Ultrashort Laser Pulse Phenomena

Fundamentals, Techniques and Applications on a Femtosecond Time Scale

Jean-Claude Diels and Wolfgang Rudolph

September 20, 2024

Contents

Chapter 1

Fundamentals

1.1 Characteristics of femtosecond light pulses

Femtosecond light pulses are electromagnetic wave packets and as such are fully described by the time and space dependent electric field. In the frame of a semi-classical treatment the propagation of such fields and the interaction with matter are governed by Maxwell's equations with the material response given by a macroscopic polarization. In this first chapter we will summarize the essential notations and definitions used throughout the book. The pulse is characterized by measurable quantities which can be directly related to the electric field. A complex representation of the field amplitude is particularly convenient in dealing with propagation problems of electromagnetic pulses. The next section expands on the choice of field representation.

1.1.1 Representation of the electric field in the time and the frequency domain

Let us consider first the temporal dependence of the electric field neglecting its spatial and polarization dependence, i.e., $\mathbf{E}(x,y,z,t) = E(t)$. A complete description can be given either in the time or the frequency domain. Even though the measured quantities are real, it is generally more convenient to use complex representation. For this reason, starting with the real $E(t)$, one defines the complex spectrum of the field strength $\tilde{E}(\Omega)$, through the complex Fourier transform ($\mathcal{F}$):

$$\tilde{E}(\Omega) = \mathcal{F}\{E(t)\} = \int_{-\infty}^{\infty} E(t)e^{-i\Omega t}dt = |\tilde{E}(\Omega)|e^{i\Phi(\Omega)} \tag{1.1}$$

In the definition (1.1), $|\tilde{E}(\Omega)|$ denotes the spectral amplitude and $\Phi(\Omega)$ is the spectral phase. Here and in what follows, complex quantities related to the field are typi-

cally written with a tilde.

Since $E(t)$ is a real function, $\tilde{E}(\Omega) = \tilde{E}^*(-\Omega)$ holds. Given $\tilde{E}(\Omega)$, the time dependent electric field is obtained through the inverse Fourier transform ($\mathcal{F}^{-1}$):

$$E(t) = \mathcal{F}^{-1}\left\{\tilde{E}(\Omega)\right\} = \frac{1}{2\pi}\int_{-\infty}^{\infty}\tilde{E}(\Omega)e^{i\Omega t}d\Omega \tag{1.2}$$

The physical meaning of this Fourier transform is that a pulse can be created by adding a number of waves of different frequency. To illustrate this point let us add $N = 2M + 1$ monochromatic fields of equal amplitude $\mathcal{E}_0$. Their frequencies Ω_n are equally spaced about a center frequency ω_ℓ and they have the same phase at $t = 0$, where they add constructively. The total field

$$E(t) = \mathcal{E}_0\cos(\omega_\ell t) + \mathcal{E}_0\sum_{n=1}^{M}\{\cos[(\omega_\ell + n\Delta\Omega)t] + \cos[(\omega_\ell - n\Delta\Omega)t]\} \tag{1.3}$$

after some algebra with trigonometric functions and geometric series, can be written as

$$E(t) = \mathcal{E}_0\left[\frac{\sin\left(\frac{N}{2}\Delta\Omega t\right)}{\sin\left(\frac{1}{2}\Delta\Omega t\right)}\right]\cos(\omega_\ell t). \tag{1.4}$$

This wave form is sketched in Fig. 1.1 for different numbers N of participating monochromatic waves. We recognize wave packets (pulses) that occur with a period T_R independent of N. Their maxima can be expected when all waves add constructively. Mathematically, this happens when the denominator in Eq. (1.4) is zero, thus $T_R = 2\pi/\Delta\Omega$. The pulses have finite length τ because the different spectral components eventually run out of phase after they all add in phase. For the packet centered at $t = 0$ this happens when the argument of the sin function in the numerator $N\Delta\Omega t/2 = \pi$. Thus, $\tau = 2\pi/(N\Delta\Omega)$. While details of these periodic wave packets will be explained later we want to point out a few things here already.

- To form a single pulse, $T_R \to \infty$, we need a continuous spectrum, which means for the frequency spacing $\Delta\Omega \to 0$.
- The length of the pulse is inversely proportional to $N\Delta\Omega$, that is, the overall spectral width covered by the participating waves.
- The rapid field oscillations are determined by the center frequency ω_ℓ, see $\cos(\omega_\ell t)$ term in Eq. (1.4). They occur independently of the term in brackets, which was responsible for the envelope of the pulse train and the repetition period. Ramifications of this will become evident when we introduce the carrier to envelope phase (CEP).

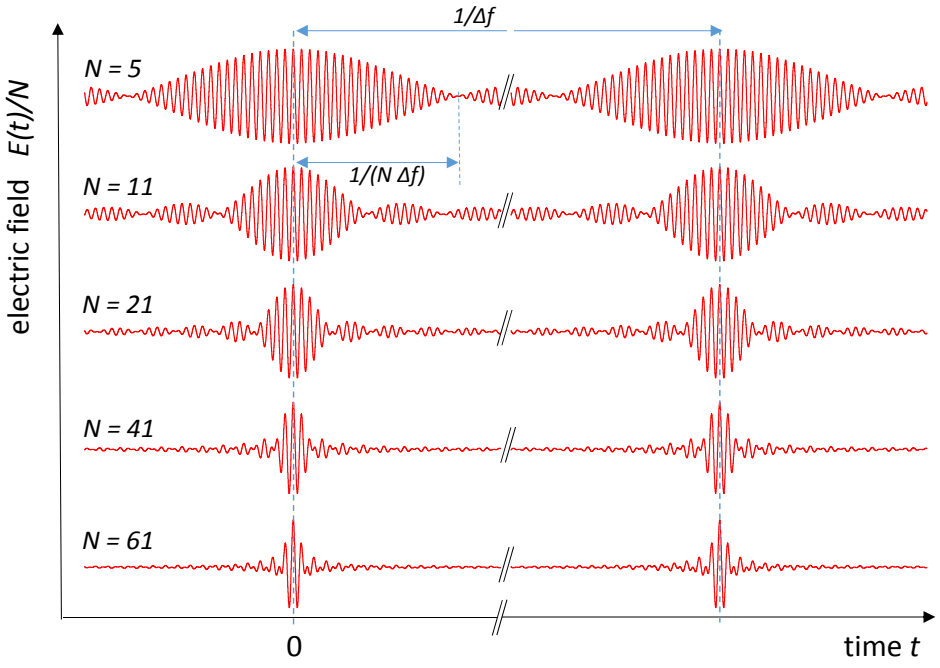

Figure 1.1: Representation of a pulse as a sum of N cosine waves equally spaced in frequency and of equal amplitude as described by Eqs. (1.3) and (1.4) for $\Delta\Omega = 0.01\Omega_0$. The graphs for different N are shifted vertically for better visibility. Note the field amplitude is divided by N and $\Delta f = \Delta\Omega/2\pi$.

For practical reasons it may not be convenient to use functions, which are non-zero for negative frequencies, as needed in the evaluation of Eq. (1.2). Frequently a complex representation of the electric field, also in the time domain, is desired. Both aspects can be satisfied by introducing a complex electric field as

$$\tilde{E}^+(t) = \frac{1}{2\pi}\int_0^\infty \tilde{E}(\Omega)e^{i\Omega t}d\Omega \tag{1.5}$$

and a corresponding spectral field strength that contains only positive frequencies:

$$\tilde{E}^+(\Omega) = |\tilde{E}(\Omega)|e^{i\Phi(\Omega)} = \begin{cases} \tilde{E}(\Omega) & \text{for} \quad \Omega \geq 0 \\ 0 & \text{for} \quad \Omega < 0 \end{cases} \tag{1.6}$$

$\tilde{E}^+(t)$ and $\tilde{E}^+(\Omega)$ are related to each other through the complex Fourier transform defined in Eq. (1.1) and Eq. (1.2), i.e.

$$\tilde{E}^+(t) = \frac{1}{2\pi}\int_{-\infty}^\infty \tilde{E}^+(\Omega)e^{i\Omega t}d\Omega \tag{1.7}$$

and

$$\tilde{E}^{+}(\Omega) = \int_{-\infty}^{\infty} \tilde{E}^{+}(t) e^{-i\Omega t} dt. \tag{1.8}$$

The real physical electric field $E(t)$ and its complex Fourier transform can be expressed in terms of the quantities derived in Eq. (1.7) and Eq. (1.8) and the corresponding quantities $\tilde{E}^{-}(t)$, $\tilde{E}^{-}(\Omega)$ for the negative frequencies. These quantities relate to the real electric field:

$$E(t) = \tilde{E}^{+}(t) + \tilde{E}^{-}(t) \tag{1.9}$$

and its complex Fourier transform:

$$\tilde{E}(\Omega) = \tilde{E}^{+}(\Omega) + \tilde{E}^{-}(\Omega) \tag{1.10}$$

Alternate Approach: the Hilbert transform .

In communications, one looks for ways to separate channels. This can be made by selecting different frequency bands with filters. Another approach is to separate signals by an abrupt phase shift. Different channels correspond thus to different phases. An abrupt phase shift of π is used in electro-optics dithering of laser gyros [1]. The Hilbert transform correspond to applying a phase shift of $\pi/2$ to the components of a signal. The Hilbert transform of a function $g(t)$ is defined as:

$$\hat{g}(t) = \frac{1}{\pi} \int_{-\infty}^{\infty} \frac{g(\tau)}{(t-\tau)} d\tau. \tag{1.11}$$

The original function can be recovered through the inverse Hilbert transform:

$$g(t) = -\frac{1}{\pi} \int_{-\infty}^{\infty} \frac{\hat{g}(\tau)}{(t-\tau)} d\tau. \tag{1.12}$$

In both cases the operation involves a convolution of $g(\tau)$ with $1/(\pi\tau)$. The Fourier transform of a convolution is the product of the Fourier transforms. The Fourier transform of $1/(\pi\tau)$ is known as the "signum function" depicted in Fig. 1.2. This sign function corresponds indeed to a phase shift of $\pi/2$ between positive and negative frequencies. The Hilbert transform $\hat{g}(t)$ is also defined as the analytical continuation of the of the function $g(t)$. Given a real function $g(t)$, one

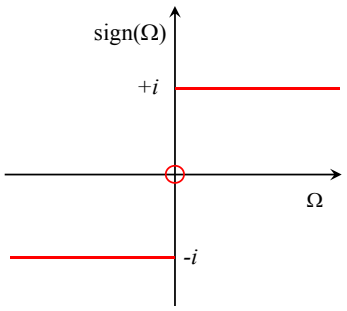

Figure 1.2: signum function sign(Ω).

defines the complex "analytic signal" $g_+(t)$ of
$g(t)$ by:

$$g_+(t) = g(t) + i\hat{g}(t), \qquad (1.13)$$

of which the Fourier transform is:

$$G_+(\Omega) = G(\Omega) + \mathrm{sgn}(\Omega)\tilde{E}(\Omega). \qquad (1.14)$$

The transformation from $G(\Omega)$ to the complex function $G_+(\Omega)$ corresponds to eliminating the negative part of the Fourier transform by adding its opposite.

This is exactly how $\tilde{E}(t)$ was defined in Section 1.1.1 above. The correspondence between the Hilbert transform notations used in system communications [2] and the notations of Section 1.1.1 is:

$G_+(Omega) = 2\tilde{E}^+(\Omega)$ as defined in Eq. (1.10)
$g_+(t) = 2\tilde{E}^+(t)$ as defined in Eq. (1.10)
$g(t) = E(t)$

This approach to introduce the complex field through Hilbert transformation is much more convoluted than the direct Fourier transform approach of the previous section. It is introduced here because it has been re-introduced recently as a new approach to nonlinear optics by Conforti *et al.* [3] and their followers [4, 5]. The context is that of defining a nonlinear polarization:

$$P(t) = \chi^{(2)} E_s(t) E_i(t). \qquad (1.15)$$

In complex notations, one often writes:

$$\tilde{P}(t) = \chi^{(2)} \tilde{E}_s(t) \tilde{E}_i(t). \qquad (1.16)$$

Instead, Conforti *et al.* [3] define the complex $\tilde{P}(t)$ by taking the Fourier transform of $P(t)$ defined by Eq (1.15), eliminating the negative part, and taking the inverse Fourier transform. No need to evoke the Hilbert transform to perform that operation. The two approaches are equivalent when the spectra of the fields E_s and E_i do not overlap.

Amplitude and phase .
It can be shown that $\tilde{E}^+(t)$ can also be calculated through analytic continuation of $E(t)$

$$\tilde{E}^+(t) = E(t) + iE'(t) \qquad (1.17)$$

where $E'(t)$ and $E(t)$ are Hilbert transforms of each other. In this sense $\tilde{E}^+(t)$ can be considered as the complex analytical correspondent of the real function $E(t)$.

The complex electric field $\tilde{E}^+(t)$ is usually represented by a product of an amplitude function and a phase term:

$$\tilde{E}^+(t) = \frac{1}{2}\mathcal{E}(t)e^{i\Gamma(t)} \tag{1.18}$$

In most practical cases of interest here the spectral amplitude will be centered around a mean frequency ω_ℓ and will have appreciable values only in a frequency interval $\Delta\omega$ small compared to ω_ℓ. In the time domain this suggests the convenience of introducing a carrier frequency ω_ℓ and of writing $\tilde{E}^+(t)$ as:

$$\boxed{\tilde{E}^+(t) = \frac{1}{2}\mathcal{E}(t)e^{i\varphi_e}e^{i\varphi(t)}e^{i\omega_\ell t} = \frac{1}{2}\tilde{\mathcal{E}}(t)e^{i\omega_\ell t}} \tag{1.19}$$

where $\varphi(t)$ is the time dependent phase, $\tilde{\mathcal{E}}(t)$ is called the complex field envelope and $\mathcal{E}(t)$ the real field envelope, respectively.

The constant phase term $e^{i\varphi_e}$ is most often of no relevance, and can be neglected. There are however particular circumstances pertaining to very short pulses where the outcome of the pulse interaction with matter depends on φ_e, often referred to as "carrier to envelope phase" (CEP). The measurement and control of φ_e can therefore be quite important. Figure 1.3(a) shows the electric field of two pulses with identical $\mathcal{E}(t)$ but different CEP $\varphi_e = 0$ and $\varphi_e = \pi/2$. It is obvious that the difference can be important in the case of nonlinear processes, such as for instance third harmonic generation creating a field proportional to the third power of the original field as shown in Fig.1.3(b).

The electric field can formally be represented in a form similar to Eq. (1.19) but the mathematical entity does not always correspond to a physically possible propagating ultrashort pulses. Since the laser pulse represents a propagating electromagnetic wave packet the dc component of its spectrum vanishes. Hence the time integral over the electric field is zero:

$$\int_{-\infty}^{\infty} E(t)dt = \int_{-\infty}^{\infty} E(t)e^{-i(\Omega=0)t}dt = \mathcal{F}\{E(t)\}_{\Omega=0} = 0. \tag{1.20}$$

It can easily be shown that Eq. (1.20) is satisfied for a pulse of the form $E(t) = \exp\left[-2\ln 2(t/\tau_p)^2\right]\cos(\omega_\ell t + \varphi_0)$ with a CEP of $\pi/2$ but not for $\varphi_e = 0$. Indeed the spectra shown in Fig. 1.3(c) support this result. The conclusion is that care must be taken when using the convenience of defining a pulse envelope for few-cycle pulses. We will discuss the carrier to envelope phase in more detail in Chapters 6 and 14.

While the description of the field given by Eqs. (1.17) through (1.19) is quite general, the usefulness of the concept of an envelope and carrier frequency as defined in Eq. (1.19) is limited to the cases where the bandwidth is only a small fraction

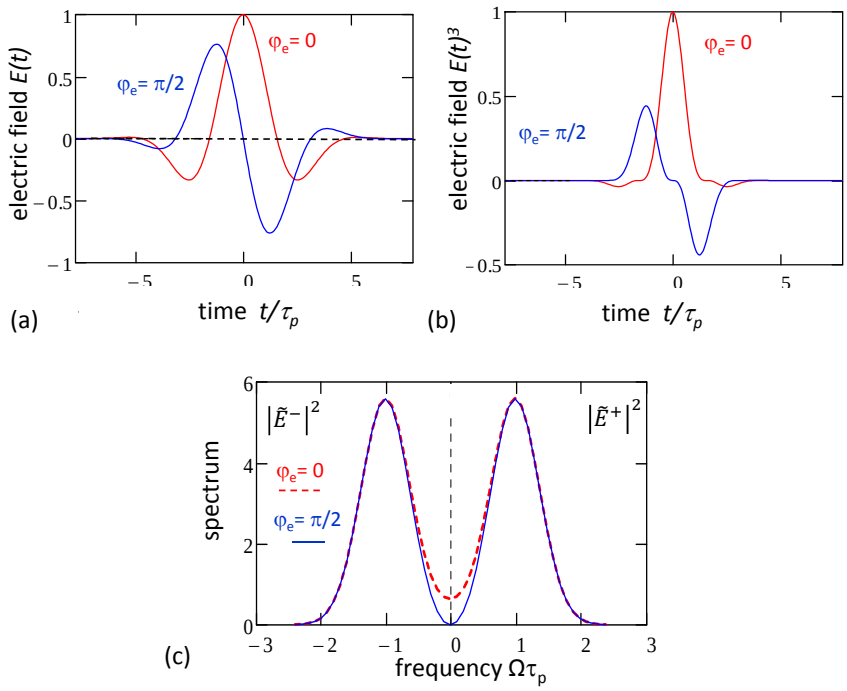

Figure 1.3: (a) Electric field of two extremely short wave forms, $E(t) = \exp\left[-2\ln 2(t/\tau_p)^2\right]\cos(\omega_\ell t + \varphi_0)$ with $\varphi_e = 0$ and $\varphi_e = \pi/2$. The full width of half maximum of the intensity envelope, τ_p, was chosen as $\tau_p = \pi/\omega_\ell$. (b) The electric field cubed of both wave forms. (c) Spectra $|\tilde{E}^-(\Omega)|^2$ and $|\tilde{E}^+(\Omega)|^2$. Note the two fields have different spectral components at $\Omega = 0$ and only the one with $\varphi = \pi/2$ describes a propagating pulse (zero dc component).

of the carrier frequency:

$$\frac{\Delta\omega}{\omega_\ell} \ll 1 \tag{1.21}$$

For inequality (1.21) to be satisfied, the temporal variation of $\mathcal{E}(t)$ and $\varphi(t)$ within an optical cycle $T = 2\pi/\omega_\ell$ ($T \approx 2$ fs for visible radiation) has to be small. The corresponding requirement for the complex envelope $\tilde{\mathcal{E}}(t)$ is

$$\left|\frac{d}{dt}\tilde{\mathcal{E}}(t)\right| \ll \omega_\ell \left|\tilde{\mathcal{E}}(t)\right| \tag{1.22}$$

Keeping in mind that today the shortest light pulses contain only a few optical cycles, one has to carefully check whether a slowly varying envelope and phase can describe the pulse behavior satisfactorily. If they do, the theoretical description of pulse propagation and interaction with matter can be greatly simplified by applying

the slowly varying envelope approximation (SVEA), as will be evident later in this chapter.

Given the spectral description of a signal, $\tilde{E}^+(\Omega)$, the complex envelope $\tilde{\mathcal{E}}(t)$ is simply the inverse transform of the translated spectral field:

$$\tilde{\mathcal{E}}(t) = \mathcal{E}(t)e^{i\varphi(t)} = \frac{1}{2\pi}\int_{-\infty}^{\infty} 2\tilde{E}^+(\Omega+\omega_\ell)e^{i\Omega t}d\Omega; \tag{1.23}$$

where the modulus $\mathcal{E}(t)$ in Eq. (1.23) represents the real envelope. The optimum

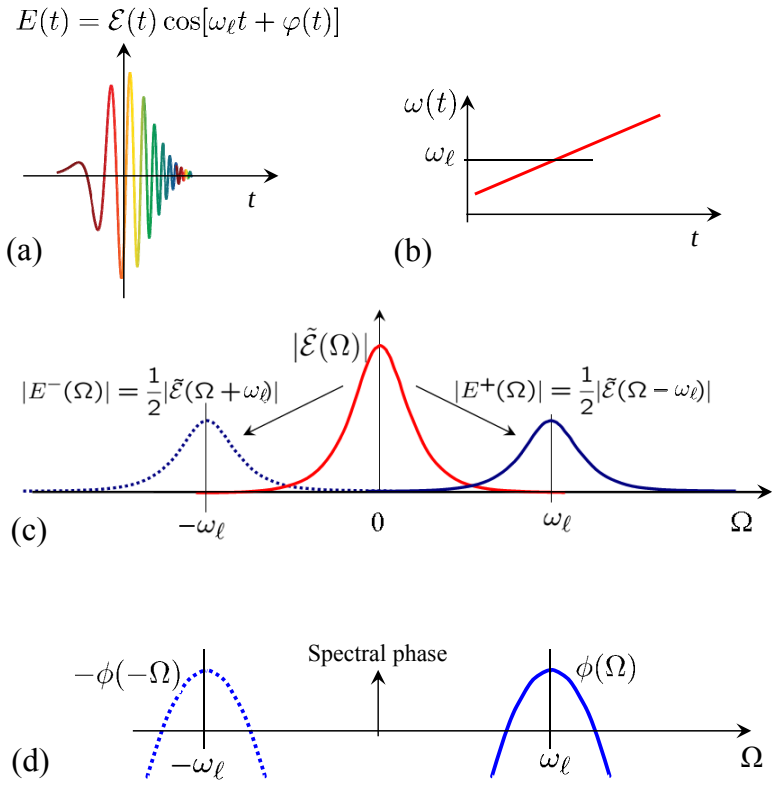

Figure 1.4: (a) Electric field, (b) time dependent carrier frequency, (c) spectral amplitude and (d) spectral phase of a linearly upchirped pulse.

"translation" in the spectral domain ω_ℓ is the one that gives the envelope $\tilde{\mathcal{E}}(t)$ with the least amount of modulation. Spectral translation of Fourier transforms is a standard technique to reconstruct the envelope of interference patterns, and is used in Chapter 10 on diagnostic techniques. The Fourier transform of the complex

envelope $\tilde{\mathcal{E}}(t)$ is the spectral envelope function:

$$\tilde{\mathcal{E}}(\Omega) = \int_{-\infty}^{\infty} \tilde{\mathcal{E}}(t) e^{-i\Omega t} dt = 2 \int_{-\infty}^{\infty} \tilde{E}^{+}(t) e^{-i(\Omega+\omega_\ell)t} dt. \tag{1.24}$$

The choice of ω_ℓ is often such that the spectral amplitude $\tilde{\mathcal{E}}(\Omega)$ is centered about the origin $\Omega = 0$.

Let us now discuss more carefully the physical meaning of the phase function $\varphi(t)$. The choice of carrier frequency in Eq. (1.19) should be such as to minimize the variation of phase $\varphi(t)$. The first derivative of the phase factor $\Gamma(t)$ in Eq. (1.18) establishes a time dependent carrier frequency (instantaneous frequency):

$$\boxed{\omega(t) = \omega_\ell + \frac{d}{dt}\varphi(t).} \tag{1.25}$$

While Eq. (1.25) can be seen as a straightforward definition of an instantaneous frequency based on the temporal variation of the phase factor $\Gamma(t)$, we will see in Section 1.1.5 that it can be rigourously derived from the Wigner distribution. For $d\varphi/dt = b = \text{const.}$, a non-zero value of b just means a correction of the carrier frequency which is now $\omega'_\ell = \omega_\ell + b$. For $d\varphi/dt = f(t)$, the carrier frequency varies with time and the corresponding pulse is said to be frequency modulated or chirped. For $d^2\varphi/dt^2 < (>)0$, the carrier frequency decreases (increases) along the pulse, which then is called down(up)chirped.

From Eq.(1.18) it is obvious that the decomposition of $\Gamma(t)$ into ω and $\varphi(t)$ is not unique. The most useful decomposition is one that ensures the smallest $d\varphi/dt$ during the intense portion of the pulse. A common practice is to identify ω_ℓ with the carrier frequency at the pulse peak. A better definition — which is consistent in the time and frequency domains — is to use the intensity weighted *average* frequency:

$$\boxed{\langle\omega\rangle = \frac{\int_{-\infty}^{\infty} |\tilde{\mathcal{E}}(t)|^2 \omega(t) dt}{\int_{-\infty}^{\infty} |\tilde{\mathcal{E}}(t)|^2 dt} = \frac{\int_{-\infty}^{\infty} |\tilde{E}^{+}(\Omega)|^2 \Omega d\Omega}{\int_{-\infty}^{\infty} |\tilde{E}^{+}(\Omega)|^2 d\Omega}} \tag{1.26}$$

The various notations are illustrated in Fig. 1.4 where a linearly up-chirped pulse is taken as an example. The temporal dependence of the real electric field is sketched in the top part of Fig 1.4. A complex representation in the time domain is illustrated with the amplitude and instantaneous frequency of the field. The positive and negative frequency components of the Fourier transform are shown in amplitude and phase in the bottom part of the figure.

1.1.2 Power, energy, and related quantities

Let us imagine the practical situation in which the pulse propagates as a beam with cross section A, and with $E(t)$ as the relevant component of the electric field. The (instantaneous) pulse power (in Watt) in a dispersionless material of refractive index n can be derived from the Poynting theorem of electrodynamics [6] and is given by

$$\mathcal{P}(t) = \epsilon_0 cn \int_A dS \, \frac{1}{T} \int_{t-T/2}^{t+T/2} E^2(t')dt' \tag{1.27}$$

where c is the velocity of light in vacuum, ϵ_0 is the dielectric permittivity and $\int_A dS$ stands for integration over the beam cross section. The power can be measured by a detector (photodiode, photomultiplier etc.) which integrates over the beam cross section. The temporal response of this device must be short as compared to the speed of variations of the field envelope to be measured. The temporal averaging is performed over one optical period $T = 2\pi/\omega_\ell$. Note that the instantaneous power as introduced in Eq. (1.27) is then just a convenient theoretical quantity. In a practical measurement T has to be replaced by the actual response time τ_R of the detector. Therefore, even with the fastest detectors available today ($\tau_R \approx 10^{-13} - 10^{-12}$s), details of the envelope of fs light pulses can not be resolved directly.

A temporal integration of the power yields the energy $\mathcal{W}$ (in Joules):

$$\mathcal{W} = \int_{-\infty}^{\infty} \mathcal{P}(t')dt' \tag{1.28}$$

where the upper and lower integration limits essentially mean "before" and "after" the pulse under investigation.

The corresponding quantity per unit area is the intensity (W/cm^2), also called fluence:

$$\begin{aligned} I(t) &= \epsilon_0 cn \frac{1}{T} \int_{t-T/2}^{t+T/2} E^2(t')dt' \\ &= \frac{1}{2}\epsilon_0 cn\mathcal{E}^2(t) = 2\epsilon_0 cn\tilde{E}^+(t)\tilde{E}^-(t) = \frac{1}{2}\epsilon_0 cn\tilde{\mathcal{E}}(t)\tilde{\mathcal{E}}^*(t) \end{aligned} \tag{1.29}$$

and the energy density per unit area (J/cm^2):

$$W = \int_{-\infty}^{\infty} I(t')dt' \tag{1.30}$$

Sometimes it is convenient to use quantities which are related to photon numbers, such as the photon flux $\mathcal{F}$ (photons/s) or the photon flux density F (photons/s/cm^2):

$$\mathcal{F}(t) = \frac{\mathcal{P}(t)}{\hbar\omega_\ell} \quad \text{and} \quad F(t) = \frac{I(t)}{\hbar\omega_\ell} \tag{1.31}$$

where $\hbar\omega_\ell$ is the energy of one photon at the carrier frequency.

The spectral properties of the light are typically obtained by measuring the intensity of the field, without any time resolution, at the output of a spectrometer. The quantity, called spectral intensity, that is measured is:

$$S(\Omega) = \mid \eta(\Omega)\tilde{E}^{+}(\Omega) \mid^2 \tag{1.32}$$

where η is a scaling factor which accounts for losses, geometrical influences, and the finite resolution of the spectrometer. Assuming an ideal spectrometer, $|\eta|^2$ can be determined from the requirement of energy conservation:

$$|\eta|^2 \int_{-\infty}^{\infty} \mid \tilde{E}^{+}(\Omega) \mid^2 d\Omega = 2\epsilon_0 cn \int_{-\infty}^{\infty} \tilde{E}^{+}(t)\tilde{E}^{-}(t)dt \tag{1.33}$$

and Parseval's theorem [7]:

$$\int_{-\infty}^{\infty} |\tilde{E}^{+}(t)|^2 dt = \frac{1}{2\pi} \int_{0}^{\infty} \mid \tilde{E}^{+}(\Omega) \mid^2 d\Omega \tag{1.34}$$

from which follows $|\eta|^2 = \epsilon_0 cn/\pi$. The complete expression for the spectral intensity [from Eq. (1.32)] is thus:

$$S(\Omega) = \frac{\epsilon_0 cn}{4\pi} \left|\tilde{\mathcal{E}}(\Omega + \omega_\ell)\right|^2 . \tag{1.35}$$

Figure 1.5 gives examples of typical pulse shapes and the corresponding spectra.

The complex quantity $\tilde{E}^{+}$ will be used most often throughout the book to describe the electric field. Therefore, to simplify notations, we will omit the superscript "+"whenever this will not cause confusion.

1.1.3 Pulse duration and spectral width

Unless specified otherwise, we define the pulse duration τ_p as the full width at half maximum (FWHM) of the intensity profile, $|\tilde{\mathcal{E}}(t)|^2$, and the spectral width $\Delta\omega_p$ as the FWHM of the spectral intensity $|\tilde{\mathcal{E}}(\Omega)|^2$. Making that statement is an obvious admission that other definitions exist. Precisely because of the difficulty of asserting the exact pulse shape, standard waveforms have been selected. The most commonly cited are the Gaussian, for which the temporal dependence of the field is:

$$\tilde{\mathcal{E}}(t) = \tilde{\mathcal{E}}_0 \exp\{-(t/\tau_G)^2\} \tag{1.36}$$

and the secant hyperbolic:

$$\tilde{\mathcal{E}}(t) = \tilde{\mathcal{E}}_0 \,\mathrm{sech}(t/\tau_s). \tag{1.37}$$

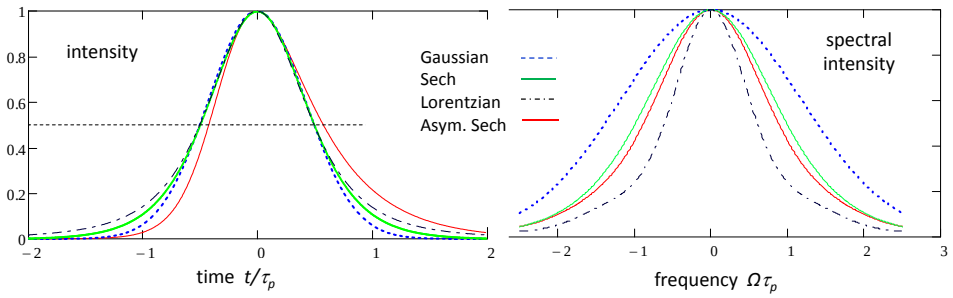

Figure 1.5: Temporal profiles and the corresponding spectra for different pulse shapes. The pulses have the same duration (FWHM τ_p) and the same peak intensity at $t = 0$. The spectra are normalized.

Gaussian pulse	$\mathcal{E}(t)$	=	$\exp\left[-1.385(t/\tau_p)^2\right]$
sech - pulse	$\mathcal{E}(t)$	=	$\mathrm{sech}[1.763(t/\tau_p)]$
Lorentzian pulse	$\mathcal{E}(t)$	=	$[1+1.656(t/\tau_p)^2]^{-1}$
asym. sech pulse	$\mathcal{E}(t)$	=	$3.08[\exp\left(1.04t/\tau_p+0.28\right)+\exp\left(-3.13t/\tau_p-0.84\right)]^{-1}$

The parameters $\tau_G = \tau_p/\sqrt{2\ln 2}$ and $\tau_s = \tau_p/1.76$ are generally more convenient to use in theoretical calculations involving pulses with these assumed shapes than the FWHM of the intensity, τ_p.

Since the temporal and spectral characteristics of the field are related to each other through Fourier transforms, the bandwidth $\Delta\omega_p$ and pulse duration τ_p cannot vary independently of each other. There is a minimum duration-bandwidth product:

$$\Delta\omega_p\,\tau_p = 2\pi\Delta\nu_p\tau_p \geq 2\pi c_B. \tag{1.38}$$

c_B is a numerical constant on the order of 1, depending on the actual pulse shape. Some examples are shown in Table 1.1. The equality holds for pulses without frequency modulation (unchirped) which are called "bandwidth limited" or "Fourier limited". Such pulses exhibit the shortest possible duration at a given spectral width and pulse shape. We refer the reader to Section 1.1.5, for a more general discussion of the uncertainty relation between pulse and spectral width based on mean-square deviations.

The shorter the pulse duration, the more difficult it becomes to assert its detailed characteristics and physical meaning. In the femtosecond domain, even the simple concept of pulse duration seems to fade away in a cloud of mushrooming definitions. Part of the problem is that it is difficult to determine the exact pulse shape. For single pulses, the typical representative function that is readily accessi-

Shape	Intensity profile $I(t)$	τ_p FWHM	Spectral profile $S(\Omega)$	$\Delta\omega_p$ FWHM	c_B	$\langle\tau_p\rangle\langle\Delta\Omega_p\rangle$ MSQ
Gauss	$e^{-2(t/\tau_G)^2}$	$1.177\tau_G$	$e^{-\frac{(\Omega\tau_G)^2}{2}}$	$2.355/\tau_G$	0.441	0.5
sech	$\mathrm{sech}^2(t/\tau_s)$	$1.763\tau_s$	$\mathrm{sech}^2\,\frac{\pi\Omega\tau_s}{2}$	$1.122/\tau_s$	0.315	0.525
Lorentz	$[1+(t/\tau_L)^2]^{-2}$	$1.287\tau_L$	$e^{-2\lvert\Omega\rvert\tau_L}$	$0.693/\tau_L$	0.142	0.7
asym. sech	$\left[e^{t/\tau_a}+e^{-3t/\tau_a}\right]^{-2}$	$1.043\tau_a$	$\mathrm{sech}\,\frac{\pi\Omega\tau_a}{2}$	$1.677/\tau_a$	0.278	
square	1 for $\lvert t/\tau_r\rvert \le 1$, 0 elsewhere	τ_r	$\mathrm{sinc}^2(\Omega\tau_r)$	$2.78/\tau_r$	0.443	3.27

Table 1.1: Examples of standard pulse profiles. The spectral values given are for bandwidth-limited (chirp-free) pulses. Note that the Gaussian is the shape with the minimum product of mean square deviation (MSQ) of the intensity and spectral intensity, see Section 1.1.5.

ble to the experimentalist is the intensity autocorrelation:

$$A_{\mathrm{int}}(\tau) = \int_{-\infty}^{\infty} I(t)I(t-\tau)dt \tag{1.39}$$

The Fourier transform of the correlation (1.39) is the real function:

$$A_{\mathrm{int}}(\Omega) = \tilde{I}(\Omega)\tilde{I}^*(\Omega) \tag{1.40}$$

where the notation $\tilde{I}(\Omega)$ is the Fourier transform of the function $I(t)$, which should not be confused with the spectral intensity $S(\Omega)$. The fact that the autocorrelation function $A_{\mathrm{int}}(\tau)$ is symmetric, hence its Fourier transform is real [7], implies that little information about the pulse shape can be extracted from such a measurement. Furthermore, the intensity autocorrelation (1.39) contains no information about the pulse phase or coherence. This point is discussed in detail in Chapter 10.

1.1.4 Gaussian pulses

Having introduced essential pulse characteristics, it seems convenient to discuss an example to which we can refer to in later chapters. We choose a Gaussian pulse with linear chirp. This choice is one of analytical convenience: the Gaussian shape is *not* the most commonly encountered temporal shape. The electric field is given by

$$\tilde{\mathcal{E}}(t) = \mathcal{E}_0 e^{-(1+ia)(t/\tau_G)^2} \tag{1.41}$$

with the pulse duration

$$\tau_p = \sqrt{2\ln 2}\,\tau_G. \tag{1.42}$$

Note that with the definition (1.41) the chirp parameter a is positive for a downchirp ($d\varphi/dt = -2at/\tau_G^2$). The Fourier transform of (1.41) yields

$$\tilde{\mathcal{E}}(\Omega) = \frac{\mathcal{E}_0\sqrt{\pi}\tau_G}{\sqrt[4]{1+a^2}} \exp\left\{i\Phi - \frac{\Omega^2{\tau_G}^2}{4(1+a^2)}\right\} \tag{1.43}$$

with the spectral phase given by:

$$\phi(\Omega) = -\frac{1}{2}\arctan(a) + \frac{a{\tau_G}^2}{4(1+a^2)}\Omega^2 \tag{1.44}$$

It can be seen from Eq. (1.43) that the spectral intensity is the Gaussian:

$$S(\omega_\ell + \Omega) = \frac{|\eta|^2\pi\mathcal{E}_0^2\tau_G^2}{\sqrt{1+a^2}} \exp\left\{-\frac{\Omega^2{\tau_G}^2}{2(1+a^2)}\right\} \tag{1.45}$$

with a FWHM given by:

$$\Delta\omega_p = 2\pi\Delta\nu_p = \frac{1}{\tau_G}\sqrt{8\ln 2(1+a^2)} \tag{1.46}$$

For the pulse duration-bandwidth product we find

$$\Delta\nu_p\tau_p = \frac{2\ln 2}{\pi}\sqrt{1+a^2} \tag{1.47}$$

Obviously, the occurrence of chirp ($a \neq 0$) results in additional spectral components which enlarge the spectral width and lead to a duration bandwidth product exceeding the Fourier limit ($2\ln 2/\pi \approx 0.44$) by a factor $\sqrt{1+a^2}$, consistent with Eq. (1.38). We also want to point out that the spectral phase given by Eq. (1.44) changes quadratically with frequency if the input pulse is linearly chirped. While this is exactly true for Gaussian pulses as can be seen from Eq. (1.44), it holds approximately for other pulse shapes. In the next section, we will develop a concept that allows one to discuss the pulse duration-bandwidth product from a more general point of view and independent of the actual pulse and spectral profile.

1.1.5 Wigner distribution, second order moments, uncertainty relations

Wigner distribution

The Fourier transform as defined in Section 1.1.1 is a widely used tool in beam and pulse propagation. In beam propagation, it leads directly to the far field pattern of

a propagating beam (Fraunhofer approximation) of arbitrary transverse profile. Similarly, the Fourier transform leads directly to the pulse temporal profile, following propagation through a dispersive medium, as we will see at the end of this chapter. The Fourier transform gives a weighted average of the spectral components contained in a signal. Unfortunately, the exact spatial or temporal location of these spectral components is hidden in the phase of the spectral field, which is most often not readily available. It is not straightforward to look at the electric field in time and make a statement about the spectral components (and vice versa) without actually taking a Fourier transform. The Wigner function tries to solve this problem by creating a mathematical entity which describes the time and spectral components at the same time, fullfilling the need for new two-dimensional representation of the waves in either the plane of space–wave vector, or time–angular frequency. Such a function was introduced by Wigner [8] and applied to quantum mechanics. The same distribution was applied to the area of signal processing by Ville [9]. Properties and applications of the Wigner distribution in Quantum Mechanics and Optics are reviewed in two recent books by Schleich [10] and Cohen [11]. A clear analysis of the close relationship between Quantum Mechanics and Optics can be found in ref. [12]. In the time–angular-frequency domain, the Wigner distribution of a function $\tilde{E}(t)$ is defined by[1]:

$$\begin{aligned} \mathcal{W}_E(t,\Omega) &= \int_{-\infty}^{\infty} \tilde{E}\left(t+\frac{s}{2}\right)\tilde{E}^*\left(t-\frac{s}{2}\right)e^{-i\Omega s}ds \\ &= \frac{1}{2\pi}\int_{-\infty}^{\infty} \tilde{E}\left(\Omega+\frac{s}{2}\right)\tilde{E}^*\left(\Omega-\frac{s}{2}\right)e^{its}ds \end{aligned} \tag{1.48}$$

One can see that the definition of the Wigner function is a local (i.e. at a given time) representation of the spectrum of the signal, since time integration yields the spectral amplitude:

$$\int_{-\infty}^{\infty} \mathcal{W}_E(t,\Omega)dt = \left|\tilde{E}(\Omega)\right|^2. \tag{1.49}$$

It is also a local (i.e. at a given spectral component) representation of the signal, since frequency integration yields the temporal intensity:

$$\int_{-\infty}^{\infty} \mathcal{W}_E(t,\Omega)d\Omega = 2\pi\left|\tilde{E}(t)\right|^2 \tag{1.50}$$

In the notation $\mathcal{W}_E$, the subscript E refers to the use of the instantaneous complex electric field $\tilde{E}$ in the definition of the Wigner function, rather than the electric field envelope $\tilde{\mathcal{E}} = \mathcal{E}\exp[i\omega_\ell t + i\varphi(t)]$ defined at the beginning of this chapter. There is a

[1] t and Ω are conjugated variables as in Fourier transforms. The same definitions can be made in the space–wavevector domain, where the variables are then x and k.

simple relation between the Wigner distribution $\mathcal{W}_E$ of the instantaneous field $\tilde{E}$, and the Wigner distribution $\mathcal{W}_\mathcal{E}$ of the real envelope amplitude $\mathcal{E}$:

$$\begin{aligned}\mathcal{W}_E(t,\Omega) &= \int_{-\infty}^{\infty} \mathcal{E}\left(t+\frac{s}{2}\right) e^{i[\omega_\ell(t+s/2)+\varphi(t+s/2)]} \\ &\quad \times \mathcal{E}^*\left(t-\frac{s}{2}\right) e^{-i[\omega_\ell(t-s/2)+\varphi(t-s/2)]} e^{-i\Omega s} ds \\ &= \int_{-\infty}^{\infty} \mathcal{E}\left(t+\frac{s}{2}\right) \mathcal{E}^*\left(t-\frac{s}{2}\right) e^{-i[\Omega-(\omega_\ell+\dot{\varphi}(t))]s} ds \\ &= \mathcal{W}_\mathcal{E}\{t, [\Omega-(\omega_\ell+\dot{\varphi})]\}. \end{aligned} \tag{1.51}$$

We will drop the subscript "E" and "$\mathcal{E}$" for the Wigner function when the distinction is not essential.

The intensity and spectral intensities are directly proportional to frequency and time integrations of the Wigner function. In accordance with Eqs. (1.29) and Eq. (1.35):

$$\frac{1}{2\sqrt{\mu_0/\epsilon}} \int_{-\infty}^{\infty} \mathcal{W}_\mathcal{E}(t,\Omega) d\Omega = I(t) \tag{1.52}$$

$$\frac{1}{2\sqrt{\mu_0/\epsilon}} \int_{-\infty}^{\infty} \mathcal{W}_\mathcal{E}(t,\Omega) dt = S(\Omega). \tag{1.53}$$

Figure 1.6 shows the Wigner distribution of an unchirped Gaussian pulse ((a), left) versus a Gaussian pulse with a linear chirp (quadratic phase modulation) ((b), right). The introduction of a quadratic phase modulation leads to a tilt (rotation) and flattening of the distribution. This distortion of the Wigner function results directly from the relation (1.51) applied to a Gaussian pulse. We have defined in Eq. (1.41) the phase of the linearly chirped pulse as $\varphi(t) = -at^2/\tau_G^2$. If $\mathcal{W}_{\text{unchirp}}$ is the Wigner distribution of the unchirped pulse, the linear chirp transforms that function into:

$$\mathcal{W}_{\text{chirp}} = \mathcal{W}_{\text{unchirp}}(t, \Omega - \frac{2at}{\tau_G^2}), \tag{1.54}$$

hence the tilt observed in Fig. 1.6. Mathematical tools have been developed to produce a pure rotation of the phase space (t, Ω). We refer the interested reader to the literature for details on the Wigner distribution and in particular on the fractional Fourier transform [13, 14]. It has been shown that such a rotation describes the propagation of a pulse through a medium with a quadratic dispersion (index of refraction being a quadratic function of frequency) [15].

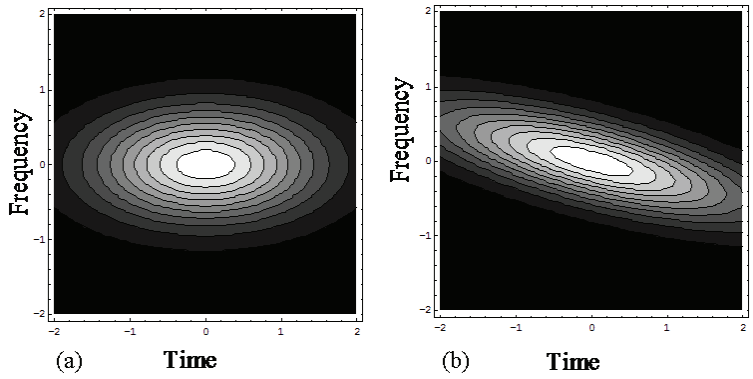

Figure 1.6: Wigner distribution for a Gaussian pulse. Left (a), the phase function $\varphi(t) = \varphi_0$ is a constant. On the right (b), Wigner distribution for a linearly chirped pulse, i.e. with a quadratic phase modulation $\varphi(t) = \alpha t^2$. The elliptical curves are lines of equal Wigner function intensity. The intensity is graded from 0 (black) to the peak (white).

Moments of the electric field

It is mainly history and convenience that led to the adoption of the FWHM of the pulse intensity as the quantity representative of the pulse duration. Sometimes pulse duration and spectral width defined by the FWHM values are not suitable measures. This is, for instance, the case in pulses with substructure or broad wings causing a considerable part of the energy to lie outside the range given by the FWHM. In these cases it may be preferable to use averaged values derived from the appropriate second–order moments. It appears in fact, as will be shown in examples of propagation, that the second moment of the field distribution is a better choice.

For the sake of generality, let us designate by $f(x)$ the field as a function of the variable x (which can be the transverse coordinate, transverse wave vector, time or frequency). The moment of order n for the quantity x with respect to intensity is defined as:

$$\langle x^n \rangle = \frac{\int_{-\infty}^{\infty} x^n |f(x)|^2 dx}{\int_{-\infty}^{\infty} |f(x)|^2 dx} \tag{1.55}$$

The first order moment, $\langle x \rangle$, is the "center of mass" of the intensity distribution, and is most often chosen as reference, in such a way as to have a zero value. For example, the center of the transverse distribution will be on axis, $x = 0$, or a Gaussian temporal intensity distribution $\mathcal{E}_0 \exp\left[-(t/\tau_G)^2\right]$ will be centered at $t = 0$. A

good criterium for the width of a distribution is the mean square deviation (MSQ):

$$\langle \Delta x \rangle = \sqrt{\langle x^2 \rangle - \langle x \rangle^2}. \tag{1.56}$$

The explicit expressions in the time and frequency domains are:

$$\langle \tau_p \rangle = \langle \Delta t \rangle = \left[\frac{1}{W} \int_{-\infty}^{\infty} t^2 I(t) dt - \frac{1}{W^2} \left(\int_{-\infty}^{\infty} t I(t) dt \right)^2 \right]^{\frac{1}{2}} \tag{1.57}$$

$$\langle \Delta \omega_p \rangle = \langle \Delta \Omega \rangle = \left[\frac{1}{W} \int_{-\infty}^{\infty} \Omega^2 S(\Omega) d\Omega - \frac{1}{W^2} \left(\int_{-\infty}^{\infty} \Omega S(\Omega) d\Omega \right)^2 \right]^{\frac{1}{2}} \tag{1.58}$$

where $S(\Omega)$ is the spectral intensity defined in Eq. (1.32). Whenever appropriate we will assume that the first-order moments are zero, which yields $\langle \Delta x \rangle = \sqrt{\langle x^2 \rangle}$.

The second moments can also be defined using the Wigner distribution [Eq. (1.48)]:

$$\langle t^2 \rangle = \frac{\int\int_{-\infty}^{\infty} t^2 \mathcal{W}_E(t,\Omega) dt d\Omega}{\int\int_{-\infty}^{\infty} \mathcal{W}_E(t,\Omega) dt d\Omega} = \frac{\int_{-\infty}^{\infty} t^2 |\tilde{E}(t)|^2 dt}{\int_{-\infty}^{\infty} |\tilde{E}(t)|^2 dt} \tag{1.59}$$

$$\langle \Omega^2 \rangle = \frac{\int\int_{-\infty}^{\infty} \Omega^2 \mathcal{W}_E(t,\Omega) dt d\Omega}{\int\int_{-\infty}^{\infty} \mathcal{W}_E(t,\Omega) dt d\Omega} = \frac{\int_{-\infty}^{\infty} \Omega^2 |\tilde{E}(\Omega)|^2 d\Omega}{\int_{-\infty}^{\infty} |\tilde{E}(\Omega)|^2 d\Omega} \tag{1.60}$$

While the above equations do not bring anything new, the Wigner distribution lets us define another quantity, which describes the coupling between conjugated variables:

$$\langle t, \Omega \rangle = \frac{\int\int_{-\infty}^{\infty} (t - \langle t \rangle)(\Omega - \langle \Omega \rangle) \mathcal{W}_E(t,\Omega) dt d\Omega}{\int\int_{-\infty}^{\infty} \mathcal{W}_E(t,\Omega) dt d\Omega}. \tag{1.61}$$

A non-zero $\langle t, \Omega \rangle$ implies that the center of mass of the spectral intensity evolves with time, as in Fig. 1.6. One can thus define an instantaneous frequency:

$$\omega(t) = \frac{\int_{-\infty}^{\infty} \Omega \mathcal{W}_E(t,\Omega) d\Omega}{\int_{-\infty}^{\infty} \mathcal{W}_E(t,\Omega) d\Omega}. \tag{1.62}$$

By substituting the definition of the Wigner distribution Eq. (1.48) in Eq. (1.62), it is possible to demonstrate rigourously the relation (1.25). Indeed, substituting the definition (1.51) in Eq. (1.62) leads to:

$$\begin{aligned} \omega(t) &= \frac{\int_{-\infty}^{\infty} \Omega \mathcal{W}_{\mathcal{E}}[t, \Omega - (\omega_\ell + \dot{\varphi})] d\Omega}{\int_{-\infty}^{\infty} \mathcal{W}_E(t,\Omega) d\Omega} \\ &= \frac{\int_{-\infty}^{\infty} [\Omega' + \omega_\ell + \dot{\varphi}(t)] \mathcal{W}_{\mathcal{E}}[t, \Omega'] d\Omega'}{\int_{-\infty}^{\infty} \mathcal{W}_E(t,\Omega) d\Omega} \\ &= \omega_\ell + \dot{\varphi}(t), \end{aligned} \tag{1.63}$$

where we used the fact that $\int \Omega' \mathcal{W}_{\mathcal{E}}(t,\Omega')d\Omega' = 0$.

There is a well known uncertainty principle between the second moment of conjugated variables. If k is the Fourier-conjugated variable of x, it is shown in Appendix B that:

$$\langle x^2\rangle\langle k^2\rangle = \frac{M^4}{4} \geq \frac{1}{4}, \tag{1.64}$$

where we have defined a shape factor "M^2", which has been extensively used to describe the departure of beam profile from the "ideal Gaussian" [16]. This relation can be applied to time and frequency:

$$\langle t^2\rangle\langle \Omega^2\rangle = \frac{M^4}{4} \geq \frac{1}{4}. \tag{1.65}$$

Equality only holds for a Gaussian pulse (beam) shape free of any phase modulation, which implies that the Wigner distribution for a Gaussian shape occupies the smallest area in the time/frequency plane. It is also important to note that the uncertainty relations (1.64) and (1.65) only hold for the pulse widths defined as the mean square deviation. For a Gaussian pulses defined by its electric field $\mathcal{E}(t) = \mathcal{E}_0 \exp\left[-(t/\tau_G)^2\right]$:

$$\begin{aligned} \langle t^2\rangle &= \frac{\tau_G^2}{4} \\ \langle \Omega^2\rangle &= \frac{1}{\tau_G^2}. \end{aligned} \tag{1.66}$$

The product of the two numbers is indeed 1/4, the minimum of the inequality (1.65). while for the products of the full width at half maximum (FWHM) of the intensity and spectral intensity (generally referred to as the "time-bandwidth product" $c_B = \tau_p \Delta\nu_p = 0.441$. In fact, the pulse time-bandwidth product product *is not minimum* for a Gaussian pulse, as illustrated in Table 1.1, which gives the value of c_B for various pulse shapes without phase modulation. It remains that, for a given pulse shape, c_B is the smallest for pulses without frequency modulation (unchirped) which are called "bandwidth limited" or "Fourier limited". Such pulses exhibit the shortest possible duration at a given spectral width and pulse shape.

If there is a frequency variation across a pulse, its spectrum will contain additional spectral components. Consequently, the modulated pulse possesses a spectral width which is larger than the Fourier limit given by column five in Table 1.1.

Relation to Quantum Mechanics

The Heisenberg uncertainty relation is contained directly in Eqs (1.64) and (1.65), when taking into account particle wave duality. Indeed, a moving particle with

energy $W = p^2/2m$ has an associated wave packet centered at the frequency $\omega = W/\hbar$. This is where the Plank constant enters into the uncertainty relation (1.65). The wave packet has a frequency distribution of second moment $\langle\Omega^2\rangle$, related by inverse Fourier transform to the temporal distribution, with a second moment in time $\langle t^2\rangle$, leading to the relation:

$$\langle t^2\rangle\langle W^2\rangle = \frac{M^4}{4} \geq \frac{\hbar^2}{4}. \tag{1.67}$$

In space, the wave packet representing the particle has a momentum $k = p/\hbar$. Hence, Equation (1.64) applied to the wave representation of a particle is the Heisenberg uncertainty relation in space:

$$\langle x^2\rangle\langle k^2\rangle = \frac{M^4}{4} \geq \frac{\hbar^2}{4}, \tag{1.68}$$

Chirped pulses

A quadratic phase modulation plays an essential role in light propagation, be it in time or space. Since a spherical wavefront can be approximated by a quadratic phase ($\varphi(x) \propto x^2$, where x is the transverse dimension) near any propagation axis of interest, imparting a quadratic spatial phase modulation will lead to focusing or de-focusing of a beam. The analogue is true in time: imparting a quadratic phase modulation ($\varphi(t) \propto t^2$) will lead to pulse compression or broadening after propagation through a dispersive medium. These problems relating to pulse propagation will be discussed in several sections and chapters of this book. In this section we attempt to clarify quantitatively the relation between a quadratic chirp in the temporal or frequency space, and the corresponding broadening of the spectrum or pulse duration, respectively. The results are interchangeable from frequency to temporal space.

Let us first assume that a laser pulse, initially unchirped, propagates through a dispersive material that leaves the pulse spectrum, $|\tilde{\mathcal{E}}(\Omega)|^2$, unchanged but produces a quadratic phase modulation in the frequency domain. The pulse spectrum is centered at the average frequency $\langle\Omega\rangle = \omega_\ell$. The average frequency does not change, hence the first nonzero term in the Taylor expansion of $\phi(\Omega)$ is

$$\phi(\Omega) = \frac{1}{2}\left.\frac{d^2\phi}{d\Omega^2}\right|_0 \langle\Omega^2\rangle, \tag{1.69}$$

where $\phi(\Omega)$ determines the phase factor of $\tilde{\mathcal{E}}(\Omega)$:

$$\tilde{\mathcal{E}}(\Omega) = \mathcal{E}(\Omega)e^{i\phi(\Omega)}. \tag{1.70}$$

The first and second order moments are, according to the definitions (1.55):

$$\langle t\rangle = \frac{\int_{-\infty}^{\infty} t\tilde{\mathcal{E}}(t)\tilde{\mathcal{E}}(t)^* dt}{\int_{-\infty}^{\infty} |\tilde{\mathcal{E}}(t)|^2 dt} = \frac{\int_{-\infty}^{\infty} \frac{d\tilde{\mathcal{E}}(\Omega)}{d\Omega}\tilde{\mathcal{E}}^*(\Omega) d\Omega}{\int_{-\infty}^{\infty} |\tilde{\mathcal{E}}(\Omega)|^2 d\Omega} = \left\langle \frac{d\phi}{d\Omega} \right\rangle \tag{1.71}$$

and

$$\begin{aligned} \langle t^2\rangle &= \frac{\int_{-\infty}^{\infty} t\tilde{\mathcal{E}}(t)t\tilde{\mathcal{E}}(t)^* dt}{\int_{-\infty}^{\infty} |\tilde{\mathcal{E}}(t)|^2 dt} = \frac{\int_{-\infty}^{\infty} \left|\frac{d\tilde{\mathcal{E}}(\Omega)}{d\Omega}\right|^2 d\Omega}{\int_{-\infty}^{\infty} |\tilde{\mathcal{E}}(t)|^2 dt} \\ &= \frac{\int_{-\infty}^{\infty} \left[\frac{d\mathcal{E}(\Omega)}{d\Omega}\right]^2 d\Omega}{\int_{-\infty}^{\infty} |\tilde{\mathcal{E}}(\Omega)|^2 d\Omega} + \left\langle \left(\frac{d\phi}{d\Omega}\right)^2 \right\rangle. \end{aligned} \tag{1.72}$$

It is left to a problem at the end of this chapter to derive these results. Since the initial pulse was unchirped and its spectral amplitude is not affected by propagation through the transparent medium, the first term in Eq. (1.72) represents the initial second order moment $\langle t^2\rangle_0$. Substituting the expression for the quadratic phase Eq. (1.69) into Eq. (1.55) for the first order moment, we find from Eq. (1.72):

$$\langle t^2\rangle = \langle t^2\rangle_0 + \left[\left.\frac{d^2\phi}{d\Omega^2}\right|_0\right]^2 \langle \Omega^2\rangle. \tag{1.73}$$

The frequency chirp introduces a temporal broadening (of the second order moment) directly proportional to the square of the chirp coefficient, $\left[\left.\frac{d^2\phi}{d\Omega^2}\right|_0\right]^2$.

Likewise we can analyze the situation where a temporal phase modulation $\varphi(t) = \left.\frac{d\varphi}{dt}\right|_0 t^2$ is impressed upon the pulse while the pulse envelope, $|\tilde{\mathcal{E}}(t)|^2$, remains unchanged. This temporal frequency modulation or chirp, characterized by the second derivative in the middle (center of mass) of the pulse, leads to a spectral broadening given by:

$$\langle \Omega^2\rangle = \langle \Omega^2\rangle_0 + \left[\left.\frac{d^2\varphi}{dt^2}\right|_0\right]^2 \langle t^2\rangle \tag{1.74}$$

where $\langle \Omega^2\rangle_0$ refers to the spectrum of the input pulse and $\langle t^2\rangle$ is the (constant) second-order moment of time.

Equations (1.73) and (1.74) demonstrate the advantage of using the mean square deviation to define the pulse duration and bandwidth, since it shows a simple relation between the broadening in the time or spectral domain, due to a chirp in the spectral or time domain, respectively independent of the pulse and spectral shape.

For the two different situations described by Eqs. (1.73) and (1.74), we can apply the uncertainty relation, Eq. (1.65),

$$\langle t^2\rangle\langle\Omega^2\rangle = \frac{M^4}{4}\kappa_c \geq \frac{1}{4}. \tag{1.75}$$

We have introduced a factor of chirp κ_c, equal to

$$\kappa_c = 1 + \frac{M^4}{4\langle t^2\rangle_0^2}\left[\left.\frac{d^2\phi}{d\Omega^2}\right|_0\right]^2 \tag{1.76}$$

in case of a frequency chirp and constant spectrum, or

$$\kappa_c = 1 + \frac{M^4}{4\langle \Omega^2\rangle_0^2}\left[\left.\frac{d^2\varphi}{dt^2}\right|_0\right]^2 \tag{1.77}$$

in case of a temporal chirp and constant pulse envelope.

In summary, using the *mean square deviation* to define the pulse duration and bandwidth:

- the duration—bandwidth product $\sqrt{\langle t^2\rangle\langle\Omega^2\rangle}$ is minimum (0.5) for a Gaussian pulse shape, without phase modulation.
- For any pulse shape, one can define a shape factor M^2 equal to the minimum duration—bandwidth product for that particular shape.
- Any quadratic phase modulation — or linear chirp — whether in frequency or time, increases the bandwidth duration product by a chirp factor κ_c. The latter increases proportionally to the second derivative of the phase modulation, whether in time or in frequency.

1.2 Pulse propagation

So far we have considered only temporal and spectral characteristics of light pulses. In this subsection we shall be interested in the propagation of such pulses through matter. This is the situation one always encounters when working with electromagnetic wave packets (at least until somebody succeeds in building a suitable trap). The electric field, now considered in its temporal and spatial dependence, is again a suitable quantity for the description of the propagating wave packet. In view of the optical materials that will be investigated, we can neglect external charges and

currents and confine ourselves to nonmagnetic and uniform media. A wave equation can be derived for the electric field vector **E** from Maxwell equations (see for instance Ref. [17]) which in Cartesian coordinates reads

$$\boxed{\left(\frac{\partial^2}{\partial x^2}+\frac{\partial^2}{\partial y^2}+\frac{\partial^2}{\partial z^2}-\frac{1}{c^2}\frac{\partial^2}{\partial t^2}\right)\mathbf{E}(x,y,z,t)=\mu_0\frac{\partial^2}{\partial t^2}\mathbf{P}(x,y,z,t)}, \tag{1.78}$$

where μ_0 is the magnetic permeability of free space. The source term of Eq. (1.78) contains the polarization **P** and describes the influence of the medium on the field as well as the response of the medium. Usually the polarization is decomposed into two parts:

$$\mathbf{P}=\mathbf{P}^L+\mathbf{P}^{NL}. \tag{1.79}$$

The decomposition of Eq. (1.79) is intended to distinguish a polarization that varies linearly ($\mathbf{P}^L$) from one that varies nonlinearly ($\mathbf{P}^{NL}$) with the field. Historically, $\mathbf{P}^L$ represents the medium response in the frame of "ordinary" optics, e.g., classical optics [18], and is responsible for effects such as diffraction, dispersion, refraction, linear losses and linear gain. Frequently, these processes can be attributed to the action of a host material which in turn may contain sources of a nonlinear polarization $\mathbf{P}^{NL}$. The latter is responsible for nonlinear optics [19–21] which includes, for instance, saturable absorption and gain, harmonic generation and Raman processes.

As will be seen in Chapters 3, both $\mathbf{P}^L$ and in particular $\mathbf{P}^{NL}$ are often related to the electric field by complicated differential equations. One reason is that no physical phenomenon can be truly instantaneous. In this chapter we will omit $\mathbf{P}^{NL}$. Depending on the actual problem under consideration, $\mathbf{P}^{NL}$ will have to be specified and added to the wave equation as a source term.

1.2.1 The reduced wave equation

Equation (1.78) is of rather complicated structure and in general can solely be solved by numerical methods. However, by means of suitable approximations and simplifications, one can derive a "reduced wave equation" which will enable us to deal with many practical pulse propagation problems in a rather simple way. We assume the electric field to be linearly polarized and propagating in the z-direction as a plane wave, i.e., the field is uniform in the transverse x, y direction. The wave equation has now been simplified to:

$$\left(\frac{\partial^2}{\partial z^2}-\frac{1}{c^2}\frac{\partial^2}{\partial t^2}\right)E(z,t)=\mu_0\frac{\partial^2}{\partial t^2}P^L(z,t) \tag{1.80}$$

As known from classical electrodynamics [17] the linear polarization of a medium is related to the field through the dielectric susceptibility χ. In the frequency domain we have

$$\tilde{P}^L(\Omega, z) = \epsilon_0 \chi(\Omega)\tilde{E}(\Omega, z) \tag{1.81}$$

which is equivalent to a convolution integral in the time domain

$$P^L(t, z) = \epsilon_0 \int_{-\infty}^{t} dt' \chi(t')E(z, t - t'). \tag{1.82}$$

Here ϵ_0 is the permittivity of free space. The finite upper integration limit, t, expresses the fact that the response of the medium must be causal. The polarization at t must not depend on electric field values at later times. For a nondispersive medium, which implies an "infinite bandwidth" for the susceptibility ($\chi(\Omega) = \text{const}$), the medium response is instantaneous, i.e., memory free. In general, $\chi(t)$ describes a finite response time of the medium which, in the frequency domain, means nonzero dispersion. This simple fact has important implications for the propagation of short pulses and time varying radiation in general. We will refer to this point several times in later chapters — in particular when dealing with coherent interaction.

The Fourier transform of (1.80) together with (1.81) yields

$$\boxed{\left[\frac{\partial^2}{\partial z^2} + \Omega^2 \epsilon(\Omega)\mu_0\right]\tilde{E}(z, \Omega) = 0} \tag{1.83}$$

where we have introduced the dielectric constant

$$\epsilon(\Omega) = [1 + \chi(\Omega)]\epsilon_0. \tag{1.84}$$

For now we will assume a real susceptibility and dielectric constant. Later we will discuss effects associated with complex quantities. The general solution of (1.83) for the propagation in the $+z$ direction is

$$\tilde{E}(\Omega, z) = \tilde{E}(\Omega, 0)e^{-ik(\Omega)z}, \tag{1.85}$$

where the propagation constant $k(\Omega)$ is determined by the dispersion relation of linear optics

$$k^2(\Omega) = \Omega^2 \epsilon(\Omega)\mu_0 = \frac{\Omega^2}{c^2} n^2(\Omega), \tag{1.86}$$

and $n(\Omega)$ is the refractive index of the material. For further consideration we expand $k(\Omega)$ about the carrier frequency ω_ℓ

$$k(\Omega) = k(\omega_\ell) + \delta k, \tag{1.87}$$

where

$$\delta k = \left.\frac{dk}{d\Omega}\right|_{\omega_\ell} (\Omega - \omega_\ell) + \frac{1}{2} \left.\frac{d^2k}{d\Omega^2}\right|_{\omega_\ell} (\Omega - \omega_\ell)^2 + \ldots \tag{1.88}$$

and write Eq. (1.85) as

$$\tilde{E}(\Omega, z) = \tilde{E}(\Omega, 0) e^{-ik_\ell z} e^{-i\delta k z}, \tag{1.89}$$

where $k_\ell^2 = \omega_\ell^2 \epsilon(\omega_\ell)\mu_0 = \omega_\ell^2 n^2(\omega_\ell)/c^2$. In most practical cases of interest, the Fourier amplitude will be centered around a mean wave vector k_ℓ, and will have appreciable values only in an interval Δk small compared to k_ℓ. In analogy to the introduction of an envelope function slowly varying in time, after the separation of a rapidly oscillating term, cf. Eqs. (1.19)– (1.22), we can define now an amplitude which is slowly varying in the spatial coordinate

$$\tilde{\mathcal{E}}(\Omega, z) = \tilde{E}(\Omega + \omega_\ell, 0) e^{-i\delta k z}. \tag{1.90}$$

Again, for this concept to be useful we must require that

$$\left|\frac{d}{dz}\tilde{\mathcal{E}}(\Omega, z)\right| \ll k_\ell \left|\tilde{\mathcal{E}}(\Omega, z)\right| \tag{1.91}$$

which implies a sufficiently small wave number spectrum

$$\left|\frac{\Delta k}{k_\ell}\right| \ll 1. \tag{1.92}$$

In other words, the pulse envelope must not change significantly while travelling through a distance comparable with the wavelength $\lambda_\ell = 2\pi/\omega_\ell$. Fourier transforming of Eq. (1.89)) into the time domain gives

$$\tilde{E}(t, z) = \frac{1}{2}\left\{\frac{1}{\pi}\int_{-\infty}^{\infty} d\Omega\, \tilde{E}(\Omega, 0) e^{-i\delta k z} e^{i(\Omega - \omega_\ell)t}\right\} e^{i(\omega_\ell t - k_\ell z)} \tag{1.93}$$

which can be written as

$$\boxed{\tilde{E}(t, z) = \frac{1}{2}\tilde{\mathcal{E}}(t, z) e^{i(\omega_\ell t - k_\ell z)}} \tag{1.94}$$

where $\tilde{\mathcal{E}}(t, z)$ is now the envelope varying slowly in space and time, defined by the term in the curled brackets in Eq. (1.93).

Further simplification of the wave equation requires a corresponding equation for $\tilde{\mathcal{E}}$ utilizing the envelope properties. Only a few terms in the expansion of $k(\Omega)$

and $\epsilon(\Omega)$, respectively, will be considered. To this effect we expand $\epsilon(\Omega)$ as series around ω_ℓ, leading to the following form for the linear polarization (1.81)

$$\tilde{P}^L(\Omega,z) = \left(\epsilon(\omega_\ell) - \epsilon_0 + \sum_{n=1}^{\infty} \frac{1}{n!} \frac{d^n\epsilon}{d\Omega^n}\Big|_{\omega_\ell} (\Omega-\omega_\ell)^n\right)\tilde{E}(\Omega,z). \tag{1.95}$$

In terms of the pulse envelope, the above expression corresponds in the time domain to

$$\begin{aligned}\tilde{P}^L(t,z) &= \frac{1}{2}\Big\{[\epsilon(\omega_\ell)-\epsilon_0]\tilde{\mathcal{E}}(t,z) \\ &+ \sum_{n=1}^{\infty}(-i)^n \frac{\epsilon^{(n)}(\omega_\ell)}{n!}\frac{\partial^n}{\partial t^n}\tilde{\mathcal{E}}(t,z)\Big\}e^{i(\omega_\ell t - k_\ell z)},\end{aligned} \tag{1.96}$$

where $\epsilon^{(n)}(\omega_\ell) = \frac{\partial^n}{\partial\Omega^n}\epsilon\Big|_{\omega_\ell}$. The term in the curled brackets defines the slowly varying envelope of the polarization, $\tilde{\mathcal{P}}^L$. The next step is to replace the electric field and the polarization in the wave equation (1.80) by Eq. (1.93) and Eq. (1.96), respectively. We transfer thereafter to a coordinate system (η,ξ) moving with the group velocity $v_g = \left(\frac{dk}{d\Omega}\Big|_{\omega_\ell}\right)^{-1}$, which is the standard transformation to a "retarded" frame of reference:

$$\xi = z \qquad \eta = t - \frac{z}{v_g} \tag{1.97}$$

and

$$\frac{\partial}{\partial z} = \frac{\partial}{\partial\xi} - \frac{1}{v_g}\frac{\partial}{\partial\eta}; \qquad \frac{\partial}{\partial t} = \frac{\partial}{\partial\eta}. \tag{1.98}$$

A straightforward calculation leads to the final result:

$$\frac{\partial}{\partial\xi}\tilde{\mathcal{E}} - \frac{i}{2}k_\ell''\frac{\partial^2}{\partial\eta^2}\tilde{\mathcal{E}} + \mathcal{D} = -\frac{i}{2k_\ell}\frac{\partial}{\partial\xi}\left(\frac{\partial}{\partial\xi} - \frac{2}{v_g}\frac{\partial}{\partial\eta}\right)\tilde{\mathcal{E}} \tag{1.99}$$

The quantity

$$\begin{aligned}\mathcal{D} &= -\frac{i\mu_0}{2k_\ell}\sum_{n=3}^{\infty}\frac{(-i)^n}{n!}\Big[\omega_\ell^2\epsilon^{(n)}(\omega_\ell) - 2n\omega_\ell\epsilon^{(n-1)}(\omega_\ell) \\ &+ n(n-1)\epsilon^{(n-2)}(\omega_\ell)\Big]\frac{\partial^n}{\partial\eta^n}\tilde{\mathcal{E}}\end{aligned} \tag{1.100}$$

contains dispersion terms of higher order, and has been derived by taking directly the second order derivative of the polarization defined by the product of envelope and fast oscillating terms in Eq. (1.96). The indices of the three resulting terms have

been re-defined to factor out a single derivative of order (n) of the field envelope. The second derivative of k:

$$\begin{aligned} k''_\ell &= \left.\frac{\partial^2 k}{\partial\Omega^2}\right|_{\omega_\ell} = -\left.\frac{1}{v_g^2}\frac{dv_g}{d\Omega}\right|_{\omega_\ell} \\ &= \frac{1}{2k_\ell}\left[\frac{2}{v_g^2} - 2\mu_0\epsilon(\omega_\ell) - 4\omega_\ell\mu_0\epsilon^{(1)}(\omega_\ell) - \omega_\ell^2\mu_0\epsilon^{(2)}(\omega_\ell)\right] \end{aligned} \tag{1.101}$$

is the group velocity dispersion (GVD) parameter. It should be mentioned that the GVD is usually defined as the derivative of v_g with respect to λ, $dv_g/d\lambda$, related to k'' through

$$\frac{dv_g}{d\lambda} = \frac{\Omega^2 v_g^2}{2\pi c}\frac{d^2k}{d\Omega^2}. \tag{1.102}$$

So far we have not made any approximations and the structure of Eq. (1.99) is still rather complex. However, we can exploit at this point the envelope properties (1.22) and (1.91), which, in this particular situation, imply:

$$\left|\frac{1}{k_\ell}\left(\frac{\partial}{\partial\xi} - \frac{2}{v_g}\frac{\partial}{\partial\eta}\right)\tilde{\mathcal{E}}\right| = \left|\frac{1}{k_\ell}\left(\frac{\partial}{\partial z} - \frac{1}{v_g}\frac{\partial}{\partial t}\right)\tilde{\mathcal{E}}\right| \ll \left|\tilde{\mathcal{E}}\right| \tag{1.103}$$

The right–hand side of (1.99) can thus be neglected if the prerequisites for introducing pulse envelopes are fulfilled. This procedure is called slowly varying envelope approximation (SVEA) and reduces the wave equation to first–order derivatives with respect to the spatial coordinate.

If the propagation of very short pulses is computed over long distances, the cumulative error introduced by neglecting the right hand side of Eq. (1.99) may be significant. In those cases, a direct numerical treatment of the second order wave equation is required.

Further simplifications are possible for a very broad class of problems of practical interest, where the dielectric constant changes slowly over frequencies within the pulse spectrum. In those cases, terms with $n \geq 3$ can be omitted too ($\mathcal{D} = 0$), leading to a greatly simplified reduced wave equation:

$$\boxed{\frac{\partial}{\partial\xi}\tilde{\mathcal{E}}(\eta,\xi) - \frac{i}{2}k''_\ell\frac{\partial^2}{\partial\eta^2}\tilde{\mathcal{E}}(\eta,\xi) = 0} \tag{1.104}$$

which describes the evolution of the complex pulse envelope as it propagates through a loss-free medium with GVD. The reader will recognize the mathematical structure of well-known equations from other areas of physics - for example, the one–dimensional Schrödinger equation and the one–dimensional heat diffusion equation.

1.2.2 Retarded frame of reference

In the case of zero GVD [$k_\ell'' = 0$ in Eq. (1.104)], the pulse envelope does not change at all in the system of local coordinates (η, ξ). This illustrates the usefulness of introducing a coordinate system moving at the group velocity. In the laboratory frame, the pulse travels at the group velocity without any distortion.

In dealing with short pulses as well as in dealing with white light (see Chapter 2) the appropriate "retarded frame of reference" is moving at the *group* rather than at the *wave* (*phase*) velocity. Indeed, while a monochromatic wave of frequency Ω travels at the phase velocity $v_p(\Omega) = c/n(\Omega)$, it is the superposition of many such waves with differing phase velocities that leads to a wave packet (pulse) propagating with the group velocity. The importance of the frame of reference moving at the group velocity is such that, in the following chapters, the notation z and t will be substituted for ξ and η, unless the laboratory frame is explicitly specified.

Some propagation problems — such as the propagation of coupled waves in nonlinear crystals discussed in Chapter 3 — are more appropriately treated in the frequency domain. As a simple exercise, let us derive the group velocity directly from the solution of the wave equation in the form of Eq. (1.89)

$$\tilde{E}(\Omega, z) = \tilde{E}(\Omega, 0) e^{-ik_\ell z} e^{-i\delta k z}. \tag{1.105}$$

The amplitude of the field spectrum $|\tilde{E}(\Omega, z)| = |\tilde{E}(\Omega, 0)|$ represented on the top left of Fig. 1.7 is not changed by propagation. We assume that the expansion of the wave vector $k(\Omega)$, Eq. (1.87), can be terminated after the linear term, that is

$$\delta k = \left.\frac{dk}{d\Omega}\right|_{\omega_\ell} (\Omega - \omega_\ell) \tag{1.106}$$

The inverse Fourier-transform of Eq. (1.105) now yields

$$\begin{aligned} \tilde{E}(t, z) &= e^{-ik_\ell z} \int_{-\infty}^{\infty} \tilde{E}(\Omega, 0) \exp\left[-i \left.\frac{dk}{d\Omega}\right|_{\omega_\ell} (\Omega - \omega_\ell) z\right] e^{i\Omega t} d\Omega \qquad (1.107) \\ &= e^{i(\omega_\ell t - k_\ell z)} \int_{-\infty}^{\infty} \tilde{E}(\Omega' + \omega_\ell, 0) e^{i(t - k_\ell' z)\Omega'}, d\Omega' \end{aligned}$$

where we substituted $\Omega = \Omega' + \omega_\ell$ and $k_\ell' = \left.\frac{dk}{d\Omega}\right|_{\omega_\ell}$ to obtain the last equation. This equation is just the inverse Fourier-transform of the field spectrum shifted to the origin (i.e., the spectrum of the envelope $\tilde{\mathcal{E}}(\Omega)$, represented on the lower left of Fig. 1.7) with the Fourier variable "time" now given by $\left(t - k_\ell' z\right)$. Carrying out the transform yields

$$\tilde{E}(t, z) = \frac{1}{2} \tilde{\mathcal{E}}(t, z) e^{i(\omega_\ell t - k_\ell z)} = \frac{1}{2} \tilde{\mathcal{E}}\left(t - k_\ell' z, 0\right) e^{i(\omega_\ell t - k_\ell z)}. \tag{1.108}$$

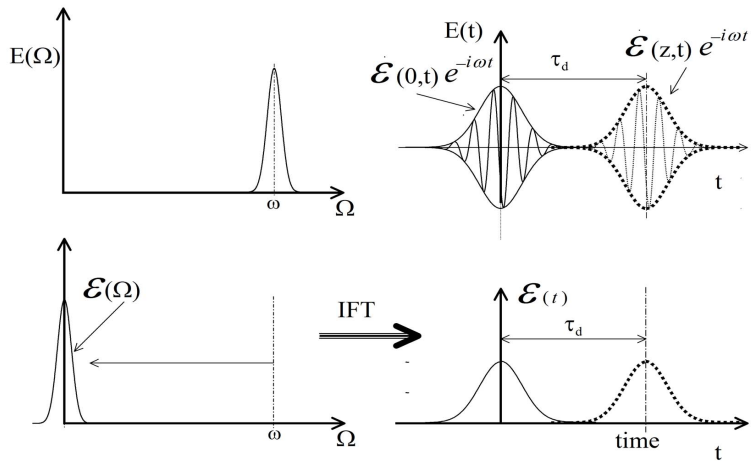

Figure 1.7: The Fourier transform amplitude ($E(\Omega, 0)$ is sketched in the upper left, and the corresponding field in the time domain on the upper right (solid line). The lower part of the figure displays the field amplitudes, $\mathcal{E}(\Omega)$ on the left, centered at the origin of the frequency scale, and the corresponding inverse Fourier transform $\mathcal{E}(t)$. Propagation in the frequency domain is obtained by multiplying the field at $z = 0$ by the phase factor $\exp(-i\tau_d\Omega)$, where $\tau_d = z/v_g$ is the group delay. In the time domain, this corresponds to delaying the pulse by an amount τ_d (right). The delayed fields $|E(z,t)|$ and $\mathcal{E}(z,t)$ are shown in dotted lines on the right of the figure.

We have thus the important result that, in the time domain, the light pulse has been delayed by an amount ($\tau_d = k'_\ell z$) proportional to distance. Within the approximation that the wave vector is a linear function of frequency, the pulse is seen to propagate without distortion with a constant group velocity v_g given by either of the three expressions:

$$\frac{1}{v_g} = \left.\frac{dk}{d\Omega}\right|_{\omega_\ell} = k'_\ell \qquad (1.109)$$

$$\frac{1}{v_g} = \frac{n_0}{c} + \frac{\omega_\ell}{c}\left.\frac{dn}{d\Omega}\right|_{\omega_\ell} \qquad (1.110)$$

$$\frac{1}{v_g} = \frac{n_0}{c} - \frac{\lambda}{c}\left.\frac{dn}{d\lambda}\right|_{\lambda}. \qquad (1.111)$$

The first term in Eqs. (1.110) and (1.111) represent the phase delay per unit length, while the second term in these equations is the change in carrier to envelope phase per unit length. We note that the dispersion of the wave vector ($dk/d\Omega$) or of

the index of refraction ($dn/d\lambda$) is responsible for a difference between the phase velocity $v_p = c/n_0$ and the group velocity v_g. In a frame of reference moving at the velocity v_g, $\tilde{\mathcal{E}}(z,t)$ remains identically unchanged. Pulse distortions thus only result from high order (higher than 1) terms in the Taylor series expansion of $k(\Omega)$. For this reason, most pulse propagation problems are treated in a retarded frame of reference, moving at the velocity v_g.

Forward/Backward propagating waves

We consider an ultrashort pulse plane wave propagating through a dielectric medium. Before the arrival of the pulse, there are no induced dipoles, and for the index of refraction we assume that of a vacuum ($n = 1$). As the dipoles are driven into motion by the first few cycles of the pulse, the index of refraction changes to the value n of the dielectric. One consequence of this causal phenomenon is the "precursor" predicted by Sommerfeld and Brillouin, see for example [17]. One might wonder if the discontinuity in index created by a short and intense pulse should not lead to a reflection for a portion of the pulse? This is an important question regarding the validity of the first order approximation to Maxwell's propagation equations. If, at $t = 0$, a short wave packet is launched in the $+z$ direction in a homogeneous medium, is it legitimate to assume that there will be no pulse generated in the opposite direction?

The answer that we give in this section is that, in the framework of Maxwell's second order equation and a linear polarization, there is no such "induced reflection". This property extends even to the nonlinear polarization created by the interaction of the light with a two-level system.

If we include the non-resonant part of the linear polarization in the index of refraction n (imaginary part of n), the remainder polarization P including all nonlinear and resonant interaction effects, adding a phenomenological scattering term σ leads to the following form of the second order wave equation:

$$\left(\frac{\partial^2}{\partial z^2}\tilde{E} - \frac{n^2}{c^2}\frac{\partial^2}{\partial t^2}\right)\tilde{E} = \mu_0\frac{\partial^2}{\partial t^2}\tilde{P} + \frac{n\sigma}{c}\frac{\partial}{\partial t}\tilde{E} \tag{1.112}$$

The polarization appearing in the right hand side can be instantaneous, or be the solution of a differential equation as in the case of most interactions with resonant atomic or molecular systems. Resonant light-matter interactions will be studied in detail in Chapter 3. The wave equation Eq. (1.112) can be written as a product of a forward and backward propagating operator. Instead of the variables t and z, it is more convenient to use the retarded time variable corresponding to the two

possible wave velocities $\pm c/n$:

$$\begin{aligned} s &= t - \frac{n}{c} z \\ r &= t + \frac{n}{c} z. \end{aligned} \tag{1.113}$$

In the new variables, Maxwell's equation (1.112) becomes:

$$\frac{\partial^2}{\partial s \partial r} \tilde{E} = \frac{c^2}{n^2} \left\{ \frac{\mu_0}{4} \left(\frac{\partial}{\partial s} + \frac{\partial}{\partial r} \right)^2 \tilde{P} + \frac{n\sigma}{c} \left(\frac{\partial}{\partial s} + \frac{\partial}{\partial r} \right) \right\} \tilde{E}. \tag{1.114}$$

We seek a solution in the form of a forward and a backward propagating field of amplitude $\tilde{\mathcal{E}}_F$ and $\tilde{\mathcal{E}}_B$:

$$\tilde{E} = \frac{1}{2} \tilde{\mathcal{E}}_F e^{i\omega_\ell s} + \frac{1}{2} \tilde{\mathcal{E}}_B e^{i\omega_\ell r}. \tag{1.115}$$

Substitution into Maxwell's Eq. (1.112):

$$\begin{aligned} & e^{i\omega_\ell s} \left[2i\omega_\ell \frac{\partial}{\partial r} + \frac{\partial^2}{\partial s \partial r} + \frac{c\sigma}{2n} \left(\frac{\partial}{\partial s} + \frac{\partial}{\partial r} + 2i\omega_\ell \right) \right] \frac{1}{2} \tilde{\mathcal{E}}_F \\ + \quad & e^{i\omega_\ell r} \left[2i\omega_\ell \frac{\partial}{\partial s} + \frac{\partial^2}{\partial s \partial r} + \frac{c\sigma}{2n} \left(\frac{\partial}{\partial s} + \frac{\partial}{\partial r} + 2i\omega_\ell \right) \right] \frac{1}{2} \tilde{\mathcal{E}}_B \\ = \quad & -\frac{\mu_0 c^2}{4n^2} \left(\frac{\partial}{\partial s} + \frac{\partial}{\partial r} \right)^2 \tilde{P}, \end{aligned} \tag{1.116}$$

which we re-write in an abbreviated way using the differential operators $\mathcal{L}$ and $\mathcal{M}$ for the forward and backward propagating waves, respectively:

$$\mathcal{L} \tilde{\mathcal{E}}_F e^{i\omega_\ell s} + \mathcal{M} \tilde{\mathcal{E}}_B e^{i\omega_\ell r} = -\frac{\mu_0 c^2}{4n^2} \left(\frac{\partial}{\partial s} + \frac{\partial}{\partial r} \right)^2 \tilde{P}. \tag{1.117}$$

In the case of a linear medium, the forward and backward wave travel independently. If, as initial condition, we choose $\tilde{\mathcal{E}}_B = 0$ along the line $r + s = 0$ ($t = 0$), there will be no back scattered wave. If the polarization is written as a slowly varying amplitude:

$$\tilde{P} = \frac{1}{2} \tilde{\mathcal{P}}_F e^{i\omega_\ell s} + \frac{1}{2} \tilde{\mathcal{P}}_B e^{i\omega_\ell r}, \tag{1.118}$$

the equations for the forward and backward propagating wave also separate if $\tilde{\mathcal{P}}_F$ is only a function of $\tilde{\mathcal{E}}_F$, and $\tilde{\mathcal{P}}_B$ only a function of $\tilde{\mathcal{E}}_B$. This is because a source term for $\tilde{\mathcal{P}}_B$ can only be formed by a "grating" term, which involves a product of $\tilde{\mathcal{E}}_B \tilde{\mathcal{E}}_F$.

It applies to a polarization created by near resonant interaction with a two-level system, using the semi-classical approximation, as will be considered in Chapters 3. The separation between forward and backward travelling waves has been demonstrated by Eilbeck [22,23] outside of the slowly-varying approximation. Within the slowly varying approximation, we generally write that the second derivative with respect to time of the polarization as $-\omega_\ell^2\tilde{\mathcal{P}}$, and therefore, the forward and backward propagating waves are still uncoupled, even when $\tilde{\mathcal{P}} = \tilde{\mathcal{P}}(\tilde{\mathcal{E}}_F, \tilde{\mathcal{E}}_B)$, provided there is only a forward propagating beam as initial condition.

1.2.3 Dispersion

For nonzero GVD ($k_\ell'' \neq 0$) the propagation problem (1.104) can be solved either directly in the time or in the frequency domain. In the first case, the solution of the partial differential equation is [24]

$$\tilde{\mathcal{E}}(t,z) = \frac{1}{\sqrt{2\pi i k_\ell'' z}} \int_{-\infty}^{\infty} \tilde{\mathcal{E}}(t',z=0) \exp\left(i\frac{(t-t')^2}{2k_\ell'' z}\right) dt'. \tag{1.119}$$

As we will see in subsequent chapters, it is generally more convenient to treat linear pulse propagation through transparent linear media in the frequency domain, since only the phase factor of the envelope $\tilde{\mathcal{E}}(\Omega)$ is affected by propagation.

It follows directly from the solution of Maxwell's equations in the frequency domain [for instance Eqs. (1.85) and (1.90)] that the spectral envelope after propagation through a thickness z of a linear transparent material is given by:

$$\tilde{\mathcal{E}}(\Omega,z) = \tilde{\mathcal{E}}(\Omega,0)e^{i\Phi(z)} = \tilde{\mathcal{E}}(\Omega,0)\exp\left(-\frac{i}{2}k_\ell''\Omega^2 z - \frac{i}{3!}k_\ell'''\Omega^3 z - \ldots\right). \tag{1.120}$$

Thus we have for the temporal envelope

$$\tilde{\mathcal{E}}(t,z) = \mathcal{F}^{-1}\left\{\tilde{\mathcal{E}}(\Omega,0)\exp\left(-\frac{i}{2}k_\ell''\Omega^2 z - \frac{i}{3!}k_\ell'''\Omega^3 z - \ldots\right)\right\}. \tag{1.121}$$

If we limit the Taylor expansion of k to the GVD term k_ℓ'', we find that an initially bandwidth-limited pulse develops a spectral phase with a quadratic frequency dependence, resulting in chirp.

We had defined a "chirp coefficient"

$$\kappa_c = 1 + \frac{M^4}{4\langle t^2\rangle_0^2}\left[\left.\frac{d\phi}{d\Omega}\right|_{\omega_\ell}\right]^2$$

when considering in Section 1.1.5 the influence of quadratic chirp on the uncertainty relation Eq. (1.75) based on the successive moments of the field distribution.

In the present case, we can identify the phase modulation:

$$\left.\frac{d\phi}{d\Omega}\right|_{\omega_\ell} = -k''_\ell z \tag{1.122}$$

Since the spectrum (in amplitude) of the pulse $|\,\tilde{\mathcal{E}}(\Omega,z)\,|^2$ remains constant [as shown for instance in Eq. (1.120)], the spectral components responsible for chirp must appear at the expense of the envelope shape, which has to become broader.

At this point we want to introduce some useful relations for the characterization of the dispersion. The dependence of a dispersive parameter can be given as a function of either the frequency Ω or the vacuum wavelength λ. The first, second and third order derivatives are related to each other by

$$\frac{d}{d\Omega} = -\frac{\lambda^2}{2\pi c}\frac{d}{d\lambda} \tag{1.123}$$

$$\frac{d^2}{d\Omega^2} = \frac{\lambda^2}{(2\pi c)^2}\left(\lambda^2\frac{d^2}{d\lambda^2} + 2\lambda\frac{d}{d\lambda}\right) \tag{1.124}$$

$$\frac{d^3}{d\Omega^3} = -\frac{\lambda^3}{(2\pi c)^3}\left(\lambda^3\frac{d^3}{d\lambda^3} + 6\lambda^2\frac{d^2}{d\lambda^2} + 6\lambda\frac{d}{d\lambda}\right) \tag{1.125}$$

The dispersion of the material is described by either the frequency dependence $n(\Omega)$ or the wavelength dependence $n(\lambda)$ of the index of refraction. The derivatives of the propagation constant used most often in pulse propagation problems, expressed in terms of the index n, are:

$$\frac{dk}{d\Omega} = \frac{n}{c} + \frac{\Omega}{c}\frac{dn}{d\Omega} = \frac{1}{c}\left(n - \lambda\frac{dn}{d\lambda}\right) \tag{1.126}$$

$$\frac{d^2k}{d\Omega^2} = \frac{2}{c}\frac{dn}{d\Omega} + \frac{\Omega}{c}\frac{d^2n}{d\Omega^2} = \left(\frac{\lambda}{2\pi c}\right)\frac{1}{c}\left(\lambda^2\frac{d^2n}{d\lambda^2}\right) \tag{1.127}$$

$$\frac{d^3k}{d\Omega^3} = \frac{3}{c}\frac{d^2n}{d\Omega^2} + \frac{\Omega}{c}\frac{d^3n}{d\Omega^3} = -\left(\frac{\lambda}{2\pi c}\right)^2\frac{1}{c}\left(3\lambda^2\frac{d^2n}{d\lambda^2} + \lambda^3\frac{d^3n}{d\lambda^3}\right) \tag{1.128}$$

The second equation, Eq. (1.127), defining the group velocity dispersion (GVD) is the frequency derivative of $1/v_g$. Multiplied by the propagation length L, it describes the frequency dependence of the group delay. It is sometimes expressed in $\mathrm{fs}^2\,\mu\mathrm{m}^{-1}$.

A positive GVD corresponds to

$$\frac{d^2k}{d\Omega^2} > 0 \tag{1.129}$$

1.2.4 Gaussian pulse propagation

For a more quantitative picture of the influence that GVD has on the pulse propagation we consider the linearly chirped Gaussian pulse of Eq. (1.41)

$$\tilde{\mathcal{E}}(t, z=0) = \mathcal{E}_0 e^{-(1+ia)(t/\tau_{G0})^2} = \mathcal{E}_0 e^{-(t/\tau_{G0})^2} e^{i\varphi(t,z=0)}$$

entering the sample. To find the pulse at an arbitrary position z, we multiply the field spectrum, Eq. (1.43), with the propagator $\exp\left(-i\frac{1}{2}k''_\ell \Omega^2 z\right)$ as done in Eq. (1.120), to obtain

$$\tilde{\mathcal{E}}(\Omega, z) = \tilde{A}_0 e^{-x\Omega^2} e^{iy\Omega^2} \tag{1.130}$$

where

$$x = \frac{\tau_{G0}^2}{4(1+a^2)} \tag{1.131}$$

and

$$y(z) = \frac{a\tau_{G0}^2}{4(1+a^2)} - \frac{k''_\ell z}{2}. \tag{1.132}$$

$\tilde{A}_0$ is a complex amplitude factor which we will not consider in what follows and τ_{G0} describes the pulse duration at the sample input. The time dependent electric field that we obtain by Fourier transforming Eq. (1.130) can be written as

$$\tilde{\mathcal{E}}(t, z) = \tilde{A}_1 \exp\left\{-\left(1 + i\frac{y(z)}{x}\right)\left(\frac{t}{\sqrt{\frac{4}{x}[x^2 + y^2(z)]}}\right)^2\right\}. \tag{1.133}$$

Obviously, this describes again a linearly chirped Gaussian pulse. For the "pulse duration" (note $\tau_p = \sqrt{2\ln 2}\,\tau_G$) and phase at position z we find

$$\tau_G(z) = \sqrt{\frac{4}{x}[x^2 + y^2(z)]} \tag{1.134}$$

and

$$\varphi(t, z) = -\frac{y(z)}{4[x^2 + y^2(z)]} t^2. \tag{1.135}$$

Let us consider first an initially unchirped input pulse ($a = 0$). The pulse duration and chirp parameter develop as:

$$\tau_G(z) = \tau_{G0}\sqrt{1 + \left(\frac{z}{L_d}\right)^2} \tag{1.136}$$

$$\frac{\partial^2}{\partial t^2}\varphi(t, z) = \left(\frac{1}{\tau_{G0}^2}\right)\frac{2z/L_d}{1 + (z/L_d)^2}. \tag{1.137}$$

We have defined a characteristic length:

$$\boxed{L_d = \frac{\tau_{G0}^2}{2k_\ell''}.} \tag{1.138}$$

For later reference let also us introduce a so-called dispersive length defined as

$$L_D = \frac{\tau_{p0}^2}{k_\ell''} \tag{1.139}$$

where for Gaussian pulses $L_D \approx 2.77 L_d$. Bandwidth limited Gaussian pulses double their length after propagation of about $0.6 L_D$. For propagation lengths $z \gg L_d$ the pulse broadening of an unchirped input pulse as described by Eq. (1.136) can be simplified to

$$\frac{\tau_G(z)}{\tau_{G0}} \approx \frac{z}{|L_d|} = \frac{2|k_\ell''|}{\tau_{G0}^2} z. \tag{1.140}$$

It is interesting to compare the result of Eq. (1.136) with that of Eq. (1.73), where we used the second moment as a measure for the pulse duration. Since the Gaussian is the shape for minimum uncertainty [Eq. (1.65)], and since $d^2\phi/d\Omega^2 = -k'' z$, one can derive the evolution equation for the mean square deviation of a Gaussian pulse in a dielectric medium:

$$\langle t^2 \rangle = \langle t^2 \rangle_0 + \left.\frac{d^2\phi}{d\Omega^2}\right|_0 \langle \Omega^2 \rangle_0 = \langle t^2 \rangle = \langle t^2 \rangle_0 + \frac{(k'')^2 z^2}{\langle t^2 \rangle_0}. \tag{1.141}$$

The latter equations reduces to Eq. (1.136) by substituting the relations between mean square deviations and Gaussian widths [Eq. (1.66)].

If the input pulse is chirped ($a \neq 0$) two different behaviors can occur depending on the relative sign of a and k_ℓ''. In the case of opposite sign, $y^2(z)$ increases monotonously resulting in pulse broadening, cf. Eq. (1.134). If a and k_ℓ'' have equal sign $y^2(z)$ decreases until it becomes zero after a propagation distance

$$z_c = \frac{\tau_{G0}^2 a}{2|k_\ell''|(1+a^2)}. \tag{1.142}$$

At this position the pulse reaches its shortest duration

$$\tau_G(z_c) = \tau_{Gmin} = \frac{\tau_{G0}}{\sqrt{1+a^2}} \tag{1.143}$$

and the time dependent phase according to Eq. (1.135) vanishes. From here on the propagation behavior is that of an unchirped input pulse of duration τ_{Gmin}, that is,

the pulse broadens and develops a time-dependent phase. The larger the input chirp ($|a|$), the shorter the minimum pulse duration that can be obtained [see Eq. (1.143)]. The underlying reason is that the excess bandwidth of a chirped pulse is converted into a narrowing of the envelope by chirp compensation, until the Fourier limit is reached. The whole procedure including the impression of chirp on a pulse will be treated in Chapter 9 in more detail.

There is a complete analogy between the propagation (diffraction) effects of a spatially Gaussian beam and the temporal evolution of a Gaussian pulse in a dispersive medium. For instance, the pulse duration and the slope of the chirp follow the same evolution with distance as the waist and curvature of a Gaussian beam, as detailed in Section 1.6. A linearly chirped Gaussian pulse in a dispersive medium is completely characterized by the position and (minimum) duration of the unchirped pulse, just as a spatially Gaussian beam is uniquely defined by the position and size of its waist. To illustrate this point, let us consider a linearly chirped pulse whose "duration" τ_G and chirp parameter a are known at a certain position z_1. The position z_c of the minimum duration (unchirped pulse) is found again by setting $y = 0$ in Eq. (1.132):

$$z_c = z_1 + \frac{\tau_G^2}{2k_\ell''}\frac{a}{1+a^2} = z_1 + a\frac{\tau_{Gmin}^2}{2k_\ell''}. \tag{1.144}$$

The position z_c is after z_1 if a and k_ℓ'' have the same sign[2]; before z_1 if they have opposite sign. All the temporal characteristics of the pulse are most conveniently defined in terms of the distance $L = z - z_c$ to the point of zero chirp, and the minimum duration τ_{Gmin}. This is similar to Gaussian beam propagation where the location of the beam waist often serves as reference. The chirp parameter a and the pulse "duration" τ_G at any point L are then simply given by

$$a(L) = L/L_d \tag{1.145}$$

$$\tau_G(L) = \tau_{Gmin}\sqrt{1+[a(L)]^2} \tag{1.146}$$

where the dispersion parameter $L_d = \tau_{Gmin}^2/(2|k_\ell''|)$. The pulse duration bandwidth product varies with distance L as

$$c_B(L) = \frac{2\ln 2}{\pi}\sqrt{1+[a(L)]^2} \tag{1.147}$$

To summarize, Fig. (1.8) illustrates the behavior of a linearly chirped Gaussian pulse as it propagates through a dispersive sample.

[2]For instance, an initially downchirped ($a > 0$) pulse at $z = z_c$ will be compressed in a medium with positive dispersion ($k'' > 0$).

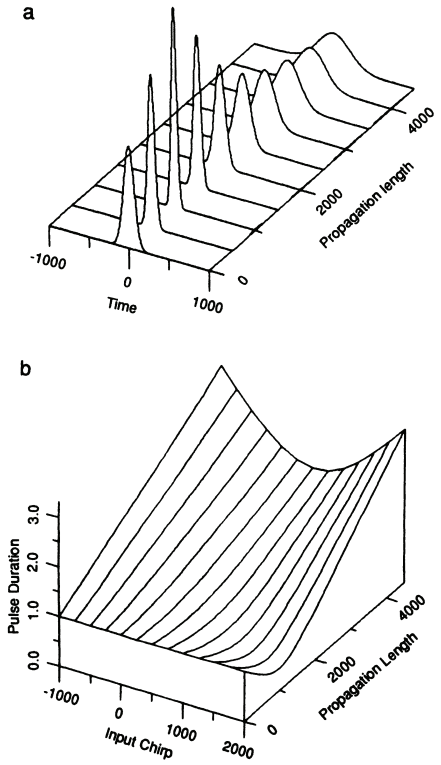

Figure 1.8: Propagation of a linearly chirped Gaussian pulse in a medium with GVD [pulse shape (a), pulse duration for different input chirp (b)].

Simple physical consideration can lead directly to a crude approximation for the maximum broadening that a bandwidth limited pulse of duration τ_p and spectral width $\Delta\omega_p$ will experience. Each group of waves centered around a frequency Ω travels with its own group velocity $v_g(\Omega)$. The difference of group velocities over the pulse spectrum becomes then:

$$\Delta v_g = \left[\frac{dv_g}{d\Omega}\right]_{\omega_\ell} \Delta\omega_p. \tag{1.148}$$

Accordingly, after a travel distance L the pulse spread can be as large as

$$\Delta\tau_p = \left|\Delta\left(\frac{L}{v_g}\right)\right| \approx \frac{L}{V_g^2}|\Delta v_g| \tag{1.149}$$

which, by means of Eqs. (1.101) and (1.148), yields:

$$\Delta\tau_p = L|k''_\ell|\Delta\omega_p. \tag{1.150}$$

Approximating $\tau_p \approx \Delta\omega_p^{-1}$, a characteristic length after which a pulse has approximately doubled its duration can now be estimated as:

$$L'_D = \frac{1}{|k''_\ell|\Delta\omega_p^2}. \tag{1.151}$$

Measuring the length in meter and the spectral width in nm the GVD of materials is sometimes given in fs/(m nm) which pictorially describes the pulse broadening per unit travel distance and unit spectral width. From Eq. (1.150) we find for the corresponding quantity

$$\boxed{\frac{\Delta\tau_p}{L\Delta\lambda} = 2\pi\frac{c}{\lambda_\ell^2}|k''_\ell|.} \tag{1.152}$$

For BK7 glass at 620 nm, $k''_\ell \approx 6\times10^{-26}\mathrm{s}^2/\mathrm{m}$, and the GVD as introduced above is about 300 fs per nm spectral width and meter propagation length.

1.2.5 Complex dielectric constant

In general, the dielectric constant, which was introduced in Eq. (1.83) as a real quantity, is complex. Indeed a closer inspection of Eq. (1.82) shows that the finite memory time of matter requires not only ϵ, χ to be frequency dependent but also that they be complex. The real and imaginary part of $\tilde{\epsilon}$, $\tilde{\chi}$ are not independent of each other but related through a Kramers–Kronig relation. The consideration of a real $\epsilon(\Omega)$ is justified as long as we can neglect (linear) losses or gain. This is valid for transparent samples or propagation lengths which are too short for these processes to become essential for the pulse shaping. For completeness we will modify the reduced wave equation (1.104) by taking into account a complex dielectric constant $\tilde{\epsilon}(\Omega)$ represented as

$$\tilde{\epsilon}(\Omega) = \epsilon(\Omega) + i\epsilon_i(\Omega). \tag{1.153}$$

Let us assume $\tilde{\epsilon}(\Omega)$ to be weakly dispersive. The same procedure introduced to derive Eq. (1.104) can be used after inserting the complex dielectric constant $\tilde{\epsilon}$ into the expression of the polarization Eq. (1.95). Now the reduced wave equation becomes

$$\frac{\partial}{\partial z}\tilde{\mathcal{E}}(t,z) - \frac{i}{2}k''\frac{\partial^2}{\partial t^2}\tilde{\mathcal{E}}(t,z) = \kappa_1\tilde{\mathcal{E}}(t,z) + i\kappa_2\frac{\partial}{\partial t}\tilde{\mathcal{E}}(t,z) + \kappa_3\frac{\partial^2}{\partial t^2}\tilde{\mathcal{E}}(t,z) \tag{1.154}$$

where

$$\kappa_1 = \frac{\omega_\ell}{2}\eta_0\epsilon_i(\omega_\ell) \tag{1.155}$$

$$\kappa_2 = \frac{1}{2}\eta_0\left[2\epsilon_i(\omega_\ell) + \omega_\ell \frac{d}{d\Omega}\epsilon_i(\Omega)\Big|_{\omega_\ell}\right] \tag{1.156}$$

$$\kappa_3 = \frac{1}{4\omega_\ell}\eta_0\left[2\epsilon_i(\omega_\ell) + 4\omega_\ell \frac{d}{d\Omega}\epsilon_i(\Omega)\Big|_{\omega_\ell} + \omega_\ell^2 \frac{d^2}{d\Omega^2}\epsilon_i(\Omega)\Big|_{\omega_\ell}\right]. \tag{1.157}$$

In the above expressions, $\eta_0 = \sqrt{\mu_0/\epsilon_0} \approx 377$ Ωms is the characteristic impedance of vacuum. For zero–GVD, and neglecting the two last terms in the right-hand side of Eq. (1.154), the pulse evolution with propagation distance z is described by

$$\frac{\partial}{\partial z}\tilde{\mathcal{E}}(t,z) - \kappa_1\tilde{\mathcal{E}}(t,z) = 0 \tag{1.158}$$

which has the solution

$$\tilde{\mathcal{E}}(t,z) = \tilde{\mathcal{E}}(t,0)e^{\kappa_1 z}. \tag{1.159}$$

The pulse experiences losses or gain depending on the sign of κ_1 and does not change its shape. Equation (1.159) states simply the Lambert-Beer law of linear optics.

An interesting situation is that in which there would be neither gain nor loss at the pulse carrier frequency, i.e., $\epsilon_i(\omega_\ell) = 0$ and $\frac{d}{d\Omega}\epsilon_i(\Omega)\big|_{\omega_\ell} \neq 0$, which could occur between an absorption and amplification line. Neglecting the terms with the second temporal derivative of $\tilde{\mathcal{E}}$, the propagation problem is governed by the equation

$$\frac{\partial}{\partial z}\tilde{\mathcal{E}}(t,z) - i\kappa_2\frac{\partial}{\partial t}\tilde{\mathcal{E}}(t,z) = 0. \tag{1.160}$$

The solution of this equation is simply

$$\tilde{\mathcal{E}}(t,z) = \tilde{\mathcal{E}}(t + i\kappa_2 z, 0). \tag{1.161}$$

To get an intuitive picture on what happens with the pulse according to Eq. (1.161), let us choose an unchirped Gaussian pulse $\tilde{\mathcal{E}}(t,0)$ [see Eq. (1.41] for $a = 0$), entering the sample at $z = 0$. From Eq. (1.161) we find:

$$\tilde{\mathcal{E}}(t,z) = \tilde{\mathcal{E}}(t,0)\exp\left[\kappa_2^2(z/\tau_G)^2\right]\exp\left[-i2\kappa_2 tz/\tau_G^2\right]. \tag{1.162}$$

The pulse is amplified, and simultaneously its center frequency is shifted with propagation distance. The latter shift is due to the amplification of one part of the pulse

spectrum (the high (low) – frequency part if $\kappa_2 < (>)0$) while the other part is absorbed. The result is a continuous shift of the pulse spectrum in the corresponding direction and a net gain while the pulse shape is preserved.

In the beginning of this section we mentioned that there is always an imaginary contribution of the dielectric constant leading to gain or loss. The question arises whether a wave equation such as Eq. (1.104), where only the real part of $\tilde{\epsilon}$ was considered, is of any practical relevance for describing pulse propagation through matter. The answer is yes, because in (almost) transparent regions the pulse change due to dispersion can be much larger than the change caused by losses. An impressive manifestation of this fact is pulse propagation through optical fibers. High-quality fibers made from fused silica can exhibit damping constants as low as 1 dB/km at wavelengths near 1 μm, where the GVD term is found to be $k'' \approx 75$ ps^2/km, see for example [25]. Consequently, a 100 fs pulse launched into a 10 m fiber loses just about 2% of its energy while it broadens by about a factor of 150. To illustrate the physics underlying the striking difference between the action of damping and dispersion, let us consider a dielectric constant $\tilde{\epsilon}(\Omega)$ originating from a single absorption line.

We will use the simple model of a classical harmonic oscillator consisting of an electron bound to a nucleus to calculate the dispersion and absorption of that line. The equation of motion of the electron is:

$$\frac{d^2r}{dt^2} + \omega_0^2 r + \frac{1}{T_c}\frac{dr}{dt} = \frac{e}{m_e}E, \tag{1.163}$$

where $\omega_0 = \sqrt{C/m_e}$ (C being the "spring constant") is the resonance frequency, m_e the electron mass, e its charge, and $1/T_c$ the damping constant. Assuming an electric field of the form $E = (1/2)\tilde{\mathcal{E}}_0 \exp(i\Omega t)$, one finds the polarization $P = N_0 er$ (N_0 being the number of oscillators (dipoles) per unit volume):

$$P(\Omega) = \frac{N_0 e^2}{m_e}\frac{E}{\omega_0^2 - \Omega^2 + i\Omega/T_c} \tag{1.164}$$

Using the general relation between polarization and electric field $P = \epsilon_0 \chi E$ we obtain an expression for the complex susceptibility:

$$\chi(\Omega) = \frac{N_0^2 e^2}{\epsilon_0 m_e}\frac{1}{\omega_0^2 - \Omega^2 + i\Omega/T_c} \tag{1.165}$$

The real and imaginary parts of the susceptibility χ can be calculated:

$$\chi_r = \frac{N_0 e^2}{\epsilon_0 m_e} \frac{(\omega_0^2 - \Omega^2)}{(\omega_0^2 - \Omega^2)^2 + \Omega^2/T_c^2} \approx \frac{N_0 e^2 T_2}{2 m_e \epsilon_0 \omega_0} \frac{\Delta\omega T_2}{1 + \Delta\omega^2 T_2^2} \tag{1.166}$$

$$\chi_i = -\frac{N_0 e^2}{\epsilon_0 m_e} \frac{(\Omega/T_c)}{(\omega_0^2 - \Omega^2)^2 + \Omega^2/T_c^2} \approx -\frac{N_0 e^2 T_2}{2 m_e \epsilon_0 \omega_0} \frac{1}{1 + \Delta\omega^2 T_2^2} \tag{1.167}$$

The second term of each equation above corresponds to the approximation of small detuning $\Delta\omega = \omega_0 - \Omega \ll \omega_o$. $1/T_2$ is the linewidth of the Lorentzian absorption line, and $T_2 = 2T_c$ will be assimilated in Chapter 3 to the phase relaxation time of the oscillators. The real and imaginary parts of the oscillator contribution to the susceptibility are responsible for a frequency dependence of the wave vector. One can write

$$k(\Omega) = \Omega \sqrt{\mu_0 \epsilon_0 \left[1 + \chi(\Omega)\right]} \approx \frac{\Omega}{c} \left[1 + \frac{1}{2}\chi(\Omega)\right] \tag{1.168}$$

For frequencies Ω being sufficiently far from resonance, i.e. $|(\omega_0 - \Omega)T_2)| = |\Delta\omega T_2| \gg 1$, but with $|\omega_\ell - \Omega| \ll \omega_\ell$ (narrow pulse spectrum), the real and imaginary parts of the propagation constant are given by:

$$k_r(\Omega) \simeq \frac{\Omega}{c} + B\frac{\Omega}{\Delta\omega T_2} \tag{1.169}$$

$$k_i(\Omega) \simeq -B\frac{\Omega}{(\Delta\omega T_2)^2}, \tag{1.170}$$

where $B = (N_0 e^2 T_2)/(4\epsilon_0 \omega_0 c m_e)$. The group velocity dispersion, responsible for pulse reshaping, is:

$$k''(\Omega) \simeq \frac{2BT_2^2\omega_0}{[\Delta\omega T_2]^3}. \tag{1.171}$$

For small travel distances L the relative change of pulse energy can be estimated from Eq. (1.85) and Eq. (1.28) to be:

$$\Delta\mathcal{W}_{rel} = 1 - \frac{\mathcal{W}(L)}{\mathcal{W}(0)} \approx -2k_i L. \tag{1.172}$$

The relative change of pulse duration due to GVD can be evaluated from Eq. (1.136) and we find:

$$\Delta\tau_{rel} = \frac{\tau_G(L)}{\tau_{G0}} - 1 \approx 2\left(\frac{k''_\ell L}{\tau_{G0}^2}\right)^2. \tag{1.173}$$

To compare both pulse distortions we consider their ratio, using Eqs. (1.170), (1.171), (1.172) and (1.173:

$$\frac{\Delta\tau_{rel}}{\Delta\mathcal{W}_{rel}} = \Delta\mathcal{W}_{rel} \frac{2}{(\Delta\omega T_2)^2} \left(\frac{T_2}{\tau_{G0}}\right)^4. \tag{1.174}$$

At given material parameters and carrier frequency, shorter pulses always lead to a dominant pulse spreading. For $T_2 = 10^{-10}$ s (typical value for a single electronic resonance), and a detuning $\Delta\omega T_2 = 10^4$, we find for example:

$$\frac{\Delta\tau_{rel}}{\Delta\mathcal{W}_{rel}} \approx \Delta\mathcal{W}_{rel}\left(\frac{1200\,\mathrm{fs}}{\tau_{G0}}\right)^4. \tag{1.175}$$

To summarize, a resonant transition of certain spectral width $1/T_2$ influences short pulse (pulse duration < 1 ps) propagation outside resonance mainly due to dispersion. Therefore, the consideration of a transparent material ($\epsilon_i \approx 0$) with a frequency dependent, real dielectric constant $\epsilon(\Omega)$, which was necessary to derive Eq. (1.104), is justified in many practical cases involving ultrashort pulses.

1.3 Interaction of light pulses with linear optical elements

Even though this topic is treated in detail in Chapter 2, we want to discuss here some general aspects of pulse distortions induced by linear optical elements. These elements comprise typical optical components, such as mirrors, prisms, and gratings, which one usually finds in all optical setups. Here we shall restrict ourselves to the temporal and spectral changes the pulse experiences and shall neglect a possible change of the beam characteristics. A linear optical element of this type can be characterized by a complex optical transfer function

$$\tilde{H}(\Omega) = R(\Omega)e^{-i\Psi(\Omega)} \tag{1.176}$$

that relates the incident field spectrum $\tilde{E}_{in}(\Omega)$ to the field at the sample output $\tilde{E}(\Omega)$

$$\tilde{E}(\Omega) = R(\Omega)e^{-i\Psi(\Omega)}\tilde{E}_{in}(\Omega). \tag{1.177}$$

Here $R(\Omega)$ is the (real) amplitude response and $\Psi(\Omega)$ is the phase response. As can be seen from Eq. (1.177), the influence of $R(\Omega)$ is that of a frequency filter. The phase factor $\Psi(\Omega)$ can be interpreted as the phase delay which a spectral component of frequency Ω experiences. To get an insight of how the phase response affects the light pulse, we assume that $R(\Omega)$ does not change over the pulse spectrum whereas $\Psi(\Omega)$ does. Thus, we obtain for the output field from Eq. (1.177):

$$\tilde{E}(t) = \frac{1}{2\pi}R\int_{-\infty}^{+\infty}\tilde{E}_{in}(\Omega)e^{-i\Psi(\Omega)}e^{i\Omega t}\,d\Omega. \tag{1.178}$$

Replacing $\Psi(\Omega)$ by its Taylor expansion around the carrier frequency ω_ℓ of the incident pulse

$$\Psi(\Omega) = \sum_{n=0}^{\infty} b_n(\Omega-\omega_\ell)^n \tag{1.179}$$

with the expansion coefficients

$$b_n = \frac{1}{n!}\frac{d^n\Psi}{d\Omega^n}\bigg|_{\omega_\ell} \tag{1.180}$$

we obtain for the pulse

$$\begin{aligned}\tilde{E}(t) &= \frac{1}{2}\tilde{\mathcal{E}}(t)e^{i\omega_\ell t} \\ &= \frac{1}{2\pi}Re^{-ib_0}e^{i\omega_\ell t}\int_{-\infty}^{+\infty}\tilde{E}_{in}(\Omega) \\ &\quad\times\exp\left(-i\sum_{n=2}^{\infty}b_n(\Omega-\omega_\ell)^n\right)e^{i(\Omega-\omega_\ell)(t-b_1)}\,d\Omega. \end{aligned}\tag{1.181}$$

By means of Eq. (1.181) we can easily interpret the effect of the various expansion coefficients b_n. The term e^{-ib_0} is a constant phase shift (phase delay) having no effect on the pulse envelope. A nonvanishing b_1 leads solely to a shift of the pulse on the time axis t; the pulse would obviously keep its position on a time scale $t' = t - b_1$. The term b_1 determines a group delay in a similar manner as the first–order expansion coefficient of the propagation constant k defined a group velocity in Eq. (1.108). The higher–order expansion coefficients produce a nonlinear behavior of the spectral phase which changes the pulse envelope and chirp. The action of the term with $n = 2$, for example, producing a quadratic spectral phase, is analogous to that of GVD in transparent media.

If we decompose the input field spectrum into modulus and phase $\tilde{E}_{in}(\Omega) = |\tilde{E}_{in}(\Omega)|\exp(i\Phi_{in}(\Omega))$, we obtain from Eq. (1.177) for the spectral phase at the output

$$\Phi(\Omega) = \Phi_{in}(\Omega) - \sum_{n=0}^{\infty}b_n(\Omega-\omega_\ell)^n. \tag{1.182}$$

It is interesting to investigate what happens if the linear optical element is chosen to compensate for the phase of the input field. For Taylor coefficients with $n \geq 2$:

$$b_n = \frac{1}{n!}\,\frac{d^n}{d\Omega^n}\Phi_{in}(\Omega)\bigg|_{\omega_\ell}. \tag{1.183}$$

A closer inspection of Eq. (1.181) shows that when Eq. (1.183) is satisfied, all spectral components are in phase for $t - b_1 = 0$, leading to a pulse with maximum peak intensity, as was discussed in previous sections. We will come back to this important point when discussing pulse compression. We want to point out the formal analogy between the solution of the linear wave equation (1.85) and Eq.(1.177) for $R(\Omega) = 1$ and $\Psi(\Omega) = k(\Omega)z$. This analogy expresses the fact that a dispersive

transmission object is just one example of a linear element. In this case we obtain for the spectrum of the complex envelope

$$\tilde{\mathcal{E}}(\Omega, z) = \tilde{\mathcal{E}}_{in}(\Omega, 0) \exp\left[-i \sum_{n=0}^{\infty} \frac{1}{n!} k_\ell^{(n)} (\Omega - \omega_\ell)^n z\right] \tag{1.184}$$

where $k_\ell^{(n)} = (d^n/d\Omega^n) k(\Omega)|_{\omega_\ell}$.

Next let us consider a sequence of m optical elements. The resulting transfer function is given by the product of the individual contributions $\tilde{H}_j(\Omega)$

$$\tilde{H}(\Omega) = \prod_{j=1}^{m} \tilde{H}_j(\Omega) = \left(\prod_{j=1}^{m} R_j(\Omega)\right) \exp\left[-i \sum_{j=1}^{m} \Psi_j(\Omega)\right] \tag{1.185}$$

which means an addition of the phase responses in the exponent. Subsequently, by a suitable choice of elements, one can reach a zero-phase response so that the action of the device is through the amplitude response only. In particular, the quadratic phase response of an element (e.g., dispersive glass path) leading to pulse broadening can be compensated with an element having an equal phase response of opposite sign (e.g., grating pair) which automatically would re-compress the pulse to its original duration. Such methods are of great importance for the handling of ultrashort light pulses. Corresponding elements will be discussed in Chapter 2.

1.4 Generation of phase modulation

At this point let us briefly discuss essential physical mechanisms to produce a time dependent phase of the pulse, i.e., a chirped light pulse. Processes resulting in a phase modulation can be divided into those that increase the pulse spectral width and those that leave the spectrum unchanged. The latter can be attributed to the action of linear optical processes. Any transparent linear medium, or spectrally "flat" reflector, can change the phase of a pulse, without affecting its spectral amplitude. The action of these elements is most easily analyzed in the frequency domain. As we have seen in the previous section, the phase modulation results from the different phase delays which different spectral components experience upon interaction. The result for an initially bandwidth-limited pulse, in the time domain, is a temporally broadened pulse with a certain frequency distribution across the envelope, such that the spectral amplitude profile remains unchanged. For an element to act in this manner its phase response $\Psi(\Omega)$ must have non-zero derivatives of at least second order as explained in the previous section.

A phase modulation that leads to a spectral broadening is most easily discussed in the time domain. Let us assume that the action of a corresponding optical element on an unchirped input pulse can be formally written as:

$$\tilde{E}(t) = T(t)e^{i\Phi(t)}\tilde{E}_{in}(t) \tag{1.186}$$

where T and Φ define a time dependent amplitude and phase response, respectively. For our simplified discussion here let us further assume that T = const., leaving the pulse envelope unaffected. Since the output pulse has an additional phase modulation $\Phi(t)$ its spectrum must have broadened during the interaction. If the pulse under consideration is responsible for the time dependence of Φ, then we call the process self-phase modulation. If additional pulses cause the temporal change of the optical properties we will refer to it as cross-phase modulation. Often, phase modulation occurs through a temporal variation of the index of refraction n of a medium during the passage of the pulse. For a medium of length d the corresponding phase is:

$$\Phi(t) = -k(t)d = -\frac{2\pi}{\lambda}n(t)d. \tag{1.187}$$

In later chapters we will discuss in detail several nonlinear optical interaction schemes with short light pulses that can produce a time dependence of n.

A time dependence of n can also be achieved by applying a voltage pulse at an electro-optic material for example. However, with the view on phase shaping of femtosecond light pulses the requirements for the timing accuracy of the voltage pulse make this technique difficult.

1.5 Beam propagation

So far we have considered light pulses propagating as plane waves, which allowed us to describe the time varying field with only one spatial coordinate. This simplification implies that the intensity across the beam is constant and, moreover, that the beam diameter is infinitely large. Both features hardly fit what we know from laser beams. Despite the fact that both features do not match the real world, such a description has been successfully applied for many practical applications and will be used in this book whenever possible. This simplified treatment is justified if the processes under consideration either do not influence the transverse beam profile (e.g., sufficiently short sample length) or allow one to discuss the change of beam profile and pulse envelope as if they occur independently from each other. The general case, where both dependencies mix, is often more complicated and, frequently, requires extensive numerical treatment. Here we will discuss solely the situation where the change of such pulse characteristics as duration, chirp, and

bandwidth can be separated from the change of the beam profile. Again we restrict ourselves to a linearly polarized field which now has to be considered in its complete spatial dependence. Assuming a propagation in the z-direction, we can write the field in the form:

$$E = E(x,y,z,t) = \frac{1}{2}\tilde{u}(x,y,z)\tilde{\mathcal{E}}(t)e^{i(\omega_\ell t - k_\ell z)} + c.c.. \tag{1.188}$$

The scalar $\tilde{u}(x,y,z)$ is to describe the transverse beam profile and $\tilde{\mathcal{E}}(t,z)$ is the slowly varying complex envelope introduced in Eq. (1.93). Note that the rapid z-dependence of E is contained in the exponential function. Subsequently, $\tilde{u}$ is assumed to vary slowly with z. Under these conditions the insertion of Eq. (1.188) into the wave equation (1.78) yields after separation of the time dependent part in paraxial approximation [16]:

$$\boxed{\left(\frac{\partial^2}{\partial x^2} + \frac{\partial^2}{\partial y^2} - 2ik_\ell\frac{\partial}{\partial z}\right)\tilde{u}(x,y,z) = 0,} \tag{1.189}$$

which is usually solved by taking the Fourier transform along the space coordinates x and y, yielding:

$$\left[\frac{\partial}{\partial z} - \frac{i}{2k_\ell}\left(k_x^2 + k_y^2\right)\right]\tilde{u}(k_x,k_y,z) = 0, \tag{1.190}$$

where k_x and k_y are the Fourier variables (spatial frequencies, wave numbers). This equation can be integrated and yields:

$$\tilde{u}(k_x,k_y,z) = \tilde{u}_0(k_x,k_y)e^{\frac{i}{2k_\ell}\left(k_x^2+k_y^2\right)z}, \tag{1.191}$$

where $\tilde{u}_0(k_x,k_y) = \tilde{u}(k_x,k_y,0)$. Paraxial approximation means that the transverse beam dimensions remain sufficiently small compared with typical travel distances of interest.

Instead of using the differential equation (1.189), one can equivalently describe the field propagation by an integral equation. The basic approach is to start with Huygens' principle, and apply the Fresnel approximation for paraxial wave propagation [16]. Assuming that the field distribution (or beam profile) $\tilde{u}(x',y',z') = \tilde{u}_0(x',y')$ is known in a plane $z = 0$; the field distribution $\tilde{u}(x,y,z)$ in a plane $z = L$ is given by:

$$\tilde{u}(x,y,z) = \frac{ie^{ik_\ell L}}{\lambda L}\int_{-\infty}^{\infty}\int_{-\infty}^{\infty}\tilde{u}_0(x',y')e^{-ik_\ell[(x'-x)^2+(y'-y)^2]/(2L)}dx'dy'. \tag{1.192}$$

This solution was obtained from Eq. (1.191) through an inverse Fourier transform and is a convolution of $\tilde{u}(x,y,0)$ and $\exp\left[-ik(x^2+y^2)/(2L)\right]$.

1.6 Analogy between pulse and beam propagation

1.6.1 Time analogy of the paraxial (Fresnel) approximation

Comparing the paraxial wave equation (1.189) and the reduced wave equation (1.104) describing pulse propagation through a GVD medium we notice an interesting correspondence. Both equations are of similar structure. In terms of the reduced wave equation the transverse space coordinates x, y in Eq. (1.189) seem to play the role of the time variable. This space-time analogy suggests the possibility of translating simply the effects related to dispersion into beam propagation properties. For instance, we may compare the temporal broadening of an unchirped pulse due to dispersion with the change of beam size due to diffraction. In this sense free-space propagation plays a similar role for the beam characteristics as a GVD medium does for the pulse envelope. To illustrate this in more detail let us start with Eq. (1.191), and, for simplicity, restrict ourselves to one dimension. Throughout this section we will also omit amplitude terms and irrelevant phase terms. The field spectrum $\tilde{u}$ at a distance z is related to the field spectrum $\tilde{u}_0$ at $z = 0$:

$$\tilde{u}(k_x, z) \propto \tilde{u}_0(k_x) e^{ik_x^2 z/(2k_\ell)}, \tag{1.193}$$

which has as inverse Fourier transform the convolution product:

$$\tilde{u}(x, z) \propto \mathcal{F}^{-1}\left\{\tilde{u}_0(k_x) e^{izk_x^2/(2k_\ell)}\right\} \propto \int_{-\infty}^{\infty} \tilde{u}_0(x') e^{-i\frac{k_\ell}{2z}(x-x')^2} dx' \tag{1.194}$$

The last expression is the well known Fresnel integral.

Let us next recall Eq. (1.120), approximated to second order, which states that the spectral field envelope $\tilde{\mathcal{E}}(\Omega)$ after propagation through a length z of a transparent material with GVD is given by[3]:

$$\tilde{\mathcal{E}}(\Omega, z) \propto \tilde{\mathcal{E}}(\Omega, 0) e^{-\frac{i}{2}k_\ell'' \Omega^2 z} \tag{1.195}$$

A comparison with Eq. (1.193) clearly shows the similarity between the diffraction and the dispersion problem. The exponential phase factor $k_x^2 z/(2k_\ell)$, which describes transverse beam diffraction in space, corresponds to the exponential phase factor $-k''\Omega^2 z/2$ which describes pulse distortion in time due to dispersion. In the time domain, Eq. (1.195) also becomes a convolution integral:

$$\tilde{\mathcal{E}}(t, z) \propto \int_{-\infty}^{\infty} \tilde{\mathcal{E}}(t', 0) e^{i\frac{(t-t')^2}{2k_\ell'' z}} dt', \tag{1.196}$$

[3]Note, for easier comparison with the diffraction problem we used here coordinates (t, z) even though they refer to a frame (η, ξ) moving with the group velocity.

which shows the expected similarities with its spatial analog Eq. (1.194).

Since Eq. (1.193) corresponded to the paraxial approximation, the analogy can be carried over to successive subsets of that approximation. It will thus apply also to Gaussian optics, and the time equivalent of the Fraunhofer approximation, as will be shown in subsequent sections.

1.6.2 Time analogy of the far-field (Fraunhofer) approximation

The Fraunhofer (far-field) approximation is obtained from the Fresnel integral by simplifying the exponent in Eq. (1.194):

$$i\frac{k_\ell}{2z}(x-x')^2 \approx -ik_\ell\frac{x}{z}x' = -ik_x x' \tag{1.197}$$

yielding:

$$\tilde{u}(x,z) \propto \int_\infty^\infty \tilde{u}_0(x')e^{-ik_x x'}\,dx' \tag{1.198}$$

Note that k_x is the projection of the k_ℓ vector in the plane of observation of the diffraction pattern. Depending on the observation geometry it is related to the spatial coordinate x in the observation plane by:

- $k_x \approx k_\ell\theta_x$, where θ_x is the angle of observation,
- $k_x = k_\ell(x/z) = k_\ell\theta_x$ for an image plane at finite distance z,
- $k_x = k_\ell(x/f)$ for observation in the focal plane of a lens with focal length f.

The corresponding transition from the Fresnel to the Fraunhofer approximation in the time domain

$$\frac{i(t-t')^2}{2k''_\ell z} \approx -\frac{itt'}{k''_\ell z}, \tag{1.199}$$

yields for the field amplitude:

$$\tilde{\mathcal{E}}(\Omega',z) \propto \int_{-\infty}^\infty \tilde{\mathcal{E}}(t',0)e^{-i\frac{tt'}{k''_\ell z}}dt', \tag{1.200}$$

which is the Fourier transform of the initial field (at $z = 0$). Here the "frequency" coordinate $\Omega' = t/(k''_\ell z)$ is related to the time coordinate t at the position of observation z, which is similar to the relationship between k_x and x discussed previously. The physical meaning of this analogy is that, after propagation of long distance in a dispersive (GVD) medium, the temporal variation of any signal is given by its Fourier transform at $z = 0$. As we will see in the next section we can even use a time lens of focal length f_T to perform paraxial "time imaging". If we observe the pulse described by Eq. (1.200) after such a lens $t = \Omega' f_T/a$.

1.6.3 Analogy between spatial and temporal imaging

The analogy between pulse and beam propagation was applied to establish a time–domain analog of an optical imaging system by Kölner and Nazarathy [26]. Optical microscopy, for example, serves to magnify tiny structures so that they can be observed by a (relatively) low–resolution system such as our eyes. The idea of the "time lens" is to magnify ultrafast (fs) transients so that they can be resolved, for example, by a relatively slow oscilloscope. Of course, the opposite direction is also possible, which would lead to data compression in space or time. Figure 1.9 compares imaging in space and time using lenses.

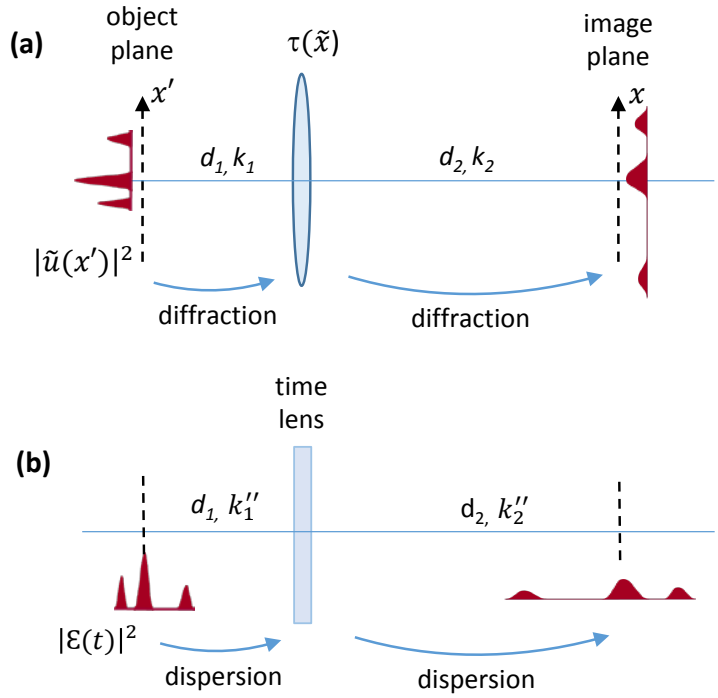

Figure 1.9: Space–time analogy of imaging. (a) Spatial imaging configuration. The "object" is a spatial intensity distribution resembling a three-pulse sequence. The "real image" shows a magnified, inverted picture. (b) The temporal imaging configuration. A GVD medium on either side of the time lens represents a dispersive length characterized by dk''. The "image" is a reversed, expanded three pulse sequence. Instead of a GVD bulk medium, grating or prism sequences can also be placed in front and behind the lens. This will be discussed in Chapter 2. (Adapted from [27].)

In the space domain, Fig. 1.9(a), we propagate the field from the object plane at $z = 0$ (transverse coordinate x') through the lens (coordinate $\tilde{x}$) to the observation

plane (coordinate x). In paraxial approximation the transfer function of a thin lens

$$\tau(\tilde{x}) = e^{ik\tilde{x}^2/(2f)} \tag{1.201}$$

adds a quadratic phase to the field at $\tilde{x}$. The two propagation steps can be described using the Fresnel integral Eq. (1.194)

$$\tilde{u}(\tilde{x}, z = d_1) \propto \int_{-\infty}^{\infty} \tilde{u}_0(x') e^{-i\frac{k_1}{2d_1}(\tilde{x}-x')^2} dx' \tag{1.202}$$

and

$$\tilde{u}(x, z = d_1 + d_2) \propto \int_{-\infty}^{\infty} \tilde{u}(\tilde{x}, z = d_1)\tau(\tilde{x}) e^{-i\frac{k_2}{2d_2}(x-\tilde{x})^2} d\tilde{x}, \tag{1.203}$$

where $k_{1,2} = 2\pi n_{1,2}/\lambda = k n_{1,2}$ are the propagation constants in the medium in front and behind the lens, respectively.

Let us evaluate this image problem for a point source in the object plane at x_0', $\tilde{u}_0(x') = u_0\delta(x' - x_0')$. This allows us to carry out the integration over x' in Eq. (1.194) to obtain $\tilde{u}(\tilde{x}, d_1)$. Inserting this result and the lens transmission function Eq. (1.201) into the second propagation integral yields

$$\tilde{u}(x, z = d_1 + d_2) \propto \int_{-\infty}^{\infty} u_0 e^{i\frac{k}{2f}\tilde{x}^2} e^{-i\frac{k_1}{2d_1}(\tilde{x}-x_0')^2} e^{-i\frac{k_2}{2d_2}(x-\tilde{x})^2} d\tilde{x}. \tag{1.204}$$

The terms of the phase ϕ in the integrand $u_0 e^{i\phi}$ can be rearranged:

$$\phi = \frac{1}{2}\left(\frac{k}{f} - \frac{k_1}{d_1} - \frac{k_2}{d_2}\right)\tilde{x}^2 + \left(\frac{k_1}{d_1}x_0' + \frac{k_2}{d_2}x\right) - \left(\frac{k_1}{2d_1}x_0'^2 + \frac{k_2}{2d_2}x^2\right) \tag{1.205}$$

Within the framework of geometric optics and the paraxial approximation the image of a point object is a point and the lens aperture (integration limits) is infinitely large. The integral Eq. (1.204) produces a Delta function

$$\tilde{u}(x, z = d_1 + d_2) \propto u_0 \int_{-\infty}^{\infty} e^{i\left(\frac{k_1}{d_1}x_0' + \frac{k_2}{d_2}x\right)\tilde{x}} d\tilde{x} \propto u_0\,\delta\left(\frac{k_1}{d_1}x_0' + \frac{k_2}{d_2}x\right) \tag{1.206}$$

if the phase term quadratic in $\tilde{x}^2$, cf. Eq. (1.205) vanishes. This requires $k_1/d_1 + k_2/d_2 = k/f$. After dividing by k we recognize the standard form of the well known imaging equation from geometric optics relating object and image distance to the focal length of the lens

$$\frac{n_1}{d_1} + \frac{n_2}{d_2} = \frac{1}{f}. \tag{1.207}$$

From the argument of the Delta function we find for the transverse magnification of an extended object $M = -n_1 d_2/(n_2 d_1)$. (Note an object extending from $x = 0$ to x_0 produces an image bounded by $x' = 0$ and x_0'.)

	diffraction	dispersion
coordinate	x	t
propagator	$e^{-i\frac{k_\ell}{2d}x^2}$	$e^{i\frac{1}{2k''_\ell d}t^2}$
	$\frac{k_\ell}{d}$	$-\frac{1}{k''_\ell d}$
lens	$e^{ik\frac{x^2}{2f}}$	$e^{-ia\frac{t^2}{2f_T}}$

Table 1.2: Corresponding terms of Fresnel diffraction and second-order dispersion (GVD).

We now want to translate the spatial imaging problem to the time domain, see Fig. 1.9(b). The equivalent of a lens with transmission function $e^{ikx^2/(2f)}$ is a quadratic phase modulator in time described by $e^{-iat^2/(2f_T)}$. Propagation (diffraction) from the object to the lens to the image plane is replaced by quadratic dispersion (GVD) in front and behind the lens. The dispersion can be introduced by propagation through a material with GVD or other optical elements as will be discussed in Chapter 2.

In principle we could now repeat the derivation of Eq. (1.207) for time imaging. Since the mathematical structure of the propagation equations in space and time are identical as pointed out previously we can simply use the equivalencies summarized in Table 1.2. After replacing the terms in the imaging equation, Eq. (1.207) we obtain for the time-lens

$$\frac{1}{d_1 k_1''} + \frac{1}{d_2 k_2''} = \frac{a}{f_T}. \tag{1.208}$$

The "magnification" in time is $M_T = -k_2'' d_2/(k_1'' d_1)$.

In this "temporal lens formula", $d_{1,2}k''_{1,2}$ are the dispersion characteristics of the object and image side, respectively, and $a/f_T = -d^2\Phi(t)/dt^2$ is the quadratic phase modulation impressed by the modulator determining the "focal length" of the time lens. As in optical imaging, to achieve large magnification with practical devices, short focal lengths are desired. For time imaging this translates into a short focal time f_T which in turn requires a suitably large phase modulation.

Note that the real image of an object can only be recognized on a screen located at a specific distance from the lens, i.e., in the image plane. At any other distance the intensity distribution visible on a screen does usually not resemble the object. Likewise, the dispersive element broadens each individual pulse (if we assume zero input chirp). It is only after the time lens and a suitably designed second dispersive element that a "pulse train" with the same contrast as the input (but stretched or compressed) emerges.

1.7 Gaussian beams and Gaussian pulses

An important particular solution of the wave equation within the paraxial approximation is the Gaussian beam (see, e.g., [28]). In order to understand better the space-time analogy for Gaussian beams/pulses, the derivation for the diffraction problem is sketched below.

1.7.1 Gaussian beams

We look for a solution to the time-free paraxial wave equation:

$$\frac{\partial \tilde{u}}{\partial z} + \frac{i}{2k_\ell}\left(\frac{\partial^2 \tilde{u}}{\partial x^2} + \frac{\partial^2 \tilde{u}}{\partial y^2}\right) = 0 \tag{1.209}$$

of the form:

$$\tilde{u}(x,y,z) = u_0 e^{-i\left[P(z)+\frac{k_\ell}{2\tilde{q}(z)}(x^2+y^2)\right]} = u_0 e^{i\Gamma} \tag{1.210}$$

The spatial derivatives needed in Eq. (1.209) are:

$$\frac{\partial \tilde{u}}{\partial z} = \left(-i\frac{dP}{dz} + i\frac{k_\ell r^2}{2\tilde{q}^2}\frac{d\tilde{q}}{dz}\right)u_0 e^{i\Gamma}, \tag{1.211}$$

and

$$\frac{\partial^2 \tilde{u}}{\partial x^2} + \frac{\partial^2 \tilde{u}}{\partial y^2} = \left(-2i\frac{k_\ell}{\tilde{q}} - \frac{k_\ell^2}{\tilde{q}^2}r^2\right)u_0 e^{i\Gamma}, \tag{1.212}$$

where $r^2 = x^2 + y^2$. Inserting the derivatives into the wave equation (1.209) and ordering with respect to terms proportional to r^0 and r^2 yields:

$$\left(-i\frac{dP}{dz} + \frac{1}{\tilde{q}}\right)r^0 u_0 e^{i\Gamma} + \frac{ik_\ell}{2\tilde{q}}\left(\frac{d\tilde{q}}{dz} - 1\right)r^2 u_0 e^{i\Gamma} = 0 \tag{1.213}$$

To satisfy this equation for all r the terms in braces must vanish. This condition produces a set of differential equations for $P(z)$ and $\tilde{q}(z)$:

$$i\frac{dP}{dz} = \frac{1}{\tilde{q}} \tag{1.214}$$

$$\frac{d\tilde{q}}{dz} = 1 \tag{1.215}$$

The last equation gives:

$$\tilde{q}(z) = q_0 + z = i\rho_0 + z \tag{1.216}$$

For reasons that will become obvious below we chose the z axis such that $\tilde{q}$ is purely imaginary at $z = 0$. We split $1/\tilde{q}$ in a real and an imaginary part:

$$\frac{1}{\tilde{q}(z)} = \frac{1}{R(z)} - \frac{i}{\rho(z)} \tag{1.217}$$

Evaluating the real and imaginary parts of Eq. (1.217) separately yields:

$$R(z) = z + \rho_0^2/z \tag{1.218}$$

and

$$\rho(z) = \rho_0(1 + z^2/\rho_0^2). \tag{1.219}$$

With $\tilde{q}(z)$ known Eq. (1.214) can now be integrated, leading to

$$P(z) = -i \ln\left(\frac{q_0 + z}{q_0}\right)$$

and

$$e^{-iP} = \frac{q_0}{q_0 + z} = \frac{1}{1 - i\frac{z}{\rho_0}} = \frac{1}{\sqrt{1 + \frac{z^2}{\rho_0^2}}} e^{i\Theta(z)}, \tag{1.220}$$

where Θ is the Guoy phase shift,

$$\Theta = \Theta(z) = \arctan(z/\rho_0). \tag{1.221}$$

$\tilde{q}(z)$ according to Eq. (1.217) and Eq. (1.220) are now inserted into our ansatz for the field, Eq. (1.210), which produces:

$$\tilde{u}(r, z) = \frac{u_0}{\sqrt{1 + z^2/\rho_0^2}} e^{-i\frac{k_\ell r^2}{2R(z)}} e^{-\frac{k_\ell r^2}{2\rho(z)}} e^{i\Theta(z)} \tag{1.222}$$

The physical meaning of the real and imaginary part of $1/\tilde{q}$ becomes clear now - $R(z)$ is the radius of curvature of the wavefront and $\rho(z)$ is related to the radius of the lateral field distribution. Often it is convenient to introduce a beam radius w at which the field has dropped to 1/e of its maximum at $r = 0$

$$w^2(z) = \frac{2}{k_\ell}\rho(z) = \frac{\lambda}{\pi}\rho(z). \tag{1.223}$$

With this substitution the Gaussian beam evolution is completely describes by

$$\tilde{u}(r, z) = u_0 \frac{w_0}{w(z)} e^{-i\frac{kr^2}{2R(z)}} e^{-\left(\frac{r}{w(z)}\right)^2} e^{i\Theta(z)} \tag{1.224}$$

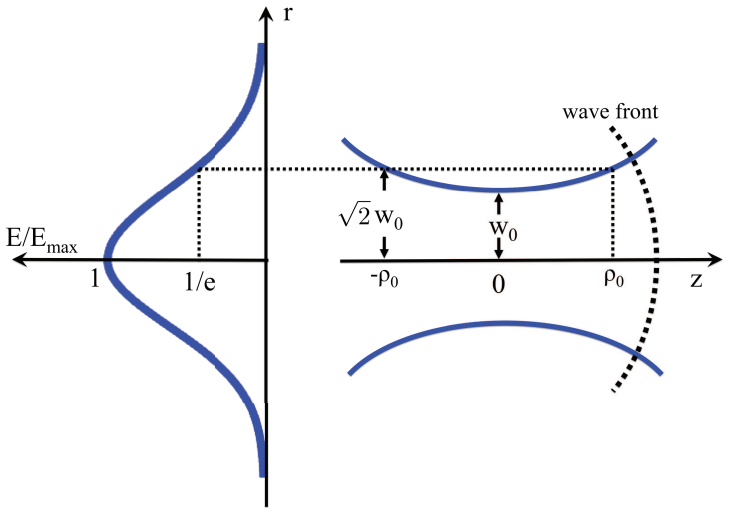

Figure 1.10: Parameters of Gaussian beams

with

$$R(z) = z\left(1 + \frac{\rho_0^2}{z^2}\right)$$

and

$$w^2(z) = w_0^2\left(1 + \frac{z^2}{\rho_0^2}\right),$$

where

$$\rho_0 = \frac{\pi}{\lambda} w_0^2$$

is the Rayleigh range with $2\rho_0$ being the confocal parameter, and w_0 is the beam waist.

Optical beams described by Eq. (1.224) exhibit a Gaussian intensity profile transverse to the propagation direction with $w(z)$ as a measure of the beam diameter, as sketched in Fig. 1.10. The origin of the z-axis ($z = 0$) is chosen to be the position of the beam waist $w_0 = w(z = 0)$. The radius of curvature of planes of constant phase is $R(z)$. Its value is infinity at the beam waist (plane phase front)[4] and at $z = \infty$. For $-\rho_0 \geq z \leq \rho_0$, the beam size is within the limits $w_0 \leq w \leq \sqrt{2}w_0$. Given the amplitude u_0 at a given beam waist and wavelength λ, the field at an arbitrary position (x, y, z) is completely predictable by means of Eqs. (1.222) to (1.224).

[4]The phase term $\Theta(z)$ in Eq. (1.222) takes on a constant value and need not be considered for $z \gg \rho_0$. A Gaussian beam at the position of its waist must not be confused with a plane wave [29].

1.7.2 Gaussian pulses

The similarity of the equations governing diffraction and pulse propagation in a GVD medium again suggest that a particular solution to the latter is a Gaussian pulse with chirp. To find such a solution to the wave equation

$$\frac{\partial\tilde{\mathcal{E}}}{\partial z}-\frac{ik''_\ell}{2}\left(\frac{\partial^2\tilde{\mathcal{E}}}{\partial t^2}\right)=0 \tag{1.225}$$

we make now an ansatz similar to Eq. (1.210) of the form

$$\tilde{\mathcal{E}}(z,t)=\mathcal{E}_0 e^{-i\left[Q+\frac{1}{2\tilde{p}}t^2\right]}. \tag{1.226}$$

The complex $\tilde{p}$ parameter replaces the complex $\tilde{q}$ parameter of Gaussian beams and, as in Eq. (1.217), is split into a sum of a real and an imaginary part:

$$\frac{1}{\tilde{p}(z)}=\frac{1}{R_T(z)}-\frac{i}{\sigma(z)}. \tag{1.227}$$

We choose the z axis such that at $z=0$ $\tilde{p}_0=i\sigma_0$ is purely imaginary ($R_T(z=0)=\infty$). Deriving the solutions for $e^{-iQ(z)}$, $R_T(z)$ and $\sigma(z)$ is straightforward with the procedure used for Gaussian beams and left to a problem at the end of this chapter. For the complex $\tilde{p}$ parameter we obtain for example:

$$\tilde{p}(z)=i\sigma_0-k''_\ell z. \tag{1.228}$$

These solutions used in Eq. (1.226) describe the propagation of a pulse with a Gaussian envelope in a GVD medium:

$$\tilde{\mathcal{E}}(z,t)=\frac{\tilde{\mathcal{E}}_0}{\sqrt[4]{1+\left(k''_\ell z/\sigma_0\right)^2}}e^{-i\frac{t^2}{2R_T(z)}}e^{-\frac{t^2}{2\sigma(z)}}e^{-\frac{i}{2}\Theta(z)} \tag{1.229}$$

with

$$R_T(z)=-k''_\ell\left[1+\frac{\sigma_0^2}{(k''_\ell z)^2}\right], \tag{1.230}$$

$$\sigma(z)=\sigma_0\left[1+\frac{(k''_\ell z)^2}{\sigma_0^2}\right], \tag{1.231}$$

and

$$\Theta(z)=\arctan\left(\frac{k''_\ell z}{\sigma_0}\right). \tag{1.232}$$

If we compare Eqs. (1.229) and (1.41) we recognize that 2σ is related to the pulse duration

$$\sigma = 2\tau_G^2 = \tau_p^2/(2\ln 2)$$

and R_T to the pulse chirp

$$\frac{1}{R_T} = -\ddot{\varphi}.$$

An unchirped pulse at $z = 0$ can only increase its duration when propagating in a GVD medium independent of the sign of k_ℓ''. This is the time equivalent of beam widening due to diffraction starting from the beam waist. The pulse develops a quadratic phase modulation (linear chirp), which corresponds to a quadratic phase factor describing a finite phase front curvature of a Gaussian beam. In the far field ($|z| \gg \rho_0$) the beam expands linearly with z. Likewise the pulse duration is proportional to z if $|k_\ell'' z| \gg \tau_{G0}$.

1.7.3 Matrices for the complex beam and pulse parameters

We saw that the complex beam parameter $\tilde{q}$ concatenates the information on beam width w and radius of curvature of the phase front R in a single complex quantity for Gaussian beams:

$$\frac{1}{\tilde{q}} = \frac{1}{R} - i\frac{\lambda}{\pi w^2} \tag{1.233}$$

Likewise the interrelated pulse parameters duration τ_G and chirp $\ddot{\varphi}$ were lumped into the complex pulse parameter $\tilde{p}$. This time equivalent of the $\tilde{q}$ parameter was:

$$\frac{1}{\tilde{p}} = -\ddot{\varphi} - \frac{2i}{\tau_G^2} \tag{1.234}$$

The propagation of Gaussian beams over distances and the action of focusing elements such as lenses and mirrors are conveniently described using 2×2 matrices known from ray optics. A sequence of such elements is the product matrix, also called system matrix. Table 1.3, second column, shows the matrix for propagation of a distance d through a medium with index n and a thin lens of focal length f.

Let us assume the Gaussian beam parameters, that is $\tilde{q}_1$, are known in a plane Σ_1. The task is to find the Gaussian beam, that is $\tilde{q}_2$, in a plane Σ_2. The two planes are separated by an optical system that can be described by an ABCD system matrix. It turns out that the complex beam parameters of input and output beam are simply related by

$$\frac{1}{\tilde{q}_2} = \frac{C + D/\tilde{q}_1}{A + B/\tilde{q}_1}. \tag{1.235}$$

From our previous discussion we expect that corresponding matrices exist that describe the modifications of a Gaussian pulse when propagating through GVD

element	space	time
distance	$\begin{pmatrix} 1 & d/n \\ 0 & 1 \end{pmatrix}$	$\begin{pmatrix} 1 & -k_\ell'' d \\ 0 & 1 \end{pmatrix}$
lens	$\begin{pmatrix} 1 & 0 \\ -1/f & 1 \end{pmatrix}$	$\begin{pmatrix} 1 & 0 \\ a/f_T & 1 \end{pmatrix}$

Table 1.3: Optical matrices for displacement and lens, and their analogs in time. Note that for the time lens $a/f_T = -\ddot{\Phi}$, where $\Phi(t)$ is a quadratic phase introduced by a modulator.

elements and (time) lenses. Indeed, we just need to substitute the corresponding quantities suggested by the imaging equations (1.207) and (1.208) and Table 1.2 in the optical matrices. The result is shown in the right column of Table 1.3.

As an example, let us analyze an "imaging" geometry similar to Fig. 1.9 now using Gaussian beams. A lens of focal length f transforms a Gaussian beam with a waist located a distance d_1 in front of it to a Gaussian beam with waist at the image distance d_2. The beam parameters just in front and behind the lens are related to each other

$$\frac{1}{\tilde{q}'} = \frac{C\tilde{q}+D}{A\tilde{q}+B} = -\frac{1}{f} + \frac{1}{\tilde{q}}, \tag{1.236}$$

where we used the elements of the lens matrix from Table 1.3. From our previous discussion, cf. Eq. (1.216), we can write the $\tilde{q}$ parameters in terms of the Rayleigh lengths ρ_0, ρ_0' and the distance to the beam waist d_1, d_2:

$$\frac{1}{\tilde{q}} = \frac{1}{i\rho_0 + d_1} \tag{1.237}$$

and

$$\frac{1}{\tilde{q}'} = \frac{1}{i\rho_0' - d_2}. \tag{1.238}$$

This together with Eq. (1.236) produces the imaging equation for Gaussian beams:

$$\frac{1}{d_1 + i\rho_0} + \frac{1}{d_2 - i\rho_0'} = \frac{1}{f} \tag{1.239}$$

Unlike in geometric optics object and image "size" (w_0 and w_0') enter explicitly through the Rayleigh range. This is a consequence of diffraction.

The equivalent situation in time is a bandwidth-limited Gaussian pulse a distance d_1 in front of a time lens (quadratic phase modulator) with equivalent focal

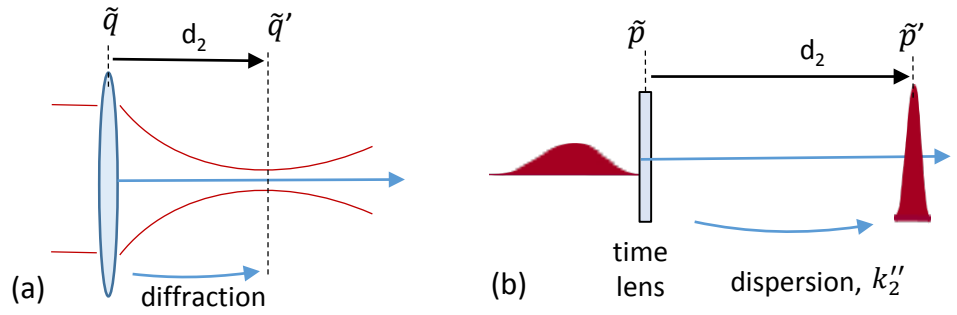

Figure 1.11: Focusing of (a) a Gaussian beam with its waist at the lens and (b) a Gaussian bandwidth-limited pulse.

"length" f_T. A Gaussian bandwidth limited pulse emerges a distance d_2 after the lens. The image equation is obtained as above using Eq. (1.228) and the right column of Table 1.3:

$$\frac{1}{k_1'' d_1 - i\sigma_0} + \frac{1}{k_2'' d_2 + i\sigma_0'} = \frac{a}{f_T} \tag{1.240}$$

Table 1.4 summarizes our comparison of Gaussian beam and pulse propagation.

As an example, Fig. 1.11 illustrates the analogy of focusing a Gaussian beam and pulse compression. Let us assume that in both cases the incident field distribution is bandwidth-limited. The complex beam, pulse parameters at the lens input - beam waist, unchirped pulse - are thus $\tilde{q} = i\rho_0$ and $\tilde{p} = -i\sigma_0$, respectively. For the case of the time-lens we obtain from Eq. (1.240) for the complex pulse parameter in the image plane:

$$\frac{1}{\tilde{p}} = \frac{1}{k_\ell'' d_2} = \frac{a}{f_T} + \frac{1}{i\sigma_0} \tag{1.241}$$

The real part of this equation yields the image distance

$$k_\ell'' d_2 = \frac{f_T}{a} \frac{1}{1 + [f_T/(a\sigma_0)]^2}, \tag{1.242}$$

and the imaginary part produces the pulse duration

$$\tau_G'^2 = 2\sigma_0' == \tau_G^2 \frac{1}{1 + \left(2a\tau_G^2/f_T\right)^2}, \tag{1.243}$$

Similarly we find the position of the beam waist after the lens to be at:

$$d_2 = f \frac{1}{1 + (f/\rho_0)^2}. \tag{1.244}$$

Gaussian pulse	**Gaussian beam**
bandwidth-limited pulse at $z = 0$ (unchirped pulse) $\tilde{\mathcal{E}}_0(t) \propto e^{-(t/\tau_{G0})^2}$ $\tilde{\mathcal{E}}_0(\Omega) \propto e^{-(\tau_{G0}\Omega/2)^2}$	beam waist at $z = 0$ (plane phase fronts) $\tilde{u}_0(x) \propto e^{-(x/w_0)^2}$ $\tilde{u}_0(k_x) \propto e^{-(k_x w_0/2)^2}$
propagation through a medium of length L (dispersion) $\tilde{\mathcal{E}}(\Omega, L) \propto \exp\left[-\left(\frac{\tau_{G0}\Omega}{2}\right)^2 - i\frac{k''_\ell L\Omega^2}{2}\right]$ $\tilde{\mathcal{E}}(t, L) \propto \exp\left[-(1+i\bar{a})\left(\frac{t}{\tau_G}\right)^2\right]$ $\propto \exp\left[-i\frac{t^2}{2\tilde{p}(L)}\right]$ $\bar{a} = L/L_d$ $\tau_G(L) = \tau_{G0}\sqrt{1+\bar{a}^2}$	free-space propagation over distance L (diffraction) $\tilde{u}(k_x, L) \propto \exp\left[-\left(\frac{w_0 k_x}{2}\right)^2 + i\frac{L{k_x}^2}{2k_\ell}\right]$ $\tilde{u}(x, L) \propto \exp\left[-(1+i\bar{b})\left(\frac{x}{w}\right)^2\right]$ $\propto \exp\left[-ik_\ell\frac{x^2}{2\tilde{q}(L)}\right]$ $\bar{b} = L/\rho_0$ $w(L) = w_0\sqrt{1+\bar{b}^2}$
chirp coefficient (slope) $\ddot{\varphi} = \frac{2\bar{a}}{1+\bar{a}^2}\,\frac{1}{\tau_{G0}^2}$	wavefront curvature $\frac{1}{R} = \frac{\bar{b}}{1+\bar{b}^2}\,\frac{1}{\rho_0}$
characteristic (dispersion) length $L_d = \frac{\tau_{G0}^2}{2k''_\ell}$	characteristic (Rayleigh) length $\rho_0 = \frac{n\pi w_0^2}{\lambda_\ell} = \frac{k_\ell w_0^2}{2}$
complex pulse parameter $\frac{1}{\tilde{p}(L)} = -\ddot{\varphi}(L) - \frac{2i}{\tau_G^2(L)}$	complex beam parameter $\frac{1}{\tilde{q}(L)} = \frac{1}{R(L)} - \frac{i\lambda_\ell}{\pi w^2(L)}$
transformation of $\tilde{p}$ between conjugate planes of a time lens (transfer function $e^{-iat^2/(2f_T)}$) $\frac{1/k''_1}{d_1 - iL_d} + \frac{1/k''_2}{d_2 + iL'_d} = \frac{a}{f_T}$	transformation of $\tilde{q}$ between conjugate planes of a lens (transfer function $e^{ikr^2/(2f)}$) $\frac{n_1}{d_1 + i\rho_0} + \frac{n_2}{d_2 - i\rho'_0} = \frac{1}{f}$

Table 1.4: Comparison of Gaussian pulses and Gaussian beams: dispersion versus diffraction

In both cases the image planes are not in the focal planes of the lenses, but further away from the lens. This is contrary to the geometric optics case discussed previously, cf. Eqs. (1.207) and (1.208). If self-diffraction can be neglected over the focal distance, $\rho_0 \gg f$, we reproduce $d_2 = f$. The corresponding condition for the time lens is that the pulse duration is much larger than the "focal time" of the lens (modulator), $\tau_G \gg \sqrt{f_T/a}$.

Figure 1.11 and Eq. (1.243) suggest the possibility of pulse compression, which will be discussed in detail in later chapters. The time-lens (modulator) impresses a linear chirp onto the bandwidth-limited input pulse resulting in spectral broadening while keeping the pulse duration unchanged. The bandwidth in excess over the Fourier limit allows the pulse to shorten while propagating through the dispersive medium on the image side until it reaches the image plane where it is bandwidth-limited again but of shorter duration. The conjugate (image) plane is to the right of the lens only if a/f_T and k''_ℓ have the same sign. If the lens produces up (down) chirp, negative (positive) GVD on the image side is necessary for chirp compensation.

In practice, electronically driven modulators are not able to reach the modulation speeds and amplitudes required for shaping fs pulses. One possible approach to create a large phase modulation is cross-phase modulation, in which a properly shaped powerful "pump" pulse creates a large index sweep (quadratic with time) in the material of the "time lens". Another approach is to use sum or difference frequency generation to impart the linear chirp of one pulse into the pulse to be "imaged". The linear chirp can be obtained by propagating of a strong pulse through a fiber. A detailed review of this "parametric temporal imaging" can be found in refs. [27,30]. The time-equivalent of a long propagation distance (large diffraction) is a large dispersion, which can be obtained with a pair of gratings, see Chapter 2.

While we treated here dispersion and diffraction separately they occur simultaneously when pulses propagate. We will discuss this and the corresponding optical matrices in Chapter 2.

1.8 Space–time effects in non-dispersive media

For very short pulses a coupling of spatial and temporal effects becomes important even for propagation in a nondispersive medium. The physical reason is that self–diffraction of a beam of finite transverse size (e.g., Gaussian beam) is wavelength dependent. A separation of time and frequency effects according to Eqs. (1.188) and (1.189) is clearly not feasible if such processes matter. One can construct a solution by solving the diffraction integral (1.192) for each spectral component. The superposition of these solutions and an inverse Fourier–transform then yields

the temporal field distribution. Starting with a field $\tilde{E}(x',y',\Omega) = \mathcal{F}\left\{\tilde{E}(x',y',t)\right\}$ in a plane $\Sigma'(x',y')$ at $z = 0$ we find for the field in a plane $\Sigma(x,y)$ at $z = L$:

$$\begin{aligned}\tilde{E}(x,y,L,t) &= \mathcal{F}^{-1}\left\{\frac{i\Omega e^{-i\Omega L/c}}{2\pi cL}\int\int dx'dy'\,\tilde{E}(x',y',\Omega)\right. \\ &\left.\times\exp\left[-i\frac{\Omega}{2Lc}\left((x-x')^2+(y-y')^2\right)\right]\right\} \qquad (1.245)\end{aligned}$$

where we have assumed a nondispersive medium with refractive index $n = 1$. Solutions can be found by solving numerically Eq. (1.245) starting with an arbitrary pulse and beam profile at a plane $z = 0$. Properties of these solutions were discussed by Christov [31]. They revealed that the pulse becomes phase modulated in space and time with a pulse duration that changes across the beam profile. Due to the stronger diffraction of long–wavelength components the spectrum on axis shifts to shorter wavelengths.

For a Gaussian beam and pulse profile at $z = 0$, i.e.,

$$\tilde{E}(x',y',0,t) \propto \exp\left(-r'^2/w_0^2\right)\exp\left(-t^2/\tau_{G0}^2\right)\exp(i\omega_\ell t)$$

with $r'^2 = x'^2 + y'^2$, the time–space distribution of the field at $z = L$ is of the form [31]:

$$\tilde{E}(r,z=L,t) \propto \exp\left(-\frac{\eta^2}{\tau_G^2}\right)\exp\left[\left(-\frac{w_0\omega_\ell\tau_{G0}}{2Lc\tau_G}r\right)^2\right]\exp\left(i\frac{\omega_\ell\tau_{G0}^2}{\tau_G^2}\eta\right) \qquad (1.246)$$

where

$$\tau_G^2 = \tau_{G0}^2 + [w_0 r/(Lc)]^2 \qquad (1.247)$$

and $\eta = \left[t - L/c - r^2/(2Lc)\right]$. This result shows a complex mixing of spatial and temporal pulse and beam characteristics. The first term in Eq. (1.246) indicates a pulse duration that increases with increasing distance r from the optical axis. For an order of magnitude estimation let us determine the input pulse duration τ_{G0} at which the pulse duration has increased to $2\tau_{G0}$ at a radial coordinate $r = w$ after the beam has propagated over a certain distance $L >> \rho_0$. From Eq. (1.247) this is equivalent to $\tau_{G0} = w_0 r/(Lc)$. For $r = w$ with $w \approx L\lambda/(\pi w)$, cf. Eq. (1.219), the pulse duration becomes $\tau_{G0} \approx \lambda/(\pi c)$. Obviously, these effects become only important if the pulses approach the single-cycle regime.

Problems

1. Verify the c_B factors of the pulse–duration–bandwidth–product of a Gaussian and sech-pulse as given in Table 1.1.

2. Calculate the pulse duration $\bar{\tau}_p$ defined as the second moment in Eq. (1.57) for a Gaussian pulse and compare with τ_p (FWHM).

3. Consider a medium consisting of particles that can be described by harmonic oscillators so that the linear susceptibility in the vicinity of a resonance is given by Eq. (1.165). Investigate the behavior of the phase and group velocity in the absorption region. You will find a region where $v_g > v_p$. Is the theory of relativity violated here?

4. Assume a Gaussian pulse which is linearly chirped in a phase modulator that leaves its envelope unchanged. The chirped pulse is then sent through a spectral amplitude–only filter of spectral width (FWHM) $\Delta\omega_F$. Calculate the duration of the filtered pulse and determine an optimum spectral width of the filter for which the shortest pulses are obtained. (Hint: For simplification you may assume an amplitude only filter of Gaussian profile, i.e., $\tilde{H}(\omega-\omega) = \exp\left[-\ln 2\left(\frac{\omega-\omega}{\Delta\omega_F}\right)^2\right]$.)

5. Derive the general expression for $d^n/d\Omega^n$ in terms of derivatives with respect to λ.

6. Assume that both the temporal and spectral envelope functions $\mathcal{E}(t)$ and $\mathcal{E}(\Omega)$, respectively, are peaked at zero. Let us define a pulse duration τ_p^* and spectral width $\Delta\omega_p^*$ using the electric field and its Fourier transform by

$$\tau_p^* = \frac{1}{|\mathcal{E}(t=0)|}\int_{-\infty}^{\infty}|\mathcal{E}(t)|dt$$

and

$$\Delta\omega_p^* = \frac{1}{|\mathcal{E}(\Omega=0)|}\int_{-\infty}^{\infty}|\mathcal{E}(\Omega)|d\Omega.$$

Show that for this particular definition of pulse duration and spectral width the uncertainty relation reads

$$\tau_p^*\Delta\omega_p^* \geq 2\pi.$$

7. Derive Eqs. (1.71) and (1.72). Hint: Make use of Parsival's theorem

$$2\pi\int_{-\infty}^{\infty}|f(t)|^2dt = \int_{-\infty}^{\infty}|f(\Omega)|^2d\Omega$$

and the fact that $\mathcal{F}\{tf(t)\} = -i\frac{d}{d\Omega}\mathcal{F}\{f(t)\}$.

8. Repeat the steps shown in the text for Gaussian beam propgation to derive the equivalent relations for Gaussian pulses, Eqs. (1.229) to (1.232).

9. A polarization — to second order in the electric field — is defined as $P^{(2)}(t) \propto \chi^{(2)} E^2(t)$. We have seen that the preferred representation for the field is the complex quantity $E^+(t) = \frac{1}{2}\mathcal{E}(t)\exp[i(\omega t + \varphi(t)]$. Give a convenient description of the nonlinear polarization in terms of $E^+(t)$, $\mathcal{E}(t)$ and $\varphi(t)$. Consider in particular second harmonic generation and optical rectification. Explain the physics associated with the various terms of $P^{(2)}$ (or $P^{+(2)}$, if you can define one).

10. Starting from the one–dimensional wave equation (1.80), show that the slowly–varying envelope approximation corresponds essentially to neglecting self-induced reflection.

Bibliography

[1] Matt Bohn and J.-C. Diels. Optimizing the frequency in dithered laser gyroscopes. *Optics Communication*, 213:331–337, 2002.

[2] S. Haykin. *Communication systems*. John Wiley & Sons., New York, 2000.

[3] M. Conforti, F. Baronio, and C. De Angelis. Nonlinear envelope equation for broadband optical pulses in quadratic media. *Physical Review A*, 81:053841, 2010.

[4] D. T. Reid. Ultra-broadband pulse evoluton in optical parametric oscillators. *Optics Express*, 19:17979–17984, 2011.

[5] A. S. Kowligy, A. Lind, D. Hickstein, D. R. Carlson, H. Timmers, N. Nader, F. C. Cruz, G.Ycas, S. B. Papp, and Scott A. Diddams. Mid-infrared frequency comb generation via cascaded quadratic nonlinearities in quasi-phase-matched waveguides. *Optics Letters*, 43:1678–1680, 2018.

[6] Eugene Hecht and Alfred Zajac. *Optics*. Addison-Wesley, ISBN 0-201-11609-X, Menlo Park, California, 1987.

[7] Willian H. Press, Brian P. Flannery, Saul E. Teukolsky, and William P. Vetterling. *Numerical Recipes*. Cambridge University Press, New York, 1986.

[8] E. Wigner. On the quantum correction for thermodynamic equilibrium. *Phys. Review*, 40:749–749, 1932.

[9] J. Ville. Theorie et applications de la notion de signal analytique. *Cables et transmissions*, 2A:61–74, 1948.

[10] W. P. Schleich. *Quantum Optics in Phase Space*. Wiley-VCH, Weinheim, 2001.

[11] L. Cohen. *Time-frequency analysis, theory and applications*. Prentice-Hall signal processing series, 1995.

[12] L. Praxmeier and K. Wókiewicz. Time and frequency description of optical pulses. *arXiv:physics*, 0502079v2:1–12, 2005.

[13] A.W. Lohmann and B.H. Soffer. Relationships between the radon-wigner and fractional fourier transforms. *J. of Optical Society of America A*, 11:1798, 1994.

[14] M.G. Raymer and D.F. McAlister M. Beck. Complex wave-field reconstruction using phase-space tomography. *Physical Review Letters*, 72:1137, 1994.

[15] H.M. Ozaktas and D. Mendlovic. Fourier transforms of fractional order and their optical interpretation. *Optics Comm.*, 101:163, 1993.

[16] Anthony E. Siegman. *Lasers*. University Science Books, Mill Valley, CA, 1986.

[17] J. D. Jackson. *Classical Electrodynamics*. John Wiley & Sons, New York, 1975.

[18] M. Born and E. Wolf. *Principles of Optics – Electromagnetic theory of propagation, interference and diffraction of light*. Pergamon Press, Oxford, New York, 1980.

[19] Y. R. Shen. *The Principles of Nonlinear Optics*. John Wiley & Sons, New York, 1984.

[20] M. Schubert and B. Wilhelmi. *Nonlinear Optics and Quantum Electronics*. John Wiley & Sons, New York, 1978.

[21] Robert W. Boyd. *Nonlinear optics*. Academic Press, third edition, 2008.

[22] J. C. Eilbeck and R. K. Bullough. The method of characteristics in the theory of resonant or nonresonant nonlinear optics. *Journal of Physics A: General Physics*, 5:820–830, 1972.

[23] J. C. Eilbeck, J. D. Gibbon, P. J. Caudrey, and R. K. Bullough. Solitons in nonlinear optics i: A more accurate description of the 2π pulse in self-induced transparency. *Journal of Physics A: Mathematical, Nuclear and General*, 6:1337–1345, 1973.

[24] Kamke. *Differentialgleichungen*. Geest and Portig, Leipzig, 1969.

[25] G. P. Agrawal. *Nonlinear Fiber Optics*. Academic Press, ISBN 0-12-045142-5, Boston, 1995.

[26] B. H. Kolner and M. Nazarathy. Temporal imaging with a time lens. *Optics Lett.*, 14:630–632, 1989.

[27] C. V. Bennett and B. H. Kolner. Principles of parametric temporal imaging, part ii: system performance. *IEEE Journal of Quantum Electronics*, 36:649–655, 2000.

[28] H. W. Kogelnik and T. Li. Laser beams and resonators. *Appl. Opt.*, 5:1550–1567, 1966.

[29] C. r. qUICK and h. c. bRYANT. Excitation of atoms passing through a TEM_{00} Gaussian laser beam at relativistic velocities. *Journal of the Optical Society of America B*, 7:708–714, 2014.

[30] C. V. Bennett and B. H. Kolner. Principles of parametric temporal imaging, part i: system configurations. *IEEE Journal of Quantum Electronics*, 36:430–437, 2000.

[31] I. P. Christov. Propagation of femtosecond light pulses. *Optics Commun.*, 53:364–367, 1985.

TO CHIRP OR NOT TO CHIRP ...

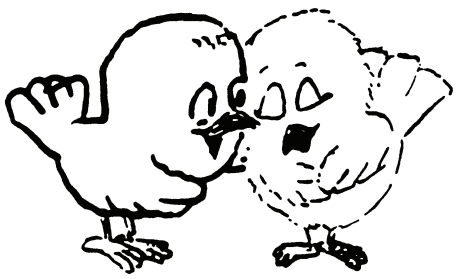

... THAT IS THE CHALLENGE

Chapter 2

Femtosecond Optics

2.1 Introduction

Whether short pulses or continuous radiation, light should follow the rules of "classical optics". There are, however, some properties related to the bending, propagation, and focalization of light that are specific to fs pulses. Ultrashort pulses are more "unforgiving" of some "defects" of optical systems, as compared to ordinary light of large spectral bandwidth, i.e., white light.[1] Studying optical systems with fs pulses helps in turn to improve the understanding and performances of these systems in white light. We will study properties of basic elements (coatings, lenses, prisms, gratings) and some simple combinations thereof. The dispersion of the index of refraction is the essential parameter for most of the effects to be discussed in this chapter. Some values are listed for selected optical materials in Table 2.1. As already noted in Chapter 1, the second derivative of the index of refraction is positive over the visible spectrum for most transparent materials, corresponding to a positive group velocity dispersion (GVD). There is a sign reversal of the GVD in fused silica around 1.3 μm, which has led to zero dispersion or negative dispersion fibers.

Often a transparent material will be characterized by a fit of the index of refraction as a function of wavelength. Values for most nonlinear materials can be found in ref. [1]. A common form is the Sellmeier equation:

$$n^2(\lambda_\ell) = 1 + \frac{B_1\lambda_\ell^2}{\lambda_\ell^2 - C_1} + \frac{B_2\lambda_\ell^2}{\lambda_\ell^2 - C_2} + \frac{B_3\lambda_\ell^2}{\lambda_\ell^2 - C_3} \tag{2.1}$$

[1] Such light can be regarded as superposition of random fluctuations (short light pulses), the mean duration of which determines the spectral width. A measurement of the light intensity, however, averages over these fluctuations.

In the case of fused silica, the parameters are[1]:

$$\begin{array}{ll} B_1 & 6.96166300 \cdot 10^{-1}\ \mu\mathrm{m}^{-2} \\ B_2 & 4.07942600 \cdot 10^{-1}\ \mu\mathrm{m}^{-2} \\ B_3 & 8.97479400 \cdot 10^{-1}\ \mu\mathrm{m}^{-2} \\ C_1 & 4.67914826 \cdot 10^{-3}\ \mu\mathrm{m}^{2} \\ C_2 & 1.35120631 \cdot 10^{-2}\ \mu\mathrm{m}^{2} \\ C_3 & 9.79340025 \cdot 10^{+1}\ \mu\mathrm{m}^{2} \end{array}$$

with the wavelength λ_ℓ expressed in microns. Another example of a possible fit function is the Laurent series formula:

$$n^2(\lambda_\ell) = A + B\lambda_\ell^2 + \frac{C}{\lambda_\ell^2} + \frac{D}{\lambda_\ell^4} + \frac{E}{\lambda_\ell^6} + \frac{F}{\lambda_\ell^8} \tag{2.2}$$

For crystalline quartz with extraordinary and ordinary index n_e and n_o, respectively, the parameters are[2]:

Parameter	for n_e	for n_o	Unit
A	$2.38490000 \cdot 10^{+0}$	$2.35728000 \cdot 10^{+0}$	
B	$-1.25900000 \cdot 10^{-2}$	$-1.17000000 \cdot 10^{-2}$	$\mu\mathrm{m}^{-2}$
C	$1.07900000 \cdot 10^{-2}$	$1.05400000 \cdot 10^{-2}$	$\mu\mathrm{m}^{2}$
D	$1.65180000 \cdot 10^{-4}$	$1.34143000 \cdot 10^{-4}$	$\mu\mathrm{m}^{4}$
E	$-1.94741000 \cdot 10^{-6}$	$-4.45368000 \cdot 10^{-7}$	$\mu\mathrm{m}^{6}$
F	$9.36476000 \cdot 10^{-8}$	$5.92362000 \cdot 10^{-8}$	$\mu\mathrm{m}^{8}$

The wavelength λ_ℓ being expressed in microns.

An interesting material for its very high index in the visible–near infrared is ZnS. The first and second order dispersion are plotted in Fig. 2.1.

We shall start this chapter with an analysis of a simple Michelson interferometer.

2.2 White light and short pulse interferometry

Incoherent radiation has received increasing attention as the poor man's fs source (even the wealthiest experimentalist will now treat bright incoherent sources with a certain amount of deference). The similarities between white light and femtosecond light pulses are most obvious when studying coherence properties, but definitely transcend the field of coherent interactions.

[2]The values for fused silica and quartz are courtesy of CVI, Albuquerque, New Mexico (www.cvi.com).

material	λ_ℓ	$n(\omega_\ell)$	$n'(\omega_\ell)$ 10^{-2}	$n'(\lambda_\ell)$ 10^{-2}	$n''(\omega_\ell)$ 10^{-3}	$n''(\lambda_\ell)$	$n'''(\omega_\ell)$ 10^{-4}	$n'''(\lambda_\ell)$
	[nm]		[fs]	[μm^{-1}]	[fs^2]	[μm^{-2}]	[fs^3]	[μm^{-3}]
BK7	400	1.5307	1.13	-13.	3.0	1.10	6.9	-12.
	500	1.5213	0.88	-6.6	2.3	.396	7.7	-3.5
	620	1.5154	0.75	-3.6	1.6	.150	13	-1.1
	800	1.5106	0.67	-2.0	0.06	0.05	39	-.29
	1000	1.5074	0.73	-1.4	-3.2	0.016	114	-.09
SF6	400	1.8674	5.8	-67.	30	7.40	214	-120
	500	1.8236	3.7	-28.	16	2.00	86	-21.
	620	1.8005	2.7	-13.	12	.70	50	-5.3
	800	1.7844	2.0	-5.9	8	.22	56	-1.2
	1000	1.7757	1.71	-3.2	4	0.08	115	-.36
SF10	400	1.7784	4.6	-54.	24	5.9	183	-98.
	500	1.7432	3.0	-22.	13	1.6	69	-17.
	620	1.7244	2.2	-11.	9	.56	42	-4.2
	800	1.7112	1.7	-5.0	6	.17	58	-1.0
	1000	1.7038	1.5	-2.8	2	0.06	132	-0.3
SF14	400	1.8185	5.3	-62.	27	6.8	187	-10.9
	500	1.7786	2.8	-25.	15	1.9	85	-2.0
	620	1.7576	2.5	-12.	10	.63	50	-4.8
	800	1.7430	1.8	-5.5	7	.20	54	-1.1
	1000	1.7349	1.6	-3.0	3.4	0.072	110	-.33
SQ1	248	1.5121	2.36	-72.	11	15.	76	-520.
	308	1.4858	1.35	-27.	4.1	3.3	23	-66.0
	400	1.4701	0.93	-11.	2.3	.86	6	-9.80
	500	1.4623	0.73	-5.5	1.8	.32	6	-2.80
	620	1.4574	0.62	-3.0	1.2	.13	13	-0.89
	800	1.4533	0.58	-1.7	-0.4	0.04	41	-0.24
	1000	1.4504	0.67	-1.3	-3.8	0.012	121	-0.08
	1300	1.4469	1.0	-1.1	-14	-.0003	446	-0.02
	1500	1.4446	1.4	-1.2	-27	-.0031	915	-0.01
LaSF9	620	1.8463	2.28	-11.2	9.04	.50		
	800	1.8326	1.76	-5.20	5.79	.17		
ZnSe	620	2.586	14.24	-30.	117.3	2.0		-15.
	800	2.511	8.35	-15.	63.3	0.69		-3.

Table 2.1: Dispersion parameters for some optical materials. BK7 is the most commonly used optical glass. The SF... are dispersive heavy flint glasses. SQ1 is fused silica. The dispersion parameters for the glasses were calculated with Sellmeir's equations and data from various optical catalogs. The data for the UV wavelengths must be considered as order of magnitude approximations. The ZnSe data are taken from Ref. [2]. Using Eqs. (1.124)–(1.128), the dispersion values given in terms of $n(\Omega)$ can easily be transformed into the corresponding values for $k(\Omega)$.

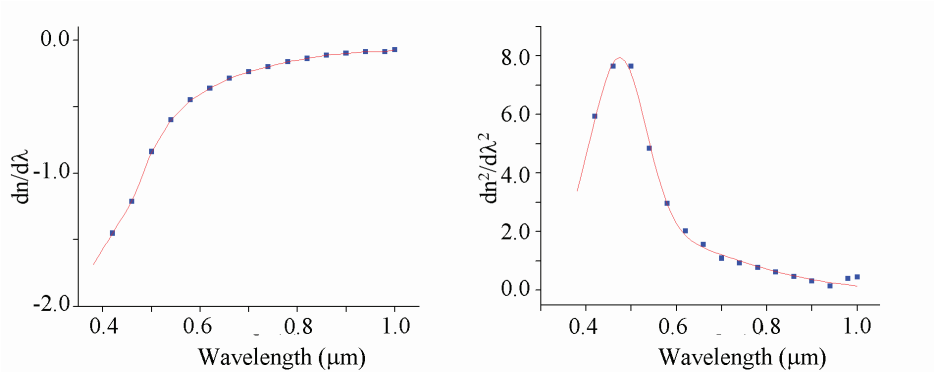

Figure 2.1: First order dispersion in μm^{-1} (left) and second order dispersion in μm^{-2} (right) of ZnS.

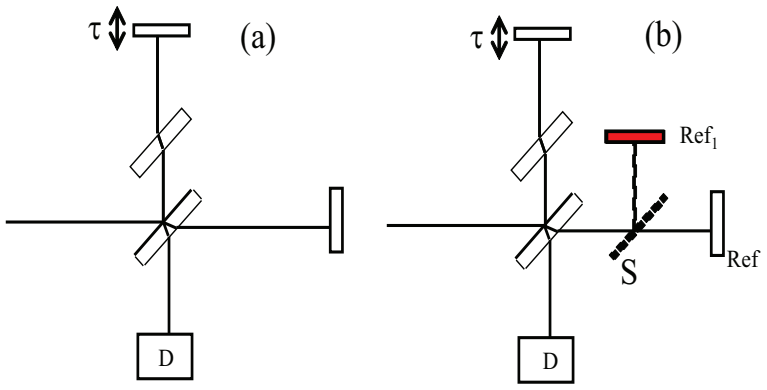

Figure 2.2: Left: balanced Michelson interferometer. Right: for the measurement of mirror dispersion, a reflecting sample is inserted between the beam splitter and the reference mirror Ref. (dotted line). The deflected beam is shown as a dashed line orthogonal to the displaced reference mirror Ref$_1$.

Let us consider the basic Michelson interferometer sketched in Fig. 2.2. The *real* field on the detector, resulting from the interferences of E_1 and E_2, is $E = E_1(t-\tau)+E_2(t)$ with τ being the delay parameter. The intensity at the output of the interferometer is given by the electric field squared averaged over one light period

T [Eq. (1.29)]:

$$\begin{aligned} I(t,\tau) &= \epsilon_0 cn \frac{1}{T}\int_{t-T/2}^{t+T/2} [E_1(t'-\tau)+E_2(t')]^2 dt' \\ &= 2\epsilon_0 cn[\tilde{E}_1^+(t-\tau)+\tilde{E}_2^+(t)][\tilde{E}_1^-(t-\tau)+\tilde{E}_2^-(t)] \\ &= \frac{1}{2}\epsilon_0 cn\Big\{\mathcal{E}_1^2(t-\tau)+\mathcal{E}_2^2(t) \\ &\quad + \tilde{\mathcal{E}}_1^*(t-\tau)\tilde{\mathcal{E}}_2(t)e^{i\omega_\ell\tau}+\tilde{\mathcal{E}}_1(t-\tau)\tilde{\mathcal{E}}_2^*(t)e^{-i\omega_\ell\tau}\Big\}. \end{aligned} \tag{2.3}$$

Here again, we have chosen to decompose the field in an amplitude function $\tilde{\mathcal{E}}$ and a phase function centered around a somewhat arbitrary average frequency of the radiation, ω_ℓ, as in Eqs. (1.18) and (1.19).

The actual signal recorded at the output of the interferometer is the intensity, $\bar{I}$, averaged over the response time τ_R of the detector. In the case of ultrashort pulses $\tau_R \gg \tau_p$ holds and what is being measured is the time integral $\int_{-\infty}^{+\infty} I(t',\tau)dt'$. We will use the notation $\langle\ \rangle$ for either integration or averaging, which results in a quantity that is time independent. Assuming thus that all fluctuations of the signal are averaged out by the detector's slow response, the measured signal reduces to the following expression:

$$\boxed{\begin{aligned} \bar{I}(\tau) &= \frac{\epsilon_0 cn}{4}\Big\{\langle\tilde{\mathcal{E}}_1^2\rangle+\langle\tilde{\mathcal{E}}_2^2\rangle+\Big\langle\tilde{\mathcal{E}}_1^*(t-\tau)\tilde{\mathcal{E}}_2(t)e^{i\omega_\ell\tau}+\tilde{\mathcal{E}}_1(t-\tau)\tilde{\mathcal{E}}_2^*(t)e^{-i\omega_\ell\tau}\Big\rangle\Big\} \\ &= \epsilon_0 cn\Big\{A_{11}(0)+A_{22}(0)+\tilde{A}_{12}^+(\tau)+\tilde{A}_{12}^-(\tau)\Big\}. \end{aligned}} \tag{2.4}$$

On the right hand side of the first line in Eq. (2.4) we recognize correlation functions similar to that in Eq. (1.39), except that they involve the electric fields rather than the intensities. In complete analogy with the definitions of the complex electric fields, the two complex functions correspond to positive and negative spectral components[3] of a correlation function $A_{12}(\tau) = \tilde{A}_{12}^+(\tau)+\tilde{A}_{12}^-(\tau)$, where, e.g., the positive frequency component is defined as:

$$\begin{aligned} \tilde{A}_{12}^+(\tau) &= \frac{1}{4}\langle\tilde{\mathcal{E}}_1^*(t-\tau)\tilde{\mathcal{E}}_2(t)e^{i\omega_\ell\tau}\rangle \\ &= \frac{1}{2}\tilde{\mathcal{A}}_{12}(\tau)e^{i\omega_\ell\tau} \end{aligned} \tag{2.5}$$

The Fourier transform of the correlation of two functions is the product of the Fourier transforms [3]:

[3] Spectrum is defined here with respect to the conjugate variable of the delay parameter τ.

$$\begin{aligned}\tilde{A}^{+}_{12}(\Omega) &= \int_{-\infty}^{\infty}\tilde{A}^{+}_{12}(\tau)e^{-i\Omega\tau}d\tau = \int_{-\infty}^{\infty}\tilde{\mathcal{A}}_{12}(\tau)e^{-i(\Omega\tau-\omega_\ell)}d\tau \\ &= \frac{1}{4}\tilde{\mathcal{E}}^{*}_{1}(\Omega-\omega_\ell)\tilde{\mathcal{E}}_{2}(\Omega-\omega_\ell) \\ &= \tilde{E}^{*}_{1}(\Omega)\tilde{E}_{2}(\Omega) \end{aligned} \tag{2.6}$$

In the ideal case of infinitely thin beam splitter, nondispersive broadband reflectors and beam splitters, $\tilde{E}_1 = \tilde{E}_2$, and the Fourier transform (2.6) is real. Correspondingly, the correlation defined by Eq. (2.5) is an electric field autocorrelation which is a symmetric function with respect to the delay origin $\tau = 0$. This fundamental property is of little practical importance when manipulating data from a real instrument, because, in the optical time domain, it is difficult to determine exactly the "zero delay" point, which requires measurement of the relative delays of the two arms with an accuracy better than 100 Å. It is therefore more convenient to use an arbitrary origin for the delay τ, and use the generally complex Fourier transformation of Eq. (2.6).

For an ideally balanced interferometer, the output from the two arms is identical, and the right–hand side of Eq. (2.6) is simply the spectral intensity of the light. This instrument is therefore referred to as a Fourier spectrometer.

Let us turn our attention to the slightly "unbalanced" Michelson interferometer. For instance, with a single beam splitter of finite thickness d', the beam 2 will have traversed $L = d'/\cos(\theta_r) = d$ (θ_r being the angle of refraction) more glass than beam 1 (Fig. 2.2). It is well known that the "white light" interference fringes are particularly elusive, because of the short coherence length of the radiation, which translates into a very restricted range of delays over which a fringe pattern can be observed. How will that fringe pattern be modified and shifted by having one beam traverse a path of length $2d$ in glass rather than in air (assumed here to be dispersionless)? Let $\tilde{E}_1(t)$ refer to the field amplitude at the detector, corresponding to the beam that has passed through the unmodified arm with the least amount of glass. Using Eq. (1.177) with $R = 1$, $\Psi(\Omega) = k(\Omega)L$ and considering only terms with $n \leq 2$ in the expansion of Ψ, cf. Eq. (1.179), we find the second beam through the simple transformation:

$$\begin{aligned}\tilde{E}_2(\Omega) &= \tilde{E}_1(\Omega)\exp\{-iL[k(\Omega)-\Omega/c]\} \\ &\approx \tilde{E}_1(\Omega)\exp\left\{-i\left[\left(k_\ell-\frac{\Omega}{c}\right)L + k'_\ell L(\Omega-\omega_\ell) + \frac{k''_\ell L}{2}(\Omega-\omega_\ell)^2\right]\right\}\end{aligned} \tag{2.7}$$

where, as outlined earlier, $(k'_\ell)^{-1} = \left(\left[\frac{dk}{d\Omega}\right]_{\omega_\ell}\right)^{-1}$ determines the group velocity of a

wave packet centered around ω_ℓ and $k''_\ell = \left[\frac{d^2k}{d\Omega^2}\right]_{\omega_\ell}$ is responsible for group velocity dispersion (GVD). The time dependent electric field is given by the Fourier transform of Eq. (2.7). Neglecting GVD we find for the complex field envelope:

$$\tilde{\mathcal{E}}_2(t) = e^{-i(k_\ell + k'_\ell \omega_\ell)L} \tilde{\mathcal{E}}_1 \left[t - (k'_\ell - 1/c)L\right]. \tag{2.8}$$

Apart from an unimportant phase factor the obvious change introduced by the glass path in one arm of the interferometer is a shift of time origin, i.e., a shift of the maximum of the correlation. This is a mere consequence of the longer time needed for light to traverse glass instead of air. The shift in "time origin" measured with the "unbalanced" versus "balanced" Michelson is

$$\begin{aligned} \Delta\tau &= \left(k'_\ell - \frac{1}{c}\right)L \\ &= \frac{L}{c}\left\{(n-1) + \omega_\ell \left[\frac{dn}{d\Omega}\right]_{\omega_\ell}\right\} \\ &= \frac{L}{c}\left\{(n-1) - \lambda_\ell \left[\frac{dn}{d\lambda}\right]_{\lambda_\ell}\right\}, \end{aligned} \tag{2.9}$$

where we replaced k'_ℓ by Eq. (1.127). The first term in the right-hand side of the second and third equation represents the temporal delay resulting from the difference of the optical pathlength in air ($n \approx 1$) and glass. The second term contains the contribution from the group velocity in glass. In the above derivation, we have not specifically assumed that the radiation consists of short pulses. It is also the case for white light continuous wave (cw) radiation that the group velocity contributes to the shift of zero delay introduced by an unbalance of dispersive media between the two arms of the interferometer.

The third (and following) terms of the expansion of $k(\Omega)$ account for the deformation of the fringe pattern observed in the recording of Fig. 2.3. The propagation can be more easily visualized in the time domain for fs pulses. The group velocity delay is due to the pulse envelope "slipping" with respect to the waves. The group velocity *dispersion* causes different parts of the pulse spectrum to travel at different velocity, resulting in pulse deformation. The result of the Michelson interferogram is a cross-correlation between the field amplitude of the "original" pulse and the signal propagated through glass.

The same considerations can be applied to white light, which can be viewed as a temporal random distribution of ultrashort pulses. The concept of incoherent radiation being constructed out of a statistical time sequence of ultrashort pulses is also useful for studying coherence in light–matter interactions, as will be studied in detail in Chapter 3 on coherent interactions.

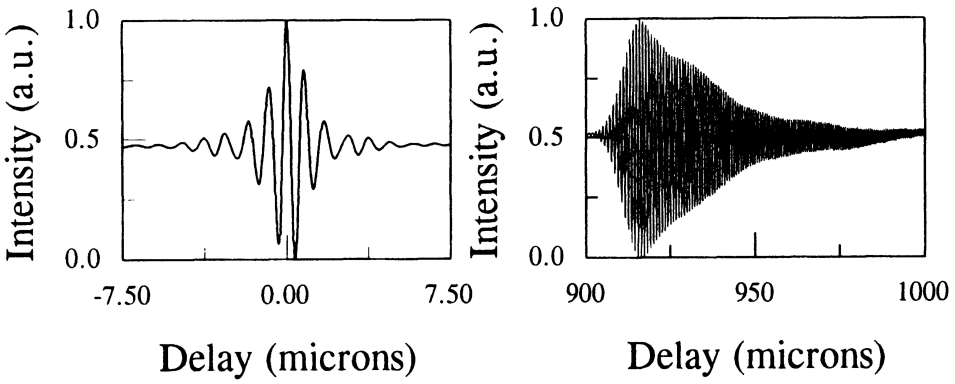

Figure 2.3: "White light" Michelson interferogram. The fringes of the balanced interferometer are shown on the left. The fringe pattern shifts to the right and is broadened by the insertion of a thin quartz plate in one arm of the interferometer.

The correlation [Eqs. (2.4) and (2.5)] is maximum for exactly overlapping statistical phase and intensity fluctuations from both arms of the interferometer. These fluctuations have a duration of the order of the inverse bandwidth of the radiation, hence can be in the fs range for broad bandwidth light. Each of these individual fs spikes will travel at the group velocity. Dispersion in group velocity causes individual frequency components of these spikes to travel at different speeds, resulting most often in pulse stretching. If the source for the interferogram of Fig. 2.3 had been a fs pulse, the recording on the right of the figure would represent the cross–correlation between the field of the stretched–out pulse $\tilde{\mathcal{E}}_2(t)$ with the original (shorter) pulse $\tilde{\mathcal{E}}_1(t)$ (of which the autocorrelation is shown on the left of the figure). Such a measurement can be used to determine the shape of the field $\tilde{\mathcal{E}}_2(t)$. The limiting case of a cross–correlation between a δ function and an unknown function yields the function directly. Indeed, the unbalanced Michelson is a powerful tool leading to a complete determination of the shape of fs signals, in amplitude and phase, as will be seen in Chapter 10.

In the case of the incoherent radiation used for the recording of Fig. 2.3, the broadened signal on the right merely reflects the "stretching" of the statistical fluctuations of the white light. This measurement however provides important information on material properties essential in fs optics. To illustrate this point we will show how the displacement of the "zero delay" point in the interferogram of Fig. 2.3 can be used to determine the first terms of an expansion of the transfer function of linear optical elements.

According to Eq. (2.6), the Fourier transform of the correlation function $\tilde{A}^+_{11}(\tau)$ measured with the balanced interferometer[4] is simply the spectral field intensity of the source. It is difficult, and not essential, to determine exactly the zero point, and therefore the measurement generally provides $\tilde{A}^+_{11}(\tau+\tau_e)\exp(i\varphi_e)$, which is the function $\tilde{A}^+_{11}(\tau)$ with an unknown phase (φ_e) and delay (τ_e) error. Similarly, the cross-correlation measured after addition of a dielectric sample of thickness $L/2$ in one arm of the interferometer (right hand side of Fig. 2.3) is $\tilde{A}^+_{12}(\tau+\tau_f)\exp\left(i\varphi_f\right)$, which is the function $\tilde{A}^+_{12}(\tau)$ with an unknown phase (φ_f) and delay (τ_f) error. The ratio of the Fourier transforms of both measurements is:

$$\begin{aligned}\frac{\tilde{A}^+_{12}(\Omega)}{\tilde{A}^+_{11}(\Omega)}\frac{e^{-i(\Omega\tau_f-\varphi_f)}}{e^{-i(\Omega\tau_e-\varphi_e)}} &= \frac{\tilde{E}_2(\Omega)}{\tilde{E}_1(\Omega)}e^{-i[\Omega(\tau_f-\tau_e)-(\varphi_f-\varphi_e)]} \\ &= e^{-i[k(\Omega)L+\Omega(\tau_f-\tau_e)-(\varphi_f-\varphi_e)]}, \end{aligned} \tag{2.10}$$

where we have made use of Eqs. (2.6) and (2.7). Unless special instrumental provisions have been made to make ($\varphi_f = \varphi_e$), and ($\tau_f = \tau_e$), this measurement will not provide the first two terms of a Taylor expansion of the dispersion function $k(\Omega)$. This is generally not a serious limitation, since, physically, the undetermined terms are only associated with a phase shift and delay of the fs pulses. The white light interferometer is an ideal instrument to determine the second and higher order dispersions of a sample. Writing the complex Fourier transforms of the interferograms in amplitude and phase:

$$\begin{aligned}\tilde{A}_{12}(\Omega) &= A_{12}(\Omega)e^{\psi_{12}(\Omega)} \\ \tilde{A}_{11}(\Omega) &= A_{11}(\Omega)e^{\psi_{11}(\Omega)}\end{aligned} \tag{2.11}$$

we find that, for an order (n) larger than 1, the dispersion is simply given by:

$$\frac{d^{(n)}k}{d\Omega^{(n)}} = -\left[\frac{d^{(n)}\psi_{12}}{d\Omega^{(n)}} - \frac{d^{(n)}\psi_{11}}{d\Omega^{(n)}}\right] \tag{2.12}$$

Equation (2.12) is not limited to dielectric samples. Instead, any optical transfer function $\tilde{H}$ which can be described by an equation similar to Eq. (1.176), can be determined from such a procedure. For instance, the preceding discussion remains valid for absorbing materials, in which case the wave vector is complex, and Eq. (2.12) leads to a complete determination of the real and imaginary part of the index of refraction of the sample versus frequency. Another example is the response of an optical mirror, as we will see in the following subsection.

[4] $\tilde{A}^+_{11}(\tau)$ corresponds to the third term $\tilde{A}^+_{12}(\tau)$ in Eq. (2.4) taken for identical beams (subscript 1 = subscript 2), not to be confused with the first term $A_{11}(0)$ in that same equation.

2.3 Dispersion of interferometric structures

2.3.1 Mirror dispersion

In optical experiments mirrors are used for different purposes and are usually characterized only in terms of their reflectivity at a certain wavelength. The latter gives a measure about the percentage of incident light intensity which is reflected. In dealing with femtosecond light pulses, one has however to consider the dispersive properties of the mirror [4, 5]. This can be done by analyzing the optical transfer function which, for a mirror, is given by

$$\tilde{H}(\Omega) = R(\Omega)e^{-i\Psi(\Omega)}. \tag{2.13}$$

It relates the spectral amplitude of the reflected field $\tilde{E}_r(\Omega)$ to the incident field $\tilde{E}_0(\Omega)$

$$\tilde{E}_r(\Omega) = R(\Omega)e^{-i\Psi(\Omega)}\tilde{E}_0(\Omega). \tag{2.14}$$

Here $R(\Omega)^2$ is the reflection coefficient and $\Psi(\Omega)$ is the phase response of the mirror. As mentioned earlier a nonzero $\Psi(\Omega)$ in a certain spectral range is unavoidable if $R(\Omega)$ is frequency dependent. Depending on the functional behavior of $\Psi(\Omega)$ (cf. Section 1.3 in Chapter 1), reflection at a mirror not only introduces a certain intensity loss but may also lead to a change in the pulse shape and to chirp generation or compensation. These effects are usually more critical if the corresponding mirror is to be used in a laser. This is because its action is multiplied by the number of effective cavity round trips of the pulse. Such mirrors are mostly fabricated as dielectric multilayers on a substrate. By changing the number of layers and layer thickness a desired transfer function, i.e., reflectivity and phase response, in a certain spectral range can be realized. As an example, Fig. 2.4 shows the amplitude and phase response of a broadband high–reflection mirror and a weak output coupler. Note that, although both mirrors have very similar reflection coefficients around a center wavelength λ_0, the phase response differs greatly. The physical explanation of this difference is that $R(\Omega)$ [or $R(\lambda)$] far from $\omega_0 = 2\pi c/\lambda_0$ (not shown) influences the behavior of $\Psi(\Omega)$ [or $\Psi(\lambda)$] near ω_0.

Before dealing with the influence of other optical components on fs pulses, let us discuss some methods to determine experimentally the mirror characteristics. In this respect the Michelson interferometer is not only a powerful instrument to analyze a sample in transmission, but it can also be used to determine the dispersion and reflection spectrum of a mirror. The interferogram from which the reference spectrum can be obtained is shown on the left of Fig. 2.3. Such a symmetric interference pattern can only be achieved in a well compensated Michelson interferometer (left part of Fig. 2.2) with identical (for symmetry) mirrors in both arms,

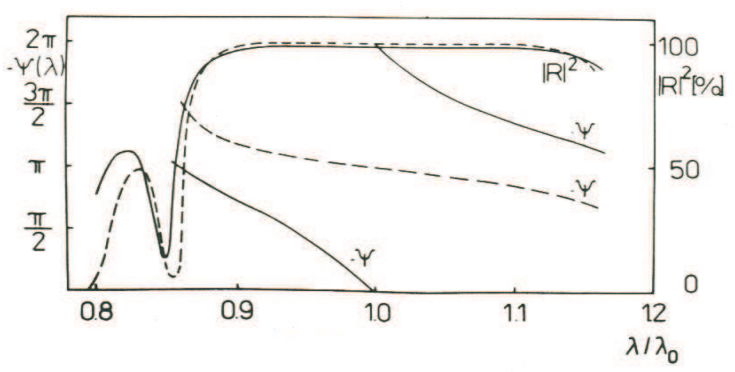

Figure 2.4: Amplitude and phase response for a high reflection multilayer mirror (dashed line) and a weak output coupler (solid line) as a function of the wavelength (from [5]).

which are also broadband (to obtain a narrow correlation pattern). For a most accurate measurement, the mirror to be measured should be *inserted* in one arm of the interferometer rather than substituted to one of the reference mirrors. Otherwise, the dispersive properties of that reference mirror cannot be cancelled. In Fig. 2.2 (left), a sample mirror is indicated as the dotted line, deflecting the beam (dashed lines) towards a displaced end mirror. As in the example of the transmissive sample, insertion of the reflective sample can in general not be done without losing the relative phase and delay references. The cross-correlation measured after substitution of the sample mirror in one arm of the interferometer (right hand side of Fig. 2.3) is $\tilde{A}^+_{12}(\tau+\tau_f)\exp\left(i\varphi_f\right)$, which is the function $\tilde{A}^+_{12}(\tau)$ with an unknown phase (φ_f) and delay (τ_f) error. The ratio of the Fourier transforms of both measurements is in analogy with Eq (2.10):

$$\begin{aligned}\frac{\tilde{A}^+_{12}(\Omega)}{\tilde{A}^+_{11}(\Omega)}\frac{e^{-i(\Omega\tau_f-\varphi_f)}}{e^{-i(\Omega\tau_e-\varphi_e)}} &= \frac{\tilde{E}_2(\Omega)}{\tilde{E}_1(\Omega)}e^{-i[\Omega(\tau_f-\tau_e)-(\varphi_f-\varphi_e)]} \\ &= R(\Omega)^2 e^{-i[2\Psi(\Omega)+\Omega(\tau_f-\tau_e)-(\varphi_f-\varphi_e)]}. \qquad (2.15)\end{aligned}$$

This function is independent of the dispersive and absorptive properties of the reference mirrors. The squared field reflection coefficient and the factor 2 in the phase account for the fact that the beam is reflected twice on the sample mirror. Both the amplitude R and phase Ψ of the transfer function $\tilde{H}(\Omega)$ can be extracted from the measurement, with the limitation that, in general, this measurement will not provide the first two terms of a Taylor expansion of the phase function $\Psi(\Omega)$. Again, this is not a serious limitation, since, physically, the undetermined terms are only associated with a phase shift and delay of the fs pulses. Using the notations of

Eqs. (2.11), the phase shift $-\Psi(\Omega)$ upon reflection of the mirror is simply given by:

$$\Psi(\Omega) = -\frac{1}{2}\left[\psi_{12}(\Omega) - \psi_{11}(\Omega) + a + b\Omega\right] \tag{2.16}$$

where a and b are constants that can generally not be determined,

The Michelson interferometer using white light is one of the simplest and most powerful tools to measure the dispersion of transmissive and reflective optics. Knox *et al.* [6] used it to measure directly the group velocity by measuring the delay induced by a sample, at selected wavelengths (the wavelength selection was accomplished by filtering white light). Naganuma *et al.* [7] used essentially the same method to measure group delays, and applied the technique to the measurement of "alpha parameters" (current dependence of the index of refraction in semiconductors) [8]. In fs lasers, the frequency dependence of the complex reflection coefficient of the mirrors contributes to an overall cavity dispersion. Such a dispersion can be exploited for optimal pulse compression, provided there is a mechanism for matched frequency modulation in the cavity. Dispersion will simply contribute to pulse broadening of initially unmodulated pulses, if no intensity or time dependent index is affecting the pulse phase, as will be discussed later. It is therefore important to diagnose the fs response of dielectric mirrors used in a laser cavity.

A direct method is to measure the change in shape of a fs pulse, after reflection on a dielectric mirror, as proposed and demonstrated by Weiner *et al.* [9]. It is clear in the *frequency domain* that the phases of the various frequency components of the pulse are being scrambled, and therefore the pulse shape should be affected. What is physically happening in the time domain is that the various dielectric layers of the coating accumulate more or less energy at different frequencies, resulting in a delay of some parts of the pulse. Therefore, significant pulse reshaping with broadband coatings occurs only when the coherence length of the pulse length is comparable to the coating thickness. Pulses of less than 30 fs duration were used in Refs. [9, 10]. As shown above, determination of the dispersion in the frequency domain can be made with a simple Michelson interferometer. The latter being a *linear measurement*, yields the same result with incoherent white light illumination or femtosecond pulses of the same bandwidth.

An alternate method, advantageous for its sensitivity, but limited to the determination of the group velocity dispersion, is to compare glass and coating dispersion inside a fs laser cavity. As will be seen in Chapter 6, an adjustable thickness of glass is generally incorporated in the cavity of mode-locked dye and solid state lasers, to tune the amount of group velocity dispersion for minimum pulse duration. The dispersion of mirrors can be measured by substituting mirrors with different coatings in one cavity position, and noting the change in the amount of glass re-

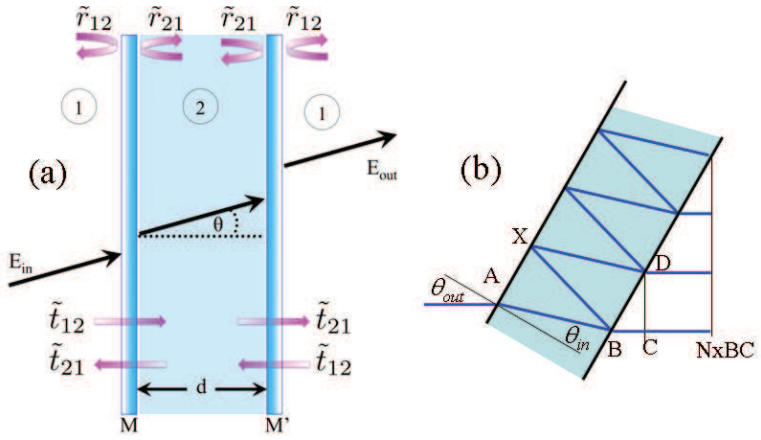

Figure 2.5: Schematic diagram of a Fabry-Perot interferometer. (a) Normal incidence. $\tilde{t}_{12}$ is the transmission from outside (1) to inside (2); $\tilde{t}_{21}$ the transmission from inside (2) to outside (1); $\tilde{r}_{12}$ the reflection from outside (1) to inside (2) and $\tilde{r}_{21}$ the reflection from inside (2) to outside (1). (b) Tilted Fabry-Perot at an angle θ_{out}. The internal angle of incidence is θ_{in}. The fields add up in phase along a wavefront at $N \times BC$ ($N \to \infty$) from B.

quired to compensate for the additional dispersion [5, 11]. The method is very sensitive, because the effect of the sample mirror is multiplied by the mean number of cycles of the pulse in the laser cavity. It is most useful for selecting mirrors for a particular fs laser cavity.

2.3.2 Fabry-Perot and Gires-Tournois interferometer

The symmetric Fabry-Perot

So far we have introduced (Michelson) interferometers only as a tool to split a pulse and to generate a certain delay between the two partial pulses. In general, however, the action of an interferometer is more complex. This is particularly true for multiple-beam devices such as a Fabry–Perot interferometer. Let us first consider a symmetric Fabry-Perot, with two identical parallel dielectric reflectors spaced by a distance d. We will use the notations $\tilde{t}_{ij}$ for the field transmission, and $\tilde{r}_{ij}$ for the field reflection, as defined in Fig. 2.5. When the Fabry-Perot is tilted, the fields add in phase along a wavefront normal to the rays (outside the Fabry-Perot) as sketched in Fig. 2.5 (b). If k_0 is the wave vector in air and k the optical path inside the Fabry-Perot, the complex field transmission function is found by

summing the successive optical path:

$$\begin{aligned}\tilde{\mathcal{T}}(\Omega) &= \tilde{t}_{12}\tilde{t}_{21}e^{-i(kAB+k_0N.BC)} + \\ &\quad \tilde{t}_{12}\tilde{t}_{21}e^{-ikBXD}\cdot\tilde{r}_{21}\tilde{r}_{21}e^{-i[kAB+k_0(N-1)BC]} \\ &\quad +\tilde{t}_{12}\tilde{t}_{21}\left(e^{-ikBXD}\cdot\tilde{r}_{21}\tilde{r}_{21}\right)^2 e^{-i[kAB+k_0(N-2)BC]}+\ldots \end{aligned} \tag{2.17}$$

The exponential $\exp[-ik_0NBC]$ can be put in factor of the whole expression. Being just a phase factor, it is generally ignored. The optical path AB is $nd/\cos\theta_{in}$, where n is the index of refraction inside the Fabry-Perot, while the difference in optical path $BXD-BC$ appearing in the power series is:

$$\frac{2nd}{\cos\theta_{in}} - 2nd\tan\theta_{in}\sin\theta_{out} = \frac{2nd}{\cos\theta_{in}} - \frac{2nd\sin^2\theta_{in}}{\cos\theta out} = \frac{2nd\cos\theta_{in}}{c}. \tag{2.18}$$

Substituting in Eq. (2.17):

$$\tilde{\mathcal{T}}(\Omega) = \tilde{t}_{12}\tilde{t}_{21}e^{-i(kd/\cos\theta_{in})}\frac{1}{1-\tilde{r}_{21}^2e^{-2ikd\cos\theta_{in}}}. \tag{2.19}$$

The dependence on tilt angle θ_{in} is somewhat counter-intuitive. The term $d/\cos\theta_{in}$ in the exponential on the numerator indicates that, as expected, the optical path length increases with angle. The exponential on the denominator $d\cos\theta_{in}$ shows instead the opposite trend, as if the optical path were to shrink as the Fabry-Perot is tilted. This is not the case, as it is a later wavefront originating at B that coincides with the one issued from C. The assumption of a plane wave of infinite extend was made in the derivation of Eq.(2.17). In a beam of limited transverse size, the sum in Eq.(2.17) is limited to a finite number N of reflections before the rays wander off the beam cross section. The number N decreases with the tilt angle θ_{in}, leading to the phase factor in the denominator turning over from $d\cos\theta_{in}$ to $d/\cos\theta_{in}$, as demonstrated experimentally in reference [12].

The total phase shift of a round-trip inside the Fabry-Perot, including the phase shift φ_r upon reflection on each mirror is:

$$\delta(\Omega) = 2\varphi_r - 2k(\Omega)d\cos\theta_{in}. \tag{2.20}$$

Introducing δ in Eq. (2.19) leads to the transfer function for the symmetrical Fabry-Perot:

$$\tilde{\mathcal{T}}(\Omega) = \tilde{t}_{12}\tilde{t}_{21}e^{-i(kd/\cos\theta_{in})}\frac{1}{1-\tilde{r}_{21}^2e^{i\delta}}, \tag{2.21}$$

where $R=|\tilde{r}_{12}|^2$ is the intensity reflection coefficient of each mirror [13]. A similar procedure leads to the field reflection:

$$\tilde{\mathcal{R}}(\Omega) = \tilde{r}_{12} + \tilde{t}_{12}\tilde{t}_{21}\tilde{r}_{21}e^{-2i(kd\cos\theta_{in})}\frac{1}{1-\tilde{r}_{21}^2e^{i\delta}}, \tag{2.22}$$

As shown in Appendix A, the phases of the field reflection and transmission coefficients of the coatings $\tilde{r}_{ij}$ and $\tilde{t}_{ij}$ have to be such that:

$$(\tilde{r}_{12}\tilde{t}^*_{21} + \tilde{r}^*_{12}\tilde{t}_{12}) + (\tilde{r}_{21}\tilde{t}^*_{12} + \tilde{r}^*_{21}\tilde{t}_{12})n = 0, \tag{2.23}$$

where n is the index of refraction of the substrate of the coating, and we considered only normal incidence. As mentioned in Appendix A, Eq. (2.23) for the symmetric interface ($n = 1$) applies also to any optical system, hence to the field reflection and transmission of the Fabry-Perot:

$$\mathcal{R}\mathcal{T}^* + \mathcal{R}^*\mathcal{T} = 0. \tag{2.24}$$

The latter equation is general, applying as well to the general expression Eqs. (2.21) and (2.22) and to the asymmetric Fabry-Perot or Gires-Tournois to be discussed next. There is however a caveat that the energy conservation (2.24) assumes that the two coatings satisfy their own energy conservation relation Eq. (2.23).

In general, the exact phase shifts of a coating are not known. Fortunately, within the frequency range where they are constant, the values of the phase shifts of the 2 coatings affect only the position of the resonances, leaving the shape and width of the transmission curve unchanged. Therefore, it is convenient to use the particular phase combination $\tilde{t}_{12}\tilde{t}_{21} - \tilde{r}_{12}\tilde{r}_{21} = 1$ and $\tilde{r}_{12} = -\tilde{r}^*_{21}$, for which the field transmission reduces to:

$$\tilde{\mathcal{T}}(\Omega) = \frac{(1-R)e^{-ikd/\cos\theta_{in}}}{1 - Re^{i\delta}} \tag{2.25}$$

For that same phase combination, one finds the complex reflection coefficient of the Fabry-Perot:

$$\tilde{\mathcal{R}}(\Omega) = \frac{\sqrt{R}\left(e^{i\delta} - 1\right)}{1 - Re^{i\delta}}. \tag{2.26}$$

One can easily verify that, if — and only if — kd is real:

$$|\mathcal{R}|^2 + |\mathcal{T}|^2 = 1. \tag{2.27}$$

Equations (2.25) and (2.26) are transfer functions for the field spectrum. The dependence on the frequency argument Ω occurs through $k = n(\Omega)\Omega/c$ and possibly $\varphi_r(\Omega)$. With $n(\Omega)$ complex, the medium inside the Fabry-Perot is either an absorbing or an amplifying medium, depending on the sign of the imaginary part of the index. We refer to a problem at the end of this chapter for a study of the Fabry-Perot with gain.

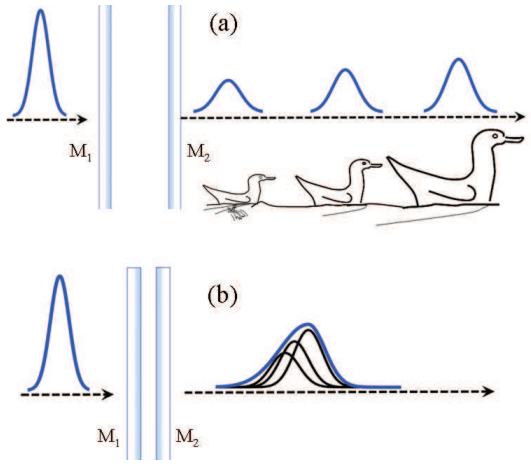

Figure 2.6: Effect of a Fabry-Perot interferometer on a light pulse. (a) If the mirror spacing is larger than the geometrical length of the incident pulse, an exponentially decaying sequence of pulses follows the Fabry-Perot, like ducklings follow mother duck. (b) If the mirror spacing is smaller than the geometric length of the incident pulse, the pulse spectrum is spectrally filtered, resulting a longer transmitted pulse.

The functions $\tilde{\mathcal{T}}(\Omega)$ and $\tilde{\mathcal{R}}(\Omega)$ are complex transfer functions, which implies that, for instance, the transmitted field is:

$$\tilde{E}_{out}(\Omega) = \mathcal{T}(\Omega)\tilde{E}_{in}(\Omega) \tag{2.28}$$

where $\tilde{E}_{in}$ is the incident field. Equation (2.28) takes into account all the dynamics of the field and of the Fabry-Perot. In the case of a Fabry-Perot of thickness $d \ll c\tau_p$, close to resonance ($\delta(\Omega) \ll 1$), the transmission function $\tilde{\mathcal{T}}(\Omega)$ is a Lorentzian, with a real and imaginary part connected by the Kramers Kronig relation. We refer to a problem at the end of this chapter to show how dispersive properties of a Fabry-Perot can be used to shape a chirped pulse.

In the case of a Fabry-Perot of thickness $d \gg c\tau_p$, the pulse spectrum covers a large number of Fabry-Perot modes. The free spectral range of the Fabry–Perot interferometer is much smaller than the spectral width of the pulse. Hence the product (2.28) will represent a frequency comb, of which the Fourier transform is a train of pulses. Intuitively indeed, we expect the transmission and/or reflection of a Fabry-Perot interferometer to consist of a train of pulses of decreasing intensity if the spacing d between the two reflecting surfaces is larger than the geometrical pulse length, [Fig. 2.6(a)]. The latter condition prevents interference between field components of successive pulses.There is however an interesting situation where

interference between successive pulses is restored. If the Fabry-Perot is inserted in the cavity of a mode-locked laser, its modes couple to those of the laser. The successive pulses form a "minicomb" intertwined with the main laser comb [12, 14, 15].

On the other hand if d is smaller than the pulse length the output field is determined by interference, as illustrated in Fig. 2.6(b). An example of a corresponding device was the dielectric multilayer mirror discussed before, which can be considered as a sequence of many Fabry–Perot interferometers. Here the free spectral range of one interferometer is much broader than the pulse spectrum and it is the behavior around a resonance which determines the shape of pulse envelope and phase. The actual pulse characteristics can easily be determined by multiplying the field spectrum of the incident pulse with the corresponding transfer function (2.25). For a multilayer mirror this function can be obtained by a multiplication of matrices for the individual layers, as detailed in Appendix A.

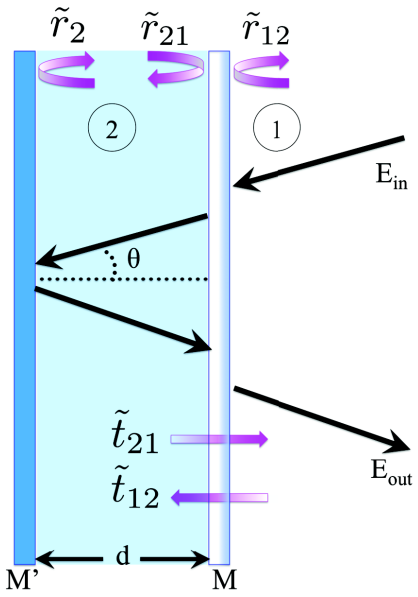

Figure 2.7: Schematic diagram of a Gires–Tournois interferometer.

The Gires-Tournois interferometer

Among the various types of interferometers that can be used for pulse shaping, we choose to detail here the Gires–Tournois interferometer [16]. This interferometer

is nothing else than an asymmetric Fabry-Perot in the limit of one reflector having a reflectivity of $R = 1$. This leads in principle to a very high and almost constant amplitude transmission while the spectral phase can be tuned continuously. This device has been used to control the GVD in a fs laser in a similar manner as gratings and prisms. The Gires–Tournois is topologically identical to a ring interferometer, with all mirrors but one being perfect reflectors. The lone transmitting mirror is used as input and output. The Gires–Tournois is also topologically identical to a high-Q microring in integrated optics, with input and output made through evanescent wave coupling to a fiber. For all these devices, the output amplitude is close to unity, whether or not the wave inside the ring is at resonance or not. It is left as an exercise at the end of this chapter to transpose the formulae of the Gires–Tournois to the situation of a ring interferometer.

The Gires–Tournois interferometer is a particular case of asymmetric Fabry-Perot interferometer with one mirror (mirror M_2) having a reflection coefficient of (almost) 1. Consequently the device is used in reflection. A simple approach is to derive an equation for the field reflection usiing the same particular phase combination $\tilde{t}_{12}\tilde{t}_{21} - \tilde{r}_{12}\tilde{r}_{21} = 1$ and $\tilde{r}_{12} = -\tilde{r}^*_{21}$ that led to Eqs. (2.25) and (2.26). The transfer function in the limit of mirror M_2 having a reflection coefficient of 1 is:

$$R(\Omega)e^{-i\Psi(\Omega)} = \frac{-r + e^{i\delta}}{1 - re^{i\delta}} \tag{2.29}$$

where δ is the phase delay[5] between two successive partial waves that leave the interferometer and r is the (real) amplitude reflection of M_1 (assumed to be non-dispersive).

The phase response determined by Eq. (2.29) can be written as

$$\Psi(\Omega) = -\arctan\left[\frac{(r^2-1)\sin\delta}{2r-(r^2+1)\cos\delta}\right] \tag{2.30}$$

Taking the derivative of both sides of this expression, and dividing by $[\tan^2\Psi + 1]$ yields:

$$\frac{d\Psi}{d\Omega} = \frac{(r^4-1) - 2r(r^2-1)\cos\delta}{(1+r^2)^2 + 4r\cos\delta[r\cos\delta - (1+r^2)]}\frac{d\delta}{d\Omega}. \tag{2.31}$$

It is interesting to find the expression for the group delay at the exact resonances, i.e. the values of Ω that make $\delta = 2N\pi$:

$$\left.\frac{d\Psi}{d\Omega}\right|_{res} = \left(\frac{r+1}{r-1}\right)\left.\frac{d\delta}{d\Omega}\right|_{res} \tag{2.32}$$

[5] In the definition of the phase delay (2.20) applied to the Gires-Tournois interferometer, θ is the *internal* angle.

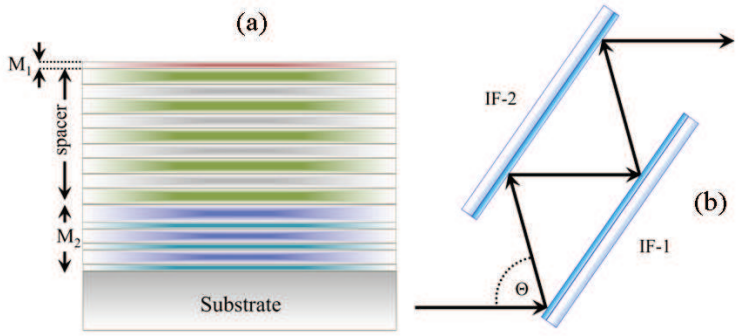

Figure 2.8: Gires-Tournois interferometer for fs light pulses using dielectric multilayers. By rotating two parallel interferometers the overall dispersion can be adjusted through a change of the external angle of incidence Θ and the number of reflections. Note, the beam direction is not changed. The lateral displacement can be compensated by a second pair of interferometers (from [17]).

The group velocity dispersion of the device is calculated from the second derivative of the expression (2.31):

$$\frac{d^2\Psi}{d\Omega^2} = \frac{(r^4-1)-2r(r^2-1)\cos\delta}{(1+r^2)^2+4r\cos\delta[r\cos\delta-(1+r^2)]}\frac{d^2\delta}{d\Omega^2} + \frac{2r(r^2-1)\sin\delta\left[4r(r^2+1)\cos\delta-4r^2\cos^2\delta-r^2-3\right]}{\{(1+r^2)^2+4r\cos\delta[r\cos\delta-(1+r^2)]\}^2}\left(\frac{d\delta}{d\Omega}\right)^2. \tag{2.33}$$

As shown in the definition Eq. (2.20), the second derivative of δ contains the group velocity dispersion ($-k$") of the material inside the interferometer. This material dispersion is enhanced by the factor $(r+1)/(r-1)$ in condition of resonance. This factor can be very large in the case a of high finesse resonator ($1-r \ll 1$).

The GVD given by Eq. (2.33) can be tuned continuously by adjusting δ which can be either through a change of the mirror separation d or through a change of the external angle of incidence Θ. Gires and Tournois [16] conceived this interferometer to adapt to optical frequencies the pulse compression technique used in radar (sending a frequency modulated pulse through a dispersive delay line). Duguay and Hansen were the first to apply this device for the compression of pulses from a He-Ne laser [18]. Since typical pulse durations were on the order of several hundred ps the mirror spacing needed to be in the order of few mm. To use the interferometer for the shaping of fs pulses the corresponding mirror spacing has to be in the order of few microns. Heppner and Kuhl [19] overcame this obvious practical difficulty by designing a Gires–Tournois interferometer on the basis of

dielectric multilayer systems, as illustrated in Fig. 2.8(a). The 100% mirror M_2 is a sequence of dielectric coatings with alternating refractive index deposited on a substrate. A certain spacer of optical thickness d consisting of a series of $\lambda/2$ layers of one and the same material is placed on top of M_2. The partially reflective surface M_1 is realized by one $\lambda/4$ layer of high refractive index. The dispersion of this compact device can be tuned by changing the angle of incidence and/or the number of passes through the interferometer. A possible arrangement which was successfully applied for GVD adjustments in fs lasers [17] is shown in Fig. 2.8(b).

Gires-Tournois as a limit of asymmetric Fabry-Perot interferometer

Using the same procedure as for the symmetric Fabry-Perot, one finds the following expressions for the transmission and reflection of the asymmetric Fabry-Perot:

$$\mathcal{T} = \frac{\tilde{t}_{12}\tilde{t}_{23}e^{-i\phi}}{1-\tilde{r}_{21}\tilde{r}_{23}e^{-2i\phi}} \tag{2.34}$$

$$\mathcal{R} = \tilde{r}_{12} + \frac{\tilde{t}_{12}\tilde{t}_{21}e^{-2i\phi}}{1-\tilde{r}_{21}\tilde{r}_{23}e^{-2i\phi}} \tag{2.35}$$

There is always a resonance dip in the reflection. Figure 2.9 show the reflection, transmission and phase for a 6 mm thickness fused silica Fabry-Perot, The reflectivities of 99% and 99.975% provide a very narrow resonance (50 MHz FWHM) and a correspondingly steep phase dispersion. Even the very high reflectivity of 99.975% does not prevent a transmission of nearly 10% at resonance.

2.3.3 Chirped mirrors

As mentioned in the previous section, the Gires-Tournois interferometer exhibits a reflectivity close to one over a broad spectrum. This was accomplished by an end mirror of high reflectivity (M_2 in Fig. 2.8). The dispersion on the other hand can be controlled by the spacer and the front mirror. This is expressed in the phase $\delta(\Omega)$ and $\varphi_r(\Omega)$ in Eq. (**??**). The problem is that both mirrors at the same time form a Fabry-Perot structure that has relatively narrow resonances and subsequently a rather complicated dispersion behavior. The most desired alternative would be a process to generate a pre-defined reflection and phase behavior, $R(\Omega)$ and $\Psi(\Omega)$. Optimization programs applied to dielectric multi-layer systems offer such an intriguing and interesting possibility. A dielectric multi-layer system consists of a sequence of films characterized by a certain refractive index n_i and thickness d_i. In principle, computer algorithms can be used to find a sequence of (d_i, n_i) combinations representing individual films that come closest to a pre-defined reflection and

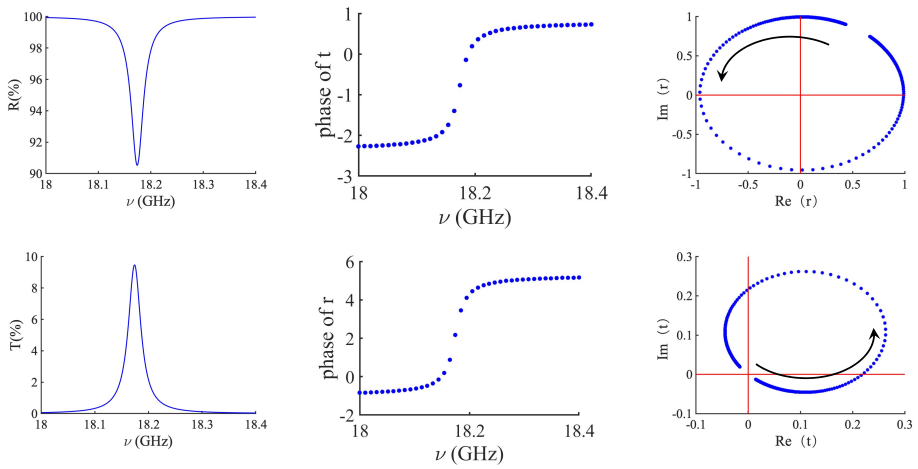

Figure 2.9: Transmission and reflection characteristics of a 6 mm Fabry-Perot with coatings of 99% and 99.975% reflectivity. (a) intensity transmission; (b) phase of the transmission transfer function, (c) imaginary versus real part of the transmission transfer function; (d) intensity reflection; (e) phase of the reflection transfer function, (f) imaginary versus real part of the reflection transfer function,

phase behavior in a certain spectral range. Of course, there are certain technical constraints that need to be considered, for example the total thickness and number of layers, the manufacturing tolerances in n_i and d_i, and the limited choice of available refractive indices n_i (suitable materials). This approach will gain importance in the future as the amplitude and phase responses needed become more and more complicated.

In many cases mirrors are desired that have a constant reflectivity and certain dispersion behavior, for example a constant amount of GVD within a pre-defined spectral range. This idea was pursued by Szipöks et al. [20], leading to what is now called chirped mirrors. The basic idea is sketched in Fig. 2.10. High-reflection mirrors typically consist of stacks of alternating high and low refractive index quarter-wave layers. A chirped mirror is a sequence of those stacks with changing resonance frequency. Wave-packets of different center frequency are thus reflected at different depths, making the group delay upon reflection a function of frequency.

Unfortunately this is an oversimplified picture that neglects subresonances in particular between the layers and the first air-film interface. This leads to a modulation of the GVD. For this reason computer optimization is necessary to tune the film parameters for a smooth dispersion curve.

Improvements in the initial layer sequence used as a starting point for the final computer optimization have been accomplished, for example, by modulating

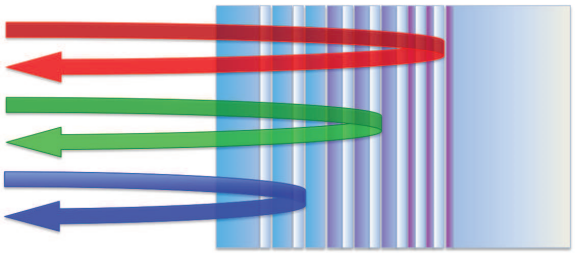

Figure 2.10: Wave packets of different center frequencies are reflected at different depths of a chirped mirror. The mirror consists of stacks of alternating high and low refractive index layers at different resonance frequencies.

the ratio of the thickness of the high- and low-index layer of the chirped mirror (double chirped mirror) [21], by superimposing a quasi-periodic modulation on the linear modulation of the layer thickness [22], and by coating the backside of the substrate [23,24]. As we will see in following chapters such mirrors have made an impressive impact on femtosecond laser source development.

2.4 Focusing elements

2.4.1 Singlet lenses

One main function of fs pulses is to concentrate energy in time and space. The ability to achieve extremely high peak power densities depends partly on the ability to keep pulses short in time, and concentrate them in a small volume by focusing. The difference between group and phase velocity in the lens material can reduce the peak intensity in the focal plane by delaying the time of arrival of the pulse front propagating through the lens center relative to the pulse front propagating along peripheral rays. The group velocity dispersion leads to reduction of peak intensity by stretching the pulse in time. As pointed out by Bor [25,26], when simple focusing singlet lenses are used, the former effect can lead to several picosecond lengthening of the time required to deposit the energy of a fs pulse on focus.

Let us assume a plane pulse and phase front at the input of a spherical lens as sketched in Fig. 2.11. According to Fermat's principle the optical path along rays from the input phase front to the focus is independent of the radius coordinate r. The lens transforms the plane phase front into a spherical one which converges in the (paraxial) focus. Assimilating air as vacuum, it is only while propagating through the lens that the pulses experience a group velocity v_g different from the phase velocity $v_p = c/n$. The result is a pulse front that is delayed with respect to the (spherical) phase front, depending on the amount of glass traversed. As we

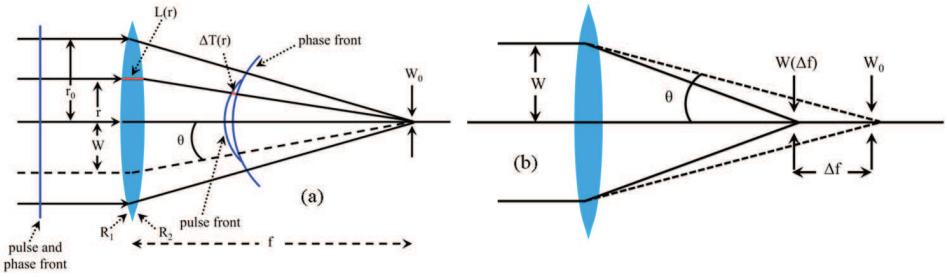

Figure 2.11: (a) delay of the pulse front with respect to the phase front, in the case of a singlet lens. (b) spread of the focal region due to chromatic aberration.

have seen in Chapter 1, the group velocity is:

$$v_g = \left(\frac{dk}{d\Omega}\right)^{-1} = \frac{c}{n - \lambda_\ell \frac{dn}{d\lambda}}, \tag{2.36}$$

where λ_ℓ is the wavelength in vacuum. The difference in propagation time between the phase front and pulse front after the lens at radius coordinate r is:

$$\Delta T(r) = \left(\frac{1}{v_p} - \frac{1}{v_g}\right) L(r), \tag{2.37}$$

where $L(r)$ is the lens thickness. The group delay $\Delta T(r)$ is also the difference of the time of arrival at the focus of pulses traversing the lens at distance r from the axis and peripheral rays touching the lens rim. Pulse parts travelling on the axis ($r = 0$) will arrive delayed in the focal plane of a positive lens compared with pulse parts traversing the lens at $r > 0$. For a spherical thin lens, the thickness L is given by

$$L(r) = \frac{r_0^2 - r^2}{2}\left(\frac{1}{R_1} - \frac{1}{R_2}\right) \tag{2.38}$$

where $R_{1,2}$ are the radii of curvature of the lens and r_0 is the radius of the lens aperture.[6] Substituting the expressions for the group velocity (2.36) and for the lens thickness (2.38) into Eq. (2.37) yields for the difference in time of arrival between a pulse passing through the lens at the rim and at r:

$$\begin{aligned} \Delta T(r) &= \frac{r_0^2 - r^2}{2c}\left(\frac{1}{R_1} - \frac{1}{R_2}\right)\left(\lambda \frac{dn}{d\lambda}\right) \\ &= \frac{r_0^2 - r^2}{2c} \lambda \frac{d}{d\lambda}\left(\frac{1}{f}\right) \end{aligned} \tag{2.39}$$

[6]Regarding sign considerations we will use positive (negative) $R_{1,2}$ for refracting surfaces which are concave (convex) towards the incident side.

where the focal length f has been introduced by $1/f = (n-1)(R_1^{-1} - R_2^{-1})$. Equation (2.40) illustrates the connection between the radius dependent pulse delay and the chromaticity $d/d\lambda(1/f)$ of the lens. For an input beam of radius r_b the pulse broadening in the focus can be estimated with the difference in arrival time $\Delta T'$ of a pulse on an axial ray and a pulse passing through the lens at r_b:

$$\boxed{\Delta T'(r_b) = \frac{r_b^2}{2c}\lambda\frac{d}{d\lambda}\left(\frac{1}{f}\right).} \tag{2.40}$$

To illustrate the effects of group velocity delay and dispersion, let us assume that we would like to focus a 50 fs pulse at the excimer laser wavelength of 248 nm (KrF) down to a spot size of 0.6 μm, using a fused silica lens (singlet) of focal distance f = 30 mm. Let us further assume that the input beam profile is Gaussian. Since the half divergence angle in the focused beam is $\theta = \lambda/(\pi w_0)$, the radius w of the Gaussian beam [radial dependence of the electric field: $\tilde{\mathcal{E}}(r) = \tilde{\mathcal{E}}(0)\exp\{-r^2/w^2\}$] incident on the lens should be approximately $\theta f = (\lambda/\pi w_0)f \approx 4$ mm. To estimate the pulse delay we evaluate $\Delta T'$ at $r_b = w$:

$$\begin{aligned}\Delta T'(r_b = w) &= \frac{w^2}{2c}\lambda\frac{d}{d\lambda}\left(\frac{1}{f}\right)\\ &= -\frac{w^2}{2cf(n-1)}\left(\lambda\frac{dn}{d\lambda}\right)\\ &= -\frac{\theta^2 f}{2c(n-1)}\left(\lambda\frac{dn}{d\lambda}\right).\end{aligned} \tag{2.41}$$

For the particular example chosen, $n \approx 1.51$, $\lambda dn/d\lambda \approx -0.17$, and the difference in time of arrival (at the focus) of the rays at $r = 0$ and $r_b = w$ is ≈ 300 fs, which can be used as a rough measure of the pulse broadening.

The effect of the chromaticity of the lens on the spatial distribution of the light intensity near the focal plane is a spread of the optical energy near the focus, because different spectral components of the pulse are focused at different points on axis. For a bandwidth limited Gaussian pulse of duration $\tau_p = \sqrt{2\ln 2}\,\tau_{G0}$ with spectral width $\Delta\lambda = 0.441\lambda^2/c\tau_p$, the focus spreads by the amount:

$$\Delta f = -f^2\,\frac{d(1/f)}{d\lambda}\Delta\lambda = -\frac{f\lambda^2}{c(n-1)}\frac{0.441}{\tau_p}\frac{dn}{d\lambda}. \tag{2.42}$$

Applying Eq. (2.42) to our example of a 30 mm fused silica lens to focus a 50 fs pulse, we find a spread of $\Delta f = 60$ μm, which is large compared to the Rayleigh range of a diffraction limited focused monochromatic beam $\rho_0 = w_0/\theta \approx 5$ μm.

We can therefore write the following approximation for the broadening of the beam: $w(\Delta f)/w_0 = \sqrt{1+(\Delta f/2\rho_0)^2} \approx (\Delta f/2\rho_0)$. Substituting the value for Δf from Eq. (2.42):

$$\frac{w(\Delta f)}{w_0} = -\frac{0.44\pi}{\tau_p}\frac{\theta^2 f}{2c(n-1)}\left(\lambda\frac{dn}{d\lambda}\right) \approx -0.44\pi\frac{\Delta T'}{\tau_p}. \tag{2.43}$$

We note that the spatial broadening of the beam due to the spectral extension of the pulse, as given by Eq. (2.43), is (within a numerical factor) the same expression as the group velocity delay [Eq. (2.41)] relative to the pulse duration. In fact, neither expression is correct, in the sense that they do not give a complete description of the spatial and temporal evolution of the pulse near the focus. An exact calculation of the focalization of a fs pulse by a singlet is presented in the subsection that follows.

In addition to the group delay effect, there is a direct temporal broadening of the pulse *in the lens itself* due to GVD in the lens material, as discussed in Section 1.5. Let us take again as an example the fused silica singlet of 30 mm focal length and of 16 mm diameter used to focus a 248 nm laser beam to a 0.6 μm spot size. The broadening will be largest for the beam on axis, for which the propagation distance through glass is $L(r=0) = d_0 = r_0^2/\{2f(n-1)\} = 2.1$ mm. Using for the second-order dispersion at 250 nm $\lambda d^2n/d\lambda^2 \approx 2.1\ \mu\text{m}^{-1}$ [25], we find from Eq. (1.136) that a 50 fs (FWHM) unchirped Gaussian pulse on axis will broaden to about 60 fs. If the pulse has an initial upchirp such that the parameter a defined in Eq. (1.41) is $a = -5$, it will broaden on axis to 160 fs. At a wavelength of 800 nm, where the dispersion is much smaller than in the UV (see Table 2.1), a bandwidth limited 50 fs pulse would only broaden to 50.4 fs.

The example above illustrates the differences between peak intensity reduction at the focal point of a lens resulting from the difference between group and phase velocity, and effects of group velocity dispersion in the lens material. The latter is strongly chirp dependent, while the former is not. The spread of pulse front arrival time in the focal plane is independent of the pulse duration and is directly related to the spot size that will be achieved (the effect is larger for optical arrangements with a large F-number). The *relative* broadening of the focus, $\propto \Delta T'/\tau_p$, is however larger for shorter pulses. The group velocity dispersion effect is pulse width dependent, and, in typical materials, becomes significant only for pulse durations well below 100 fs in the VIS and NIR spectral range.

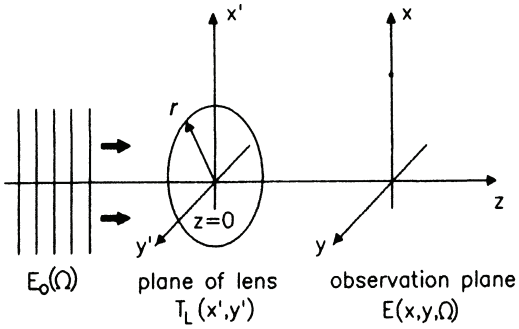

Figure 2.12: Diffraction geometry for focusing.

2.4.2 Space-time distribution of the pulse intensity at the focus of a lens

The geometrical optical discussion of the focusing of ultrashort light pulses presented above gives a satisfactory order of magnitude estimate for the temporal broadening effects in the focal plane of a lens. We showed this type of broadening to be associated with chromatic aberration. Frequently the experimental situation requires an optimization not only with respect to the temporal characteristics of the focused pulse, but also with respect to the achievable spot size. To this aim we need to analyze the space-time distribution of the pulse intensity in the focal region of a lens in more detail. The general procedure is to solve either the wave equation (1.78), or better the corresponding diffraction integral[7], which in Fresnel approximation was given in Eq. (1.192). However, we cannot simply separate space and time dependence of the field with a product ansatz (1.188) since we expect the chromaticity of the lens to induce an interplay of both. Instead we will solve the diffraction integral for each "monochromatic" Fourier component of the input field $\tilde{E}_0(\Omega)$ which will result in the field distribution in a plane (x,y,z) behind the lens, $\tilde{E}(x,y,z,\Omega)$. The time-dependent field $\tilde{E}(x,y,z,t)$ then is obtained through the inverse Fourier transform of $\tilde{E}(x,y,z,\Omega)$ so that we have for the intensity distribution:

$$I(x,y,z,t) \propto |\mathcal{F}^{-1}\{\tilde{E}(x,y,z,\Omega)\}|^2. \tag{2.44}$$

The geometry of this diffraction problem is sketched in Fig. 2.12. Assuming plane waves of amplitude $E_0(\Omega) = E_0(x',y',z'=0,\Omega)$ at the lens input, the dif-

[7] For large F numbers the Fresnel approximation may no longer be valid, and the exact diffraction integral including the vector properties of the field should be applied.

fraction integral to be solved reads, apart from normalization constants:

$$E(x,y,z,\Omega) \propto \frac{\Omega}{c}\int\int E_0(\Omega)T_L(x',y')T_A(x',y')e^{-i\frac{k}{2z}\left[(x'-x)^2+(y'-y)^2\right]}dx'dy' \quad (2.45)$$

where T_L and T_A are the transmission function of the lens and the aperture stop, respectively. The latter can be understood as the lens rim in the absence of other beam limiting elements. The lens transmission function describes a radially dependent phase delay which in case of a thin, spherical lens can be written:

$$T_L(x',y') = \exp\left\{-i\frac{\Omega}{c}\left[nL(r') + d_0 - L(r')\right]\right\} \quad (2.46)$$

with $r'^2 = x'^2 + y'^2$ and

$$L(r') = d_0 - \frac{r'^2}{2}\left(\frac{1}{R_1} - \frac{1}{R_2}\right) = d_0 - \frac{r'^2}{2(n-1)f}, \quad (2.47)$$

where d_0 is the thickness in the lens center. Note that because of the dispersion of the refractive index n, the focal length f becomes frequency dependent. For a spherical opening of radius r'_0 the aperture function T_A is simply:

$$T_A(r') = \begin{cases} 1 & \text{for} \quad x'^2 + y'^2 = r'^2 \le r'^2_0 \\ 0 & \text{otherwise} \end{cases} \quad (2.48)$$

If we insert Eq. (2.47) into Eq. (2.46) we can rewrite the lens transmission function as:

$$T_L(x',y') = \exp\left\{-i\left[k_g(\Omega)d_0 - \left(k_g(\Omega) - \frac{\Omega}{c}\right)\frac{r'^2}{2}\left(\frac{1}{R_1} - \frac{1}{R_2}\right)\right]\right\}, \quad (2.49)$$

where

$$k_g(\Omega) = \frac{\Omega}{c}n(\Omega) \quad (2.50)$$

is the wave vector in the glass material. Substituting this transmission function in the diffraction integral Eq.(2.45) we find for the field distribution in the focal plane:

$$\begin{aligned} E(\Omega) \quad \propto \quad & \frac{\Omega}{c}e^{-ik_g(\Omega)d_0}\int\int T_A E_0(\Omega)\exp\left[i\left(k_g(\Omega) - \frac{\Omega}{c}\right)\frac{r'^2}{2}\left(\frac{1}{R_1} - \frac{1}{R_2}\right)\right] \\ & \times e^{-i\frac{k}{2z}\left[(x'-x)^2+(y'-y)^2\right]}dx'dy' \end{aligned} \quad (2.51)$$

The exponent of the second exponential function is radially dependent and is responsible for the focusing, while the first one describes propagation through a dispersive material of length d_0. For a closer inspection let us assume that the glass

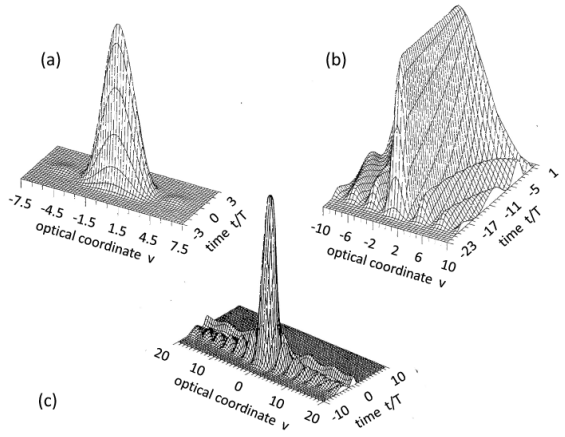

Figure 2.13: Space-time distribution of the pulse intensity in the focal plane of a lens: (a) Focusing without chromatic or spherical aberration, (b) Focusing with chromatic aberration $\tau/T = 20$. The input pulse was chosen to vary as $e^{-(t/T)^2}$. v is the optical coordinate defined as $v = r_0' k_\ell \sqrt{x^2+y^2}/f_\ell$ and $\tau = T'(r_0) = \left|\frac{r_0'^2\lambda}{2fc(n-1)} n'(\lambda)\right|$ is a measure for the dispersion (from [27]). (c) Focusing with chromatic and spherical aberration. The intensity distribution in the plane of the marginal focus is shown (from [28]).

material is only weakly dispersive so that we may expand $k_g(\Omega)$ and $[k_g(\Omega) - \Omega/c]$ up to second order. In both exponential functions this will result in a sum of terms proportional to $(\Omega - \omega_\ell)^m$ $(m = 0, 1, 2)$. According to our discussion in the section about linear elements, optical transfer functions which have the structure $\exp[-ib_1(\Omega - \omega_\ell)]$ give rise to a certain pulse delay. Because b_1 is a function of r' this delay becomes radius dependent, a result which has already been expected from our previous ray-optical discussion. The next term of the expansion $(m = 2)$ is responsible for pulse broadening in the lens material.

A numerical evaluation of Eq. (2.51) and subsequent inverse Fourier transform [Eq. (2.44)] allows one to study the complex space-time distribution of the pulse intensity behind a lens. An example is shown in Fig. 2.13. In the aberration-free case we recognize a spatial distribution corresponding to the Airy disc and no temporal distortion. The situation becomes more complex if chromaticity plays a part. We see spatial as well as temporal changes in the intensity distribution. At earlier times the spatial distribution is narrower. This can easily be understood if we remember that pulses from the lens rim (or aperture edge) arrive first in the focal plane and are responsible for the field distribution. At later times pulses from inner parts of the lens arrive. The produced spot becomes larger since the effective aperture size is smaller. If we use achromatic doublets (cf. next Section 2.4.3) the exponential proportional to $(\Omega - \omega_\ell)$ in the corresponding diffraction integral does not appear. The only broadening then is due to GVD in the glass material.

Interesting effects occur if spherical aberration is additionally taken into account [28] which is essential to correctly model strong focusing with singlet lenses. As known from classical optics, spherical aberration results in different focal planes for beams passing through the lens at different r. Since ultrashort pulses passing through different lens annuli experience the same delay, almost no temporal broadening occurs for the light which is in focus, as illustrated in Fig. 2.13(c). The space-time distribution in the focal area can differ substantially from that obtained with a purely chromatic lens.

To measure the interplay of chromatic and spherical aberration in focusing ultrashort light pulses, one can use an experimental setup as shown in Fig. 2.14(a). The beam is expanded and sent into a Michelson interferometer. One arm contains the lens to be characterized, which can be translated so as to focus light passing through certain lens annuli onto mirror M_1. Provided the second arm has the proper length, an annular interference pattern can be observed at the output of the interferometer. The radius of this annulus is determined by the setting of Δf. If no spherical aberration is present, an interference pattern is observable only for $\Delta f \approx 0$ and a change of the time delay by translating M_2 would change the radius of the interference pattern. With spherical aberration present, at a certain Δf, an interference pattern occurs only over a delay corresponding to the pulse duration

while the radius of the annulus remains constant. This can be proved by measuring the cross-correlation, i.e., by measuring the second harmonic signal as function of the time delay. The width of the cross-correlation does not differ from the width of the autocorrelation which is measured without the lens in the interferometer arm. Figure 2.14(b) shows the position of the peak of the cross-correlation as function of Δf and the corresponding r, respectively. For comparison, the delay associated with chromatic aberration alone is also shown (dashed curve).

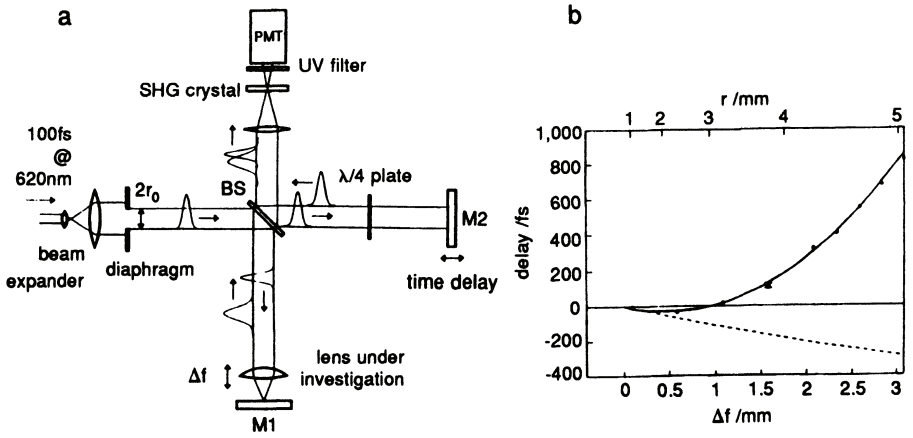

Figure 2.14: (a) Correlator for measuring the effect of chromatic and spherical aberration on the focusing of fs pulses. (b) Measured pulse delay (data points) as a function of the lens position (Δf — deviation from the paraxial focus) and the corresponding radial coordinate r of light in focus. The solid line is obtained with ray–pulse tracing; the dashed curve shows the effect of chromatic aberration only. Lens parameters: $f_0 = 12.7$ mm, BK7 glass (from [29]).

2.4.3 Achromatic doublets

The chromaticity of a lens was found to be the cause for a radial dependence of the time of arrival of the pulse at the focal plane, as was shown by Eq.(2.40). Therefore one should expect achromatic optics to be free of this undesired pulse lengthening. To verify that this is indeed the case, let us consider the doublet shown in Fig. 2.15. The thicknesses of glass traversed by the rays in the media of index n_1 and n_2 are L_1 and L_2 and are given by:

$$L_1 = d_1 - \frac{r^2}{2}\left(\frac{1}{R_1} - \frac{1}{R_2}\right) \tag{2.52}$$

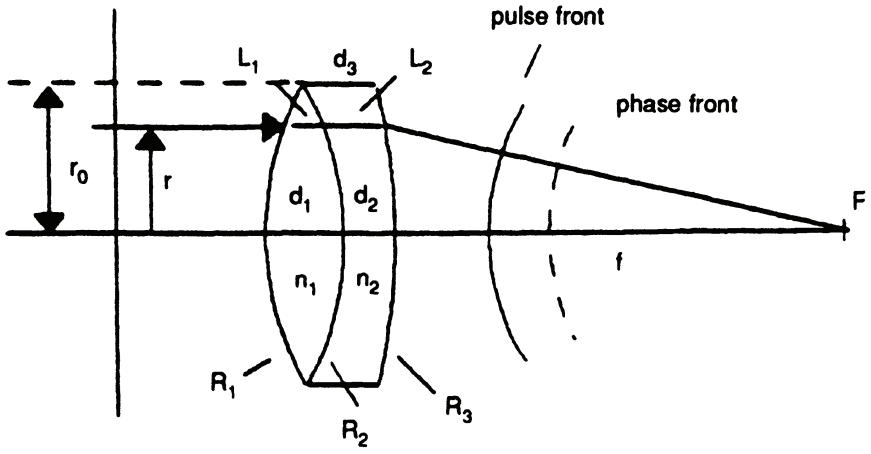

Figure 2.15: Ray tracing in an achromat (from [25]).

and

$$L_2 = d_2 - \frac{r^2}{2}\left(\frac{1}{R_2} - \frac{1}{R_3}\right) \tag{2.53}$$

where $d_{1,2}$ is the center thickness of lens 1,2. The inverse of the focal length of the doublet lens is:

$$\frac{1}{f} = (n_1 - 1)\left(\frac{1}{R_1} - \frac{1}{R_2}\right) + (n_2 - 1)\left(\frac{1}{R_2} - \frac{1}{R_3}\right). \tag{2.54}$$

The condition of achromaticity $\frac{d}{d\lambda}(1/f) = 0$ gives an additional relation between the radii of curvature R_i and the indices n_i. The expression for the transit time in glass [25] in which we have inserted the chromaticity of the doublet is:

$$\boxed{T(r) = \frac{d_1}{c}\left\{n_1 - \lambda\frac{dn_1}{d\lambda}\right\} + \frac{d_2}{c}\left\{n_2 - \lambda\frac{dn_2}{d\lambda}\right\} + \frac{\lambda r^2}{2c}\frac{d}{d\lambda}\left(\frac{1}{f}\right).} \tag{2.55}$$

Equation (2.55) indicates that, for an achromatic doublet for which the third term on the right hand side vanishes, the transit time has no more radial dependence. The phase front and wave front are thus parallel, as sketched in Fig. 2.15. In this case, the only mechanism broadening the pulse at the focus is group velocity dispersion. The latter can be larger than with singlet lenses since achromatic doublets usually contain more glass.

2.4.4 Focusing mirrors

Another way to avoid the chromatic aberration and thus pulse broadening is to use mirrors for focusing. With spherical mirrors and on-axis focusing the first aberration to be considered is the spherical one. The analysis of spherical aberration of mirrors serves also as a basis to the study of spherical aberration applied to lenses.

Let us consider the situation of Fig. 2.16, where a plane pulse- and wavefront impinge upon a spherical mirror of radius of curvature R. The reflected rays are the tangents of a caustic — the curve commonly seen as light reflects off a coffee cup. Rays that are a distance r off-axis intersect the optical axis at point T which differs from the paraxial focus F in the paraxial focal plane Σ'. The difference in arrival time between pulses travelling along off-axis rays and on-axis pulses in the paraxial focal plane is:

$$\Delta T = \frac{1}{c}\left[\overline{VQ} - \left(\overline{PS} + \frac{R}{2}\right)\right]. \tag{2.56}$$

Through simple geometrical considerations on can find an expression for ΔT in the form of an expansion in powers of (r/R). The first non-zero term of that expansion is:

$$\Delta T = \frac{3}{4}\frac{R}{c}\left(\frac{r}{R}\right)^4. \tag{2.57}$$

Likewise, one obtains for the geometrical deviation from the paraxial focus in Σ':

$$x = \frac{R}{2}\left(\frac{r}{R}\right)^3. \tag{2.58}$$

For a beam diameter $D = 3$ mm and a focal length $f = 25$ mm the arrival time difference amounts to only 0.1 fs and the deviation from the paraxial focus $x \approx 1$ μm. The numbers increase rapidly with beam size; $\Delta T \approx 13$ fs, $x \approx 25$ μm for $D = 10$ mm, for example.

In experimental situations where even a small aberration should be avoided, parabolic mirrors can advantageously be used to focus collimated input beams. An example requiring such optics is upconversion experiments where fluorescence with fs rise time from a large solid angle has to be focused tightly, without modifying its temporal behavior. Elliptical mirrors should be used to focus light emerging from a point source. However, since parabolic mirrors are more readily available, a combination of parabolic mirrors may be used in lieu of an ellipsoid.

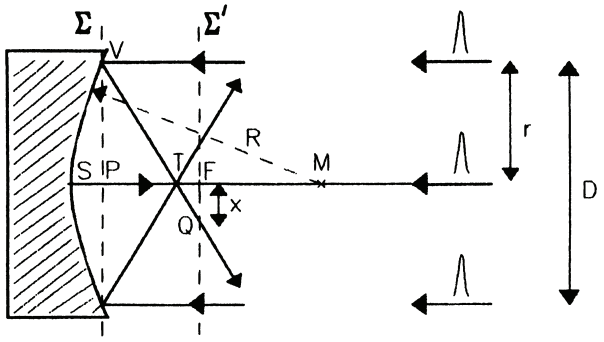

Figure 2.16: Focusing of light pulses by a spherical mirror.

2.5 Elements with angular dispersion

2.5.1 Introduction

Besides focusing elements there are various other optical components which modify the temporal characteristics of ultrashort light pulses through a change of their spatial propagation characteristics.

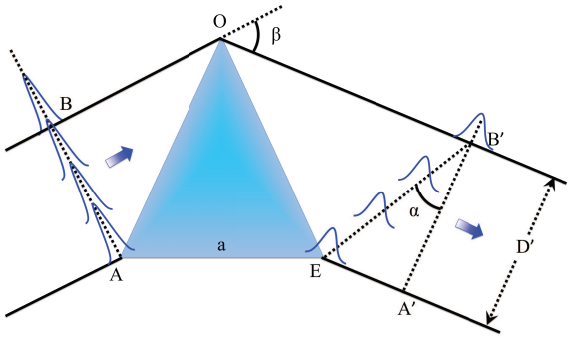

Figure 2.17: Pulse front tilt introduced by a prism. The position of the (plane) wavefronts is indicated by the dashed lines $\overline{AB}$ and $\overline{A'B'}$.

Even a simple prism can provide food for thought in fs experiments. Let us consider an expanded parallel beam of short light pulses incident on a prism, and diffracted by the angle $\beta = \beta(\Omega)$, as sketched in Fig. 2.17. As discussed in Chapter 1, a Gaussian beam with beam waist w_0 self diffracts by an angle of approximately $\theta = \lambda/\pi w_0$. In the case of a short pulse (or white light), this diffraction has to be combined with a spectral diffraction, since the light is no longer monochromatic, and different spectral components will be deflected by the prism with

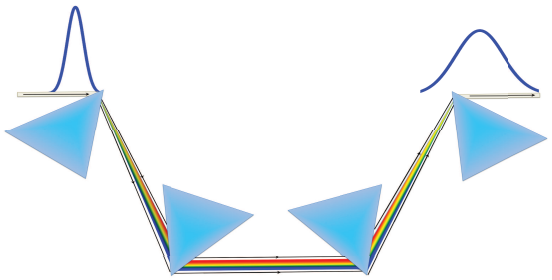

Figure 2.18: Pulse broadening in a four prism sequence.

a different angle $\beta = \beta(\Omega)$. If the pulse is sufficiently short, both effects are of the same order of magnitude, resulting in a complex space-time problem that can no longer be separated. Throughout this section, whether considering group delays or group velocity dispersion, we will consider sufficiently broad beams, and sufficiently short propagation distances L_p behind the prism. This will allow us to neglect the change in beam diameter due to propagation and spectral diffraction after the prism. In most cases we will also approximate the beam with a flat profile. At the end of this chapter the interplay of of propagation and spectral diffraction effects will be discussed for Gaussian beams.

As discussed by Bor *et al.* [26], the prism introduces a tilt of the pulse front with respect to the phase front. As in lenses, the physical origin of this tilt is the difference between group and phase velocity. According to Fermat's principle the prism transforms a phase front $\overline{AB}$ into a phase front $\overline{A'B'}$. The transit times for the phase and pulse fronts along the marginal ray $\overline{BOB'}$ are equal ($v_p \sim v_g$ in air). In contrast the pulse is delayed with respect to the phase in any part of the ray that travels through a certain amount of glass. This leads to an increasing delay across the beam characterized by a certain tilt angle α. The maximum arrival time difference in a plane perpendicular to the propagation direction is $(D'/c)\tan\alpha$.

Before discussing pulse front tilt more thoroughly, let us briefly mention another possible prism arrangement where the above condition for L_p is not necessary. Let us consider for example the symmetrical arrangement of four prisms sketched in Fig. 2.18. During their path through the prism sequence, different spectral components travel through different optical distances. At the output of the fourth prism all these components are again equally distributed in one beam. The net effect of the four prisms is to introduce a certain amount of GVD leading to broadening of an unchirped input pulse. We will see later in this chapter that this particular GVD can be interpreted as a result of angular dispersion and can have a sign opposite to that of the GVD introduced by the glass material constituting the prisms.

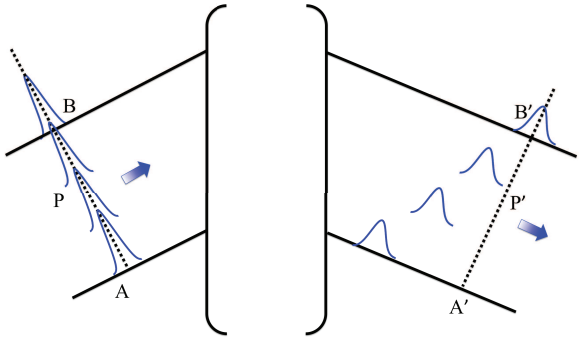

Figure 2.19: Delay of the pulse front with respect to the phase front.

2.5.2 Tilting tilt of pulse fronts of pulse fronts

In an isotropic material the direction of energy flow — usually identified as ray direction — is always orthogonal to the surfaces of constant phase (*wave fronts*) of the corresponding propagating wave. In the case of a beam consisting of ultrashort light pulses, one has to consider in addition planes of constant intensity (*pulse fronts*). For most applications it is desirable that these pulse fronts be parallel to the phase fronts and thus orthogonal to the propagation direction. In the section on focusing elements we have already seen how lenses cause a radially dependent difference between pulse and phase fronts. This leads to a temporal broadening of the intensity distribution in the focal plane. There are a number of other optical components which introduce a tilt of the pulse front with respect to the phase front and to the normal of the propagation direction, respectively. One example was the prism discussed in the introduction of this section. As a general rule, the pulse front tilting should be avoided whenever an optimum focalization of the pulse energy is sought. There are situations where the pulse front tilt is desirable to transfer a temporal delay to a transverse coordinate. Applications exploiting this property of the pulsefront tilt are pulse diagnostics (Chapter 10) and travelling wave amplification (Chapter 8.1).

The general approach for tilting pulse fronts is to introduce an optical element in the beam path which retards the pulse fronts as a function of a coordinate transverse to the beam direction. This is schematically shown in Fig. 2.19 for an element that changes only the propagat ion direction of a (plane) wave. Let us assume that a wavefront $\overline{AB}$ is transformed into a wavefront $\overline{A'B'}$. From Fermat's principle it follows that the optical pathlength P_{OL} between corresponding points at the wavefronts $\overline{AB}$ and $\overline{A'B'}$ must be equal:

$$P_{OL}(BB') = P_{OL}(PP') = P_{OL}(AA'). \tag{2.59}$$

Since the optical pathlength corresponds to a phase change $\Delta\Phi = 2\pi P_{OL}/\lambda$, the propagation time of the wavefronts can be written as

$$T_{phase} = \frac{\Delta\Phi}{\omega_\ell} \tag{2.60}$$

where we referred to the center frequency of the pulse. This phase change is given by

$$\Delta\Phi = \int_P^{P'} k(s)ds = \frac{\omega_\ell}{c}\int_P^{P'} n(s)ds = \omega_\ell \int_P^{P'} \frac{ds}{v_p(s)} \tag{2.61}$$

where s is the coordinate along the beam direction. In terms of the phase velocity the propagation time is

$$T_{phase} = \int_P^{P'} \frac{ds}{v_p(s)}. \tag{2.62}$$

The propagation time of the pulse fronts however, T_{pulse}, is determined by the group velocity

$$T_{pulse} = \int_P^{P'} \frac{ds}{v_g(s)} = \int_P^{P'} \left|\frac{dk}{d\Omega}\right|_{\omega_\ell} ds. \tag{2.63}$$

From Eqs. (2.62) and (2.63) the difference in propagation time between phase front and pulse front becomes

$$\Delta T(P,P') = T_{phase} - T_{pulse} = \int_P^{P'} \left(\frac{1}{v_p} - \frac{1}{v_g}\right) ds = \int_P^{P'} \left[\frac{k_\ell}{\omega_\ell} - \left|\frac{dk}{d\Omega}\right|_{\omega_\ell}\right] ds, \tag{2.64}$$

which can be regarded as a generalization of Eq. (2.37).

A simple optical arrangement to produce pulse front tilting is an interface separating two different optical materials – for instance air (vacuum) and glass (Fig. 2.20). At the interface F the initial beam direction is changed by an angle $\beta = \gamma - \gamma'$ where γ and γ' obey Snell's law $\sin\gamma = n(\omega_\ell)\sin\gamma'$. The point A of an incident wavefront $\overline{AB}$ is refracted at time $t = t_0$. It takes the time interval T_{phase} to recreate the wavefront $\overline{A'B'}$ in medium 2, which propagates without distortion with a phase velocity $v_p = c/n(\omega_\ell)$. The time interval T_{phase} is given by

$$T_{phase} = \frac{n\overline{AA'}}{c} = \frac{\overline{BB'}}{c} = \frac{\overline{PF} + n\overline{FP'}}{c} = \frac{D\,\tan\gamma}{c}. \tag{2.65}$$

The beam path from B to B' is through a nondispersive material and thus pulse front and wavefront coincide at B'. In contrast the phase front and pulse front propagate different distances during the time interval T_{phase} in medium 2 and thus become separated. Since in (most) optical materials the group velocity is smaller than the

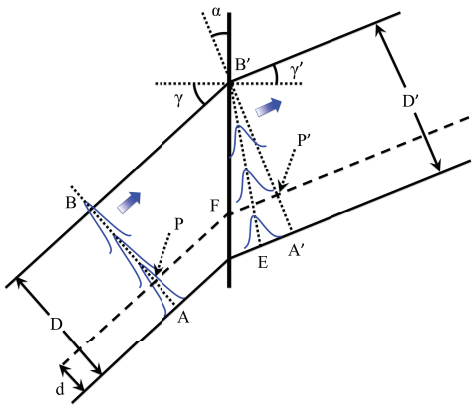

Figure 2.20: Pulse front tilt through refraction at an interface.

phase velocity the pulse front is delayed with respect to the phase front. In our case this delay increases linearly over the beam cross section. The characteristic tilt angle α between pulse and phase fronts is given by

$$\tan\alpha = \frac{\overline{EA'}}{D'}. \tag{2.66}$$

From simple geometrical considerations we find for the two distances

$$\overline{EA'} = \left(\frac{c}{n} - v_g\right) T_{phase} = \left(\frac{c}{n} - v_g\right) \frac{D}{c} \tan\gamma \tag{2.67}$$

and

$$D' = D\frac{\cos\gamma'}{\cos\gamma} = D\frac{\sqrt{n^2 - \sin^2\gamma}}{n\cos\gamma}. \tag{2.68}$$

Inserting Eqs. (2.67) and (2.68) in Eq. (2.66) and using the expression for the group velocity, we obtain for α

$$\tan\alpha = \frac{\omega_\ell n'(\omega_\ell)}{\omega_\ell n'(\omega_\ell) + n(\omega_\ell)} \frac{\sin\gamma}{\sqrt{n^2 - \sin^2\gamma}}. \tag{2.69}$$

Following this procedure we can also analyze the pulse front at the output of a prism, cf. Fig. 2.17. The distance $\overline{EA'}$ is the additional pathlength over which the phase has travelled as compared to the pulse path. Thus, we have

$$\overline{EA'} = v_p \left[\frac{a}{v_g} - \frac{a}{v_p}\right] = a\omega_\ell n'(\omega_\ell) \tag{2.70}$$

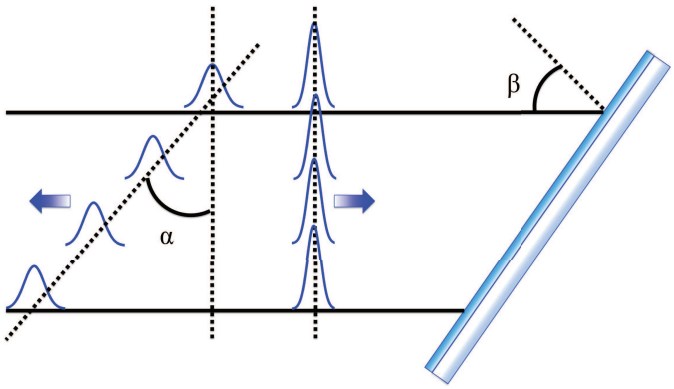

Figure 2.21: Pulse front tilt produced by diffraction at a grating in Littrow configuration.

which results in a tilt angle

$$\tan\alpha = \frac{a}{b}\omega_\ell n'(\omega_\ell) = -\frac{a}{b}\lambda_\ell \left.\frac{dn}{d\lambda}\right|_{\lambda_\ell} \tag{2.71}$$

where $b = D'$ is the beam width.

As pointed out by Bor [26], there is a general relation between pulse front tilt and the angular dispersion $d\beta/d\lambda$ of a dispersive device which reads

$$\boxed{\tan\alpha = \lambda\left|\frac{d\beta}{d\lambda}\right|.} \tag{2.72}$$

The latter equation can be proven easily for a prism, by using the equation for the beam deviation, $d\beta/d\lambda = (a/b)(dn/d\lambda)$, in Eq. (2.71). Similarly to prisms, gratings produce a pulse front tilt, as can be verified easily from the sketch of Fig. 2.21. To determine the tilt angle we just need to specify the angular dispersion in Eq. (2.72) using the grating equation.

2.5.3 GVD through angular dispersion!angular dispersion — General

Angular dispersion has been advantageously used for a long time to resolve spectra or for spectral filtering, utilizing the spatial distribution of the frequency components behind the dispersive element (e.g., prism, grating). In connection with fs optics, angular dispersion has the interesting property of introducing GVD. At first glance this seems to be an undesired effect. However, optical devices based on angular dispersion, which allow for a continuous tuning of the GVD can be designed. This idea was first implemented in [30] for the compression of chirped

pulses with diffraction gratings. The concept was later generalized to prisms and prism sequences [31]. Simple expressions for two and four prism sequences are given in [32, 33]. From a general point of view, the diffraction problem can be treated by solving the corresponding Fresnel integrals [30, 34, 35]. We will sketch this procedure at the end of this chapter. Another successful approach is to analyze the sequence of optical elements by ray-optical techniques and calculate the optical beam path P as a function of Ω. From our earlier discussion we expect the response of any linear element to be of the form:

$$R(\Omega)e^{-i\Psi(\Omega)} \tag{2.73}$$

where the phase delay Ψ is related to the optical pathlength P_{OL} through

$$\Psi(\Omega) = \frac{\Omega}{c} P_{OL}(\Omega). \tag{2.74}$$

$R(\Omega)$ is assumed to be constant over the spectral range of interest and thus will be neglected.

We know that non-zero terms $[(d^n/d\Omega^n)\Psi \neq 0]$ of order $n \geq 2$ are responsible for changes in the complex pulse envelope. In particular

$$\frac{d^2}{d\Omega^2}\Psi(\Omega) = \frac{1}{c}\left(2\frac{dP_{OL}}{d\Omega} + \Omega\frac{d^2P_{OL}}{d\Omega^2}\right) = \frac{\lambda^3}{2\pi c^2}\frac{d^2P_{OL}}{d\lambda^2} \tag{2.75}$$

is related to the GVD parameter. We recall that, with the sign convention chosen in Eq. (2.73), the phase factor Ψ has the same sign as the phase factor $k_\ell L$. Consistent with the definition given in Eq. (1.128) a positive GVD corresponds to $\frac{d^2\Psi}{d\Omega^2} > 0$. In this chapter, we will generally express $\frac{d^2\Psi}{d\Omega^2}$ in fs^2.

The relation between angular dispersion and GVD can be derived through the following intuitive approach. Let us consider a light ray which is incident onto an optical element at point Q, as in Fig. 2.22. At this point we do not specify the element, but just assume that it causes angular dispersion. Thus, different spectral components originate at Q under different angles, within a cone represented by the patterned area in the figure. Two rays corresponding to the center frequency ω_ℓ of the spectrum, $\vec{r}_0$, and to an arbitrary frequency Ω, $\vec{r}_\Omega$, are shown in Fig. 2.22. The respective wavefronts S are labelled with subscript "0" (for the central frequency ω_ℓ) and "Ω" (for the arbitrary frequency Ω). The planes S_Ω, S_0 and S'_Ω, S'_0 are perpendicular to the ray direction and represent (plane) wave fronts of the incident light and diffracted light, respectively. Let P_0 be our point of reference and be located on $\vec{r}_0$ where $\overline{QP_0} = L$. A wavefront S'_Ω of $\vec{r}_\Omega$ at P_Ω is assumed to intersect $\vec{r}_0$ at P_0. The optical pathlength $\overline{QP_\Omega}$ is thus

$$\overline{QP_\Omega} = P_{OL}(\Omega) = P_{OL}(\omega_\ell)\cos\alpha = L\cos\alpha \tag{2.76}$$

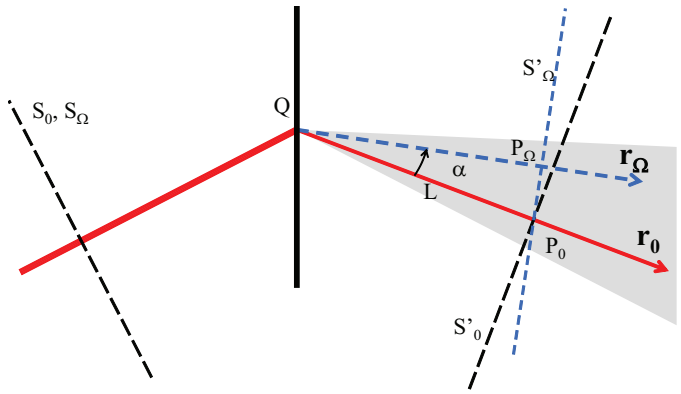

Figure 2.22: Angular dispersion causes GVD. The solid line in the middle of the figure represents the angular dispersive element, providing a frequency dependent deflection of the beam at the point of incidence Q. The different frequency components of the pulse spread out in the patterned area.

which gives for the phase delay

$$\Psi(\Omega) = \frac{\Omega}{c} P_{OL}(\Omega) = \frac{\Omega}{c} L \cos\alpha \tag{2.77}$$

The dispersion constant responsible for GVD is obtained by twofold derivation with respect to Ω:

$$\begin{aligned} \left.\frac{d^2\Psi}{d\Omega^2}\right|_{\omega_\ell} &= -\frac{L}{c}\left\{\sin\alpha\left[2\frac{d\alpha}{d\Omega} + \Omega\frac{d^2\alpha}{d\Omega^2}\right] + \Omega\cos\alpha\left(\frac{d\alpha}{d\Omega}\right)^2\right\}\Bigg|_{\omega_\ell} \\ &\approx -\frac{L\omega_\ell}{c}\left(\left.\frac{d\alpha}{d\Omega}\right|_{\omega_\ell}\right)^2 \end{aligned} \tag{2.78}$$

where $\sin\alpha = 0$ and $\cos\alpha = 1$ if we take the derivatives at the center frequency of the pulse, $\Omega = \omega_\ell$. The quantity $(d\alpha/d\Omega)|_{\omega_\ell}$, responsible for angular dispersion, is a characteristic of the actual optical device to be considered. It is interesting to note that the dispersion parameter is always negative independently of the sign of $d\alpha/d\Omega$ and that the dispersion increases with increasing distance L from the diffraction point. Therefore angular dispersion always results in negative GVD.

Differentiation of Eq. (2.78) results in the next higher dispersion order

$$\begin{aligned}\left.\frac{d^3\Psi}{d\Omega^3}\right|_{\omega_\ell} &= -\frac{L}{c}\left\{\cos\alpha\left[3\left(\frac{d\alpha}{d\Omega}\right)^2+3\Omega\frac{d\alpha}{d\Omega}\frac{d^2\alpha}{d\Omega^2}\right]\right.\\ &+ \left.\sin\alpha\left[3\frac{d^2\alpha}{d\Omega^2}+\Omega\frac{d^3\alpha}{d\Omega^3}-\Omega\left(\frac{d\alpha}{d\Omega}\right)^3\right]\right\}\Bigg|_{\omega_\ell}\\ &\approx -\frac{3L}{c}\left[\left(\frac{d\alpha}{d\Omega}\right)^2+\Omega\frac{d\alpha}{d\Omega}\frac{d^2\alpha}{d\Omega^2}\right]\Bigg|_{\omega_\ell}, \end{aligned} \tag{2.79}$$

where the last expression is a result of $\alpha(\omega_\ell) = 0$.

The most widely used optical device for angular dispersion are prisms and gratings. To determine the dispersion introduced by them we need to specify not only the quantity $\alpha(\Omega)$ in the expressions derived above, but also the optical surfaces between which the path is being calculated. Indeed, we have assumed in the previous calculation that the beam started as a plane wave (plane reference surface normal to the initial beam) and terminates in a plane normal to the ray at a reference optical frequency ω_ℓ. The choice of that terminal plane is as arbitrary as that of the reference frequency ω_ℓ (cf. Chapter 1, Section 1.1.1). After some propagation distance, the various spectral component of the pulse will have separated, and a finite size detector will only record a portion of the pulse spectrum.

Therefore, the "dispersion" of an element has only meaning in the context of a particular application, that will associate reference surfaces to that element. This is the case when an element is associated with a cavity, as will be considered in the next section. In the following sections, we will consider combinations of elements of which the angular dispersion is compensated. In that case, a natural reference surface is the normal to the beam.

2.5.4 GVD of a cavity containing a single prism dispersion!prism

Dispersion control is an important aspect in the development of fs sources. The most elementary laser cavity as sketched in Fig. 2.23 has an element with angular dispersion. The dispersive element could be the Brewster angle laser rod itself. The cavity will be typically terminated by a curved mirror. The two reference surfaces to consider are the two end-mirror of the cavity. We have seen that negative GVD is typically associated with angular dispersion, and positive GVD with the propagation through a glass prism or laser rod [8]. One might therefore expect to be

[8] It is generally the case — but not always — that optical elements in the visible have positive GVD.

able to tune the GVD in the arrangement of Fig. 2.23 from a negative to a positive value.

A Gaussian beam approach of such a cavity is presented below.

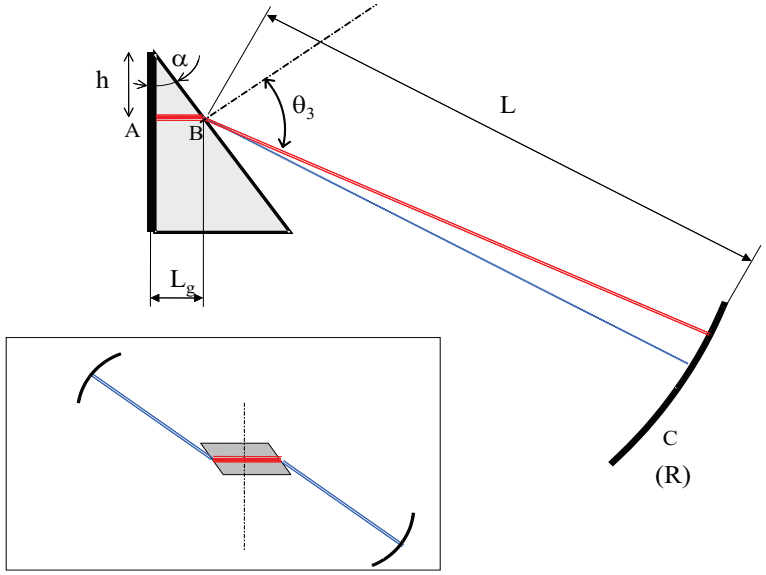

Figure 2.23: Example of a cavity with a single right angle prism. The side of the right angle is an end mirror of the cavity. The cavity is terminated by a curved mirror of radius of curvature R, at a distance L from the Brewster angle exit face of the prism. Stability of the cavity requires that $L + \overline{AB}/n < R$. Translation of the prism allows for an adjustment of the pathlength in glass L_g. The inset shows that this calculation applies to a symmetric cavity with a Brewster-angle laser rod and two spherical mirrors.

The cavity is terminated on one end by the plane face of the prism, on the other end by a spherical mirror of curvature R. The prism–mirror distance measured at the central frequency ω_ℓ is L. The beam originates from a distance h from the apex of the prism (angle α), such that the pathlength in glass can be written as $a = h\tan\alpha$. For the sake of notation simplification, we define $b = \frac{L}{2}\left(1 - \frac{L}{R}\right)$. The Gaussian parameters for this cavity are the beam waist w_0, the Rayleigh range $\rho_0 = \pi n w_0^2/\lambda$, related to the mirror curvature by

$$R = (L + a) + \frac{\rho_0^2}{L + a}. \tag{2.80}$$

The total phase shift for one half cavity round-trip is $\Psi(\Omega) = \Psi_{AB}(\Omega) + \Psi_{BC}(\Omega)$. The phase shift through the glass here is $-k(\Omega)L_g = -\Psi_{AB}(\Omega)$, with $\Psi_{AB}(\Omega)$ given

by:

$$\Psi_{AB}(\Omega) = \arctan\frac{a}{\rho_0} = \arctan\frac{u}{n(\Omega)\Omega}, \tag{2.81}$$

where we have defined $u = 2ac/w_0^2 = 2hc\tan\alpha/w_0^2$. Expanding in a Taylor series:

$$\begin{aligned}\Psi_{AB}(\Omega) &= \Psi_0 + \left.\frac{d\Psi}{d\Omega}\right|_{\omega_\ell}\Delta\Omega + \frac{1}{2}\left.\frac{d^2\Psi}{d\Omega^2}\right|_{\omega_\ell}(\Delta\Omega)^2 + \ldots \\ &\approx \Psi_0 + \frac{u}{n^2\Omega^2+u^2}\left[\Omega\frac{dn}{d\Omega} + n(\Omega)\right]_{\omega_\ell}\Delta\Omega + \\ &\quad \frac{1}{2}\left\{\frac{u}{n^2\Omega^2+u^2}\left[2\frac{dn}{d\Omega} + \Omega\frac{d^2n}{d\Omega^2}\right]_{\omega_\ell} - \frac{2un^2\Omega}{n^2\Omega^2+u^2}\left[\Omega\frac{dn}{d\Omega} + n(\Omega)\right]_{\omega_\ell}\right\}(\Delta\Omega)^2,\end{aligned} \tag{2.82}$$

where $\Delta\Omega = \Omega - \omega_\ell$.

For the path in air, we assume the cavity close enough to concentric, so that $\rho_0 \ll a$ and the geometric approximation applies to the path BC. We have thus a phase shift $-k\overline{BC} = -\Psi_{BC}(\Omega)$, with

$$\Psi_{BC}(\Omega) = \frac{\Omega}{c}\left[L + \frac{L}{2}\left(1 - \frac{L}{R}\right)\Delta\theta^2\right] = \frac{\Omega}{c}\left[L + b\Delta\theta^2\right], \tag{2.83}$$

where $\Delta\theta$ is the departure of dispersion angle from the diffraction angle at ω_ℓ. Within the small angle approximation, we have for $\Delta\theta$:

$$\Delta\theta \approx \Delta\Omega\frac{\sin\alpha}{\cos\theta_3}\frac{dn(\Omega)}{d\Omega} = \Delta\Omega\frac{dn(\Omega)}{d\Omega}. \tag{2.84}$$

The last equality ($\sin\alpha = \cos\theta_3$) applies to the case where θ_3 equals the Brewster angle. The GVD dispersion of this cavity is thus:

$$\begin{aligned}\left.\frac{d^2\Psi}{d\Omega^2}\right|_{\omega_\ell} &= \left.\frac{d^2\Psi_{AB}}{d\Omega^2}\right|_{\omega_\ell} + \left.\frac{d^2\Psi_{BC}}{d\Omega^2}\right|_{\omega_\ell} \\ &= \frac{u}{n^2\omega_\ell^2+u^2}\left(2\frac{dn}{d\Omega} + \Omega\frac{d^2}{d\Omega^2}\right)_{\omega_\ell} - \frac{2un^2\omega_\ell}{n^2\omega_\ell^2+u^2}\left[\Omega\frac{dn}{d\Omega} + n(\Omega)\right]_{\omega_\ell} + \frac{2b\omega_\ell}{c}\left(\left.\frac{dn}{d\Omega}\right|_{\omega_\ell}\right)^2\end{aligned} \tag{2.85}$$

or, using the wavelength dependence of the index of refraction, and taking into account that, for the Brewster prism, $\tan\alpha = 1/n(\omega_\ell)$:

$$\begin{aligned}&\left.\frac{d^2\Psi}{d\Omega^2}\right|_{\omega_\ell} = \\ &\frac{u}{n^2\omega_\ell^2+u^2}\left(\frac{\lambda}{2\pi c}\right)\left(\lambda^2\frac{d^2n}{d\lambda^2}\right)\Bigg|_{\lambda_\ell} - \frac{2un^2\omega_\ell}{n^2\omega_\ell^2+u^2}\left[n - \lambda\frac{dn}{d\lambda}\right]_{\omega_\ell} + b\frac{\lambda^3}{\pi c^2}\left(\frac{dn}{d\lambda}\right)^2\Bigg|_{\lambda_\ell}\end{aligned} \tag{2.86}$$

The stability of the cavity requires that $R > L$, and that the coefficients a and b be positive. In the visible range, most glasses have a positive GVD dispersion ($k" > 0$ or $d^2n/d\lambda^2 > 0$).

The purpose of this exercise is to caution against applying blindly the angular dispersion formula of Eq. (2.86), derived for propagation from one plane wavefront to another plane waveront. In this case, propagating from a beam waist to a curved wavefront, the angular dispersion contribution has a positive sign.

Femtosecond pulses have been obtained through adjustable GVD compensation with a single prism in a dye ring laser cavity [36]. As in the case of Fig. 2.23, the spectral narrowing that would normally take place because of the angular dispersion of the prism was neutralized by having the apex of the prism at a waist of the resonator. In that particular case, the adjustable positive dispersion of the prism provided pulse compression because of the negative chirp introduced by saturable absorption below resonance, as detailed in Chapter 6.

2.5.5 Group velocity control with pairs of prisms ixdispersion !prism

Pairs of elements

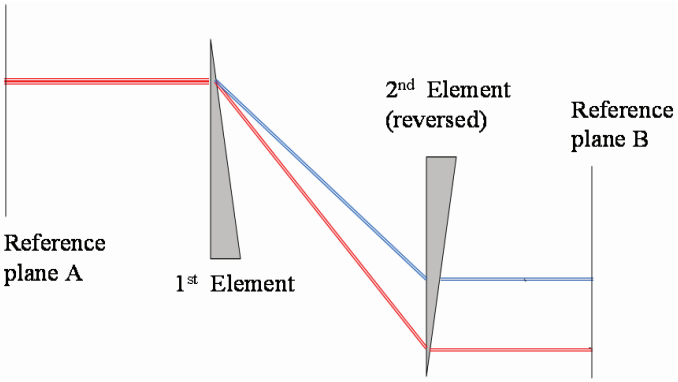

Figure 2.24: Pair of elements with angular dispersion arranged for zero net angular dispersion. The elements are most often prisms or gratings.

In most applications, a second element will be associated to the first one, such that the angular dispersion introduced by the first element is compensated, and all frequency components of the beam are parallel again, as sketched in Fig. 2.24. The elements will generally be prisms or gratings.

As before, we start from a first reference surface A normal to the beam. It seems then meaningful to chose the second reference surface B at the exit of the

system that is normal to the beam. There is no longer an ambiguity in the choice of a reference surface, as in the previous section with a single dispersive element. At any particular frequency, Fermat's principle states that the optical pathes are equal from a point of the wavefront A to the corresponding point on the wavefront B. This is not to say that these distances are not frequency dependent. The spectral components of the beam are still separated in the transverse direction. For that reason, a pair of prisms or gratings provides a way to "manipulate" the pulse spectrum by spatially filtering (amplitude or phase filter) the various Fourier components.

Calculation for matched isosceles prisms.

One of the most commonly encountered case of Fig. 2.24, is that where the two angular dispersive elements are isosceles prisms. Prisms have the advantage of smaller insertion losses, which is particularly important with the low gain solid state lasers used for fs applications.

There are numerous contributions to the group velocity dispersion that makes this problem rather complex:

a) Group velocity dispersion due to propagation in glass for a distance L.

b) Group velocity dispersion introduced by the changes in optical path L in each prism, due to angular dispersion.

c) Group velocity dispersion due to the angular dispersion after one prism, propagation of the beam over a distance ℓ, and as a result propagation through different thicknesses of glass at the next prism.

These considerations by themselves are sufficient to write an expression for the second order dispersion of a pair of prism, using the properties established earlier in this chapter for the relation between angular dispersion and second order dispersion. This expression differs from the most commonly used expression for calculation the dispersion of a pair of prisms [32]. The shortcomings of the latter expressions are:

- The expression of Fork and Gordon [32] implies that the separation between the prisms has both a positive and negative effect, which is not correct.

- The only optical path considered is that between the two prisms; the beam displacement after the second prism is not calculated.

- The expression applies only for the case of tip to tip propagation in the prisms

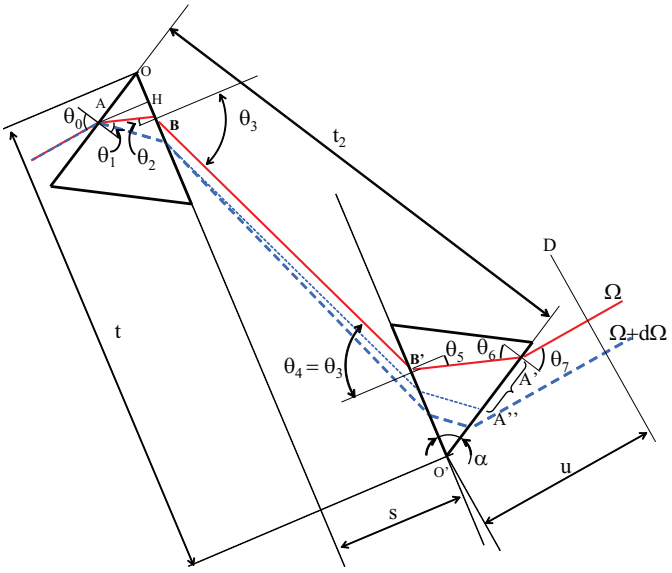

Figure 2.25: Typical two prisms sequence as used in fs laser cavities. The relative position of the prisms is defined by the distance t and the spacing s between the parallel faces OB and $O'B'$. The initial beam enters the prism at a distance $\overline{OA} = a$ from the apex. The distance t_2 between the parallel faces OA and $O'A'$ is $t_2 = t\sin\alpha + s\cos\alpha$. The solid line $ABB'A'D$ traces the beam path at an arbitrary frequency Ω. The beam at the frequency upshifted by $d\Omega$ is represented by the dashed line. The dotted line indicates what the optical path would be in the second prism, if the distance $\overline{BB'}$ were reduced to zero (this situation is detailed in Fig. C.1). "D" is a point on the phase front a distance u from the apex O' of the second prism. In most cases we will associate the beam path for a ray at Ω with the path of a ray at the center frequency ω_ℓ.

In addition to the simple derivation based on the properties of angular dispersion, a rigorous derivation has been made by calculating exactly the optical pathways between parallel wavefronts before and after the pair of prisms [37]. The details of this calculation are reproduced in Appendix C. The result is in agreement with the easily derivable equation based on the properties (a), (b) and (c) cited above:

$$\left.\frac{d^2\Psi}{d\Omega^2}\right|_{\omega_\ell} = \frac{L_g}{c}\left[2\left.\frac{dn}{d\Omega}\right|_{\omega_\ell} + \omega_\ell \left.\frac{d^2n}{d\Omega^2}\right|_{\omega_\ell}\right] - \frac{\omega_\ell}{c}(L)\left(\left.\frac{d\theta_3}{d\Omega}\right|_{\omega_\ell}\right)^2 - \frac{n\omega_\ell}{c}L_g\left(\left.\frac{d\theta_1}{d\Omega}\right|_{\omega_\ell}\right)^2 \quad (2.87)$$

This equation applies to any pair of identical isosceles prisms in the parallel face configuration represented in Fig. 2.25, for an arbitrary angle of incidence. L is the distance between prisms along the beam at ω_ℓ, and L_g is the total distance of glass traversed. The group velocity dispersion is simply the sum of three contributions:

1. The (positive) GVD due to the propagation of the pulse through a thickness of glass L_g.

2. The negative GVD contribution due to the angular dispersion $d\theta_3/d\Omega$ applied to Eq. (2.78) over a distance $\overline{BB'} = s/\cos\theta_3$.

3. The negative GVD contribution due to the angular dispersion $d\theta_1/d\Omega$ (deflection of the beam at the first interface) applied to Eq. (2.78) over a distance L_g in the glass of index n.

In most practical situations it is desirable to write Eq. (C.18) in terms of the input angle of incidence θ_0 and the prism apex angle α. The necessary equations can be derived from Snell's law and Eq. (C.16):

$$\begin{aligned}\frac{d}{d\Omega}\theta_1 &= \frac{1}{n}\left[n^2 - \sin^2(\theta_0)\right]^{-\frac{1}{2}}\left[n\cos\theta_0\frac{d\theta_0}{d\Omega} - \sin\theta_0\frac{dn}{d\Omega}\right] \\ \frac{d}{d\Omega}\theta_3 &= \left[1 - n^2\sin^2(\alpha-\theta_1)\right]^{-\frac{1}{2}}\left[n\cos(\alpha-\theta_1)\frac{d\theta_1}{d\Omega} + \sin(\alpha-\theta_1)\frac{dn}{d\Omega}\right],\end{aligned} \quad (2.88)$$

where $\theta_1 = \arcsin\left(n^{-1}\sin\theta_0\right)$ and $d\theta_0/d\Omega = 0$.

For the particular case of Brewster angle prisms and minimum deviation (symmetric beam path through the prism for $\Omega = \omega_\ell$), we can make the substitutions

$d\theta_1/dn = -1/n^2$, and $d\theta_3/dn = 2$. Using $\theta_0 = \theta_3 = \theta_4 = \theta_7$, the various angles are related by:

$$\begin{aligned} \tan\theta_0 &= n \\ \sin\theta_0 = \cos\theta_1 &= \frac{n}{\sqrt{1+n^2}} \\ \cos\theta_0 = \sin\theta_1 &= \frac{1}{\sqrt{1+n^2}} \\ \sin\alpha &= \frac{2n}{n^2+1} \end{aligned} \tag{2.89}$$

The total second order dispersion in this case becomes:

$$\boxed{\left.\frac{d^2\Psi}{d\Omega^2}\right|_{\omega_\ell} = \frac{L_g}{c}\left[2\left.\frac{dn}{d\Omega}\right|_{\omega_\ell} + \omega_\ell \left.\frac{d^2n}{d\Omega^2}\right|_{\omega_\ell}\right] - \frac{\omega_\ell}{c}\left(4L + \frac{L_g}{n^3}\right)\left(\left.\frac{dn}{d\Omega}\right|_{\omega_\ell}\right)^2,} \tag{2.90}$$

In terms of wavelength:

$$\boxed{\left.\frac{d^2\Psi}{d\Omega^2}\right|_{\omega_\ell} = \frac{\lambda_\ell^3}{2\pi c^2}\left[L_g \left.\frac{d^2n}{d\lambda^2}\right|_{\lambda_\ell} - \left(4L + \frac{L_g}{n^3}\right)\left(\left.\frac{dn}{d\lambda}\right|_{\lambda_\ell}\right)^2\right].} \tag{2.91}$$

In many practical devices, $L >> L_g$ and the second term of Eq. (2.91) reduces to $L(dn/d\lambda)^2$.

It is left as a problem at the end of this chapter to calculate the exact third order dispersion for a pair of prisms. If the angular dispersion in the glass can be neglected ($L >> L_g$), the third order dispersion for a Brewster angle prism is:

$$\begin{aligned} &\Psi'''_{\text{tot}}(\omega_\ell) \approx \\ &\quad \frac{\lambda_\ell^4}{(2\pi c)^2 c}\left[12L\left(n'^2\left[1 - \lambda_\ell n'(n^{-3} - 2n)\right] + \lambda_\ell n' n''\right) - L_g(3n'' + \lambda_\ell n''')\right]. \end{aligned} \tag{2.92}$$

To simplify the notation, we have introduced n', n'' and n''' for the derivatives of n with respect to λ taken at λ_ℓ.

The presence of a negative contribution to the group velocity dispersion due to angular dispersion offers the possibility of tuning the GVD by changing $L_g = g/\sin\theta_0$ (g is the thickness of the glass slab formed by bringing the two prisms together, as shown in Fig. C.1) in Appendix C. A convenient method is to simply translate one of the prisms perpendicularly to its base, which alters the glass path while keeping the beam deflection constant. It will generally be desirable to avoid

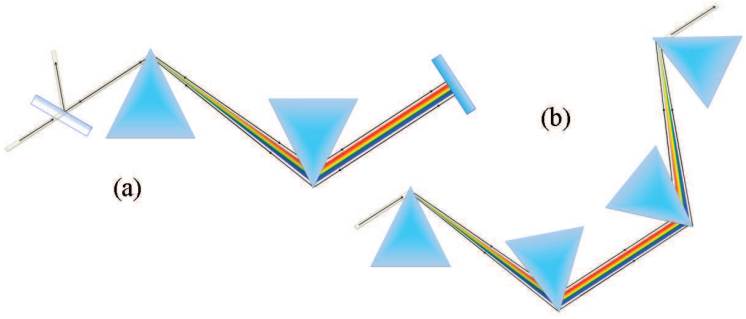

Figure 2.26: Set-ups for adjustable GVD without transverse displacement of spectral components. (a) two prisms followed by end mirror (configuration used mostly in linear cavities). (b) 4 prisms (used in ring cavities). The GVD is tuned by translating one or more prisms into the beam.

a transverse displacement of spectral components at the output of the dispersive device. Two popular prism arrangements which do not separate the spectral components of the pulse are sketched in Fig. 2.26. The beam is either sent through two prism, and retro-reflected by a plane mirror, or sent directly through a sequence of four prisms. In these cases the dispersion as described by Eq. (C.18) doubles. The values of Ψ'', Ψ''', etc. that are best suited to a particular experimental situation can be predetermined through a selection of the optimum prism separation $s/\cos\theta_3$, the glass pathlength L_g, and the material (cf. Table 2.1). Such optimization methods are particularly important for the generation of sub-20 fs pulses in lasers [38, 39] that use prisms for GVD control.

In this section we have derived analytical expressions for dispersion terms of increasing order, in the case of identical isoceles prism pairs, in exactly antiparallel configuration. It is also possible by methods of pulse tracing through the prisms to determine the phase factor at any frequency and angle of incidence [32, 33, 40–42]. The more complex studies revealed that the GVD and the transmission factor R [as defined in Eq. (2.73)] depend on the angle of incidence and apex angle of the prism. In addition, any deviation from the Brewster condition increases the reflection losses. An example is shown in Fig. 2.27.

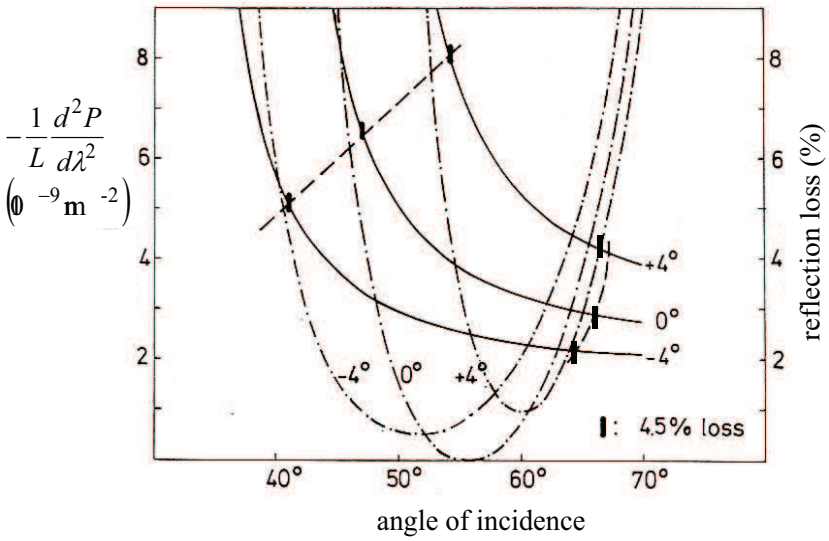

Figure 2.27: Dispersion (solid lines) and reflection losses (dash-dotted lines) of a two-prism sequence (SQ1 - fused silica) as a function of the angle of incidence on the first prism surface. Symmetric beam path through the prism at the central wavelength is assumed. Curves for three different apex angles (-4^o, 0^o, 4^o) relative to $\alpha = 68.9^o$ (apex angle for a Brewster prism at 620 nm) are shown. The tic marks on the dashed lines indicate the angle of incidence and the dispersion where the reflection loss is 4.5%. (from [33]).

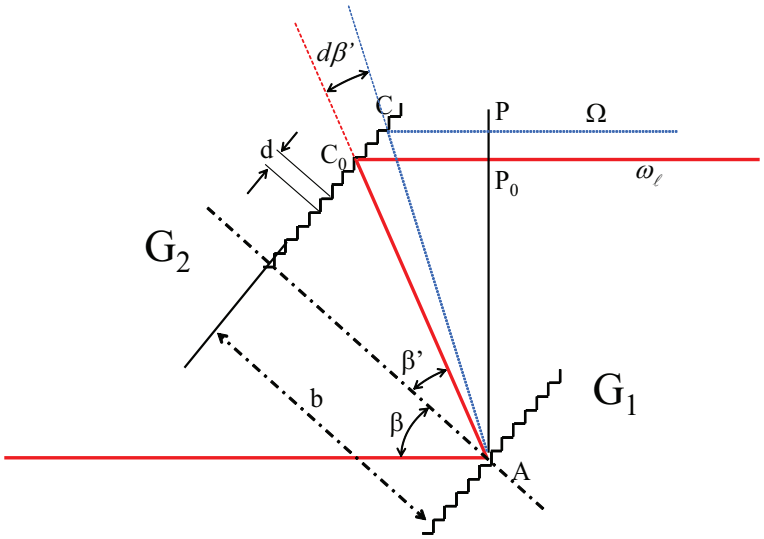

Figure 2.28: Two parallel gratings produce GVD without net angular dispersion. For convenience a reference wavefront is assumed so that the extension of $\overline{PP_0}$ intersects G_1 at A.

2.5.6 GVD introduced by gratings gratings

Gratings can produce larger angular dispersion than prisms. The resulting negative GVD was first utilized by Treacy to compress pulses of a Nd:glass laser [30]. In complete analogy with prisms, the simplest practical device consists of two identical elements arranged as in Fig. 2.28 for zero net angular dispersion. The dispersion introduced by a pair of parallel gratings can be determined by tracing the frequency dependent ray path. The optical path length $\overline{ACP}$ between A and an output wavefront $\overline{PP_o}$ is frequency dependent and can be determined with help of Fig. (2.28) to be:

$$\overline{ACP} = \frac{b}{\cos(\beta')}\left[1+\cos(\beta'+\beta)\right] \tag{2.93}$$

where β is the angle of incidence, β' is the diffraction angle for the frequency component Ω and b is the normal separation between G_1 and G_2. If m is the order of diffraction, the angle of incidence and the diffraction angle are related through the grating equation

$$\sin\beta' - \sin\beta = \frac{2m\pi c}{\Omega d} \tag{2.94}$$

where d is the grating constant. The situation with gratings is however different than with prisms, in the sense that the optical path of two parallel rays out of grating G_1 impinging on adjacent grooves of grating G_2 will see an optical path

difference $\overline{CP} - \overline{C_0P_0}$ of $m\lambda$, m being the diffraction order. Thus, as the angle β' changes with wavelength, the phase factor $\Omega\overline{ACP}/c$ increments by $2m\pi$ each time the ray $\overline{AC}$ passes a period of the ruling of G_2 [30]. Because only the relative phase shift across $\overline{PP_0}$ matters, we may simply count the rulings from the (virtual) intersection of the normal in A with G_2. Thus, for the mth order diffraction we find for $\Psi(\Omega)$:

$$\Psi(\Omega) = \frac{\Omega}{c}\overline{ACP}(\Omega) - 2m\pi\frac{b}{d}\tan(\beta'). \tag{2.95}$$

The group delay is given by:

$$\begin{aligned}\frac{d\Psi}{d\Omega} &= \left(\frac{b}{c}\right)\frac{1+\cos(\beta+\beta')}{\cos\beta'} + \frac{\Omega b}{c\cos^2\beta'}\{\sin\beta'\,[1+\cos(\beta+\beta')] \\ &\quad -\cos\beta'\sin(\beta+\beta')\}\frac{d\beta'}{d\Omega} + \frac{2m\pi}{d}\frac{b}{\cos^2\beta'}\frac{d\beta'}{d\Omega} \\ &= \left(\frac{b}{c}\right)\frac{1+\cos(\beta+\beta')}{\cos\beta'} = \frac{\overline{ACP}(\Omega)}{c}.\end{aligned} \tag{2.96}$$

In deriving the last equation, we have made use of the grating equation $\sin\beta' - \sin\beta = 2\pi c/(\Omega d)$. Equation (2.96) shows remarkable properties of gratings. The group delay is simply equal to the phase delay, and not explicitly dependent on the grating order. The carrier to envelope delay is zero. The second order derivative, obtained by differentiation of Eq. (2.96), is:

$$\begin{aligned}\frac{d^2\Psi}{d\Omega^2} &= \frac{b}{c}\frac{1}{\cos^2\beta'}\{\sin\beta'\,[1+\cos(\beta+\beta')] - \cos\beta'[\sin(\beta+\beta')]\}\frac{d\beta'}{d\Omega} \\ &= \left(\frac{b}{d}\right)\frac{2m\pi}{\omega_\ell\cos\beta'}\left.\frac{d\beta'}{d\Omega}\right|_{\omega_\ell} = \frac{-4\pi^2m^2c}{\omega_\ell^3\cos^2\beta'}\frac{L}{d^2},\end{aligned} \tag{2.97}$$

where we have again made use of the grating equation, and used the distance $L = b/\cos\beta'$ between the gratings along the ray at $\Omega = \omega_\ell$. Using wavelengths instead of frequencies:

$$\boxed{\left.\frac{d^2\Psi}{d\Omega^2}\right|_{\omega_\ell} = -\frac{\lambda_\ell}{2\pi c^2}\left(\frac{m\lambda_\ell}{d}\right)^2\frac{L}{\cos^2\beta'(\lambda_\ell)}.} \tag{2.98}$$

where $\cos^2\beta'(\omega_\ell) = 1 - [2\pi c/(\omega_\ell d) + \sin\beta]^2$. The third derivative can be written as

$$\left.\frac{d^3\Psi}{d\Omega^3}\right|_{\omega_\ell} = -\frac{3}{\omega_\ell}\left.\frac{d^2\Psi}{d\Omega^2}\right|_{\omega_\ell}\left[1 + \frac{2}{3}\frac{m\lambda_\ell}{d}\frac{sin\beta'}{\cos^2\beta'}\right]. \tag{2.99}$$

To decide when the third term in the expansion [as defined in Eq. (1.179)] of the phase response of the grating needs to be considered we evaluate the ratio

$$R_G = \left|\frac{b_3(\Omega-\omega_\ell)^3}{b_2(\Omega-\omega_\ell)^2}\right| = \left|\frac{\Psi'''(\omega_\ell)}{3\Psi''(\omega_\ell)}\right||\Omega-\omega_\ell| \approx \frac{\Delta\omega_p}{\omega_\ell}\left[1 + \frac{2}{3}\frac{m\lambda_\ell}{d}\frac{sin\beta'}{\cos^2\beta'}\right] \tag{2.100}$$

where the spectral width of the pulse $\Delta\omega_p$ was used as an average value for $|\Omega-\omega_\ell|$. Obviously it is possible to minimize (or tune) the ratio of second- and third- order dispersion by changing the grating constant and the angle of incidence. The second order dispersion increases with the square of the ratio $m\lambda_\ell/d\cos\beta'$, thus faster than the ratio R_G that is proportional to that quantity. Grazing incidence, multiple order may be considered when very large dispersion needs to be achieved on a relatively narrow bandwidth.

The derivation of Eq. (2.98) could have been shortened considerably by using the general relation between angular dispersion and GVD, Eq. (2.78). Indeed, deriving from Eq. (2.94) the angular dispersion of a grating

$$\left.\frac{d\beta'}{d\Omega}\right|_{\omega_\ell} = -\frac{2\pi c}{\omega_\ell^2 d\cos\beta'}, \tag{2.101}$$

and inserting in Eq. (2.78), we also obtain Eq. (2.98).

2.5.7 Grating pairs for pulse compressors

For all practical purpose, a pulse propagating from grating G_1 to G_2 can be considered as having traversed a linear medium of length L characterized by a negative dispersion. We can write Eq. (2.98) in the form of:

$$\left.\frac{d^2\Psi}{d\Omega^2}\right|_{\omega_\ell} = k_\ell'' L = -\left\{\frac{\lambda_\ell}{2\pi c^2}\left(m\frac{\lambda_\ell}{d}\right)^2 \frac{1}{\cos^2\beta'(\omega_\ell)}\right\} L. \tag{2.102}$$

Referring to Table 1.4 of Chapter 1, a bandwidth limited Gaussian pulse of duration τ_{G0}, propagating through a dispersive medium characterized by the parameter k_ℓ'', broadens to a Gaussian pulse of duration τ_G

$$\tau_G = \tau_{G0}\sqrt{1+\left(\frac{L}{L_d}\right)^2}, \tag{2.103}$$

with a linear chirp of slope:

$$\ddot{\varphi} = \frac{2L/L_d}{1+(L/L_d)^2}\,\frac{1}{\tau_{G0}^2} \tag{2.104}$$

where the parameter L_d relates both to the parameters of the grating and to the minimum (bandwidth limited) pulse duration:

$$L_d = \frac{\tau_{G0}^2}{2|k_\ell''|} = \pi\left(\frac{c\tau_{G0}}{m\lambda_\ell}\right)^2 \frac{d}{\lambda_\ell}\cos^2\beta'(\omega_\ell). \tag{2.105}$$

Conversely, a pulse with a positive chirp of magnitude given by Eq. (2.104) and duration corresponding to Eq. (2.103) will be compressed by the pair of gratings to a duration τ_{G0}. A pulse compressor following a pulse stretcher is used in numerous amplifications systems and will be dealt with in Chapter 8.1. The "compressor" is a pair of gratings with optical path L, designed for a compression ratio $\tau_G/\tau_{G0} = L/L_d$ [9]. The ideal compressor of length L will restore the initial (before the stretcher) unchirped pulse of duration τ_0. To a departure x from the ideal compressor length L, corresponds a departure from the ideal unchirped pulse of duration τ_0:

$$\tau_G = \tau_{G0}\sqrt{1+\frac{x^2}{L_d^2}}. \tag{2.106}$$

This pulse is also given a chirp coefficient (cf. Table 1.4) $\bar{a} = x/L_d$.

In most compressors, the transverse displacement of the spectral components at the output of the second grating can be compensated by using two pairs of gratings in sequence or by sending the beam once more through the first grating pair. As with prisms, the overall dispersion then doubles. Tunability is achieved by changing the grating separation b. Unlike with prisms, however, the GVD is always negative. The order of magnitude of the dispersion parameters of some typical devices is compiled in Table 2.2.

The choice between gratings and prism for controllable dispersion is not always a simple one. Prisms pairs have lower losses than gratings (the total transmission through a grating pair usually does not exceed 80%), and are therefore the preferred intracavity dispersive element. Gratings are often used in amplifier chain where extremely high compression and stretching ratio are desired, which implies a small L_d. It should be noted however that L_d is not only determined by the properties of the prism or grating, but is also proportional to τ_{G0}^2 as shown by Eq. (2.105). Therefore, prisms stretcher-compressors are also used in medium power amplifiers for sub-20 fs pulses. The disadvantage of prisms is that the beam has to be transmitted through glass, which, for high power pulses, is a nonlinear medium.

2.5.8 Combination of focusing and angular dispersive elements

A disadvantage of prism and grating sequences is that for achieving large GVD the length L between two diffraction elements becomes rather large, cf. Eq.(2.78). As proposed by Martinez *et al.* [43] the GVD of such devices can be considerably increased (or decreased) by using them in connection with focusing elements such as telescopes. Let us consider the optical arrangement of Fig. 2.29, where a telescope is placed between two gratings.

[9] In all practical cases with a pair of gratings, $(L/L_d)^2 \gg 1$.

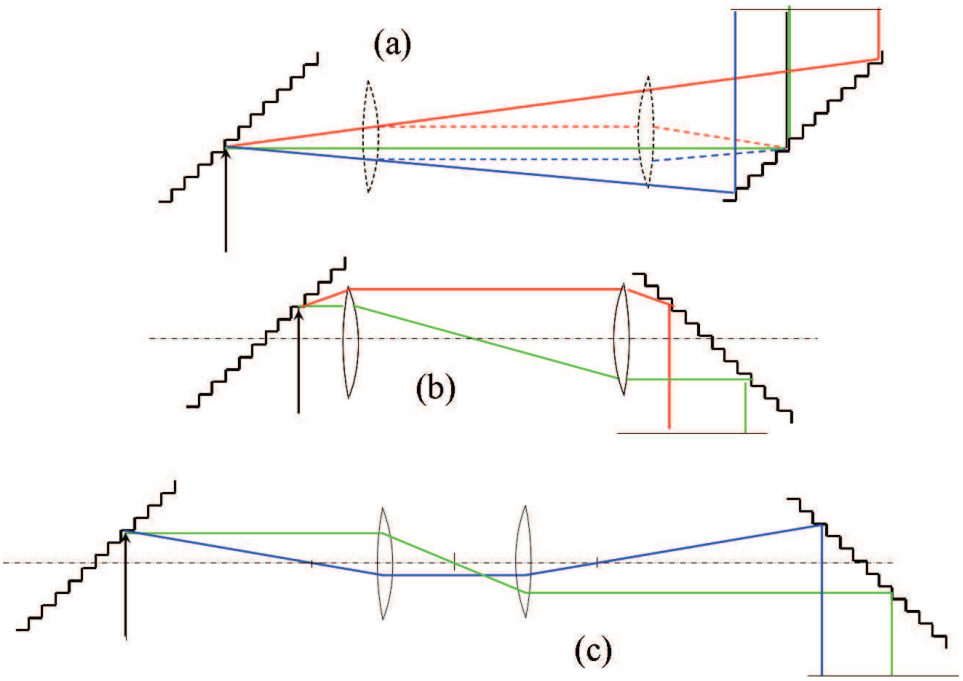

Figure 2.29: Combination of a grating pair and a telescope. (a) Comparison of a standard two grating combination of negative dispersion, and a zero-dispersion arrangement. The solid lines show the beam paths in the standard configuration, as discussed in the previous section and in Fig. 2.28. The total phase shift is largest for the red beam and smallest for the blue beam. The dashed line corresponds to the zero-dispersion configuration, where the gratings are both at a focal point of each lens, and the lens are spaced by two focal distances. It is easily seen that all the optical paths are equal length. (b) Positive dispersion configuration. The spacing between the gratings is smaller than $4f$, while the lens spacing remains $2f$. The green beam has a longer optical path than the red beam. (c) The grating spacing is larger than 4f (the lenses being still $2f$ apart). This is still a negative dispersion configuration: the blue beam has a shorter optical path than the green beam.

Device	λ_ℓ [nm]	ω_ℓ [fs^{-1}]	Ψ'' [fs^2]
fused silica (L_g = 1 cm)	620	3.04	535
	800	2.36	356
Brewster prism	620	3.04	-760
pair, fused silica			
L = 50 cm	800	2.36	-523
grating pair	620	3.04	-9.3 10^4
b = 20 cm; $\beta = 0^o$			
d = 1.2 μm	800	2.36	-3 10^5

Table 2.2: Values of second-order dispersion for typical devices.

The solid lines in Fig. 2.29(a) show the optical path through a pair of parallel gratings, for beam of decreasing wavelength from red (top) to blue (bottom). With two lenses inserted between the gratings, such that the distance between gratings $L = 4f$, all optical paths are rigourously equal (zero dispersion configuration). Therefore, Eq. (2.98) is still valid, provided the distance L between gratings is replaced by $L - 4f$. Since the telescope implies an image inversion, the orientation of the second grating should be reversed, as in Fig. 2.29(b), in which the distance L is smaller than $4f$. The sign of $L - 4f$ is negative, making the second order dispersion Eq. (2.98) *positive*. The green optical path experiences several additional 2π phase shifts on the grating as compared to the red one. Such an arrangement is used in amplifier systems to stretch pulses (chirped pulse amplification [44, 45]. When the distance between gratings is increased beyond $L = 4f$ [Fig. 2.29(c)] the blue beam experiences a larger phase shift than the green beam, indicating negative dispersion.

More generally, as shown in Fig. 2.30, the grating-lens configuration does no need to be symmetrical, neither do the lenses need to have the same focal distance. Let Δ be the distance from the left grating to the left lens of focal distance f, and Δ' the distance from the right grating to the right lens of focal distance f', the overall dispersion is given by:

$$\boxed{\left.\frac{d^2\Psi}{d\Omega^2}\right|_{\omega_\ell} = -\frac{\omega_\ell}{c}\left(\left.\frac{d\alpha}{d\Omega}\right|_{\omega_\ell}\right)^2\left(\Delta + M^2\Delta'\right)} \tag{2.107}$$

where a magnification factor $M = f'/f$ has been introduced. Indeed, the angular dispersion of G_1 is magnified by M to $M(d\alpha/d\Omega)$. For the second grating to produce a parallel output beam its dispersion must be M times larger than that of G_1.

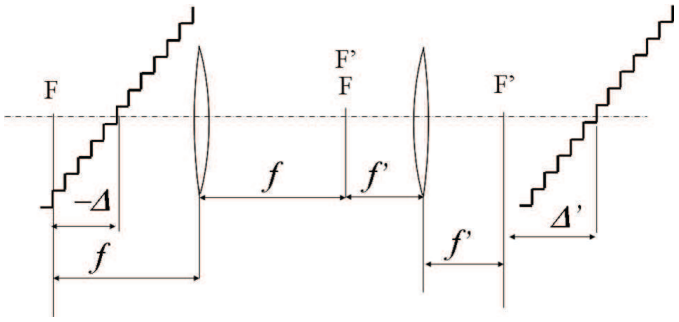

Figure 2.30: Most general configuration of grating-lens combination.

Matrix tools have been developed to compute the propagation of Gaussian beams through a system of gratings. The matrices used are 3×3, an extension of the conventional $ABCD$ matrices for Gaussian beams, with an additional column containing two additional terms to account for angular dispersion. Details can be found in references [46–48].

In summary, the use of telescopes in connection with grating or prism pairs allows us to increase or decrease the amount of GVD as well as to change the sign of the GVD. Interesting applications of such devices include the recompression of pulses after very long optical fibers [43] and extreme pulse broadening (> 1000) before amplification [44]. A more detailed discussion of this type of dispersers, including the effects of finite beam size, can be found in [35].

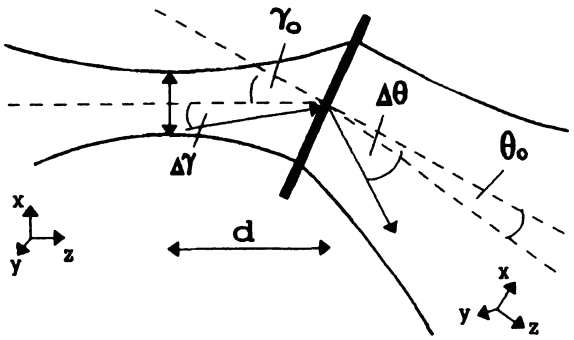

Figure 2.31: Interaction of a Gaussian beam with a disperser.

2.6 Wave-optical description of angular dispersive elements

Because our previous discussion of pulse propagation through prisms, gratings, and other elements was based on ray-optical considerations, it failed to give details about the influence of a finite beam size. These effects can be included by a wave-optical description which is also expected to provide new insights into the spectral, temporal, and spatial field distribution behind the optical elements. We will follow the procedure developed by Martinez [35], and use the characteristics of Gaussian beam propagation, i.e., remain in the frame of paraxial optics.

First, let us analyze the effect of a single element with angular dispersion as sketched in Fig. 2.31. The electric field at the disperser can be described by a complex amplitude $\tilde{U}(x,y,z,t)$ varying slowly with respect to the spatial and temporal coordinate:

$$E(x,y,z,t) = \frac{1}{2}\tilde{U}(x,y,z,t)e^{i(\omega_\ell t - k_\ell z)} + c.c. \tag{2.108}$$

Using Eq. (1.210) the amplitude at the disperser can be written as

$$\tilde{U}(x,y,t) = \tilde{\mathcal{E}}_0(t)\exp\left[-\frac{ik_\ell}{2\tilde{q}(d)}(x^2+y^2)\right] = \tilde{U}(x,t)\exp\left[\frac{-ik_\ell y^2}{2\tilde{q}(d)}\right] \tag{2.109}$$

where $\tilde{q}$ is the complex beam parameter, d is the distance between beam waist and disperser, and $\tilde{\mathcal{E}}_0$ is the amplitude at the disperser. Our convention shall be that x and y refer to coordinates transverse to the respective propagation direction z. Further, we assume the disperser to act only on the field distribution in the x direction, so that the field variation with respect to y is the same as for free space propagation of a Gaussian beam. Hence, propagation along a distance z changes the

last term in Eq. (2.109) simply through a change of the complex beam parameter $\tilde{q}$. According to Eq. (1.216) this change is given by

$$\tilde{q}(d+z) = \tilde{q}(d) + z. \tag{2.110}$$

To discuss the variation of $\tilde{U}(x,t)$ it is convenient to transfer to frequencies $\bar{\Omega}$ and spatial frequencies ρ applying the corresponding Fourier transforms

$$\tilde{U}(x,\bar{\Omega}) = \int_{-\infty}^{\infty} \tilde{U}(x,t) e^{-i\bar{\Omega}t} dt \tag{2.111}$$

and

$$\tilde{U}(\rho,\bar{\Omega}) = \int_{-\infty}^{\infty} \tilde{U}(x,\bar{\Omega}) e^{-i\rho x} dx. \tag{2.112}$$

A certain spatial frequency spectrum of the incident beam means that it contains components having different angles of incidence. Note that $\bar{\Omega}$ is the variable describing the spectrum of the envelope (centered at $\bar{\Omega} = 0$), while $\Omega = \bar{\Omega} + \omega_\ell$ is the actual frequency of the field. In terms of Fig. 2.31 this is equivalent to a certain angular distribution $\Delta\gamma$. The spatial frequency ρ is related to $\Delta\gamma$ through

$$\Delta\gamma = \frac{\rho}{k_\ell}. \tag{2.113}$$

For a plane wave, $\tilde{U}(\rho,\bar{\Omega})$ exhibits only one non-zero spatial frequency component which is at $\rho = 0$. The disperser not only changes the propagation direction ($\gamma_0 \rightarrow \theta_0$) but also introduces a new angular distribution $\Delta\theta$ of beam components which is a function of the angle of incidence γ and the frequency $\bar{\Omega}$

$$\begin{aligned} \Delta\theta &= \Delta\theta(\gamma,\Omega) \\ &= \left.\frac{\partial\theta}{\partial\gamma}\right|_{\gamma_0} \Delta\gamma + \left.\frac{\partial\theta}{\partial\Omega}\right|_{\omega_\ell} \bar{\Omega} \\ &= \alpha\Delta\gamma + \beta\bar{\Omega}. \end{aligned} \tag{2.114}$$

The quantities α and β are characteristics of the disperser and can easily be determined, for example, from the prism and grating equations.[10] By means of Eq. (2.113) the change of the angular distribution $\Delta\gamma \rightarrow \Delta\theta$ can also be interpreted as a transformation of spatial frequencies ρ into spatial frequencies $\rho' = \Delta\theta k_\ell$ where

$$\rho' = \alpha k_\ell \Delta\gamma + k_\ell \beta\bar{\Omega} = \alpha\rho + k_\ell\beta\bar{\Omega}. \tag{2.115}$$

[10] For a Brewster prism adjusted for minimum deviation we find $\alpha = 1$ and $\beta = -(\lambda^2/\pi c)(dn/d\lambda)$. The corresponding relations for a grating used in diffraction order m are $\alpha = \cos\gamma_0/\cos\theta_0$ and $\beta = -m\lambda^2/(2\pi cd\cos\theta_0)$.

Just behind the disperser we have an amplitude spectrum $\tilde{U}_T(\rho', \bar{\Omega})$ given by

$$\tilde{U}_T(\rho', \bar{\Omega}) = C_1 \tilde{U}\left(\frac{1}{\alpha}\rho' - \frac{k_\ell}{\alpha}\beta\bar{\Omega}, \bar{\Omega}\right) \tag{2.116}$$

where C_1 and further constants C_i to be introduced are factors necessary for energy conservation that shall not be specified explicitly. In spatial coordinates the field distribution reads

$$\begin{aligned}
\tilde{U}_T(x, \bar{\Omega}) &= \int_{-\infty}^{\infty} \tilde{U}_T(\rho', \bar{\Omega}) e^{i\rho' x} d\rho' \\
&= C_1 \int_{-\infty}^{\infty} \tilde{U}\left(\frac{1}{\alpha}\rho' - \frac{k_\ell}{\alpha}\beta\bar{\Omega}, \bar{\Omega}\right) e^{i\rho' x} d\rho' \\
&= C_1 \int_{-\infty}^{\infty} \tilde{U}(\rho, \bar{\Omega}) e^{i\alpha\rho x} e^{ik_\ell\beta\bar{\Omega}x} d(\alpha\rho) \\
&= C_2 e^{ik_\ell\beta\bar{\Omega}x} \tilde{U}(\alpha x, \bar{\Omega}).
\end{aligned} \tag{2.117}$$

The disperser introduces a phase factor $\exp\left(ik_\ell\beta\bar{\Omega}x\right)$ and a magnification factor α. For the overall field distribution we obtain with Eqs. (2.109), (2.110), and (2.117)

$$\tilde{U}_T(x, y, \bar{\Omega}) = C_3 \tilde{\mathcal{E}}_0(\bar{\Omega}) e^{ik_\ell\beta\bar{\Omega}x} \exp\left[-\frac{ik_\ell}{2\tilde{q}(d)}\left(\alpha^2 x^2 + y^2\right)\right]. \tag{2.118}$$

The field a certain distance L away from the disperser is connected to the field distribution Eq. (2.118) through a Fresnel transformation which describes the free space propagation. Thus, it can be written as

$$\begin{aligned}
\tilde{U}_T(x, y, L, \bar{\Omega}) &= C_4 \exp\left[\frac{-ik_\ell y^2}{2\tilde{q}(d+L)}\right] \int \tilde{\mathcal{E}}_0(\bar{\Omega}) e^{ik_\ell\beta\bar{\Omega}x'} \\
&\times \exp\left[-i\frac{k_\ell}{2\tilde{q}(d)}\alpha^2 x'^2\right] \exp\left[-\frac{i\pi}{L\lambda}(x - x')^2\right] dx'.
\end{aligned} \tag{2.119}$$

Solving this integral yields an analytical expression for the spectral amplitude

$$\begin{aligned}
\tilde{U}_T(x, y, L, \bar{\Omega}) &= C_5 \tilde{\mathcal{E}}_0(\bar{\Omega}) \exp\left[-ik_\ell \frac{x^2}{2L}\right] \\
&\times \exp\left[-ik_\ell \frac{y^2}{2\tilde{q}(d+L)}\right] \exp\left\{\frac{ik_\ell L}{2} \frac{\tilde{q}(d)}{\tilde{q}(d+\alpha^2 L)} \left[\frac{x^2}{L^2} + 2\frac{\beta x}{L}\bar{\Omega} + \beta^2\bar{\Omega}^2\right]\right\}.
\end{aligned} \tag{2.120}$$

The phase term proportional to $\bar{\Omega}^2$ is responsible for GVD according to our discussion in the section on linear elements. As expected from our ray-optical treatment,

this term increases with increasing distance L and originates from angular dispersion β. The term linear in $\bar{\Omega}$ varies with the transverse coordinate x. It describes a frequency variation across the beam and accounts for different propagation directions of different spectral components. We know that exponentials proportional to $b_1\bar{\Omega}$ result in a pulse delay, as discussed previously following Eq. (1.181). Since $b_1 \propto x$ the pulse delay changes across the beam — a feature which we have called tilt of pulse fronts. This proves the general connection between angular dispersion and pulse front tilting introduced earlier in a more intuitive way.

For a collimated input beam and $\alpha = 1$ we can estimate

$$\frac{\tilde{q}(d)}{\tilde{q}(d+\alpha^2 L)} \approx 1 \tag{2.121}$$

and the temporal delay becomes $b_1 = k_\ell \beta x$. Looking at the beam at a certain instant the corresponding spatial delay is $k_\ell \beta x c$. Thus, we find for the tilt angle α

$$|\tan\alpha| = \left|\frac{d}{dx}(k_\ell \beta x c)\right| = \omega_\ell \left|\frac{d\theta}{d\bar{\Omega}}\Big|_{\bar{\Omega}=0}\right| = \lambda_\ell \left|\frac{d\theta}{d\lambda}\Big|_{\lambda_\ell}\right| \tag{2.122}$$

which confirms our previous results, cf. Eq. (2.72). With the same approximation we obtain for the GVD term:

$$\frac{d^2\Psi}{d\bar{\Omega}^2} = 2b_2 = -k_\ell L\beta^2 = -\frac{L\omega_\ell}{c}\left(\frac{d\theta}{d\Omega}\Big|_{\omega_\ell}\right)^2 \tag{2.123}$$

in agreement with Eq. (2.78).

For compensating the remaining angular dispersion we can use a properly aligned second disperser which has the parameters $\alpha' = 1/\alpha$ and $\beta' = \beta/\alpha$. According to our general relation for the action of a disperser (2.117) the new field distribution after this second disperser is given by

$$\begin{aligned} \tilde{U}_F &= C_2 e^{ik_\ell \frac{\beta}{\alpha}\bar{\Omega}x}\tilde{U}_T\left(\frac{x}{\alpha}, y, L, \bar{\Omega}\right) \\ &= C_6\tilde{\mathcal{E}}_0(\bar{\Omega})e^{\frac{i}{2}k_\ell\bar{\Omega}^2\beta^2 L}\exp\left\{\frac{-ik_\ell}{2}\left[\frac{(x+\alpha\beta\bar{\Omega}L)^2}{\tilde{q}(d+\alpha^2 L)} + \frac{y^2}{\tilde{q}(d+L)}\right]\right\}, \end{aligned} \tag{2.124}$$

which again exhibits the characteristics of a Gaussian beam. Hence, to account for an additional propagation over a distance L', we just have to add L' in the arguments of $\tilde{q}$. As discussed by Martinez [35] $\alpha \neq 1$ gives rise to astigmatism (the position of the beam waist is different for the x and y directions) and only for a well-collimated input beam does the GVD not depend on the travel distance L'

after the second disperser. For $\alpha = 1$ and $q(d + L + L') \approx q(0)$ (collimated input beam) the field distribution becomes

$$\boxed{\tilde{U}_F(x, y, L, \bar{\Omega}) = C_6 \tilde{\mathcal{E}}_0(\bar{\Omega}) e^{\frac{i}{2} k_\ell \beta^2 L \bar{\Omega}^2} \exp\left\{ -\frac{(x + \beta \bar{\Omega} L)^2 + y^2}{w_0^2} \right\}.} \tag{2.125}$$

The first phase function is the expected GVD term. The $\bar{\Omega}$ dependence of the second exponential indicates the action of a frequency filter. At constant position x, its influence increases with increasing $(\beta \bar{\Omega} L / w_0)^2$, i.e., with the ratio of the lateral displacement of a frequency component Ω and the original beam waist. The physics behind is that after the second disperser, not all frequency components can interfere over the entire beam cross-section, leading to an effective bandwidth reduction and thus to pulse broadening. If the experimental situation requires even this to be compensated, the beam can be sent through an identical second pair of dispersers (e.g., prisms). Within the approximations introduced above we just have to replace L by $2L$ in Eqs. (2.124),(2.125). For a well collimated beam ($\beta \bar{\Omega} L / w_0 \ll 1$) this results in

$$\tilde{U}_{F2}(x, y, L, \bar{\Omega}) = C_7 \tilde{\mathcal{E}}_0(\bar{\Omega}) e^{i k_\ell \beta^2 L \bar{\Omega}^2} e^{-(x^2 + y^2)/w_0^2}. \tag{2.126}$$

In this (ideal) case the only modification introduced by the dispersive element is the phase factor leaving the beam characteristics unchanged.

It is quite instructive to perform the preceding calculation with a temporally chirped input pulse as in Eq. (1.41) having a Gaussian spatial as well as temporal profile [35]:

$$\tilde{\mathcal{E}}_0(t) = \mathcal{E}_0 e^{-(1+ia)(t/\tau_G)^2} e^{-(x^2 + y^2)/w_0^2}. \tag{2.127}$$

The (temporal) Fourier transform yields

$$\tilde{\mathcal{E}}_0(\bar{\Omega}) = C_8 \exp\left(i \frac{\bar{\Omega}^2 \tilde{\tau} a}{4} \right) \exp\left(-\frac{\bar{\Omega}^2 \tilde{\tau}^2}{4} \right) \exp\left(-\frac{x^2 + y^2}{w_0^2} \right) \tag{2.128}$$

with $\tilde{\tau}^2 = \tau_G^2 / (1 + a^2)$, where according to our discussion following Eq. (1.47) $\tau_G / \tilde{\tau}$ is the maximum possible shortening factor after chirp compensation. This pulse is to travel through an ideal two-prism sequence described by Eq. (2.125) where βL has to be chosen so as to compensate exactly the quadratic phase term of the input pulse Eq. (2.128). Under this condition the insertion of Eq. (2.128) into Eq. (2.125) yields

$$\tilde{U}_F(x, y, \bar{\Omega}, L) = C_9 e^{-\bar{\Omega}^2 \tilde{\tau}^2 / 4} \exp\left[-\frac{(x + \beta \bar{\Omega} L)^2 + y^2}{w_0^2} \right]. \tag{2.129}$$

The time dependent amplitude obtained from Eq. (2.129) after inverse Fourier transform is

$$\tilde{\mathcal{E}}(t) = C_{10}\exp\left(\frac{-t^2}{\tilde{\tau}^2(1+u^2)}\right)\exp\left[\left(\frac{-x^2}{(1+u^2)w_0^2} - \frac{y^2}{w_0^2}\right)\right]\exp\left[\frac{-iu^2xt}{(1+u^2)\beta L}\right], \quad (2.130)$$

where $u = 2\beta L/(\tilde{\tau}w_0)$. The last exponential function accounts for a frequency sweep across the beam which prevents the different frequency components from interfering completely. As a result, the actual shortening factor is $\sqrt{1+u^2}$ times smaller than the theoretical one, as can be seen from the first exponential function. The influence of such a filter can be decreased by using a large beam size. A measure of this frequency filter, i.e., the magnitude of the quantity $(1+u^2)$, can be derived from the second exponent. Obviously the quantity $(1+u^2)$ is responsible for a certain ellipticity of the output beam which can be measured.

2.7 Optical matrices optical matrix for dispersive systems

In Chapter 1 we pointed out the similarities between Gaussian beam propagation and pulse propagation. Even though this fact has been known for many years [30, 49], it was only recently that optical matrices have been introduced to describe pulse propagation through dispersive systems [46, 50–53] in analogy to optical ray matrices. The advantage of such an approach is that the propagation through a sequence of optical elements can be described using matrix algebra. Dijaili *et al.* [52] defined a 2×2 matrix for dispersive elements which relates the complex pulse parameters (cf. Table 1.4) of input and output pulse, $\tilde{p}$ and $\tilde{p}'$, to each other. Döpel [50] and Martinez [51] used 3×3 matrices to describe the interplay between spatial (diffraction) and temporal (dispersion) mechanisms in a variety of optical elements, such as prisms, gratings and lenses, and in combinations of them. The advantage of this method is the possibility to analyze complicated optical systems such as femtosecond laser cavities with respect to their dispersion — a task of increasing importance, as attempts are being made to propagate ultrashort pulses near the bandwidth limit through complex optical systems. The analysis is difficult since the matrix elements contain information pertaining to both the optical system and of pulse.

One of the most comprehensive approaches to describe ray and pulse characteristics in optical elements by means of matrices is that of Kostenbauder [53]. He defined 4×4 matrices which connect the input and output ray and pulse coordinates to each other. As in ray optics, all information about the optical system is carried in the matrix while the spatial and temporal characteristics of the pulse are

represented in a ray-pulse vector $(x, \Theta, \Delta t, \Delta\nu)$. Its components are defined by position x, slope Θ, time t and frequency ν. These coordinates have to be understood as *difference quantities* with respect to the coordinates of a *reference pulse*. The spatial coordinates are similar to those known from the ordinary $\begin{pmatrix} A & B \\ C & D \end{pmatrix}$ ray matrices. However, the origin of the coordinate system is defined now by the path of a diffraction limited reference beam at the average pulse frequency. This reference pulse has a well-defined arrival time at any reference plane; the coordinate Δt, for example, is the difference in arrival time of the pulse under investigation. In terms of such coordinates and using a 4×4 matrix, the action of an optical element can be written as

$$\begin{pmatrix} x \\ \Theta \\ \Delta t \\ \Delta\nu \end{pmatrix}_{out} = \begin{pmatrix} A & B & 0 & E \\ C & D & 0 & F \\ G & H & 1 & I \\ 0 & 0 & 0 & 1 \end{pmatrix} \begin{pmatrix} x \\ \Theta \\ \Delta t \\ \Delta\nu \end{pmatrix}_{in} \tag{2.131}$$

where A, B, C, D are the components of the ray matrix and the additional elements are

$$E = \frac{\partial x_{out}}{\partial \Delta\nu_{in}}\,, \quad F = \frac{\partial \Theta_{out}}{\partial \Delta\nu_{in}}\,, \quad G = \frac{\partial \Delta t_{out}}{\partial x_{in}}\,, \quad H = \frac{\partial \Delta t_{out}}{\partial \Theta_{in}}\,, \quad I = \frac{\partial \Delta t_{out}}{\partial \Delta\nu_{in}}. \tag{2.132}$$

The physical meaning of these matrix elements is illustrated by a few examples of elementary elements in Fig. 2.32. The occurrence of the zero-elements can easily be explained using simple physical arguments, namely (i) the center frequency must not change in a linear (time invariant) element and (ii) the ray properties must not depend on t_{in}. It can be shown that only six elements are independent of each other [53] and therefore three additional relations between the nine nonzero matrix elements exists. They can be written as

$$\begin{aligned} AD - BC &= 1 \\ BF - ED &= \lambda_\ell H \\ AF - EC &= \lambda_\ell G. \end{aligned} \tag{2.133}$$

Using the known ray matrices [54] and Eq. (2.132), the ray-pulse matrices for a variety of optical systems can be calculated. Let us construct as an example the matrix for an air-glass interface. The various elements can be calculated directly from Snell's law. Let Θ_{in} be the angle of incidence, and Θ_{out} the angle of refraction.

A system matrix can be constructed as the ordered product of matrices corresponding to the elementary operations (as in the example of the prism constructed from the product of two interfaces and a propagation in glass). An important feature of a system of dispersive elements is the frequency dependent optical beam

matrix element	function	example
E	position dispersion	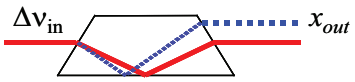
F	angular dispersion	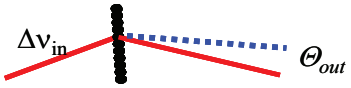
G	tilt of pulse front	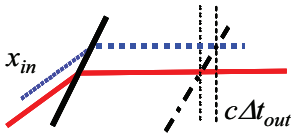
H	delay due to angular disp.	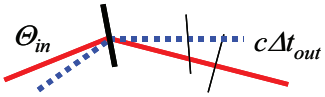
I	delay due to spectrum	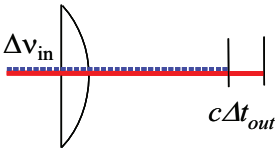

Figure 2.32: Illustration of the function performed by the matric elements E, F, G, H, and I. The path of the reference beam at the central wavelength is represented by the solid line, while the dotted line indicates the displaced path caused by Θ_{in}, x_{in} or $\Delta\nu_{in}$. A dispersive prism introduces a transverse wavelength dependent displacement of the beam, x_{out}. To a change in optical frequency $\Delta\nu_{in}$ from the central frequency ν_ℓ corresponds an angular deviation Θ_{out} at a dispersive interface. At the same dispersive interface, to a transverse displacement x_{in} left of the interface corresponds an energy front tilt $\Delta t_{out} = G x_{in}$ right of the interface. There is also a contribution to the energy front tilt associated with the angular dispersion, which is $\Delta t_{out} = H\Theta_{in}$. Finally, on axis of a lens which has chromatic aberration, the displaced wavelength suffers a delay $\Delta t_{out} = I\Delta\nu_{in}$.

path P, and the corresponding phase delay Ψ. This information is sufficient for geometries that do not introduce a change in the beam parameters. Examples which have been discussed in this respect are four-prism and four-grating sequences illuminated by a well-collimated beam.

As shown in Ref. [53], Ψ can be expressed in terms of the coordinates of the

Lens or Mirror ($\mathcal{M}_L$)	**Brewster Prism** ($\mathcal{M}_{BP}$)
$\begin{pmatrix} 1 & 0 & 0 & 0 \\ -1/f & 1 & 0 & 0 \\ 0 & 0 & 1 & 0 \\ 0 & 0 & 0 & 1 \end{pmatrix}$	$\begin{pmatrix} 1 & L_g/n^3 & 0 & -\frac{SL_g}{n^3} \\ 0 & 1 & 0 & -2S \\ -\frac{2S}{\lambda_\ell} & -\frac{L_gS}{n^3\lambda_\ell} & 1 & \frac{L_gS^2}{n^3\lambda_\ell}+2\pi L_g k''_\ell \\ 0 & 0 & 0 & 1 \end{pmatrix}$
f — focal length	$S = 2\pi \left.\frac{\partial n}{\partial\Omega}\right\|_{\omega_\ell}$, L_g — mean glass path
Dispersive Slab ($\mathcal{M}_{DS}$)	**Grating** ($\mathcal{M}_G$)
$\begin{pmatrix} 1 & L/n & 0 & 0 \\ 0 & 1 & 0 & 0 \\ 0 & 0 & 1 & 2\pi L k''_\ell \\ 0 & 0 & 0 & 1 \end{pmatrix}$	$\begin{pmatrix} -\frac{\cos\beta'}{\cos\beta} & 0 & 0 & 0 \\ 0 & -\frac{\cos\beta}{\cos\beta'} & 0 & \frac{c(\sin\beta'-\sin\beta)}{\lambda_\ell \sin\beta'} \\ \frac{\sin\beta-\sin\beta'}{c\sin\beta} & 0 & 1 & 0 \\ 0 & 0 & 0 & 1 \end{pmatrix}$
$k''_\ell = \left.\frac{d^2k}{d\Omega^2}\right\|_{\omega_\ell}$, L_g – thickness of slab	β – angle of incidence, β' – diffraction angle

Table 2.3: Examples of Ray-Pulse Matrices

system matrix as

$$\Psi = \frac{\pi\Delta\nu^2}{B}(EH - BI) - \frac{\pi}{B\lambda_\ell}Q(\Delta\nu) \tag{2.134}$$

where

$$Q(\Delta\nu) = \begin{pmatrix} x_{in} & x_{out} \end{pmatrix}\begin{pmatrix} A & -1 \\ -1 & D \end{pmatrix}\begin{pmatrix} x_{in} \\ x_{out} \end{pmatrix} + 2\begin{pmatrix} E & \lambda_0 H \end{pmatrix}\begin{pmatrix} x_{in} \\ x_{out} \end{pmatrix} \tag{2.135}$$

and x_{in}, x_{out} are the position coordinates of the input and output vectors, respectively. The argument $\Delta\nu$ of Q and Ψ is the cyclic frequency coordinate relative to the pulse central frequency $\Delta\nu = (\Omega - \omega_\ell)/2\pi$. The calculations according to Eq. (2.134) have to be repeated for a set of frequencies to obtain $\Psi(\nu)$. From $\Psi(\nu)$ we can then determine chirp and temporal behavior of the output pulses using the

relation (1.177) for linear elements without losses. For pulses incident on-axis ($x_{in} = 0$), Eq. (2.135) yields for the phase response

$$\Psi_M(\Delta\nu) = \frac{1}{4\pi B}\left[\left(EH - BI - \frac{1}{\lambda_\ell} DE^2\right)\Delta\nu^2 - 4\pi EH\Delta\nu\right], \tag{2.136}$$

where the index M is to express the derivation of the phase response from the ray-pulse matrix. Information about the temporal broadening can also be gained directly from the matrix element I since $\Delta t_{out} = \Delta t_{in} + \Delta\nu I$. Wave packets centered at different frequencies need different times to travel from the input to the exit plane which gives an approximate broadening of $I\Delta\nu$ for a bandwidth limited input pulse with a spectral width $\Delta\omega_\ell = 2\pi\Delta\nu_\ell$. For on-axis propagation ($x_{in} = x_{out} = 0$) we find $Q(\Delta\nu) = 0$ and the dispersion is given by the first term in Eq. (2.134). For a dispersive slab, for example, we find from Table 2.3:

$$\Psi_M = \frac{1}{2} L_g k''_\ell (\Omega - \omega_\ell)^2 \tag{2.137}$$

which agrees with Eq. (1.184) and the accompanying discussion.

As another example let us discuss the action of a Brewster prism at minimum deviation and analyze the ray-pulse at a distance L_a behind it. The system matrix is the product of ($\mathcal{M}_{BP}$) and ($\mathcal{M}_{DS}$) for free space, which is given by

$$\begin{pmatrix} 1 & B + L_a & 0 & E + FL_a \\ 0 & 1 & 0 & F \\ G & H & 1 & I \\ 0 & 0 & 0 & 1 \end{pmatrix}. \tag{2.138}$$

For the sake of simplicity the elements of the prism matrix have been noted A,B,...,H. For the new position and time coordinate we obtain

$$x_{out} = x_{in} + (B + L_a)\Theta_{in} + (E + FL_a)\Delta\nu \tag{2.139}$$

and

$$\Delta t_{out} = Gx_{in} + H\Theta_{in} + \Delta t_{in} + I\Delta\nu. \tag{2.140}$$

Let us next verify the tilt of the pulse fronts derived earlier. The pulse front tilt can be understood as an arrival time difference Δt_{out} which depends on the transverse beam coordinate x_{out}. The corresponding tilt angle α' is then

$$\tan\alpha' = \frac{\partial(c\Delta t_{out})}{\partial x_{out}} = c\frac{\partial\Delta t_{out}}{\partial x_{in}}\frac{\partial x_{in}}{\partial x_{out}} = cG. \tag{2.141}$$

After we insert G for the Brewster prism, the tilt angle becomes (cf. Table 2.3):

$$\tan\alpha' = -2\omega_\ell \left.\frac{\partial n}{\partial \Omega}\right|_{\omega_\ell} = 2\lambda_\ell \left.\frac{\partial n}{\partial \lambda}\right|_{\lambda_\ell}. \tag{2.142}$$

This result is equivalent to Eq. (2.71) if we use $a/b = 2$, which is valid for Brewster prisms. The different signs result from the direction of the x-axis chosen here.

As a final example we want to apply the matrix formalism to discuss the field distribution behind a two-prism sequence used for pulse compression, such as the one sketched in Fig. 2.25. We assume that one prism is traversed at the apex while the second is responsible for a mean glass path L_g. The corresponding system matrix is obtained by multiplying matrix (2.138) from the left with the transposed[11] matrix of a Brewster prism. The result is

$$\begin{pmatrix} 1 & \frac{L_g}{n^3} + L_a & 0 & -S\left[\frac{L_g}{n^3} + 2L_a\right] \\ 0 & 1 & 0 & 0 \\ 0 & \frac{S}{\lambda_\ell}\left[\frac{L_g}{n^3} + 2L_a\right] & 1 & -\frac{S^2}{\lambda_\ell}\left[\frac{L_g}{n^3} + 4L_g\right] - 2\pi k''_\ell L_g \\ 0 & 0 & 0 & 1 \end{pmatrix}. \tag{2.143}$$

To get a simplified expression, we make the assumption that $L_g \ll L_a$, which allows us to neglect terms linear in L_g in favor of those linear in L_a, whenever they appear in a summation. For the second derivative of the phase response (2.136) we find

$$\Psi''(\omega_\ell) = L_g k''_\ell - \frac{8\pi}{\lambda_\ell} L_a \left(\left.\frac{dn}{d\Omega}\right|_{\omega_\ell}\right)^2 \tag{2.144}$$

which is consistent with the exact solution Eq. (C.18), within the approximation of $L_g \ll L_a$, implying negligible angular dispersion inside the prisms.

It is well known that ray matrices can be used to describe Gaussian beam propagation, e.g., [54]. The beam parameter of the output beam is connected to the input parameter by

$$\tilde{q}_{out} = \frac{A\tilde{q}_{in} + B}{C\tilde{q}_{in} + D}. \tag{2.145}$$

Kostenbauder [53] showed that, in a similar manner, the ray-pulse matrices contain all information which is necessary to trace a generalized Gaussian beam through the optical system. Using a 2×2 complex "beam" matrix ($\tilde{Q}_{in}$), the amplitude of a generalized Gaussian beam is of the form

$$\exp\left[-\frac{i\pi}{\lambda_\ell}\begin{pmatrix} x_{in} & x_{out} \end{pmatrix}\left(\tilde{Q}_{in}\right)^{-1}\begin{pmatrix} x_{in} \\ t_{in} \end{pmatrix}\right] \tag{2.146}$$

[11] Note that the second prism has an orientation opposite to the first one.

which explicitly varies as

$$\exp\left[-\frac{i\pi}{\lambda_\ell}\left(\tilde{Q}^r_{xx}x^2_{in}+2\tilde{Q}^r_{xt}x_{in}t_{in}-\tilde{Q}^r_{tt}t^2_{in}\right)\right]$$
$$\times\quad \exp\left[\frac{\pi}{\lambda_\ell}\left(\tilde{Q}^i_{xx}x^2_{in}+2\tilde{Q}^i_{xt}x_{in}t_{in}-\tilde{Q}^i_{tt}t^2_{in}\right)\right], \tag{2.147}$$

where $\tilde{Q}^r_{ij}$, $\tilde{Q}^i_{ij}$ are the real and imaginary coordinates of the matrix $(\tilde{Q}_{in})^{-1}$ and $\tilde{Q}_{xt}=-\tilde{Q}_{tx}$. The first factor in Eq.(2.147) expresses the phase behavior and accounts for the wave front curvature and chirp. The second term describes the spatial and temporal beam (pulse) profile. Note that unless $\tilde{Q}^{r,i}_{xt}=0$ the diagonal elements of $(\tilde{Q}_{in})$ do not give directly such quantities as pulse duration, beam width, chirp parameter, and wave front curvature. One can show that the field at the output of an optical system is again a generalized Gaussian beam where in analogy to (2.145) the generalized beam parameter $(\tilde{Q}_{out})$ can be written as

$$\left(\tilde{Q}_{out}\right)=\frac{\begin{pmatrix}A & 0\\ G & 1\end{pmatrix}\left(\tilde{Q}_{in}\right)+\begin{pmatrix}B & E/\lambda_\ell\\ H & I/\lambda_\ell\end{pmatrix}}{\begin{pmatrix}C & 0\\ 0 & 0\end{pmatrix}\left(\tilde{Q}_{in}\right)+\begin{pmatrix}D & F/\lambda_\ell\\ 0 & 1\end{pmatrix}}. \tag{2.148}$$

The evaluation of such matrix equations is quite complex since it generally gives rather large expressions. However, the use of advanced algebraic formula-manipulation computer codes makes this approach practicable.

2.8 Numerical approaches

The analytical and quasi-analytical methods to trace pulses give much physical insight but fail if the optical systems become too demanding and/or many dispersion orders have to be considered.

There are commercial wave and ray tracing programs available that allow one to calculate not only the geometrical path through the system but also the associated phase. Thus complete information on the complex field distribution (amplitude and phase) in any desired plane is retrievable.

Problems

1. Dispersion affects the bandwidth of wave-plates. Calculate the maximum pulse duration for which a 10^{th} order quarter wave plate can be made of

crystalline quartz, at 266 nm, using the parameters given with Eq. (2.2). We require that the quarter-wave condition still be met with 5% accuracy at $\pm (1/\tau_p)$ of the central frequency. What is the thickness of the wave-plate?

2. We consider here a Fabry-Perot cavity containing a gain medium. To simplify, we assume the gain to be linear and uniform in the frequency range around a Fabry-Perot resonance of interest. Consider this system to be irradiated by a tunable probe laser of frequency ν_p.

   a Find an expression for the transmission and reflection of this Fabry-Perot with gain as a function of the frequency of the probe laser.

   b Find the gain for which the expression for the transmission tends to infinity. What does it mean?

   c Describe how the gain modifies the transmission function of the Fabry-Perot (linewidth, peak transmission, peak reflection). Sketch the transmission versus frequency for low and high gain.

   d With the probe optical frequency tuned to the frequency for which the empty (no gain) Fabry-Perot has a transmission of 50%, find its transmission factor for the value of the gain corresponding to lasing threshold.

3. Calculate the transmission of pulse propagating through a Fabry-Perot interferometer. The electric field of the pulse is given by $E(t) = \mathcal{E}(t)e^{i\omega_\ell t}$, where $\mathcal{E}(t) = \exp(-|t|/\tau)$ and $\tau = 10$ ns. The Fabry Perot cavity is 1 mm long, filled with a material of index $n_0 = 1.5$, and both mirrors have a reflectance of 99.9%. The wavelength is 1 μm. What is the transmission linewidth (FWHM) of this Fabry-Perot? Find analytically the shape (and duration) of the pulse transmitted by this Fabry Perot, assuming exact resonance.

4. Consider the same Fabry-Perot as in the previous problem, on which a Gaussian pulse (plane wave) is incident. The frequency of the Gaussian pulse is 0.1 ns^{-1} below resonance. Calculate (numerically) the shape of the pulse transmitted by this Fabry Perot, for various values of the pulse chirp a. The pulse envelope is:

$$\tilde{\mathcal{E}}(t) = e^{-(1+ia)(\frac{t}{\tau_G})^2}.$$

   Is there a value of a for which the pulse transmitted has a minimum duration?

5. Consider the Gires–Tournois interferometer. (a) As explained in the text, the reflectivity is R = constant = 1, while the phase shows a strong variation with frequency. Does this violate the Kramers–Kronig relation? Explain your answer. (b) Derive the transfer function (**??**).

6. Derive an expression for the space-time intensity distribution of a pulse in the focal plane of a chromatic lens of focal length $f(\lambda)$. To obtain an analytical formula make the following assumptions. The input pulse is bandwidth-limited and exhibits a Gaussian temporal and transverse spatial profile. The lens has an infinitely large aperture and the GVD can be neglected. [Hint: You can apply Gaussian beam analysis for each spectral component to obtain the corresponding field in the focal plane. Summation over spectral contributions (Fourier back-transform) gives then the space-time field distribution.]

7. Calculate the third order dispersion for a pair of isosceles prisms, not necessarily used at the minimum deviation angle, using the procedure that led to Eq. (C.18). Compare with Eq. (2.92).

8. Calculate the optimum pair of prisms to be inserted into the cavity of a femtosecond pulse laser at 620 nm. The criterium is that the prism pair should provide a 20% GVD tunability around -800 fs^2, and the next higher-order dispersion should be as small as possible. With the help of Table 2.1 choose a suitable prism material, calculate the apex angle of the prisms for the Brewster condition at symmetric beam path, and determine the prism separation. If needed, assume a beam diameter of 2 mm to estimate a minimum possible glass path through the prisms.

9. Derive the ray-pulse matrix (2.143) for a pair of Brewster prisms. Verify the second-order dispersion given in relation (C.18), without the assumption of $L_g \ll L_a$.

10. Derive the delay and aberration parameter of a spherical mirror as given in Eqs. (2.56) and (2.57). Explain physically what happens if a parallel input beam impinges on the mirror with a certain angle α.

11. A parallel beam with plane pulse fronts impinges on a circular aperture with radius R centered on the optic axis. The pulse is unchirped and Gaussian. Estimate the frequency shift that the diffracted pulse experiences if measured with a detector placed on the optic axis. Give a physical explanation of this shift. Make a numerical estimate for a 100 fs and a 10 fs pulse. Can this effect be used to obtain ultrashort pulses in new spectral regions by placing diffracting apertures in series? [Hint: you can start with Eq. (2.51) and take out the lens terms. For mathematical ease you can let $R \to \infty$).] Note that a frequency shift (of the same origin) occurs when the on-axis pulse spectrum of a Gaussian beam is monitored along its propagation path.

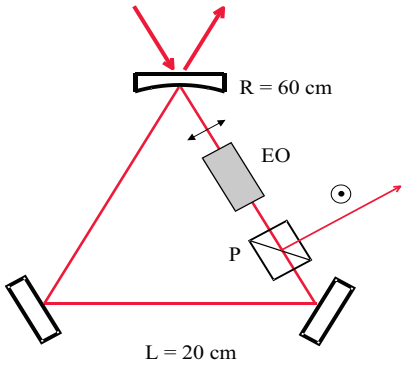

Figure 2.33: Ring resonator. Consider the electro-optic switch (EO, Pockel's cell) and the polarizing beam splitter only for part (d). The polarization of the beam circulating in the cavity gets rotated from the plane of the ring into the orthogonal direction when an electrical pulse is applied to the Pockel's cell, and extracted from the cavity by a polarizing beam splitter. The risetime of the electrical pulse is short compared to the cavity round-trip time.

12. Consider the 3-mirror ring resonator sketched in Fig. 2.33. Two of the mirrors are flat and 100% reflecting, while one mirror of field reflectivity $r = 0.9999\%$ and 60 cm curvature, serves as input and output of this resonator. We are operating at a wavelength of 800 nm. The perimeter of the ring is 60 cm. A beam with a train of pulses, of average incident power of $P_0 = 1$ mW is sent, properly aligned, into the input path of this resonator.

    a Calculate the size and location of the beam waist w_0 of the fundamental mode of this resonator, and the size of the beam (w) at the output mirror. Explain why the output power P_2 does not depend on the wavelength.

    b Derive an expression for the field inside the resonator E_i as a function of the input field E_0.

    c Consider this passive cavity being irradiated from the outside by a train of femtosecond pulses, for its use as a photon storage ring. Show that two conditions need to be fulfilled for this cavity to be exactly resonant, which may not always be simultaneously met.

    d Let us assume next that the train of pulses, with a wavelength near 800 nm, corresponds to exactly a "resonance" of this resonator, both

in frequency and repetition rate. A fast electro-optic switch is included in the ring, such that it directs the electromagnetic wave out of the resonator for a round-trip time of the cavity, every N round-trip times (cavity dumping). The switch opens in a time short compared to the round-trip time. Explain how this device can be used to create short output pulses with a larger single-pulse energy than the incident pulses. What energy could be obtained in the case of (i) $N = 100$ and (ii) $N = 5000$.

Bibliography

[1] V. G. Dmitriev, G. G. Gurzadyan, and D. N. Nikogosyan. *Handbook of Nonlinear Material*. Springer-Verlag, Berlin, 1999.

[2] F. J. Duarte. Dye lasers. In F. J. Duarte, editor, *Tunable Lasers Handbook*. Academic Press, Boston, 1994.

[3] Willian H. Press, Brian P. Flannery, Saul E. Teukolsky, and William P. Vetterling. *Numerical Recipes*. Cambridge University Press, New York, 1986.

[4] S. DeSilvestri, P. Laporta, and O. Svelto. The role of cavity dispersion in cw mode-locked lasers. *IEEE J. Quantum Electron.*, QE-20:533–539, 1984.

[5] W. Dietel, E. Dopel, K. Hehl, W. Rudolph, and E. Schmidt. Multilayer dielectric mirrors generated chirp in femtosecond dye ring lasers. *Optics Comm.*, 50:179–182, 1984.

[6] W. H. Knox, N. M. Pearson, K. D. Li, and C. A. Hirlimann. Interferometric measurements of femtosecond group delay in optical components. *Optics Lett.*, 13:574–576, 1988.

[7] K. Naganuma, K. Mogi, and H. Yamada. Group delay measurement using the fourier transform of an interferometric cross-correlation generated by white light. *Optics Lett.*, 7:393–395, 1990.

[8] K. Naganuma and H. Yasaka. Group delay and alpha-parameter measurement of 1.3 micron semiconductor traveling wave optical amplifier using the interferometric method. *IEEE J. Quantum Electron.*, 27:1280–1287, 1991.

[9] A. M. Weiner, J. G. Fujimoto, and E. P. Ippen. Femtosecond time-resolved reflectometry measurements of multiple-layer dielectric mirrors. *Opt. Lett.*, 10:71–73, 1985.

[10] A. M. Weiner, J. G. Fujimoto, and E. P. Ippen. Compression and shaping of femtosecond pulses. In D. H. Auston and K. B. Eisenthal, editors, *Ultrafast Phenomena IV*, pages 11–15, New York, 1984. Springer-Verlag.

[11] J.-C. Diels, W. Dietel, E. Dopel, J. J. Fontaine, I. C. McMichael, W. Rudolph, F. Simoni, R. Torti, H. Vanherzeele, and B. Wilhelmi. Colliding pulse femtosecond lasers and applications to the measurement of optical parameters. In D.H. Auston and K. B. Eisenthal, editors, *Ultrafast Phenomena IV*, pages 30–34, New York, 1984. Springer-Verlag.

[12] Koji Masuda, James Hendrie, Jean-Claude Diels, and Ladan Arissian. Envelope, group and phase velocities in a nested frequency comb. *Journal of Physics B*, 49:085402, 2016.

[13] M. Born and E. Wolf. *Principles of Optics – Electromagnetic theory of propagation, interference and diffraction of light*. Pergamon Press, Oxford, New York, 1980.

[14] James Hendrie, Matthias Lenzner, Hanieh Akhamiardakani, Jean-Claude Diels, and Ladan Arissian. Impact of resonant dispersion on the sensitivity of intracavity phase interferometry and laser gyros. *Optics Express*, 24:30402–304010, 2016.

[15] James Hendrie, Ning Hsui, and Jean-Claude Diels. Control of frequency combs with passive resonators. *Sensors*, 23:1066, 2023.

[16] J. Desbois, F. Gires, and P. Tournois. A new approach to picosecond laser pulse analysis and shaping. *IEEE J. Quantum Electron.*, QE-9:213–218, 1973.

[17] J. Kuhl and J. Heppner. Compression of fs optical pulses with dielectric multi-layer interferometers. *IEEE J. Quantum Electron.*, QE-22:182–185, 1986.

[18] M. A. Duguay and J. W. Hansen. Compression of pulses from a mode-locked He-Ne laser. *Appl.Phys.Lett.*, 14:14–15, 1969.

[19] J. Heppner and J. Kuhl. Intracavity chirp compensation in a colliding pulse mode-locked laser using thin-film interferometers. *Appl.Phys.Lett.*, 47:453–455, 1985.

[20] R. Szipöks, K. Ferenz, C. Spielman, and F. Krausz. Chirped multilayer coatings for broadband dispersion control in femtosecond lasers. *Opt. Lett.*, 19:201–203, 1994.

[21] F. X. Kärtner, N. Matuschek, T. Schibli, U. Keller, H. A. Haus, C. Heine, R. Morf, V. Scheuer, M. Tilsch, and T. Tschudi. Design and fabrication of double chirped mirrors. *Opt. Lett.*, 22:831–833, 1997.

[22] G. Tempea, F. Krausz, C. Spielman, and K. Ferenz. Dispersion control over 150 THz with chirped dielectric mirrrors. *IEEE Selected Topics in Quant. Electron.*, 4:193–196, 1998.

[23] G. Tempea, V. Yakovlev, B. Bacovic, F. Krausz, and K. Ferenz. Tilted-front interface chirped mirrors. *J. Opt. Soc. Am. B*, 18:1747–1750, 2001.

[24] N. Matuschek, L. Gallmann, D. H. Shutte, G. Steinmeyer, and U. Keller. Back-side coated chirped mirrors with smooth ultra-broadband dispersion characteristics. *Appl. Phys. B*, 71:509–522, 2000.

[25] Z. Bor. Distortion of femtosecond laser pulses in lenses and lens systems. *Journal of Modern Optics*, 35:1907–1918, 1988.

[26] Z. Bor. Distorsion of femtosecond laser pulses in lenses. *Optics Letters*, 14:119–121, 1989.

[27] M. Kempe, W. Rudolph, U. Stamm, and B. Wilhelmi. Spatial and temporal transformation of femtosecond laser pulses by lenses and lens systems. *J. Opt. Soc. Am.*, B9:1158–1165, 1992.

[28] M. Kempe and W. Rudolph. The impact of chromatic and spherical aberration on the focusing of ultrashort light pulses by lenses. *Opt. Lett.*, 18:137–139, 1993.

[29] M. Kempe and W. Rudolph. Femtosecond pulses in the focal region of lenses. *Phys. Rev.*, A48:4721–4729, 1993.

[30] E. B. Treacy. Optical pulse compression with diffraction gratings. *IEEE J. Quantum Electron.*, QE-5:454–460, 1969.

[31] F. J. Duarte and J. A. Piper. Dispersion theory of multiple prisms beam expanders for pulsed dye lasers. *Optics Comm.*, 43:303–307, 1982.

[32] R. L. Fork, O. E. Martinez, and J. P. Gordon. Negative dispersion using pairs of prism. *Opt. Lett.*, 9:150–152, 1984.

[33] V. Petrov, F. Noack, W. Rudolph, and C. Rempel. Intracavity dispersion compensation and extracavity pulse compression using pairs of prisms. *Exp. Technik der Physik*, 36:167–173, 1988.

[34] C. Froehly, B. Colombeau, and M. Vampouille. Shaping and analysis of picosecond light pulses. *Progress of Modern Optics*, XX:115–125, 1981.

[35] O. E. Martinez. Grating and prism compressor in the case of finite beam size. *J.Opt.Soc.Am.B*, 3:929–934, 1986.

[36] W. Dietel, J. J. Fontaine, and J.-C. Diels. Intracavity pulse compression with glass: a new method of generating pulses shorter than 60 femtoseconds. *Optics Letters*, 8:4–6, 1983.

[37] Ladan Arissian, Jean-Claude Diels, and Andreas Velten. Group velocity control by atomic nonlinear response in a laser cavity. In *CLEO, 2007*, page 130 (MC4), Baltimore, MA, 2007. Optical Society of America.

[38] P. F. Curley, Ch. Spielmann, T. Brabec, F. Krausz, E. Wintner, and A. J. Schmidt. Operation of a fs Ti:sapphire solitary laser in the vicinity of zero group-delay dispersion. *Opt. Lett.*, 18:54–57, 1993.

[39] M. T. Asaki, C. P. Huang, D. Garvey, J. Zhou, H. Kapteyn, and M. M. Murnane. Generation of 11 fs pulses from a self-mode-locked Ti:sapphire laser. *Opt. Lett.*, 18:977–979, 1993.

[40] O. E. Martinez, J. P. Gordon, and R. L. Fork. Negative group-velocity dispersion using diffraction. *J. Opt. Soc. Am.*, A1:1003–1006, 1984.

[41] F. J. Duarte. Generalized multiple-prism dispersion theory for pulse compression in ultrafast dye lasers. *Opt. and Quant.Electr.*, 19:223–229, 1987.

[42] C. P. J. Barty, C. L. Gordon III, and B. E. Lemoff. Multiterawatt 30-fs Ti:sapphire laser system. *Optics Lett.*, 19:1442–1444, 1994.

[43] O. E. Martinez. 3000 times grating compressor with positive group velocity dispersion: application to fiber compensation in the 1.3-1.6 μm region. *IEEE J. of Quantum Electron.*, 23:59–64, 1987.

[44] M. Pessot, P. Maine, and G. Mourou. 1000 times expansion compression of optical pulses for chirped pulse amplification. *Optics Comm.*, 62:419, 1987.

[45] M. Pessot, J. Squier, G. Mourou, and G. Vaillancourt. Chirped-pulse amplification of 100-fs pulses. *Optics Lett.*, 14:797–799, 1989.

[46] O. E. Martinez. Matrix formalism for pulse compressors. *IEEE J.Quantum Electron.*, QE-24:2530–2536, 1988.

[47] R. Guther. The *ABCD*-matrix for holographic gratings. *Optica Acta*, 11:97–104, 1981.

[48] A. E. Siegman. *ABCD*-matrix elements for a curved diffraction grating. *Journal of the Optical Society of America A*, 2:1793, 1985.

[49] S. A. Akhmanov, A. P. Sukhorov, and A. S. Chirkin. Nontationary phenomena and space-time analogy in nonlinear optics. *Sov. Phys. JETP*, 28:748–757, 1969.

[50] E. Doepel. Matrix formalism for the calculation of group delay and group-velocity dispersion in linear optical elements. *J. Mod. Opt.*, 37:237–242, 1990.

[51] O. E. Martinez. Matrix formalism for dispersive cavities. *IEEE J.Quantum Electron.*, QE-25:296–300, 1989.

[52] S. P. Dijaili, A. Dienes, and J. S. Smith. ABCD matrices for dispersive pulse propagation. *IEEE J. Quantum Electron.*, QE-26:1158–1164, 1990.

[53] A. G. Kostenbauder. Ray-pulse matrices: A rational treatment for dispersive optical systems. *IEEE J. Quantum Electron.*, QE-26:1148–1157, 1990.

[54] Anthony E. Siegman. *Lasers*. University Science Books, Mill Valley, CA, 1986.

Chapter 3

Semi-Classical Light–Matter Interaction

Introduction

Most fields of science are taught following historical developments. For instance, geometry started with cartesian coordinates, in which circles, ellipses hyperbolae are totally different and unrelated objects. Going from cartesian to slanted coordinates, one realizes that circles are just a particular case of ellipses. It took projective coordinates to realize that circles, ellipses and hyperbolae are just one object. Teaching analytical geometry in particularizing from the general projective coordinates towards the more narrow minded cartesian one, gives a much richer and elegant understanding of geometry.

The same can be said of light-matter interaction, in particular nonlinear optics. We have taken the conventional approach in the preceding chapters, by describing matter as an ensemble of electric dipoles, which respond linearly to the electric field. The next step, if we follow the "historical" approach, would be to expand the polarization in a power series of the applied field, to describe nonlinear optics. Another aspect of the same "weak field" nonlinearities is typically presented by a quantum mechanical perturbation treatment. In most nonlinear optics treatments, there is a chapter suggesting that it is the index of refraction that should be expanded in a power series of the intensity. Then it is suggested that the power expansion is sometimes invalid. Finally, there is generally a chapter on "short pulse nonlinear optics".

It would be a daunting, but very useful task, to re-organize the field from the more general view of atom-field interaction, proceeding by successive approximations, down to the most particular case of classical nonlinear optics. A more

modest approach will be used here, limited to semi-classical models of electron - atom - molecule near-resonant interactions, to non-resonant nonlinear optics. Nearly all problems of linear and nonlinear optics are generally treated in a stationary approximation. Ultrashort pulses are bringing the awareness that not all situation can be treated as "steady-state", the latter being an asymptotic limit of a transient behavior.

3.1 Light-electron interaction

In the description of matter by an "index of refraction" or a "polarization", one tends to forget that the nature of light-matter interaction is simply re-radiation of electrons driven by the optical field. Electrons are accelerated by a combination of the applied electromagnetic field of the light and the field of other particles, and follow trajectories dependent on the light polarization. The moving electrons radiate a field that adds to that of the light, resulting in phase and amplitude changes of the optical field. This situation is traditionally described by an isotropic, polarization independent, polarizability, or index of refraction of a plasma. It is shown in the next subsection that this description does not match the response of free electrons created by tunnel ionization. It will be shown next how this case of free electrons connect to the conventional steady state response of a plasma.

3.1.1 Free electrons after tunnel ionization

Free electrons can be produced by ionization of a molecule under a high optical field. There are two channels of strong field ionization: multiphoton or tunneling. The two regimes are distinguished by the Keldysh parameter γ [1]:

$$\gamma = \sqrt{\frac{I_p}{2U_p}}, \tag{3.1}$$

where I_p is the ionization potential, and U_p is the ponderometive energy or the average kinetic energy of a free electron oscillating in the laser field. If e and m_e are the charge and mass of the electron; ω the (angular) frequency of the light field of amplitude $\mathcal{E}$:

$$U_p = \frac{e^2\mathcal{E}^2}{4m_e\omega^2}. \tag{3.2}$$

U_p expressed in eV as a function of the light intensity I_ℓ in W/cm^2 and the wavelength λ in microns is:

$$U_p = 9.33 \cdot 10^{-14} I_\ell \lambda^2 \tag{3.3}$$

In the "quasistatic limit" of $\gamma < 1$ the dressed Coulomb barrier is essentially static as seen by the electrons and the method of releasing the electrons is dominated by *tunneling*. For $\gamma > 1$ the electron release is most likely described by photon absorption, and *multiphoton* features are more dominant [2]. The difference between tunneling and multiphoton is easily recognized in measurements of velocity mapping imaging (VMI) where the electron momentum distribution following ionization is measured [3]. We consider here as an example the case of ionization by a fs pulse at 800 nm where a tunneled electron leaves its parent atom/molecule instantaneously along the direction of light polarization, at the moment of ionization, with zero velocity [4]. The electrons leave the atom from a Rydberg state that typically has an orbit radius one order of magnitude larger than the atomic radius. Formulae can be found in the literature for the tunneling rate and the ratio of electron production for various polarization [5,6]. We are here just interested in following the motion of the electron, subjected to the force F due to a combination of the optical field E and a Coulomb field F_c:

$$F = -qE + F_c = ma, \tag{3.4}$$

where a is the acceleration of the electron of mass m and charge q. In this classical approach, we neglect the magnetic force on the electron. The tunneled electron is released at time t_0 in the optical field given by:

$$E = \frac{\mathcal{E}(t,r)}{\sqrt{1+\varepsilon}}\left[\cos\omega(t-t_0)\vec{x} + \varepsilon\sin\omega(t-t_0)\vec{y}\right], \tag{3.5}$$

where ε defines the light polarization ($\varepsilon = 0$ for linear polarization) and $\mathcal{E}(r,t)$ is the envelope of the field. At any time $t \geq t_0$, the velocity of the electron is given by:

$$v = \frac{q\mathcal{E}(t,r)}{m\omega}(\sin\omega t\ \vec{x} - \varepsilon\cos\omega t\ \vec{y}) + \vec{y}\varepsilon\frac{q\mathcal{E}(t_0,r_0)}{m\omega}. \tag{3.6}$$

In circular polarization ($\varepsilon = 1$), the electron acquires a drift velocity $v_d = q\mathcal{E}(t_0,r_0)/(m\omega)$ along $\vec{y}$, long after the laser pulse is gone. At the moment of ionization $t_0 = 0$, the electron velocity is zero, hence there must be a drift term to fulfill the initial condition. Let us consider a pulse of intensity of $2.8{\cdot}10^{14}$ W/cm^2 as is realized in a light filament in air (see Section **??**). To this circularly polarized pulse corresponds a field peak amplitude of 4.62×10^8 V/cm, the drift velocity of the electron ionized by this field is $3.45\cdot10^4$ cm/s or 1.6 atomic units.

The position of the electron is

$$r = \frac{qE_0}{m\omega^2}(-\cos\omega t\vec{x} - \vec{y}\epsilon\sin\omega t) + \vec{y}\epsilon\frac{qE_0}{m\omega}t + r_0 + \frac{qE_0}{m\omega^2}\vec{x}. \tag{3.7}$$

It means that the electron having the negative charge will oscillate in the same direction and phase of the laser field. Consistently with neglecting the magnetic forces, we ignore the motion out of the polarization plane "xy plane". The coordinates of the electron are:

$$x = \frac{qE_0}{m\omega^2}(-\cos\omega t) + x_0 + \frac{qE_0}{m\omega^2} \tag{3.8}$$

$$y = \epsilon\frac{qE_0}{m\omega}t(-\frac{\sin\omega t}{\omega t} + 1). \tag{3.9}$$

The initial position is taken to be 10 times the atomic radius of nitrogen which is 65 picometers or 0.65/0.52918 = 1.22 atomic units. The amplitude of the oscillation is $qE_0/(m\omega^2)$ = 1.4 nm corresponding to 27.7 atomic units. Within the 200 femtosecond of a circularly circularly polarized pulse, the electron ionized at the peak has moved $qE_0/(m\omega)t$ which is $1.23{\cdot}10^2$ nm or $6.52\cdot10^3$ atomic units in 100 fs.

The radiation of a non-relativistic moving charge [7] is expressed as

$$\Delta E = \frac{q}{\epsilon_0 c}\frac{\vec{n}\times(\vec{n}\times\dot{\vec{\beta}})}{R} + \frac{qd}{\epsilon_0 R^2}. \tag{3.10}$$

where $\beta = v/c$, ϵ_0 is the vacuum permittivity, $\vec{n} = \vec{R}/R$ is the unit vector of the observation point $\vec{R}$ and "d" is the displacement of the charge that can be calculated at time t from the position equations (3.9). Note that there are two terms in the electron response: the first one is the "radiation term", and is only relevant at very high intensities. In our example of $2.8{\cdot}10^{14}$ W/cm^2 considered here, it is two orders of magnitude smaller than the second term. Since the latter involves the distance from the parent ion to the electron, it is called the "dipole term". The classical definition of the polarization relates to this dipole term, generally defined as $P = Nqd$, where N is the density of electrons. This definition relates to the second term of Eq. (3.10) in an homogeneous medium where $R^{-3} = N$, and the field of the electron cloud reacting to the applied field is $\Delta E = P/\epsilon_0$.

The electron trajectories in the first ps after ionization and their emission into the applied field is a deterministic problem that can only be solved by numerical calculations. Some calculations of the transient response of the electron cloud in linear polarization were reported by Romanov and Levis [8]. An example of the transient response is reproduced in Fig. 3.1.

For mixed gases the contribution of each material (in the absence of interaction) can be calculated separately. The distance between electrons changes with time and position. The response of the electrons is a field ΔE, calculated for each point in space as a function of time, which modifies the applied field: $E(z+\Delta z) = E(z) + \Delta E$.

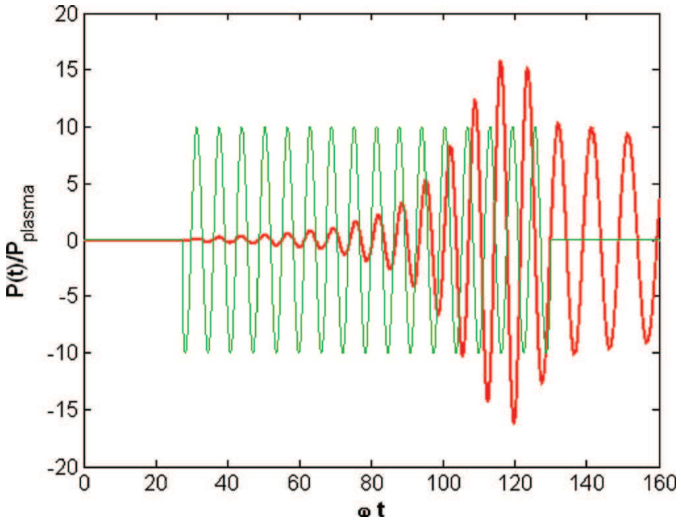

Figure 3.1: The cumulative polarization response of a medium that is being tenuously ionized by a laser pulse with rectangular envelope. The laser electric field oscillations are shown for comparison, not to scale. (from [8])

The radiated field ΔE is related to the traditional notion of index of refraction $n(z,t)$ (no longer a constant) by the propagation equation written in the slowly varying envelope approximation and in retarded time:

$$\frac{\Delta E}{E} = -ik\Delta z = -i\frac{2\pi n}{\lambda}\Delta z \tag{3.11}$$

Note that this approach is not restricted to a particular motion. If the medium is excited by multiple laser frequencies or existing nuclear and electromagnetic fields, they all contribute in the motion of the electron and therefore its radiation.

The response due to the dipole radiation of the electrons at position r is calculated by time integration of Eq. (3.6) and inserted in the dipole term of radiation equation Eq. (3.10).

$$\Delta E_p(t,r) = \frac{qd(t,r)}{R(t,r)^2\epsilon_0} = \frac{q^2\mathcal{E}(t,r)}{2m\omega^2 R(t,r)^2\epsilon_0}, \tag{3.12}$$

in which $\tilde{E}(t,r)$ is the pulse envelope. Note that the dipole radiation exists only during the laser pulse. In this particular case the radiation of the moving electron agrees with the Drude model, which is detailed in Section 3.1.2 that follows. It leads to an index of refraction

$$\Delta n = -\frac{{\omega_p}^2}{\omega^2} = -\frac{Nq^2}{2\epsilon_0 m\omega^2}, \tag{3.13}$$

where ω_P is a time dependent plasma frequency that depends on the density of electrons N at each instant. Note that in a general case the motion of an electron is influenced by existing electromagnetic fields, collisions and Coulomb forces, and therefore the refractive index of electrons can not be defined solely by the density. Tunneled electrons with circularly polarized light withhold a drift velocity [Eq. (3.6)] that is determined by the field value at the moment of ionization. The spiral motion of the tunneled electrons results in generating an expanding sphere in time. The electromagnetic fields in the presence of moving matter are related through Maxwell's equations, suitably modified to include the effects of motion upon the electric and magnetic properties of matter [9]. We assume that the expanding electron sphere in time has the constituent parameters of free space ($\mu = \mu_0$ and $\epsilon = \epsilon_0$). Let us assume that the expanding electron sphere is a perfect conductor with the field zero for $r < b$, where b is the radius of the sphere. One relation is necessary to complete the set of basic equations, which is Ohm's law for a perfect moving conductor

$$E + v \times \mu_0 H = 0. \tag{3.14}$$

Here v is the velocity of a macroscopic element of volume of the moving conductor. The solutions of Maxwell's equations inside and outside the expanding sphere have to be matched across a moving surface. Due to the requirement of regularity at infinity, the problem is defined only by the magnetic vector potential ' A .

$$H = -\frac{1}{\mu_0}\nabla \times A \tag{3.15}$$

$$E = -\frac{\partial A}{\partial t} \tag{3.16}$$

and is the solution of

$$\nabla^2 A - \frac{1}{c^2}\frac{\nabla A^2}{\nabla t^2} = -\mu_0 J, \tag{3.17}$$

where J is the electric current density. Using the Green's function, the field at distance r from the center of a sphere moving with constant velocity [10] is

$$E = -\frac{\mu_0}{c^2}\frac{3Hv^3}{(1-v/c)^2(1+2v/c)}\left[\frac{T}{rc} + \frac{T^2}{2r^2}\right], \tag{3.18}$$

where $T = t - r/c$. In the case of tunneled electrons with circularly polarized light $r = R$ is the distance between the electrons , v is the expansion velocity of the sphere (the drift velocity $qE(t_0, r_0)/(m\omega)$ in Eq. (3.6) and $T = a/v - R/c$ where "a" is the radius of the sphere at a given time.

The total response at each point in the beam cross section at a given time "t'" is calculated by adding all the responses of expanding spheres from the initial ionization time $t_i = -\infty$ to the final observation time $t_f = t'$, weighted by the probability

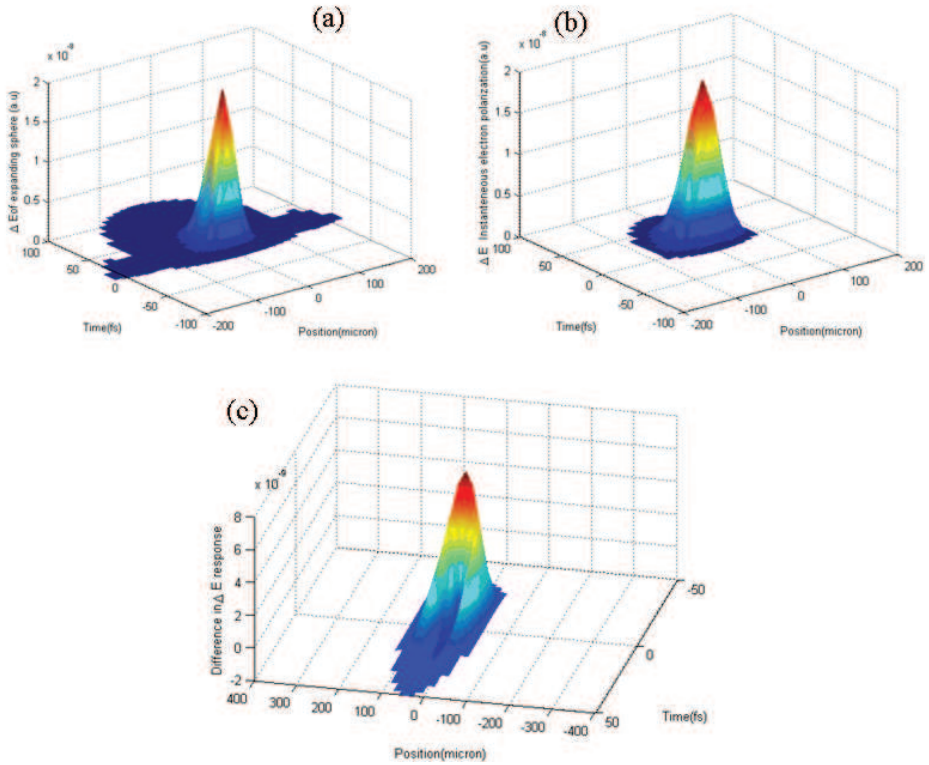

Figure 3.2: a) Radiation field of expanding spherical conductors b) Dipole radiation c) Difference between Dipole radiation and radiation due to the drift motion

of ionization at the moment of ionization t_i .

$$\Delta E_d(t_f, r) = -i \int_{t_i=-\infty}^{t_f=t'} 3\frac{\mu_0}{c^2} W(t_i) \frac{E(t)v(t_i)^3}{(1-v(t_i)/c)^2(1+2v(t_i)/c)} \left[\frac{T}{Rc} + \frac{T^2}{2R^2}\right] dt. \quad (3.19)$$

The refractive index due to the expansion of electron spheres [Fig. 3.2(a)] is compared to the dipole radiation [Fig. 3.2(b)] with circularly polarized light. The difference between the two is presented in Fig. 3.2(c). The dipole index is stronger in the first half of the pulse. The index due to the drift is stronger in the central portion of the beam profile and in later times of the laser pulse. Note that the two responses have a 90^o degree phase difference; the dipole index is a real index, and the drift index is an imaginary one (absorption index). The drift index (imaginary) of tunneled electrons with linear polarization is neglected because of their low drift velocity and the index is mostly due to dipole radiation (real index).

Another point of view in connecting microscopic effects such as light polari-

zation to macroscopic effects in high fields can be seen through conservation of energy. In the strong field ionization [11] conservation of energy imposes that

$$N_{\text{photon}}h\omega = I_p + U_p + K, \tag{3.20}$$

where K is the kinetic energy of the electrons and N_{photon} is the number of absorbed photons in the ionization process. I_p is the energy required to release an electron and U_p is the ponderomotive energy [Eq. (3.2)] due to the oscillation of electrons with the applied field.

3.1.2 Steady state limit: the Drude model

It is easy to associate a characteristic resonant frequency to an oscillator with a positive and negative charge. Associating the resonant frequency of Eq. (7.7) with a homogeneous electron plasma may seem less obvious. If an electron moves in the plasma from its equilibrium position, there will be a restoring force. The larger the number of surrounding electrons, the larger the restoring force, which explains the density dependence of the resonant frequency.

Let us consider a volume of electrons, of density n_0. The equation of motion of electrons under the influence of an electric field, neglecting collisions and magnetic forces, is:

$$m_e\frac{dv}{dt} = -eE + e[v\times B] - m_e\nu_c v \tag{3.21}$$

Note that in the equation of motion of the electron, the electric field can be the Coulomb field from the surrounding electrons. Let us consider a perturbation δn_e from the equilibrium density of the electrons n_0. We will for simplicity neglect collisions and the magnetic force in the following derivation. Expressing that the change in the number of electrons per unit time in a infinitesimal volume is equal to a source term, minus the current of particles out of that volume, leads to the conservation equation for the electrons:

$$\left(\frac{\partial n}{\partial t} + \nabla nv = \text{Source terms}\right). \tag{3.22}$$

with $n = n_0 + \delta n_e$ and $\delta n_e \ll n_0$. In the velocity $v = v_0 + \delta v$, we assume no drift velocity ($\delta v = 0$. The conservation equation (without source term – the plasma is at equilibrium), neglecting the second order product $\delta n\delta v$, leads to:

$$\nabla\cdot\delta v = \frac{-1}{n_0}\frac{\partial n}{\partial t}. \tag{3.23}$$

Taking the divergence of Gauss law, and using the equation of motion (3.21):

$$\nabla\cdot eE = \frac{ne^2}{\epsilon_0} = m_e\nabla\cdot\frac{dv}{dt} \approx m_e\frac{d}{dt}\nabla\cdot\delta v = m_e\frac{d}{dt}\left(\frac{-1}{n_0}\frac{\partial n}{\partial t}\right) \tag{3.24}$$

which leads to the differential equation for the plasma density:

$$\frac{\partial^2 n}{\partial t^2} = -\left(\frac{n_0 e^2}{m_e \epsilon_0}\right) n = -\omega_p^2 n, \tag{3.25}$$

which shows that indeed, density fluctuations in a plasma of electron have a resonant frequency.

The fluctuation of the density (position) of electrons gives rise to an electric field. Considering that there is no other electric field (no applied field), using Ampere law:

$$\begin{aligned} \nabla \times H &= J + \frac{\partial D}{\partial t} \\ D &= \epsilon E \\ J &= -nqv \\ & \frac{\partial}{\partial t}\left(\epsilon \frac{\partial E}{\partial t} = nqv\right) \\ \frac{\partial^2 E}{\partial t^2} &= \frac{n_0 q}{\epsilon_0}\frac{\partial v}{\partial t} \end{aligned}$$

where we have set the magnetic field to zero. Since $\partial v/\partial t = -qE/m_e$ from the equation of motion,

$$\frac{\partial^2 E}{\partial t^2} = -\left(\frac{n_0 q^2}{m \epsilon_0}\right) E \tag{3.26}$$

we see that the density fluctuation themselves give rise to the emission of a field at the plasma frequency ω_p.

The classical treatment of electron in plasma is not very different from the bound electron: it a is stationary solution of a driven oscillator, based on a fundamental assumptions that the medium response is isotropic and stationary. In particular, the density term that defines the plasma frequency is never a constant when dealing with fs pulses.

3.2 Transitions with bound electrons

3.2.1 Introduction: the classical oscillator and Maxwells equations

The classical approach is to calculate the motion of the bound electron, modeled as a dipole. The electron is at a (small) distance d from the positive ion. It oscillates with the applied electric field. This is the classical oscillator model. The Coulomb field produces a restoring force, which leads to a resonance frequency. One introduces a damping term. A similar model is used for the plasma. The result is that,

away from resonance, under the influence of an optical oscillating field at ω, the motion of the electron follows the frequency of the applied field, in phase, and is thus $d = d_0 \cos \omega t$. At a point of observation at a distance R from the dipole, the field due to the dipole is:

$$\Delta E = \frac{q^2}{4\pi R^2}\left[1 - \frac{R^2}{(R+d)^2}\right] \approx \frac{2q^2 d}{4\pi R^3} \tag{3.27}$$

Putting that in Maxwell's propagation equation:

$$\frac{\partial^2 E}{\partial z^2} - \frac{1}{c^2}\frac{\partial^2 (E + \Delta E)}{\partial t^2} = 0 \tag{3.28}$$

or

$$\frac{\partial^2 E}{\partial z^2} - \frac{1}{c^2}\frac{\partial^2 E}{\partial t^2} = \frac{1}{c^2}\frac{\partial^2 \Delta E}{\partial t^2} = \frac{\omega^2}{c^2}\Delta E. \tag{3.29}$$

Using:

$$\begin{aligned} E &= \frac{1}{2}\mathcal{E} e^{i(\omega t - kz)} \\ \Delta E &= \frac{1}{2}\Delta\mathcal{E} e^{i(\omega t - kz)} \end{aligned}$$

we find:

$$-2ik\frac{\partial \mathcal{E}}{\partial z} - 2i\frac{\omega}{c^2}\frac{\partial \mathcal{E}}{\partial t} = \frac{\omega^2}{c^2}\Delta\mathcal{E}, \tag{3.30}$$

and

$$\frac{\partial \mathcal{E}}{\partial z} + \frac{1}{c}\frac{\partial \mathcal{E}}{\partial t} = -i\frac{\omega}{2c}\Delta\mathcal{E}, \tag{3.31}$$

Even though we started from a $\Delta\mathcal{E}$ in phase with the applied field, after insertion in the propagation equation it appears that its envelope is adding 90 degrees out of phase with the applied field, as is the case of an index of refraction.

It appears as if, by the time the electron re-radiates, the wave has already moved by a distance of $\lambda/4$.

3.3 Semi-classical approach to light matter interaction

In a semi-classical approach, the field is treated classically, and the atom quantum mechanically. The basic physics is essentially the same as discussed in the previous classical section: the electromagnetic field of light excites the motion of electrons bound to the atom. The electrons being bound to the atom/molecule, the

re-radiation into the field is that of the dipole term in Eq. (3.10). In that dipole radiation term, the only varying parameter is the distance d between charges, which is found by solving the time dependent Schrödinger equation for the atomic system,

$$H\psi = i\hbar\frac{\partial\psi}{\partial t}, \tag{3.32}$$

where the Hamiltonian H is the atomic system Hamiltonian H_0 perturbed by the dipolar term:

$$H = H_0 + (qd)E. \tag{3.33}$$

The atomic system is characterized by a set of energy levels $\hbar\omega_k$, eigenvalues of the equation:

$$H_0\psi_k = \hbar\omega_k\psi_k. \tag{3.34}$$

The wave function solution ψ is found by inserting in Eq. (3.32) the expansion:

$$\psi(t) = \sum a_k(t)\psi_k, \tag{3.35}$$

and solving for the coefficients $a_k(t)$. The reaction field per electron $(qd(t)/\epsilon_0)$ that radiates back into the applied field is calculated by taking the expectation value of the position r:

$$\Delta E = \langle\psi|qr|\psi\rangle/\epsilon_0. \tag{3.36}$$

The polarization $P = \epsilon_0\Delta E$ is in general defined by a differential equation, where the driving term is the total electric field applied to the atomic system, which can have components at different frequencies. The initial conditions are given by the state of the system *prior* to the application of the field. In practical situation, the total field may be given by a combination of m pulses a various frequencies:

$$E(t) = \frac{1}{2}\sum_{j=1}^{j=m}\left\{\tilde{\mathcal{E}}_j(t)e^{i\omega_{\ell,j}-\vec{k}_j\cdot\vec{r}}\right\} \tag{3.37}$$

where some of the fields $\tilde{\mathcal{E}}_j$ may be generated from the time dependent polarization. One should not forget that the interaction will always have a particular aim, which is either to create a particular state of matter characterized by the wave function ψ [or equivalently the set of time dependent coefficients $a_k(t)$], or create a particular reaction field $\Delta E(t)$ or polarization $P(t)$. In the latter case, one will want to compress or modulate the applied field, or create new frequency components. One will generally seek a particular combination of atomic system (levels) and fields depending on the goal that one seeks to achieve, most often seeking near resonance or proximity of certain transition frequencies between levels and light frequencies.

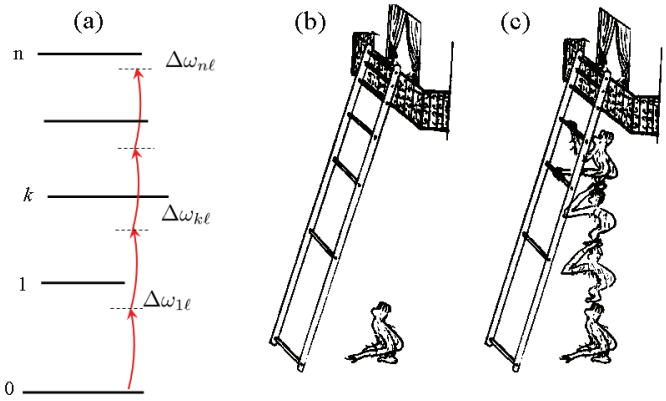

Figure 3.3: (a) The main approximation in this approach is to consider the interaction of the light only with n levels connected by a combination of photons of frequency $\omega_{\ell,j}$. The important parameters are the dipole moments of the transitions, and the detunings $\Delta\omega_{k,\ell} = \omega_{k,\ell} - \sum_{j=1}^{j=k} \omega_{\ell,j}$. (b) A typical problem will be to create an inversion with a stack of unequally spaced levels, or for a "Romeo" to reach the balcony of his "Juliet" with a lousy ladder. The solution (c) is the multiphoton approach.

We will first investigate the situation of *cascade transitions*, applicable when each photon of frequency $\omega_{\ell,k}$ finds a near resonance with a pair of levels, as sketched in Fig. 3.3(a). An example of related physical situation is to excite a stack of rotational levels. These levels are in general an anharmonic ladder. A single pulse excitation may only reach to the first step, as illustrated by the "Romeo" of Fig. 3.3(b) trying to reach his "Juliet" with an anharmonic ladder. The smart approach that can be taken is to create a properly timed and phased sequence of pulses or "Romeos" to reach the top of the ladder, as in Fig. 3.3(c). Rotational level inversion can be engineered with ultrashort IR pulses [12]. They are also taking place in the propagation of ultrashort intense pulses in air [13]. Cascade excitation can be exploited to create a complete population inversion in atomic vapors [14].

Situations can be created where most detuning — except one — can be neglected. The interaction with the off-resonant levels can be considered nearly instantaneous: the response time is of the order of the inverse of the detuning. One can find a stationary ("adiabatic") solution for the coefficients a_k associated with the off-resonant levels. The interaction reduces to a set of differential equations involving the near resonant levels, which, for times sufficiently short that relaxation effects (radiative and non-radiative decays, collisional relaxation) are negligible, can often be represented by a "Bloch vector" model. We will see under which condition these equations reduce first to rate equations, next to the classical non-

resonant instantaneous linear and nonlinear polarization.

Semi-classical approach applied to cascade excitation of multilevel systems One can also use a multiple wavelength source, each wavelength of the source being resonant with successive dipole transitions. If in addition the sum of the n photon frequencies is resonant with a particular level, we have a case of "cascade n-photon resonance". This problem can be solved formally in all generality from Schrödinger's equations. From the general solution, we can particularize to the case of identical fields, off-resonance intermediate levels, multiphoton resonance.P For simplicity, we will limit ourselves here to a three-level system. The procedure followed here is easily generalized to n-levels.

We consider a bichromatic laser pulse described by:

$$\begin{aligned} E(t) &= \mathcal{E}_1(t)\cos[\omega_{\ell,1}t+\varphi_1(t)] \\ &+ \mathcal{E}_2(t)\cos[\omega_{\ell,2}t+\varphi_2(t)]+\ldots. \end{aligned} \tag{3.38}$$

Note that we are not using at this point the complex notations. As it is often the case in nonlinear optics, one has to be careful to include both the positive and negative frequencies at the onset.

The relevant three level system is sketched in Fig. 3.4. The detunings are defined as:

$$\begin{aligned} \Delta_1 &= \omega_{01}-\omega_{\ell,1} \\ \Delta_2 &= \omega_{02}-(\omega_{\ell,1}+\omega_{\ell,2}) \end{aligned} \tag{3.39}$$

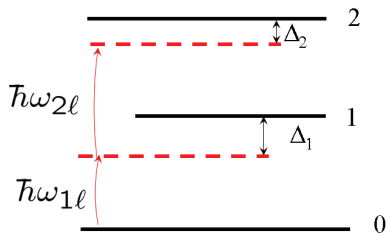

Figure 3.4: Sketch showing the three levels 0, 1 and 2, the light frequencies $\hbar\omega_{1\ell}$ and $\hbar\omega_{2\ell}$ and the detunings.

The coupling with the multilevel (three) system is through the dipole interaction term in the time dependent Schrödinger equation:

$$H\psi = i\hbar\frac{\partial\psi}{\partial t}, \tag{3.40}$$

with:

$$H = H_0 + H' = H_0 - p \cdot E(t) \tag{3.41}$$

where p is the dipole moment. The wave function ψ is written as a linear combination of the wave function of the unperturbed atomic system ψ_k:

$$\psi(t) = \sum_k a_k(t)\psi_k \tag{3.42}$$

which leads to a system of differential equations for the coefficients $a_k(t)$:

$$\frac{da_k}{dt} = -i\omega_k a_k + \sum_j \frac{i}{2\hbar} p_{k,j}[\tilde{\mathcal{E}}_1 e^{i\omega_{\ell,1}t} + \tilde{\mathcal{E}}_2 e^{i\omega_{\ell,2}t} + c.c.]a_j \tag{3.43}$$

The "rotating frame" approximation for this particular situation is:

$$\begin{aligned} a_0 &= c_0 \\ a_1 &= e^{i\omega_{\ell,1}t}\, c_1 \\ a_2 &= e^{i(\omega_{\ell,1}+\omega_{\ell,2})t}\, c_2 \end{aligned} \tag{3.44}$$

In substituting in Eqs. (3.43), it is important to keep only the slowly varying terms (as compared to the light frequency or transition frequency). This is the step where we see the importance of having defined the field as a real quantity, i.e. with both positive and negative frequencies. The positive field frequencies combine with negative going frequencies, and vice versa, to give:

$$\begin{aligned} \frac{dc_0}{dt} &= \frac{i}{2\hbar} p_{1,0}\tilde{\mathcal{E}}_1^*(t)\, c_1 \\ \frac{dc_1}{dt} &= -i\Delta_1 c_1 + \frac{i}{2\hbar} p_{0,1}\tilde{\mathcal{E}}_1(t)c_0 + \frac{i}{2\hbar} p_{2,1}\tilde{\mathcal{E}}_2^*(t)c_2 \\ \frac{dc_2}{dt} &= -i\Delta_2 c_2 + \frac{i}{2\hbar} p_{1,2}\tilde{\mathcal{E}}_2(t)c_1 \end{aligned} \tag{3.45}$$

or in general, applicable to a n-level system:

$$\frac{dc_k}{dt} = -i\Delta_k c_k + \frac{i}{2\hbar} p_{k-1,k}\tilde{\mathcal{E}}(t)c_{k-1} + \frac{i}{2\hbar} p_{k,k+1}\tilde{\mathcal{E}}^*(t)c_{k+1}. \tag{3.46}$$

This systems takes a simpler form is we define the Rabi frequencies as:

$$\begin{aligned} \tilde{E}_1 &= \frac{i}{\hbar} p_{1,0}\tilde{\mathcal{E}}_1 \\ \tilde{E}_2 &= \frac{i}{\hbar} p_{2,1}\tilde{\mathcal{E}}_2. \end{aligned} \tag{3.47}$$

Substituting:

$$\boxed{\begin{array}{rcl}\dfrac{dc_0}{dt} &=& 0+\dfrac{1}{2}\tilde{E}_1^* c_1+0\\ \dfrac{dc_1}{dt} &=& -\dfrac{1}{2}\tilde{E}_1 c_0 - i\Delta_1 c_1+\dfrac{1}{2}\tilde{E}_2^* c_2\\ \dfrac{dc_2}{dt} &=& 0-\dfrac{1}{2}\tilde{E}_2 c_1 - i\Delta_2 c_2\end{array}}$$

or in matrix form:

$$\boxed{\frac{d}{dt}\begin{pmatrix} c_0\\ c_1\\ c_2\end{pmatrix}=\begin{pmatrix} 0 & \frac{1}{2}\tilde{E}_1^* & 0\\ -\frac{1}{2}\tilde{E}_1 & i\Delta_1 & \frac{1}{2}\tilde{E}_2^*\\ 0 & -\frac{1}{2}\tilde{E}_2 & -i\Delta_2\end{pmatrix}\begin{pmatrix} c_0\\ c_1\\ c_2\end{pmatrix}} \tag{3.48}$$

This is the basics of the treatment of a cascade of multilevel systems. The extension to a larger number of transitions is straightforward. A basic approximation is that any level k is connected by a dipole transition to a level $k+1$ and $k-1$.

The system of equations (3.48) is easy to solve numerically. One is generally not interested in expressing the results as a matrix of c coefficients, but instead the 3×3 matrix of the density matrix elements $\rho_{ij} = c_i c_j^*$. The diagonal elements $c_i c_i^*$ represent the populations of the level i. The off-diagonal elements $c_i c_j^*$ are a measure of the amplitude excitation at the frequency $\omega_j - \omega_i$, and will be directly connected to the polarization, as we have already seen in the case of the two level system.

This matrix formalism is most useful in reaching a desired population distribution. This approach can be used in systems where the density of levels is such that one can generally find a "ladder" of levels to climb. An example of application is given in Appendix **??**. It is shown in that appendix how a properly phased sequence of pulses can create a complete population inversion in the vibro-rotational level structure of CH_3F. It can also be applied to the less crowded level structure of atomic transitions. The example of inverting a two-photon transition in sodium vapor, with the purpose of creating a bichromatic artificial guide-star, is treated in Appendix **??** In the case of atomic transitions, the more often considered case is to have the intermediate level – or intermediates levels – far off resonance. In that case, the equation for that particular (or these particular) intermediate level(s) can be considered to be steady state, and the system of equation is reduced. This is the "adiabatic approximation", which will be solved in Section 3.3.1.

3.3.1 Adiabatic approximation; multiphoton Bloch model

If the detuning of the intermediate level 1 is larger than the transition rates: the second Eq. (3.48) can be considered to be in steady state, and one can solve for the

coefficient c_1:

$$c_1 = \frac{i}{2\Delta_1}\left(E_1 c_0 - E_2^* c_2\right). \tag{3.49}$$

By substituting this solution in the other two equations, the three level system has been reduced to a two-level system, where the ground and upper state are not connected by a dipole transition. These equation can be represented by a "Bloch vector" model, in which a "pseudo-polarization" vector rotates around a "pseudo-electric-field" vector with an angular velocity given by a Rabi frequency that is now proportional to the square of the electric field amplitude. Substituting the solution (3.49) into the other two equations:

$$\begin{aligned} \dot{c}_0 &= \frac{i}{4\Delta_1}\left(E_1 c_0 - E_2^* c_2\right) E_1 \\ \dot{c}_2 &= -\frac{i}{4\Delta_1} E_1 E_2 c_0 + \frac{i}{4\Delta_1} E_2 E_2^* c_2 - i\Delta_2 c_2. \end{aligned} \tag{3.50}$$

Defining:

$$\begin{aligned} \tilde{Q}_2 &= -i c_0 c_2^* \\ W_2 &= c_2 c_2^* - c_0 c_0^* \end{aligned} \tag{3.51}$$

leads to the following set of equations:

$$\boxed{\begin{aligned} \dot{\tilde{Q}}_2 &= i\left\{\Delta_2 + \frac{1}{4\Delta_1}\left[|E_1|^2 - |E_2|^2\right]\right\}\tilde{Q}_2 - \frac{E_1 E_2}{2\Delta_1} W_2 \\ \dot{W}_2 &= \frac{1}{2\Delta_1} Re\left[E_1 E_2 \tilde{Q}^*\right]. \end{aligned}} \tag{3.52}$$

We recognize here Bloch's equations for a two-level system [15], if we define a two photon Rabi frequency $\kappa_2 \mathcal{E}^2$, where:

$$\boxed{\kappa_2 = \frac{\kappa_1 \kappa_2}{2\Delta_1} = \frac{p_{01} p_{12}}{\hbar^2 \Delta_1}.} \tag{3.53}$$

In general, more than one intermediate level may be involved in the calculation of the two-photon Rabi frequency. This simply means than instead of the single term in the right hand side of Eq. (3.53), there will be a sum over i, the latter designing the index of an intermediate level with detuning Δ_i [essentially replacing all indices "1" by "i" in Eq. (3.53)].

Note a small complexity appearing in the detuning: a time dependent detuning $\Delta\omega_2(t)$ has to be substituted to the constant detuning Δ_2:

$$\Delta\omega_2(t) = \Delta_2 + \frac{1}{4\Delta_1}\left[|E_1|^2 - |E_2|^2\right]. \tag{3.54}$$

The substitution leads to the Maxwell'Bloch multiphoton system of equations:

$$\dot{\tilde{Q}}_2 = i\Delta\omega_2(t)\tilde{Q}_2 - \kappa_2\tilde{\mathcal{E}}^2 W - \frac{\tilde{Q}_2}{T_2} \quad (3.55)$$

$$\dot{W} = Re\left[\kappa_2\tilde{\mathcal{E}}^2\tilde{Q}^*\right] - \frac{W - W_0}{T_1} \quad (3.56)$$

$$\frac{\partial\tilde{\mathcal{E}}}{\partial z} = -\alpha_2\tilde{Q}_2\tilde{\mathcal{E}}^* - \frac{\alpha}{2}\tilde{\mathcal{E}} + \eta\alpha_2\tilde{\mathcal{E}}_3\tilde{Q}^* \quad (3.57)$$

$$\frac{\partial\tilde{\mathcal{E}}_3}{\partial z} = -\eta\alpha_2\tilde{Q}_2\tilde{\mathcal{E}} - \frac{\alpha_3}{2}\tilde{\mathcal{E}}_3 \quad (3.58)$$

$$(3.59)$$

Q_2 is the amplitude of some atomic "excitation" oscillating at the frequency of the two-photon transition, or 2 ω. It is thus natural to expect that the field opposing the driving field (hence responsible for two-photon transition) is given by the combination $Q_2\tilde{\mathcal{E}}^*$ which would be the amplitude of an oscillation at the frequency $2\omega - \omega = \omega$. A rigorous derivation of the polarization shows that this is indeed the case [16]. An additional contribution to a time varying polarization comes from the fact that the atom has a different polarizability in the ground state versus the upper state. Therefore, as the populations swing up and down under the influence of the field, there will be a modulation of the polarization proportional to the population difference. This has a negative impact on phase matching in third harmonic generation. A fourth equation has been added to the set (3.52), with the combination of $Q_2\tilde{\mathcal{E}}$, expected to oscillate at the frequency $3\omega_\ell$. This is the term responsible for two-photon resonant third harmonic generation discussed in the next section.

The system of Eqs. (3.55) through (3.57) can easily be generalized to multiphoton resonant interaction, where n- rather than 2- photons are near resonance with two atomic levels [17, 18]. In most of the cases, a geometric representation applies, as sketched in Fig. 3.5(a). The n-photon have created a matter excitation at frequency $n\omega$, which is represented by a a three dimensional "pseudo-vector" $\vec{Q}(Q_r, Q_i, W)$, where W is proportional to the population difference between the resonant levels. The geometric interpretation of the Eqs. (3.55,3.56) is that the time evolution of the vector $\vec{Q}$ results from a rotation of the $\vec{Q}$ around a pseudo-vector $\vec{\mathcal{E}}(\mathcal{E}_r.\mathcal{E}_r, \Delta\omega)$ with an angular velocity proportional to $|\vec{\mathcal{E}}|$. The third component of the pseudo-vector $\vec{\mathcal{E}}$ is the detuning between $n\omega_\ell$ and the near resonant level, as modified by an eventual Stark shift.

In the set of Eqs. (3.55) through (3.57), the phase $\varphi(t)$ of the field does not appear explicitly. An equivalent form of equations that is preferred for analytical treatments is obtained by the substitution $Q = (iu + v)\exp(i\varphi)$. The geometrical representation of the interaction is that given in Fig. 3.5(b), where the medium resonance is described by the vector $\vec{\mathcal{P}}(u, v, W)$. Here also the motion of the vector

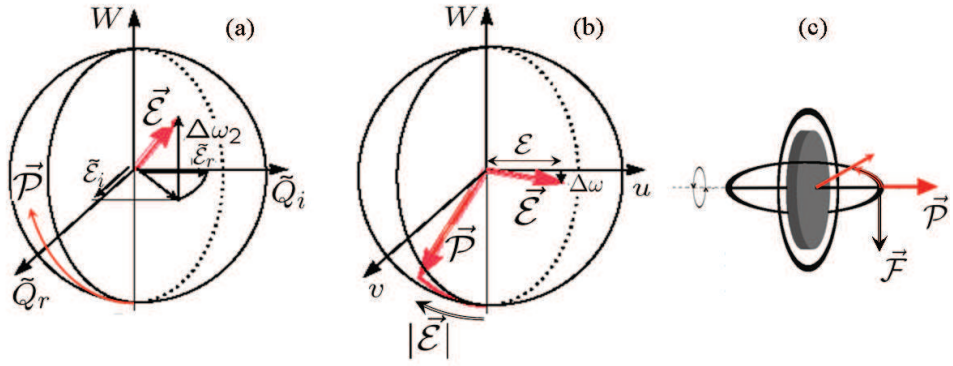

Figure 3.5: Bloch vector model for the near resonant interaction between light and an atomic system. The first two components of $\vec{Q}$ are $-iQ_r + Q_i = \rho_{1n}$ where ρ_{1n} is the single- or multi-photon resonant matrix element between the ground state and the resonant level. In (a), the field is represented by its real and imaginary parts. In (b), the field is represented by its amplitude $\mathcal{E}$ and phase φ, and $Q = (iu + v)\exp(i\varphi)$. The closest analogy to the generalized polarization is not an oscillating spring, but a gyroscope as represented in (c).

$\vec{\mathcal{P}}$ is a rotation about the pseudo-electric field vector $\vec{\mathcal{E}}(\mathcal{E}^n, 0, \Delta\omega - dot\varphi)$. This particular model will be dealt with in more details when discussing linear optics as a limiting case of coherent interaction (Section 3.3.4). It is seen here that the fundamental mechanical analogy of resonant excitation of matter by a light pulse is not an harmonic force driving a spring near its resonance, but a gyroscope. Indeed, as shown in Fig. 3.5(c), the vector $\vec{\mathcal{P}}$ is represented by the shaft of a gyroscope of angular momentum $I\omega$, If a force $\vec{\mathcal{F}}$ is applied to the cage of the gyroscope, the axis $\vec{\mathcal{P}}$ will precess following an equation of motion $\partial\vec{\mathcal{P}}/\partial t \propto \vec{\mathcal{P}} \times \vec{\mathcal{F}}$.

3.3.2 Optimizing harmonic conversion

Long wavelength lasers being generally more efficient, frequency conversion by harmonic generation is often used to generate shorter wavelength. Gases and atomic vapors have often been used as nonlinear media because of their higher damage threshold as compared to nonlinear crystals. The set of equations presented in the previous section provides a guide to the choice of nonlinear material. If the medium has a two photon resonance, the generation length for a maximum third harmonic generation will be reduced.In the set of Eqs. the function Q has a maximum value, limited by the radius of the Bloch sphere. At the maximum value of Q, the propagation equations appear to be describing just linear gain or linear absorption.

3.3.3 Coherent Raman scattering

It is essentially the same model/equations as in the previous section, with the level 2 "folded down". The notations are $\tilde{\mathcal{E}}_1$ at $\omega_{\ell,1}$ for the Raman pump, $\tilde{\mathcal{E}}_2$ at $\omega_{\ell,2}$ for the Stokes signal; the ground level is "0", the upper level (connected by dipole transition) "1", and the Raman transition is $0 \to 2$.

Stimulated Stokes Backward Raman Scattering

The system of Maxwell-Bloch equations reduces now to:

$$\begin{aligned}
\dot{\tilde{Q}}_r &= i\Delta\omega_2(t)\tilde{Q}_r - \kappa_2\tilde{\mathcal{E}}_1\tilde{\mathcal{E}}_2^* W - \frac{\tilde{Q}_r}{T_2} \\
\dot{W} &= Re\left[\kappa_2\tilde{\mathcal{E}}_1\tilde{\mathcal{E}}_2^*\tilde{Q}_r^*\right] - \frac{W - W_0}{T_1} \\
\frac{\partial\tilde{\mathcal{E}}_2}{\partial z} - \frac{1}{c}\frac{\partial\tilde{\mathcal{E}}_2}{\partial t} &= -\alpha_s\tilde{Q}_r^*\tilde{\mathcal{E}}_1 \\
\frac{\partial\tilde{\mathcal{E}}_1}{\partial z} + \frac{1}{c}\frac{\partial\tilde{\mathcal{E}}_1}{\partial t} &= -\alpha_p\tilde{Q}_r\tilde{\mathcal{E}}_2
\end{aligned} \tag{3.60}$$

The fields, with their complete exponential dependence, are

$$\begin{aligned}
E_1 &= \tilde{\mathcal{E}}_1 e^{i(\omega_{\ell,1}t - k_1 z)} \\
E_2 &= \tilde{\mathcal{E}}_1 e^{i(\omega_{\ell,2}t + k_2 z)}
\end{aligned} \tag{3.61}$$

The Raman excitation has the harmonic dependence:

$$\tilde{Q}e^{i[(\omega_{\ell,1} - \omega_{\ell,2})t - (k_1 + k_2)z]} \tag{3.62}$$

All these exponential dependence are consistent with the above equations.

The coefficients α_s and α_p should contain the respective optical frequencies, in order to satisfy energy conservation.

3.3.4 Single photon coherent propagation

Whether we are dealing with molecular or atomic transitions, the situation can arise where the ultrashort duration of the optical pulse becomes comparable with – or even less than – the phase relaxation time of the excitation. In the frequency domain, the pulse spectrum is broader than the homogeneous linewidth defined in the first section of Chapter 3. If the pulse is so short that its spectrum becomes much larger than the inhomogeneous linewidth, the medium response becomes similar to that of a single atom. It may seem like a simplified situation when the excitation occurs in a time shorter than all inter-atomic interaction. It is in fact quite to the contrary: in dealing with longer pulses, the faster phase relaxation time of the induced excitation simplifies the light matter response. One is used to dealing with a steady state rather than the "transient" response of light-matter interaction.

We will start from the semi-classical equations for the interaction of near resonant radiation with an ensemble of two-level systems inhomogeneously broadened around a frequency ω_{ih}. The extension to multilevel systems will be discussed in the next section. We refer to the book by Allen and Eberly for more detailed developments [19].

In this section we chose a density matrix approach to derive the interaction equations for a near resonant two-level system, of ground state $|0\rangle$ and upper state $|1\rangle$, excited by the field $E(t)$. The density matrix equation for this two-level system is:

$$\dot{\rho} = \frac{1}{i\hbar}\left[H_0 - pE,\, \rho\right] \tag{3.63}$$

where H_0 is the unperturbed Hamiltonian, and p the dipole moment which is parallel to the polarization direction of the field. Introducing the complex field through $E = \tilde{E}^+ + \tilde{E}^-$ in Eq. (3.63) leads to the following differential equations for the diagonal and off-diagonal matrix elements:

$$\dot{\rho}_{11} - \dot{\rho}_{00} = \frac{2p}{\hbar}\left[i\rho_{01}\tilde{E}^- - i\rho_{10}\tilde{E}^+\right] \tag{3.64}$$

$$\dot{\rho}_{01} = i\omega_0\rho_{01} + \frac{ip\tilde{E}^+}{\hbar}\left[\rho_{11} - \rho_{00}\right] \tag{3.65}$$

where ω_0 is the resonance frequency of the two-level system. It is generally convenient to define a complex "pseudo polarization" amplitude $\tilde{Q}$ by

$$i\rho_{01}p\bar{N} = \frac{1}{2}\tilde{Q}\exp(i\omega_\ell t) \tag{3.66}$$

where $\bar{N} = \bar{N}_0 g_{inh}(\omega_0 - \omega_{ih})$ and $\bar{N}_0$ is the total number density of the two-level systems. The real part of $\tilde{Q}$ will describe the attenuation (or amplification for an

initially inverted system) of the electric field. Note that $\tilde{Q} = i\tilde{\mathcal{P}}$ where $\tilde{\mathcal{P}}$ is the slowly varying polarization envelope defined in Eq. (**??**). Further we introduce a normalized population inversion:

$$w = p\bar{N}(\rho_{11} - \rho_{00}). \tag{3.67}$$

The complete system of interaction and propagation equations can now be written as:

$$\begin{aligned}
\dot{\tilde{Q}} &= i(\omega_0 - \omega_\ell)\tilde{Q} - \kappa\tilde{\mathcal{E}}w - \frac{\tilde{Q}}{T_2} && (3.68)\\
\dot{w} &= \frac{\kappa}{2}[\tilde{Q}^*\tilde{\mathcal{E}} + \tilde{Q}\tilde{\mathcal{E}}^*] - \frac{w - w_0}{T_1} && (3.69)\\
\frac{\partial\tilde{\mathcal{E}}}{\partial z} &= -\frac{\mu_0\omega_\ell c}{2n}\int_0^\infty \tilde{Q}(\omega_0')g_{inh}(\omega_0' - \omega_{ih})d\omega_0'. && (3.70)
\end{aligned}$$

The quantity $\kappa\mathcal{E}$ with $\kappa = p/\hbar$ is the Rabi frequency. T_1 and T_2 are respectively the energy and phase relaxation times. Most of the energy conserving relaxations are generally lumped in the phase relaxation time T_2. Equation (3.70) has been obtained from Eq. (**??**) by integrating over the polarization of subensembles with resonance frequency ω_0'. The set of Eqs. (3.68)–(3.70) is generally designated as Maxwell–Bloch equations.

Another common set of notations to describe the light-matter interaction uses only real quantities, such as the in-phase (v) and out-of phase (u) components of the pseudo-polarization $\tilde{Q}$, and, for the electric field $\tilde{\mathcal{E}}$, its (real) amplitude $\mathcal{E}$ and its phase φ. Defining

$$\tilde{Q} = (iu + v)e^{i\varphi} \tag{3.71}$$

and substituting in the above system of equations leads to the usual form of Bloch equations[1] for the subensemble of two-level systems having a resonance frequency ω_0.

$$\begin{aligned}
\dot{u} &= (\omega_0 - \omega_\ell - \dot{\varphi})v - \frac{u}{T_2} && (3.72)\\
\dot{v} &= -(\omega_0 - \omega_\ell - \dot{\varphi})u - \kappa\mathcal{E}w - \frac{v}{T_2} && (3.73)\\
\dot{w} &= \kappa\mathcal{E}v - \frac{w - w_0}{T_1} && (3.74)
\end{aligned}$$

[1]These equations are the electric-dipole analogues of equations derived by F. Bloch [20] to describe spin precession in magnetic resonance.

where the initial value for w at $t = -\infty$ is

$$w_0 = p\bar{N}(\rho_{11}^{(e)} - \rho_{00}^{(e)}). \tag{3.75}$$

The propagation equation Eq. (3.70), in terms of $\tilde{\mathcal{E}}$ and φ, becomes

$$\boxed{\begin{aligned} \frac{\partial \mathcal{E}}{\partial z} &= -\frac{\mu_0 \omega_\ell c}{2n} \int_0^\infty v(\omega_0') g_{inh}(\omega_0' - \omega_{ih}) d\omega_0' \qquad (3.76) \\ \frac{\partial \varphi}{\partial z} &= -\frac{\mu_0 \omega_\ell c}{2n} \int_0^\infty \frac{u(\omega_0')}{\mathcal{E}} g_{inh}(\omega_0' - \omega_{ih}) d\omega_0'. \qquad (3.77) \end{aligned}}$$

The motion of the pseudopolarization vector $\vec{\mathcal{P}}$ (initially pointing downwards along the w axis) is a rotation around the pseudo-electric field vector $\vec{\mathcal{E}}$ with an angular velocity proportional to the amplitude of that vector. (b) In the complex amplitude representation, the phase of the electric field determines the particular vertical plane containing the pseudo-electric field vector $\vec{\mathcal{E}}$.

The vector representation of Feynman *et al.* [15], for the interaction equations is particularly useful in the description of coherent phenomena. The representation is a cinematic representation of the set of equations (3.72), (3.73), and (3.74). For simplicity, we consider first an undamped isolated two-level system ($T_1 = T_2 = T_3 = \infty$), and construct a fictitious vector $\vec{\mathcal{P}}$ of components (u, v, w), and a pseudo-electric field vector $\vec{\mathcal{E}}$ of components $(\kappa\mathcal{E}, 0, -\Delta\omega)$. The detuning is defined as $\Delta\omega = \omega_0 - \omega_\ell - \dot{\varphi}$. The system of Eqs. (3.72)–(3.74) are then the cinematic equations describing the rotation of a pseudo-polarization vector $\vec{\mathcal{P}}$ rotating around the pseudo-electric vector $\vec{\mathcal{E}}$ with an angular velocity given by the amplitude of the vector $\vec{\mathcal{E}}$ [Fig. 3.5(a)]. The vectorial form of Eqs. (3.72)- (3.74) is thus:

$$\boxed{\partial\vec{\mathcal{P}}/\partial t = \vec{\mathcal{E}} \times \vec{\mathcal{P}}} \tag{3.78}$$

Depending on whether the two-level system is initially in the ground state or inverted, the pseudo-polarization vector is initially pointing down or up. Since we have assumed no relaxation, the length of the pseudo-polarization vector is a constant of the motion, and the tip of the vector moves on a sphere. The conservation of length of the pseudo-polarization vector can be verified directly from the set of Bloch's equations. Indeed, the sum of each equation (3.72), (3.73) and (3.74) multiplied by u, v, and w, respectively, yields after integration:

$$u^2 + v^2 + w^2 = w_0^2 \tag{3.79}$$

which is satisfied for each subensemble of two-level systems. As shown in Fig. 3.5(a), a resonant excitation ($\Delta\omega = 0$)) will tip the pseudo-polarization vector by an angle

$\theta_0 = \int_{-\infty}^{\infty} \kappa \mathcal{E} dt$ in the (v, w) plane. For a sufficiently intense pulsed excitation, it is possible to achieve complete population inversion when $\theta_0 = \pi$. The effect of phase relaxation (homogeneous broadening) is to shrink the pseudo-polarization vector as it moves around. To take into account inhomogeneous broadening, we have to consider an ensemble of pseudo-polarization vectors, each corresponding to a different detuning $\Delta\omega$.

A similar representation can be made for the system of Eqs. (3.68)–(3.69). The pseudo-polarization vector is then the vector $\vec{Q}(Q_i, Q_r, w)$ rotating around a pseudo-electric field vector $\vec{\mathcal{E}}(\kappa\tilde{\mathcal{E}}_r, \kappa\tilde{\mathcal{E}}_i, -\Delta\omega)$ [Fig. 3.5(b)]. Physically, the first two components of the pseudo-polarization vector $\vec{Q}$ represent the dipolar resonant field that opposes the applied external field (and is thus responsible for absorption).

3.4 From transient to stationary interaction

Most classical linear and nonlinear optics, which is treated in the next chapter, treats the linear and nonlinear polarizations as being instantaneous. Therefore, it be understood as a steady-state approximation of the equations covered in the preceding sections.

3.4.1 Rate equations

We have seen how the semiclassical interaction in multilevel systems can be reduced to a two-level system, described by Bloch's equations, if the near resonance of a pair of levels dominates. The next most common situation is when dealing with pulses long compared with the phase relaxation time. If the light field envelope is slowly varying with respect to T_2, Bloch's equations reduce to the standard rate equations. For pulses longer than the dephasing time T_2, the two first Bloch equations (3.72), (3.73) are stationary on the time scale of the pulse. Solving these equations for u, v, and substituting v into the third equation (3.74) for the population difference, leads to the rate equation:

$$\dot{w} = -\frac{\mathcal{E}^2(\kappa^2 T_1 T_2)}{1 + \Delta\omega^2 T_2^2} \frac{w}{T_1} - \frac{w - w_0}{T_1} = -\frac{I}{I_{soff} T_+ 1} w - \frac{w - w_0}{T_1} \tag{3.80}$$

Equation (3.80) defines a saturation field at resonance $\tilde{\mathcal{E}}_{s0} = 1/(\kappa\sqrt{T_1 T_2})$. Off resonance, a larger field $\tilde{\mathcal{E}}_{soff} = \tilde{\mathcal{E}}_{s0}\sqrt{1 + \Delta\omega^2 T_2^2}$ is required to saturate the same transition. To that off-resonance saturation field corresponds a saturation intensity I_{soff}.

For pulses much shorter than the energy relaxation time $\tau_p \ll T_1$ and purely homogeneoulsy broadened media the rate equation (3.80) can be integrated together

with the propagation equation (3.70) which yields for the transmitted intensity

$$I(z,t) = I_0(t)\frac{e^{W(t)/W_s}}{e^{-a} - 1 + e^{W(t)/W_s}} \tag{3.81}$$

In this last equation $W(t) = \int_{-\infty}^{t} I_0(t)dt$, and $a = \sigma_{01}^{(0)} w_0 z/p$ is the linear gain/absorption coefficient. Equation (3.81) corresponds can be written in terms of photon flux F:

$$\boxed{F(z,t) = F_0(t)\frac{e^{2\sigma_{01}\bar{W}_0(t)}}{e^{-a} - 1 + e^{2\sigma_{01}\bar{W}_0(t)}}} \tag{3.82}$$

where $\bar{W}_0(t) = \int_{-\infty}^{t} F_0(t')dt' = 1/(\hbar\omega_\ell)\int_{-\infty}^{t} I_0(t')dt'$ (I_0 intensity of the incident pulse), cf. Eqs. (1.29), (1.30), and

$$a = \sigma_{01}\Delta N^{(e)} z \tag{3.83}$$

is the absorption ($\Delta N^{(e)} < 0$) or amplification ($\Delta N^{(e)} > 0$) coefficient corresponding to a sample of length z. $\bar{W}_0(t)$ is a measure of the incident pulse energy (area) density until time t in units of (photons)/cm^2. The total incident energy density is $\hbar\omega_\ell \bar{W}_0(t = \infty) = \hbar\omega_\ell \bar{W}_{0,\infty} = W_0$. The transmitted energy density $W(z,t) = \hbar\omega_\ell \bar{W}(z,t)$ is obtained by integrating Eq. (3.82) with respect to time and can be written as

$$\boxed{W(z,t) = \hbar\omega_\ell \int_{-\infty}^{t} F(z,t')dt' = W_s \ln\left[1 - e^{a}\left(1 - e^{W_0(t)/W_s}\right)\right],} \tag{3.84}$$

where $W_s = \hbar\omega_\ell/(2\sigma_{01})$ is the saturation energy density of the medium. With Eq. (**??**), in the limit $\tau_p \ll T_1$, we can express the population inversion as

$$\boxed{\Delta N(z,t) = \Delta N^{(e)} e^{-2\sigma_{01}\bar{W}(z,t)} = \frac{\Delta N^{(e)}}{1 - e^{a}[1 - e^{W_0(t)/W_s}]}.} \tag{3.85}$$

Femtosecond pulse propagation through a homogeneously broadened saturable medium in the limit of $T_2 \ll \tau_p \ll T_1$ is completely determined by two parameters: the saturation energy density W_s and the linear absorption (gain) coefficient a. Equation (3.81) is particularly useful in calculating pulse propagation in amplifiers, as further detailed in Chapter 8.1.

3.4.2 Steady-state approximation: linear and nonlinear optics

Steady state solutions of the first two Bloch's equation (field variations slow compared to T_2 lead to the rate equation (after insertion of these solutions in the third Bloch equation).

$$\tilde{Q} = \frac{\kappa\tilde{\mathcal{E}}T_2 w}{1 - i\Delta\omega T_2}. \tag{3.86}$$

or, in terms of u and v:

$$u = -\frac{\Delta\omega T_2 \kappa \mathcal{E} T_2 w}{1+\Delta\omega^2 T_2^2} \tag{3.87}$$

$$v = -\frac{\kappa \mathcal{E} T_2 w}{1+\Delta\omega^2 T_2^2}. \tag{3.88}$$

Substituting v in the third Bloch equation (3.74) leads to the rate equation discussed in the previous Section [Eq. (3.80)]

Linear optics is the steady state solution of all three equations.

$$u = -\frac{\Delta\omega T_2 \kappa \mathcal{E} T_2 w}{1+\Delta\omega^2 T_2^2+\kappa^2\mathcal{E}^2 T_1 T_2} \tag{3.89}$$

$$v = -\frac{\kappa \mathcal{E} T_2 w}{1+\Delta\omega^2 T_2^2+\kappa^2\mathcal{E}^2 T_1 T_2} \tag{3.90}$$

$$w = \frac{w_0(1+\Delta\omega^2 T_2^2)}{1+\Delta\omega^2 T_2^2+\kappa^2\mathcal{E}^2 T_1 T_2} = \frac{w_0}{1+\frac{I}{I_{soff}}} \tag{3.91}$$

where we used the off-resonance saturation intensity defined in Eq. (3.80).

3.5 Small motions at the bottom of the sphere

Bloch's equations can be solved analytically in the weak short pulse limit, i.e., for pulses that do not induce significant changes in population and have a duration short compared to the phase relaxation time T_2. The interaction equation (3.68) can be written in the integral form:

$$\tilde{Q}(t) = \int_{-\infty}^{t} \kappa \mathcal{E} w e^{-i[(\omega_0-\omega_\ell)t'-\varphi(t')]} dt' \tag{3.92}$$

For weak pulses $w \approx w_0$) and the right hand side of Eq. (3.92) at $t = \infty$ is proportional to the Fourier transform of $\kappa\tilde{\mathcal{E}}w$. Thus we have:

$$|\tilde{Q}|^2 = u^2+v^2 = \kappa^2 w_0^2 |\tilde{\mathcal{E}}(\omega_0-\omega_\ell)|^2 \tag{3.93}$$

$$\approx -2w_0(w_\infty - w_0) \tag{3.94}$$

where $\tilde{\mathcal{E}}(\omega_0-\omega_\ell)$ is the amplitude of the Fourier transform of the field envelope at the line center frequency ω_0. The last equality results from the conservation of the length of the pseudo-polarization vector ($u^2+v^2+w^2 = w_0^2$ = constant). The

approximation is made that the change in population is small: $w_\infty^2 = [w_0 + (w_\infty - w_0)]^2 \approx w_0^2 + 2w_0(w_\infty - w_0)$. The final expression is:

$$(w_\infty - w_0) = -\frac{\kappa^2 w_0}{2}|\tilde{\mathcal{E}}(\omega_0 - \omega_\ell)|^2. \tag{3.95}$$

This is a close connection to linear optics. Equation (3.93) tells us that the amplitude of the dipolar field that opposes the applied field is proportional to the Fourier component of the applied field at the dipole resonant frequency. The form of Eq. (3.95) is of equal physical importance, since it relates the energy absorbed by the two-level system to the spectral intensity of the light at the resonance frequency. The approximations made to arrive to this conclusion are more general than the steady-state approximations of the previous section.

3.6 Light-molecule interaction

Molecules have two additional types of motion compared to atoms: they can *rotate* around their axes of symmetry and concurrently *vibrate* to and from because of the restoring force between their atoms. These additional degrees of freedom bring features to the molecular spectra that are not present in atomic spectra.

Molecular structures vary in term of their symmetry and consequently their behavior. This section we only discuss the spectra of diatomic molecules, which can easily be extended to more complex molecules.

3.6.1 Rigid rotator model

The Schrödinger equation of a rotating light object bound by a restoring force to a very heavy stationary object is:

$$-\frac{\hbar^2}{2\mu}\Big[\frac{1}{r^2}\Big(r\frac{\partial}{\partial r}\Big)\Big(r\frac{\partial}{\partial r}\Big)+\frac{1}{r}\frac{\partial}{\partial r}-\frac{1}{\hbar^2 r^2}\mathrm{J}^2\Big]\Psi(r,\theta,\varphi)=\Big[E-V(r)\Big]\Psi(r,\theta,\varphi) \tag{3.96}$$

where $\mu = m_1 m_2/(m_1+m_2)$ is the reduced mass of the objects, $V(r)$ is the bonding potential and (r,θ,φ) are the spherical coordinate components. J is the angular momentum operator which commutes with its z-component; $[\mathrm{J}^2,\mathrm{J}_z]=0$. One can assume that the displacement of the particle from its equilibrium point is negligible. The Hamiltonian of a rotating quantum object is therefore

$$H_{\mathrm{rot}} = \frac{\mathrm{J}_X^2}{2I_{XX}}+\frac{\mathrm{J}_Y^2}{2I_{YY}}+\frac{\mathrm{J}_Z^2}{2I_{ZZ}} \tag{3.97}$$

where I_{XX}, I_{YY} and I_{ZZ} are the moments of inertia, μr^2, around the body-fixed (X,Y,Z) axes. Ψ can be separated to radial and angular parts as $\Psi = R(r)Y(\theta,\varphi)$. Angular solutions of the Schrödinger equation above are shown to be spherical harmonics, $Y_{j,m}(\theta,\varphi)$, with the eigenvalues of

$$\mathrm{J}^2\ Y_{j,m}(\theta,\varphi) = J(J+1)\hbar^2\ Y_{j,m}(\theta,\varphi) \tag{3.98}$$

$$\mathrm{J}_z\ Y_{j,m}(\theta,\varphi) = m\hbar\ Y_{j,m}(\theta,\varphi) \tag{3.99}$$

with $J = 0,1,2,\ldots$ and $m \le |J|$.

We focus on the case of a linear molecule for which $I_{XX} = I_{YY} = I$, $I_{ZZ} \approx 0$. From $\mathrm{J}^2 = \mathrm{J}_X^2+\mathrm{J}_Y^2+\mathrm{J}_Z^2$ the rotation of molecule creates a series of discrete states with energies

$$E_{\mathrm{rot}} = \frac{J(J+1)\hbar^2}{2I} \tag{3.100}$$

In spectroscopy it is more popular to consider the rotational energy terms in units of wavenumber, therefore, for the rigid rotator model we introduce

$$F(J) = \frac{h}{8\pi^2 cI} J(J+1) = B\, J(J+1) \tag{3.101}$$

where B is the rotational constant in units of cm^{-1} , h is the Planck's constant and c the speed of light.

3.6.2 Oscillator Model of Diatomic Molecules

Atoms in a diatomic molecule are bound together by a restoring force caused by their electrons cloud. This force can be approximated by a linear function of displacement from an equilibrium point, i.e., $F(r) = -k(r - r_e)$. This model is equivalent to the classical harmonic oscillator.

For the radial part of 3.96 the potential energy is

$$V(r) = \frac{1}{2}kr^2 \tag{3.102}$$

Solutions of Schrödinger equation of a harmonic oscillator can be found in many introductory quantum mechanics books. The vibrational states have energies of

$$E_{\mathrm{vib}} = \hbar\omega_{\mathrm{vib}}(v + \frac{1}{2}) \tag{3.103}$$

with $v = 0, 1, 2, \ldots$ where

$$\omega_{\mathrm{vib}} = \sqrt{\frac{k}{\mu}} \tag{3.104}$$

In spectroscopic units (cm^{-1}), the vibrational energy is

$$G(v) = \frac{\hbar\omega_{\mathrm{vib}}}{hc}(v + \frac{1}{2}) = \omega(v + \frac{1}{2}) \tag{3.105}$$

This shows that the energies of the harmonic oscillator are equally spaced, contrary to the rotational energies of a rigid rotator.

Although the harmonic oscillator model is sufficient to address the features of molecular spectra for small values of v, for higher values this model is not precise enough. This is due to the shape of vibration potential curve. We expect that if atoms of a molecule move far from their equilibrium value, the molecule dissociates, i.e., it splits into separate atoms. Equivalently, the potential curve flattens for large values of r. In other words the potential curve is deformed from the parabolic shape of the harmonic oscillator model.

Consequently the vibration potential of the anharmonic oscillator is a polynomial with displacement terms of higher order added to the potential of the harmonic oscillator. Energy levels of the solutions of the Schrödinger equations for the anharmonic oscillator (in cm^{-1}) are:

$$G(v) = \omega_e(v+\frac{1}{2}) - \omega_e\ x_e(v+\frac{1}{2})^2 + \omega_e\ y_e(v+\frac{1}{2})^3 + \ldots \tag{3.106}$$

Values of ω_e, $\omega_e x_e$ and $\omega_e y_e$ decrease rapidly, e.g. these values for the $X^1\Sigma_g^+$ electronic state of N_2 molecule are $\omega_e = 2358.57$, $\omega_e x_e = 14.324$ and $\omega_e y_e = -0.00226$. Anharmonicity removes the equality of distances between energy states that is valid for harmonic oscillator. From Eq. (3.106) the spacing between vibrational levels decreases as v increases.

3.6.3 Nonrigid rotator Model of Diatomic Molecules

In Section 3.6.1 the rotator is assumed to be rigid, i.e. the distance between the center of gravity and the rotating object is constant over one rotation period. However, spectral observation proves this assumption to be an approximation. Variation of internuclear distance because of molecular vibration affects the rotational motion in two ways. First, a classical picture of rotation requires a centrifugal force to compensate the restoring force. In classical paradigm of rotation we have

$$\mu\omega^2 r = \frac{J^2}{\mu r^3} \tag{3.107}$$

and the equation of centrifugal force and restoring force is

$$r - r_e = \frac{J^2}{\mu r_e^3 k} \tag{3.108}$$

where r_e is the vibration equilibrium position where assumption can be made that $r - r_e \approx r_e$ as the displacement of molecule from its equilibrium position is very small. The energy of a vibrating rotator is

$$E = \frac{J^2}{2\mu r_e^2} + \frac{1}{2}k(r-r_e)^2 = \frac{J^2}{2\mu r_e^2} - \frac{J^4}{2\mu^2 r_e^6 k}. \tag{3.109}$$

The quantum mechanical Hamiltonian of this system is obtained by substituting the angular momentum operator. The eigenvalues of such an Hamiltonian (in units of cm^{-1}) are

$$\begin{aligned} E &= \frac{1}{hc}\Big[\frac{\hbar^2}{2\mu r_e^2}J(J+1) - \frac{\hbar^4}{2\mu^2 r_e^6 k}J^2(J+1)^2\Big] \\ &= B\ J(J+1) - D\ J^2(J+1)^2 \end{aligned} \tag{3.110}$$

As a result the centrifugal distortion decreases the spacing between rotational energies. In Eq. (3.110) higher terms can be introduced if anharmonicity is involved. However, they play a less important roles as their amounts are negligible compared to the first two constants.

The second way that vibrations change the rotational motion is that the variation of internuclear distance manipulates the amount of moment of inertia, I, as it is a function of $(r - r_e)$. This in turn affects the values of B and D as

$$B_v = B_e - \alpha(v + \frac{1}{2}) \tag{3.111}$$

$$D_v = D_e - \beta_e(v + \frac{1}{2}) \tag{3.112}$$

Here, higher terms are neglected as their effect is negligible. In conclusion the amount of energy that a molecule contains due to its rotation and vibration is

$$\begin{aligned} T = \omega_e(v + \frac{1}{2}) - \omega_e x_e(v + \frac{1}{2})^2 + \omega_e y_e(v + \frac{1}{2})^3 + \dots \\ + B_v J(J+1) - D_v J^2(J+1)^2 + \dots \end{aligned} \tag{3.113}$$

3.6.4 Molecular alignment by linearly polarized laser field

General formalism

Interaction of laser light with a molecule without permanent dipole moment induces a dipole moment, μ, by separating the centers of positive and negative charges. This dipole moment is proportional to the electric field by polarizability tensor, α. Laser makes the induced dipole moment to be aligned along the same direction as the electric field. Assuming a molecule with diagonal polarizability tensor, the energy of the molecule inside the electric field is changed as

$$\begin{aligned} E &= -\frac{1}{2}\vec{\mu}\cdot\vec{\mathcal{E}} \\ &= -\frac{1}{2}\Big(\alpha_{XX}\mathcal{E}_X^2 + \alpha_{YY}\mathcal{E}_Y^2 + \alpha_{ZZ}\mathcal{E}_Z^2\Big). \end{aligned} \tag{3.114}$$

Hence, for a molecule with $\alpha_{XX} = \alpha_{YY} = \alpha_\perp$ and $\alpha_{ZZ} = \alpha_\parallel$ the energy is

$$E = -\frac{\mathcal{E}_0^2}{2}\,\Delta\alpha\,\cos^2\theta, \tag{3.115}$$

where $\Delta\alpha = \alpha_\parallel - \alpha_\perp$ and $\mathcal{E} = \mathcal{E}_0\cos\theta\hat{Z}$ with θ being the angle between the molecule's axis of symmetry along $\hat{Z}$ and the electric field polarization axis. This

implies that the molecule rotates to align itself along the field axis, $\theta = 0$, so as to maintain a minimum energy.

However, for a molecule one needs to treat the interaction quantum mechanically to reveal the full dynamics. The Hamiltonian of the interaction between the induced dipole moment and the electric field, for the case that the frequency of the electric field is far from any electronic and vibrational transition is [21]:

$$H_{\text{int}} = -\frac{1}{4}\sum_{\rho\rho'} \mathcal{E}_\rho \alpha_{\rho\rho'} \mathcal{E}'_\rho = -\frac{1}{4}\sum_{\rho\rho'}\sum_{kk'} \mathcal{E}_\rho \, \langle\rho|k\rangle \alpha_{kk'} \langle k'|\rho'\rangle \mathcal{E}^*_{\rho'} \tag{3.116}$$

where $\alpha_{\rho\rho'}$ and $\alpha_{kk'}$ are the polarizability tensors in body-fixed and space-fixed frames. k, ρ and $\langle\rho|k\rangle$ are the body-fixed frame $(\hat{X}, \hat{Y}, \hat{Z})$, space-fixed frame $(\hat{x}, \hat{y}, \hat{z})$ and elements of Euler transformation matrix from one frame to the other, respectively.

Molecule	$B_0(\text{cm}^{-1})$	$D_0(\text{cm}^{-1})$	$\Delta\alpha_\nu(\text{Å}^3)$	g_{even}	g_{odd}
N_2	1.989581	5.76×10^{-6}	0.93	2	1
O_2	1.4297	4.839×10^{-6}	1.15	0	1
CO_2	0.3902	0.135×10^{-6}	2	1	0

Table 3.1: Molecular rotational properties of N_2, O_2 and CO_2 [22, 23]

Here we only consider a linearly polarized field, $\mathcal{E} = \mathcal{E}_0\hat{z}$, and linear molecules, $I_{ZZ} \approx 0$, $I_{XX} = I_{YY} = I$ where I is the moment of inertia in Eq. (3.97) and $\alpha_{ZZ} = \alpha_\parallel$, $\alpha_{XX} = \alpha_{YY} = \alpha_\perp$. An explicit form of Eq. (3.116) for this special case is

$$H_{\text{int}} = -\frac{\mathcal{E}_0^2}{4}\,\Delta\alpha\,\cos^2\theta \tag{3.117}$$

which has the similar form as Eq. (3.115) with the same definition of $\Delta\alpha$. Rotational properties are briefly listed in table 3.1. The total Hamiltonian of a linear molecule interacting with a linearly polarized field is obtained by adding Eq. (3.97) and Eq. (3.117): $H = H_{\text{rot}} + H_{\text{int}}$. Note that Eq. (3.97) for a linear molecule has energies as in Eq. (3.100). The solution of the time-dependent Schrödinger equation is a linear combination of spherical harmonics in Eq. (3.98) of the form $\sum_{jm} a_{j,m} Y_{j,m}(\theta, \varphi)$.

The expectation value of the molecule's polar angle, $\langle\cos^2\theta\rangle$, is a measure that quantifies how the molecule aligns with respect to the space-fixed frame. Note that revealing the complete 3-D orientation of molecule needs the expectation value of all the Euler angles to be calculated. This is beyond the scope of this text and curious reader is encouraged to consult the reference [24]. $\sqrt{\langle \text{J}^2\rangle} \approx \langle \text{J}\rangle$ is used to define the dynamics of rotational states during the interaction.

A molecular ensemble has a thermal distribution over rotational states that is defined by Boltzmann statistics

$$P(E_J) = \frac{1}{Z}\, g_J\, (2J+1)\, \exp\Big(-\frac{E_J}{k_B T}\Big), \tag{3.118}$$

where Z, g_J (cf. table 3.1), k_B are the partition function, nuclear spin statistics and the Boltzmann constant. The $(2J+1)$ term accounts for the number of degenerate states with same energy but different m.

Hence, the expectation value of any observable should be calculated by

$$\langle \cos^2\theta \rangle = \frac{1}{Z} \sum_{J,m} g_J\, \exp(-\frac{E_J}{k_B T}) \langle \cos^2\theta \rangle_{J,m} \tag{3.119}$$

where the Boltzmann distribution is used to average the $\langle \cos^2\theta \rangle$ for the rotational states initially in J and m state.. $\langle \cos^2\theta \rangle_{J,m}$ means that we assume that initially only $|J,m\rangle = 1$; we then calculate $\langle \cos^2\theta \rangle$ and multiply it by its thermal weight. The same operation is performed for the rest of the states, and sum the results.

Dependence of the Hamiltonian on $\cos^2\theta$ allows Raman-type transitions with $\Delta J = 0, \pm 2$ and $\Delta m = 0$ selection rules between rotational states [22]. Transitions redistribute the population of rotational states during the interaction. Here we discuss the importance of the interaction duration, or in other words the duration of the electric field.

Adiabatic versus impulsive alignment

In the absence of any electric field, the rotational period of a molecule is $\tau_{\text{rot}} = 1/(2Bc)$ with B defined in Eq. 3.101. This period establishes a scale to define two regimes of interaction with respect to the pulse duration τ: *adiabatic* regime ($\tau > \tau_{\text{rot}}$) and *nonadiabatic* or *impulsive* regime $\tau < \tau_{\text{rot}}$. The response to the laser field is different in the two temporal regions. Analytical treatments can be found in reference [25] to understand this difference. The numerical simulations presented in Figs 3.6 and 3.7 illustrate the difference between the two regimes. Let us assume first that the molecule is at zero temperature so that initially only $J = 0$ is populated. In the adiabatic regime [Fig. 3.6 (center)], the $J > 0$ states start to populate as the pulse rises, with the maximum J being reached at the peak of pulse maximum. However, as the pulse slope turns negative, the population rolls back to $J = 0$, and the system returns to its initial state upon the pulse turn-off. This scenario requires the pulse duration to be longer than the rotational period, so that the rotational states have sufficient time to transit back to the initial state. Figure 3.7 (center) shows the $\sqrt{J(J+1)}$ for adiabatic case. This verifies that the pulse escalates the J value from

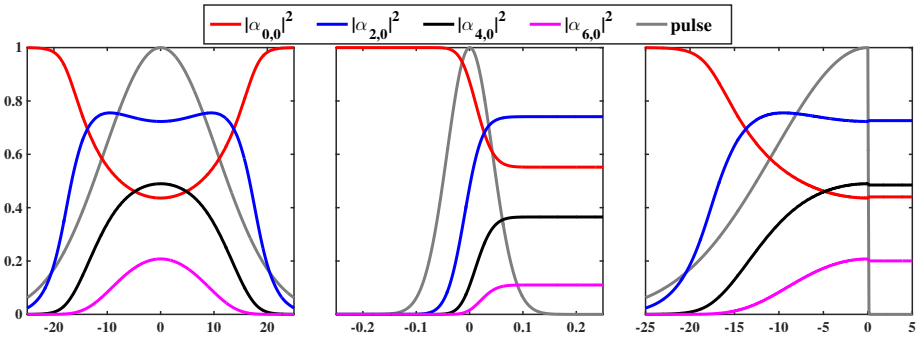

Figure 3.6: Dynamics of wavefunction coefficients, $a_{J,M}$ as function of time for N_2 at T=0°K for different pulse durations. (left) [τ_{on} = 25 ps, τ_{off} = 25 ps], (middle) [τ_{on} = 100 fs, τ_{off} = 100 fs] and (right) [τ_{on} = 25 ps, τ_{off} = 100 fs]. Normalized pulse shape is shown with grey line. Abscissa is in picoseconds time unit. τ_{on} is the rising half-width at half-maximum of the rising side of pulse and τ_{off} is the rising half-width at half-maximum of the falling side of pulse.

zero to a maximum and then this value is dropped as the pulse declines. Also, $\langle\cos^2\theta\rangle$ suggests that the molecule is aligned toward the electric field direction as the pulse enters and when it disappears molecules are left randomly aligned, as they were at the beginning.

Figure 3.7 (left) shows the $\sqrt{J(J+1)}$ for adiabatic case. This verifies that the pulse escalates the J value from zero to a maximum and then this value is dropped as the pulse declines. Also, $\langle\cos^2\theta\rangle$ suggests that the molecule is aligned toward the electric field direction as the pulse enters and when it disappears molecules are left randomly aligned, as they were at the beginning.

In Figure 3.7 (middle) average amount $\sqrt{J(J+1)}$ at the end of pulse duration is nonzero i.e. molecule gains angular momentum. After the pulse turn-off, these states evolve freely and beat just like a superposition of sinusoidal functions with different frequencies. Effect of superposition of states emerges in the value of $\langle\cos^2\theta\rangle$. It is obvious that even after the interaction is terminated molecules change their angle with the space-fixed frame. This oscillatory effect is called "rotational revivals" with period equal to the τ_{rot}. It should be noted that these alignment revivals are hindered by the damping effects which are not discussed in this text.

Value of $\sqrt{J(J+1)}$ is shown in Figure 3.7 with blue dashed line. It shows that in case of nonadiabatic alignment that molecule is left in $J > 0$ states contrary to the adiabatic alignment that angular momentum is zero. Figure 3.6 and Figure 3.7 (right) show the case that τ_{on} = 25 ps (adiabatic turn-on) and τ_{on} = 100 fs (nonadiabatic turn-off). This case inherits the properties of adiabatic and nonadiabatic cases. The most striking differences of this with nonadiabatic interaction is that the

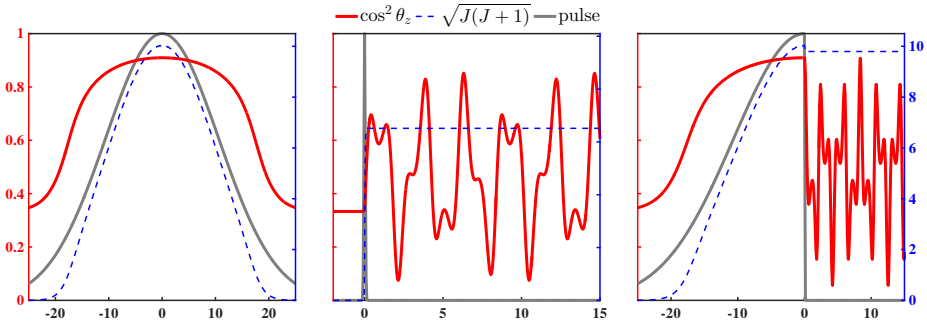

Figure 3.7: Dynamics of $\langle\cos^2\theta\rangle$ (red, left ordinate) and $\sqrt{\langle J(J+1)\rangle}$ (blue, right ordinate) with same conditions as in Figure 3.6. (left) [τ_{on} = 25 ps, τ_{off} = 25 ps], (middle) [τ_{on} = 100 fs, τ_{off} = 100 fs] and (right) [τ_{on} = 25 ps, τ_{off} = 100 fs]. Normalized pulse shape is shown with grey line. Abscissa is in picoseconds time unit.

value of $\sqrt{J(J+1)}$ is higher, i.e. more rotational states contribute to the dynamics of the molecule. As a result the beating between these states which is observable in $\langle\cos^2\theta\rangle$ quantity results in sharper features for Figure 3.7 (right). In other words, broader wavepacket in J space is equivalent of sharper alignment peaks. For this hybrid type of interaction, simulations show that the vertical separation between peaks and dips of $\langle\cos^2\theta\rangle$ are more pronounced.

Numerical results of Eq. (3.119) are shown in Figure 3.8 for nitrogen, oxyegn and air molecules ensemble at T=295°K interacting with a linear pulse. Air is assumed to consist of 78% nitroegn and 22% oxygen. Pulse has a Gaussian temporal shape with full-width at half-maximum of 60 femtosecond and peak intensity is 50 TW/cm^2. Higher temperature requires more rotational states to be considered in Eq. (3.119) according to Eq. (3.118). Similar to Figure 3.7 (middle), after the pulse declines molecular wavepacket beats at multiples of rotational frequency. After integral multiples of τ_{rot}, "full-revival", molecule's rotational states have $2n\pi$ phase. This moment occurs at 8.34 ps for N_2 and 11.66 ps for O_2.

The local maxima represent alignment of molecules in direction of laser polarization i.e. the angle between the laser polarization and the molecular axis is reduced while the minima show the antialignment of molecules i.e. the angle between the laser polarization and the molecular axis is increased. Angular shape of molecule at alignment and anti-alignment instances are presented in middle and right panel of Figure 3.9, respectively. Contrary to the angular shape of molecule before the interaction with the pulse that is sphere, Figure 3.9, at the alignment molecule is stretched along the polarization axis while it becomes flat in the plane perpendicular to the polarization at the anti-alignment moment.

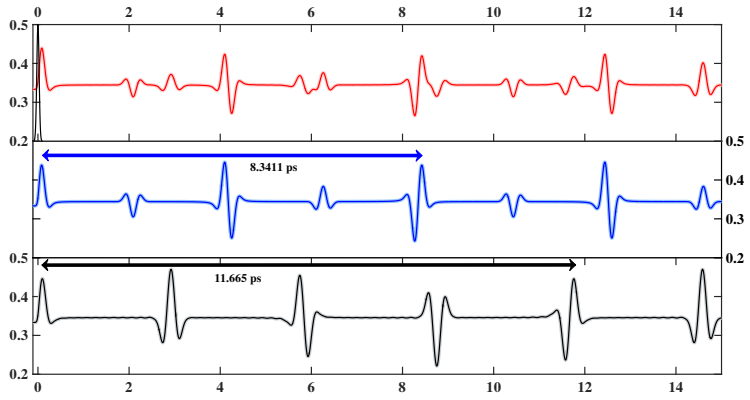

Figure 3.8: Nondissipative $\langle \cos^2\theta \rangle$ of O_2 (bottom), N_2 (middle) and air (top). Air is assumed to be a mixed ensemble of 78% of N_2 and 22% of O_2. Electric field is a 60 fs, 50 TWcm^{-2} linearly polarized pulse (shown in top plot with black solid line. Abscissa is in picoseconds

Figure 3.8 shows that the transition from alignment to antialignment and vice versa is very fast compared to the rotational period. This fast transition is important in many applications as we will discuss in section **??**

3.6.5 Orientational index of refraction

This section deals with the reaction of the molecules rotated by the light field on the light field itself. This reaction is due to the fact that the molecules have a different (linear) index of refraction along their different axis of symmetry.

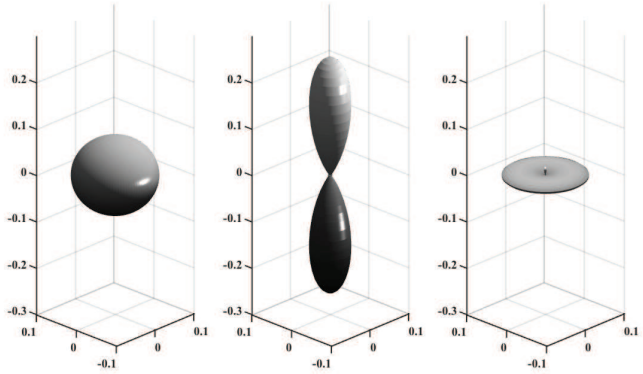

Figure 3.9: Angular distribution of N_2 molecule at T=0°K in absence of aligning pulse (left), in alignment instance near the full-revival (middle) and anti-alignment near full-revival (right).

Bibliography

[1] L. V. Keldysh. Ionization in the field of a strong electromagnetic wave. *Soviet Physics JET*, 20(5):1307–1314, 1965.

[2] V. S. Popov. Tunnel and multiphoton ionization of atoms and ions in a strong laser field (kelysh theory). *Phys.-Usp*, 47:855, 2004.

[3] L. Arissian, C. Smeenk, F. Turner, C. Trallero, A. V. Sokolov, D. Villeneuve A. Staudte, and P B Corkum. Direct test of laser tunneling with electron momentum imaging. *Physical Review Letters*, 105:133002, 2010.

[4] M. Y.Ivanov, M. Spanner, and O. Smirnova. anatomy of strong field ionization. *J. Mod.Phys*, 52:165–184, 2005.

[5] V. P. Krainov. Ionization rates and energy and angular distributions at the barrier-suppression ionization of complex atoms and atomic ions. *J. Opt. Soc. Am. B*, 14:425, 1997.

[6] L. Arissian and J.-C. Diels. Ultrafast electron plasma index; an ionization perspective. *Journal of Lasers, Optics & Photonics*, 1:107–111, 2014.

[7] J. D. Jackson. *Classical Electrodynamics 2nd ed.* McGraw-Hill, New York, 1975.

[8] D. A. Romanov and R. J. Levis. Postionization medium evolution in a laser filament: A uniquely nonplasma response. *Physical Review E*, E86:046408, 2012.

[9] R. M. Fano, L. J. Chu, and R. B. Adler. *Electromagnetic Fields, Energy and Forces*. John Wiley and Sons, Inc.,, New York, 1960.

[10] L. C Bahiana. *Electromagnetic induction on an expanding conducting sphere*. PhD thesis, Massachusetts Institute of Technology, 1964.

[11] C. Smeenk, L. Arissian, B. Zhou, A. Mysyrowicz, D. M. Villeneuve, A. Staudte, and P. B. Corkum. Partitioning of the linear photon momentum in multiphoton ionization. *Physical Review Letters*, 106:193002, 2011.

[12] J.-C. Diels and S. Besnainou. Multiphoton coherent excitation of molecules. *J. Chem. Phys.*, 85:6347–6355, 1986.

[13] NRC Michael Spanner, Steacie Institute for Molecular Sciences. Mechanisms of inversion in the N_2^+ air laser. *to be published*, 2016.

[14] J. Biegert and J. C. Diels. Feasibility study to create a polychromatic guidestar in atomic sodium. *Physical Review A*, 67:043403–1–043403–11, 2003.

[15] R. P. Feynman, F. L. Vernon, and R. W. Hellwarth. Geometrical representation of the Schroedinger equation for solving maser problems. *J. Appl. Phys.*, 28:49–52, 1957.

[16] J.-C. Diels and A. T. Georges. Coherent two-photon resonant third and fifth harmonic VUV generation in metal vapors. *Phys. Rev. A*, 19:1589–1591, 1979.

[17] J.-C. Diels, N. Nandini, and A. Mukherjee. Multiphoton coherences. *Physica Acta*, T23:206–210, 1988.

[18] N. Mukherjee, A. Mukherjee, and J.-C. Diels. Four-photon coherent resonant propagation and transient wave mixing: Application to the mercury atom. *Phys. Rev. A*, A38:1990–2004, 1988.

[19] L. Allen and J. H. Eberly. *Optical Resonances and Two-level Atoms*. John Wiley & Sons, 1975.

[20] F. Bloch. Magnetic resonances. *Phys. Rev.*, 70:460, 1946.

[21] Tamar Seideman and Edward Hamilton. Nonadiabatic alignment by intense pulses. concepts, theory, and directions. In P.R. Berman and C.C. Lin, editors, *Advances In Atomic, Molecular, and Optical Physics*, volume 52, pages 289 – 329. Academic Press, 2005.

[22] G. Herzberg. *Molecular Spectra and Molecular Structure: I. Spectra of Diatomic Molecules*. Van Nostrand, New York, 1950.

[23] A. Lofthus and P. H. Krupenie. The spectrum of molecular nitrogen. *J. Phys. Chem. Ref. Data*, 6:113–307, 1977.

[24] Jakob Juul Larsen, Kasper Hald, Nis Bjerre, Henrik Stapelfeldt, and Tamar Seideman. Three dimensional alignment of molecules using elliptically polarized laser fields. *Phys. Rev. Lett.*, 85:2470–2473, Sep 2000.

[25] Tamar Seideman. On the dynamics of rotationally broad, spatially aligned wave packets. *The Journal of Chemical Physics*, 115(13):5965–5973, 2001.

Chapter 4

Neo-classical Light–Matter Interaction

In the previous chapter, the quantum mechanical response of the medium interacting with a light field was calculated. We arrived to classical linear and nonlinear polarization in the limit of stationary response, i.e. pulses much longer than the matter relaxation times. This is the situation that occurs when the pulse spectrum does not cover any resonant transition. Non-resonant optical processes are particularly useful in femtosecond phenomena because they can lead to conversion of optical frequencies with minimum losses. Nonlinear non-resonant phenomena are currently exploited to make use of the most efficient laser sources, which are only available at few wavelengths, to produce shorter pulses at different wavelengths (nonlinear frequency conversion and compression) and amplify them (parametric amplification). In contrast to the previous section where the interaction was dominated by a resonance, we will be dealing with situations where the light frequency is far away from optical resonances. Nonlinear crystals lend themselves nearly ideally to frequency conversion with ultrashort pulses because their nonlinearity is electronic and typically non-resonant from the near UV through the visible to the near IR spectral region. Therefore, the processes involved respond nearly instantaneously on the time scale of even the shortest optical pulse. There appears to be no limit in the palette of frequencies that can be generated through nonlinear optics, from dc (optical rectification) to infrared (difference frequency generation and optical parametric generation and amplification), to visible, and to UV (sum frequency generation). The shorter the pulse, the higher the peak intensity for a given pulse energy (and thus the more efficient the nonlinear process).

For cw light of low intensity, a medium with a non-resonant nonlinearity appears completely transparent and merely introduces a phase shift. For pulses, as

discussed in Chapter 1, dispersion has to be taken into account, which can lead to pulse broadening and shortening depending upon the input chirp, and to phase modulation effects. The light–matter interaction is linear, i.e., there is a linear relationship between input and output field, which results in a constant spectral intensity. A typical example is the pulse propagation through a piece of glass. The situation becomes much more complex if the pulse intensity is large, which can be achieved by focusing or/and using amplified pulses. The high electric field associated with the propagating pulse is no longer negligibly small as compared to typical local fields inside the material such as inner atomic (inner molecular) fields and crystal fields. The result is that the material properties are changed by the incident field and thus depend on the pulse. The induced polarization which is needed as source term in the wave equation is formally described by the relationship

$$\begin{aligned} P = \epsilon_0 \chi(E) E &= \epsilon_0 \chi^{(1)} E + \epsilon_0 \chi^{(2)} E^2 + \epsilon_0 \chi^{(3)} E^3 + ... + \epsilon_0 \chi^{(n)} E^n + ... \\ &= P^{(1)} + P^{(2)} + ... + P^{(n)} + ... \end{aligned} \tag{4.1}$$

The quantities $\chi^{(n)}$ are known as the nonlinear optical susceptibilities of n^{th} order where $\chi^{(1)}$ is the linear susceptibility introduced in Eq. (1.81). The ratio of two successive terms is roughly given by

$$\left| \frac{P^{(n+1)}}{P^{(n)}} \right| = \left| \frac{\chi^{(n+1)} E}{\chi^{(n)}} \right| \approx \left| \frac{E}{E_{mat}} \right| \tag{4.2}$$

where E_{mat} is a typical value for the inherent electrical field in the material. For simplicity we have taken both E and P as scalar quantities. Generally, $\chi^{(n)}$ is a tensor of order $(n+1)$ which relates an n-fold product of vector components E_j to a certain component of the polarization of n^{th} order,[1] $P^{(n)}$; see, for example, [1–3].

4.1 Non-instantaneous response

For Eq. (4.1) to be valid in the time domain, we must assume that the sample responds instantaneously to the electric field: in other words, it does not exhibit a memory. The polarization at an instant $t = t_0$ must depend solely on field values at $t = t_0$. As discussed in the previous section for resonant interaction, a non-instantaneous response and memory effects, respectively, are a result of phase and energy relaxation processes. They become noticeable if they proceed on a time scale of the pulse duration or longer. Fortunately, in non-resonant light–matter interaction many processes are well described by an instantaneous response even

[1] Note that this product can couple up to n different input fields depending upon the conditions of illumination.

when excited by pulses with durations of the order of 10^{-14} s. This is generally true for nonlinear effects of electronic origin. Often however, the motion of the much heavier atomic nuclei and molecules contribute to the material response. In such a case, memory effects are likely to occur on a fs time scale, and the nth-order polarization depends on the history of the field:

$$P^{(n)}(t) = \epsilon_0 \int\int ... \int \chi^{(n)}(t_1, t_2, ..., t_n) E(t-t_1) E(t-t_1-t_2) ... \\ \times E(t-t_1-...-t_n) dt_1 dt_2 ... dt_n, \tag{4.3}$$

which illustrates the influence of the electric field components at earlier times.

Let us discuss the meaning of a memory of the nonlinear polarization for the case of $n = 2$. The nonlinear polarization of second order is responsible for second harmonic generation or frequency mixing or parametric amplification:

$$P^{NL}(t) = P^{(2)}(t) = \epsilon_0 \int\int \chi^{(2)}(t_1, t_2) E_1(t-t_1) E_2(t-t_1-t_2) dt_1 dt_2, \tag{4.4}$$

where E_1 and E_2 are optical fields, which can be identical, and $\chi^{(2)}$ is the susceptibility of second order. Note that, even though the expression (4.4) is a time convolution, its Fourier transform is not a simple product, but also a convolution in the frequency domain. This convolution takes a simple form in the case of an instantaneous nonlinearity:

$$\chi^{(2)}(t_1, t_2) = \chi_0^{(2)} \delta(t-t_1) \delta(t-t_2). \tag{4.5}$$

In the time domain, the corresponding nonlinear polarization is:

$$P^{NL}(t) = \epsilon_0 \chi_0^{(2)} E_1(t) E_2(t), \tag{4.6}$$

By taking directly the Fourier transform of this expression, we find that the nonlinear polarization in the frequency domain is a convolution:

$$P^{NL}(\Omega) = \int P^{NL}(t) e^{-i\Omega t} dt = \epsilon_0 \chi_0^{(2)} \int E_1(\Omega - \Omega') E_2(\Omega') d\Omega'. \tag{4.7}$$

For monochromatic waves and long pulses, where the fields can be approximated by δ-functions in the frequency domain, Eq. (4.7) reduces to a product.

Equation (4.7) fails as soon as the nonlinear response can no longer be considered to be instantaneous. We will now show how one can find the general expression for a nonlinear polarization of second order, cf. Eq. (4.4), in the frequency domain. Fourier-transforming Eq. (4.4) yields:

$$P^{NL}(\Omega) = \epsilon_0 \int\int \chi^{(2)}(t_1, t_2) \left[\int E_1(t-t_1) E_2(t-t_1-t_2) e^{-i\Omega t} dt \right] dt_1 dt_2 \tag{4.8}$$

where we have changed the order of integration. The expression in brackets, $C(t_1, t_2, \Omega)$, is the Fourier transform of a product, which can be written as the convolution of the FT's of the factors, $e^{-i\Omega t_1}E_1(\Omega)$ and $e^{-i\Omega(t_1+t_2)}E_2(\Omega)$:

$$C(t_1, t_2, \Omega) = \int e^{-i\Omega'(t_1+t_2)}E_2(\Omega')e^{-i(\Omega-\Omega')t_1}E_1(\Omega-\Omega')d\Omega' \tag{4.9}$$

After inserting Eq. (4.9) into Eq. (4.8) the polarization in the frequency domain reads

$$P^{NL}(\Omega) = \epsilon_0 \int\int \chi^{(2)}(t_1, t_2)\,[C(t_1, t_2, \Omega)]\,dt_1 dt_2. \tag{4.10}$$

Inserting Eq. (4.9) into Eq. (4.10) and changing the order of integration, we find

$$P^{NL}(\Omega) = \epsilon_0 \int E_2(\Omega')E_1(\Omega-\Omega')\chi^{(2)}(\Omega, \Omega')d\Omega', \tag{4.11}$$

where

$$\chi^{(2)}(\Omega, \Omega') = \int\int \chi^{(2)}(t_1, t_2)e^{-i\Omega' t_2}e^{-i\Omega t_1}dt_1 dt_2. \tag{4.12}$$

The result of Eq.(4.11) is easily generalized to higher order susceptibilities. If the susceptibility is not frequency dependent we reproduce the result of Eq. (4.7). This is again a manifestation of the fact that an instantaneous response (no memory) is characterized by nondispersive material properties.

4.2 Pulse propagation

To study pulse propagation in a nonlinear optical medium we can proceed as in the previous section. To the linear wave equation for the electric field, which contains the $\chi^{(1)}$ contribution, we add the nonresonant nonlinear polarization. As result we obtain the wave equation with the nonlinear polarization as source term:

$$\left(\frac{\partial}{\partial z}\tilde{\mathcal{E}} - \frac{i}{2}k''_\ell\frac{\partial^2}{\partial t^2}\tilde{\mathcal{E}} + \mathcal{D}\right)e^{i(\omega_\ell t - k_\ell z)} + c.c. = i\frac{\mu_0}{k_\ell}\frac{\partial^2}{\partial t^2}P^{NL}. \tag{4.13}$$

The polarization appearing in the right hand side can be instantaneous, or be the solution of a differential equation as in the case of most interactions with resonant atomic or molecular systems, see previous section and Chapter **??**. If we represent the polarization as a product of a slowly varying envelope $\tilde{\mathcal{P}}$ and a term oscillating with an optical frequency ω_p, $e^{i\omega_p t}$, the right-hand side of Eq. (4.13) can be written as

$$\frac{\partial^2}{\partial t^2}\left(\tilde{\mathcal{P}}e^{i\omega_p t} + c.c.\right) = \left(\frac{\partial^2}{\partial t^2}\tilde{\mathcal{P}} + 2i\omega_p\frac{\partial}{\partial t}\tilde{\mathcal{P}} - \omega_p^2\tilde{\mathcal{P}}\right)e^{i\omega_p t} + c.c.. \tag{4.14}$$

In order to compare the magnitude of the individual terms we approximate $(\partial/\partial t)\tilde{\mathcal{P}}$ with $\tilde{\mathcal{P}}/\tau_p$ which yields for the ratio of two successive members of the sum in the brackets $\omega_p\tau_p$. Therefore, if the pulse duration is (much) longer than an optical period, that is $\omega_p\tau_p = 2\pi\tau_p/T_p \gg 1$, we may neglect the first two terms in favor of $\omega_p^2\tilde{\mathcal{P}}$. This will simplify the further evaluation of Eq. (4.13) significantly.

As pointed out earlier the SVEA becomes questionable if the pulses contain only few optical cycles. Brabec and Krausz [4] derived a propagation equation under less stringent conditions. If

$$|(\partial/\partial z)\tilde{\mathcal{E}}| << k_\ell|\tilde{\mathcal{E}}| \tag{4.15}$$

and

$$|(\partial/\partial t)\tilde{\mathcal{E}}| << \omega_\ell|\tilde{\mathcal{E}}| \tag{4.16}$$

or

$$\left|1 - \frac{v_p}{v_g}\right| << 1 \tag{4.17}$$

are satisfied pulse propagation in the presence of a nonlinear polarization of slowly-varying amplitude $\mathcal{P}^{(NL)}$ and dispersion can be described by

$$\left[\frac{\partial}{\partial z} + \frac{i}{2k_\ell}\left(1 - \frac{i}{\omega_\ell}\frac{\partial}{\partial t}\right)^{-1}\nabla_\perp^2 - \frac{\alpha_0}{2} + i\hat{D}\right]\tilde{\mathcal{E}} = -i\frac{\omega_\ell c\mu_0}{2n_0}\left(1 - \frac{i}{\omega_0}\frac{\partial}{\partial t}\right)\tilde{\mathcal{P}}^{(NL)}, \tag{4.18}$$

where

$$\hat{D} = \frac{\alpha_1}{2}\frac{\partial}{\partial t} + \sum_{m=2}^{\infty}\frac{1}{m!}\left(k_m + i\frac{\alpha_m}{2}\right)\left(-i\frac{\partial}{\partial t}\right)^m$$

with

$$\alpha_m = \frac{\partial^m}{\partial\Omega^m}\left[\mathrm{Im}\,k(\Omega)\right]_{\omega_\ell} \quad \text{and} \quad k_m = \frac{\partial^m}{\partial\Omega^m}\left[\mathrm{Re}\,k(\Omega)\right]_{\omega_\ell},$$

see Appendix F. The coordinates z, t refer to a frame moving with the group velocity of the pulse. The additional time derivatives of the nonlinear polarization and the diffraction term ($\nabla_\perp^2$) become important for extremely short pulses. This propagation equation was termed "slowly evolving envelope equation". In many materials phase and group velocity are not much different and condition (4.17) is satisfied. Conditions (4.15) and (4.17) can be combined to the "slowly evolving wave approximation" [4]

$$\left|\frac{\partial}{\partial z}E\right| << k_\ell|E|, \tag{4.19}$$

which states that the amplitude and phase of the electric field must not change significantly over a propagation distance of the order of a wavelength.

In general, when a nonlinear polarization is involved, there will not be just one propagation equation of the form of Eq. (4.14), but as many as the number of waves that participate in the nonlinear optical process. For instance, a third order polarization excited by a field at frequency ω_ℓ will create a polarization at $3\omega_\ell = \omega_\ell + \omega_\ell + \omega_\ell$, and a polarization at $\omega_\ell = \omega_\ell - \omega_\ell + \omega_\ell$. The first process is generation of a third harmonic field, and the second is either two-photon absorption or a nonlinear index of refraction, depending on the phase of the nonlinear susceptibility. The generated field at $3\omega_\ell$ will propagate, and interfere with the field at $3\omega_\ell$ produced at a different location by the fundamental. The third harmonic field may also lead to the generation of other frequencies, through the third order process. For instance, there will be re-generation of the fundamental frequency through the third order process $\omega_\ell = 3\omega_\ell - \omega_\ell - \omega_\ell$, and the latter field will also interfere with the propagated fundamental. The third harmonic may also create a 9^{th} harmonic through the nonlinear susceptibility. At a minimum, there will be at least two differential equations of the form Eq. (4.14), with a third order susceptibility, corresponding to the fundamental and third harmonic fields. More equations have to be added if more frequencies are generated.

It is beyond the scope of the book to give a detailed description of the various possible nonlinear effects and excitation schemes. The reader is referred to the standard texts on nonlinear optics, for example Schubert and Wilhelmi [1], Boyd [2], Bloembergen [3] and Shen [5]. Here we shall restrict ourselves to a nonlinearity of second order that is responsible for second harmonic generation (SHG), optical parametric amplification (OPA), and to a nonlinearity of third order describing (self) phase modulation [(S)PM].

The tensor character of the nonlinear susceptibility describes the symmetry properties of the material. For all substances with inversion symmetry, $\chi^{(2n)} = 0$ ($n = 1, 2...$) holds, and therefore no second harmonic processes can be observed in isotropic materials and centrosymmetric crystals for example. In contrast, third-order effects are always symmetry allowed. However, even in isotropic materials, the tensor character of the nonlinear susceptibility should not be ignored. The electric field of the light itself can break the symmetry, leading to interesting polarization rotation effects.

In the following sections we will discuss various examples of nonlinear optical processes with short light pulses. The propagation of the corresponding wave packets at carrier frequency ω_i is described by a group velocity v_i for which

$$\boxed{\frac{1}{v_i} = \frac{n(\omega_i)}{c} + \frac{\omega_i}{c}\left.\frac{dn}{d\Omega}\right|_{\omega_i}} \tag{4.20}$$

holds. Sometimes it will also be necessary to specify the polarization direction, $\hat{e}_j$, of the waves participating in the nonlinear process.

Unless stated otherwise we will assume that the nonlinear susceptibility is much faster than the time scale of interest (pulse duration). This will allow us to simplify the derivations by applying the concept of an instantaneous material response. Also, to simplify the discussion on effects typical for the conversion of very short light pulses, we will usually neglect any change in intensity due to focusing effects; an approximation, which generally holds for nonlinear materials shorter than the Rayleigh range. An exception is when self-focusing occurs, a nonlinear effect discussed in Section 4.7.

4.3 Second harmonic generation (SHG)

Second harmonic generation has gained particular importance in ultrashort pulse physics as a means for frequency conversion and nonlinear optical correlation. Owing to the characteristics of ultrashort pulses, a number of new features unknown in the conversion of cw light have to be considered [6–10]. We will examine first the relatively simple case of type I SHG, in which the fundamental wave propagates as an ordinary (o) or extraordinary (e) wave, producing an extraordinary or ordinary second harmonic (SH) wave, respectively. We will briefly discuss at the end of this section the more complex case of type II SHG, in which the nonlinear polarization, responsible for the generation of a second harmonic propagating as an e wave, is proportional to the product of the e and o components of the fundamental. We will see that group velocity mismatch between the fundamental and the SH leads generally to a reduced conversion efficiency and pulse broadening. Under certain circumstances, however, it is possible to have simultaneously high conversion efficiency and efficient compression of the second harmonic in presence of group velocity mismatch. Second harmonic is only a particular case of sum frequency generation. Therefore, in some of the subsections to follow, we will treat in parallel second harmonic generation and the more general case of sum frequency generation.

4.3.1 Type I second harmonic generation

Let us assume a light pulse incident upon a second harmonic generating crystal. The electric field propagating inside the material consists of the original (fundamental) field (subscript $i = 1$) and the second harmonic field (subscript $i = 2$). The total field obeys a wave equation similar to Eq. (4.13) with a nonlinear polarization

of second-order as source term:

$$\left[\left(\frac{\partial}{\partial z}+\frac{1}{v_1}\frac{\partial}{\partial t}-\frac{ik_1''}{2}\frac{\partial^2}{\partial t^2}\right)\tilde{\mathcal{E}}_1+\mathcal{D}_1\right]e^{i(\omega_1 t-k_1 z)} + \frac{k_2}{k_1}\left[\left(\frac{\partial}{\partial z}+\frac{1}{v_2}\frac{\partial}{\partial t}-\frac{ik_2''}{2}\frac{\partial^2}{\partial t^2}\right)\tilde{\mathcal{E}}_2+\mathcal{D}_2\right]e^{i(\omega_2 t-k_2 z)}+c.c.=i\frac{\mu_0}{k_1}\frac{\partial^2}{\partial t^2}P^{(2)} \tag{4.21}$$

where the second-order polarization can be written as

$$P^{(2)}=\epsilon_0\chi^{(2)}\frac{1}{4}\left[\tilde{\mathcal{E}}_1 e^{i(\omega_1 t-k_1 z)}+\tilde{\mathcal{E}}_2 e^{i(\omega_2 t-k_2 z)}+c.c..\right]^2 \tag{4.22}$$

Since the group velocities v_1 and v_2 are not necessarily equal there is no coordinate frame in which both the fundamental and SH pulses are at rest. Therefore z and t are the (normal) coordinates in the laboratory frame. With the simplifications introduced above for the polarization, we obtain two coupled differential equations for the amplitude of the fundamental wave

$$\boxed{\left(\frac{\partial}{\partial z}+\frac{1}{v_1}\frac{\partial}{\partial t}-\frac{ik_1''}{2}\frac{\partial^2}{\partial t^2}\right)\tilde{\mathcal{E}}_1+\mathcal{D}_1=-i\chi^{(2)}\frac{\omega_1^2}{4c^2k_1}\tilde{\mathcal{E}}_1^*\tilde{\mathcal{E}}_2 e^{i\Delta k z}} \tag{4.23}$$

and for the second harmonic (SH) wave

$$\boxed{\left(\frac{\partial}{\partial z}+\frac{1}{v_2}\frac{\partial}{\partial t}-\frac{ik_2''}{2}\frac{\partial^2}{\partial t^2}\right)\tilde{\mathcal{E}}_2+\mathcal{D}_2=-i\chi^{(2)}\frac{\omega_2^2}{4c^2k_2}\tilde{\mathcal{E}}_1^2 e^{-i\Delta k z},} \tag{4.24}$$

where $\Delta k = 2k_1(\omega_1)-k_2(\omega_2)$ is the wave vector mismatch calculated with the wave vector values at the carrier frequency of the fundamental and second-harmonic. Since k_1, k_2 are functions of the orientation of the wave vector with respect to the crystallographic axis, it is often possible to find crystals, beam geometry and beam polarizations, for which $\Delta k = 0$ (phase matching) is achieved [1–3]. Note that in the case of ultrashort pulses the wave vectors vary over the bandwidth of the pulse. This variation caused by the linear polarization has already been taken into account by the time derivatives on the left-hand sides of Eqs. (4.23) and (4.24), cf. Eq. (1.100).

Type I — small conversion efficiencies

Small conversion efficiencies occur at low input intensities and/or small length of the nonlinear medium and nonlinear susceptibility. Under these circumstances we

may assume that the fundamental pulse does not suffer losses. If we assume in addition that $k_1'' = k_2'' = \mathcal{D}_1 = \mathcal{D}_2 \approx 0$ we find for the fundamental pulse, using Eq. (4.23), $\tilde{\mathcal{E}}_1(t,z) = \tilde{\mathcal{E}}_1(t - z/v_1)$. The fundamental pulse travels distortionless in a frame moving with the group velocity v_1. This expression can be inserted into the generating equation for the SH, Eq. (4.24). Integration with respect to the propagation coordinate yields for the SH at $z = L$:

$$\tilde{\mathcal{E}}_2\left(t - \frac{L}{v_2}, L\right) = -i\frac{\chi^{(2)}\omega_2^2}{4c^2k_2}\int_0^L \tilde{\mathcal{E}}_1^2\left[t - \frac{z}{v_2} + \left(\frac{1}{v_2} - \frac{1}{v_1}\right)z\right]e^{-i\Delta kz}dz. \tag{4.25}$$

Using the correlation theorem, Eq. (4.25) can be transformed into the frequency domain:

$$\tilde{\mathcal{E}}_2(\Omega, L) = -i\frac{\chi^{(2)}\omega_2^2}{4c^2k_2}\int \tilde{\mathcal{E}}_1(\Omega')\tilde{\mathcal{E}}_1(\Omega - \Omega')d\Omega' \int_0^L e^{i\left[(v_2^{-1} - v_1^{-1})\Omega - \Delta k\right]z}dz. \tag{4.26}$$

After integration with respect to the propagation coordinate we obtain for the SH field

$$\begin{aligned}\tilde{\mathcal{E}}_2(\Omega, L) = \\ -i\frac{\chi^{(2)}\omega_2^2 L}{4c^2k_2}\operatorname{sinc}\left\{\left[\left(\frac{1}{v_2} - \frac{1}{v_1}\right)\Omega - \Delta k\right]\frac{L}{2}\right\}\int \tilde{\mathcal{E}}_1(\Omega')\tilde{\mathcal{E}}_1(\Omega - \Omega')d\Omega'\end{aligned} \tag{4.27}$$

and for the spectral intensity of the SH (apart from the conversion factor from field squared to intensity):

$$\begin{aligned}|\tilde{\mathcal{E}}_2(\Omega, L)|^2 = \\ \left(\frac{\chi^{(2)}\omega_2^2 L}{4c^2k_2}\right)^2 \operatorname{sinc}^2\left\{\left[\left(\frac{1}{v_2} - \frac{1}{v_1}\right)\Omega - \Delta k\right]\frac{L}{2}\right\}\left|\int \tilde{\mathcal{E}}_1(\Omega')\tilde{\mathcal{E}}_1(\Omega - \Omega')d\Omega'\right|^2.\end{aligned} \tag{4.28}$$

Maximum conversion is achieved for zero group velocity mismatch ($v_1 = v_2$) and zero phase mismatch ($\Delta k = 0$).

The term $(v_2^{-1} - v_1^{-1})z$ in the argument of $\tilde{\mathcal{E}}_1$ in Eq. (4.25) describes the walk-off between the second harmonic pulse and the pulse at the fundamental wavelength owing to the different group velocities. The result is a broadening of the second harmonic pulse, as can be seen from Fig. 4.1. Only for crystal lengths

$$L \ll L_D^{SHG} = \frac{\tau_{p1}}{|v_2^{-1} - v_1^{-1}|} \tag{4.29}$$

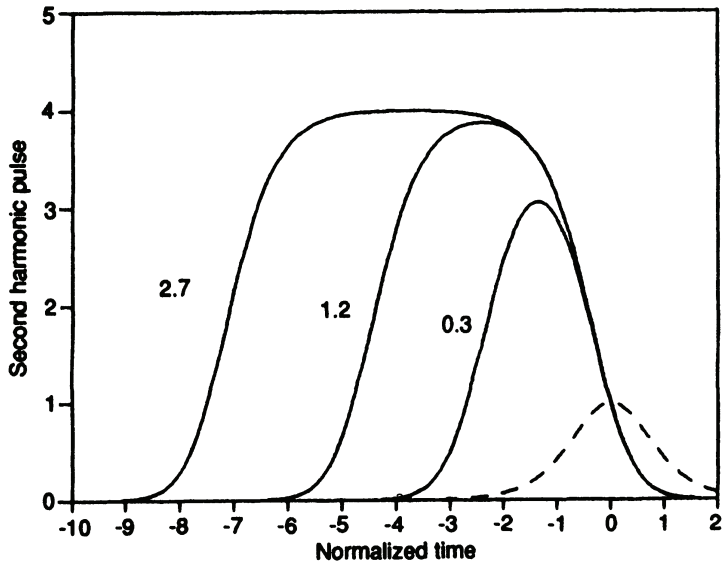

Figure 4.1: Second harmonic pulse at different, normalized crystal lengths, L/L_D^{SHG} according to Eq. (4.25). (−−− input sech - pulse; the intensity is not to scale)

can the influence of the group velocity mismatch on the shape of the second-harmonic pulse be neglected. In this case the SHG intensity varies with the square of the product of crystal length and intensity of the fundamental, cf. Eq. (4.25). Because of this quadratic dependence, the second harmonic pulse is shorter than the fundamental pulse (by a factor $\sqrt{2}$ for Gaussian pulses). For $L \gg L_D^{SHG}$ the pulse duration is determined by the walk-off and approaches a value of $L \times |v_2^{-1} - v_1^{-1}|$, the peak power remains constant, and the energy increases linearly with L. Of course, one needs to avoid this regime if short second harmonic pulses are required. The group velocity mismatch between the fundamental and SH pulse is listed in Table 4.1 for some typical crystals used for SHG. Similar conclusions can be drawn from the frequency domain solution for the SH pulse. The group velocity mismatch causes the SHG process to act as a frequency filter, cf. Eq.(4.28). The bandwidth becomes narrower with increasing crystal length. In addition, the sinc^2 term in Eq. (4.28) introduces a modulation of the spectrum of the second harmonic. The period of that modulation can serve to estimate the group velocity mismatch $(v_2^{-1} - v_1^{-1})$ of the particular crystal used.

It is interesting to note what happens when the phase matching condition is not satisfied ($\Delta k \neq 0$). The introduction of $\exp(-i\Delta kz)$ in the integrand of Eq. (4.25) produces a second harmonic output that varies periodically with the propagation

crystal	λ [nm]	θ [°]	$(v_2^{-1} - v_1^{-1})$ [fs/mm]
KDP	550	71	266
	620	58	187
	800	45	77
	1000	41	9
$LiIO_3$	620	61	920
	800	42	513
	1000	32	312
BBO	500	52	680
	620	40	365
	800	30	187
	1000	24	100
	1500	20	5

Table 4.1: Phase matching angle θ and group velocity mismatch $(v_2^{-1} - v_1^{-1})$ for type-I phase matching (oo-e) in some negative uni-axial crystals. The data were obtained from Sellmeier equations, see [11–13].

distance. The periodicity length is given by

$$L_P^{SHG} = \frac{2\pi}{\Delta k} \tag{4.30}$$

if group velocity mismatch can be neglected. In such cases it is recommended to work with crystal lengths $L < L_P^{SHG}$.

Type I — large conversion efficiencies

The simple approach of the previous section does no longer apply to conversion efficiencies larger than a few tens of percent. We have to consider the depletion of the fundamental pulse as the second harmonic pulse grows according to the complete system of differential equations (4.23), (4.24). In the phase and group velocity matching regime, the second harmonic energy approaches its maximum value asymptotically. Because of their lower intensities, the pulse wings reach this "saturation" regime later and the second harmonic pulse duration τ_{p2} broadens until it reaches a value that is approximately given by the duration of the fundamental pulse τ_{p1}. Therefore, even a moderate energy conversion requires very high conversion efficiencies for the peak intensities. Figure 4.2 shows schematically the conversion efficiencies in various regimes for zero group velocity mismatch (long pulses).

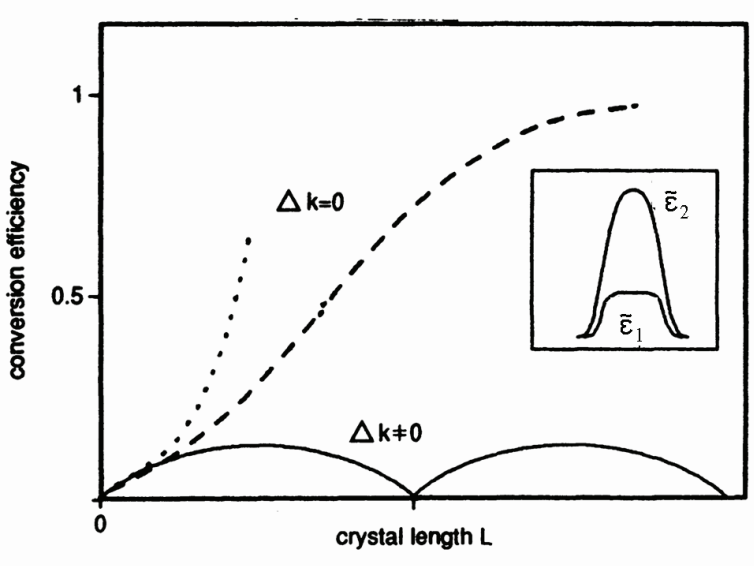

Figure 4.2: Conversion efficiencies neglecting $(\cdots)$ and taking into account $(- - -)$ depletion of the fundamental wave. The inset illustrates the shaping of the SH and fundamental pulse in the crystal.

With the inclusion of group velocity and phase mismatch, the processes involved in SHG become very complex. Numerical studies of Eqs. (4.23) and (4.24) in [14–16] reveal pulse splitting and a periodical behavior of the conversion efficiency with propagation length under certain circumstances. The complexity results partly from the fact that the phase of the fundamental wave becomes dependent on the conversion process. For cw light, the phase of the fundamental wave can easily be obtained from Eqs. (4.23) and (4.24) and reads [15]

$$\varphi_1(z) = \frac{1}{2}\arccos\left[\frac{c^2 k_1 \tilde{\mathcal{E}}_2(z)}{\chi^{(2)}\omega_1^2 \tilde{\mathcal{E}}_1^2(z)}\Delta k\right] - \frac{\pi - \Delta k z}{4}. \tag{4.31}$$

This phase is responsible for a new phase mismatch $\Delta k_{\text{eff}} z = \varphi_2(z) - 2\varphi_1(z)$ which, as opposed to the Δk introduced earlier, is a function of the field amplitudes. The result is that the conversion efficiency drops more rapidly for spectral components for which $\Delta k \neq 0$. Thus, the SH process acts like an intensity dependent spectral filter for short pulses, reducing the conversion efficiency and leading to distortions of the temporal profile. As shown experimentally by Kuehlke and Herpers [17], an optimum input intensity can exist for maximum energy conversion of fs pulses. Usually these conversion efficiencies do not exceed a few tens of percent.

There is another interesting consequence of the nonlinear phase. In most cases,

for both the SH and the fundamental fields, we have to consider a certain dependence of the field amplitudes on the transverse spatial coordinate (beam profile). According to Eq. (4.31) this leads to a phase $\phi_1(x,y,z)$, which can result in focusing or defocusing of the fundamental wave [18]. This lensing effect is similar to self-focusing based on the Kerr effect that will be discussed in Section 4.7. There, the self-lensing will be introduced as the result of a nonlinear polarization of third-order, $P^{(3)}$, as opposed to the former case of Eq. (4.31), which is derived from a second order nonlinear polarization.

Type I — compensation of the group velocity mismatch

A nonzero group velocity mismatch limits the frequency-doubling efficiency of femtosecond light pulses to a few tens of percents. It is interesting to note that the group velocity mismatch is equivalent to the fact that the phase matching condition does not hold over the entire pulse spectrum. We want to leave the actual workout of this fact to one of the problems at the end of this chapter. Generally, it is not possible to match the group velocities by choosing suitable materials while keeping the phase matching condition for the center frequencies, $\Delta k = 0$, as indicated in Table 4.1. However, since phase matching is achieved most often by angular tuning, simultaneous phase matching of an extended spectrum is feasible by realizing different angle of incidence for different spectral components. Corresponding practical arrangements for fs light pulses were suggested in Refs. [19] and [20], and implemented for sum frequency generation to 193 nm [21]. In Fig. 4.3, two

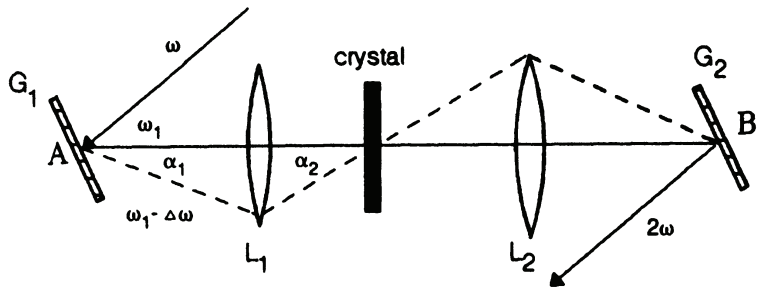

Figure 4.3: Frequency doubler for ultrashort (broadband) light pulses (adapted from [19]).

gratings, G_1 and G_2, are used to disperse and re-collimate the beam, respectively. Two achromatic lenses (or telescopes [20]) image A onto the crystal and onto B to ensure zero group velocity dispersion. The combination of L_1 and G_1 enables different angles of incidence for different spectral components. The desired magnification of lens L_1 is determined by the angular dispersion of the first grating $a_1 = d\beta/d\Omega$ and the derivative of the phase matching angle $a_2 = d\theta/d\Omega$

$$M_1 = \frac{d\theta/d\Omega}{d\beta/d\Omega}. \tag{4.32}$$

The magnification of the second lens has to be chosen likewise, taking into account the doubled frequency at the output of the crystal.

4.3.2 Second harmonic type II: equations for arbitrary phase mismatch and conversion efficiencies

Treatment in the time domain

As pointed out before there is no analytical solution to the general problem of SH generation. Numerical procedures have to be used to describe the propagation of the fundamental and the SH pulses under the combined action of (linear) dispersion and nonlinear effects. The possible effects are particularly complex and interesting in type II SH generation.

Type II SH generation involves the interaction of three waves, the SH, and an ordinary (o) and extraordinary (e) fundamental. Group velocity mismatch of these three waves does not always lead to pulse broadening. In the case of second harmonic generation type II, it is possible to achieve significant pulse compression at either the fundamental or the up-converted frequency.

To describe type II frequency conversion we extend the system of equations (4.23) and (4.24). We choose a retarded time frame of reference travelling with the second harmonic signal at its group velocity v_2. The fundamental pulse has a component $\tilde{\mathcal{E}}_o(t)\exp[i(\omega_1 t - k_o z)]$ propagating as an ordinary wave (subscript o) at the group velocity v_o, and a component $\tilde{\mathcal{E}}_e(t)\exp[i(\omega_1 t - k_e z)]$ propagating as an extraordinary wave (subscript e) at the group velocity v_e. The system of equations describing the evolution of the fundamental pulses $\tilde{\mathcal{E}}_o$ and $\tilde{\mathcal{E}}_e$, and the generation of the second harmonic wave $\tilde{\mathcal{E}}_2$ is:

$$\left[\frac{\partial}{\partial z}+\left(\frac{1}{v_o}-\frac{1}{v_2}\right)\frac{\partial}{\partial t}\right]\tilde{\mathcal{E}}_o+\mathcal{D}_o = -i\chi^{(2)}\frac{\omega_1^2}{4c^2k_o}\tilde{\mathcal{E}}_e^*\tilde{\mathcal{E}}_2e^{i\Delta k\,z} \quad (4.33)$$

$$\left[\frac{\partial}{\partial z}+\left(\frac{1}{v_e}-\frac{1}{v_2}\right)\frac{\partial}{\partial t}\right]\tilde{\mathcal{E}}_e+\mathcal{D}_e = -i\chi^{(2)}\frac{\omega_1^2}{4c^2k_e}\tilde{\mathcal{E}}_o^*\tilde{\mathcal{E}}_2e^{i\Delta k\,z} \quad (4.34)$$

$$\frac{\partial}{\partial z}\tilde{\mathcal{E}}_2+\mathcal{D}_2 = -i\chi^{(2)}\frac{\omega_1^2}{c^2k_2}\tilde{\mathcal{E}}_e\tilde{\mathcal{E}}_0e^{-i\Delta k\,z}, \quad (4.35)$$

where $\Delta k = k_o + k_e - k_2$ is the wave vector mismatch calculated at the pulse carrier frequency. The phase matching condition $\Delta k_0 = k_o(\omega_1) + k_e(\omega_1) - k_2(2\omega_1) = 0$ implies that the *phase velocities* are matched. The fact that the waves at ω_1 and ω_2 remain in phase does not necessarily imply that *pulses* reach simultaneously the end of the crystal. The three wave packets propagate at *group velocities* v_o, v_e, and v_2 that, in general, are different. The expression Eq. (4.27) found for type-I SH generation without pump depletion can be regarded a special solution of Eqs. (4.33-4.35).

SHG for short pulses — treatment in the frequency domain

When dealing with the conversion of very short pulses, it is not sufficient to include dispersion only up to first order, that is $\mathcal{D} = 0$. For $\mathcal{D} \neq 0$, however, the system of equations (4.33)-(4.35) contains higher-order time derivatives whose treatment is numerically difficult. The problem can be stated more clearly in the frequency domain, using the complete functional dependence of the k vectors (or the indices of refraction), rather than power series. We start from the wave equation for the electric field

$$\left(\frac{\partial^2}{\partial z^2}-\frac{1}{c^2}\frac{\partial^2}{\partial t^2}\right)\tilde{\mathbf{E}}(t,z) = \mu_0\frac{\partial^2}{\partial t^2}\left[\tilde{\mathbf{P}}^L(t,z)+\tilde{\mathbf{P}}^{NL}(t,z)\right] \quad (4.36)$$

where the electric field is the sum of the three participating waves

$$\tilde{\mathbf{E}}(t,z) = \hat{\mathbf{e}}_\mathbf{o}\tilde{E}_o(t,z)+\hat{\mathbf{e}}_\mathbf{e}\tilde{E}_e(t,z)+\hat{\mathbf{e}}_\mathbf{e}\tilde{E}_2(t,z) \quad (4.37)$$

and the nonlinear polarization

$$\tilde{\mathbf{P}}^{NL}(t,z) = \epsilon_0\chi^{(2)}\Big[\tilde{E}_o(t,z)\tilde{E}_e(t,z)\hat{\mathbf{e}}_\mathbf{e}+\tilde{E}_2(t,z)\tilde{E}_o^*(t,z)\hat{\mathbf{e}}_\mathbf{e}+\tilde{E}_2(t,z)\tilde{E}_e^*(t,z)\hat{\mathbf{e}}_\mathbf{o}\Big]. \quad (4.38)$$

Without loss of generality, we have assumed that the second harmonic field $\tilde{\mathbf{E}}_\mathbf{2}$ propagates as an extraordinary wave with polarization vector $\hat{\mathbf{e}}_\mathbf{e}$. The nonlinear polarization terms are responsible for the evolution of the SH, the fundamental e-wave and the fundamental o-wave, respectively.

Following the same procedure as in Section 1.2, we take the Fourier transform of Eq.(4.36):

$$\left[\frac{\partial^2}{\partial z^2} + \mu_0\Omega^2\epsilon(\Omega)\right]\tilde{\mathbf{E}}(\Omega,z) = -\mu_0\Omega^2\tilde{\mathbf{P}}^{NL}(\Omega,z) \tag{4.39}$$

where we used the expressions (1.81) for the linear polarization and Eq. (1.84) for the dielectric constant. The nonlinear polarization in the frequency domain is a sum of three convolution integrals; the first member of the sum, for example, is $\epsilon_0\chi^{(2)}\hat{e}_e\int E_o(\Omega',z)E_e(\Omega-\Omega',z)d\Omega'$.

For the electric field components we make the ansatz

$$\tilde{E}_q(\Omega,z) = \frac{1}{2}\tilde{a}_q(\Omega,z)e^{-ik_q(\Omega)z}. \tag{4.40}$$

where the subscript q stands for "o", "e", or "2". The amplitudes $\tilde{a}_q(\Omega,z)$ peak at the central frequencies of the corresponding pulse. The ansatz is a solution of the linear wave equation [$\tilde{\mathbf{P}}^{NL}(\Omega,z)$=0 in Eq.(4.39)]. Hence $k_q(\Omega) = \Omega n_q(\Omega)/c = \Omega\sqrt{\mu_0\epsilon(\Omega)}$. Inserting the ansatz into Eq. (4.39) and separating out the three field components according to polarization and frequency yields

$$\begin{aligned}
\frac{\partial}{\partial z}\tilde{a}_2(\Omega,z) &= \frac{-i\Omega^2\chi^{(2)}}{4c^2k_2(\Omega)}\int\tilde{a}_o(\Omega',z)\tilde{a}_e(\Omega-\Omega',z)e^{i\left[-k_o(\Omega')-k_e(\Omega-\Omega')+k_2(\Omega')\right]z}d\Omega' \\
&\quad + \frac{i}{2k_2(\Omega)}\frac{\partial^2}{\partial z^2}\tilde{a}_2(\Omega,z) \qquad (4.41)\\
\frac{\partial}{\partial z}\tilde{a}_o(\Omega,z) &= \frac{-i\Omega^2\chi^{(2)}}{4c^2k_o(\Omega)}\int\tilde{a}_2(\Omega',z)\tilde{a}_e^*(\Omega-\Omega',z)e^{i\left[k_o(\Omega')+k_e(\Omega-\Omega')-k_2(\Omega')\right]z}d\Omega' \\
&\quad + \frac{i}{2k_o(\Omega)}\frac{\partial^2}{\partial z^2}\tilde{a}_o(\Omega,z) \qquad (4.42)\\
\frac{\partial}{\partial z}\tilde{a}_e(\Omega,z) &= \frac{-i\Omega^2\chi^{(2)}}{4c^2k_e(\Omega)}\int\tilde{a}_2(\Omega',z)\tilde{a}_o^*(\Omega-\Omega',z)e^{i\left[k_e(\Omega')+k_o(\Omega-\Omega')-k_2(\Omega')\right]z}d\Omega' \\
&\quad + \frac{i}{2k_e(\Omega)}\frac{\partial^2}{\partial z^2}\tilde{a}_e(\Omega,z). \qquad (4.43)
\end{aligned}$$

The sum of the three equations (4.41) is equivalent to the second order wave equation (4.39) or (4.36). There is however an approximation involved in splitting the single wave equation in a system of three equations, namely that the spectral range of the pulses E_o and E_e centered at ω_ℓ and $2\omega_\ell$ do not overlap. For numerical calculations, it is more convenient to consider field amplitudes shifted to zero frequency:

$$\begin{aligned}
\tilde{\mathcal{E}}_2(\Delta\Omega = \Omega - 2\omega_\ell) &= \tilde{a}_2(\Omega,z)\\
\tilde{\mathcal{E}}_o(\Delta\Omega = \Omega - \omega_\ell) &= \tilde{a}_o(\Omega,z)\\
\tilde{\mathcal{E}}_e(\Delta\Omega = \Omega - \omega_\ell) &= \tilde{a}_e(\Omega,z), \qquad (4.44)
\end{aligned}$$

where we have dropped for simplicity of notation the variable z in the argument of the field amplitudes on the left of Eqs. (4.44). These fields are the Fourier transforms of the envelopes defined in Chapter 1, Eq. (1.18). The envelope was defined in Eq. (1.18) with a similar ansatz as Eq. (4.40), hence not involving any SVEA. In situations where the SVEA applies, these shifted amplitudes [Eq. (4.44)] become identical to the spectral amplitudes defined in Eq. (1.18). The set of equations (4.41) can easily be written for the spectral field envelopes defined in Eqs. (4.44).

The set of coupled equations (4.41) with (4.44) is convenient for a numerical treatment. No other assumption or approximation has been made, except that the spectra of the fundamental and second harmonic do not overlap, in order to be able to split a single Maxwell's second order propagation equation into three coupled differential equations. The dispersion of the material is contained in the frequency dependence of the wave vectors $k_q^2(\Omega) = \Omega^2 n^2(\Omega)/c^2$. The second derivative of the envelope with respect to z can generally be neglected, unless the spectral envelope of the field changes on length scales of the wavelength.

It should be noted that no moving frame of reference has been adopted in this section. Hence, the fields are propagating at their respective group velocities. A more convenient representation of the solution uses a frame of reference propagating at one of the group velocities, for instance that of the second harmonic (see also Section 4.3.1). The temporal (complex) envelopes in this frame of reference moving at the velocity v_2 are obtained from the solutions $\tilde{\mathcal{E}}_i(\Delta\Omega, z)$ through the transformation:

$$\tilde{\mathcal{E}}_2(t,z) = \int_{-\infty}^{\infty} \tilde{\mathcal{E}}_2(\Delta\Omega,z) e^{-i[k_2(\Delta\Omega)-\frac{\Delta\Omega}{v_2}]z} e^{-i\Delta\Omega t} d\Delta\Omega \tag{4.45}$$

$$\tilde{\mathcal{E}}_o(t,z) = \int_{-\infty}^{\infty} \tilde{\mathcal{E}}_o(\Delta\Omega,z) e^{-i[k_o(\Delta\Omega)-\frac{\Delta\Omega}{v_2}]z} e^{-i\Delta\Omega t} d\Delta\Omega \tag{4.46}$$

$$\tilde{\mathcal{E}}_e(t,z) = \int_{-\infty}^{\infty} \tilde{\mathcal{E}}_e(\Delta\Omega,z) e^{-i[k_e(\Delta\Omega)-\frac{\Delta\Omega}{v_2}]z} e^{-i\Delta\Omega t} d\Delta\Omega. \tag{4.47}$$

4.3.3 Pulse shaping in second harmonic generation (type II)

In this section we will describe the situation where group velocity mismatch can be utilized to shape (shorten) ultrashort light pulses as a result of nonlinear frequency conversion.

Akhmanov et al. [22] analyzed the situation where a SH pulse and a fundamental pulse are simultaneously incident on a nonlinear crystal with $v_2 > v_1$. If a short SH pulse is launched in the trailing edge of a long fundamental pulse the SH will extract energy from various parts of the fundamental while moving through

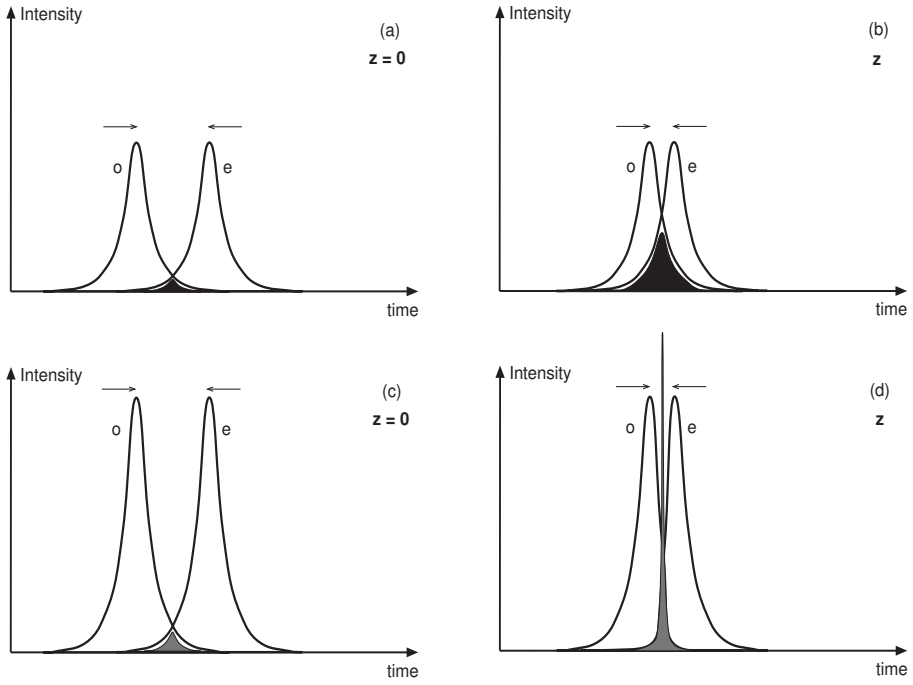

Figure 4.4: The three interacting pulses — fundamental ordinary, fundamental extraordinary and second harmonic — are represented in a temporal frame of reference moving with the group velocity of the second harmonic.

the fundamental pulse due to the group velocity mismatch. High peak powers of the second harmonic and considerable pulse shortening were predicted.

Similar effects can be expected in type II phase-matching. Here another degree of freedom, the group velocity mismatch ($v_o - v_e$) of the ordinary and extraordinary fundamental, can be adjusted. Consider a phase matched situation ($\Delta k = 0$) where again a short second harmonic pulse, of sufficient intensity to deplete the fundamental, is seeded at the trailing edge of a longer fundamental pulse at the input of the nonlinear crystal. This situation leading to pulse compression [10,23], was first implemented with subpicosecond pulses in [24,25]. Subsequently, pulse compression through second harmonic generation in very long (5-6 cm) KDP (KH_2PO_4) and KD^*P (KD_2PO_4) crystals was predicted [23] and demonstrated [26]. We will describe in a subsequent section a similar compression mechanism in synchronously pumped optical parametric oscillators [27–30].

Let us now discuss the situation where the group velocity of the SH is intermediate between the two fundamental waves, $v_o < v_2 < v_e$ and assume that the e-wave pulse enters the crystal delayed with respect to the o-wave pulse. A second harmo-

nic will be generated at the temporal overlap between the two pulses, as sketched in Fig. 4.4(a). In a frame of reference moving at the group velocity of the second harmonic, the two fundamental pulses will travel towards each other. After some propagation distance, the overlap of the fundamentals increases, and so does the second harmonic intensity (Fig. 4.4(b)). However, if the fundamental pulses are sufficiently intense as sketched in Figs. 4.4(c) and (d), the intensity of the second harmonic may be large enough to deplete the fundamentals. As a result, the spatial overlap of the two (depleted) fundamentals remains small, as they move into each other (Fig. 4.4(d)).

An interesting situation arises when the walk-off lengths for the two fundamental pulses, $L_e = \tau_p/(v_e^{-1} - v_2^{-1})$ and $L_o = \tau_p/(v_o^{-1} - v_2^{-1})$, are equal and opposite in sign, and only three or four times longer than the crystal length. This case was analyzed in detail by Wang and Dragila [10] and Stabinis *et al.* [23]. The crystal angle θ; the walk-off lengths for a 12 ps pulse at 1.06 μm, and their ratio m are listed in Table 4.2 for second harmonic generation type II in KDP and DKDP. In order

crystal	θ	L_o (cm)	L_e (cm)	$\|m\|$
KDP	59.2°	20.9	-15.8	1.32
DKDP	53.5°	28.1	-20.0	1.40

Table 4.2: Relevant constants for second harmonic generation type II in KDP and DKDP at 1.06 μm. m is the ratio of the walk-off lengths.

to generate compressed second-harmonic pulses, the faster e wave is sent delayed with respect to the o wave into the crystal. A second harmonic "seed" originates from the short overlap region between the two e and o fundamental pulses. As this second harmonic propagates through the crystal it is amplified, while the overlap between all three pulses increases. Because of its faster group velocity, the second harmonic always sees an un-depleted o wave at its leading edge. Compression of the second harmonic results from the differential amplification of the leading edge with respect to the trailing edge. Implementation of this compression requires an accurate control of the pulse intensity, hence a well defined temporal profile, and a square or super Gaussian beam profile. Compression factors in excess of 30 have been observed [26, 31].

4.3.4 Group velocity control in SHG through pulse front tilt

The condition of second harmonic group velocity intermediate between the ordinary and extraordinary fundamentals cannot in general be met at any wavelength, for any crystal. It is however possible to adjust the group velocity through a tilt

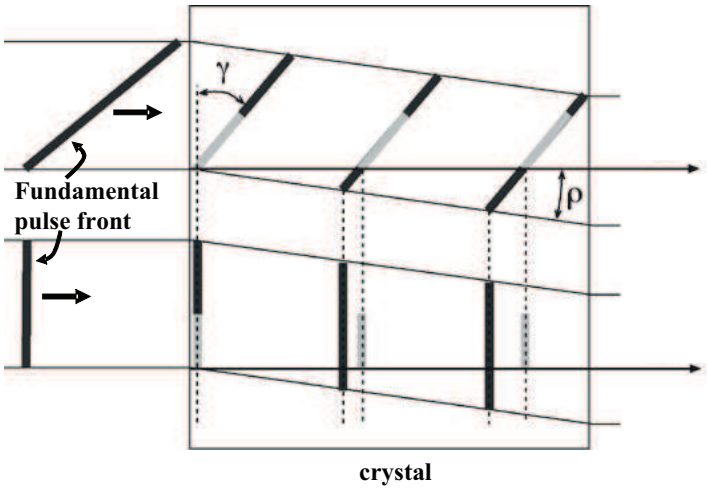

Figure 4.5: SHG using tilted pulse fronts. The wave vector of the (o-wave) SH is perpendicular to the entrance face of the crystal. Top figure - the pulse front of the fundamental (dark bar) is tilted by an amount compensating the group velocity mismatch of fundamental and SH (grey bar) pulse exactly. Bottom figure - the input pulse front is not tilted. The different group velocities of fundamental and SH pulse lead to walk-off.

of the energy front with respect to the phase-front. Figure 4.5 illustrates the basic principle in the case of a degenerate type I process. As shown in the lower part of the figure, the temporal overlap of the interacting pulses decreases because of the lower velocity of the SH pulse relative to the fundamental pulse. Furthermore, the spatial overlap decreases because of the walk-off (ρ in the figure) of the fundamental wave from the second harmonic wave. These two negative effects can however be used in conjunction with pulse front tilt to match the relative velocities of the two pulses, as illustrated in the upper part of Fig. 4.5. Loosely speaking: seen in the frame of reference of the SH wave, the lateral walk-off of the fundamental beam decrease the component of the pulse velocity along the direction of propagation of the SH just to match its (group) velocity.

Unfortunately, for femtosecond pulses, it is not practical to generate a large pulse front tilt. For instance, a pulse front tilt of the order of 40 degrees would be required for second harmonic type II generation and compression in BBO of a 800 nm pulse of a Ti:Sapphire laser in collinear interaction [32]. A dispersive element like a prism with a ratio of beam diameter to base length of 20 (in the case of SF 10 glass) would be needed to achieve the required energy front tilt of 40 degrees.

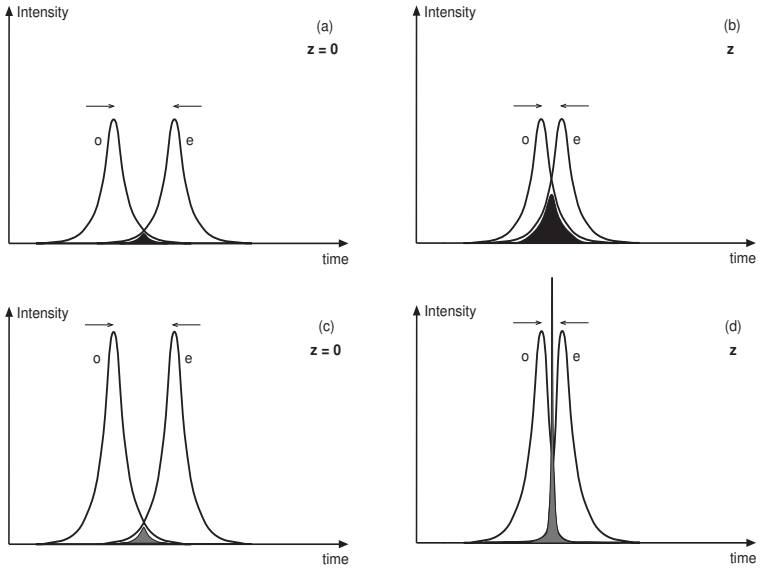

Figure 4.6: Geometry for pre-compensation the pulse front tilt resulting from propagation through an interface (the pulse fronts are depicted as dotted lines) using prisms. For the chosen type II SHG of 800 nm pulses: $\theta = 2°$, which is the internal angle of the fundamental beams for non-collinear interaction. In order to match the energy fronts of both fundamentals, an external pulse front tilt of $\gamma = 0.6°$ for $\beta = 1.6°$ is required. Also sketched in the figure are thin SF10 prisms (a/b = 0.2) to realize the desired γ .

Dispersion in the glass would lead to large pulse broadening and phase modulation.

A better approach for group velocity matching in SHG as well as in parametric three-wave interactions of fs pulses is to use a non-collinear geometry [33, 34]: Table 4.3 shows how the group velocities of the participating waves can be changed from the collinear to the non-collinear case (here for an internal angle of 2 degrees) leading to conditions for compression. The sketch of the interaction geometry in Fig. 4.6 shows that it is possible to obtain the respective group velocities through manipulation of the angles of incidence in the crystal and the energy tilt produced by a prism. Figure 4.6 pertains to the case of non-collinear interacting plane waves inside a 250 μm long BBO crystal, cut for type II second-harmonic generation of laser pulses at 800 nm.

The situation sketched in Fig. 4.6 was simulated with the system of equations Eqs (4.41), (4.42) and (4.43), with the substitution of Eqs. (4.44) for the case of a 10 fs fundamental pulse with a 20 fs pre-delay of the fundamental e with respect of the fundamental o. Successive intensity profiles are plotted in Figs. 4.7. The 10 fs fundamental pulse gives rise to a 2.5 fs second harmonic. Even in this extreme

geometry	fundamental (o) v_o (10^8 m/s)	second-harmonic (e) v_2 (10^8 m/s)	fundamental (e) v_e (10^8 m/s)
collinear	1.780	1.755	1.843
non-collinear	1.798	1.905	1.934

Table 4.3: Group velocities for the o, e and second-harmonic e waves. Values are calculated for type II second-harmonic generation of 800 nm radiation for collinear and non-collinear (internal angle is 2 degrees) interaction in BBO crystals.

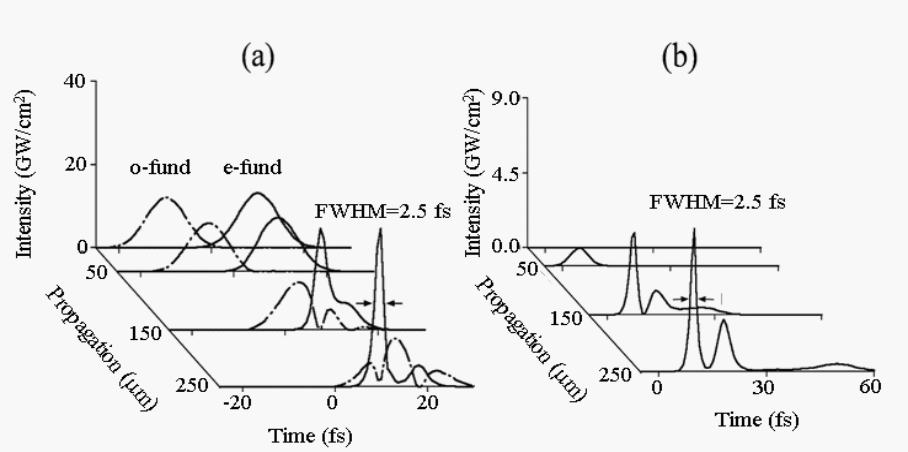

Figure 4.7: Calculated fundamental (a) and second-harmonic waves (b) as they propagate and interact inside a 250 μm long BBO crystal (note the different scales for (a) and (b)). Group velocity mismatch leads to a compressed second-harmonic pulse with a FWHM of 2.5 fs (b), for 10 fs fundamental input pulses. Furthermore, considerable pulse reshaping can be seen for the extraordinary fundamental in (a), leading to a shortened FWHM from 10 fs to 2.5 fs with a shoulder. Pulse energies were 400 μJ for each fundamental pulse, at a FWHM of 10 fs with a pre-delay of 20 fs of the e-fundamental with respect to the o-fundamental.

case of pulse compression, the maximum value for $\partial^2\tilde{\mathcal{E}}/\partial z^2$ is 200 times smaller than $2k\partial\tilde{\mathcal{E}}/\partial z$, and the second order partial derivatives can therefore be neglected in Eqs. (4.41), (4.42) and (4.43). Figure 4.7(b) shows a peak intensity of 9 GW/cm^2 for the 2.5 fs second-harmonic for initial peak intensities for the fundamental pulses of roughly 13 GW/cm^2. This indicates 70% conversion in intensity.

4.4 Optical parametric interaction

4.4.1 Coupled field equations

Similar considerations as in the previous section can be made for a number of other nonlinear processes of second order used for generating pulses at new frequencies. Figure 4.8 shows schematically three possible situations. In parametric

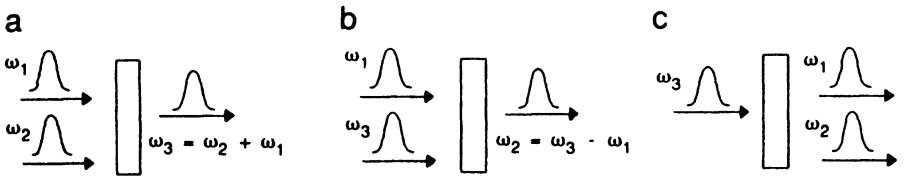

Figure 4.8: Nonlinear optical processes of second order for generating pulses of new frequencies. (a) parametric up-conversion, (b) parametric down-conversion, (c) parametric oscillation.

up-conversion two pulses of frequencies ω_1 and ω_2, respectively, are sent through a nonlinear medium (crystal) and produce a pulse of frequency $\omega_3 = \omega_1 + \omega_2$. In parametric down-conversion a pulse with the difference frequency is generated. In parametric oscillation, a single pulse of frequency ω_3 generates two pulses of frequency ω_1 and ω_2 such that $\omega_1 + \omega_2 = \omega_3$. Which process occurs depends on the realization of the phase matching condition. In principle, to obtain a fs output pulse through up- or down-conversion, it is sufficient to have only one fs input pulse. The second input can be a longer pulse or even cw light. Mokhtari *et al.* [35], for example, mixed 60 fs pulses at 620 nm from a dye laser with 85 ps pulses from a Nd:YAG laser (1064 nm) to obtain up converted fs pulses at 390 nm. Parametric frequency mixing of two fs input pulses were reported, for example, in [36] and [37]. If the input pulse (pump pulse) is sufficiently strong, two pulses of frequencies ω_1 and ω_2, for which the phase matching condition is satisfied, can arise. In this case, noise photons which are always present in a broad spectral range can serve as seed light. This process is known as optical parametric oscillation; the generated pulses are called idler and signal pulses — the usual convention being that the signal is the generated radiation with the shorter wavelength.

With similar assumptions that allowed us to derive the equations for SHG, we obtain three coupled differential equations for the interaction of the three optical fields as shown in Fig. 4.8:

$$\left(\frac{\partial}{\partial z} + \frac{1}{v_1}\frac{\partial}{\partial t}\right)\tilde{\mathcal{E}}_1 - \frac{i}{2}k_1''\frac{\partial^2}{\partial t^2}\tilde{\mathcal{E}}_1 + \mathcal{D}_1 = -i\chi^{(2)}\frac{\omega_1^2}{4c^2k_1}\tilde{\mathcal{E}}_2^*\tilde{\mathcal{E}}_3 e^{i\Delta kz} \tag{4.48}$$

$$\left(\frac{\partial}{\partial z}+\frac{1}{v_2}\frac{\partial}{\partial t}\right)\tilde{\mathcal{E}}_2-\frac{i}{2}k_2''\frac{\partial^2}{\partial t^2}\tilde{\mathcal{E}}_2+\mathcal{D}_2=-i\chi^{(2)}\frac{\omega_2^2}{4c^2k_2}\tilde{\mathcal{E}}_1^*\tilde{\mathcal{E}}_3e^{i\Delta kz} \tag{4.49}$$

$$\left(\frac{\partial}{\partial z}+\frac{1}{v_3}\frac{\partial}{\partial t}\right)\tilde{\mathcal{E}}_3-\frac{i}{2}k_3''\frac{\partial^2}{\partial t^2}\tilde{\mathcal{E}}_3+\mathcal{D}_3=-i\chi^{(2)}\frac{\omega_3^2}{4c^2k_3}\tilde{\mathcal{E}}_1\tilde{\mathcal{E}}_2e^{-i\Delta kz} \tag{4.50}$$

where $\Delta k = k_1(\omega_1)+k_2(\omega_2)-k_3(\omega_3)$, and the higher order dispersion terms defined in Eqs. (1.99), (1.100) have been included. The conversion efficiencies are maximum if the phase matching condition, $\Delta k = 0$, is satisfied. The description of the various processes in Fig. 4.8 by Eqs. (4.48)–(4.50) differs only in the initial conditions, that is the field amplitudes at the crystal input. This system of equations is analogous to the ones encountered for second harmonic generation. For relatively weak pulses, conversion efficiencies are low, and the group velocity dispersion contributes to a broadening of the generated radiation.

As in the case of SHG, there is a particularly interesting regime which combines the complexities of short pulses, high intensity and long interaction lengths. The pulses have to be sufficiently short that simultaneous phase matching cannot be achieved over the pulse bandwidth. The crystal length and pulse intensities are sufficiently high for regeneration of the pump to occur. These conditions are also referred to as "giant pulse regime", or sometimes "nonlinear parametric generation".

4.4.2 Synchronous pumping

Higher efficiencies can be obtained by placing the nonlinear crystal in an optical resonator for the signal pulse. The crystal is then pumped by a sequence of pulses whose temporal separation exactly matches the resonator round trip time. In this manner, the signal pulse passes through the amplifying crystal many times before it is coupled out. Laenen *et al.* [38] pumped the crystal with a train of 800 fs pulses from a frequency doubled Nd:glass laser and produced 65–260 fs signal pulses which were tunable over a range from 700 to 1800 nm.

Intracavity pumping of an optical parametric oscillator (OPO) is also possible to take advantage of the high intracavity pulse power for the pumping. This technique was demonstrated by Edelstein *et al.* [39], by placing the OPO crystal in the resonator of a fs dye laser, and building a second resonator around the crystal for the signal pulse. At repetition frequencies of about 80 MHz, the mean output power of the parametric oscillator was on the order of several milliwatts. A high gain, short lifetime laser such as a dye or semiconductor laser is desirable, because the mode-locking of such a laser is less sensitive to feedback from the faces of the crystal. Intracavity pumping of an optical parametric oscillator has however also been demonstrated in a Ti:sapphire laser [40] which has a long gain lifetime.

4.4.3 Chirp amplification

So far we have been concerned with amplitude modulation effects in nonlinear mixing. Phase modulation introduces an element of complexity that one generally tries to avoid, in particular in the conditions of "giant pulse compression" discussed previously. It has been recognized however that second order interactions can be used to generate or amplify a phase modulation. We will consider here as an example chirp amplification that can take place in parametric processes.

The frequencies of the three interacting pulses obey the relation

$$\omega_3(t) = \omega_1(t) + \omega_2(t). \tag{4.51}$$

If we substitute for the time dependent frequencies $\omega_i(t) = \omega_i + \dot{\varphi}_i(t)$ $(i = 1, 2, 3)$, we obtain for the phases

$$\dot{\varphi}_3(t) = \dot{\varphi}_2(t) + \dot{\varphi}_1(t). \tag{4.52}$$

In addition, for efficient parametric oscillation, the phase matching condition must be satisfied, which now implies

$$k_3[\omega_3(t)] = k_2[\omega_2(t)] + k_1[\omega_1(t)]. \tag{4.53}$$

For $|\dot{\varphi}_i| \ll \omega_i$ and linearly chirped pump pulses a Taylor expansion of Eq. (4.53) yields

$$\left.\frac{dk_3}{d\Omega}\right|_{\omega_3} \dot{\varphi}_3(t) = \left.\frac{dk_2}{d\Omega}\right|_{\omega_2} \dot{\varphi}_2(t) + \left.\frac{dk_1}{d\Omega}\right|_{\omega_1} \dot{\varphi}_1(t). \tag{4.54}$$

The chirps at the three frequencies are thus related by the *group* velocities v_i. From Eqs. (4.52) and (4.54), a relation between the chirp of idler and signal pulses and pump pulse can be found:

$$\dot{\varphi}_1 = p\dot{\varphi}_3 \tag{4.55}$$

$$\dot{\varphi}_2 = (1-p)\dot{\varphi}_3, \tag{4.56}$$

where p is the chirp enhancement coefficient:

$$p = \left(\frac{v_3^{-1} - v_2^{-1}}{v_1^{-1} - v_2^{-1}}\right), \tag{4.57}$$

and v_i are the group velocities at the respective frequencies ω_i.

Equation (4.57) indicates that chirp amplification is most pronounced in a condition of degeneracy where $\omega_1 \approx \omega_2$. The mechanism of chirp amplification can also be understood by means of the tuning curves. For instance, Fig. 4.9 shows the tuning curves for phase matching (type I) in KDP. A small change in pump

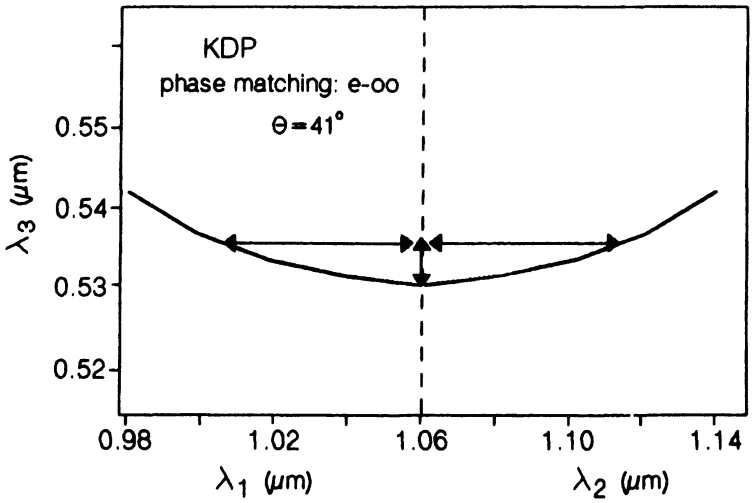

Figure 4.9: Tuning curves of a KDP optical parametric oscillator, pumped at a wavelength of $\lambda_3 = 0.53\,\mu$m (from [41]).

wavelength λ_3 results in a strong change of signal wavelength. As a result, a slightly chirped pump pulse generates signal and idler with enhanced (and opposite) chirp [41]. The signal pulses with enhanced chirp can be compressed in a grating pair compressor. Using the natural chirp of frequency doubled pulses from a Nd:glass laser, pulses of 50 fs at 920 nm were obtained by this technique [41].

4.5 Third order susceptibility

4.5.1 Fundamentals

The third order contribution to the nonlinear polarization in an isotropic medium is [2]:

$$\begin{aligned}
\tilde{P}_x^{(3)} &= \epsilon_0 \chi^{(3)} \sum_{j=x,y} \left[\tilde{E}_x \tilde{E}_j \tilde{E}_j^* + \tilde{E}_j \tilde{E}_x \tilde{E}_j^* + \tilde{E}_j \tilde{E}_j \tilde{E}_x^* \right] \\
&= \epsilon_0 \chi^{(3)} \left\{ 2 \left[|\tilde{E}_x|^2 + |\tilde{E}_y|^2 \right] \tilde{E}_x + \tilde{E}_x |\tilde{E}_x|^2 + \tilde{E}_y \tilde{E}_y \tilde{E}_x^* \right\} \\
&= 3\epsilon_0 \chi^{(3)} \left\{ \left[|\tilde{E}_x|^2 + \frac{2}{3} |\tilde{E}_y|^2 \right] \tilde{E}_x + \frac{1}{3} (\tilde{E}_x^* \tilde{E}_y) \tilde{E}_y \right\}, \qquad (4.58)
\end{aligned}$$

[2] We consider here only the terms in the polarization oscillating at the same optical frequency as the driving field.

where we consider the $\hat{x}$ component of the polarization, under the influence of a light pulse propagating along z, with field components along $\hat{x}$ and $\hat{y}$. If there is only a component of the field along x:

$$\tilde{P}_x^{(3)} = 3\epsilon_0 \chi^{(3)} |\tilde{E}_x|^2 \tilde{E}_x. \tag{4.59}$$

In the transparent region of many materials, $\chi^{(3)}$ can be approximated by a real quantity, and the nonlinear polarization results in an index of refraction that depends nonlinearly on the propagating field. Usually the lowest order of this dependence is expressed by one of the following equivalent relations

$$\boxed{\begin{aligned} n &= n_0 + n_2 |\tilde{\mathcal{E}}(t)|^2 \\ &= n_0 + 2n_2 \langle E^2(t) \rangle \\ &= n_0 + \bar{n}_2 I(t), \end{aligned} \qquad (4.60)}$$

where $\bar{n}_2 = 2n_2/(\epsilon_0 c n_0)$. The quantity n_2 is called nonlinear index coefficient and describes the strength of the coupling between the electric field and the refractive index. The most often quoted quantities are n_2 in esu units, and $\bar{n}_2$ in cm^2/W. The conversion factor between the two quantities is:

$$\bar{n}_2(\text{cm}^2/\text{W}) = \frac{2}{(300)^2 n_0} \sqrt{\frac{\mu_0}{\epsilon_0}} n_2(\text{esu}) \approx \frac{8.378}{n_0} \cdot 10^{-3} n_2(\text{esu}) \tag{4.61}$$

Origin	Example	$\bar{n}_2$ [cm^2/W]	Response time [s]
electronic			
nonresonant	glass	10^{-16}—10^{-15}	10^{-15}—10^{-14}
	air	10^{-18}—10^{-19}	10^{-14}—10^{-13}
resonant	semic. doped glass	10^{-10}	10^{-11}
molecular motion	CS_2	10^{-12}	10^{-12}

Table 4.4: Examples of nonlinear refractive index parameters

Many different physical processes can account for an intensity dependent change in index of refraction due to a third-order nonlinearity. Table 4.4 gives some examples. As a rule of thumb, the larger the nonlinearity, the longer the corresponding response time. For fs pulse excitation, it is only a (nonresonant) nonlinearity of electronic origin that can be considered to be without inertia. The corresponding nonlinear refractive index can be described by relations (4.60), and is a result of an

optical nonlinearity of third order. If only one pulse is incident on the sample the complete (including terms not oscillating at ω_ℓ) polarization reads

$$\tilde{P}^{(3)} = \epsilon_0 \chi^{(3)} E^3 = \epsilon_0 \chi^{(3)} \left(\frac{3}{8} |\tilde{\mathcal{E}}|^2 \tilde{\mathcal{E}} e^{i\omega_\ell t} + \frac{1}{8} \tilde{\mathcal{E}}^3 e^{3i\omega_\ell t} \right) + c.c. \tag{4.62}$$

assuming an instantaneous response. The terms with $3\omega_\ell$ in the argument of the exponential function describe third harmonic generation. In the cases where this latter process is sufficiently weak not to impact the propagation of the wave at ω_ℓ, one can show from Eq. (4.62) that

$$n_2 = \frac{3\chi^{(3)}}{8n_0}, \tag{4.63}$$

(see Problem 3 at the end of this chapter). The intensity dependence of n implies a refractive index varying in time and space. The temporal variation, as discussed in Chapter 1 [Eq. (1.187)], leads to a pulse chirp. The (transverse) spatial refractive index dependence leads to lensing effects. These processes are called self-phase modulation (SPM) and self-focusing (SF), respectively. In most cases self-focusing is undesirable and is avoided by minimizing the sample length and/or working with uniform beam profiles whenever possible.

To describe SPM we can substitute Eq. (4.62) into the wave equation (4.13). Let us first recall the approximations needed to derive the simple expression for the second derivative of the polarization used in the previous subsection. These approximations lead to an estimate of the first correction terms. If the nonlinearity is not perfectly inertialess (i.e., does not respond instantaneously to the electric field), we have to compute the polarization using the integral expression (4.3). For response times smaller than the pulse duration, the Fourier transform of Eq. (4.3) can be expanded into a Taylor series about ω_ℓ. Termination of the series after the second term and back-transformation into the time domain yields for the polarization, in terms of the field envelope:

$$\tilde{P}^{(3)}(t) = \frac{3}{8}\epsilon_0 \left[\chi^{(3)} |\tilde{\mathcal{E}}|^2 \tilde{\mathcal{E}} + i \left. \frac{\partial \chi^{(3)}}{\partial \Omega} \right|_{\omega_\ell} \frac{\partial}{\partial t} \left(|\tilde{\mathcal{E}}|^2 \tilde{\mathcal{E}} \right) \right] e^{i(\omega_\ell t - k_\ell z)} + c.c. \tag{4.64}$$

The above expression (4.64) restates once more that a non-zero response time τ_r leads to a frequency dependence of the susceptibility. The critical parameter is the spectral variation of this susceptibility over the frequency range covered by the pulse spectrum. To study nonlinear propagation problems, the slowly varying envelope approximation is generally applied to the polarization, as expressed in

Eq. (4.14). Inserting the expansion (4.64) into the second derivative of the polarization (4.14) and keeping terms up to the first temporal derivative lead to:

$$i\frac{\mu_0}{k_\ell}\frac{d^2}{dt^2}P^{(3)} = \left[-i\frac{n_2 k_\ell}{n_0}|\tilde{\mathcal{E}}|^2\tilde{\mathcal{E}} - \beta\frac{\partial}{\partial t}\left(|\tilde{\mathcal{E}}|^2\tilde{\mathcal{E}}\right) + ...\right]e^{i(\omega_\ell t - k_\ell z)} + c.c. \tag{4.65}$$

where

$$\beta = \frac{n_2}{c}\left(2 - \frac{\omega_\ell}{\chi^{(3)}}\left.\frac{\partial\chi^{(3)}}{\partial\Omega}\right|_{\omega_\ell}\right). \tag{4.66}$$

It should be remembered that the temporal derivative in Eq. (4.65) becomes important if the light period is not negligibly short compared to the pulse duration. Equations (4.65) and (4.66) indicate that the first-order correction to the SVEA and the finite response time of the nonlinear susceptibility (the two summands forming β) have the same action on pulse propagation. Corrections to the SVEA may also be important in the spatial (transverse) propagation of the beam as indicated in Eq. (4.18).

Pulse propagation through transparent media which is affected by SPM and dispersion has played a key role in fiber optics. For a review we refer to the monograph by Agrawal [42]. In this chapter we will discuss the physics behind SPM and neglect group velocity dispersion. In Chapter 9 we shall describe effects associated with the interplay of SPM and group velocity dispersion.

4.5.2 Short samples with instantaneous response

For interaction lengths much shorter than the dispersion length L_D, and for an instantaneous nonlinearity, the wave equation (4.13) with the source term (4.65) simplifies to

$$\frac{\partial}{\partial z}\tilde{\mathcal{E}}(z,t) = -i\frac{3\omega_\ell^2\chi^{(3)}}{8c^2k_\ell}|\tilde{\mathcal{E}}^2|\tilde{\mathcal{E}} = -i\frac{n_2 k_\ell}{n_0}|\tilde{\mathcal{E}}|^2\tilde{\mathcal{E}} \tag{4.67}$$

after applying the SVEA to the polarization term. For real $\chi^{(3)}$, substituting $\tilde{\mathcal{E}} = \mathcal{E}\exp(i\varphi)$ into Eq. (4.67) and separating the real and imaginary parts result in an equation for the pulse envelope

$$\frac{\partial}{\partial z}\mathcal{E} = 0 \tag{4.68}$$

and for the pulse phase

$$\frac{\partial\varphi}{\partial z} = -\frac{n_2 k_\ell}{n_0}|\mathcal{E}|^2. \tag{4.69}$$

Obviously the pulse amplitude $\mathcal{E}$ is constant in the coordinate system travelling with the group velocity, that is, the pulse envelope remains unchanged, $\mathcal{E}(t,z) =$

$\mathcal{E}(t,0) = \mathcal{E}_0(t)$. Taking this into account, we can integrate Eq. (4.69) to obtain for the phase

$$\boxed{\varphi(t,z) = \varphi_0(t) - \frac{k_\ell n_2}{n_0} z \mathcal{E}_0^2(t)} \tag{4.70}$$

which results in a phase modulation given by

$$\frac{\partial \varphi}{\partial t} = \frac{d\varphi_0}{dt} - \frac{n_2 k_\ell}{n_0} z \frac{d}{dt} \mathcal{E}_0^2(t). \tag{4.71}$$

This result can be interpreted as follows. The refractive index change follows the pulse intensity instantaneously. Thus, different parts of the pulse "feel" different refractive indices, leading to a phase change across the pulse. Unlike the phase modulation associated with group velocity dispersion, this self-phase modulation (SPM) produces new frequency components and broadens the pulse spectrum. To characterize the SPM it is convenient to introduce a nonlinear interaction length

$$L_{NL} = \frac{n_0}{n_2 k_\ell \mathcal{E}_{0m}^2} \tag{4.72}$$

where $\mathcal{E}_{0m}$ is the peak amplitude of the pulse. The quantity z/L_{NL} represents the maximum phase shift which occurs at the pulse peak, as can be seen from Eq. (4.71). Figure 4.10 shows some examples of the chirp and spectrum of self-phase modulated pulses. Because n_2 is mostly positive far from resonances (see Problem 4 at the

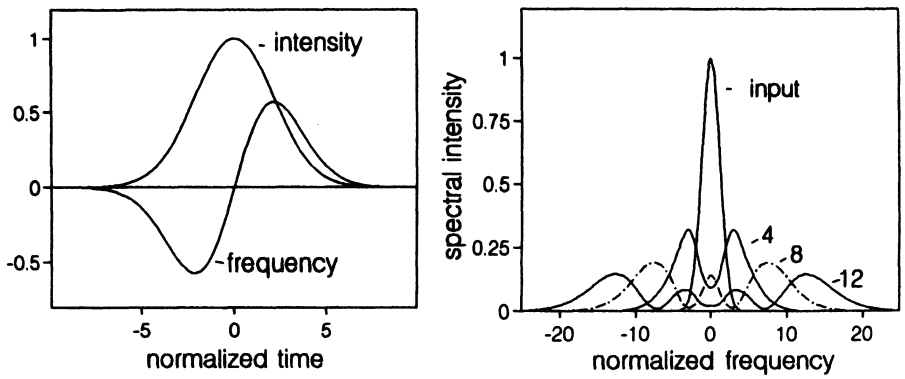

Figure 4.10: Frequency modulation and spectrum of self-phase modulated Gaussian pulses for different propagation lengths z/L_{NL}.

end of this chapter), upchirp occurs in the pulse center. We also see that SPM can

introduce a considerable spectral broadening. This process as well as some nonlinear processes of higher order can be used to generate a white light continuum, as discussed later in this chapter.

For an order of magnitude estimate let us determine the frequency change $\delta\omega$ over the FWHM of a Gaussian pulse. Substituting $\mathcal{E}_{0m}e^{-2\ln 2(t/\tau_p)^2}$ for $\mathcal{E}_0(t)$ in Eq. (4.71) yields

$$\delta\omega\tau_p = \frac{8\ln 2}{\sqrt{2}}\frac{z}{L_{NL}}. \tag{4.73}$$

For $z = L_{NL}$ the normalized frequency sweep is $\delta\omega\tau_p \approx 4$. Note that the original pulse duration bandwidth product of the unchirped Gaussian input pulse was $\Delta\omega\tau_p \approx 3$.

A pulse can also be phase modulated in the field of a second pulse if both pulses interact in the medium. The phase of pulse 1 is then determined by

$$\frac{\partial\varphi_1}{\partial z} = -\frac{n_2 k_\ell}{n_0}\left(|\tilde{\mathcal{E}}_1|^2 + 2|\tilde{\mathcal{E}}_2|^2\right)\tilde{\mathcal{E}}_1. \tag{4.74}$$

This offers the possibility of phase modulating weak pulses by means of a strong pulse. Both pulses can differ in their wavelength, duration, polarization state, etc.. This process is known as cross phase modulation and has found several interesting applications [43]. For example, it is possible to transfer information from one pulse train to another by induced spectral changes [44].

4.5.3 Short samples and non-instantaneous response

For very short pulses and/or a non-instantaneous sample response, the source term given by Eq. (4.65) with $\beta \neq 0$ must be incorporated in the wave equation. The pulse propagation is now governed by

$$\frac{\partial}{\partial z}\tilde{\mathcal{E}} + i\frac{n_2 k_\ell}{n_0}|\tilde{\mathcal{E}}|^2\tilde{\mathcal{E}} + \beta\frac{\partial}{\partial t}\left(|\tilde{\mathcal{E}}|^2\tilde{\mathcal{E}}\right) = 0. \tag{4.75}$$

Comparison with Eqs. (1.98) and (1.99) suggests that the term with a time derivative can be interpreted as an intensity dependent group velocity. For $\beta > (<)\ 0$ the pulse center is expected to travel slower (faster) than the trailing edge. This causes a steepening of the trailing (leading) edge of the pulse, known as "self-steepening." It is similar to the formation of shock waves in acoustics. It is not necessarily associated with a slow response of the polarization, since $\beta = 2$ for $\partial\chi^{(3)}/\partial\omega\big|_{\omega_\ell} = 0$, from the definition of Eq. (4.66). This shock term can also be identified with the second term of the right-hand side in Eq. (4.18). One notes that this first order correction to the SVEA is a loss term, rather than a dispersive term. It can be interpreted as the energy required to drive the nonlinear index.

To solve Eq. (4.75) we again substitute the complex pulse amplitude by a product of an envelope and a phase function to obtain

$$\frac{\partial}{\partial z}\mathcal{E} + 3\beta\mathcal{E}^2\frac{\partial}{\partial t}\mathcal{E} = 0 \tag{4.76}$$

and

$$\frac{\partial}{\partial z}\varphi + \beta\mathcal{E}^2\frac{\partial}{\partial t}\varphi = -\frac{n_2 k_\ell}{n_0}\mathcal{E}^2. \tag{4.77}$$

The equation for the envelope can be solved independently of the phase equation. Its solution can formally be written as [45]

$$\mathcal{E}(z,t) = \mathcal{E}\Big(z = 0, t - 3\beta z\mathcal{E}^2(t,z)\Big). \tag{4.78}$$

For a Gaussian input pulse, $\mathcal{E}_{0m}e^{-(t/\tau_G)^2}$, we find

$$\mathcal{E}(z,t) = \mathcal{E}_{0m}\exp\left\{-\left[\frac{t - 3\beta z\mathcal{E}^2(z,t)}{\tau_G}\right]^2\right\}, \tag{4.79}$$

which contains the envelope implicitly. Figure 4.11 shows the pulse envelope for different values of $3\beta z/\tau_G$. In order to observe the shock pulse with $|d\mathcal{E}/dt| \to \infty$,

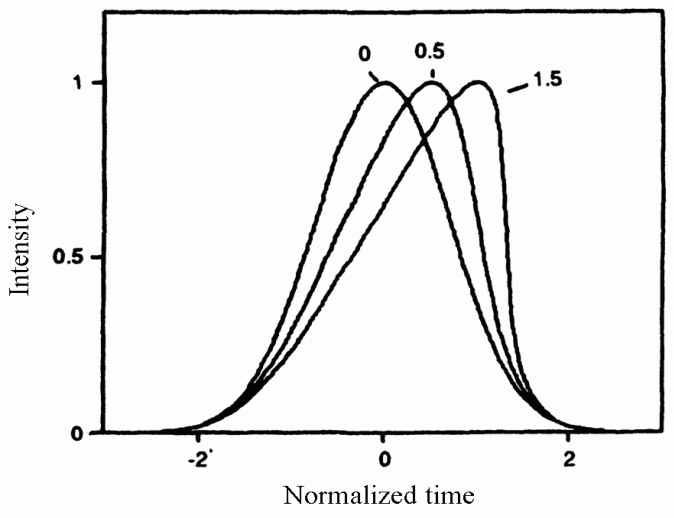

Figure 4.11: Pulse envelope according to Eq. (4.79) for different values of $3\beta z/\tau_G$.

the shock term in the propagation should dominate other terms such as dispersion (neglected here for the sake of simplicity). This, for example, is the case for filamentation (self-focusing) in air and is responsible for the associated white light or "conical emission" (Section 4.6 and 14.2.2).

The envelope function can be inserted in Eq. (4.77) to obtain an implicit (analytical) solution for the phase [45], which, however, is rather complex. A numerical evaluation of the pulse spectrum $|\mathcal{F}\{\tilde{\mathcal{E}}(t,z)\}|^2$ reveals an asymmetric behavior, which is expected, since we are now dealing with SPM of asymmetric pulses. Such spectra were reported by Knox *et al.* [46], for example, as result of SPM of 40 fs pulses in glass. Rothenberg and Grischkowsky directly measured the steepening of pulses in propagating through optical glass fibers [47].

It should also be noted that SPM in connection with saturation, which was discussed earlier, is a particular example of a time dependent sample response. In the case of saturation, there is a memory effect associated with the change of occupation numbers, with a characteristic time determined by the corresponding (energy) relaxation time.

4.5.4 Counter-propagating pulses and third-order susceptibility

In a laser cavity, we may encounter the situation where counter-propagating pulses meet in a nonlinear medium. The standing wave formed at the intersection of the colliding pulses creates a phase (real third-order susceptibility) or an amplitude grating (purely imaginary third-order susceptibility, resulting in two-photon absorption). The grating formed by the nonlinear interaction will diffract each beam into the direction of the other. As illustrated in Fig. 4.12, the transmitted forward propagating field (affected by the nonlinear susceptibility) is combined with the part of the counter-propagating field that is diffracted to the right. Experimentally, these two contributions being undistinguishable, we observe only the total forward propagating pulse at the right of the sample as a "transmitted" beam. When the incident counter-propagating intensities are different, it appears as if the medium had a different transfer function for the forward and backward propagating beams, as explained below. In what follows we will assume that the medium is much thinner than the pulse length, $d << \tau_p c$.

Let us assume two counter-propagating beams $\tilde{E}_1 = (1/2)\tilde{\mathcal{E}}_1 \exp[i(\omega_\ell t - kz)]$ and $\tilde{E}_2 = (1/2)\tilde{\mathcal{E}}_2 \exp[i(\omega_\ell t + kz)]$. From Eq. (4.59), we find for the third-order polarization responsible for phase modulation and two-photon absorption:

$$\begin{aligned} P^{(3)} &= 3\epsilon_0\chi^{(3)}(\tilde{E}_1+\tilde{E}_2)(\tilde{E}_1+\tilde{E}_2)^*(\tilde{E}_1+\tilde{E}_2)+c.c. \\ &= 3\epsilon_0\chi^{(3)}\left\{|\tilde{E}_1|^2+|\tilde{E}_2|^2+\tilde{E}_1\tilde{E}_2^*+\tilde{E}_1^*\tilde{E}_2\right\}\left\{\tilde{E}_1+\tilde{E}_2\right\}+c.c. \\ &= \frac{3}{8}\epsilon_0\chi^{(3)}\left\{\left(|\tilde{\mathcal{E}}_1|^2+2|\tilde{\mathcal{E}}_2|^2+\tilde{\mathcal{E}}_1\tilde{\mathcal{E}}_2^* e^{-2ik_\ell z}\right)\tilde{\mathcal{E}}_1 e^{i(\omega_\ell t-k_\ell z)}\right. \\ &\quad \left.+\left(2|\tilde{\mathcal{E}}_1|^2+|\tilde{\mathcal{E}}_2|^2+\tilde{\mathcal{E}}_1^*\tilde{\mathcal{E}}_2 e^{2ik_\ell z}\right)\tilde{\mathcal{E}}_2 e^{i(\omega_\ell t+k_\ell z)}\right\}+c.c.. \end{aligned} \tag{4.80}$$

We recognize in Eq. (4.80) a forward and a backward propagating field, and two

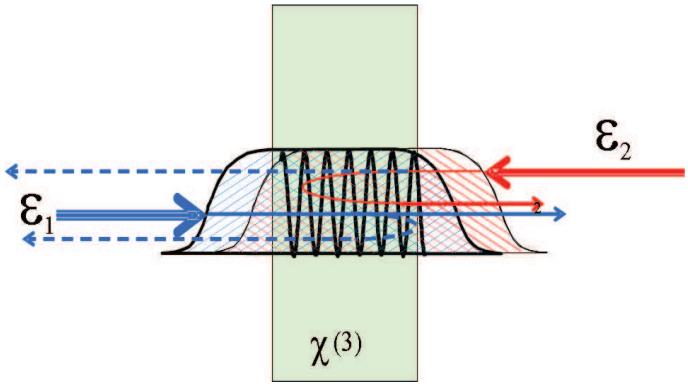

Figure 4.12: Geometry of the interaction of counter-propagating pulses in a medium with a third order nonlinear susceptibility. The standing wave field produces a grating that diffracts (reflects) the waves. What is observed exiting the sample is the sum of the transmitted and reflected fields.

terms involving higher order spatial Fourier components. Even in the case of an homogeneous medium, the terms in $\exp(\pm 2ikz)$ lead to a coupling through a higher order (fifth order) process, which we will neglect. We will see in the exercise at the end of the chapter that these terms become important if the nonlinear susceptibility has a periodic structure on the scale of the wavelength. The forward propagating nonlinear polarization is:

$$\tilde{P}^{(3)}_{\text{forward}} = \frac{1}{2}\tilde{\mathcal{P}}^{(3)}_1 e^{i(\omega_\ell t - k_\ell z)} = \frac{3}{8}\epsilon_0 \chi^{(3)}\left(|\tilde{\mathcal{E}}_1|^2 + 2|\tilde{\mathcal{E}}_2|^2\right)\tilde{\mathcal{E}}_1 e^{i(\omega_\ell t - k_\ell z)}. \tag{4.81}$$

In the retarded frame of reference, and in the slowly varying envelope approximation, the field amplitude varies as, cf. Eq.(**??**):

$$\frac{\partial \tilde{\mathcal{E}}_1}{\partial z} = -i\frac{\mu_0 \omega_\ell c}{2n_0}\tilde{\mathcal{P}}^{(3)}_1. \tag{4.82}$$

Up to this point, no assumption has been made for the complex third order susceptibility, which we will assume to be of the form:

$$\chi^{(3)} = \chi^{(3)}_r - i\chi^{(3)}_i. \tag{4.83}$$

The real part of the third order susceptibility leads to the nonlinear index n_2 as was expressed in Eq. (4.63):

$$n_2 = \frac{3\chi^{(3)}_r}{8n_0}$$

For the case of real $\chi^{(3)}$, inserting Eq. (4.81) into Eq. (4.82) results in the following propagation equation for $\tilde{\mathcal{E}}_1$

$$\begin{aligned}\frac{\partial\tilde{\mathcal{E}}_1}{\partial z} &= -i\frac{\omega_\ell}{c}\frac{3}{8}\frac{\chi_r^{(3)}}{n_0}\left(|\tilde{\mathcal{E}}_1|^2+2|\tilde{\mathcal{E}}_2|^2\right)\tilde{\mathcal{E}}_1 \\ &= -i\frac{\omega_\ell}{c}n_2\left(|\tilde{\mathcal{E}}_1|^2+2|\tilde{\mathcal{E}}_2|^2\right)\tilde{\mathcal{E}}_1 = -ik_{NL}\tilde{\mathcal{E}}_1, \end{aligned} \tag{4.84}$$

where k_{NL} represents a nonlinear propagation constant. This equation describes self- and cross-phase modulation. The factor of 2 in front of $|\tilde{\mathcal{E}}_2|^2$ leads to the asymmetry in the induced phase mentioned in the introduction if the two counter-propagating beams have different amplitudes. There is no energy exchange between the two beams in case of a real susceptibility $\chi^{(3)}$.

Case of two-photon absorption The imaginary part of the third order susceptibility is responsible for two-photon absorption. For purely imaginary $\chi^{(3)}$ the propagation equation for the pulse amplitude becomes

$$\frac{\partial\tilde{\mathcal{E}}_1}{\partial z} = -\frac{\omega_\ell}{c}\frac{3}{8}\frac{\chi_i^{(3)}}{n_0}\left(|\tilde{\mathcal{E}}_1|^2+2|\tilde{\mathcal{E}}_2|^2\right)\tilde{\mathcal{E}}_1 = -\frac{\beta_2}{2}\left(|\tilde{\mathcal{E}}_1|^2+2|\tilde{\mathcal{E}}_2|^2\right)\tilde{\mathcal{E}}_1, \tag{4.85}$$

which leads to the definition of the two-photon absorption coefficient β_2:

$$\beta_2 = \frac{3}{4}\frac{\omega_\ell}{cn_0}\chi_i^{(3)}. \tag{4.86}$$

In terms of intensities, the expression for the attenuation of beam 1 in presence of beam 2 is:

$$\frac{dI_1}{dz} = -\beta_2\left(I_1+2I_2\right)I_1. \tag{4.87}$$

Again, it is only when the two counter-propagating beams have equal intensity that the relative attenuation of both beams is equal.

4.6 Continuum generation

One of the most impressive (and simplest) experiments with ultrashort light pulses is the generation of a white light continuum. At the same time continuum generation with laser pulses is one of the most complex and difficult-to-analyze processes as it combines spatial and temporal effects and their interplay. This is one reason while the spectral supercontinuum has remained an area of active theoretical and experimental research until today. For reviews on this subject see [48], and the special issue [49] for a summary of recent research.

Provided the pulse is powerful enough, focusing into a transparent material results in a substantial spectral broadening. The output pulse appears on a sheet of paper as a white light flash, even if the exciting pulse is in the near IR or near UV spectral range. This is often accompanied by colors distributed in rings. Continuum generation was first discovered with ps pulses by Alfano and Shapiro [50] and has since been applied to numerous experiments. One of the most attractive fields of application is time-resolved spectroscopy, where the continuum pulse is used as an ultrafast spectral probe.

Spectral super-broadening was observed in many different (preferably transparent) materials including liquids, solids, and gases. Essential processes contributing to the continuum generation are common to all. Figure 4.13 shows as an example a white light continuum generated in a solid with near IR fs pulses [51] and in gas with UV fs pulses [52]. As can be seen, the continuum does not have a "flat" uniform spectrum. A broad palette of fs laser sources is still desirable to create a continuum with a maximum energy concentration in any particular wavelength range. Continuum generation is a rather complex issue which involves changes in the temporal and spatial beam characteristics. With fs pulses, the do-

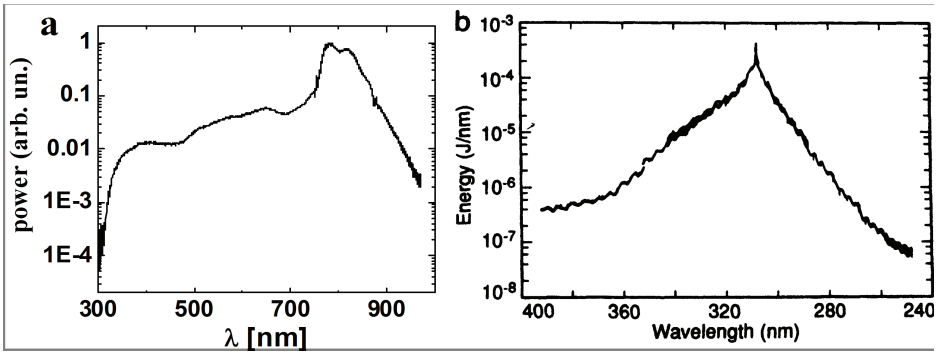

Figure 4.13: Femtosecond spectral super-broadening. (a) In a 0.5-mm CaF_2 sample with 20 fs pulses at 800 nm (adapted from [51]). (b) In a 60 cm long Ar cell (40 atm). The pump pulses (4 mJ, 308 nm, 160 fs) were focused with a 50 cm lens (from [52]).

minant process and the starting mechanism leading to spectral super-broadening is SPM due to an intensity dependent refractive index. However, a number of other nonlinear effects play a role as well. The interplay of self-focusing (see Section **??**) and various nonlinear processes make the exact treatment of the continuum generation with short pulses extremely complex. Indeed, an inspection of Fig. 4.13 shows that the spectral features cannot be explained by the action of SPM alone. Other nonlinear effects that are likely to contribute are parametric four-wave mixing and Raman scattering. The strong anti-Stokes component visible in Fig. 4.13 is likely

due to multi-photon excitation of the dielectric material followed by avalanche ionization [53]. The resulting electron plasma in the conduction band produces a fast rise of a negative refractive index component that can explain the dominant broadening toward the shorter wavelengths. As will be explained in the next section SPM is associated with self-focusing leading to extremely high intensities where the beam collapses. It is at this point where the continuum generating nonlinear processes are most effective.

The continuum pulse at the sample output is chirped. This is due to the time dependence of the nonlinear optical processes, which produces various spectral components at different parts within the pulse. Another origin of chirp is the propagation of the generated continuum from the point of beam collapse through the medium, and all optical elements (including the path through air) leading to the detector. The chirp of the continuum was measured by fs frequency-domain interferometry [54] and transient-grating diffraction [51] for example. The dispersive processes account for most of the chirp of the continuum for pulses < 50 fs. This is illustrated in Fig. 4.14.

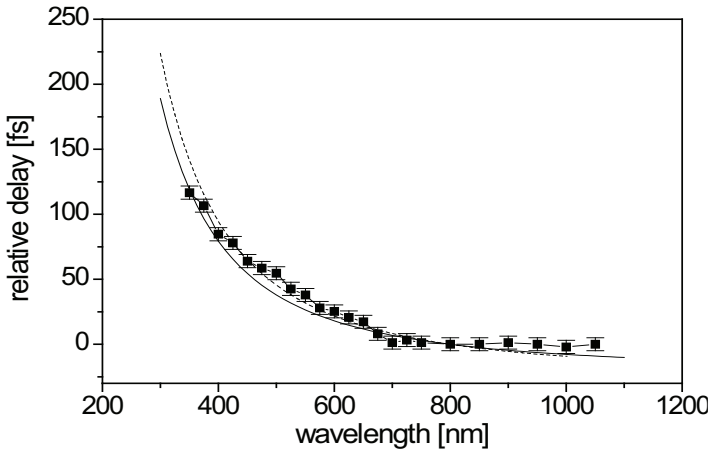

Figure 4.14: Spatio-temporal distribution of a fs white-light continuum after propagation through 1 m air (640 Torr). Solid line: dispersion expected from the 1 m path through the atmosphere, dotted line: atmospheric path and 0.11 mm of CaF_2 (the distance from the beam collapse to the exit face of the crystal). (adapted from [51]).

Sending the continuum pulse through a proper element with group velocity dispersion can result in pulse compression (see Chapter 9). The "ideal" fs continuum pulse is thus a nearly bandwidth-limited fs pulse which is considerably shorter than the original pump pulse. Such continuum pulses enabled optical spectroscopy with time resolution better than 10 fs [55, 56].

Traditionally continua were generated in bulk materials with amplified fs pulses. Dispersion and the associated pulse broadening together with the finite propagation length until beam collapse limited the effective material length. This changed with the introduction of microstructured fibers [57] and tapered fibers [58]. These fibers either shift the wavelength of zero dispersion to regions were fs oscillator pulses were readily available and/or reduce the dispersion while increasing the nonlinearity. Because of the possible large propagation lengths at constant beam diameter (guided modes) the overall nonlinear interaction length can be greatly increased, which allowed the generation of continua with nJ and sub-nJ pulses directly from oscillators, and even using cw light (e.g., [59]). Using pulses directly from Ti:sapphire oscillators, continua covering almost two decades from ≈ 380 nm to 1600 nm were obtained.

An interesting application of the continuum is in metrology. Under certain circumstances, that will be discussed in Chapter 6, the continuum extends the regular mode structure of a mode-locked laser, making it possible to perform frequency mixing experiments over more than one octave in frequency.

4.7 Self-focusing

The nonlinearities of a medium affect both the temporal and spatial dependence of the electric field of the light. In the previous sections we have avoided this difficulty by assuming a uniform beam profile or neglecting nonlinear space-time coupling effects. However, any nonlinear interaction strong enough to affect the pulse temporal profile will also affect its transverse profile. One example is second harmonic generation, slightly off-exact phase matching condition (large nonlinear phase shifts), or at large conversion efficiencies. As sketched in the inset of Fig. 4.2, an initially Gaussian temporal profile will be depleted predominantly in the center, resulting in a flattened shape. The same interaction will also transform an initially Gaussian beam into a profile with a flat top.

In this section we will consider as an important example the problem of self-focusing. The intensity dependent index of refraction causes an initially collimated beam to become focused in a medium with $n_2 > 0$. It is the same intensity dependence of the refractive index that causes self-phase modulation of a fs pulse, as we have seen in the previous section.

4.7.1 Critical power

The action of a nonuniform intensity distribution across the beam profile on a nonlinear refractive index results in a transverse variation of the index of refraction,

leading either to focusing or defocusing. Let us assume a cw beam with a Gaussian profile $I = I_0 \exp\left(-2r^2/w^2\right)$, and a positive $\bar{n}_2$, as is typical for a nonresonant electronic nonlinearity. The refractive index decreases monotonically from the beam center with increasing radial coordinate. One can define a "self-trapping" power $P_{cr,1}$ as the power for which the wavefront curvature (on axis) due to diffraction is exactly compensated by the change in the wavefront curvature due to the self-lensing over a small propagation distance Δz. We assume that the waist of the Gaussian beam is at the input boundary of the nonlinear medium ($z = 0$). Within the paraxial approximation, diffraction results in a spherical curvature of the wavefront at a small distance Δz from the beam waist:

$$\varphi_{\text{diff}}(\Delta z) = -\frac{k_\ell \Delta z}{2\rho_0^2} r^2, \tag{4.88}$$

where ρ_0 is the Rayleigh range. This result is obtained by approximating $1/R \approx \Delta z/\rho_0^2$ in Eq. (1.218). The action of the nonlinear refractive index results in a radial dependence of the phase after a propagation distance Δz:

$$\varphi_{\text{sf}}(r, \Delta z) = -\bar{n}_2 \frac{2\pi}{\lambda} \Delta z I_0 e^{-(2r^2/w_0^2)} \approx -\bar{n}_2 \frac{2\pi}{\lambda_\ell} \Delta z I_0 \left(1 - 2\frac{r^2}{w_0^2}\right), \tag{4.89}$$

where the last equation is an approximation of the wavefront near the beam center. This equation follows from Eq. (4.70) after replacing $n_2 \mathcal{E}_0^2$ by $\bar{n}_2 I(r)$. The input beam has the critical power $P_{cr,1} = \int 2\pi r I(r) dr$ when the radial parts of Eqs. (4.88) and (4.89) compensate each other:

$$P_{cr,1} = I_0 \frac{\pi w_0^2}{2} = \frac{\lambda^2}{8\pi n_0 \bar{n}_2} \tag{4.90}$$

where we have made use of $\rho_0 = \pi w_0^2 n_0/\lambda$. One says that the beam is "self-trapped" because neither diffraction nor focusing seems to occur. This value of critical power is also derived by Marburger [60] by noting that the propagation equation is equivalent to that describing a particle moving in a one-dimensional potential. The condition for which the potential is "attractive" (leads to focusing solutions) is $P \geq P_{cr,1}$. One can define another critical power $P_{cr,2}$ as the power for which the phase factor on axis of the Gaussian beam, $\arctan(z/\rho_0)$, exactly compensates the nonlinear phase shift $\bar{n}_2 I_0$:

$$P_{cr,2} = \frac{\lambda_\ell^2}{4\pi n_0 \bar{n}_2}. \tag{4.91}$$

This second value of the critical power is also obtained by assuming that the beam profile remains Gaussian, and deriving an expression for "scale factor" $f(z) =$

$w(z)/w_0$ [61, 62] as a function of distance z. The function $f(z)$ reaches zero after a finite distance if the power exceeds the value $P_{cr,2}$.

Another common approach to defining a "self trapping" power is to approximate the radial beam profile by a flat top of diameter d [2]. The refractive index inside the tube of diameter d is $n = n_0 + \bar{n}_2 I_0$. The critical angle for total internal reflection, α, is determined by $\sin\alpha = n_0/(n_0 + \bar{n}_2 I_0)$. The beam is trapped inside the tube if the diffraction angle $\theta_d \approx 1.22\lambda/(2n_0 d)$ is equal to $\theta_{cr} = \pi/2 - \alpha$. From this condition and using the fact that $\bar{n}_2 I_0 << n_0$ one can derive the critical power $P_{cr,3} = I_0 \pi d^2/4$:

$$P_{cr,3} = \frac{(1.22)^2 \pi \lambda_\ell^2}{32 n_0 \bar{n}_2} \tag{4.92}$$

These three approaches, summarized in Table 4.5, define a critical power of the form:

$$P_{cr} = a \frac{\lambda_\ell^2}{n_0 \bar{n}_2} \tag{4.93}$$

phase on axis	wavefront curv.	waveguide
$\frac{2\pi}{\lambda_\ell}\bar{n}_2 I_0 z = \arctan\frac{z}{\rho_0}$	$\frac{2\pi}{\lambda_\ell}\bar{n}_2 I_0 = -\frac{k_\ell r^2}{2R}$	$\theta_{cr} = \theta_d$
$P_{cr} = \frac{1}{4\pi}\frac{\lambda_\ell^2}{n_0\bar{n}_2}$	$P_{cr} = \frac{1}{8\pi}\frac{\lambda_\ell^2}{n_0\bar{n}_2}$	$P_{cr} = \frac{(1.22)^2\pi}{32}\frac{\lambda_\ell^2}{n_0\bar{n}_2}$

Table 4.5: Three approaches to defining a critical power for self-focusing. They differ by the coefficient a in Eq. (4.93).

The point of agreement between these different definition is the existence of a critical *power* rather than a critical intensity. This result is not surprising, since, for a given power, both the diffraction to be compensated and the lensing effect (nonlinear index) are inversely proportional to the beam diameter. It is not possible without numerical calculation to predict exactly the evolution of the beam at powers close to any of these "critical powers". The Gaussian characteristic of the beam will be altered. Only numerical calculation can determine the fate of the beam over long propagation distances. Calculations made in steady state conditions have demonstrated the existence of a critical power $P_{cr} \approx 3.77 P_{cr,1} \approx 1.03 P_{cr,2}$, corresponding to the value of $a \approx 0.142$ in Eq. (4.93) [60].

A laser beam whose power exceeds the critical power reaches a focus after a finite propagation distance – the self-focusing length z_{SF}. Even for cw beams the

exact treatment of beam propagation in an n_2 medium can only be done numerically. According to such a simulation

$$z_{SF} \approx \frac{0.183\rho_0}{\sqrt{(\sqrt{P/P_{cr}} - 0.852)^2 - 0.0219}} \tag{4.94}$$

see, for example, ref. [60]. Here ρ_0 is the Rayleigh range of the original beam assumed to have a beam waist at the sample input.

With some restrictive assumptions one can derive an approximate self-focusing length analytically, which shows a similar structure as Eq. (4.94). We will sketch this approach at the end of Section 4.8.1.

4.7.2 The nonlinear Schrödinger equation

Let us consider the propagation of a laser beam along the direction z, in a medium characterized by a linear index of refraction n, a third order nonlinear polarization, and a linear loss/gain coefficient α [cf. Eq. (4.62)]. The nonlinear polarization

$$\tilde{P}^{(3)}_{NL} = \frac{3}{8}\epsilon_0\chi^{(3)}|\tilde{\mathcal{E}}|^2\tilde{\mathcal{E}}e^{i(\omega_\ell t - kz)}. \tag{4.95}$$

is to be substituted into the wave equation (1.78), with the field given by Eq (1.94). If we assume a steady state condition (no time dependence) the equation describing the spatial dependence of the electric field is:

$$\left[\frac{\partial}{\partial z} + \frac{i}{2k_\ell}\left(\frac{\partial^2}{\partial x^2} + \frac{\partial^2}{\partial y^2}\right) + i\frac{3\omega_\ell^2}{8c^2k_\ell}\chi^{(3)}|\mathcal{E}|^2 - \frac{\alpha}{2}\right]\tilde{\mathcal{E}} = 0 \tag{4.96}$$

The prefactor in front of the nonlinear term can also be written as $3\omega_\ell^2\chi^{(3)}/(8c^2k_\ell) = n_2k_\ell/n_0$. One recognizes in Eq. (4.96) a three-dimensional generalization of the nonlinear Schrödinger equation [63]:

$$i\frac{\partial\psi}{\partial z} - a\frac{\partial^2\psi}{\partial x^2} - b|\psi|^2\psi + c\psi = 0. \tag{4.97}$$

The last term of Eq. (4.96) is a linear gain or absorption associated with the imaginary part of the linear index of refraction. In one dimension, these equations were shown by Zakharov and Shabat [64] to have steady state solutions labeled "solitons". These solitons correspond to a balance between the self-focusing and the diffraction. The physical reality is however more complex than can be included in the nonlinear Schrödinger Eq. (4.97). Indeed, once the nonlinearity exceeds the threshold to overcome diffraction, the beam collapses to a point (see next section).

In order to obtain a dynamically stable solution in the transverse dimension, it is necessary to include a higher order nonlinearity in the polarization to prevent this collapse, as demonstrated below.

If we consider a short pulse propagating as a plane wave through an infinite medium with the nonlinear polarization of Eq. (4.95), the temporal evolution of the field is given by a similar nonlinear Schrödinger equation:

$$\left[\frac{\partial}{\partial z} - \frac{ik''}{2}\frac{\partial^2}{\partial t^2} + i\frac{n_2 k_\ell}{n_0}|\mathcal{E}|^2 - \frac{\alpha}{2}\right]\tilde{\mathcal{E}} = 0, \tag{4.98}$$

where the independent variables are now z and t. The soliton solution to Eq. (4.98) results from a balance between dispersion and self-phase modulation caused by the nonlinear polarization. The condition for the existence of a temporal soliton is that (anomalous) dispersion $\frac{ik''}{2}\frac{\partial^2}{\partial t^2}$ balances self-temporal-lensing (positive self-phase modulation) $\frac{in_2 k_\ell}{n_0}|\mathcal{E}|^2\tilde{\mathcal{E}}$. Normal dispersion and a negative self-phase modulation can also lead to soliton solutions [65]. A more detailed discussion of solitons is given in Chapter 5, Section 5.5.

4.8 Beam trapping and filaments

Once the beam power is sufficient for self-focusing to overcome diffraction, the beam collapses to a point. In general, after the beam has collapsed, it diffracts. However, numerous experiments have shown self-guiding of high peak power infrared femtosecond pulses through the atmosphere [66–70]. Similar observations were made in the UV [71, 72]. After reaching the focus, the light appeared to trap itself in self-induced waveguides or "filaments" of the order of 100 μm diameter. Before addressing problems specific to ultrashort pulses we will discuss a steady state model to illustrate the possibility of beam self-trapping.

4.8.1 Beam trapping

We start with the time-free wave equation

$$\left[\frac{\partial}{\partial z} + \frac{i}{2k_\ell}\left(\frac{\partial^2}{\partial x^2} + \frac{\partial^2}{\partial y^2}\right)\right]\tilde{\mathcal{E}}(x,y,z) = -ik_{NL}\tilde{\mathcal{E}}(x,y,z). \tag{4.99}$$

For the nonlinear propagation constant on the right-hand side we assume a nonlinear refractive index due to a Kerr nonlinearity and a contribution of next order.

$$k_{NL} = \frac{\omega_\ell}{c}\left(n_2|\tilde{\mathcal{E}}|^2 + n_3|\tilde{\mathcal{E}}|^3\right) \tag{4.100}$$

A physical system that can give rise to a negative n_3 will be introduced later. A general solution to Eq. (4.99) is only possible by numerical means. To illustrate the possibility of beam trapping we will analyze the term on the right hand side of the wave equation near in the vicinity of the beam center. Assuming a Gaussian beam profile, $\tilde{\mathcal{E}} = \mathcal{E}_0(w_0/w)\exp\left(-r^2/w^2\right)$, over a propagation distance Δz, the medium introduces a phase factor

$$\phi_{NL}(r) = k_{NL}\Delta z = \frac{\omega_\ell}{c}\left[n_2\frac{\mathcal{E}_0^2 w_0^2}{w^2}e^{-2r^2/w^2} + n_3\frac{\mathcal{E}_0^3 w_0^3}{w^3}e^{-3r^2/w^2}\right]\Delta z. \tag{4.101}$$

The curvature of the r dependent phase on axis determines the focusing characteristics of a slice of thickness Δz. For $n_3 = 0$ this is the phase factor that was discussed in Section 4.7.1 and was found responsible for self-focusing. The curvature of the phase term in the vicinity of the beam center is

$$\left.\frac{d^2}{dr^2}\phi_{NL}(r)\right|_{r\approx 0} = -Q\left[1 + \mathcal{E}_0 w_0\left(\frac{n_3}{w n_2}\right)\right] \tag{4.102}$$

where $Q = 4\omega_\ell n_2\tilde{\mathcal{E}}_0^2 w_0^2\Delta z/(cw^4)$. For $n_2 > 0$ as is the case in most materials and $n_3 < 0$ we have the situation that the term in brackets can change sign depending on the ratio $n_3/(n_2 w)$ for given input beam ($\tilde{\mathcal{E}}_0 w_0$). For $n_2 w > (<) n_3$ the material will act like a positive (negative) lens. A positive lens tends to decrease w upon propagation until at some point the sign of the phase term reverses leading to negative lensing. This in turn increases w until the process is reversed again. This suggests the possibility of a periodically changing beam diameter (trapped beam) even if diffraction is included. The effect of the latter is that the phase curvature should have a certain positive value depending on w before the beam actually contracts. Similar beam trapping can be expected from contributions that are of order $m > 2$ if the sign of n_m is negative. The nonlinear refractive indices have their origin in nonlinear susceptibilities of order $m + 1$. The Kerr effect, $\chi^{(3)}$ producing a nonlinear index n_2, is one example, which we discussed in detail before.

Let us know briefly describe a physical system that can produce a negative n_3. Let us assume that the beam propagates through a gas that can be ionized by a three-photon absorption. The free electrons (density N_e) can recombine with the positive ions and a steady state will be reached.

$$\frac{d}{dt}N_e = \sigma^{(3)}|\tilde{\mathcal{E}}|^6 N_0 - \beta_{ep}N_e^2 = 0 \tag{4.103}$$

Here $\sigma^{(3)}$ is a 3-photon absorption cross section, N_0 is the number density of atoms, and β_{ep} is the two-body recombination constant. From Eq. (4.103) we can obtain

the steady-state density of free electrons as a function of the laser field

$$N_{eq} = \sqrt{\frac{\sigma^{(3)} N_0}{\beta_{ep}}} |\tilde{\mathcal{E}}|^3. \tag{4.104}$$

The (small) change of the refractive index $\Delta\tilde{n}$ associated with the laser generated free electrons can be estimated with the Drude model:

$$\tilde{n}^2 = (1 + \Delta\tilde{n})^2 \approx 1 + 2\Delta\tilde{n} = 1 + \frac{\omega_p^2}{\omega_\ell^2}\left(1 - i\frac{\gamma}{\omega_\ell}\right). \tag{4.105}$$

where $\omega_p^2 = N_{eq}^2 e^2/(m\epsilon_0)$ is the plasma frequency and γ is the dephasing rate determined by collisions. With the equilibrium electron density from Eq. (4.104) the change of the refractive index becomes:

$$\Delta\tilde{n} = \sqrt{\frac{\sigma^{(3)} N_0}{\beta_{ep}}} \frac{e^2}{2\omega_\ell^2 m\epsilon_0}\left(1 - i\frac{\gamma}{\omega_\ell}\right)|\tilde{\mathcal{E}}|^3. \tag{4.106}$$

The index change is complex: the imaginary part accounts for free-electron absorption, the real part determines the nonlinear index n_3 used in Eq. (4.100).

Numerical solutions of Eq. (4.99) with the nonlinear k-vector (4.100) and n_3 due to three-photon ionization [73] show several features that are very similar to those observed with fs filamented pulses. The power loss with distance plotted in Fig. 4.15 is remarkably low, after an initial drop. The explanation for the low losses can be found in the plot of electron density and beam size $w(z)$ of Fig. 4.15. As the beam size decreases towards its minimum value w_{min}, the electron density reaches a peak, before falling back to an insignificant value as the beam expands. The beam waist w appears to "ricochet" at every period on the minimum value. In most cases, the loss mechanism is effective only for a small fraction of the period of oscillation of the beam. The loss decreases with distance because that fraction of period spent at the shortest dimension w decreases with distance. This phenomenon is the steady state analogue of "dynamic replenishment" observed for fs filaments in numerical simulations by Mlejnek *et al.* [74].

Equation (4.99) with an n_2 nonlinearity allows one to derive an approximate expression for the self-focusing length z_{SF}, see for example [5]. To this end we insert the ansatz of a Gaussian beam profile

$$\tilde{\mathcal{E}} = \mathcal{E}_0[w_0/w(z)]\exp\left(-r^2/w(z)^2\right)$$

and assume that the Gaussian beam shape is maintained throughout the propagation (focusing). The beam waist w_0 is at the sample input ($z = 0$). Within the frame of

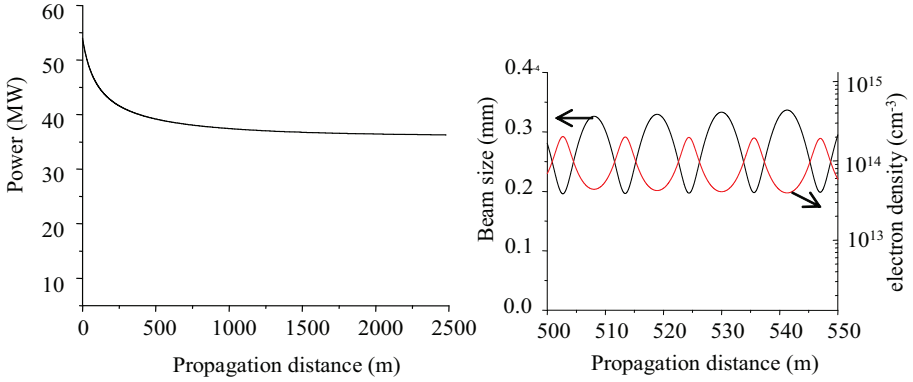

Figure 4.15: Numerical simulation of the nonlinear propagation of a 60 MW cw Gaussian UV (250 nm) beam in air. Left - plot of beam power versus distance. Right - beam size and electron density versus propagation distance [73].

paraxial optics we approximate the nonlinear term by

$$n_2|\tilde{\mathcal{E}}|^2 \approx n_2\mathcal{E}_0^2\frac{w_0^2}{w^2(z)}\left[1-2\frac{r^2}{w^2(z)}\right]. \tag{4.107}$$

Sorting the powers of r and setting the prefactors to zero results in a second-order differential equation for the beam waist:

$$\frac{d^2}{dz^2}w(z) = -\frac{4}{k_\ell^2}\left(\frac{P}{P_{cr}}-1\right)\frac{1}{w^3(z)}, \tag{4.108}$$

where P is the (constant) beam power and P_{cr} is the critical power defined as $P_{cr,1}$ in Eq. (4.90). The solution to this differential equation is

$$w^2(z) = w_0^2 - \frac{w_0^2}{\rho_0^2}\left(\frac{P}{P_{cr}}-1\right)z^2 \tag{4.109}$$

where $\rho_0 = kw_0^2/2$ is the Rayleigh range. Provided that $P > P_{cr}$, the beam collapses at a distance equal to the self-focusing length $z = z_{SF}$, where

$$z_{SF} = \frac{\rho_0}{\sqrt{P/P_{cr}-1}}. \tag{4.110}$$

4.8.2 Ultra-short pulse self focusing

An exact treatment of short-pulse self focusing is very complex as it involves the inclusion of many different nonlinear effects combined with propagation effects.

The general approach is to start with Eq. (4.18) and specify the nonlinear polarization of the material in which the pulse propagates. For example, by specifying the nonlinear polarization as the Kerr effect and the Raman effect, one arrives at a generalized nonlinear Schödinger equation often used to describe pulse propagation in fibers and in bulk materials leading to filaments:

$$\begin{aligned}\frac{\partial\tilde{\mathcal{E}}}{\partial z} &= \frac{\alpha_0}{2}\tilde{\mathcal{E}} + i\hat{D} - \frac{i}{2k_\ell}\left(1 - \frac{i}{\omega_\ell}\frac{\partial}{\partial_z}\right)^{-1}\nabla_\perp^2\tilde{\mathcal{E}} \\ &- i\gamma(1-f_R)\left(1 - \frac{i}{\omega_\ell}\frac{\partial}{\partial_t}\right)|\tilde{\mathcal{E}}|^2\tilde{\mathcal{E}} \\ &+ i\gamma f_R\left[1 - \frac{i}{\omega_\ell}\frac{\partial}{\partial t}\right]\left\{\tilde{\mathcal{E}}\int_0^\infty h_R(t')|\tilde{\mathcal{E}}(t-t')|^2dt'\right\} \qquad (4.111)\end{aligned}$$

where f_R indicates the fraction of the nonlinearity that is a delayed Raman contribution, as opposed to the "instantaneous" electronic contribution. $\gamma = \pi\bar{n}_2 n_0/(377\lambda)$ is the effective nonlinearity. The Raman response function is given by $h_R(t)$. When applied to fibers [42], the transverse Laplacian term is no longer relevant.

Numerical solutions of Eq. (4.111) exist for different propagation problems (material parameters), see for example refs. [74–81]. The results vary due to the complexity of the equation and the fact that some of the material parameters in Eq. (4.111) are not well known. Comparison of the numerical results with experiments is hampered by the difficulties encountered when measuring the parameters of the propagating pulse and the filaments. We will discuss some of the properties of self-focusing associated with short pulses and leading to filaments in more detail in Chapter 14.

4.9 Problems

1. Verify the temporal behavior of the polarization and occupation number as given in Eqs. (**??**) and (**??**).

2. Estimate the absolute value of the refractive index change at a frequency off resonance by $\Delta\omega_F/2$ which is caused by saturation of a homogeneously broadened, absorbing transition with Lorentzian profile. The change in the absorption at resonance at the pulse center was measured to be 50%. The pulse duration τ_p is much larger than the energy relaxation time T_1. The small signal absorption coefficient is α_0.

3. Show that the nonlinear refractive index coefficient is related to the third-order susceptibility through $n_2 = 3\chi^{(3)}/(8n_0)$ [cf. Eq. (4.63)].

4. Starting from the density matrix equations of a two-level system, find an approximate expression for n_2 which is valid for ω_ℓ far from a single resonance. In particular, comment on the statement following Eq. (4.72) that n_2 is mostly positive.

5. Chirp enhancement through parametric interaction provides an interesting possibility to compress pulses. To illustrate this, let us consider the following simplified model. An initially unchirped Gaussian pulse is sent through a group velocity dispersive element, e.g., a block of glass of length L and GVD parameter k'', leading to linearly chirped output pulses (chirp parameter a). This pulse now serves as a pump in a parametric process producing a (Gaussian) output pulse of the same duration but with an increased chirp parameter (of opposite sign), $a' = -Ra$. A second piece of glass of suitable length can be used to compress this pulse. Calculate the total compression factor in terms of L and R. Note that this configuration would allow us to control the achievable compression factor simply by changing the group velocity dispersion (e.g., L) of the first linear element that controls the initial chirp.

6. Consider the situation of Section 4.5.4 relating to the interaction of two counter-propagating pulses in a nonlinear medium characterized by a third order nonlinear susceptibility $\chi^{(3)}$. The purpose of this problem is to compare the counter-propagating interaction in the case of the homogeneous medium with the case of a set of Multiple Quantum Wells (MQW's) separated by a wavelength, as sketched in Fig. 4.16.

   For the homogeneous medium, the nonlinear susceptibility is uniform and equal to $\chi^{(3)}$. The stratified medium is assumed to be made of N (infinitely thin) quantum wells separated by half a wavelength, each quantum well having a susceptibility $\chi^{(3)}\delta(kz - j\pi)/N$. The medium susceptibility $\chi^{(NL)}$ can thus be represented by:

$$\chi^{(NL)}(z) = \sum_{j=1}^{N} \frac{\chi^{(3)}}{N} \delta(kz - j\pi) \tag{4.112}$$

   Insert this susceptibility in Eq. (4.80), and average (integrate) over the thickness of the medium, to find an average third-order polarization. Show that the coupling term in this polarization, which in an homogenous medium would average to zero, has now a contribution of the same order as the other terms.

   It is interesting to contrast the result from the MQW with that of the homogeneous medium. First, the nonlinear polarization is larger in the case of

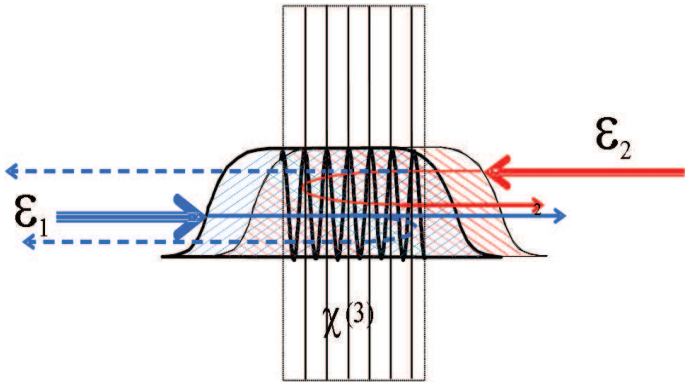

Figure 4.16: Geometry of counter-propagating wave interaction in a medium with a third order nonlinear susceptibility concentrated in quantum wells. We assume the spacing between quantum wells to have a negligible nonlinear susceptibility. The quantum wells are located at the antinodes of the standing wave field, resulting in a maximum interaction between the nonlinear medium and the light field.

the MQW sample: if the fields are equal, $\mathcal{P}_1^{(3)} = 4\epsilon_0\chi^{(3)}|\mathcal{E}_1^2|\mathcal{E}_1$ to be compared with $\mathcal{P}_1^{(3)} = 3\epsilon_0\chi^{(3)}|\mathcal{E}_1^2|\mathcal{E}_1$ in the homogeneous case. Second, the "non-reciprocity" due to cross phase modulation which appears in the homogeneous case, is not present in the MQW geometry. Show that, for the change in index, instead of $\Delta n_{\rm nl} = n_2(\tilde{\mathcal{E}}_1^2 + 2\tilde{\mathcal{E}}_2^2)$ for the forward beam, in the homogeneous case — a consequence of Eq. (4.84) —, we have

$$\Delta n_{\rm nl} = n_2\left(\tilde{\mathcal{E}}_1^2 + \tilde{\mathcal{E}}_2^2 + 2\mathcal{E}_1\mathcal{E}_2\right) = \frac{3\chi^{(3)}}{8n_0}\left(\tilde{\mathcal{E}}_1^2 + \tilde{\mathcal{E}}_2^2 + 2\mathcal{E}_1\mathcal{E}_2\right), \tag{4.113}$$

an expression that is the same for both directions of propagation. This is basically a result from the fact that the emission of layers of dipoles (spaced by a wavelength) in the forward and backward directions is equal [82].

Bibliography

[1] M. Schubert and B. Wilhelmi. *Nonlinear Optics and Quantum Electronics*. John Wiley & Sons, New York, 1978.

[2] W. Boyd. *Nonlinear Optics*. Academic Press, New York, 1991.

[3] N. Bloembergen. *Nonlinear Optics*. World Scientific Publishing Company, Singapore, 1996.

[4] T. Brabec and F. Krausz. Nonlinear optical pulse propagation in the single-cycle regime. *Phys. Rev. Lett.*, 78:3282–3284, 1997.

[5] Y. R. Shen. *The Principles of Nonlinear Optics*. John Wiley & Sons, New York, 1984.

[6] R. C. Miller. Second harmonic generation with a broadband optical maser. *Phys. Lett.*, A26:177–178, 1968.

[7] J. Comly and E. Garmire. Second harmonic generation from short light pulses. *Appl. Phys. Lett.*, 12:7–9, 1968.

[8] S. A. Akhmanov, A. S. Chirkin, K. V. Drabovich, A. I. Kovrigin, R. V. Khokhlov, and A. P. Sukhorukov. Nonstationary nonlinear optical effects and ultrashort light pulse formation. *IEEE J. of Quantum Electron.*, 4:598–605, 1968.

[9] W. H. Glenn. Second harmonic generation by ps optical pulses. *IEEE J. Quantum Electron.*, QE-5:281–290, 1969.

[10] Y. Wang and R. Dragila. Efficient conversion of picosecond laser pulses into second-harmonic frequency using group-velocity-dispersion. *Phys. Rev. A*, 41:5645–5649, 1990.

[11] F. Zernicke. Refractive indices of ADP and KDP between 200nm and 1500nm. *J. Opt. Soc. Am.*, 54:1215–1220, 1964.

[12] M. Choy and R. L. Byer. Accurate second-order susceptibility measurements of visible and infrared optical pulses. *Phys.Rev.*, B14:1693–1706, 1976.

[13] K. Kato. Second harmonic generation to 2058 å in β-bariumborate. *IEEE J. Quantum Electron.*, QE-22:1013–1014, 1986.

[14] Y. N. Karamzin and A. P. Sukhorukov. Limitation on the efficiency of frequency doublers of picosecond light pulses. *Sov. J. Quantum Electron.*, 5:496–500, 1975.

[15] R. C. Eckardt and J. Reintjes. Phase matching limitations of high efficiency second harmonic generation. *IEEE J. Quantum Electron.*, QE-20:1178–1187, 1984.

[16] N. C. Kothari and X. Carlotti. Transient second harmonic generation: influence of effective group velocity dispersion. *J. Opt. Soc. Am. B*, 5:756–764, 1988.

[17] D. Kuehlke and U. Herpers. Limitation of the second harmonic conversion of intense femtosecond pulses. *Opt. Commun.*, 69:75–80, 1988.

[18] L. A. Ostrovski. Self-action of light in crystals. *JETP Lett.*, 5:272–274, 1967.

[19] G. Szabo and Z. Bor. Broadband frequency doubler for femtosecond light pulses. *Appl. Phys.*, B50:51–54, 1990.

[20] O. E. Martinez. Achromatic phase matching for second harmonic generation of femtosecond light pulses. *IEEE J. Quantum Electron.*, QE-25:2464–2468, 1989.

[21] Th. Hofmann, K. Mossavi, F. K. Tittel, and G. Szabo. Spectrally compensated sum-frequency mixing scheme for generation of broadband radiation at 193 nm. *Optics Lett.*, 17:1691–1693, 1992.

[22] S. A. Akhmanov, A. P. Sukhorov, and A. S. Chirkin. Nontationary phenomena and space-time analogy in nonlinear optics. *Sov. Phys. JETP*, 28:748–757, 1969.

[23] A. Stabinis, G. Valiulis, and E. A. Ibragimov. Effective sum frequency pulse compression in nonlinear crystals. *Optics Comm.*, 86:301–306, 1991.

[24] Y. Wang and B. Luther Davies. Frequency-doubling pulse compressor for picosecond high power neodymium laser pulses. *Opt. Lett.*, 17:1459–1461, 1992.

[25] P. Heinz, A. Laubereau, A. Dubietis, and A. Piskarskas. Fiberless two-step parametric compression of sub-picosecond laser pulses. *Lithuanian Phys. Rev.*, 33:314–317, 1993.

[26] A. Umbrasas, J. C. Diels, G. Valiulis, J. Jacob, and A. Piskarskas. Generation of femtosecond pulses through second harmonic compression of the output of a Nd:YAG laser. *Opt. Lett.*, 20:2228–2230, 1995.

[27] A. Umbrasas, J. C. Diels, J. Jacob, and A. Piskarskas. Parametric oscillation and compression in KTP crystals. *Opt. Lett.*, 19:1753–1755, 1994.

[28] J. D. V. Khaydarov, J. H. Andrews, and K. D. Singer. Pulse compression in a synchronously pumped optical parametric oscillator from group-velocity mismatch. *Opt. Lett.*, 19:831–833, 1994.

[29] J. D. V. Khaydarov, J. H. Andrews, and K. D. Singer. 20-fold pulse compression in a synchronously pumped optical parametric oscillator. *Appl. Phys. Lett.*, 65:1614–1616, 1994.

[30] L. Lefort, S.D. Butterworth, Y.P. Svirko, K. Puech, D. C. Hanna, and D.H. Jundt. Generation of fs pulses from order of magnitude pulse compression in a cw synchronously pumped optical parametric oscillator. In *CLEO '98, San Francisco, USA*. OSA, 1998.

[31] Jens Biegert, Vaclav Kubecek, and Jean-Claude Diels. Pulse compression: Type II second harmonic pulse compression. In John G. Webster, editor, *Encyclopedia of Electrical and Electronics Engineering (#17)*, volume 17, pages 446–454. IEEE, 1998.

[32] J. Biegert and J. C. Diels. Compression of pulses of a few optical cycles through harmonic conversion. *Journal of Optical Society B*, 18:1218–1226, 2001.

[33] T. R. Zhang, H. R.Choo, and M. C.Downer. Phase and group velocity matching for second harmonic generation of femtosecond pulses. *Appl. Opt.*, 29:3927–3933, 1990.

[34] P. DiTrapani, A. Andreoni, C. Solcia, P. Foggi, R. Danielius, A Dubietis, and A. Piskarskas. Matching of group velocities in three-wave parametric interaction with femtosecond pulses and application to traveling-wave generators. *J. Opt. Soc. B*, 12:2237–2244, 1995.

[35] A. Mokhtari, A. Chebira, and J. Chesnoy. Subpicosecond fluorescence dynamics of dye molecules. *Journal of the Optical Soc. of Am. B*, B-7:1551–1557, 1990.

[36] T. Elsaesser and M. C. Nuss. Femtosecond pulses in the mid-infrared generated by down conversion of a traveling wave dye laser. *Opt. Lett.*, 16:411–413, 1991.

[37] T. M. Jedju and L. Rothberg. Tunable femtosecond radiation in the mid-infrared for time resolved absorption in semiconductors. *Appl. Opt.*, 27:615–618, 1988.

[38] R. Laenen, H. Graener, and A. Laubereau. Broadly tunable femtosecond pulses generated by optical parametric oscillation. *Opt. Lett.*, 15:971–973, 1990.

[39] D. C. Edelstein, E. S. Wachman, and C. L. Tang. Broadly tunable high repetition rate femtosecond optical parametric oscillator. *Appl. Phys. Lett.*, 54:1728–1730, 1989.

[40] Xianmei Meng, Raphael Quintero, and Jean-Claude Diels. Intracavity pumped optical parametric bidirectional ring laser as a differential interferometer. *Opt. Comm*, 233:167–172, 2004.

[41] A. Jankauskas, A. Piskarskas, D. Podenas, A. Stabinis, and A. Umbrasas. New nonlinear optical methods of powerful femtosecond pulse generation and dynamic interferometry. In Z. Rudzikas, A. Piskarskas, and R. Baltramiejunas, editors, *Proceedings of the V international symposium on Ultrafast Phenomena in Spectroscopy*, pages 22–32, Vilnius, 1987. World Scientific.

[42] G. P. Agrawal. *Nonlinear Fiber Optics*. Academic Press, ISBN 0-12-045142-5, Boston, 1995.

[43] R. R. Alfano, Q. X. Li, T. Jimbo, J. T. Manassah, and P. P. Ho. Induced spectral broadening of a weak ps pulse in glass produced by an intense ps pulse. *Opt. Lett.*, 14:626–628, 1986.

[44] W. Rudolph, J. Krueger, P. Heist, and W. Wilhelmi. Ultrafast wavelength shift of light induced by light. In *ICO-15*, page 1319. SPIE, 1990.

[45] D. Anderson and M. Lisak. Nonlinear asymmetric self phase modulation and self steepening of pulses in long waveguides. *Phys. Rev. A*, 27:1393–1398, 1983.

[46] W. H. Knox, R. L. Fork, M. C. Downer, R. H. Stolen, and C. V. Shank. Optical pulse compression to 8 fs at a 5 kHz repetition rate. *Appl. Phys. Lett.*, 46:1120–1121, 1985.

[47] J. E. Rothenberg and D. Grischkowsky. Observation of the formation of an optical intensity shock and wave breaking in the nonlinear propagation of pulses in optical fibers. *Phys. Rev. Lett.*, 62:531–533, 1989.

[48] R. R. Alfano, editor. *The Supercontinuum Laser Source*. Springer, New York, Berlin, 1989.

[49] A. Zheltikov (Ed.). Special issue on Supercontinuum Generation. *Appl. Phys. B*, 77:143–376, 2003.

[50] R. R. Alfano and S. L. Shapiro. Observation of self-phase modulation and small-scale filaments in crystals and glasses. *Phys. Rev. Lett.*, 24:592–594, 1970.

[51] J. Zeller, J. Jasapara, W. Rudolph, and M. Sheik-Bahae. Spectro-temporal characterization of a fs white light continuum by transient-grating diffraction. *Opt. Commun.*, 185:133–137, 2000.

[52] J. H. Glownia, J. Misewich, and P. P. Sorokin. Ultrafast ultraviolet pump probe apparatus. *J.Opt.Soc.Am.*, B3:1573–1579, 1986.

[53] A. Brodeur and S. L. Chin. Ultrafast white-light continuum generation and self-focusing in transparent condensed media. *J. Opt. Soc. Am. B*, 16:637–650, 2000.

[54] E. Tokunaga, Q. Terasaki, and T. Kobayashi. Induced phase modulation of chirped continuum pulses studied with a femtosecond frequency-domain interferometer. *Optics Lett.*, 18:370–372, 1992.

[55] W. H. Knox, M. C. Downer, R. L. Fork, and C. V. Shank. Amplifier femtosecond optical pulses and continuum generation at 5 kHz repetition rate. *Opt. Lett.*, 9:552–554, 1984.

[56] R. L. Fork, C. H. Cruz, P. C. Becker, and C. V. Shank. Compression of optical pulses to six femtoseconds by using cubic phase compensation. *Opt. Lett.*, 12:483–485, 1987.

[57] J. K. Ranka, R. .S. Windeler, and A. J. Stentz. Visible continuum generation in air-silica microstructure optical fibers with anomalous dispersion at 800 nm. *Optics Lett.*, 25:25–27, 2000.

[58] T. A. Birks, W. J. Wadsworth, and P. S. Russel. Supercontinuum generation in tapered fibers. *Optics Lett.*, 25:1415–1417, 2000.

[59] J. W. Nicholson, A. K. Abeeluck, C. Headley, M. F. Yan, and C. G. Jorgensen. Pulsed and continuous-wave supercontinuum generation in highly nonlinear, dispersion-shifted fibers. *Appl. Phys. B*, 77:211–218, 2003.

[60] J. H. Marburger. Self-focusing. In J. H. Sanders and S. Stendholm, editors, *Progr. Quantum Electron.*, volume 4, pages 35–110. Pergamon, Oxford, 1977.

[61] S. A. Akhmanov, A. P. Sukhorukov, and R. V. Khokhlov. Self focusing and self trapping of intense light beams in a nonlinear medium. *Sov. Phys JETP*, 23:1025–1033, 1966.

[62] S. A. Akhmanov, A. P. Sukhorukov, and R. V. Khokhlov. Development of an optical waveguide in the propagation of light in a nonlinear medium. *Sov. Phys JETP*, 24:198–201, 1967.

[63] Eryk Infeld and George Rowlands. *Nonlinear waves, solitons and chaos*. Cambridge University Press, ISBN 0-521-37937-7, New York, 1990.

[64] V. E. Zakharov and A. B. Shabat. Exact theory of two-dimensional self-focusing and one-dimensional self-modulation of waves in nonlinear media. *Sov. Phys. JETP*, 34:62–69, 1972.

[65] J.-C. Diels, W. Dietel, J. J. Fontaine, W. Rudolph, and B. Wilhelmi. Analysis of a mode-locked ring laser: chirped-solitary-pulse solutions. *J. Opt. Soc. Am. B*, 2:680–686, 1985.

[66] E. T. J. Nibbering, P. F. Curley, G. Grillon, B. S. Prade, M. A. Franco, F. Salin, and A. Mysyrowicz. Conical emission from self-guided femtosecond pulses in air. *Opt. Lett.*, 21:62–64, 1996.

[67] A. Braun, G. Korn, X. Liu, D. Du, J. Squier, and G. Mourou. Self-channeling of high-peak-power femtosecond laser pulses in air. *Optics Lett.*, 20:73–75, 1995.

[68] L. Woeste, S. Wedeking, J. Wille, P. Rairouis, B. Stein, S. Nikolov, C. Werner, S. Niedermeier, F. Ronneberger, H. Schillinger, and R. Sauerbrey. Femtosecond atmospheric lamp. *Laser und Optoelektronik*, 29:51–53, 1997.

[69] B. La Fontaine, F. Vidal, Z. Jiang, C. Y. Chien, D. Comtois, A. Desparois, T. W. Johnston, J.-C. Kieffer, and H. Pepin. Filamentation of ultrashort pulse laser beams resulting from their propagation over long distances in air. *Physics of Plasmas*, 6:1615–1621, 1999.

[70] P. Rairoux, H. Schillinger, S. Niedermeier, M. Rodriguez, F. Ronneberger, R. Sauerbrey, B. Stein, D. Waite, C. Wedeking, H. Wille, L. Woeste, and C. Ziener. Remote sensing of the atmosphere using ultrashort laser pulses. *Appl. Phys. B*, 71:573–580, 2000.

[71] Xin Miao Zhao, Patrick Rambo, and Jean-Claude Diels. Filamentation of femtosecond UV pulses in air. In *QELS, 1995*, volume 16, page 178 (QThD2), Baltimore, MA, 1995. Optical Society of America.

[72] J. Schwarz, P. K. Rambo, J.-C. Diels, M. Kolesik, E. Wright, and J. V. Moloney. Uv filamentation in air. *Optics Comm.*, 180:383–390, 2000.

[73] J. Schwarz and J.-C. Diels. Analytical solution for uv filaments. *Phys. Rev. A*, 65:013806–1—013806–10, 2001.

[74] M. Mlejnek, E. M. Wright, and J. V. Moloney. Dynamic spatial replenishment of femtosecond pulse propagating in air. *Opt. Lett.*, 23:382–384, 1998.

[75] G. Fibich and G. C. Papanicolaou. Self-focusing in the perturbed and unperturbed nonlinear Schrödinger equation in critical dimension. *SIAM J. Applied Math.*, 60:183–240, 1998.

[76] G. Fibich and A. L. Gaeta. Critical power for self-focusing in bulk media and in a hollow waveguides. *Optics Lett.*, 29:1772–1774, 2004.

[77] A. L. Gaeta. Catastrophic collapse of ultrashort pulses. *Phys. Rev. Lett.*, 84:3582–3585, 2000.

[78] N. Aközbek, C. M. Bowden, A. Talebpour, and S. L. Chin. Femtosecond pulse propagation in air: Variational analysis. *Phys. Rev. B*, 61:4540–4549, 2000.

[79] G. Fibich, S. Eisenmann, B. Ilan, and A. Zigler. Control of multiple filamentation in air. *Optics Lett.*, 25:335–337, 2000.

[80] A. Couairon and L. Bergé. Light filaments in air for ultraviolet and infrared wavelengths. *Phys. Rev. Lett*, 88:13503–1—13503–4, 2002.

[81] P. Bennett and A. B. Aceves. Parallel numerical integration of maxwell's full-vector equations in nonlinear focusing media. *Physica D*, 184:352–375, 2003.

[82] Paul Pulaski and Jean-Claude Diels. Demonstration of a nonreciprocal multiple-quantum-well structure leading to unidirectional operation of a ring laser. In *CLEO'98*, page 469, San Francisco, 1998. Optical Society of America.

Chapter 5

Semi-quantum Light-matter Interaction

5.1 Short review of Quantum Mechanics

The purpose of this chapter is not to be a complete course in quantum mechanics, but to provide some "scientific literacy" to the experimentalist to gain understanding of the extensive work that has been made in quantum related ultrashort pulse phenomena.

5.1.1 Wigner distribution and particle-wave duality

We have seen in Chapter 1, Section 1.1.5 that the time bandwidth product is always larger or equal to 1/2 if the pulse durations are defined as the second moment of the field [Eq. (1.65)]. The same applies to the conjugate variables of space and spatial frequency [Eq. (1.64)]. The equalities apply exclusively to the Gaussian shaped field. The leap to the Heisenberg uncertainty relation involves only introducing wave-particle duality. To a particle of energy W corresponds a wave of frequency $\omega = W/\hbar$, hence a bandwidth $\langle \Omega^2 \rangle = \frac{\langle W^2 \rangle}{\hbar^2}$. From this and Eq. (1.65) result the basic energy-time uncertainty:

$$\langle t^2 \rangle \langle W^2 \rangle \geq \frac{\hbar^2}{4}. \tag{5.1}$$

Similarly in space, to a particle with momentum p corresponds a wave with momentum $\hbar k$, hence a bandwidth $\langle k^2 \rangle = \frac{\langle p^2 \rangle}{\hbar^2}$. From this and Eq. (1.64) result the basic momentum-space uncertainty:

$$\langle x^2 \rangle \langle p^2 \rangle \geq \frac{\hbar^2}{4}. \tag{5.2}$$

5.1.2 Uncertainty principle applied to interferometers

The passive interferometer

We can easily apply the latter uncertainty principle to estimate a lower limit of the resolution achievable by a Michelson interferometer terminated by a free mass m [1], assuming all other components perfectly rigid (Fig. 5.1). From the uncertainty relation (5.2) we have: $\Delta p_{min} = \frac{\hbar}{2\Delta x}$, which, over a measurement time τ, leads to a contribution to $\Delta x(\tau)$ of: $\Delta x(\tau) = \frac{\Delta p}{m} \times \tau \rightarrow \frac{\hbar}{2\Delta x} \times \frac{\tau}{m}$, From which we extract the minimum fluctuation:

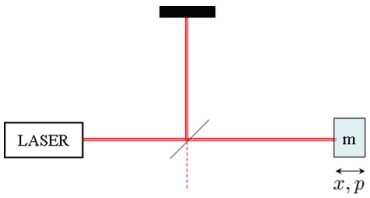

Figure 5.1: Estimating the quantum limit of a Michelson terminated by a free moving mass m

$$\Delta x(\tau) = \sqrt{\frac{\hbar\tau}{2m}}. \tag{5.3}$$

This is the minimum position uncertainty for a free moving mass m for a measurement time τ, hence a lower limit of the resolution of a Michelson.

The active interferometer

The same approach can be applied to the corresponding active-Michelson (intracavity phase interferometer as described in [2]) to estimate a lower resolution limit. In the passive interferometer we want to minimize the uncertainty in the number of photons leaking through the detection port when the interferometer is resonant. In the active interferometer instead, it is directly the phase difference per cavity round-trip that is measured or a frequency $\Delta\nu = \nu_\ell \frac{\Delta(L)}{L}$, where ΔL is the length difference between the two branches of the interferometer, and $\nu_\ell = 2\pi\omega_\ell$ is the optical frequency.

Since the minimum measurement time is one period of measured signal or $\tau = 1/\Delta\nu$, using the result of the previous section for Δx:

$$\Delta\nu = \nu_\ell \frac{\Delta x}{2L} = \nu_{opt} \frac{1}{2L} \sqrt{\frac{\hbar}{2m\Delta\nu}} \tag{5.4}$$

from which we extract the uncertainty in beat frequency $\Delta\nu$:

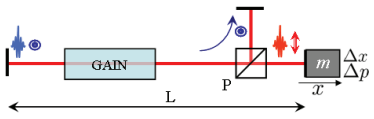

Figure 5.2: Estimating the quantum limit of active Michelson [2] terminated by a free moving mass m

$$\Delta\nu = \left(\frac{\nu_{opt}}{2L}\right)^{2/3} \left(\frac{\hbar}{2m}\right)^{1/3}. \tag{5.5}$$

Taking $\nu_\ell = 10^{15}$ Hz, $m = 1$ kg in a $L = 1$ m laser cavity leads to $\Delta\nu = 0.025$ Hz, close to measurements performed with unstabilized lasers [3]. Both Eqs (5.3)

and (5.5) refer to a quantum limit in the absence of photons. An estimate of the photon noise contribution will be given in Section 5.8.3.

5.1.3 The ubiquitous Schrödinger equation

Particle-wave duality can also be invoked to justify a wave equation, with a wave $\psi(x,t)$ propagating in time and space. Differentiation with respect to t corresponds to multiplication by $i\omega$,

$$i\omega\psi \equiv \frac{\partial\psi}{\partial t}. \tag{5.6}$$

Similarly, differentiation with respect to x implies multiplication by $-ik$, hence

$$-k^2\psi \equiv \frac{\partial^2\psi}{\partial x^2}.$$

Expressing the energy as a function of the momentum,

$$\hbar\omega \equiv \frac{p^2}{2m} \equiv \frac{\hbar^2k^2}{2m},$$

and combining with Eq. (5.6) leads directly to Schrödinger's equation:

$$i\hbar\frac{\partial\psi}{\partial t} = \frac{\hbar^2k^2}{2m}\psi = -\frac{\hbar^2}{2m}\frac{\partial^2\psi}{\partial x^2}. \tag{5.7}$$

More generally in 3 dimensions and including a potential V:

$$i\hbar\frac{\partial\psi}{\partial t} = -\frac{\hbar^2}{2m}\nabla^2\psi + V(\vec{r}). \tag{5.8}$$

The Schrödinger equation is adapted at many sauces, partly fashion, partly to take advantage of the extensive study of this type of equation. For instance, a huge number of phenomena can be represented by a system of N equations of the form (only two equations are considered here):

$$\frac{d}{dt}\begin{pmatrix}\tilde{\mathcal{E}}_1\\ \tilde{\mathcal{E}}_2\end{pmatrix} = \begin{pmatrix}\tilde{r}_{11} & \tilde{r}_{12}\\ \tilde{r}_{21} & \tilde{r}_{22}\end{pmatrix}\begin{pmatrix}\tilde{\mathcal{E}}_1\\ \tilde{\mathcal{E}}_2\end{pmatrix} = \|R\|\cdot\|E\|. \tag{5.9}$$

Multiplying left and right by $i\hbar$ leads to $i\hbar\frac{d}{dt}\|E\| = i\hbar\|R\|\cdot\|E\|$. Substituting $\psi = \|E\|$ and $H = i\hbar\|R\|$ and we are back to the Schrödinger equation:

$$i\hbar\frac{\partial\psi}{\partial t} = H\psi.$$

There are a lot of mathematical analysis, and numerous analytical and numerical methods to solve for the eigenvalues and eigenfunctions of this equation. The eigenvalues are real if H is Hermitian. The energy is conserved if H is anti-Hermitian.

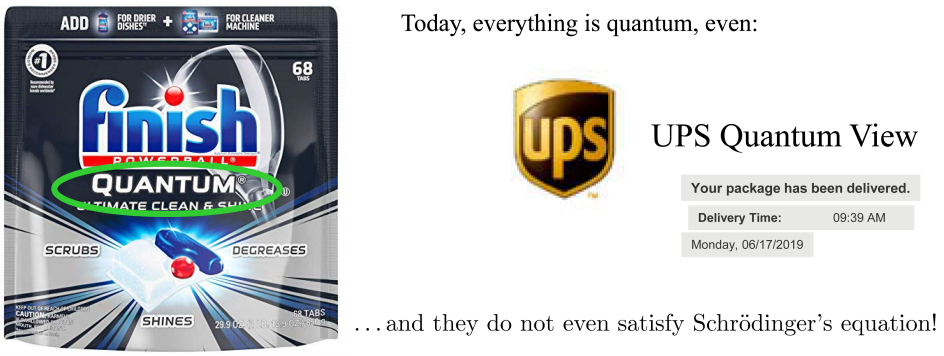

Figure 5.3: Quantum physics is the fashion!

Even Maxwell's equations are converted to Schrödinger's

For a stationary field, the one dimensional Maxwell's propagation equation in the SVEA approximation reduces to:

$$-2ik\frac{\partial \mathcal{E}}{\partial z}+\frac{\partial^2 \mathcal{E}}{\partial x^2}=\frac{\mu_0 \omega c}{2}\mathcal{P}. \tag{5.10}$$

Taking $\mathcal{P}=\epsilon_r\epsilon_0\mathcal{E}$ and re-arranging the terms:

$$\frac{\partial \mathcal{E}}{\partial z}=\frac{1}{2k}\frac{\partial^2 \mathcal{E}}{\partial x^2}+V(x)\mathcal{E}=\frac{1}{2k}\frac{\partial^2 \mathcal{E}}{\partial x^2}+\frac{\omega}{2c}\epsilon\mathcal{E}=\frac{1}{2k}\frac{\partial^2 \mathcal{E}}{\partial x^2}+k[\epsilon_{rr}(x)+i\epsilon_{ri}(x)]\mathcal{E}. \tag{5.11}$$

This is indeed of the form of:

$$i\frac{\partial \psi}{\partial z}=H\psi.$$

5.2 Hermitian versus non-Hermitian "interlude"

There is a point in trying to model various phenomena in the form of Schrödinger equations: there has been extensive studies on how different types of solutions to these equations correlate with properties of the Hamiltonian. A considerable amount of classical optical problems have exploited the wealth of basic information of quantum operators. This justifies including the present section outlining basic properties of the Hamiltonian.

The standard approach to solve Schrödinger-like equations is to look for eigenvalues and eigenfunctions. One of the first postulates of quantum mechanics that students are taught is that all operators must be Hermitian. That is, if $\hat{A}$ is some operator, then $\hat{A}=\hat{A}^\dagger$, where $\dagger$ is the conjugate transpose. The reason for

this restriction is simply that these operators correspond to physical observables which therefore must be real. It is a common linear algebra exercise to show that Hermitian matrices always have real eigenvalues.

Theorem 1. *All Hermitian operators have real eigenvalues*

Proof. If $|\psi\rangle$ is an eigenvector of the operator $\hat{A}$ with eigenvalue a then,

$$\begin{aligned} \hat{A}|\psi\rangle &= a|\psi\rangle \\ \langle\psi|\hat{A}|\psi\rangle &= \langle\psi|a|\psi\rangle \\ &= a\langle\psi|\psi\rangle . \end{aligned} \tag{5.12}$$

Similarly,

$$\begin{aligned} \langle\psi|\hat{A}|\psi\rangle^{\dagger} &= \langle\psi|a|\psi\rangle^{\dagger} \\ \langle\psi|\hat{A}^{\dagger}|\psi\rangle &= a^{*}\langle\psi|\psi\rangle . \end{aligned} \tag{5.13}$$

Since $\hat{A}$ is Hermitian, $\hat{A} = \hat{A}^{\dagger}$, which leads to the conclusion that (5.12)=(5.13). Thus, $a = a^{*}$, which is only true if a is real. □

Other useful properties of Hermitian operators include that they conserve probability through unitary transformations, $U = e^{i\hat{A}}$, and they force an orthonormal basis since their eigenvectors are orthogonal. These seem to be common sense requirements of any operator since any useful theorem should include observables (real eigenvalues), conserve energy (unitary transformations), and create a reasonable space to make calculations (orthogonal eigenvectors).

In 1998, however, Carl Bender showed that some non-Hermitian Hamiltonians (energy operators) can still result in real eigenvalues if they are invariant under parity and time inversion (referred to as $\mathcal{PT}$-symmetry) [4]. In fact, they went on to claim that $\mathcal{PT}$-symmetry is actually the broader requirement of operators i.e. that every Hermitian operator is $\mathcal{PT}$-symmetric.

To make this more concrete, consider the non-Hermitian Hamiltonian used in [4],

$$\hat{H} = \hat{p}^2 + \hat{x}^2(i\hat{x}). \tag{5.14}$$

Inverting space (parity) changes the sign of the momentum and space operators such that the parity operator induces the change,

$$\hat{\mathcal{P}}: \qquad \hat{p} \to -\hat{p} \qquad \text{and} \qquad \hat{x} \to -\hat{x}. \tag{5.15}$$

Inverting time leaves the space operator as is, but negates the imaginary unit, which also causes the momentum operator to flip sign so that the time inversion operator causes,

$$\hat{\mathcal{T}}: \qquad \hat{p} \to -\hat{p} \qquad \text{and} \qquad i \to -i. \tag{5.16}$$

With these rules it follows that the Hamiltonian of Eq. (5.14) is $\mathcal{PT}$-symmetric since,

$$\hat{\mathcal{P}}\hat{\mathcal{T}}\hat{H} = (-\hat{p})^2 + (-\hat{x})^2(-i)(-\hat{x}) = \hat{p}^2 + \hat{x}^2(i\hat{x}) = \hat{H}. \tag{5.17}$$

The Hamiltonian of Eq. (5.14) has been shown by Carl Bender [4] to have purely real eigenvalues, which led to the conclusion that operator Hermiticity is a sufficient but not necessary requirement for quantum mechanical operators. This has birthed the field of Non-Hermitian quantum mechanics, which has been called an analytic continuation of Hermitian quantum mechanics in the same manner that $\hat{H} = \hat{p}^2 + \hat{x}^2(i\hat{x})$ is a continuation of the Hermitian harmonic oscillator Hamiltonian $\hat{H} = \hat{p}^2 + \hat{x}^2$ into the complex plane.

In order to show that *any* $\mathcal{PT}$-symmetric Hamiltonian has real eigenvalues, a few definitions must be made. First, inverting space and time twice should leave the system unchanged,

$$(\hat{\mathcal{P}}\hat{\mathcal{T}})^2 = 1. \tag{5.18}$$

Second, if a Hamiltonian is $\mathcal{PT}$-symmetric, then it must commute with the $\hat{\mathcal{P}}\hat{\mathcal{T}}$ operator,

$$[\hat{H}, \hat{\mathcal{P}}\hat{\mathcal{T}}] = 0. \tag{5.19}$$

Last, $\hat{H}$ and $\hat{\mathcal{P}}\hat{\mathcal{T}}$ operate in the same space. In other words, every eigenfunction of $\hat{H}$ is also an eigenfunction of $\hat{\mathcal{P}}\hat{\mathcal{T}}$,

$$\text{if} \qquad \hat{H}\,|\phi\rangle = E\,|\phi\rangle \qquad \text{then} \qquad \hat{\mathcal{P}}\hat{\mathcal{T}}\,|\phi\rangle = \lambda\,|\phi\rangle\,, \tag{5.20}$$

where E and λ are eigenvalues. This actually isn't a definition, but a postulate as it is not always satisfied. Another operator, C, has since been defined to ensure this is satisfied so that the necessary and sufficient condition of real eigenvalues is that the Hamiltonian commutes with the $\hat{\mathcal{P}}\hat{\mathcal{T}}\hat{C}$ operators [1]. If this is true, then the state is termed to have, "unbroken symmetry", with the opposite resulting in, "broken symmetry".

Theorem 2. *All Hamiltonians exhibiting unbroken $\mathcal{PT}$-symmetry have real eigenvalues.*

Proof. Unbroken $\mathcal{PT}$-symmetry means that Eq. (5.20) must be true. First it must be shown that the eigenvalue of the $\hat{\mathcal{P}}\hat{\mathcal{T}}$ operator, λ, is a pure phase.

$$\hat{\mathcal{P}}\hat{\mathcal{T}}\,|\psi\rangle = \lambda\,|\psi\rangle\,. \tag{5.21}$$

[1] Note that this C operator is not equivalent to the charge operator in particle physics but is denoted with the same symbol due to its similar properties

Now multiply both sides by $\hat{\mathcal{P}}\hat{\mathcal{T}}$ and then take advantage of Eq. (5.18) twice.

$$\begin{aligned}(\hat{\mathcal{P}}\hat{\mathcal{T}})^2|\psi\rangle &= \hat{\mathcal{P}}\hat{\mathcal{T}}\lambda|\psi\rangle \\ |\psi\rangle &= \hat{\mathcal{P}}\hat{\mathcal{T}}\lambda|\psi\rangle \\ |\psi\rangle &= \hat{\mathcal{P}}\hat{\mathcal{T}}\lambda(\hat{\mathcal{P}}\hat{\mathcal{T}})^2|\psi\rangle \end{aligned} \tag{5.22}$$

Because the $\hat{\mathcal{P}}\hat{\mathcal{T}}$ operator switches the sign of the imaginary unit, it is an antilinear operator. This means that $\hat{\mathcal{P}}\hat{\mathcal{T}}\lambda\hat{\mathcal{P}}\hat{\mathcal{T}} = \lambda^*$ and thus,

$$|\psi\rangle = \lambda^*\lambda|\psi\rangle\,. \tag{5.23}$$

Therefore $|\lambda|^2 = 1$ which is only true if $\lambda = e^{i\phi}$ i.e. a pure phase.

Since the Hamiltonian operates in the same space as the $\hat{\mathcal{P}}\hat{\mathcal{T}}$ operator (unbroken symmetry), this allows it to operate on the same eigenvector,

$$\begin{aligned}\hat{H}|\psi\rangle &= a|\psi\rangle \\ \hat{\mathcal{P}}\hat{\mathcal{T}}\hat{H}|\psi\rangle &= \hat{\mathcal{P}}\hat{\mathcal{T}}a|\psi\rangle \\ &= \hat{\mathcal{P}}\hat{\mathcal{T}}a(\hat{\mathcal{P}}\hat{\mathcal{T}})^2|\psi\rangle \end{aligned} \tag{5.24}$$

Taking advantage of the fact the $\hat{H}$ and $\hat{\mathcal{P}}\hat{\mathcal{T}}$ commute allows the LHS to be rearranged and $\hat{\mathcal{P}}\hat{\mathcal{T}}$ to operate on $|\psi\rangle$ such that,

$$\begin{aligned}\hat{H}\hat{\mathcal{P}}\hat{\mathcal{T}}|\psi\rangle &= \hat{\mathcal{P}}\hat{\mathcal{T}}a(\hat{\mathcal{P}}\hat{\mathcal{T}})^2|\psi\rangle \\ \hat{H}\lambda|\psi\rangle &= \hat{\mathcal{P}}\hat{\mathcal{T}}a\hat{\mathcal{P}}\hat{\mathcal{T}}\lambda|\psi\rangle \\ \lambda a|\psi\rangle &= a^*\lambda|\psi\rangle \end{aligned} \tag{5.25}$$

Considering the fact that λ is a phase means that $a = a^*$ i.e. the eigenvalues are real. □

An important observable difference between Hermitian and non-Hermitian systems appears near singularities. A Hermitian singularity is called a diabolical point (DP), where the eigenvalues are degenerate but the eigenvectors remain orthogonal. Non-Hermitian singularities, on the other hand, are termed exceptional points (EPs) and result in a coalescing of both the eigenvalues and eigenvectors. The eigenvectors are not orthogonal and therefore no longer span the space, but split into the complex plane. One area where this new quantum formalism is being employed is in laser systems since they are inherently non-Hermitian due to gain/loss dynamics. The coalescing of the eigenvalues and eigenvectors at the EP has led to many newly observed laser phenomena due to the ability to remove certain allowed modes. The space surrounding the EP singularity is characterized by a square-root

dependence which is being exploited in optics to enhance the sensitivity of many different systems [5–16].

Laser sensor research is one specific field that has attempted to benefit from this new formalism. Typically, laser sensors operate from a diabolical point (for instance zero response for zero input signal), and the quantity to be measured lifts the system out of the singularity linearly. If a laser sensor is placed at an exceptional point, the quantity to be measured lifts the system out of the singularity nonlinearly, which can lead to an enhancement of response of the sensor near an EP.

In order to make this discussion more concrete, let us take a specific example of the laser gyroscope. It has been shown that a mode-locked laser can be represented as a 2-level quantum system [17]. This makes the transition to representing a laser system with the language of Non-Hermitian quantum mechanics straightforward. Consider a single cavity mode-locked laser gyroscope as in Fig. 5.4. There are two counter-propagating electric fields of amplitude $\tilde{\mathcal{E}}_1$ and $\tilde{\mathcal{E}}_2$. The Sagnac phase shift $\Delta\phi$ creates a differential phase shift at each round-trip, such that as the fields are interfered on a detector, a periodic signal ($|\tilde{\mathcal{E}}_1 + \tilde{\mathcal{E}}_2|^2$) at a beat frequency $\Delta\nu = \Delta\phi/(2\pi\tau_{rt})$ is recorded. In the absence of coupling between the fields, the mode equations for the field amplitudes are of the form of Eq. (5.9), which can be put in the form of a Schrödinger equation:

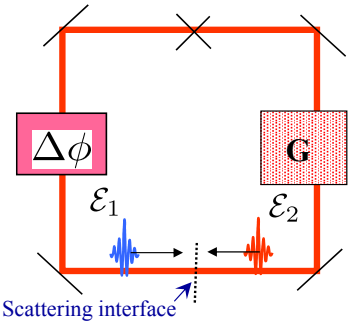

Figure 5.4: Laser gyro topology. Two pulses are counter-circulating in a ring cavity of round-trip time τ_{rt}, experiencing a differential phase shift $\Delta\phi$ at each round-trip.

$$i\frac{d}{dt}\begin{pmatrix}\tilde{\mathcal{E}}_1\\ \tilde{\mathcal{E}}_2\end{pmatrix} = \begin{pmatrix}\Delta/2 & 0\\ 0 & -\Delta/2.\end{pmatrix}\begin{pmatrix}\tilde{\mathcal{E}}_1\\ \tilde{\mathcal{E}}_2\end{pmatrix}. \tag{5.26}$$

The matrix is Hermitian, has eigenvalues $\lambda_\pm = \pm\Delta/2$, and orthogonal eigenvectors, ($[0,1]$ and $[1,0]$), such that the electric field solutions are,

$$\tilde{\mathcal{E}}_{1,2} = \mathcal{E}_{1,2}e^{i\lambda_\pm t}. \tag{5.27}$$

Notice the singularity at $\Delta = 0$. Here the eigenvalues become 0, but the eigenstates remain unchanged since the vectors are not dependent on Δ. This is the definition of a diabolic point. When the two fields are interfered in time, the detector records $|\tilde{\mathcal{E}}_1 + \tilde{\mathcal{E}}_2|^2$ which is a signal oscillating at the beat frequency Δ. The diabolic point is at $\Delta = 0$ with the beat frequency increasing linearly with Δ.

In order to observe an EP, we add a non-conservative coupling S into the two mode equations:

$$i\frac{d}{dt}\begin{pmatrix}\tilde{\mathcal{E}}_1\\ \tilde{\mathcal{E}}_2\end{pmatrix}=\begin{pmatrix}\Delta/2 & iS\\ iS & -\Delta/2.\end{pmatrix}\begin{pmatrix}\tilde{\mathcal{E}}_1\\ \tilde{\mathcal{E}}_2\end{pmatrix}. \tag{5.28}$$

The matrix is non-Hermitian owing to the off-diagonal elements, but $\mathcal{PT}$-symmetric since inverting space and time gives the exact same system. The eigenvalues are $\lambda_{1,2} = \pm\sqrt{(\Delta/2)^2 - S^2}$. Unlike the previous case, the eigenvectors are no longer constant:

$$|\psi_\pm\rangle = \begin{bmatrix} \frac{1}{iS}\left(-\frac{\Delta}{2} \pm \sqrt{\left(\frac{\Delta}{2}\right)^2 - S^2}\right) \\ 1 \end{bmatrix}. \tag{5.29}$$

Combining the eigenvalues and eigenvectors leads to the expression for the electric fields,

$$\tilde{\mathcal{E}}_{1,2} = \mathcal{E}_{1,2}\left[\frac{1}{iS}\left(-\frac{\Delta}{2} \pm \sqrt{\left(\frac{\Delta}{2}\right)^2 - S^2}\right)e^{i\lambda_+ t} + e^{i\lambda_- t}\right]. \tag{5.30}$$

The important part to notice here is that there is a singularity at $\Delta/2 = S$. At this point, which is the exceptional point, there is a coalescing of both eigenvectors and eigenvalues. Notice that if Δ decreases from this point, the system splits into the complex plane. This is an example of broken $\mathcal{PT}$-symmetry. If Δ increases past the exceptional point the system enters an unbroken-symmetry regime and the beat frequency increases from 0 with a square-root dependence, which is well known as the gyroscope response near the dead band [18].

It should be remembered that this approach has been applied to a classical physics problem. Its usefulness is in the utilization of mathematical tools developed for quantum mechanics. More importantly, it helps the researcher in getting support by convincing his sponsor that he is doing "quantum physics".

5.3 From the classical to quantum harmonic oscillator

5.3.1 The mechanical oscillator

The equation of motion for the classical harmonic oscillator is:

$$\frac{dp}{dt} = -k_s q, \tag{5.31}$$

where k_s is the spring constant and kq the restoring force. The momentum p is related to

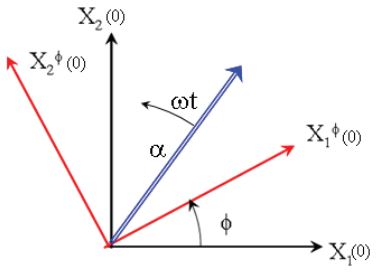

Figure 5.5: The classical state for the field of amplitude α represented in the $X_1(0)X_2(0)$ coordinates.

the displacement q by:

$$m\frac{dq}{dt} = p. \tag{5.32}$$

Elimination of p leads to the second order equation:

$$\frac{d^2q}{dt^2} + \omega_0^2 q = 0, \tag{5.33}$$

where $\omega_0^2 = k_s/m$. The classical harmonic oscillator has the harmonic solution $\alpha(\omega) = \alpha(0)e^{i(\omega t+\phi)}$, which we can write as $\alpha = (Q+iP)/\sqrt{2}$. $Q = (\alpha+\alpha^*)/\sqrt{2}$ and $P = (\alpha-\alpha^*)/i\sqrt{2}$ represent two quadratures of the oscillation. Traditional notations for the two quadratures [1] are $Q \to X_1$ and $P \to X_2$. More generally, one defines the quadrature with respect to some phase Φ:

$$\begin{aligned} X_1^\phi &= \frac{\alpha e^{i\phi} + \alpha^* e^{-i\phi}}{\sqrt{2}} \\ X_2^\phi &= \frac{\alpha e^{i\phi} - \alpha^* e^{-i\phi}}{i\sqrt{2}} \\ &\to \alpha = \frac{X_1^\phi + iX_2^\phi}{\sqrt{2}} e^{-i\phi}. \end{aligned} \tag{5.34}$$

The Hamiltonian is the sum of the kinetic and potential energies:

$$H = \frac{1}{2}\left(\frac{p^2}{m} + kq^2\right). \tag{5.35}$$

5.3.2 The harmonic oscillator — connection with optics

The classical Maxwell equations can be expressed in terms of a scalar potential Φ and a vector potential A.

$$B = \nabla \times A \tag{5.36}$$

$$E = -\nabla\Phi - \frac{\partial A}{\partial t}. \tag{5.37}$$

Coulomb gauge:

$$\nabla \dot{A} = 0$$

The scalar potential satisfies then Poisson's equation:

$$\nabla\Phi = \frac{1}{4\pi\epsilon}\int \frac{\rho(r')}{|r-r'|} d^3r. \tag{5.38}$$

In the absence of charges, one derives for A the wave equation:

$$\nabla^2 A - \frac{n^2}{c^2}\frac{\partial^2 A}{\partial t^2} = -\mu_0 J. \tag{5.39}$$

In vacuum or linear dielectric, we expand the vector potential A in a set of orthogonal solutions of the wave equation, in (periodic) boundary conditions:

$$A = \Sigma_k A_k \left(e^{-ik.r} + c.c.\right), \tag{5.40}$$

where:

$$k_x = \frac{2\pi N_x}{L_x},\ \frac{2\pi N_y}{L_y},\ \frac{2\pi N_z}{L_z}.$$

The Coulomb gauge condition is satisfied if $k \cdot A = 0$. The Fourier components A_k must satisfy the wave Eq. (5.39):

$$k^2 A_k(t) + \frac{n^2}{c^2}\frac{\partial^2 A_k(t)}{\partial t^2} = 0 \tag{5.41}$$

which can be re-written as:

$$\frac{\partial^2 A_k(t)}{\partial t^2} + \omega_k^2 A_k(t) = 0, \tag{5.42}$$

which is reminiscent of Eq. (5.33). From Eqs (5.37) and (5.36):

$$E_k = -i\omega_k A_k e^{i(\omega_k t - k.r)} \tag{5.43}$$

$$B_k = ikA_k e^{i(\omega_k t - k.r)} \tag{5.44}$$

The electromagnetic energy in the mode k occupying a volume V_k is: $W_k = \epsilon_0 E_k^2 V_k/2 = \epsilon\omega_k^2 V_k |A_k|^2/2$, which we use to define a dimensionless vector potential $\mathcal{A}_k$:

$$\mathcal{A} = \sqrt{\frac{\epsilon_0 \omega_k^2 V_k}{2W_k}} A_k \tag{5.45}$$

At this point we are in perfect analogy with the classical mechanical oscillator, and the transition to quantum mechanics applies equally to both systems.

5.3.3 Going Quantum

Background

The transition to quantum mechanics consists simply in replacing the observables by operators: $p \to \hat{p}$ and $q \to \hat{q}$. The reader familiar with Poisson brackets will

know that Eqs. (5.31) and (5.32) can be derived directly from the Hamiltonian. In quantum mechanics, the Poisson brackets are replaced by the commutators. We know the Heisenberg uncertainty principle applies to position-momentum, which implies that the commutator (demonstration in Appendix E):

$$[\hat{q}, \hat{p}] = i\hbar. \tag{5.46}$$

This is satisfied if:

$$\hat{p} = -i\hbar \frac{\partial}{\partial \hat{q}} \tag{5.47}$$

Indeed:

$$[\hat{q}, \hat{p}] = \hat{q}\hat{p} - \hat{p}\hat{q} = -i\hbar \left(\hat{q} \frac{\partial}{\partial \hat{q}} - \frac{\partial}{\partial \hat{q}} \hat{q} \right) = i\hbar. \tag{5.48}$$

These products are operators on function of $\hat{q}$. Derivatives with respect to $\hat{q}$ on powers of $\hat{q}$ act like normal derivatives. Supposing the operator (5.48) is applied to the term $c_j q^j$ of a Taylor expansion of a function $\psi(q)$:

$$-i\hbar c_j \left(\hat{q} \frac{\partial}{\partial \hat{q}} - \frac{\partial}{\partial \hat{q}} \hat{q} \right) q^j = -i\hbar c_j \left(\hat{q}\, j q^{j-1} - (j+1) q^j \right) = -i\hbar \left(j q^j - (j+1) q^j \right) = i\hbar c_j q^j. \tag{5.49}$$

The equations of motion for the (quantum) harmonic oscillator are:

$$\frac{d\hat{q}}{dt} = -\frac{i}{\hbar}[\hat{q}, \hat{H}] = \frac{i}{m}\hat{p}. \tag{5.50}$$

where the Hamiltonian was defined in Eq. (5.35), and

$$\frac{d\hat{p}}{dt} = -\frac{i}{\hbar}[\hat{p}, \hat{H}] = -k\hat{q}. \tag{5.51}$$

Normalized variables:

$$\hat{Q} = \sqrt{\frac{k}{\hbar\omega_0}}\hat{q} \quad \text{and} \quad \hat{P} = -i\frac{\partial}{\partial \hat{Q}}. \tag{5.52}$$

The commutator of these two operators is i (and not $i\hbar$). This implies for the uncertainty relation $\langle \hat{Q}^2 \rangle \langle \hat{P}^2 \rangle \geq 1/4$. Substituting in the Hamiltonian:

$$\hat{H} = \frac{\hbar\omega_0}{2}\left(\hat{Q}^2 + \hat{P}^2 \right) = \frac{\hbar\omega_0}{2}\left(\hat{Q}^2 - \frac{\partial^2}{\partial \hat{Q}^2} \right). \tag{5.53}$$

An essential difference with the classical treatment is that we can no longer write $\left(\hat{Q}^2 + \hat{P}^2 \right) = \left(\hat{Q} - i\hat{P} \right)\left(\hat{Q} + i\hat{P} \right)$. Indeed, applying the same argument as in the derivation of Eq. (5.48), we find that the commutator $[\hat{Q}, \hat{P}] = i$. These new normalized

variables allow for a straightforward connection between the mechanical harmonic oscillator and optics, as will be shown in the next section. The Heisenberg equations of motion are now:

$$\begin{aligned} \frac{d\hat{P}}{dt} &= -\frac{i}{\hbar}[\hat{P},\hat{H}] = -\omega_0\hat{Q} \\ \frac{d\hat{Q}}{dt} &= -\frac{i}{\hbar}[\hat{Q},\hat{H}] = \omega_0\hat{P}. \end{aligned} \tag{5.54}$$

In the classical treatment, one of the two observable is eliminated, leading to a second order differential equation. Instead, the following transformation leads to two uncoupled differential equations:

$$\begin{aligned} \hat{A} &= \frac{1}{\sqrt{2}}(\hat{Q}+i\hat{P}) \\ \hat{A}^\dagger &= \frac{1}{\sqrt{2}}(\hat{Q}-i\hat{P}) \end{aligned} \tag{5.55}$$

In these new operators, the Heisenberg equations of motion become:

$$\begin{aligned} \frac{d\hat{A}}{dt} &= -i\omega_0\hat{A} \\ \frac{d\hat{A}^\dagger}{dt} &= i\omega_0\hat{A}^\dagger \end{aligned} \tag{5.56}$$

since $[\hat{Q},\hat{P}] = i$, we have also the commutation relations $[\hat{A},\hat{A}^\dagger] = 1$. More importantly, we have:

$$\hat{A}^\dagger\hat{A} = \frac{1}{2}\left[\hat{Q}-i\hat{P}\right]\left[\hat{Q}+i\hat{P}\right] = \left[\hat{Q}^2+\hat{P}^2+i\hat{Q}\hat{P}-i\hat{P}\hat{Q}\right] \tag{5.57}$$

Since $\hat{Q}^2+\hat{P}^2 = \frac{2}{\hbar\omega}H$ and $i\hat{Q}\hat{P}-i\hat{P}\hat{Q} = -1$, the Hamiltonian is:

$$\boxed{\hat{H} = \hbar\omega_0\left(\hat{A}^\dagger\hat{A}+\frac{1}{2}\right).} \tag{5.58}$$

Eigenstates: The Schrödinger equation with the Hamiltonian (5.53) is:

$$\boxed{i\hbar\frac{d}{dt}\psi = \hat{H}\psi = E\psi = \frac{\hbar\omega_0}{2}\left(\hat{Q}^2+\hat{P}^2\right)\psi = \frac{\hbar\omega_0}{2}\left(\hat{Q}^2-\frac{\partial^2}{\partial\hat{Q}^2}\right)\psi.} \tag{5.59}$$

The solutions are the Hermite Gaussian polynomials with the eigenvalues:

$$E_n = \hbar\omega_0(n+\frac{1}{2}) \tag{5.60}$$

Associating with Eq. (5.58) leads to identifying $\hat{A}^\dagger\hat{A}$ as the number operator. It can be shown [19] that the operator $\hat{A}^\dagger$ applied to the eigenfunction ψ_n transforms it into the eigenfunction ψ_{n+1}, making it the "creator" operator. Similarly, $\hat{A}$ is the annihilator operator.

We have thus:

$$\begin{aligned} \hat{A}|n\rangle &= \sqrt{n}|n-1\rangle \\ \hat{A}^\dagger|n\rangle &= \sqrt{n+1}|n+1\rangle. \end{aligned} \tag{5.61}$$

The ground state $|0\rangle$ is defined as zero-photon number $\langle|\hat{A}^\dagger\hat{A}|\rangle = 0$ by:

$$\hat{A}|0\rangle = 0|0\rangle. \tag{5.62}$$

Uncertainty relations for P and Q

From the definitions (5.55) we extract the in-phase and quadrature components[2]:

$$\begin{aligned} \hat{Q} &= \frac{1}{\sqrt{2}}(\hat{A}^\dagger + \hat{A}) \\ \hat{P} &= \frac{1}{\sqrt{2}}(\hat{A}^\dagger - \hat{A}) \end{aligned} \tag{5.63}$$

which have as commutator:

$$[Q,P] = \frac{1}{2i}\left\{(\hat{A}^\dagger + \hat{A})(\hat{A}^\dagger - \hat{A}) - (\hat{A}^\dagger - \hat{A})(\hat{A}^\dagger + \hat{A})\right\} = \frac{1}{2i}\left\{2[\hat{A},\hat{A}^\dagger]\right\} = i. \tag{5.64}$$

The commutator leads directly to an uncertainty relation (demonstration in Appendix E)

$$\langle\hat{P}^2\rangle\langle\hat{Q}^2\rangle \geq \frac{1}{4}. \tag{5.65}$$

Vacuum state

The ground state or vacuum state defined in Eq. (5.62) is a minimum uncertainty state. The expectation value of both quadratures of the field is zero: $\langle 0|\hat{A}^\dagger + \hat{A}|0\rangle = 0$, and $\langle 0|\hat{A}^\dagger - \hat{A}|0\rangle = 0$. The number of photons in the ground state is also zero:

$$\langle 0|\hat{A}^\dagger\hat{A}|0\rangle = 0. \tag{5.66}$$

However, for the same operator product in reverse order:

$$\langle 0|\hat{A}\hat{A}^\dagger|0\rangle = 1, \tag{5.67}$$

[2]The description of a harmonic function presuppose always a phase reference. Given a classical amplitude at time $t = 0$ $\alpha(0) = Q(0) + iP(0)$, $\alpha(t) == \alpha(0)\exp(i\omega t) == [Q(0)\cos\omega t - P(0)\sin\omega t] + i[P(0)\cos\omega t + Q(0)\sin\omega t] = Q(t) + iP(t)$ $Q = (\alpha + \alpha^*)/\sqrt{2}$ and $P(\alpha - \alpha^*)/\sqrt{2}$ are the in-phase and $\pi/2$ out of phase components of the oscillation, traditionally referred to as the "quadrature" components.

which relates to the non-zero commutator (5.64). Even in the ground state, there is a contribution to the mean square field.

Coherent states

The classical coherent states have a complex phase space amplitude $\alpha = Q + iP$ (normalized units). One can show that the states of the quantum harmonic oscillator most closely resembling their classical counterparts are eigenstates of the complex amplitude operator $\hat{A}$:

$$\hat{A}|\alpha\rangle = \alpha|\alpha\rangle. \tag{5.68}$$

These states are called "coherent states". The expectation values of observables are the classical values. For instance:

$$\langle\alpha|\hat{Q}|\alpha\rangle = \langle\alpha|\frac{\hat{A}+\hat{A}^\dagger}{2}|\alpha\rangle = \frac{\alpha+\alpha^*}{\sqrt{2}} = Q; \tag{5.69}$$

the same applying to $\hat{P}$.

Using the number states as a basis, we can write for the coherent states:

$$|\alpha\rangle = \sum_n c_n|n\rangle \tag{5.70}$$

Using the coherent state definition Eq. (5.68):

$$\hat{A}|\alpha\rangle = \sum_n c_n\hat{A}|n\rangle = \sum_n c_n\sqrt{n}|n-1\rangle \tag{5.71}$$

Projecting both sides of this equation on a number state $\langle m|$, one derives the recursion equation $c_{m+1} = (\alpha/\sqrt{m+1})c_n$, which, after normalization leads to the probability distribution of occupation number n:

$$P_n = |C_n|^2 = e^{-|\alpha|^2}\frac{(|\alpha|^2)^n}{n!} = e^{-\langle n\rangle}\frac{(\langle n\rangle)^n}{n!} \tag{5.72}$$

which is the Poisson distribution of classical light, with an average photon number $\langle n\rangle$, and a standard deviation of $\sqrt{\langle n\rangle} = |\alpha|$. This rms (root mean square) deviation is known as the shot noise. It represents the minimum uncertainty for a perfectly stable classical intensity due to quantum randomness at the detection. For a large number of photons, the distribution is almost Gaussian.

The coherent state $|\alpha\rangle$ is represented in Fig. 5.6 in its coordinates, using the notations of Eqs. (5.34) and Fig. 5.5. We have $\hat{A} = (\hat{X}_1 + i\hat{X}_2)/\sqrt{2}$, $[\hat{X}_1, \hat{X}_2] = i$, $\langle\Delta\hat{X}_1^2\Delta\hat{X}_2^2\rangle \geq 1/4$ for any quadrature (hence $\langle\Delta\hat{X}_1^{\phi 2}\Delta\hat{X}_2^{\phi 2}\rangle \geq 1/4$. The vector OM has the length $|\alpha|$, which, according to Poisson' statistics, is also then minimum photon number uncertainty:

$$\pm\Delta N = \pm\sqrt{\langle N\rangle} = |\alpha| = \sqrt{Q^2+P^2} = OM \tag{5.73}$$

It has been shown in Section 1.1.5 that the minimum uncertainty corresponds to a Gaussian, or a circle of radius 1/2 in the $X_1(0)X_2(0)$ coordinates. From Fig. 5.6:

$$\Delta\varphi = \frac{\text{circle radius}}{OM} = \frac{1}{2} \times \frac{1}{\Delta N}. \tag{5.74}$$

This is a simple (albeit not rigorous) demonstration that the uncertainty relation applies not only to the quadratures of the field but also on phase-photon number:

$$\Delta N \Delta\varphi \geq \frac{1}{2}. \tag{5.75}$$

A more rigorous demonstration is given in Appendix E.

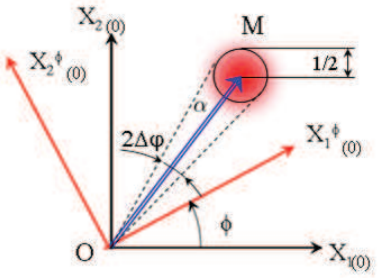

Figure 5.6: The classical state for the field of amplitude α represented in the $X_1(0)X_2(0)$ coordinates.

5.4 Squeezing

The concept of squeezing is as diverse as that of "quantum", and the question "what does the word "squeezing" evoke for you?" should make the day of a psychiatrist.

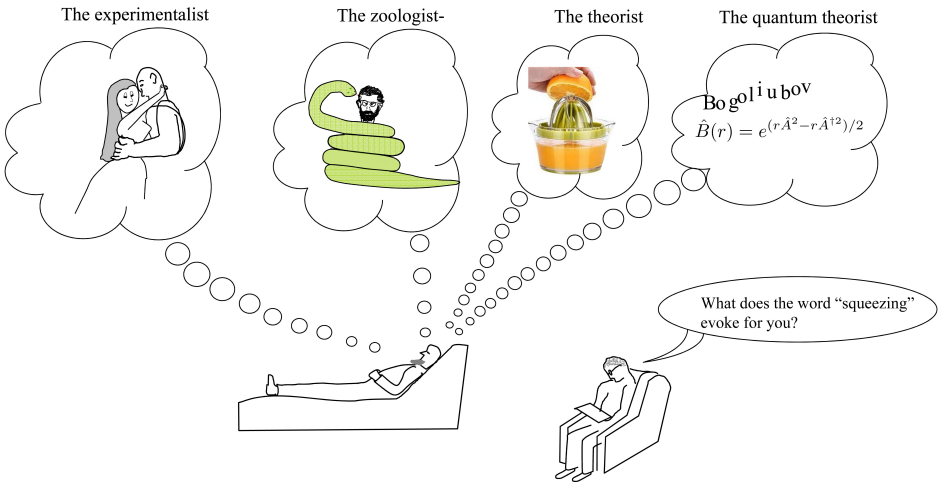

A squeezed state is defined as a state at the minimum uncertainty of the harmonic oscillator, but with unequal variances in conjugate quadrature. A few examples of squeezed states are shown in Fig. 5.7. The dispersion is minimal along X_2 for M_1, along X_1 for M_2, along the phase φ for M_3 and the amplitude for M_4.

5.4.1 Squeezed vacuum states

Let us consider the unitary transformation:

$$\hat{B}(r) = e^{(r\hat{A}^2 - r\hat{A}^{\dagger 2})/2}. \tag{5.76}$$

It can be shown (through Taylor series expansion), that:

$$\hat{B}^\dagger \hat{A} \hat{B} = \cosh(r)\hat{A} - \sinh(r)\hat{A}^\dagger = \mu\hat{A} - \nu\hat{A}^\dagger. \tag{5.77}$$

This transformation is known as the Bogoliubov transformation [20]. The hyperbolic functions implies that the coefficients μ and ν are not arbitrary, but related by the constraint that $|\mu|^2 - |\nu|^2 = 1$. This operator appears in the derivation of phase sensitive amplification by the degenerate optical parametric amplifier, as will be described in Section 5.4.4. If we apply this transformation to the in-phase and in quadrature operators $\hat{X}_1$ and $\hat{X}_2$ we find:

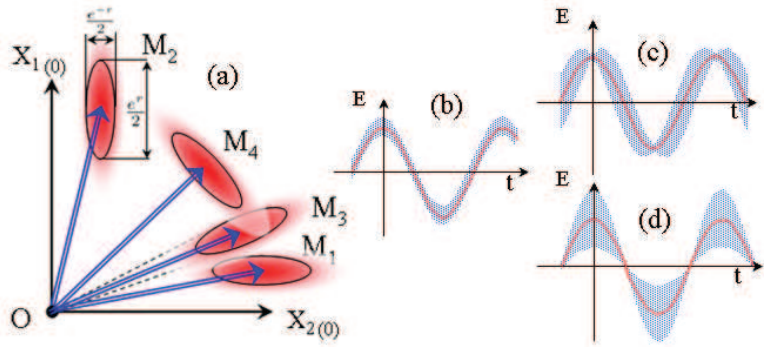

Figure 5.7: (a) Examples of squeezing along quadrature components (M_1 and M_2) or phase and amplitude (M_3) and (M_4). With the phase space rotating at the optical frequency ω, the projection of the quantum field onto a fixed axis corresponds to the electric field as shown in (b), (c) and (d). In these graphs the solid red lines are the expectation value of the electric field, and the blue dotted patterned regions represents the uncertainty in the electric field. (b) corresponds to a weak coherent state. (c) is for a state squeezed in amplitude, and (d) in phase.

$$\begin{aligned}
\hat{B}^\dagger \hat{X}_1 \hat{B} &= \frac{1}{\sqrt{2}}\left(\hat{B}^\dagger \hat{A}\hat{B} + \hat{B}^\dagger \hat{A}^\dagger \hat{B}\right) \\
&= \frac{1}{\sqrt{2}}\left[(\cosh r)\hat{A} - (\sinh r)\hat{A}^\dagger + (\cosh r)\hat{A}^\dagger - (\sinh r)\hat{A}\right] \\
&= (\cosh r - \sinh r)\left(\frac{\hat{A}+\hat{A}^\dagger}{\sqrt{2}}\right) = e^{-r}\hat{X}_1. \qquad (5.78)
\end{aligned}$$

The same derivation leads to:

$$\hat{B}^\dagger(r)\hat{X}_2\hat{B} = e^{r}\hat{X}_2. \qquad (5.79)$$

Applying the operator $\hat{B}$ to the vacuum state $|0\rangle$, one creates a new vacuum state $|0_r\rangle = \hat{B}|0\rangle$. The mean square deviation for the quadratures of that transformed vacuum state are:

$$\begin{aligned}
\langle 0_r|\Delta\hat{X}_1^2|0_r\rangle &= \langle 0_r|\hat{X}_1^2|0_r\rangle = \langle 0|(\hat{B}^\dagger\hat{X}_1\hat{B})^2|0\rangle = e^{-2r}\langle 0|\hat{X}_1^2|0\rangle = \frac{e^{-2r}}{4} \\
\langle 0_r|\Delta\hat{X}_2^2|0_r\rangle &= e^{2r}\langle 0|\hat{X}_2^2|0\rangle = \frac{e^{2r}}{4}. \qquad (5.80)
\end{aligned}$$

If $\Delta X_1 = e^{-r}/2$, then $\Delta X_2 = e^{r}/2$, and we have indeed a minimum uncertainty state $\Delta\hat{X}_1\Delta\hat{X}_2 \geq 1/4$. r is known as the squeezing parameter (Fig. 5.7). For a vacuum state, the expectation values of $\hat{A}$ satisfy $\langle|\hat{A}|^2\rangle = \langle|\hat{A}^\dagger|^2\rangle = \langle\hat{A}^\dagger\hat{A}\rangle = 0$ and $\langle\hat{A}\hat{A}^\dagger\rangle =$

1. Squeezed vacuum contains photons, as illustrated in Fig. 5.8(a). The photon number in the squeezed state is:

$$\langle|\hat{B}^\dagger \hat{B}|\rangle = \langle|(\mu^* \hat{A}^\dagger - \nu^* \hat{A})(\mu \hat{A} - \nu \hat{A}^\dagger)|\rangle = |\nu|^2. \tag{5.81}$$

Only an even photon number is seen in Fig. 5.8(a). This is a direct consequence of the definition of the operator $\hat{B}$ in Eq. (5.76) which involves only squared annihilation and creation operators. Squeezed vacuum shows a periodic variation of fluctuations as a function of the quadrature phase ϕ, as illustrated in Fig. 5.8(b).

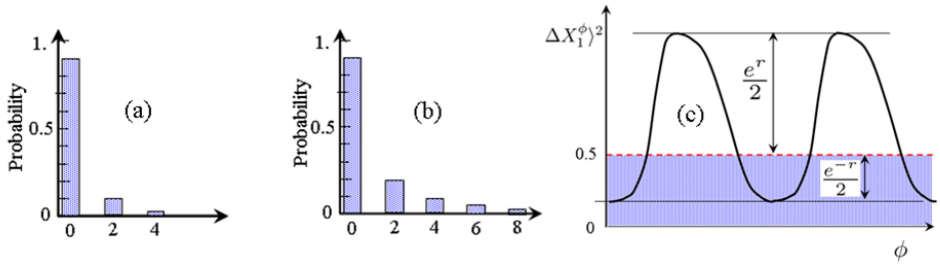

Figure 5.8: (a) Photon number probability of squeezed vacuum for $r = 0.5$, $\alpha = 0$. (b) Photon number probability of squeezed vacuum for $r = 1$, $\alpha = 0$. (c) variation of fluctuations as a function of the quadrature phase ϕ. The shaded area indicates the "shot noise" level.

5.4.2 Measuring squeezed states

Since squeezed light has phase dependent properties, the detection should be based on interference. The simplest example is that of homodyne detection using a single detector and a beam splitter to combine the light to be analyzed with a strong local oscillator [Fig. 5.9(a)]. The field amplitude sent to the detector is $\mathcal{E}_{out} = \tilde{t}\mathcal{E} + \tilde{r}\mathcal{E}_L$ where $\mathcal{E}$ is the input field and $\mathcal{E}_L$ the local oscillator. We have the well known property that the phase upon reflection and transmission are $\pi/2$ from each others (see Appendix A). For the quantized fields:

$$\hat{A}^\dagger_{out}\hat{A}_{out} = |t|^2 \hat{A}^\dagger \hat{A} + |r|^2 \hat{B}^\dagger \hat{B} + \tilde{t}^* \tilde{r} \hat{A}^\dagger \hat{B} + \tilde{t}\tilde{r}^* \hat{A}\hat{B}^\dagger. \tag{5.82}$$

Taking the local oscillator to be a coherent state $\beta_L|\exp(i\phi_l)$, the average number of output photons is:

$$\langle \hat{N}_{out} \rangle = \hat{A}^\dagger_{out}\hat{A}_{out} = |t|^2\langle \hat{N} \rangle + |r|^2|\beta_L|^2 + 2|\beta_L||t||r|\langle \hat{A}(\phi_L + \frac{\pi}{2})\rangle, \tag{5.83}$$

where

$$\langle \hat{A}(\phi) \rangle = \frac{\hat{A}e^{-i\phi} + \hat{A}^{\dagger}e^{i\phi}}{2}. \tag{5.84}$$

By calculating the fluctuations $\langle \Delta \hat{N}^2_{out} \rangle = \langle \hat{N}^2_{out} \rangle - \langle \hat{N}_{out} \rangle^2$, one finds that the output fluctuations are the sum of the shot noise of the local oscillator reflected by the beam splitter, and the transmitted quadrature fluctuations from the input. The shot noise contribution can be made negligible if $|r| \ll |t|$, while having an intense local oscillator such that $|r| * 2|\beta_L|^2 \gg |t|^2 \langle \hat{N} \rangle$. Then:

$$\langle \Delta \hat{N}^2_{out} \rangle = 4|\beta_L|^2 |t|^2 |r|^2 \langle \Delta \hat{X}^2(\phi + \frac{\pi}{2}) \rangle. \tag{5.85}$$

For a squeezed input, as a function of the phase of the local oscillator, the noise fluctuations at the detector will follow the pattern of Fig. 5.8(c).

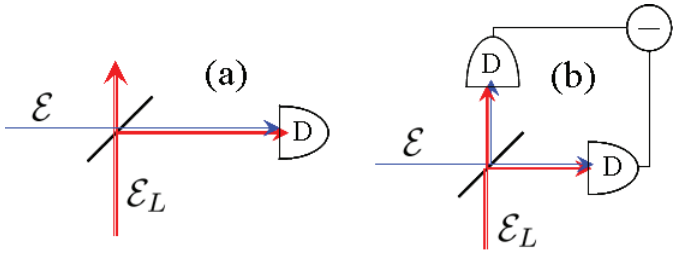

Figure 5.9: (a) Homodyne detection with a single detector. The beam splitter has a high transmission, low reflectivity. (b) Homodynedetection with a 50/50 beam splitter, and differential detection.

Homodyne detection can also be made with a 50/50 beam splitter and two detectors. From the preceding discussion, it is clear that the fluctuations of the coherent local radiation are subtracted out between the two detectors. If the input radiation is squeezed, there is a $\Delta\pi/2$ phase difference between the two arms. The phase dependence of the difference signal seen by the two detector is as in Eq. (5.83), and, as function of the phase of the local oscillator, follow the pattern of Fig. 5.8(c).

5.4.3 Squeezed states and shot noise in a passive interferometer

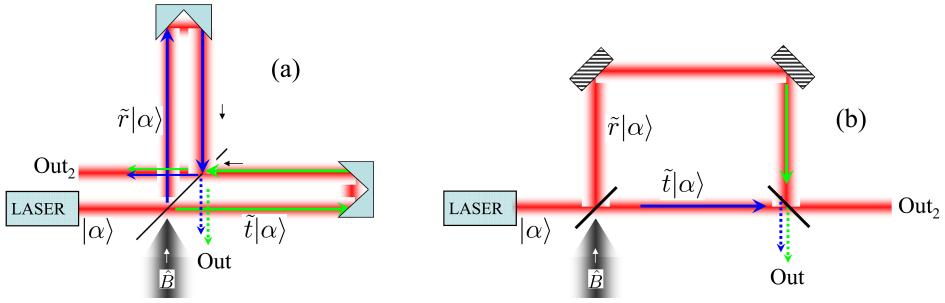

Figure 5.10: Passive Michelson (a) and Mach Zehnder (b) interferometers. We assume perfectly balanced interferometers operating close to destructive interference at the output marked *out*; constructive at output marked out_2 (dotted lines). The laser is assumed to produce a perfect coherent state $|\alpha\rangle$. In both cases there is a vacuum state input $\hat{B}$.

The first application of squeezing was to improve the detection of a Michelson Interferometer beyond the shot noise limit [1]. In the interferometers sketched in Fig. 5.10, a strong coherent field $|\alpha\rangle$ is split into two arms by a beam splitter of complex field reflectivity $\tilde{r}$ and transmissivity $\tilde{t}$ which are orthogonal in phase (cf. Appendix A), implying $r^2 - t^2 = 1$ in the case of 50/50 beam splitters. Therefore if the two arms of the interferometer are exactly equal, destructive interference occurs towards out_2, and constructive interference towards the output port (dotted lines in the figure). We will assume that the optical paths are adjusted for destructive interference towards the output ports, and $|r| = |t| = 1/\sqrt{2}$. Let us consider, in addition to the annihilation operator $\hat{A}$ for the coherent field, an input $\hat{B}$ entering from the output ports. The interfering modes at the output lead to:

$$\hat{B}_{out} = \left(\tilde{r}\hat{A} + \tilde{t}\hat{B}\right)\tilde{t} - \left(\tilde{t}\hat{A} + \tilde{r}\hat{B}\right)\tilde{r} = (\tilde{t}^2 - \tilde{r}^2)\hat{B} = \hat{B}. \tag{5.86}$$

Let us next consider that the two arms of the interferometers are slightly unequal, with the green arrow beam (in Figure 5.10) reaching an output plane with a phase φ_g, and the blue arrow beam with a phase φ_b. The phase difference $\varphi = \varphi_b - \varphi_g$ is

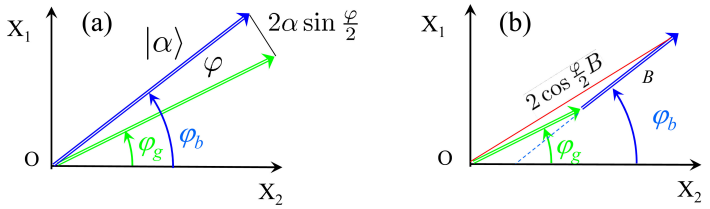

Figure 5.11: Phasor diagram.

small. It is easy to see from the phasor diagram of Fig. 5.11 that the interference at the output is:

$$\begin{aligned}\hat{B}_{out} &= \frac{1}{\sqrt{2}}\left[(\hat{A}+\hat{B})e^{i\varphi_b} - (\hat{A}+\hat{B})e^{i\varphi_g}\right] \\ &= \frac{1}{2}\left[2i\sin\frac{\varphi}{2}\hat{A} + 2\cos\frac{\varphi}{2}\hat{B}\right]e^{i(\varphi_b+\varphi_g)/2}. \end{aligned} \tag{5.87}$$

A photodetector at the output measures the photon number, which is $\langle\hat{B}^\dagger\hat{B}\rangle$. The number operator at the output is:

$$\hat{B}^*_{out}\hat{B}_{out} = \sin^2\frac{\varphi}{2}\hat{A}^\dagger\hat{A} + \cos^2\frac{\varphi}{2}\hat{B}^\dagger\hat{B} - i\sin\frac{\varphi}{2}\cos\frac{\varphi}{2}(\hat{A}^\dagger\hat{B} - \hat{B}^\dagger\hat{A}). \tag{5.88}$$

The first term on the right hand side is the classical signal (φ small). If the input $\hat{B}$ is a standard vacuum state, the photon number $\hat{B}^\dagger\hat{B}$ is zero. The third term is the interference between the vacuum state input and the classical state of the laser. The expectation value of the square of the last term in Eq. 5.88 is (derivation in Appendix E):

$$\begin{aligned}\langle(\hat{A}^\dagger\hat{B} - \hat{B}^\dagger\hat{A})^2\rangle &= \langle N\rangle\langle(\hat{B}e^{-i\phi} - \hat{B}^\dagger e^{i\phi})^2\rangle - \langle\hat{B}^\dagger\hat{B}\rangle \\ &= 4\langle\hat{N}\rangle\langle\Delta\hat{B}_2^2\rangle - \langle\hat{N}_b\rangle. \end{aligned} \tag{5.89}$$

Here, $\hat{N}$ and $\hat{N}_b$ are the number operators of the coherent input and vacuum input, respectively, and $\Delta\hat{B}_2 = (i/\sqrt{2})(\hat{B}^\dagger - \hat{B})$ is the phase quadrature of the vacuum input. In the case of a normal vacuum input (un-squeezed), the photon number is zero ($\langle\hat{N}_b\rangle = 0$) and the expression (5.89) reduces to $4\langle\hat{N}\rangle\langle\Delta\hat{B}_2^2\rangle = 4\langle\hat{N}\rangle\times(1/4) = \langle\hat{N}\rangle$). The shot-noise limit for the detection of a coherent signal of N photons is $\sqrt{N}$. Even though we assumed a perfect Michelson where even the correlated fluctuations in the two arms are correlated and cancel out at the output, the introduction of the vacuum state at the output port returns the same basic uncertainty in the measurement. If the vacuum input were squeezed, such that $\langle\Delta\hat{B}_2^2\rangle < 1/4$, the expression (5.89) reduces to less than $\langle\hat{N}\rangle$. In the case of squeezed vacuum, we have also that $\langle\hat{N}_b\rangle > 0$.

5.4.4 Producing squeezed states

Classical Optical Parametric Amplifier (OPA)

Non-degenerate OPA

Amplifiers based on population inversion provide phase insensitive gain, in contrast to Optical Parametric Amplifiers (OPA). In this Chapter, instead of the

electric field, we will use the fields normalized to the square of the frequencies $\tilde{\mathcal{E}}_i/\sqrt{\omega_i} = F_i$. Let us consider first the case of the non-degenerate OPA, in which a pump $\tilde{\mathcal{E}}_p$ at ω_p amplifies a signal $\tilde{\mathcal{E}}_s$ at ω_s generating an idler $\tilde{\mathcal{E}}_i$ at $\omega_i = \omega_p - \omega_s$. Assuming for simplicity phase and group velocity matching, the set of coupled equations for the OPA in the retarded frame reduces to:

$$\begin{aligned} \frac{\partial F_p}{\partial z} &= -i\kappa F_i F_s \\ \frac{\partial F_s}{\partial z} &= -i\kappa F_p F_i^* \\ \frac{\partial F_i}{\partial z} &= -i\kappa F_p F_s^*. \end{aligned} \tag{5.90}$$

Assuming κ real (real nonlinear susceptibility, no nonlinear absorption), it can easily be verified that the total energy is conserved, which is to be expected since each pump photon produces one signal and one idler photon. In most cases of interest in this section, the pump will be a strong coherent field, and the depletion negligible. Then the system of 3 coupled equations reduces to [3]:

$$\begin{aligned} \frac{\partial F_s}{\partial z} &= -i\tilde{\gamma} F_i^* \\ \frac{\partial F_i^*}{\partial z} &= i\tilde{\gamma} F_s \end{aligned} \tag{5.91}$$

where $\tilde{\gamma} = i\kappa F_p$. This set of differential equations has as solution:

$$\begin{pmatrix} F_s(z) \\ F_i^*(z) \end{pmatrix} = \begin{pmatrix} \cosh(\gamma z) & -\sinh(\gamma z) \\ -\sinh(\gamma z) & \cosh(\gamma z) \end{pmatrix} \cdot \begin{pmatrix} F_s(0) \\ F_i^*(0) \end{pmatrix} \tag{5.92}$$

Degenerate OPA In the case of the degenerate OPA, $\omega_i = \omega_s$, but $F_s \equiv \tilde{\mathcal{E}}_s$ and $F_i \equiv \tilde{\mathcal{E}}_i$ are still distinguishable, as being separate photons with different phase and possibly different polarization. We still have the relationship between the phase of the pump φ_p, the signal φ_s and that of the idler φ_i:

$$\varphi_p - \varphi_s - \varphi_i = 0.$$

If the phase of the pump is taken as reference ($\varphi_p = 0$), and a signal with phase $\varphi_s = \pi/2$ is injected, the coupled equations 5.91 give:

$$\begin{aligned} \frac{\partial \mathcal{E}_s}{\partial z} &= -i\kappa \mathcal{E}_p (i\mathcal{E}_i) = \kappa \mathcal{E}_p \mathcal{E}_i \\ \frac{\partial F_i^*}{\partial z} &= -i\kappa \mathcal{E}_p (-i\mathcal{E}_s) = -\kappa \mathcal{E}_p \mathcal{E}_s. \end{aligned} \tag{5.93}$$

[3] Note that this approximation is at the expense of the energy conservation, which remains rigorously true. One can derive the conservation of photon number from the set of Eqs. 5.90: $\sum(\partial|F_j|^2/\partial z) = 0$ ($j = p, s, i$). The same conservation law does not apply to Eqs. 5.91

Depending on the relative phase of pump and signal, there is exponential growth for one wave and exponential decay for the other.

If ψ is the phase of the pump [$\tilde{\mathcal{E}}_p = \mathcal{E}_p \exp(i\psi)$], then $\tilde{\gamma} = \gamma \exp(i\psi)$, and the solution (5.92) becomes:

$$\begin{pmatrix} \tilde{\mathcal{E}}_s(z) \\ \tilde{\mathcal{E}}_s^*(z) \end{pmatrix} = \begin{pmatrix} \cosh(\gamma z) & -\sinh(\gamma z)e^{i\psi} \\ -\sinh(\gamma z)e^{-i\psi} & \cosh(\gamma z) \end{pmatrix} \cdot \begin{pmatrix} \tilde{\mathcal{E}}_s(0) \\ \tilde{\mathcal{E}}_s^*(0) \end{pmatrix}. \tag{5.94}$$

Quantum Optical Parametric Amplifier

The extension from the previous section is rather straightforward, making the same approximation of intense and un-depleted pump. The fields being replaced by operators, the quantum equivalent of Eq. (5.91) is:

$$\begin{aligned} \frac{\partial \hat{A}_s}{\partial z} &= -\tilde{\gamma}\hat{A}_i^\dagger \\ \frac{\partial \hat{A}_i^\dagger}{\partial z} &= \tilde{\gamma}\hat{A} \end{aligned} \tag{5.95}$$

where $\tilde{\gamma} = i\kappa F_p$. In the degenerate case. setting $\tilde{\gamma} = \gamma \exp\{-i\psi\}$, the solution for the transformed signal operators $\hat{B}$ and $\hat{B}^\dagger$ is:

$$\begin{pmatrix} \hat{B}_s \\ \hat{B}_s^\dagger \end{pmatrix} = \begin{pmatrix} \cosh(\gamma z) & -\sinh(\gamma z)e^{i\psi} \\ -\sinh(\gamma z)e^{-i\psi} & \cosh(\gamma z) \end{pmatrix} \cdot \begin{pmatrix} \hat{A}_s(0) \\ \hat{A}_s^\dagger(0) \end{pmatrix} = \begin{pmatrix} \mu & -\nu \\ -\nu^* & \mu \end{pmatrix} \cdot \begin{pmatrix} \hat{A}_s(0) \\ \hat{A}_s^\dagger(0) \end{pmatrix} \tag{5.96}$$

This is the Bogoliubov transformation, which we have seen in Section 5.4.1 to transform the vacuum state into a squeezed vacuum state. We have indeed from the matrix product $\hat{B}_s = \mu\hat{A}_s - \nu\hat{A}_s^\dagger$, and the determinant of the matrix satisfies the condition $|\mu|^2 - |\nu|^2 = 1$. Using the in-phase and quadrature operators defined in Eq. (5.63) and in Fig. 5.6; $\hat{X}_1 = (1/\sqrt{2})(\hat{A} + i\hat{A}^\dagger)$ and $\hat{X}_2 = (1/\sqrt{2}i)(\hat{A} - i\hat{A}^\dagger)$, and choosing a phase reference such that $\psi = 0$, the set of Eqs. (5.96) becomes:

$$\begin{pmatrix} \hat{X}_1(z) \\ \hat{X}_2(z) \end{pmatrix} = \begin{pmatrix} e^{-\gamma z} & 0 \\ 0 & e^{\gamma z} \end{pmatrix} \cdot \begin{pmatrix} \hat{X}_1(0) \\ \hat{X}_2(0) \end{pmatrix} \tag{5.97}$$

One quadrature growth exponentially, while the other decays exponentially. The product of the two exponentials being 1, the transformed state remains a minimum uncertainty state.

Application to frequency combs

As indicated in the previous paragraph, squeezing with degenerate parametric amplification takes place between the quadrature components $\hat{X}_1$ and $\hat{X}_2$. This is expected, since the parametric amplification process is phase sensitive. Detection will

thus require a local oscillator in phase with one of these components for instance $\hat{X}_1$. Experimental work has been initially aimed a creating continuous sources of squeezed radiation, addressing for instance the need to reduce the noise in Michelson interferometers (LIGO) beyond the classical limit. Another need arose for accurate time of flight measurements, using trains of fs pulses (see Chapter 6). As proposed by Jun Ye [21], the fixed ratio between the light period (≈ 2.5 fs) and the ns spacing between mode-locked pulses opens the possibility to do distance and timing measurements with a large dynamic range. Interferometric cross-correlations with Michelson structures (Chapter 2 and Chapter 10) combine a scale ranging from meters (envelope correlation) to a fine structure of the order of a fraction of wavelength. In the frequency domain, this corresponds to performing time domain reflectometry with a plurality of wavelengths, which are the modes of the frequency comb.

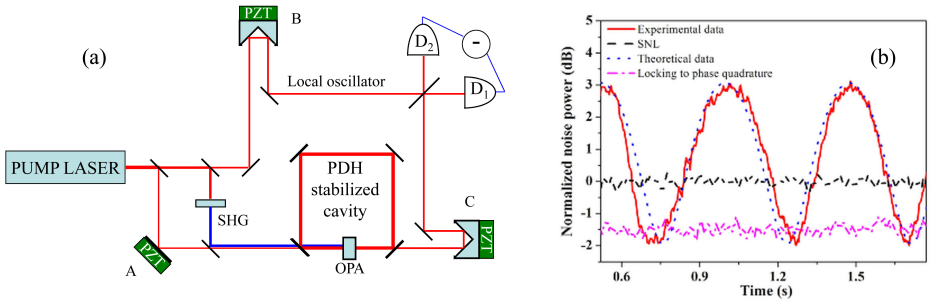

Figure 5.12: Squeezing through degenerate OPA (adapted from [22]). (a) Sketch of the experimental configuration. A mode-locked Ti:sapphire laser is frequency doubled to pump an OPA crystal at degeneracy. A fraction of the fundamental laser beam is used as a seed for amplification. The phase of the seed with respect to the pump is adjusted with the piezoelectric driven mirror *PZT A*. The effective amplification length is extended by inserting the OPA crystal in a cavity synchronized to the mode-locked source, and stabilized by the Pound Drever Hall technique [23]. With the PDH cavity pumped below threshold, the amplified seed is interfered with the local oscillator in a balanced homodyne detection (detectors D_1 and D_2). The relative phase of the local oscillator and amplified seed is adjusted by *PZT B*. An additional scan can be provided by *PST C* for comparison of the timing accuracy with and without (pump beam blocked) squeezing. (b) Difference noise level at 2 MHz as the phase between LO and seed is being scanned (red line). The black dashed line shows the shot noise limit, and the magenta dash-dotted line the noise level when locking to the phase quadrature. The dotted blue line is a theoretical curve (see reference [22]).

Measurement of a pm displacement based on degenerate Optical Parametric Amplification (OPA) [22] is taken as example of squeezed passive interferometry.

A simplified diagram of the experiment is shown in Fig. 5.12, adapted from Fig. 1 of reference [22]. The pump pulses are frequency doubled from the primary mode-locked Ti:sapphire laser from which the seed pulse is derived. The relative phase of the seed with respect to the pump is adjusted via a piezoelectrically driven mirror *A* in Fig. 5.12(a). The squeezing derived in the previous Section 5.4.4 occurs for degenerate parametric amplification, and not oscillation. To compensate for the small gain due to the shortness of the crystal, the seed pulse is cycled in a cavity synchronized with the pump cavity. The pump pulse energy is kept below the threshold for optical parametric oscillation. The amplified seed is mixed with the local oscillator pulse in a balanced detector configuration. The relative phase between the amplified seed and local oscillator is controlled by the *PZT B* applied to the delay line reflector.

To take advantage of the $1/f$ dependence of the noise (see Section 5.8), the balanced detection is performed at 2 MHz. As the phase of the local oscillator relative to that of the pump is being scanned, Fig. 5.12(b) the difference signal noise signal between D_2 and D_1 shows the characteristic variation of squeezing and anti-squeezing (red line). The red dashed line shows the noise level with the phase (*PZT B*) locked for minimum amplitude noise.

To relate the noise squeezing to a time measurement, a modulation at 2 MHz with a peak amplitude of 8.4 pm is applied to the mirror driven by *PZT C*. The spectrum analyzer records a peak at 2 MHz of 3 dB above the shot noise level in the absence of squeezing (OPA not pumped). This same peak is 3.8 dB above the noise level with the phase (*PZT B*) locked for minimum amplitude noise. Translating the displacement of 8.4 pm into a time of flight, Wang *et al* [22] report a shot noise limited minimum measurable timing variation of the signal pulses relative to a pump derived reference of $2.8 \cdot 10^{-20}$s. This timing accuracy is reduced by a factor of 1.17, or 1.5 dB, through the squeezing arrangement of Fig. 5.12. To put this value in perspective, Intracavity Phase Interferometry (without squeezing) discussed in Section 5.8.3 has sub-fm accuracy, or a minimum measurable timing variation of 10^{-24} s.

There are numerous nonlinear interactions that can modify the "uncertainty circle". Most relevant in the context of ultrashort phenomena are those associated with nonlinear propagation, Kerr effect and solitons, topics discussed in the next sections of this chapter.

5.5 Solitons in time

Solitons can be defined as a mathematical steady state solution of a propagation equation. A more restrictive definition is that it should be solution of the nonlinear Schrödinger equation, which will be derived in this chapter. In the time domain, the nonlinear Schrödinger equation will describe the temporal shape of a pulse confined by other means in the two transverse dimensions. This equation can be derived in space, in which case the soliton may represent the steady state transverse shape of a beam propagating in a nonlinear medium, where no temporal dependence is assumed. The stability of the solution of the nonlinear Schrödinger equation depends on the dimensionality of the problem addressed.

5.5.1 Mechanism of pulse compression by propagation

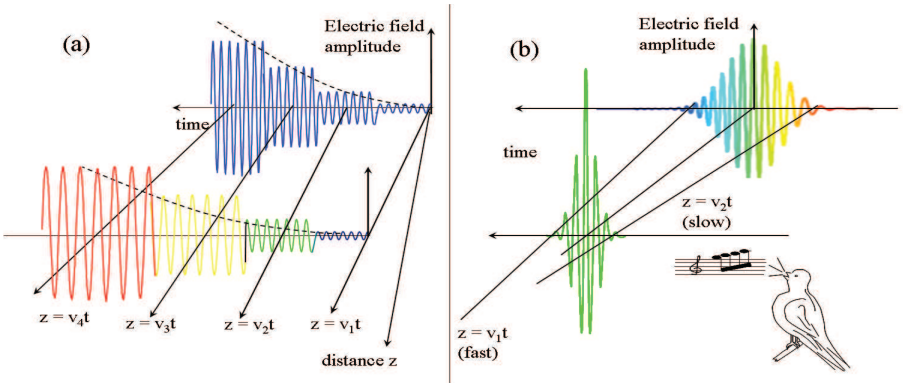

Figure 5.13: (a) Generation of new optical frequencies by propagation of a pulse in a medium where the wave velocity increases with intensity. The optical signal of increasing intensity is shown as having a stepwise increase on its leading edge (the time axis is pointing left, for a better visualization of a pulse propagating to the right). The different intensities propagate at velocities v_1, v_2, v_3 and v_4 with $v_4 < v_3 < v_2 < v_1$. As a result, the pulse optical frequencies decrease with time along the pulse (or the wavelengths increase along the pulse) after some propagation distance. (b) Through the process shown in (a), one has generated an "upchirped" pulse, i.e. a pulse of which the optical frequency increases with time. This is exactly what the little bird on the bottom of the picture is singing. This pulse is now sent through a medium with negative dispersion (i.e. a medium in which the higher frequencies (blue) propagate faster than the lower frequencies (red). As a result, the tail of the pulse catches up with the pulse leading edge, resulting in pulse compression.

A pulse of light consists of a superposition of waves propagating at their phase

velocity, with a common crest. The broader the range of frequencies involved the shorter the pulse. There are two mechanisms in the production of short pulses: A mechanism —dubbed "nonlinear" because the speed of light depends on the pulse intensity — by which the range of frequencies is extended, and another one called "dispersion", studied in detail in Chapter 1, by which the waves that constitute the pulse propagate at different frequencies.

The speed of light is highest in vacuum: $c = 299792458$ m/s. As it propagates through matter, it is slowed down by the interaction with atoms and molecules, resulting in a velocity $v = c/n$ where n is the index of refraction.. There are numerous mechanisms resulting in an intensity dependent wave velocity. The oldest one involves water waves, and relates to the fist observation of solitons. "Solitary propagation" was discovered long before the mathematical equation even existed, by the engineer and shipbuilder John Scott Russell (1808-1882) [24] who named it "*the wave of translation*". In 1834 he was riding by the Grand Union Canal at Hermiston, Glasgow, and observed that when a canal boat stopped, its bow wave continued onward at a well-defined elevation of the water at constant speed. It was only in the 1960's that the name "soliton" was coined when the phenomenon was rediscovered by the American physicist Martin Kruskal. Details of the early history of the soliton can be found in a book by Robin K. Bullough [25]. The soliton took up so much importance in all areas of physics and laser optics that a recreation of the observation of John Russell was organized for the 150th anniversary of his observation. Fig 5.14 shows a picture of a re-creation of that event.

The term "Kerr effect" nearly always associated with nonlinear wave velocity certainly does not apply to water waves. The velocity of the water wave is affected by the depth of the canal in which it propagates. The intensity of the water wave is related to its crest. The shallower the canal, the more the water wave velocity will be affected by the height of the wave relative to the canal depth. Not recognizing this fact led to a first unsuccessful reconstruction of the original observation of Russell.

Solitons in the time domain have been realized by numerous methods. Requirements are spatial confinement of the beam, and phase modulation and dispersion of opposite sign. Femtosecond lasers have been the first soliton sources [26], in which the beam confinement is periodic, with the repetition rate of the cavity round-trip frequency. In a first demonstration, the phase modulation was created by saturation of an absorber below resonance. The saturation sweeps the near resonant contribution of the index from a high value at low power to a low saturated value, resulting in a *downchirp* [27, 28]. Generation of solitons by mode-locked lasers has most often positive self-phase modulation of the electronic Kerr effect, and negative dispersion provided by pairs of prisms (see Chapter 2) or negative dispersion mirrors. One notable exception is the replacement of Kerr nonlinearity by cascade second

Figure 5.14: Recreation of the soliton in 1984– soliton home page, Heriot Watt University http://www.ma.hw.ac.uk/solitons/index.html

order nonlinearity [29].

5.5.2 The 1D nonlinear Schrödinger equation

A mode-locked laser can be summarized as a laser cavity, in which a single pulse circulates. A pulse train results from the transmission of the intracavity pulse through an output mirror, at each round trip. As a pulse circulates inside the cavity, it will be shaped by various processes such as Kerr modulation, dispersion. If a train of identical pulses have to emerge through the output mirror, it is essential that the propagation of the intracavity pulse through an infinite medium representing the content of the laser cavity leads to steady state. In any laser, losses and gain compensate each other. At the femtosecond level, pulse shaping is dominated by dispersive effects, and we can neglect the influence of gain and saturable absorption on pulse shaping. The pulse shaping mechanism is a combination of self-phase modulation and dispersion at each round trip. The self-phase modulation results from a nonlinear index of refraction $n_2 I$ (I being the intensity in W cm^{-2}, n_2 being the nonlinear index in cm^2 W^{-1} of a nonlinear element of length ℓ in the cavity). It has been shown [30] that the localized elements can be replaced

by their value averaged over the cavity length, if that cavity length is smaller than a characteristic distance. The dispersion k''_{av} results from the second derivative of a cavity averaged k_{av} wave vector with respect to frequency. In what follows, we will neglect higher order terms in Kerr effect and in dispersion. The evolution of a pulse in the mode-locked laser cavity can be approximated as a propagation (of a non-diffracting beam) through an infinite lossless medium, with an intensity dependent index of refraction nonlinearity (n_2) and a dispersion of opposite sign. The pulse evolution generally converges towards a steady-state solution, designated as "soliton", which can be explained as follows. The nonlinearity is responsible for spectral broadening, and the dispersion, make the frequency components produced in the trailing part of the pulse travel faster than the low frequency components of the pulse leading edge. Therefore, the tendency of pulse broadening owing to the exclusive action of group velocity dispersion can be counterbalanced.

The effect of group velocity dispersion is to create a pulse broadening and a down-chirp (in a medium of negative dispersion). The medium of negative dispersion is characterized by a wave vector $k(\Omega)$ averaged over the cavity:

$$k(\Omega) = k_{av0} + k'_{av}(\Omega - \omega) + k''_{av}\frac{(\Omega-\omega)^2}{2} + \dots \tag{5.98}$$

The transmission of a pulse characterized by its spectral field, $\tilde{\mathcal{E}}(\Omega-\omega)$, through a medium of length L with the average k vector of Eq. (5.98), is given by

$$\tilde{\mathcal{E}}(\Omega-\omega)e^{-ik(\Omega)L} \approx \tilde{\mathcal{E}}(\Omega-\omega)e^{-ik''_{av}L\frac{(\Omega-\omega)^2}{2}} \approx \tilde{\mathcal{E}}(\Omega-\omega)\left[1 - \frac{i(\Omega-\omega)^2 k''_{av}}{2}L\right], \tag{5.99}$$

where we have omitted the first and second terms of the expansion, responsible respectively for a constant phase shift, and a group delay. After inverse Fourier transformation, the effect of dispersion change the field after a round-trip to:

$$\left[1 + \frac{ik''_{av}L}{2}\frac{\partial^2}{\partial t^2}\right]\tilde{\mathcal{E}}(t) = \left[1 + \frac{i\psi''}{2}\frac{\partial^2}{\partial t^2}\right]\tilde{\mathcal{E}}(t) \tag{5.100}$$

where we have defined $\psi(\Omega)$ as the total phase factor through the cavity, combining the phase shift by mirrors, transparent elements, eventual prism pairs, The total dispersion for a single passage through the cavity is then the second derivative with respect to angular frequency ψ''.

Let us assume next that the cavity contains an element with a nonlinear index $n = n_0 + n_2 I$ of length ℓ. The modified field after this element is:

$$\tilde{\mathcal{E}}(t,\ell) = \tilde{\mathcal{E}}(t,0)e^{-ik_{NL}\ell} \approx \tilde{\mathcal{E}}(t,0)\left[1 - i\frac{\omega}{c}\ell\frac{n_2}{\eta_0}|\tilde{\mathcal{E}}|^2\right]. \tag{5.101}$$

One can generally assume that the change per round-trip is small and consider the cavity length L to be an infinitesimal length increment. Combining the elements/round-trip Eqs. (5.100) and (5.101), and expressing the change per infinitesimal distance increment ∂z:

$$i\frac{\partial\tilde{\mathcal{E}}}{\partial z} = -\frac{\psi''}{2P}\frac{\partial^2\tilde{\mathcal{E}}}{\partial t^2} + \frac{\omega}{c}\frac{n_2}{\eta_0}\frac{\ell}{L}|\tilde{\mathcal{E}}|^2\tilde{\mathcal{E}}. \tag{5.102}$$

One can use the $k = \omega/c$ vector to normalize the distance z. As discussed in previous chapters, balance phase modulation and dispersion requires that k'' and n_2 have opposite sign. Since in most physical situations n_2 is positive [4], solitons propagation will generally require that ψ'' be negative. As shown in Chapter 2 k'' in transparent materials is positive in the visible. A combination of mirrors, prisms or gratings can be devised to create a negative dispersion. In the near infrared, k'' is negative in glasses, and in particular in fibers. A natural time unit is $\tau_0 = \sqrt{-\psi''/kL}$. The Kerr effect serves to normalize the fields to a characteristic field $\mathcal{E}_0 = \sqrt{(\eta_0 P)/(n_2\ell)}$. In these normalized variables, the nonlinear Schrödinger equation for the field $u = \tilde{\mathcal{E}}/\mathcal{E}_0$ is:

$$i\frac{\partial u}{\partial z} = \frac{1}{2}\frac{\partial^2 u}{\partial t^2} + |u|^2 u \tag{5.103}$$

5.5.3 The first order soliton

Normalized units

The first order solution to Eq. (5.103) is a sech pulse, which we can define by substituting the trial solution $u = A\,\mathrm{sech}\,\frac{t}{\tau_s}\exp(-i\beta z)$ into Eq. (5.103). The substitution yields:

$$\beta A\,\mathrm{sech}\,\frac{t}{\tau_s}e^{-i\beta z} = A(\frac{1}{\tau_s})^2 e^{-i\beta z}\left[\frac{1}{2}\,\mathrm{sech}\,\frac{t}{\tau_s} - \mathrm{sech}^3\,\frac{t}{\tau_s}\right] + A^3\,\mathrm{sech}^3\,\frac{t}{\tau_s}e^{-i\beta z} \tag{5.104}$$

Equation (5.104) is satisfied if the normalized pulse duration $\tau_s = 1/A$ and the correction to the wave vector $\beta = A^2/2$. The steady state solution representing the first order soliton is:

$$u = A\ \mathrm{sech}(At)\ e^{-iA^2 z/2} \tag{5.105}$$

In these normalized units, there is an infinite family of solutions of "order 1", defined as the product of peak amplitude A by pulse duration τ_s being unity. In general, for initial conditions of the form $A\,\mathrm{sech}(t/\tau)$, periodic solutions may be found. They are labeled n-order solitons if $A\tau = n$ (n integer).

[4] An important exception is that of cascaded second order nonlinearities where an effective negative n_2 can be produced [31].

It should be noted that the correct pulse area is:

$$\theta_s = \int_{-\infty}^{\infty} \frac{1}{\tau_s} \operatorname{sech} \frac{t}{\tau_s} dt = \pi. \tag{5.106}$$

As in Self-Induced-Transparency (SIT) (cf. next section 5.6), the pulse energy is inversely proportional to the pulse duration. The shorter the pulse duration, the higher the intensity, and the shorter the soliton period.

Non-normalized units

The concepts of time, distance, frequency and phase may be hidden using the normalized form of the nonlinear Schödinger equation. Referring to Eq. (5.102), the non-normalized nonlinear Schrödinger equation can be written as:

$$i\frac{\partial \tilde{\mathcal{E}}}{\partial z} = -\frac{k''}{2}\frac{\partial^2 \tilde{\mathcal{E}}}{\partial t^2} + \frac{\omega n_2}{c\eta_0}|\tilde{\mathcal{E}}|^2\tilde{\mathcal{E}}. \tag{5.107}$$

where z is the distance in meter, t the time in seconds, k'' the dispersion in s^2/m, and $\omega n_2/(c\eta_0)$ the Kerr effect coefficient in m^3/V^2 (with n_2 in m^2/W, η_0 in Ohms). Referring to a mode-locked laser cavity, we are replacing localized elements by distributed quantities — essentially taking the ratio $\ell/P = 1$. Instead of the field $\tilde{\mathcal{E}}$, it will be convenient for future sections to introduce a normalized field $\tilde{\mathcal{A}}$: Introducing the beam cross-section S:

$$\tilde{\mathcal{A}} = \frac{\tilde{\mathcal{E}} \times \sqrt{S}}{\sqrt{2\eta_0 \hbar \omega}}. \tag{5.108}$$

With this definition the "field" $\mathcal{A}$ is in units of $s^{-1/2}$, such that the "energy";

$$\int_{-\infty}^{\infty} |\tilde{\mathcal{A}}|^2 dt = N_{ph} \tag{5.109}$$

is the total photon number in the pulse. With this new field unit, the nonlinear Schrödinger equation takes the form:

$$\boxed{i\frac{\partial \tilde{\mathcal{A}}}{\partial z} = -\frac{\psi''}{2L}\frac{\partial^2 \tilde{\mathcal{A}}}{\partial t^2} + K|\tilde{\mathcal{A}}|^2\tilde{\mathcal{A}},} \tag{5.110}$$

where

$$K = \frac{\omega}{c}\frac{\ell}{L}\frac{2\hbar\omega n_2}{S} \tag{5.111}$$

In the case of solid state fs lasers, it is common that the Rayleigh range in the solid is shorter than the crystal length. In that case, the length ℓ has to be replaced by the rayleigh range $2\pi n w^2/\lambda$ and Eq. (5.111) has to be replaced by:

$$K = \frac{8\pi}{\lambda^2 L} n\hbar\omega n_2. \tag{5.112}$$

Note that the dependence in the size of the beam waist w has been eliminated. The dimension of K is inverse velocity.

Following the same procedure as in the previous section, with the Anzatz for the field $\tilde{\mathcal{A}} = A \operatorname{sech} \frac{t}{\tau_s} \exp(-i\beta z)$, we find after substitution in Eq. (5.110):

$$\beta A \operatorname{sech} \frac{t}{\tau_s} e^{-i\beta z} = -\frac{\psi''}{2L} A (\frac{1}{\tau_s})^2 e^{-i\beta z} \left[\frac{1}{2} \operatorname{sech} \frac{t}{\tau_s} - \operatorname{sech}^3 \frac{t}{\tau_s} \right] + A^3 \operatorname{sech}^3 \frac{t}{\tau_s} e^{-i\beta z}. \tag{5.113}$$

The correction to the wave vector is now $\beta = -\psi''/(4L\tau_s^2)$, and the relation between amplitude and pulse duration becomes:

$$\boxed{A\tau_s = \sqrt{\frac{-\psi''}{2LK}}.} \tag{5.114}$$

This last relation clearly established that a first order soliton can only exist if ψ'' and K have opposite sign.

More generally, the field of the soliton of order 1 is:

$$\tilde{\mathcal{A}} = -A \operatorname{sech}\left(\frac{t - t_c}{\tau_s} - \frac{\psi'' \Delta\omega}{L\tau_s} z \right) e^{i[\Delta\omega(t-t_c) + (KA^2/2)z - (\psi''\Delta\omega^2/2L)z + \varphi]}. \tag{5.115}$$

The second term in the envelope indicates that, if there is a frequency drift $\Delta\omega$ of the soliton, its group delay will be affected because of the dispersion k''. The second term in the exponential is the nonlinear phase shift $kn_2 I_0 z$, while the last one is the phase shift due to dispersion.

Using Eq. (5.114) to eliminating A in Eq. (5.115):

$$\tilde{\mathcal{A}} = \frac{1}{\tau_s} \sqrt{\frac{\psi''}{KL}} \operatorname{sech}\left(\frac{t - t_c}{\tau_s} - \frac{\psi'' \Delta\omega}{L\tau_s} z \right) e^{i\left[\Delta\omega(t-t_c) - (\psi'' z/2L)(\frac{1}{\tau_s^2} + \Delta\omega^2) + \varphi\right]}. \tag{5.116}$$

The amplitude A or the pulse duration τ_s are also linked to the photon number N_{ph}:

$$N_{ph} = \int_{-\infty}^{\infty} |\tilde{\mathcal{A}}|^2 dt = \frac{-\psi''}{2KL} \frac{1}{\tau_s} \int_{-\infty}^{\infty} \operatorname{sech}^2 x dx = \frac{-\psi''}{KL} \frac{1}{\tau_s}. \tag{5.117}$$

which implies the simple expression for the pulse energy

$$\text{Pulse energy} = \frac{-\psi''\hbar\omega}{KL\tau_s} \tag{5.118}$$

Some relations between N_{ph}, pulse duration and amplitude are listed below:

$$\frac{KA^2}{2} = \frac{-\psi''}{4L\tau_s^2} = \frac{-\psi''^2}{4K^2L^2\tau_s^2} \times \frac{K^2L}{\psi''} = N_{ph}^2\frac{K^2L}{4\psi''} \tag{5.119}$$

$$A = \frac{1}{\tau_s}\sqrt{\frac{-\psi''}{2KL}} = \frac{N_{ph}}{\sqrt{2}}\sqrt{\frac{KL}{-\psi''}} \tag{5.120}$$

$$N_{ph}\tau_s = \frac{-\psi''}{KL} \tag{5.121}$$

$$\frac{\partial\tau_s}{\partial N_{ph}} = -\frac{k''}{KN_{ph}^2} = -\frac{KL}{\psi''}\tau_s^2 \tag{5.122}$$

Soliton perturbation

Let us add to the evolution equation (5.110) some perturbation $F(\tilde{\mathcal{A}}, \tilde{\mathcal{A}}^*, z)$:

$$i\frac{\partial\tilde{\mathcal{A}}}{\partial z} = -\frac{k''}{2}\frac{\partial^2\tilde{\mathcal{A}}}{\partial t^2} + K|\tilde{\mathcal{A}}|^2\tilde{\mathcal{A}} + F(\tilde{\mathcal{A}}, \tilde{\mathcal{A}}^*, z). \tag{5.123}$$

Assuming the perturbation is small, we want to find how the soliton solution is modified by writing:

$$\tilde{\mathcal{A}}(z,t) = \left\{A\,\text{sech}[\frac{t}{\tau_s}] + \Delta\tilde{\mathcal{A}}(z,t)\right\}e^{-betaz} \tag{5.124}$$

where $A\,\text{sech}\left(\frac{t}{\tau_s}\right)$ is the unperturbed solution at $z = 0$. It should be noted that the Kerr term is of the form:

$$(\tilde{\mathcal{A}}_0 + \Delta\tilde{\mathcal{A}}(t))(\tilde{\mathcal{A}}_0^* + \Delta\tilde{\mathcal{A}}(t)^*)(\tilde{\mathcal{A}}_0 + \Delta\tilde{\mathcal{A}}(t)) = 2|\tilde{\mathcal{A}}_0|^2\Delta\tilde{\mathcal{A}}(t) + \tilde{\mathcal{A}}_0^2\Delta\tilde{\mathcal{A}}_0^* + \tilde{\mathcal{A}}_0^2\tilde{\mathcal{A}}_0^*, \tag{5.125}$$

where higher order terms have been neglected. We insert the Ansatz (5.124) into Eq. (5.123) to solve the nonlinear Schrödinger equation ro first order in the perturbation $\Delta\tilde{\mathcal{A}}(z,t)$:

$$\begin{aligned} i\frac{\partial\Delta\tilde{\mathcal{A}}(z,t)}{\partial z} &= \frac{k''}{2}\frac{\partial^2\Delta\tilde{\mathcal{A}}(z,t)}{\partial t^2} + 2K|\tilde{\mathcal{A}}_0(z,t)|^2\Delta\tilde{\mathcal{A}}(z,t) + K\tilde{\mathcal{A}}_0(z,t)^2\Delta\tilde{\mathcal{A}}(z,t)^* \\ &+ F(\tilde{\mathcal{A}}, \tilde{\mathcal{A}}^*, z)e^{-i\beta z}. \end{aligned} \tag{5.126}$$

This can be written in the condensed form:

$$\mathcal{L}(\Delta\tilde{\mathcal{A}}) + \mathcal{L}(F) = 0, \tag{5.127}$$

$$\mathcal{L} = -i\frac{\partial}{\partial z} + \left[\frac{k''}{2}\frac{\partial^2}{\partial t^2} + 2K|\tilde{\mathcal{A}}_0(z,t)|^2 + K\tilde{\mathcal{A}}_0(z,t)^2()^*\right]. \tag{5.128}$$

From Eq. (5.116) one identifies four free parameters or degrees of freedom to characterize the soliton:

1. the soliton amplitude or photon number N_{ph},
2. the phase φ,
3. the frequency shift $\Delta\omega$,
4. the pulse center position t_c.

These parameters will evolve with distance. The perturbation $\Delta\tilde{\mathcal{A}}(z,t)$ in Eq. (5.124) can be expanded to first order in the perturbation parameters δN, $\delta\varphi$, $\delta\omega$ and δt_c:

$$\Delta\tilde{\mathcal{A}}(z,t) = \frac{\partial\tilde{\mathcal{A}}_0}{\partial N_{ph}}\delta N + \frac{\partial\tilde{\mathcal{A}}_0}{\partial\varphi}\delta\varphi + \frac{\partial\tilde{\mathcal{A}}_0}{\partial\Delta\omega}\delta\omega + \frac{\partial\tilde{\mathcal{A}}_0}{\partial t_c}\delta t_c \tag{5.129}$$

In performing the derivatives of $\tilde{\mathcal{A}}(z,t)$, we start from the initial condition: $\tilde{\mathcal{A}} = A_0\,\mathrm{sech}\left(\frac{t}{\tau_s}\right)$meaning we choose initially a centered pulse ($t_c = 0$), zero phase, at resonance ($\Delta\omega = 0$). By performing the successive derivatives, we find how the soliton is affected by a variation of each of the 4 free parameters.

Phase perturbation

$$\boxed{\left|\frac{\partial\tilde{\mathcal{A}}}{\partial\varphi}\right|_0 = iA_0\,\mathrm{sech}\left(\frac{t}{\tau_s}\right)} \tag{5.130}$$

Referring to Eq. (5.129), this last Eq. (5.130) being proportional to the soliton shape and added in quadrature, implies that a phase perturbation will have no other effect than to modify the soliton phase by $\delta\varphi\Delta z$ without affecting any other parameter, such as the soliton shape, position, energy, phase, or frequency.

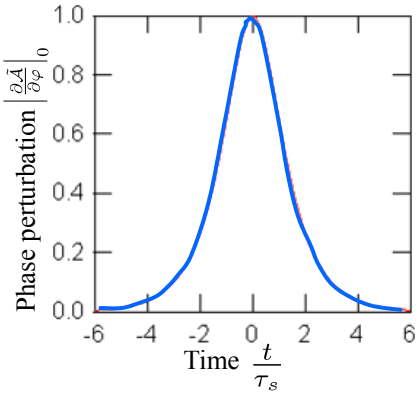

Figure 5.15: Phase perturbation: a simple rotation of the phasor of the soliton.

Soliton position perturbation

The derivative of the soliton with respect to its position t_c yields $\left|\frac{\partial\tilde{\mathcal{A}}}{\partial t_c}\right|_0 = -\frac{A_0}{\tau_s}\,\mathrm{sech}\left(\frac{t}{\tau_s}\right)\tanh\left(\frac{t}{\tau_s}\right)$.The change proportional to the derivative implies an additional change in position: the leading edge is depleted, the trailing edge enhanced, implying a delay of the soliton. Similarly to the phase perturbation, no other parameter of the soliton is affected.

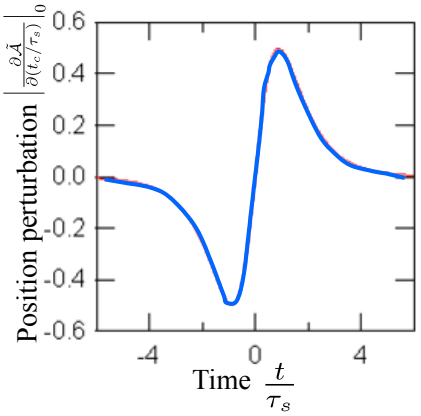

Figure 5.16: Position perturbation.

Photon-number perturbation For the derivative with respect to N_{ph}, we notice a dependence on N_{ph} in the amplitude A (Eq. (5.120), and in the pulse duration τ_s (Eq. (5.122).

$$\left|\frac{\partial\tilde{\mathcal{A}}}{\partial N_{ph}}\right|_0 = \frac{1}{\sqrt{2}}\sqrt{\frac{K}{k''}}\,\mathrm{sech}\left(\frac{t}{\tau_s}\right) + \frac{1}{2}\frac{t}{\tau_s}\sqrt{\frac{K}{-k''}}\,\mathrm{sech}\left(\frac{t}{\tau_s}\right)\tanh\left(\frac{t}{\tau_s}\right) \tag{5.131}$$

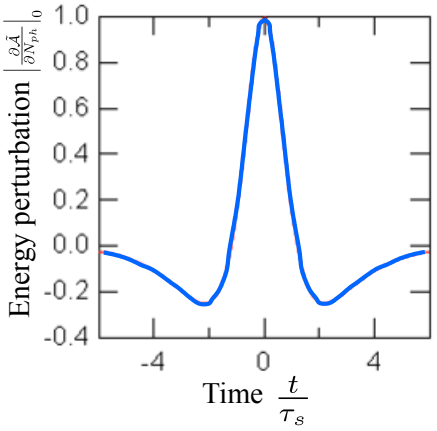

Figure 5.17: Photon-number perturbation.

Noting that

$$A_0 K t/(2k'') = (t/2\tau_s)\sqrt{K/k''},$$

leads to the symmetric function:

$$\boxed{\left|\frac{\partial\tilde{\mathcal{A}}}{\partial N_{ph}}\right|_0 = -\frac{1}{2}\sqrt{\frac{K}{-k''}}\left\{1-\frac{t}{\tau_s}\tanh\frac{t}{\tau_s}\right\}\mathrm{sech}\left(\frac{t}{\tau_s}\right)} \tag{5.132}$$

This function is plotted in Fig. 5.17. A perturbation causing an increase in photon number leads to a depletion of the leading and trailing edges, while the number of photons is increased in the center, implying a pulse compression. The soliton is a stable entity for the total number of photons. An increase in peak intensity should result in a larger Kerr effect, hence a phase shift. Indeed, this is seen by introducing the perturbation $\left|\frac{\partial\tilde{\mathcal{A}}}{\partial N_{ph}}\right|_0$ via Eq. (5.129) into the Schrödinger equation for the perturbation [Eq. (5.126)]: the second derivative with respect to time introduces a term proportional to $\left|\frac{\partial\tilde{\mathcal{A}}}{\partial\varphi}\right|_0$.

$$\mathcal{L}\left(|\frac{\partial\tilde{\mathcal{A}}}{\partial N_{ph}}|_0\right) \propto \frac{1}{N_{ph}}\left|\frac{\partial\tilde{\mathcal{A}}}{\partial\varphi}\right|_0 . \tag{5.133}$$

Soliton frequency perturbation

The derivative with respect to detuning is:

$$\boxed{\left|\frac{\partial\tilde{\mathcal{A}}}{\partial\Delta\omega}\right|_0 = \frac{1}{\tau_s}\sqrt{\frac{-k''}{2K}}it\,\mathrm{sech}\left(\frac{t}{\tau_s}\right)} \tag{5.134}$$

which implies a time dependent phase shift. A change in frequency should result in a change in position, since the group velocity is frequency dependent. Indeed, this is seen by introducing the perturbation $\left|\frac{\partial\tilde{\mathcal{A}}}{\partial\Delta\omega}\right|_0$ via Eq. (5.129) into the Schrödinger equation for the perturbation [Eq. (5.126)]: the second derivative with respect to time introduces a term proportional to $\mathrm{sech}(t/\tau_s)\tanh(t/\tau_s)$, or a cumulative position shift.

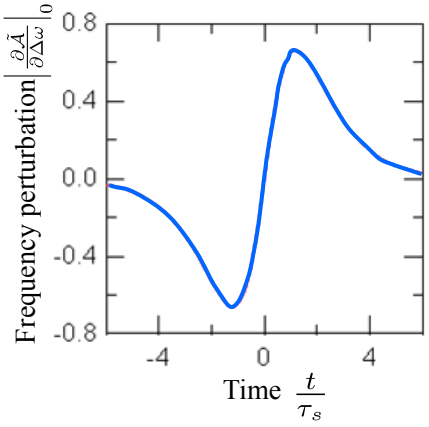

Figure 5.18: Frequency perturbation.

$$\mathcal{L}\left(|\frac{\partial\tilde{\mathcal{A}}}{\partial\Delta\omega}|_0\right) \propto \tau_s^2\left|\frac{\partial\tilde{\mathcal{A}}}{\partial t_c}\right|_0 . \tag{5.135}$$

5.5.4 Stability of solitons

First order solitons are stable, in the sense that if a soliton of order > 0.5 or < 1.5 (area between $\pi/2$ and $3\pi/2$) is launched, it will evolve towards a single soliton or order one [32]. The threshold for soliton formation is higher if a chirped pulse is launched [33]. An example of the reshaping of a chirped Gaussian towards a soliton is shown in Fig 5.19. The excess frequency components related to the chirp propagate at lower and higher velocity than the soliton, separating from the main pulse.

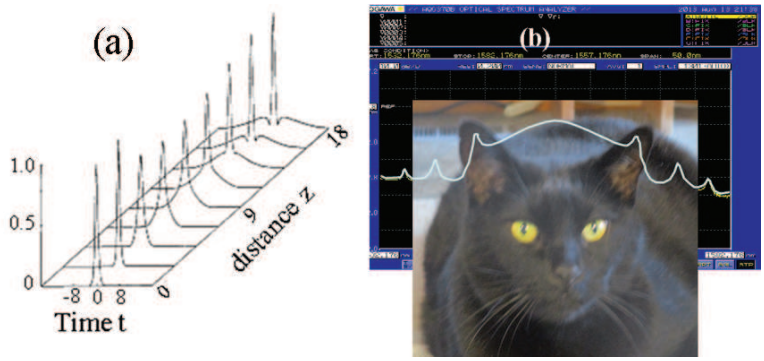

Figure 5.19: Evolution of a chirped pulse of order 1 (area π) into a soliton. (a) in time domain. (b) Final soliton spectrum, showing the Kelly sidebands [34] (adapted from [33].

A purely dispersive system will not evolve towards a pulse. Given a pulse of area < 0.5 or a weak cw field as initial condition, the right hand side of Eq. (5.103) is near zero, and there is no evolution towards a pulse. Any positive feedback, such as saturable absorption or Kerr lensing, will contribute towards an evolution towards a pulse. Following the approach of Haus *et al* [35], we add the elements to complete the evolution Eq. (**??**). The expanded equation is:

$$i\frac{\partial \mathcal{E}}{\partial \chi} = \psi + ig\left(1 + \frac{1}{\Delta\omega_g^2}\frac{\partial^2}{\partial t^2}\right)\tilde{\mathcal{E}} - iL\left(1 - \alpha_s\frac{|\tilde{\mathcal{E}}|^2}{\mathcal{E}_s^2}\right)\tilde{\mathcal{E}} - \frac{k''P}{2}\frac{\partial^2\mathcal{E}}{\partial t^2} + \frac{n_2\omega\ell}{2\eta c}|\mathcal{E}|^2\mathcal{E}, \quad (5.136)$$

The various terms of this equation are a second order (quadratic) approximation of the particular physical phenomenon represented.

- g is the linear gain/round-trip.
- The term $\frac{1}{\Delta\omega_g^2}\frac{\partial^2}{\partial t^2}$ is a parabolic approximation of the gain bandwidth, inverse Fourier transformed in the time domain.

- L is the loss/cavity round-trip.
- α_s is the saturable fraction of these losses.
- ψ is the phase shift per round-trip (in case if differs slightly from 2π

The normalize form of Eq. (5.136) is:

$$i\frac{\partial \mathcal{E}}{\partial \chi} = \psi + i(G-L) + \frac{1}{2}\Big(i\kappa_g - 1\Big)\Big)\frac{\partial^2}{\partial t^2}\tilde{\mathcal{E}} + \left(1 - i\kappa_L)\frac{|\tilde{\mathcal{E}}|^2}{\mathcal{E}_s^2}\right)\tilde{\mathcal{E}}. \tag{5.137}$$

Some terms in this equation have more than one more interpretations. The dispersion term has an imaginary component due to the bandwidth of the gain. The imaginary part of the Kerr nonlinearity was introduces as saturable loss. It can also result from four wave mixing. Eq. (5.137) has the steady state solution [36]:

$$\tilde{\mathcal{E}}(t) = \mathcal{E}_0 \,\mathrm{sech}(t/\tau_s) e^{iK\ln[\mathrm{sech}(t/\tau_s)]} \tag{5.138}$$

To study the stability — or simply the practical existence — of the stationary solution, one should start from initial condition departing from the stationary solution. Following a pulse evolution in the time domain amounts to cycle the Eq. (5.137) from round-trip to round-trip, leading either to identical pulses from round-trip to round trip — the simple stable soliton — or something that periodically oscillate. The stability of the solutions has been investigated by H. Haus and followers [35, 37–39]. The conclusion is that there is no stable solution without saturable absorption. And yet, there are lasers generating frequency combs that do not appear to have saturable losses [40–43]. This question is still being debated.

5.6 Other type of soliton: the "2π" pulse

The property of a pulse propagating without distortion nor losses is not limited to dielectric media. A famous example is that of a pulse propagating in an absorbing medium consisting in an ensemble of two-level systems (inhomogeneously broadened absorber), a phenomenon call Self-Induced Transparency (SIT) [44].

We have introduced in Chapter 3 the system of Eqs. (3.72, 3.73, 3.74, 3.76, 3.77) describing the interaction between an absorbing medium and a two-level system. There is a vector representation of these equations [45], which is particularly useful in the context of intense pulse propagation in near resonant systems. To recall the results of Chapter 3, one constructs a fictitious vector $\vec{\mathcal{P}}$ of components (u, v, w), and a pseudo-electric field vector $\vec{\mathcal{E}}$ of components $(\kappa\mathcal{E}, 0, -\Delta\omega)$. The detuning is defined as $\Delta\omega = \omega_0 - \omega_\ell - \dot{\varphi}$. The system of Eqs. (3.72)–(3.74) are then the cinematic equations describing the rotation of a pseudo-polarization vector $\vec{\mathcal{P}}$

rotating around the pseudo-electric vector $\vec{\mathcal{E}}$ with an angular velocity given by the amplitude of the vector $\vec{\mathcal{E}}$. The vectorial form of Eqs. (3.72)- (3.74) was given in Eq. (3.78).

Key assumption in SIT is that the pulse duration be short compared to phase and energy relaxation times, which implies that the total energy in the system can be conserved, and that the length of the pseudo-polarization vector is conserved. The sum of each equation (3.72), (3.73) and (3.74) multiplied by u, v, and w, respectively, yields after integration:

$$u^2 + v^2 + w^2 = w_0^2 \tag{5.139}$$

which is satisfied for each sub-ensemble of two-level systems. As was shown in Fig. 3.5(a), a resonant excitation ($\Delta\omega = 0$)) will tip the pseudo-polarization vector by an angle $\theta_0 = \int_{-\infty}^{\infty} \kappa\mathcal{E}dt$ in the (v, w) plane. For a sufficiently intense pulsed excitation, it is possible to achieve complete population inversion when $\theta_0 = \pi$. The effect of phase relaxation (homogeneous broadening) is to shrink the pseudo-polarization vector as it moves around. To take into account inhomogeneous broadening, we have to consider an ensemble of pseudo-polarization vectors, each corresponding to a different detuning $\Delta\omega$.

For a pulse at resonance, the area θ_0 fully describes in which state the medium is left. It can be seen directly from the vector model of Fig. 3.5(a), or by direct integration of Bloch's equations (3.72), (3.73) and (3.74) for exact resonance [$\omega_\ell = \omega_0$ and $\dot{\varphi(t)} = 0$] and negligible relaxation ($T_1 \approx \infty$ and $T_2 \approx \infty$), that:

$$w_\infty = w(t = \infty) = w_0 \cos\theta_0. \tag{5.140}$$

Similarly, one finds that the polarization (absorptive component) is proportional to $\sin\theta_0$. A "π pulse" is thus a pulse that will completely invert a two-level system, leaving it in a pure state with no macroscopic polarization. A "2π pulse" will leave the system in the ground state, having completed a cycle of population inversion and return to ground state.

Because the area involves the integral of the electric field amplitude rather than the pulse intensity, higher energy densities will be required to achieve the same area with shorter pulses. Therefore, experiments of single photon coherent resonant interactions with fs pulses require intensities at which higher order nonlinear optical effects may have to be taken into account. Another consequence of the electric field amplitude dependence of the area is that, in an absorbing medium, it is possible to have the area conserved, or even growing with distance, while the energy is decreasing. Such a situation arises when the pulse duration increases with distance.

For inhomogeneously broadened media an "area theorem" can be derived which tells us exactly how the pulse area evolves with propagation distance. With the assumptions that the pulses are at resonance ($\omega_\ell = \omega_{ih}$), and shorter than both the energy relaxation time T_1 and the phase relaxation time T_2, a time integration of Eq. (3.76), taking into account Bloch's equations (3.72) through (3.74), yields the *area theorem* [44]:

$$\boxed{\frac{d\theta_0}{dz} = \frac{\alpha_0}{2}\sin\theta_0.} \tag{5.141}$$

where

$$\alpha_0 = \frac{\pi\mu_0\omega_\ell\, cp}{\hbar n} w_0(\omega_{ih}) = \frac{\pi\kappa^2\hbar\omega_\ell}{\epsilon_0 cnp} w_0(\omega_{ih}) \tag{5.142}$$

is the linear absorption coefficient (at resonance) for the inhomogeneously broadened transition. $w_0(\omega_{ih})$ is the initial inversion density at the transition center ($\omega_0' = \omega_{ih}$).

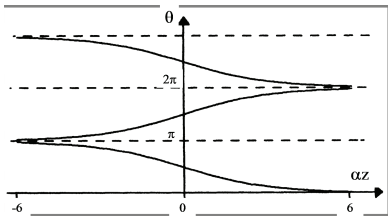

Figure 5.20: Graphic solution of the area theorem equation. The area is plotted as a function of distance (in units of linear absorption length (α_0^{-1}) for an absorbing medium. There is only one point on the set of curves that corresponds to any given area. The origin of distance is the abscissa corresponding to the initial area. From this initial point, a pulse will propagate to the right in an absorbing medium, to the left in an amplifier. Any initial area will evolve asymptotically with distance towards the limits 0, 2π, ..., $2N\pi$ (N integer) in an absorbing medium. The asymptotic limits are π, 3π, ..., $(2N+1)\pi$ in an amplifier.

The low intensity limit of Eq. (5.141) ($\sin\theta_0 \approx \theta_0$) is the exponential attenuation law (Beer's law). A remarkable feature of Eq. (5.141) is that it points to *area conserving pulses*. Indeed, for any pulse of area equal to a multiple of π, the area is conserved. This is true, for instance, for a "zero-area" pulse, which is not necessarily a zero energy pulse. A signal consisting of two pulses π out of phase has an area equal to zero, but an energy equal to twice the single pulse energy. Such a pulse sequence propagates without loss of "area" through a resonant medium.

The area theorem tells us in addition which of the steady state areas are stable solutions. For a pulse with an initial area smaller than π, the right side of Eq. (5.141) is negative, and the area as well as the pulse energy will decay with distance as the pulse is absorbed. On the other hand, if the pulse area is initially between π and 2π, θ *increases* with distance. With such a pulse, a population inversion has been achieved, and the pulse tail is amplified. The stimulated emission at the pulse tail results in pulse stretching, and hence an increase in pulse area with distance. The pulse energy, however, still decreases with distance in the reshaping process. Pulse reshaping proceeds until the area reaches the value of 2π. Once the pulse reshaping is completed, the electric field envelope has acquired a well

defined and stable hyperbolic secant (sech) shape and propagates without further distortion or attenuation through the resonant absorbing medium. This phenomenon is called *self-induced transparency*. Pulses of initial area $2n\pi$ break up into n "2π"pulses. It can easily be verified, by substitution into Eqs. (3.72) through (3.74) that the envelope given by:

$$\mathcal{E}(t) = \frac{2}{\kappa\tau_s}\,\mathrm{sech}\left(\frac{t}{\tau_s} - \frac{z}{\tau_s v_e}\right). \tag{5.143}$$

is a solution of Bloch's equations. The pulse given by Eq. (5.143) has an area of 2π, and a duration (FWHM) of $1.763\tau_s$. This solution is valid on- and off- resonance. In Eq. (5.143), $v_e \ll c$ is the envelope velocity of the 2π pulse. For a pulse duration short compared to the inverse (inhomogeneous) linewidth of the absorber, the envelope velocity is given by $v_e = 2/(\alpha_0\tau_s)$. This slow velocity essentially expresses that the first half $(\tau_s/2)$ of the pulse is absorbed in a distance α_0^{-1}, to be restored to the second half by stimulated emission.

5.6.1 Comparison between "2π" pulses and solitons

Stability

Energy is conserved in soliton pulse propagation, because only dispersive elements are involved. In the case of SIT, the total energy in the resonant light–matter system is conserved because the pulses are shorter than the energy relaxation time T_1, and no energy is dissipated into the bath. The pulse energy density was defined in Eq. (1.30):

$$W = \frac{1}{2}\epsilon_0 cn\int_{-\infty}^{\infty}\mathcal{E}^2 dt = \frac{1}{2}\sqrt{\epsilon/\mu_0}\int_{-\infty}^{\infty}\mathcal{E}^2 dt. \tag{5.144}$$

A simple energy conservation law can be derived by integrating Eq. (3.76) over time, after multiplying both sides by $\mathcal{E}$ and using the third Bloch equation (3.74):

$$\begin{aligned}\frac{dW}{dz} &= \sqrt{\frac{\epsilon}{\mu_0}}\int_{-\infty}^{\infty}\mathcal{E}\frac{\partial\mathcal{E}}{\partial z}dt \\ &= -\frac{\mu_0\omega_\ell\, c}{2}\sqrt{\frac{\epsilon}{\mu_0}}\int_{-\infty}^{\infty}\int_{0}^{\infty} v(\omega_0')\mathcal{E}g_{inh}(\omega_0'-\omega_{ih})d\omega_0' dt \\ &= -\frac{\hbar\omega_\ell}{2p}\int_0^{\infty}\Big[w_\infty(\omega_0') - w_0(\omega_0')\Big]g_{inh}(\omega_0'-\omega_{ih})d\omega_0'\end{aligned} \tag{5.145}$$

The population difference (per unit volume) $(w_\infty - w_0)/p$ integrated over the inhomogeneous transition is a measure of the energy stored in the medium, as a consequence of the energy lost by the pulse, dW/dz.

Both in soliton propagation and SIT, the pulse area tends to the stationary value (2π for SIT, π for soliton) where it remains constant. If the initial value is less than the asymptotic one, one may wonder how the area can increase while the energy is conserved? This is possible through pulse reshaping: pulse stretching can result in an increase in pulse area at constant energy.

"Pulse cleaning"

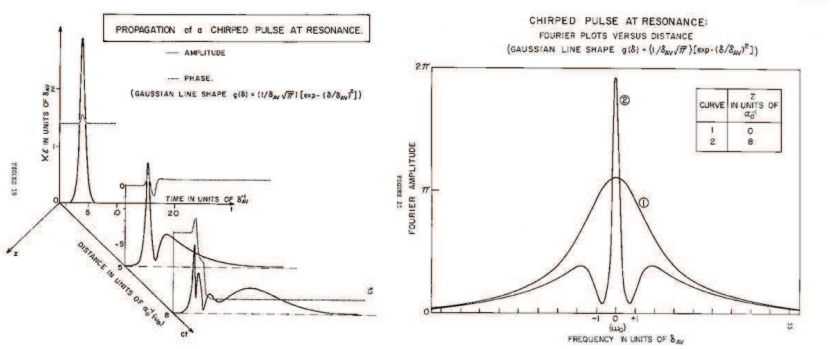

Figure 5.21: Propagation of a chirped pulse of initial area 3.5, and evolution towards a 2π pulse. Left: in the (retarded) time domain. Right: in frequency. The excess frequencies propagate at a faster velocity and are overtaken by the slow propagating 2π pulse. In frequency, the small signals shed away from the main pulse.

Both self-induced transparency and soliton propagation act as a filter to create bandwidth limited pulses. Whether at or off resonance, the 2π pulse is created at the original pulse frequency [46]. In SIT, the envelope velocity, of the order of one absorption length (at the pulse frequency) per pulse duration is considerably less than the phase and group velocities in the medium. Therefore, the slow moving distortionless 2π sech lets itself be overtaken by all spectral components considered as noise. This pulse cleaning is illustrated in Fig. 5.21. In addition to the separation in time, the low intensity are pushed away from resonance. The expression derived below (Section 5.6.1) shows that frequency shift, away from resonance, is the largest for weak signals. The situation is very similar to the evolution of an initially chirped pulse towards a soliton shown in Fig. 5.19. In both cases, "bumps" appear on both sides of the pulse spectrum, giving the pulse spectrum cats ears in the case of solitons in fibers (Fig. 5.19). In the case of SIT, there is a resonance involved, and the spectrum does not shed its background symmetrically for pulses off-resonance [46].

Frequency shift with distance

Bloch's equations describe the transient response of the complex polarization for a two-level system. The pulse frequency is no longer a conserved quantity in the presence of a transient polarization. An expression can be derived from Bloch's equations that establishes quantitatively the evolution of the average carrier frequency of a pulsed signal as it propagates through the medium. The notation $\langle\dot{\varphi}\rangle$ is used for the average phase derivative (average deviation of the frequency from ω_ℓ):

$$\langle\dot{\varphi}\rangle = \frac{\int_{-\infty}^{\infty}\mathcal{E}^2\dot{\varphi}dt}{\int_{-\infty}^{\infty}\mathcal{E}^2dt} = \frac{1}{2W}\left[\sqrt{\frac{\epsilon}{\mu_0}}\int_{-\infty}^{\infty}\mathcal{E}^2\dot{\varphi}dt\right]. \tag{5.146}$$

Multiplying both sides by W and taking the derivative we obtain:

$$\begin{aligned}\frac{d(W\langle\dot{\varphi}\rangle)}{dz} &= W\frac{d\langle\dot{\varphi}\rangle}{dz} + \langle\dot{\varphi}\rangle\frac{dW}{dz} \\ &= \frac{1}{2}\sqrt{\frac{\epsilon}{\mu_0}}\frac{d}{dz}\int_{-\infty}^{\infty}\mathcal{E}^2\dot{\varphi}dt\end{aligned} \tag{5.147}$$

The last term of Eq. (5.147) can be directly calculated using the Maxwell-Bloch equations. In particular, we can insert the time derivative of Eq. (3.77) in this equation:

$$\begin{aligned}&\frac{1}{2}\sqrt{\frac{\epsilon}{\mu_0}}\int_{-\infty}^{\infty}\left(\mathcal{E}^2\frac{\partial\dot{\varphi}}{\partial z} + \dot{\varphi}\frac{\partial\mathcal{E}^2}{\partial z}\right)dt \\ &\quad= -\frac{\omega_\ell}{4}\int_{-\infty}^{\infty}dt\int_0^{\infty}d\omega_0'\,g_{inh}(\omega_0'-\omega_{ih})\left[\dot{u}\mathcal{E}-u\dot{\mathcal{E}}+2v\mathcal{E}\dot{\varphi}\right] \\ &\quad= -\frac{\omega_\ell}{2}\int_0^{\infty}d\omega_0'\int_{-\infty}^{\infty}dt\,g_{inh}(\omega_0'-\omega_{ih})[\dot{u}\mathcal{E}+\dot{\varphi}v\mathcal{E}] \\ &\quad= -\frac{\omega_\ell}{2}\int_0^{\infty}d\omega_0'\int_{-\infty}^{\infty}dt\,g_{inh}(\omega_0'-\omega_{ih})\left[(\omega_0'-\omega_\ell)v\mathcal{E}-\frac{u\mathcal{E}}{T_2}\right]\end{aligned} \tag{5.148}$$

where we have made use of the first Bloch equation (3.72). We have already derived an expression for the evolution of the pulse energy density W. Combining Eqs. (5.145),(5.147), and (5.148) yields the following expression for the evolution with propagation distance of the pulse carrier frequency:

$$\boxed{\frac{d\langle\dot{\varphi}\rangle}{dz} = \frac{\omega_\ell}{2\kappa W}\int_0^{\infty}g_{inh}(\omega_0'-\omega_{ih})\left[\omega_0'-\omega_\ell-\langle\dot{\varphi}\rangle\right](w_\infty-w_0)\,d\omega_0' + \frac{2\langle k\rangle}{T_2}.} \tag{5.149}$$

In analogy to the definition of the average frequency in Chapter 1 [cf. Eq. (1.26)], we have introduced the average contribution to the propagation vector due to the

resonant dispersion of the two-level system:

$$\begin{aligned} \langle k \rangle &= \frac{\int_{-\infty}^{\infty} \mathcal{E}^2 (\partial\varphi/\partial z) dt}{\int_{-\infty}^{\infty} \mathcal{E}^2 \, dt} \\ &= \frac{\omega_\ell}{4W} \int_0^\infty d\omega_0' \int_{-\infty}^{\infty} dt \; g_{inh}(\omega_0' - \omega_{ih}) u \mathcal{E} \end{aligned} \tag{5.150}$$

The polarization amplitude u — and hence the resonant contribution to the wave vector $\langle k \rangle$ — will shrink with time in presence of phase relaxation (finite T_2). The corresponding temporal modulation of the polarization is responsible for the second term of the right-hand side of Eq. (5.149). For very short pulses, however, ($\tau_p \ll T_2$), this second term can be neglected.

5.7 Quantum Solitons

As shown in the previous section, A rigorous theory of the quantum theory of solitons is far beyond the scope of this chapter. We will limit ourselves to a qualitative description of the operators involved, trying to explain the physics while referring to the literature for a deeper understanding.

5.7.1 Kerr Effect

We have seen in Chapter 4 that, for interaction lengths much shorter than the dispersion length L_D, and for an instantaneous nonlinearity, the wave equation (4.13) with the source term (4.65) simplifies to

$$\frac{\partial}{\partial z}\tilde{\mathcal{E}}(z,t) = -i\frac{3\omega_\ell^2\chi^{(3)}}{8c^2k_\ell}|\tilde{\mathcal{E}}^2|\tilde{\mathcal{E}} = -i\frac{n_2}{n_0}k_\ell\tilde{\mathcal{E}}^*\tilde{\mathcal{E}}\tilde{\mathcal{E}}. \tag{5.151}$$

This equation is equivalent to the normalized Eq. (5.103) from the previous section with the dispersion term neglected. After numerous complex manipulations [19], one can derive the corresponding Heisenberg equation of motion for the creation/annihilation operators:

$$\frac{\partial}{\partial z}\hat{A}(t) = -iK\hat{A}^\dagger(t)\hat{A}(t)\hat{A}(t), \tag{5.152}$$

which resembles Eq. (5.151) where the fields $\tilde{\mathcal{E}}$ and $\tilde{\mathcal{E}}^*$ have been replaced by the annihilation ($\hat{A}$) and creation ($\hat{A}$) operators. Let us consider radiation propagation along a fiber with Kerr coefficient. The initial locus of the exp(−2) points of the probability distribution starts as the circle of minimum uncertainty for a coherent state input. The equation of motion conserves the photon number leaving the operator $\hat{A}^\dagger(t)\hat{A}(t)$ independent of z. Integrating Eq. (5.152) from $z = 0$ to $z = L$ yields:

$$\hat{A}(L,t) = e^{-iK\hat{A}^\dagger(0,t)\hat{A}(0,t)L}\hat{A}(0,t) \tag{5.153}$$

With the approximation that the change is small:

$$\hat{A}(L,t) = A_0(L,t) + \Delta\hat{A}(L,t) \tag{5.154}$$

where $A_0(L,t)$ is the classical phase shifted field:

$$A_0(L,t) = e^{-iK|A(0,t)|^2L}A(0,t) \tag{5.155}$$

Substituting into Eq. (5.153) the approximation (5.154) and the classical field (5.155).

$$\begin{aligned} A_0(L,t) + \Delta\hat{A}(L,t) &= e^{-iKL[A_0^* + \Delta\hat{A}_0^\dagger][A_0 + \Delta\hat{A}_0]} \times [A_0 + \Delta\hat{A}_0] \\ &\approx e^{-iKL[|A_0|^2 + \Delta\hat{A}_0^\dagger A_0 + \Delta\hat{A}_0 A_0^*]} \times [A_0 + \Delta\hat{A}_0] \\ &\approx e^{-iKL|A_0|^2}\left[A_0 - iKL|A_0|^2\Delta\hat{A}_0 + \Delta\hat{A}_0 - iKLA_0^2\Delta\hat{A}_0^\dagger - iKLA_0\Delta\hat{A}_0^\dagger\Delta\hat{A}_0 - iKLA_0^*\Delta\hat{A}_0^2\right] \end{aligned} \tag{5.156}$$

where, for clarity of representation, we have used, for the operators, the notation $\Delta\hat{A}_0$ for $\Delta\hat{A}(0,t)$ and $\Delta\hat{A}_0^\dagger$ for $\Delta\hat{A}^\dagger(0,t)$; and for the coherent fields the notation A_0 for $A_0(0,t)$ and A_0^* for $A^*(0,t)$. Equating the first order terms:

$$\begin{aligned}\Delta\hat{A}(L,t) &\approx e^{-iKL|A_0|^2}\left\{\left[1-iKL|A_0|^2\right]\Delta\hat{A}_0 - iKLA_0^2\Delta\hat{A}_0^\dagger\right\}\\ &= e^{-iKL|A_0|^2}\left[\mu\Delta\hat{A}_0 - \nu\Delta\hat{A}_0^\dagger\right],\end{aligned} \tag{5.157}$$

which we recognize as the Bogoliubov transformation (cf. Sections 5.4.1 and 5.4.4)with

$$\begin{aligned}\mu &= 1 - iKL|A_0|^2\Delta\hat{A}_0 = 1 - i\Phi\\ \nu &= iKLA_0^2\Delta\hat{A}_0^\dagger = -i\Phi e^{2\arg[A_0]}.\end{aligned} \tag{5.158}$$

The transformation (5.157) satisfies indeed the relation $|\mu|^2 - |\nu|^2 = 1$. Let us assume we start with a coherent state of zero phase $\arg[A_0(0,t) = 0$, as indicated by the blue arrow in Fig. 5.22. After a distance L, the state has rotated by an angle Φ (dashed arrow in Fig. 5.22), as can be seen by equating the zero-order terms of Eq. (5.156). The initial circular uncertainty changes into an ellipse, that remains between the concentric circles drawn from the extrema of the uncertainty circle. This is understandable, since the Kerr effect affects only the phase and not the amplitude of the field. Because the Bogoliubov transformation is unitary, the area of the ellipse remains equal to the area of the initial uncertainty circle.

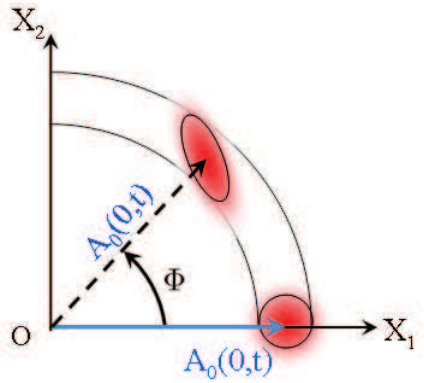

Figure 5.22: Squeezing by Kerr effect.

5.7.2 The quantum nonlinear Schrödinger equation

Normalized equations

We have derived in Section 5.5.2 a dimensionless nonlinear Schrödinger equation, using a field u normalized by means of the Kerr effect, the wavelength is chosen as distance unit, and the time is normalized through the second order dispersion. The quantum mechanical correspondent of the classical Eq. (5.103) is:

$$i\frac{\partial\hat{A}}{\partial z} = \frac{1}{2}\frac{\partial^2\hat{A}}{\partial t^2} + \hat{A}^\dagger\hat{A}\hat{A}. \tag{5.159}$$

It is worth noting here that in most original papers and textbooks (see for instance [19, 47, 48]), the time and space coordinates have been interchanged. A discussion on this flip of coordinates can be found in Appendix D. We have chosen to use here the conventional retarded frame of reference attached to the moving soliton.

In analyzing the quantum mechanical nonlinear Schrödinger equation, one proceeds in a similar way as for the analysis of the Kerr effect alone, by decomposing the operator $\hat{A}$ in a large classical part $u_0(z,t)$ and a perturbation δU : $\hat{A} = u_0 + \delta U$. We assume next that the fluctuations δU are split into a soliton perturbation $\Delta\hat{A}$ and a non-soliton (radiation) component f: $\delta U = \Delta\hat{A} + f$. The zero-order approximation of Eq. (5.159) is:

$$i\frac{\partial u_0}{\partial z} = \frac{1}{2}\frac{\partial^2 u_0}{\partial t^2} + u_0^* u_0 u_0. \tag{5.160}$$

which has as solution:

$$u_0(z,t) = A_0 \ \mathrm{sech}\left(\frac{t}{\tau_s}\right) e^{-iA_0^2 z/2 + i\phi} \tag{5.161}$$

with $\tau_s = 1/A_0$ for the first order soliton.

Let us use the notation $\mathcal{L}$ for the operator:

$$\mathcal{L} = -i\frac{\partial}{\partial z} + \frac{1}{2}\frac{\partial^2}{\partial t^2} + 2|u_0|^2 + u_0^2. \tag{5.162}$$

The equation for the variation $\mathcal{L}\Delta\hat{A} + \mathcal{L}f = 0$ is, to first order:

$$\mathcal{L}f = -\left[-i\frac{\partial\Delta\hat{A}}{\partial z} + \frac{1}{2}\frac{\partial^2\Delta\hat{A}}{\partial t^2} + 2|u_0|^2\Delta\hat{A} + u_0^2\Delta\hat{A}^\dagger\right]. \tag{5.163}$$

Due to the nonlinearity, the equations couple $\Delta\hat{A}$ and $\Delta\hat{A}^\dagger$ so that Eq. (5.163) corresponds to two coupled equations. Linear equations of motion of an operator are in one to one correspondence with linear equations of motion of the classical evolution equation. The integration can proceed classically, and the classical transfer functions apply directly to the quantum problem. It is therefore not surprising that a detailed derivation of the solution of the quantum soliton perturbation problem, which can be found in [19, 49], lead to the same conclusion as the perturbation of the classical soliton outlined in Section 5.5.3. When the Ansatz $\delta U = \Delta\hat{A} + f$ is introduced into the linearized nonlinear Schrödinger equation, we find that no new function are generated. A perturbation in the number of photon number propagated unperturbed, but affects the phase through the Kerr effect. A perturbation in frequency also propagates undisturbed, but results in a pulse center displacement through the frequency dependence of the group velocity.

While the photon number perturbation does not change to first order with propagation, the phase is affected via the Kerr effect. Similarly, a perturbation frequency $\Delta\omega$ is stable to first order, but it affects the position of the soliton center via the the group velocity dispersion (second derivative term in the soliton equation)

The quantum soliton evolution can be understood directly from the uncertainty principle. The number of photons is an invariant in the soliton propagation. The Kerr effect causes a quantum diffusion in phase, associated with a squeezing in photon number as shown in Section 5.7.1. The time-frequency uncertainty implies a position (soliton center t_c) diffusion.

5.7.3 Soliton squeezing experiment in fibers

A diagram of a typical soliton squeezing experiment [50] is sketched in Fig. 5.23(a). This is an all fiber experiment that could also be realized with discrete components. For the sake of clarity, the various functions of the fiber components are represented in block diagrams. The principle of the experiment is to interfere, in a Mach Zehnder interferometer, a soliton with a dispersive wave produced by the same source. The Kerr effect distorts the soliton coherent-symmetrical noise distribution in the upper arm of the interferometer. The resultant crescent shaped distribution is rotated by interference with an auxiliary pulse sent through the lower arm of the interferometer. The 180 fs pulses at 1540 nm are first split into orthogonally pola-

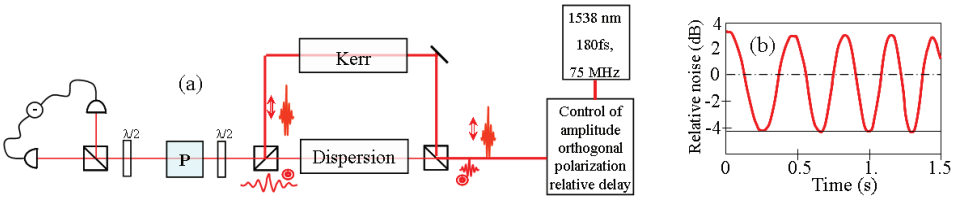

Figure 5.23: (a) Block diagram of the soliton squeezing experiment in a Mach-Zehnder fiber interferometer [50]. (b) The sum photocurrent noise is plotted as a function of relative phase between the two inputs to the Mach Zehnder.

rized pulses of intensity ratio 1 to 10, into branches of a Michelson interferometer. The output of that interferometer is a sequence of two orthogonally polarized pulses with adjustable relative delay and phase. The pulse polarized in the plane of the figure is sent as a soliton to the upper branch of the Mach Zehnder. The other (weak) pulse is sent through a very dispersive branch of the Mach Zehnder. The orthogonally polarized components at the output of the Mach Zehnder are projected as equal components onto the axis of a polarizer (P). The signal is analyzed on a balanced homodyne detector, as a function of the relative phase of the two

pulses injected in the Mach Zehnder. The sum photocurrent noise is plotted as a function of relative phase in Fig. 5.23(b) (red curve).

5.7.4 Experiments in fiber involving soliton collision

It was already recognized in the early times of self-induced-transparency that solitons can collide, and pass through each other while conserving their properties. Computer simulations have also shown this property to extend to solitons in fibers. In the case of quantum solitons, the position and phase of one of the collision protagonist is modified by an amount dependent upon the velocity and photon number (intensity) of the other. The phase change $\Delta\varphi_1$ of soliton 1, after colliding with soliton 2, can be approximated by [47, 51]:

$$\Delta\varphi_1 \approx \frac{4N_2}{N_{av}(v_2 - v_1)}, \tag{5.164}$$

where v_i and N_i are the velocities and photon numbers of the respective solitons, and N_{av} the average photon number. The larger the photon number (intensity), the larger the Kerr effect, dominated by mutual modulation, hence the dependence on the photon number of the other soliton. The phase shift is inversely proportional to the velocity difference: the larger the velocity difference, the shorter the interaction time.

5.8 Noise measurements and cancelation

5.8.1 Phase, frequency noise and power spectral density

The limits of most measurements are set by various kinds of spurious signals which can be defined as noise. They include perturbations caused mechanical vibration, air currents, dark current noise in detectors, laser noise, *etc*... perturbations usually uncorrelated with the data.

The topic of noise is quite exhaustive, as different theories have been established for electronic noise, noise in communications, noise in frequency combs, soliton noise, quantum noise... This topic has generated numerous complex books [19, 52] and articles. In most articles, the notations and nomenclature are derived from radio frequency. In our representation of a complex field $E(t) = (1/2)\mathcal{E}(t)\exp[i(\omega_\ell t + \varphi(t)]$ phase or frequency noise is generally caused by slow (compared to ω_ℓ) fluctuations in the phase factor φ. As is traditional with RF oscillators [53], instead of using the phase fluctuations in the time domain, one takes the Fourier trans-

form of $\varphi(t)$ to define a $\varphi(2\pi\Omega) = \varphi(f)$ with dimension of radian/Hz[5]. The phase noise Power Spectral Density (PSD) is traditionally defined as the mean square deviation $S_\varphi(f) = \langle\varphi^2\rangle = \int_{-\infty}^{\infty} \varphi(f)^2 df$ in units of radian^2/Hz. Another popular approach is to take the Fourier transform of the instantaneous frequency fluctuation $\nu(t) = (1/2\pi)d\varphi(t)/dt$, take its Fourier transform $\nu(f) = \nu(2\pi\Omega)$ in units of Hz/Hz. The frequency noise PSD is defined as the mean square deviation $S_\nu(f) = \langle\nu^2\rangle = \int_{-\infty}^{\infty} \nu(f)^2 df$ in units of Hz^2/Hz. Given a source centered at f_c, the common measure of noise is its linewidth FWHM, which can be measured by heterodyning the source with a perfect monochromatic source and taking the FWHM of the beat signal. Unlike the FWHM which is simply a number, the PSD is a function of f. Analytical relations between the FWHM and the PSD can be found in the literature for various noise statistics [53]. For instance, for a white frequency noise, the linewidth is simply related to the PSD at the central frequency:

$$\Delta\nu = \pi S_\nu(f_c). \tag{5.165}$$

Most of these "trivial" noise mentioned at the beginning of this paragraph is generally more troublesome at low frequencies, with its (PSD) showing a distribution roughly proportional to $1/f$ (falling by 10 dB per decade of frequency). This is only a coarse approximation, but the reason that most feedback loops are designed with a gain decreasing with frequency by a factor 10 for each decade of frequency.

5.8.2 Shot noise and Johnson noise

For an ideal photodetector of 100% quantum efficiency, the Poisson statistics of a coherent optical beam is reflected in the photocurrent i. The photoelectron have thus also a Poisson statistics, with the root mean square deviation $\sqrt{\sigma_{Ne}^2} = \sqrt{\langle N_e^2 - \langle N_e\rangle^2\rangle} =$. In a bandwidth B, the average number of electrons is $\langle N_e\rangle \approx i/Be$. The RMS noise current in a bandwidth B is then the square root of this number, times the bandwidth and the electron charge e:

$$i_{rms} = Be\sqrt{\langle N_e\rangle} = \sqrt{2eiB}, \tag{5.166}$$

where a mysterious factor 2 appears because of the equivalent noise bandwidth of a one second averaging window is 0.5Hz [54]. The rms noise current Is quite small in application with cw beams of narrow bandwidth. For instance, for 1 Hz bandwidth, with 10 mW beam impinging on a 0.3A/W sensitivity detector creates a current

[5]Not to be confused with the phase $\phi(\Omega)$ of the Fourier transform, which is of course dimensionless.

response of 3 mA, while the shot noise current is only 30 pA. Equation 5.166 can be used to define a power signal to noise ratio:

$$SNR = \frac{i^2}{i_{rms}^2} = \frac{i}{2eB}. \tag{5.167}$$

Another source of noise is the thermal or Johnson noise associated with the load resistance R_ℓ used with the detector. The equivalent current i_t associated with this noise is:

$$i_\ell = \sqrt{\frac{4kT\ B}{R_\ell}}. \tag{5.168}$$

This contribution increases for fast detection, because of the bandwidth increase, and the fact that small values of load resistance are used to minimize the $R_\ell C$ time response of the detector. The latter problem can be alleviated through the use of transimpedance amplifiers.

The sensitivity of most measurement is directly related to the signal to noise ratio. One classical method is to chop the signal and use a lock-in amplifier for detection. Because of the $1/f$ frequency dependence of the noise, a high chopping frequency is desired, implying a high frequency lock-in amplifier. The ultimate method to eliminate the low frequency noise is to send the laser beam in an interferometer (for instance Mach Zehnder or Michelson). One branch carries the signal beam to be affected by the measurement, the other a reference beam shifted in frequency. The shifting can be made by either an acousto-optic frequency shifter, or an electro-optic modulator. An alternative is to use as a source a mode-locked laser emitting two correlated combs [2]. The carrier frequency of these combs can be as high as half the laser repetition rate, which can be in the GHz range [55]. The purpose of these frequency shifted methods is to have a beat signal translated up to a high frequency outside of the $1/f$ region, where the background noise is low. These methods improve the power spectral density of the noise in the detected signal, usually reaching the shot noise limit.

5.8.3 Noise in Intracavity Phase Interferometry

Most optical measurement use an square law detector to measure a change in amplitude of a signal to be detected. They are therefore subject to the shot noise limitation addressed in the previous section. This section describes another measurement technique based directly on measuring the phase of an optical signal, independently of the amplitude, hence not directly subjected to the shot noise limit. A single mode-locked laser can produce two frequency combs that are correlated. Therefore, interfering these two frequency combs produces a beat note many orders

of magnitude narrower than a single mode of either comb. Using the mode-locked laser with two pulses circulating in the cavity is a technique known as Intracavity Phase Interferometry (IPI) [2]. The physical quantity to be measured induces a relative phase shift $\Delta\varphi$ between the two pulses at each round-trip. As a result, the two frequency combs issued from the laser have different optical frequencies, and the superposition of these two combs produces a beating at a frequency proportional to the phase difference. As in heterodyne interferometry where a laser beam is made to interfere with a frequency shifted (outside the "1/f" region) clone in an interferometer, the noise is improved to the shot noise limit. Indeed, in IPI a phase difference is measured in a time interval of one cavity round-trip time, or $\approx$ 10 ns, only affected by the noise components near 100 MHz. However, we are not concerned with amplitude noise, since it is the frequency of the beat signal that constitutes the measurement.

A topological sketch of ring and linear laser implementations is shown in Fig. 5.24. Two pulses circulate in the cavities, meeting at a point indicated by a cross. There is no phase coupling between the two pulses if the crossing point is in a medium that does not backscatter. This can be obtained either by a flowing saturable absorber, or an Optical Parametric Oscillator (OPO) crystal as a gain me-

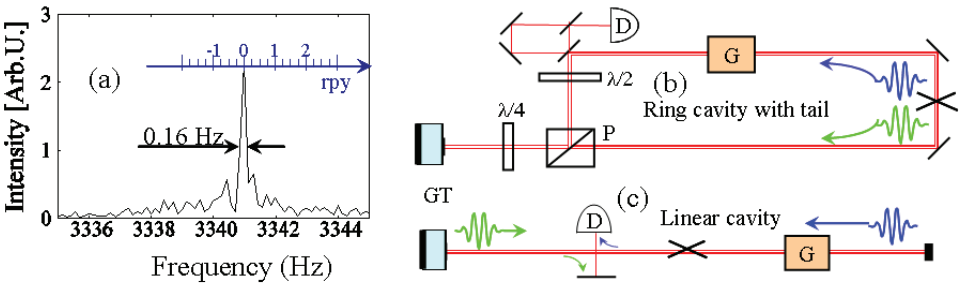

Figure 5.24: (a) Typical IPI response (b)Sketch of a ring cavity for IPI. (c) Sketch of a linear IPI cavity.

dium (the crossing point is then controlled by the delay between two oppositely directed pump pulses), or by having the circulating pulses be orthogonally polarized. In Fig. 5.24, GT designates the end mirror that can be a Gires-Tournois interferometer for enhancement of the IPI response [56].

The beat note frequency $\Delta\nu$ measured in IPI is:

$$\Delta\nu = \nu\frac{\Delta L}{L} = \frac{\Delta\varphi}{2\pi\tau_{ph}}, \tag{5.169}$$

where ν is the optical frequency, ΔL the difference between the two arms of the

interferometer, L the cavity length, and τ_{ph} the cavity round-trip time at the phase velocity.

A crude estimate of the quantum limit of IPI measurements can be made using the uncertainty relation between phase and photon number (5.75). Let us consider an IPI laser with a $P = 10$ mW power, producing a beat note with a bandwidth $\Delta\nu_b \approx 1$Hz, which corresponds to a phase shift resolution of 10^{-8} radian as in reference [3]. The photon flux being $P/h\nu$, during the measurement time of $1/\Delta_b\nu = 1$ s The photon number $\langle N\rangle$ is:

$$\langle N\rangle \approx \frac{P}{h\nu\Delta_b\nu} \approx \frac{10^{-2}}{6.6\cdot 10^{-34}\times 3\cdot 10^{14}} = (1/20)10^{18}. \tag{5.170}$$

Assuming a coherent beam, the minimum phase uncertainty is:

$$\Delta\varphi_{min} \approx \frac{1}{2\langle\Delta N\rangle} = \frac{1}{2\sqrt{\langle N\rangle}} \approx 0.25\cdot 10^{-8}, \tag{5.171}$$

estimate remarkably close to the measured value in reference [3].

Bibliography

[1] Carlton M. Caves, Kip S. Thorne, Ronald W. P. Drever, Vernon D. Sandberg, and Mark Zimmermann. Quantum-mechanical noise in an interferometer. *Physical Review D*, 23(8):1694–1708, 1981.

[2] L. Arissian and J.-C. Diels. Intracavity phase interferometry: frequency comb sensors inside a laser cavity. *Laser & Photonics Rev*, 8:799–826, 2014.

[3] Andreas Velten, Andreas Schmitt-Sody, and Jean-Claude Diels. Precise intracavity phase measurement in an optical parametric oscillator with two pulses per cavity round-trip. *Optics Letters*, 35:1181–1183, 2010.

[4] Carl M. Bender and Stefan Boettcher. Real spectra in non-hermitian hamiltonians having $\mathcal{PT}$ symmetry. *Phys. Rev. Lett.*, 80:5243–5246, Jun 1998.

[5] Ramy El-Ganainy, Konstantinos G. Makris, Mercedeh Khajavikhan, Ziad H. Musslimani, Stefan Rotter, and Demetrios N. Christodoulides. Non-hermitian physics and pt symmetry. *Nature Physics*, 14:11–19, 01 2018.

[6] Brian Baum, Mark Lawrence, David Barton, Jennifer Dionne, and Hadiseh Alaeian. Active polarization control with a parity-time-symmetric plasmonic resonator. *Phys. Rev. B*, 98:165418, Oct 2018.

[7] Ashok Kodigala, Thomas Lepetit, and Boubacar Kanté. Exceptional points in three-dimensional plasmonic nanostructures. *Phys. Rev. B*, 94:201103, Nov 2016.

[8] Tamar Goldzak, Alexei A. Mailybaev, and Nimrod Moiseyev. Light stops at exceptional points. *Phys. Rev. Lett.*, 120:013901, Jan 2018.

[9] Weijian Chen, Şahin Kaya Özdemir, Guangming Zhao, Jan Wiersig, and Lan Yang. Exceptional points enhance sensing in an optical microcavity. *Nature*, 548:192–196, 08 2017.

[10] Jan Wiersig. Enhancing the sensitivity of frequency and energy splitting detection by using exceptional points: Application to microcavity sensors for single-particle detection. *Phys. Rev. Lett.*, 112:203901, May 2014.

[11] Hossein Hodaei, Mohammad-Ali Miri, Matthias Heinrich, Demetrios N. Christodoulides, and Mercedeh Khajavikhan. Parity-time–symmetric micrroring lasers. *Science*, 346(6212):975–978, 2014.

[12] Wenlong Yang, Matthew Springer, James Strohaber, Alexandre Kolomenski, Hans Schuessler, George Kattawar, and Alexei Sokolov. Spectral phase retrieval from interferometric autocorrelation by a combination of graduated optimization and genetic algorithms. *Opt. Express*, 18(14):15028–15038, Jul 2010.

[13] A. Guo, G. J. Salamo, D. Duchesne, R. Morandotti, M. Volatier-Ravat, V. Aimez, G. A. Siviloglou, and D. N. Christodoulides. Observation of $\mathcal{PT}$-symmetry breaking in complex optical potentials. *Phys. Rev. Lett.*, 103:093902, Aug 2009.

[14] Chengyong Feng, Xiaozhen Xu, and Jean-Claude Diels. Generation of 300 ps laser pulse with 1.2 J energy by stimulated Brillouin scattering in water at 532 nm. *Opt. Lett.*, 39(12):3367–3370, 2014.

[15] Jiangang Zhu, Şahin Kaya Özdemir, Lina He, and Lan Yang. Controlled manipulation of mode splitting in an optical microcavity by two rayleigh scatterers. *Opt. Express*, 18(23):23535–23543, Nov 2010.

[16] Hossein Hodaei, Absar U. Hassan, Steffen Wittek, Hipolito Garcia-Gracia, Ramy El-Ganainy, Demetrios N. Christodoulides, and Mercedeh Khajavikhan. Enhanced sensitivity at higher-order exceptional points. *Nature*, 548:187–191, 08 2017.

[17] Andreas Schmitt-Sody, Ladan Arissian, Andreas Velten, Jean-Claude Diels, and Dave Smith. Rabi cycling of two pulses in a mode-locked ring laser cavity with electro-optical control. *Physical Review A*, 78:063802, 2008.

[18] Luke Horstman, Ning Hsu, James Hendrie, David Smith, and Jean-Claude Diels. Exceptional points and the ring laser gyroscope. *Photon. Res.*, 8(3):252–256, Mar 2020.

[19] Hermann A. Haus. *Electromagnetic noise and quantum optical measurements*. Springer, Berlin,m Heidelberg, 2000.

[20] N. N. Bogoliubov and D. V. Shikkov. *Introduction to the theory of quantized fields*. Interscience, New York, 1959.

[21] J. Ye. Absolute measurement of a long, arbitrary distance to less than an optical fringe. *Opt. Lett.*, 29:1153–1155, 2004.

[22] Shaofeng Wang, Xiao Xiang, Nicolas Treps, Claude Fabre, Tao Liu, Shougang Zhang, and Ruifang Dong. Sub-shot-noise interferometric timing mea-

surement with a squeezed frequency comb. *Physical Review*, 175:256–266, 2018.

[23] K. H. Drever, J. L. Hall, F. V. Kowalski, J. Hough, G. M. Ford, A. J. Munley, and H. W. Ward. Laser phase and frequency stabilization using an optical resonator. *Appl. Phys.B*, 31:97–105, 1983.

[24] J. S. Russell. Report on wave. In *Report of the fourteenth meeting of the British Association for the Advancement of Science*, pages 311–390, York, 1844.

[25] R K Bullough. The wave, "par excellence", the solitary, progressive great wave of equilibrium of the fluid - an early history of the solitary wave. In M Lakshmanan, editor, *Solitons*, pages 150–281. Springer Series in Nonlinear Dynamics, 1988.

[26] J.-C. Diels, W. Dietel, J. J. Fontaine, W. Rudolph, and B. Wilhelmi. Analysis of a mode-locked ring laser: chirped-solitary-pulse solutions. *J. Opt. Soc. Am. B*, 2:680–686, 1985.

[27] W. Dietel, J. J. Fontaine, and J.-C. Diels. Intracavity pulse compression with glass: a new method of generating pulses shorter than 60 femtoseconds. *Optics Letters*, 8:4–6, 1983.

[28] J. J. Fontaine, W. Dietel, and J.-C. Diels. Chirp in a mode-locked ring dye laser. *IEEE J. of Quantum Electron.*, QE-19:1467, 1983.

[29] X. Liu, L. Qian, and F. Wise. High-energy pulse compression by use of negative phase shifts produced by the cascade $\chi^{(2)} : \chi^{(2)}$ nonlinearity. *Optics Letters*, 24:1777–1779, 1999.

[30] V. E. Zakharov and A. B. Shabat. Exact theory of two-dimensional self-focusing and one-dimensional self-modulation of waves in nonlinear media. *Sov. Phys. JETP*, 34:62–69, 1972.

[31] Richard DeSalvo, David J. Hagan, G. Stegeman, and Eric W. Van Stryland. Self-focusing and self-defocusing by cascaded second-order effects in KTP. *Optics Letters*, 17:28–30, 1993.

[32] Junkichi Satsuma and Nobuo Yajima. Initial value problems of one-dimensional self-modulation of nonlinear waves in dispersive media. *Supplement of the Progress of Theoretical Physics*, 12:284–306, 1974.

[33] C. Desem and P. L. Chu. Effect of chirping on solution propagation in single-mode optical fibers. *Optics Letters*, 11:248–250, 1986.

[34] S. M. J. Kelly. Characteristic sideband instability of periodically amplified average soliton. *Electron. Lett.*, 28:806–807, 1992.

[35] H. A. Haus, J. G. Fujimoto, and E. P. Ippen. Structures for additive pulse mode locking. *J. Opt. Soc. Am. B*, 8:2068–2076, 1991.

[36] O. E. Martinez, R. L. Fork, and J. P. Gordon. Theory of passively mode locked lasers for the case of a nonlinear complex propagation coefficient. *J.Opt.Soc.Am.*, B2:753–760, 1985.

[37] H. A. Haus. Theory of mode-locking with a fast saturable absorber. *J. Appl. Phys.*, 46:3049, 1975.

[38] H. A. Haus. Theory of mode-locking with a slow saturable absorber. *IEEE J. of Quantum Electron.*, QE-11:736–746, 1975.

[39] F. X. Kaertner and I.D. Jungand U. Keller. Soliton mode-locking with saturable absorbers. *IEEE J. Sel. Top. Quantum Electron.*, 2:540, 1996.

[40] P. Del'Haye, A. Schliesser, O. Arcizet, T. Wilken, R. Holzwarth, and T. J. Kippenberg. Optical frequency comb generation from a monolithic microresonator. *Nature*, 450:7173, 2007.

[41] L. Kornaszewski, G. Maker, G. P. A. Malcolm, M.Butkus, E. U. Rafailov, and C. J. Hamilton. Sesamfree modelocked semiconductor disk laser. *Laser Photonics Review*, 6:L20–L23, 2007.

[42] Christoph Weber, Lorenzo L. Columbo, Mariangela Gioannini, Stefan Breuer, and Paolo Bardella. Threshold behavior of optical frequency comb self-generation in an inas/ingaas quantum dot laser. *Optics Letters*, 44:3478–3481, 2019.

[43] Andreas Hugi, Gustavo Villares, Stéphane Blaser, HC Liu, and Jérome Faist. Mid-infrared frequency comb based on a quantum cascade laser. *Nature*, 492:229–233, 2012.

[44] S. McCall and E. L. Hahn. Self-induced transparency. *Phys. Rev.*, 183:457, 1969.

[45] R. P. Feynman, F. L. Vernon, and R. W. Hellwarth. Geometrical representation of the Schroedinger equation for solving maser problems. *J. Appl. Phys.*, 28:49–52, 1957.

[46] J.-C. Diels and E. L. Hahn. Carrier-frequency distance dependence of a pulse propagating in a two-level system. *Phys. Rev. A*, A-8:1084–1110, 1973.

[47] H. A. Haus, K. Watanabe, and Y. Yamamoto. Quantum-nondemolition measurement of optical solitons. *J. Opt. Soc. Am. B.*, 6:1138–1148, 1989.

[48] H. A. Haus and Y. Lai. Quantum theory of soliton squeezing: a linearized approach. *J. 716*, pages 386–392, 1990.

[49] D. J. Kaup. Perturbation theory for solitons in optical fibers. *Physical Review A*, 42:5689–5694, 1990.

[50] M. Fiorentino, Jay E. Sharping, Prem Kumar, Dmitry Levandovsky, and Michael Vasilyev. Soliton squeezing in a mach-zehnder fiber interferometer. *Phy. Rev. A*, 64:031801, 2001.

[51] P. D. Drummond, R. M. Shelby, and S. R. Friberg amd Y. Yamamoto. Quantum solitons in optical fibres. *Nature*, 365:307–313, 1993.

[52] William H. Louisell. *Radiation and Noise In Quantum Electronics*. Radiation and Noise In Quantum Electronics, New York, 1964.

[53] D. B. Sullivan, D. W. Allan, D. A. Howe, and F. L. Walls. Characterization of clocks and oscillators. *NIST Technical Note*, 1337:TN–1–TN–187, 1990.

[54] Phillip C. D. Hobbs. Reaching the shot noise limit. *Optics and Photonlcs News*, pages 17–23, April 1991.

[55] A. Bartels, D. Heinecke, and S. A. Diddams. Passively mode-locked 10 ghz femtosecond ti:sapphire laser. *Optics Letters*, 33:1905–1907, 2008.

[56] James Hendrie, Matthias Lenzner, Hanieh Akhamiardakani, Jean-Claude Diels, and Ladan Arissian. Impact of resonant dispersion on the sensitivity of intracavity phase interferometry and laser gyros. *Optics Express*, 24:30402–304010, 2016.

Chapter 6

Ultrashort Sources I - Fundamentals

6.1 Introduction

The standard source of ultrashort pulses is a mode-locked laser. Fundamental properties of the radiation emitted by such a source, both in time and frequency domains, are presented in this first section. Section 6.2 exposes the main theoretical models to predict the shape of the pulses generated in such a laser. General considerations about the evolution of the pulse energy are given in Section 6.3. Section 6.4 is dedicated to the analysis of the main components of the laser, outlining the mechanism of pulse shaping of each element (or groups of elements). Of course, the laser resonator itself has its role in the mode-locked operation. The remainder of this chapter, Section 6.5 is therefore dealing with the properties of the laser cavity.

6.1.1 Superposition of cavity modes

Central to the generation of ultrashort pulses is the laser cavity with its longitudinal and transverse modes. A review of the mode spectrum of a laser cavity is contained in Section 6.5.1. "Mode-locked" operation requires a well defined mode structure. As will be shown below, mode-locking refers to establishing a phase relationship between longitudinal modes. A transverse mode structure will generally contribute to amplitude noise (at frequencies corresponding to the differences between mode frequencies). Most fs lasers operate in a single TEM_{00} transverse mode. A typical laser cavity can support a large number of longitudinal modes. In the absence of transverse mode structure, we can consider that the laser can operate on any of the

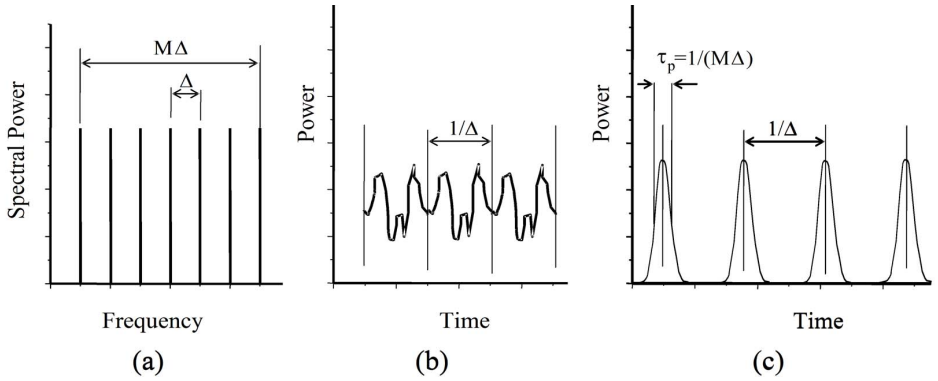

Figure 6.1: Spectral amplitude of a set of equally spaced cavity modes (a), and possible field amplitudes in the time domain, (b) and (c), that belong to this spectrum. In (b), the modes have a random phase distribution. In (c), all modes are "locked" to the same phase.

longitudinal modes of index m, whose frequency ν_m satisfies the condition

$$\nu_m = \frac{mc}{2\sum_i n_i(\nu_m)L_i} \equiv \frac{mc}{2n(\nu_m)L} \tag{6.1}$$

where m is a positive integer and $n_i(\nu_m)L_i$ is the optical pathlength at the frequency ν_m of the cavity element i of length L_i. The total pathlength $OL = \sum_i n_i(\nu_m)L_i$ is the sum of the optical pathlengths of all cavity elements. We will formally write $OL = n(\nu)L$, where L is the geometrical cavity length and n is an effective average refractive index. We will first consider the ideal textbook case where the mode spacing $\Delta = \nu_{m+1} - \nu_m = c/(2nL)$ is constant, which implies that n is nondispersive for frequencies within the laser gain bandwidth.

The electric field of a laser that oscillates on M adjacent longitudinal modes of frequency $\omega_m = 2\pi\nu_m = \omega_\ell + 2\pi m\Delta$ with equal field amplitude $\mathcal{E}_0/2$ can be written as

$$\tilde{E}^+(t) = \frac{1}{2}\tilde{\mathcal{E}}(t)e^{i\omega_\ell t} = \frac{1}{2}\mathcal{E}_0 e^{i\omega_\ell t}\sum_{m=(1-M)/2}^{(M-1)/2} e^{i(2m\pi\Delta t+\phi_m)}, \tag{6.2}$$

where we now count m from $(1-M)/2$ to $(M-1)/2$. Here ϕ_m is the phase of mode m, which is random for a free-running laser. The mode spectrum is centered about a cavity mode of frequency $\omega_\ell = 2\pi p\Delta$, where p is a large positive integer. The laser field, except for a phase factor, is a repeating pattern with a periodicity of $1/\Delta$, since, for any integer q,

$$\tilde{E}^+\left(t + \frac{1}{\Delta}q\right) = \tilde{E}^+(t)e^{i\omega_\ell q/\Delta} \tag{6.3}$$

as can be verified using Eq. (6.2). This periodicity is the cavity round-trip time $\tau_{RT} = 1/\Delta$. For random phases ϕ_m, the average laser intensity $\langle I \rangle = M\mathcal{E}_0^2/(2\sqrt{\mu_0/\epsilon})$ is the sum of the intensity of the individual modes. This follows from the fact that the length of the sum vector of M unit field vectors of random phase, cf. Eq. (6.2), is equal to $\sqrt{M}$.

For any particular distribution of phases, the time dependent laser power can be written as:

$$P(t) \propto \mathcal{E}_0^2[M + f(t)]. \tag{6.4}$$

Here $|f(t)| < M$ carries the information on the time dependence of the periodic laser output. This follows from the fact that the length of the sum vector of M unit vectors of random phase is equal to $\sqrt{M}$ (random walk). Note that each member of the sum in Eq. (6.2) represents such unit vector.

Forcing all the modes to have an equal phase ϕ_0 — a procedure called "mode-locking" — implies in the time domain that all the waves of different frequency will add constructively at one point, resulting in a very intense and short burst of light [Fig. 6.1(c)]. For the case of M oscillating modes of equal amplitude the sum in Eq. (6.2) can be calculated analytically and the total electric field is

$$\tilde{E}^+(t) = \frac{1}{2}\tilde{\mathcal{E}}(t)e^{i\omega_\ell t} = \frac{1}{2}\mathcal{E}_0 e^{i\phi_0} e^{i\omega_\ell t}\frac{\sin(M\pi\Delta t)}{\sin(\pi\Delta t)}. \tag{6.5}$$

For large M this corresponds to a train of single pulses spaced by $\tau_{RT} = 1/\Delta$. The "duration" of one of such burst, τ_p , can be estimated from Eq. (6.5):

$$\boxed{\tau_p \approx \frac{1}{M\Delta}.} \tag{6.6}$$

If we identify $M\Delta$ with the spectral width $\Delta\nu$ of the laser output we recognize the relationship $\tau_p \approx 1/\Delta\nu$ from Chapter 1. The ratio τ_{RT}/τ_p is thus a measure of the number of longitudinal modes oscillating in phase. For example, to produce a train of 10-fs pulses with a period of 10 ns about 10^6 modes are required.

At the pulse peak the contribution of the M modes add constructively to produce a field amplitude $\mathcal{E}(t = t_{peak}) = M\mathcal{E}_0$. Unlike the case of the random superposition of modes, the peak intensity is now equal to the product of the intensity of a single mode and the square of the number of modes: $I(t) = \mathcal{E}^2/(2\sqrt{\mu_0/\epsilon}) = M^2\mathcal{E}_0^2/(2\sqrt{\mu_0/\epsilon})$. Note that both the free-running and mode-locked laser described here have identical mode combs given by Eq. (6.2) (sketched in Fig. 6.1). Within that description, the average power of the free-running and mode-locked train are both equal to M times the power of each mode[1]. The peak power of the pulsed

[1]This is a coarse approximation that does not consider the interaction of the light with the gain medium. In an actual laser, the emission of each mode is not the same in cw or mode-locked operation.

output exceeds that of the cw free-running laser by a factor M.

6.1.2 Cavity modes and modes of a mode-locked laser

The above description assumes equally spaced modes. This is no longer true if the refractive index is a function of frequency, $n = n(\nu)$, which is the case for a typical laser cavity. The mode-spacing at frequency ν can be estimated by

$$\Delta(\nu) \approx \frac{c}{2Ln(\nu)}\left[1 + \frac{\nu}{n(\nu)}\frac{dn}{d\nu}\right]^{-1}. \tag{6.7}$$

To derive this results we approximated $n(\nu_{m+1}) \approx n(\nu_m) + \frac{dn}{d\nu}\Delta$ in Eq. (6.1). The actual frequency dependence of the mode spacing depends on the cavity dispersion that was lumped into $n(\nu)$. The Fourier transform of a non-uniform frequency comb is a non periodic, non-uniform pulse train. To illustrate this point we consider a cavity dispersion that leads to a mode spacing that varies linearly with the mode index. The frequency of cavity mode m can then be written as

$$\omega_m = \omega_\ell + 2\pi(1 + m\gamma_d)m\Delta, \tag{6.8}$$

where γ_d is the dispersion coefficient. The superposition of M cavity modes of equal amplitude and phase produces an electric field

$$\tilde{E}^+(t) = \frac{1}{2}\tilde{\mathcal{E}}(t)e^{i\omega_\ell t} = \frac{1}{2}\tilde{\mathcal{E}}_0 e^{i\omega_\ell t}\sum_{m=(1-M)/2}^{(M-1)/2} e^{i2\pi(1+m\gamma_d)m\Delta t}. \tag{6.9}$$

Unlike in the case of equally spaced modes shown in Eqs. (6.2) and (6.3), the field amplitude, the intensity and the power $P(t)$ are not periodic. At $t = 0$ all cavity modes are in phase producing the maximum possible field amplitude. After one round trip the modes still interfere mostly constructively and produce another pulse with a somewhat smaller amplitude. This scenario persists over a number of round trips until, roughly speaking, the mode at the end of the spectrum [mode index $(M-1)/2$] becomes π out of phase with the central mode. From Eq. (6.9) one expects this to happen after about $q_M \approx 2(M^2\gamma_d)^{-1}$ round trips. Note that we can interpret the term quadratic in m in Eq. (6.9) as a phase term for mode m that changes with time. Depending on the actual value of Δ and γ_d further round trips lead to random superposition of modes with different phases. As a result the individual pulses become broader, have unequal spacing and fluctuating amplitudes.

Figure 6.2 shows as an example the maximum of the field amplitude during one round trip as a function of the round trip number for $M = 101$ and $\gamma_d = 10^{-5}$.

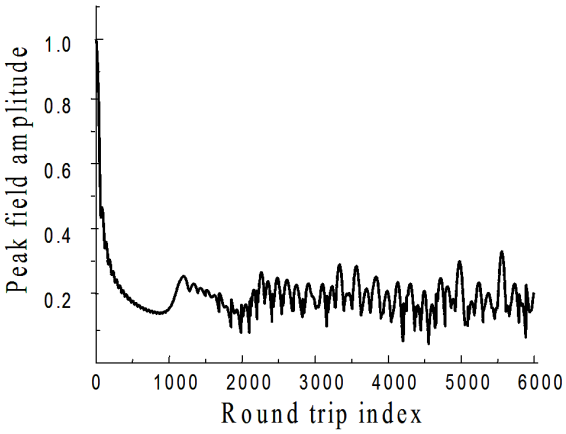

Figure 6.2: Pulse train produced by a set of $M = 101$ cavity modes whose frequencies are not equally spaced, $\omega_m = \omega_\ell + 2\pi(1 + m\gamma_d)m\Delta$, where $\gamma_d = 10^{-5}$.

So far we have referred to modes of a hypothetical cavity and their superposition. In a mode-locked laser, even though $n = n(\nu)$, the pulse spacing (in time) and the mode spacing (in frequency) are constants [2]. The theory of the mode-locked laser shows this transformation of the unequal mode spacing of the passive cavity into a perfect comb to be the result of an interplay of dispersion and nonlinear optical processes. Before elaborating on this surprising result, let us describe two sets of experiments that further demonstrate the difference between cavity modes and the Fourier transform of a mode-locked laser. The experiments were performed on a standard Ti:sapphire linear laser as depicted in the left of Fig. 6.3. In a first experiment the laser was operated in continuous-wave (cw) mode. The bandwidth and center frequency of that laser can be controlled by translating intracavity slits [1, 2]. The beat frequency of longitudinal modes that oscillate in a narrow frequency spectrum equals the mode spacing frequency Δ. It was found that the mode spacing frequency is not a constant across the tuning range of the laser, but follows the expected frequency dependence given by Eq. (6.7). The inverse mode spacing frequency would correspond to the pulse repetition frequency if the laser were mode-locked and the spectrum limited to a narrow range about ν. Mode-locking that laser is similar to the orthodontist intervention on the mode comb.

One can perform a similar measurement on the same laser, mode-locked after opening the bandwidth limiting slit, and selecting a particular wavelength range of

[2]The Fourier transform of a regular pulse train is a comb of frequency spikes. Here the term "mode spacing" refers to the spacing between the teeth of that comb, and not between the actual longitudinal modes of the laser cavity.

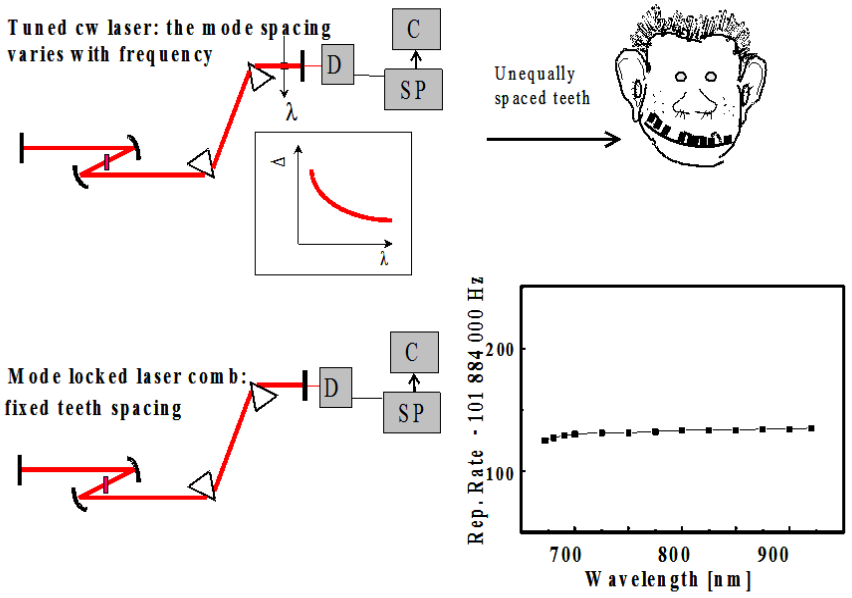

Figure 6.3: Top left: a standard Ti:sapphire laser operated in cw mode. As the wavelength (optical frequency) is being tuned, the beat note between adjacent modes changes due to dispersion of the cavity. Bottom left: the same laser is mode-locked, and portions of the output spectrum are selected with a spectrometer. The "mode spacing" of the fs comb is recorded as a function of wavelength (bottom right) either with a frequency counter or spectrum analyzer. The small change of the repetition rate arises from a thermal expansion of the cavity during the measurement. (D - detector, C - counter or spectrum analyzer, SP = spectrometer)

the spectrum with a spectrometer, as sketched on the lower left of Fig. 6.3. The laser emits a train of pulses of 9 fs duration, spanning a 200 nm broad spectrum. A 0.2 nm bandwidth of the output spectrum of the laser is selected with a spectrometer and sent onto a fast photodiode. The signal was recorded with a frequency counter and a spectrum analyzer [3] as shown on the lower right of Fig. 6.3. The sensitivity of the spectrum analyzer (spectral resolution 1 Hz) allows the measurement to extend far into the wings of the mode-locked spectrum, greater than 50 dB down from the center peak. The repetition rate of the different wavepackets does not vary as a function of frequency or wavelength over a total span of 250 nm. It is the nonlinear phase shift due to the mode-locking mechanism (in this case the Kerr-modulation) that compensates for the group velocity dispersion. Such a result is expected, since the different wavepackets formed with any group of modes should

all travel at the same group-delay, or they will not produce a pulse that "stays together" after several round trips. It is also consistent with the Fourier transform of an infinite train of equally spaced pulses, which produces a comb of equally spaced spectral components.

A recent experiment [4] with a stabilized laser has confirmed that "teeth" of the frequency comb, which is the Fourier transform of the pulse train, are equally spaced throughout the pulse bandwidth to 3.0 parts in 10^{17}.

6.1.3 The "perfect" mode-locked laser

The "perfect" mode-locked laser produces a continuous train of *identical* pulses at a constant repetition rate. Such a "perfect" mode-locked laser has to be stabilized to minimize, for example, length fluctuations due to thermal expansion and vibrations.

A mode-locked fs laser requires a broadband gain medium, which will typically sustain over 100,000 longitudinal modes. The *train* of pulses results from the leakage of a single pulse travelling back and forth in a cavity of constant length. The round-trip time of the cavity is thus a constant, implying a perfectly regular comb of pulses in the time domain. The frequency spectrum of such a pulse train is a perfect frequency comb, with equally spaced teeth, at variance with the unequal comb of longitudinal modes of a non-mode-locked cw laser.

The historical and standard textbook definition of "mode-locking" presented in the previous section originates from the description of the laser in the frequency domain, where the emission is considered to be made up of the sum of the radiation of each of these (longitudinal) modes. This description can still be applied to the "ideal" mode-locked laser considered in this section, if a fictitious perfect comb with equal tooth spacing is substituted to the real longitudinal modes of the cavity. This frequency description of "mode-locking" is equivalent to having, in the time domain, a continuous single frequency carrier, sampled at equal time intervals τ_{RT} by an envelope function, as shown in the top part of Fig. 6.4.

Our ideal mode-locked laser emits a train of equally spaced pulses with a period τ_{RT}, which corresponds to a comb of modes in the spectral domain whose spacing is constant, $\Delta = 1/\tau_{RT}$. Consequently the mode frequency can be expressed as

$$\nu_m = f_0 + m\Delta = f_0 + \frac{m}{\tau_{RT}}, \tag{6.10}$$

where m is the mode index that now starts at $m = 0$. Note that $f_0 < \Delta$ is non-zero in general. This is different from the "cold" cavity referred to in the introduction of this chapter, where the mode frequencies are solely determined by the optical pathlength of the cavity $Ln(\nu)$. In cases where the index can be approximated by a

constant over the gain bandwidth, the group velocity is equal to the phase velocity, and the mode frequencies are integer multiples of Δ.

While the pulse envelope peaks again exactly after one round trip time τ_{RT} the phase of a mode with index m changes by

$$2\pi\nu_m\tau_{RT} = 2\pi f_0\tau_{RT} + 2\pi m\Delta\tau_{RT} = 2\pi f_0\tau_{RT} + 2\pi m. \tag{6.11}$$

Apart from multiples of 2π each mode acquires an additional phase with respect to the pulse envelope

$$\phi_{CE} = 2\pi f_0\tau_{RT}. \tag{6.12}$$

This is illustrated in Fig. 6.4. Since the phase shift ϕ_{CE} is independent of the mode index it leads to a slippage of the phase of the carrier frequency with respect to the pulse envelope. The frequency f_0 responsible for this slippage is called "carrier to envelope offset" (CEO). One can also interpret the relative shift of envelope

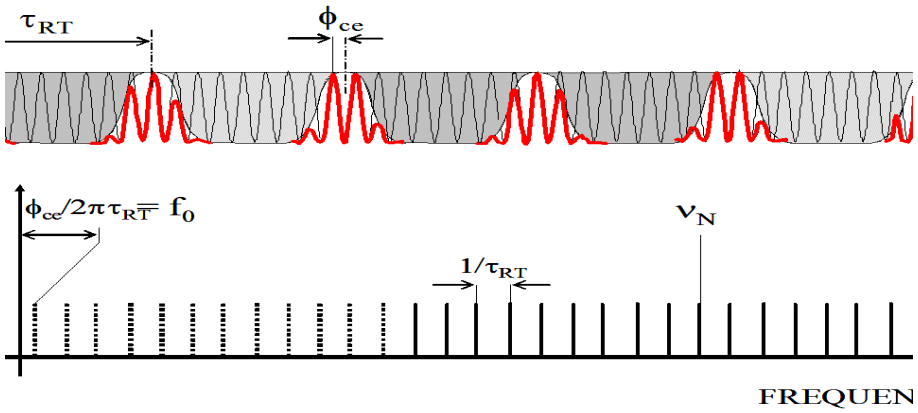

Figure 6.4: Top: a pure carrier at a frequency ν_N is modulated periodically by envelopes, at regular time intervals τ_{RT}. Bottom: the corresponding frequency picture. A comb of δ functions in frequency, is extended to near zero frequency. The frequency f_0 of the first "mode"is the carrier to envelope offset.

and carrier as the result of the difference of phase and group velocity. An average group velocity can be defined as $\bar{v}_g = 2L/\tau_{RT}$. The time a phase front of a mode of index N needs to complete one roundtrip ($2L$) is N/ν_N, which suggest to define an average phase velocity $\bar{v}_p = 2L\nu_n/N$. The delay between the pulse envelope and an arbitrary point on the phase front can now be written as

$$\tau_{CE} = 2L\left(\frac{1}{\bar{v}_g} - \frac{1}{\bar{v}_p}\right) = (\tau_{RT} - N/\nu_N), \tag{6.13}$$

which yields for the phase

$$\phi_{CE} = 2\pi\nu_N\tau_{CE} = 2\pi(\tau_{RT}\nu_N - N). \tag{6.14}$$

It is only when $f_0 = 0$ that the repetition rate is an integer number of optical cycles of an oscillating mode, cf. Eqs. (6.14) and (6.12).

The ability to measure (or control) f_0 implies that one is able to establish a link between the optical frequencies of the mode comb (ν_m) and the radio-frequency ($1/\tau_{RT}$). Let us assume for instance that one optical mode at ν_N of the laser is linked to an optical frequency standard and that $f_0 = 0$ so that there are N optical cycles $1/\nu_N$ within the pulse period τ_{RT}. Under these conditions, the repetition rate can be considered to be a radio-frequency standard with a relative linewidth, $\Delta\nu/\nu$, N times narrower than that of the optical reference.

The existence of a perfectly regular frequency comb has revolutionized the field of metrology. Such a comb can be used as a ruler to measure the spacing between any pairs of optical frequencies ν_1 and ν_2. The technique is similar to a standard measurement of length with a ruler. One measures the beat note $\Delta\nu_1$ between the source at ν_1 and the closest tooth —assigned the index m_1 — of the frequency comb, as well as the beat note $\Delta\nu_2$ between the source at ν_2 and the neighboring tooth m_2 of the frequency comb. The frequency difference between the two sources is $\nu_2 - \nu_1 = \Delta\nu_2 - \Delta\nu_1 + (m_2 - m_1)/\tau_{RT}$.

We will discuss the frequency rulers and the mode-locked laser as time standard in Chapter 14. Details on stabilization techniques as well as frequency standards can be found in ref. [5].

6.1.4 The "common" mode-locked laser

The expression "mode-locking" suggests equidistant longitudinal modes of the laser cavity emitting in phase. As mentioned in the previous section, this frequency description of "mode-locking" is equivalent to having, in the time domain, a continuous single frequency carrier, sampled at equal time intervals by an envelope function. Unless sophisticated stabilization techniques as described in section 14.4 are used, an ordinary mode-locked laser does not at all fit the above description. We shall use the term common mode-locked laser when the cavity length is not stabilized across the spectrum. In such a common situation, each cavity mirror is subject to vibrational motions. A typical mechanical resonance is around 100 Hz, with a motion amplitude ΔL of up to 1 μm. Because of that motion, the position of the longitudinal modes of the cavity is not fixed in time. As the cavity length L drifts, so does the mode frequency ν_m and the repetition rate $1/\tau_{RT}$. From Eq. (6.10), we can express the change in mode frequency $\Delta\nu_m$ due to a change in cavity length

ΔL:

$$\Delta\nu_m = \left(\frac{df_0}{dL} + m\frac{d\Delta}{dL}\right)\Delta L = \left(\frac{df_0}{dL} - \frac{m}{\tau_{RT}^2}\frac{d\tau_{RT}}{dL}\right)\Delta L. \tag{6.15}$$

It depends on the specifics of the mode-locked laser how the CEO f_0 and and the round-trip time (group velocity) vary individually with L.

Pulse train coherence

Because of this change of the carrier frequency, the repetition rate and the carrier to envelope offset, one can no longer talk of an output pulse train made of identical pulses. The difference between the properties of the radiation from an ultra-stable "frequency comb" as opposed to the common "mode-locked laser" can be established in a coherence measurement. Coherence can be measured with a Mach-Zehnder interferometer, as sketched in Fig. 6.5. In the case of a single pulse, the interference contrast is zero for an optical delay Δx of the interferometer exceeding the coherence length of the pulse. The interferogram will resemble that shown in Fig. 2.3. In the case of a pulse train from a "perfect" mode-locked laser, as the delay of the interferometer is being scanned, an identical fringe pattern re-appears at delays equal to an integer multiple q of the pulse spacing τ_{RT}. In a "common" mode-locked laser, the visibility of these re-occurring fringes will decay with increasing q. To explain this loss in fringe contrast let us assume that at each delay Δx we measure a signal from N pulse pairs. The signal at the detector

$$S(q,\Delta x) = \eta^2 \sum_{i=1}^{N} \left\langle \mathcal{E}(t)\left[\cos(\omega_\ell t + \phi_i) + \cos\left(\omega_\ell t + \phi_{i+q} + k\Delta x\right)\right]^2 \right\rangle. \tag{6.16}$$

Here ϕ_i is the relative phase of the carrier with respect to the peak of the pulse envelope and $\langle\rangle$ denotes time integration over the pulse envelope and carrier period. After performing the time integration we obtain

$$S(q,\Delta x) = W_0 \sum_{i=1}^{N}\left[1 + \cos\left(\phi_i - \phi_{i+q} - k\Delta x\right)\right], \tag{6.17}$$

where W_0 is the energy of one pulse pair. Since N is typically a large number $\sum\cos\left(\phi_i - \phi_{i+q} - k\Delta x\right) \approx 0$ if the phase difference $\delta\phi_i = \phi_i - \phi_{i+q}$ is random, which results in zero fringe contrast.

The change in cavity length ΔL will result in a mode shift $\Delta\nu_m$ given by Eq. (6.15), resulting in a total phase shift $q\Delta\nu_m\tau_{RT}$. Let us use as an estimate for $\Delta\nu_m$ the value of $\nu_m\Delta L/L$. The fringes will disappear for the value of ΔL that makes this phase shift of the order of unity. Since $\Delta\nu_m$ is an optical frequency, it

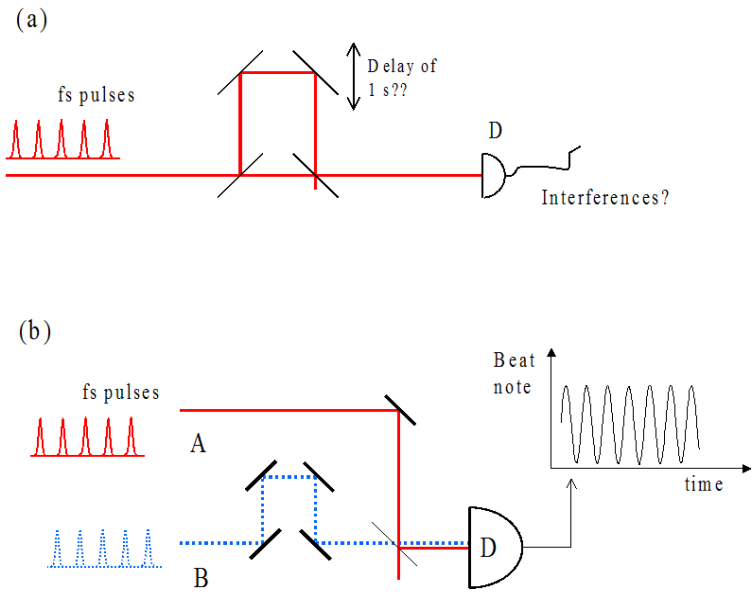

Figure 6.5: Pulse train coherence measured by a Mach-Zehnder interferometer. (a) A fringe pattern is observed around delays that are multiples of the pulse period, $m\tau_{RT}$. The fringe contrast deteriorates with increasing m for trains from "common" mode-locked lasers. (b) The coherence of an unknown source A can be measured by optical beating with an ideal reference source B, provided both sources have the same repetition rate. An optical delay is required to ensure that the pulse of each train interfere at the detector. The bandwidth of the beat note carries the information on the coherence properties.

takes only a few round-trips in a typical laser to reach that value. It has been possible, however, to stabilize lasers to have a pulse train coherent over delays 14 orders of magnitude larger than the single pulse duration or $q \approx 10^8$, as will be shown in Chapter 14.

The method discussed above is obviously not practical for measuring the coherence of a pulse train over many inter-pulse spacings as the required optical delay line can exceed hundreds of km. Another method to measure the coherence of a common source A is to compare it with a perfectly coherent source B (lower part of Fig. 6.5). Let us assume that both mode-locked lasers are locked[3] to the same

[3]This "locking" does not necessarily imply stabilization: a synchronously pumped optical parametric oscillator and its pump laser have by design the same repetition rate. So does the two outputs of a bidirectional mode-locked ring laser.

repetition rate $1/\tau_{RT}$. From Eq. (6.15), it results that the mode-frequency fluctuations are all equal to carrier-to-envelope fluctuations $d\nu_m/dL = df_0/dL$ if τ_{RT} is constant. Let us assume that the CEO of source (B), $f_{B,0}$, is kept constant by a control unit while the carrier frequency of source (A), $f_{A,0}$, is let to fluctuate. If the two pulse trains are made to interfere on a detector, a beat note will be observed. Using Eq. (6.10) to define the frequencies of the mode combs we find for the beat frequency

$$f_b(t) = |f_{B,0} - f_{A,0}(t)|. \tag{6.18}$$

The observation of $f_b(t)$ over a certain time period allows one to measure the bandwidth of this beat note. The inverse of the bandwidth is the coherence time of the source (B). A convolution of the bandwidths of each source is involved if the CEO's of both sources fluctuate.

As an example, Fig. 6.6 shows the beat note and and its spectrum produced by two pulse trains of equal repetition rate. In this particular case of an unstabilized laser source, mechanical vibrations constantly change the cavity length, resulting in excursions of the cavity mode frequency of the order of one MHz. The beat note bandwidth however can be extremely narrow ($\approx$ 1 Hz) if, as is the case in Fig. 6.6, identical cavity length fluctuations in the two resonators from which the interfering pulse trains originate. This large degree of mutual coherence indicated by the narrow beat note bandwidth proves that the cavity does have an influence on the pulse train.

There is a simple method to generate two pulse trains that have the same repetition rate and are subject to the same cavity fluctuations. The method consists in constructing a single ring or linear resonator that emits two pulse trains of the same repetition rate but different mode frequencies, as will be described in Chapter 14. The two pulse trains from such a source produced the beat note shown in Fig. 6.6. A bandwidth of less than 1 Hz is observed due to the fact that the cavity length fluctuations change the mode comb of the two interfering pulses in a similar way.

To illustrate this let us assume one of the mirrors moves with a constant velocity v relative to the cavity axis. In the time domain picture, both counterpropagating pulses reflected off this mirror experience a Doppler shift $\Delta\nu_{dop} = 2(v/c)\nu_N$. This leaves the beat note (difference frequency) unchanged. It also is instructive to analyze the mode comb of a cavity, which for simplicity we assume to be empty, under the condition of a moving mirror. The cavity length changes according to $L_0 + vt$. From Eq. (6.1), the mode comb frequencies the mode frequencies can be expected to change according to

$$\nu_m(t) = \frac{mc}{2(L_0 + vt)}. \tag{6.19}$$

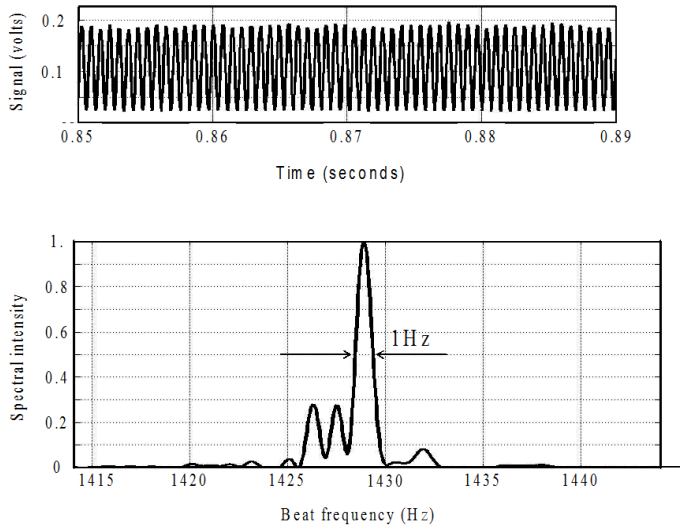

Figure 6.6: Top: portion of a 1.5 second long beat note recorded between two femtosecond pulse trains of the same repetition rate. The two pulse trains are issued from a common cavity. Lower figure: the Fourier transform of the full 1.5 s recording. The bandwidth of the central peak of the beat note spectrum is only 1 Hz wide. The side peaks are due to the fact that the beat note drifts over longer periods of time, due to a small rocking motion of the optical table (gyroscopic response)and/or air currents (Fresnel drag).

For small velocities, the frequency change during on round trip $\tau_{RT} = 2d/c$

$$\Delta\nu_m = \nu_m(t) - \nu_m(t + 2d/c) = \frac{2v}{c}\nu_m(t) = \Delta\nu_{dop} \tag{6.20}$$

is equal to the Doppler shift. These considerations are only valid within the approximations that the change in cavity length at each round-trip is much smaller than the wavelength, and that the relative change in velocity during a cavity lifetime is small compared to unity. Thus for all practical situations relating to mechanical vibrations of a cavity, the pulse frequency changes because of the Doppler shift at each reflection on a moving mirror, but the Doppler shifted mode frequency ν_N remains resonant with the cavity mode ν_m. A consequence of the equality between the Doppler shift and the cavity resonance shift expressed by Eq. (6.19) is that the cavity modes follow the same temporal evolution for both senses of circulation in a ring cavity [4]. This fact explains why pulse trains generated in opposite sense of cir-

[4] In that particular case the repetition rate is locked to the same value, and both terms in Eq. (6.15) are equal for both intracavity pulses.

culation in ring cavities can be mutually coherent. Figure 6.6 is thus also a demonstration that the pulse train emitted by an unstabilized laser possesses properties pertinent to the resonator. This fact in itself is remarkable, considering that radiation should completely fill a cavity in order to define the cavity modes, and that a femtosecond pulse occupies only one part in a million of the cavity length. The beat note of Fig. 6.6 is an indication that the femtosecond pulse has started from noise distributed over the whole laser, noise that contained the mode structure of the cavity and maintained it through the compression process, shaping and evolution towards the fs pulse. The 1 Hz bandwidth of the beat note in Fig. 6.6 signifies that the mode structure of the cavity is remembered over at least 10^8 round-trips.

Time- versus frequency-domain description of a mode-locked laser

There are two basic approaches to describe the operational principle of a "perfect" mode-locked laser: the frequency, and the time-domain approach. The frequency-domain picture that we have stressed so far considers the oscillation of a number of equally spaced (by Δ) longitudinal modes of amplitude $\mathcal{E}_m$ and phase ϕ_0, whose frequencies ν_m are given by Eq. (6.10). Some mechanism is then introduced to lock the relative phases of the modes to each other so that their coherent superposition produces a periodic pulse train in the time domain:

$$\tilde{\mathcal{E}}(t)e^{i\omega_\ell t} = \sum_{m=1}^{M} \mathcal{E}_m e^{i\phi_0} e^{i2\pi\nu_m t}. \tag{6.21}$$

This locking can be accomplished through active, passive, and a combination of those techniques. Most femtosecond lasers utilize some kind of passive mode-locking, where intensity-dependent loss and/or dispersion mechanisms favor pulsed over continuous radiation. The problem with the frequency-domain picture is the difficulty to treat the various processes in the laser including the coupling between the large number of modes to predict the pulse parameters $M, \mathcal{E}_m, \nu_m$, and ϕ_0. Recall that the mode frequencies ν_m are not given by the dispersion of the "cold" cavity, cf. Eq. (6.7), but establish themselves in the process of mode-locking. Therefore the simple picture presented in the beginning of this chapter can only serve as a qualitative description of the mode-locking process.

We have seen in the previous section that the frequency domain picture, in which all longitudinal modes within the gain bandwidth oscillate in phase, is an oversimplification. The ratio of the laser cavity length to the pulse duration would be a measure of the number of modes oscillating in phase. Typically, for a meter long laser producing a train of 100 fs pulses, there would be over 100,000 longitudinal modes contributing to the pulse bandwidth. Because of the dispersion

of the intracavity elements, the longitudinal modes are not equidistant over that range. Moreover, since a real laser resonator is not infinitely rigid, one cannot even talk of a fixed set of modes. Therefore, the most common approach to model a mode-locked laser is to analyze, in the time domain, the shaping mechanisms of one (sometimes more) pulse(s) travelling back and forth in a linear cavity, or circulating in a ring cavity. This is the description that will generally be followed in this book, and in particular in this chapter, Sections 6.2 and 6.3. In this picture the function of the cavity is not to establish a comb of modes but rather to force the circulating field to interact periodically with the cavity elements. Most analyses follow one of two main routes - (i) the evolution of the pulse from noise (spontaneous emission) and (ii) the characterization of a "steady-state" where the circulating pulse reproduces itself after an integer number (ideally one) of round trips. In either case, the result is the complex pulse envelope $\tilde{\mathcal{E}}(t)$ rather than the frequency domain parameters M, ν_m and, $\mathcal{E}_m$.

In the case of passive mode-locking, some intensity dependent loss or dispersion mechanism is used to favor operation of pulsed over continuous radiation. Another type of mode-locking mechanism is active: a coupling is introduced between cavity modes, "locking" them in phase. Between these two classes are "hybrid" and "doubly mode-locked" lasers in which both mechanisms of mode locking are used. In parallel to this categorization in "active" and "passive" lasers, one can also classify the lasers as being modulated inside (the most common approach) or outside (usually in a coupled cavity) the laser.

6.1.5 Basic elements and operation of a fs laser

There are a few basic elements essential to a fs laser:

- a broadband ($\Delta\nu_g \gg 1$ THz) gain medium
- a laser cavity
- an output coupler
- a dispersive element
- a phase modulator
- a gain/loss process controlled by the pulse intensity or energy.

The items listed above refer more to a function than to physical elements. For instance, the gain rod in a Ti:sapphire laser can cumulate the functions of gain (source of energy), phase modulator (through the Kerr effect), loss modulation

(through self lensing), and gain modulation. To reach femtosecond pulse durations, there is most often a dispersive mechanism of pulse compression present, with phase modulation to broaden the pulse bandwidth, and dispersion (positive or negative, dependent on the sign of the phase modulation) to eliminate the chirp and compress the pulse. It is the dispersion of the whole cavity that has to be factored in the calculation of pulse compression. This interplay of nonlinear and dispersion processes is responsible for the perfect (equally spaced) mode comb of the mode-locked laser even if the dispersion of the "cold" cavity calls for unequally spaced cavity modes.

The radiation builds up from noise as in any oscillator. In continuously pumped lasers, the noise is due to spontaneous emission from the active medium. The evolution from noise to a regular train of pulses has been the object of numerous theories and computer simulations since the first mode-locked laser was operated (see, for instance, [6]). The pump power has to exceed a given threshold P_{th} for this transition from noise to pulsed operation to occur. This threshold is sometimes higher than the power required to sustain mode-locking: a mode-locked laser will not always restart if its operation has been interrupted. Such a hysteresis is sometimes observed with dye lasers, and is common with Ti:sapphire lasers. Generally, it is a loss or gain modulation that is at the origin of the pulse formation.

Emergence of a pulse from noise is only the first stage of a complex pulse evolution. Subsequently, the pulse — which may contain sub fs noise spikes and be as long as the cavity round-trip time — will be submitted to several compression mechanisms that will bring it successively to the ps and fs range. Progress in ultrashort pulse generation has resulted from the understanding of compression mechanisms that can act at the shortest time scale. Most of this chapter will be devoted to the analysis of the most common compression schemes. First, a loss (saturable absorption) and gain (synchronous pumping, gain saturation) mechanism will steepen the leading and trailing edges of the pulse, reducing its duration down to a few ps. Dispersive mechanisms — such as self-phase modulation and compression — take over from the ps to the fs range.

There are mechanisms of pulse broadening that prevent pulse compression from proceeding indefinitely in the cavity. The most obvious and simple broadening arises from the bandwidth limitation of the cavity (bandwidth of the difference spectrum of gain and losses). The bandwidth limit of the amplifier medium has been reached in some (glass lasers, Nd:YAG lasers), but not all, lasers. Other pulse width limitations arise from higher order dispersion of optical components and nonlinear effects (four wave mixing coupling in dye jets, two-photon absorption, Kerr effect, etc...).

The pulse evolution in a cw pumped laser leads generally to a "steady state," in which the pulse reproduces itself after an integer number of cavity round trips

(ideally one). The pulse parameters are such that gain and loss, compression and broadening mechanisms, as well as shaping effects, balance each other.

6.2 Circulating pulse model

6.2.1 General round-trip model

As mentioned in the previous section, the simplest model for a practical mode-locked laser is that of a pulse circulating in the cavity. The pulse travels successively through the different resonator elements, each contributing to the pulse shaping in a particular manner. The block diagram of Fig. 6.7 is the basis for the most commonly used theoretical description of such lasers. Which elements need to be considered and in which order will depend on the type of laser to be modelled. Each block of the diagram of Fig. 6.7 can represent a real physical element or a function rather than a physical element. For instance, the "saturable loss" in Fig. 6.7 can represent either a saturable absorber, or the contribution of all elements that give rise to an intensity or energy dependent transmission.

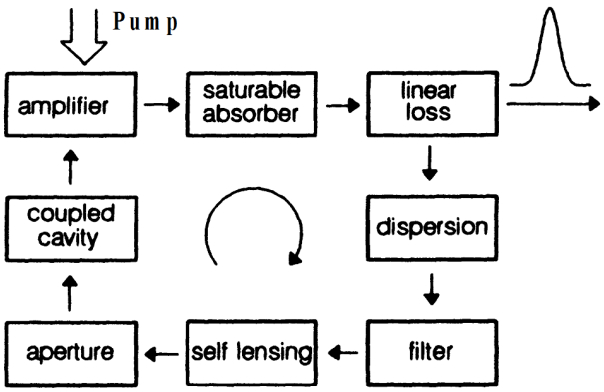

Figure 6.7: Schematic representation of the circulating pulse model describing a fs laser.

If we describe symbolically the action of each resonator element by an operator function T_i, the field after the $(n+1)$-th round trip can be written in terms of the field before that round trip as

$$\tilde{\mathcal{E}}^{(n+1)}(t) = (T_N T_{N-1} ... T_2 T_1)\tilde{\mathcal{E}}^{(n)}(t), \tag{6.22}$$

where we have numbered the resonator elements from 1 to N. If the parameters of the laser elements are suitably chosen, the fields $\tilde{\mathcal{E}}^{(i)}$ will evolve towards a steady-

state pulse, which reproduces itself (apart from a constant phase factor ϕ_0) after subsequent round trips, i.e., $\tilde{\mathcal{E}}^{(n+1)} = \tilde{\mathcal{E}}^{(n)}$ for n being large enough. The resulting steady-state condition

$$\tilde{\mathcal{E}}(t)e^{i\phi_0} = (T_N T_{N-1} ... T_2 T_1)\tilde{\mathcal{E}}(t), \tag{6.23}$$

has been the basis for numerous analytical models[5]. These models usually assume certain beam and pulse shapes with parameters that are determined from Eq. (6.23). In most cases the operators have to be suitably approximated to allow for analytical treatment. We will discuss this procedure in detail in the next sections. While the analytical or semi-analytical solutions give much insight into the physical mechanisms involved in fs lasers the complexity of the processes often calls for numerical modelling.

The round trip model illustrated in Fig. 6.7 is well suited for a numerical treatment. Starting from noise (spontaneous emission) the field is traced through each cavity round trip. The main advantages of this approach are

- Ease of incorporating various processes and optical elements with complicated transfer functions, leading to the modelling of virtually any laser.
- There is no need to make restrictive approximations for the transfer functions. This allows one for example to follow the evolution of both the temporal and spatial field profile.
- The evolution of the mode-locked pulse from noise can be predicted as can the response of the laser to external disturbances.
- One is not limited to the time or frequency domain. By using Fast Fourier Transforms (FFT), one can chose to model any phenomena in the most appropriate frame (for instance: phase modulation in the time domain, dispersion in the frequency domain)

Even though the transient evolution towards steady state may take thousands of round trips, the modelling can generally be implemented with a personal computer. The main disadvantage of a computer model that includes a plethora of processes is that it is difficult to get a clear physical picture of the laser operation.

6.2.2 Continuous model

If the change in electric field introduced by each element of the cavity, at each round-trip, is small, the pulse evolution can be modelled by a differential equation.

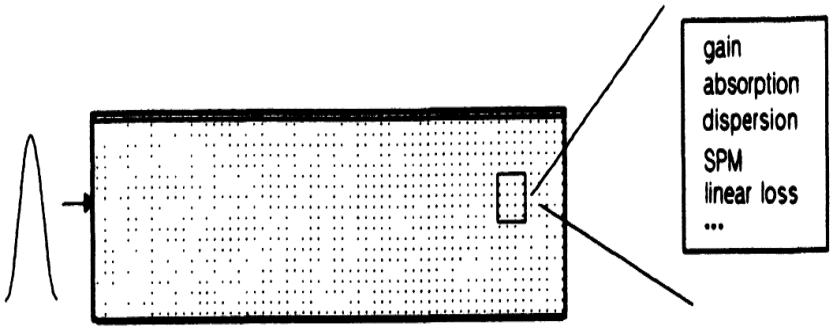

Figure 6.8: Representation of a fs laser as an infinitely long medium with the distributed properties of the cavity

An additional simplification is to assume that the pulse evolves along the mode of a stable cavity, and thus the spatial pulse evolution is decoupled from the temporal evolution. Since the change per element and per round-trip is assumed to be infinitesimal, the order of the elements in the cavity does not matter, and the laser is equivalent to an infinitely long medium, in which the resonator elements are uniformly distributed (Fig. 6.8). This "continuous model" in which the resonator elements are replaced by a uniform medium is similar to the propagation of a pulse in a fiber.

The continuous model is aimed at searching for a stationary pulse, which is a shape-preserving signal propagating through this model medium. Such a pulse is called a soliton of first order or fundamental soliton. Pulses which reproduce after a certain periodicity length are labelled solitons of higher order. In an actual laser, the "higher order solitons" will reproduce after a given number of resonator round trips. We have seen some examples of solitons in Chapter 3 and Chapter **??**. One of the simplest cavity model leading to solitons is that of a laser with linear gain balancing linear losses, and a combination of self-phase modulation and dispersion. This particular soliton model and the related equations are discussed in more detail in the following section.

Solitons in femtosecond lasers

The existence of solitons is related to a particular structure of the equations governing propagation through the composite medium. No exact soliton solutions have been found in any model incorporating most of the resonator elements. However,

[5] A more general definition expresses that the pulse reproduces itself every m round trips, i.e. $\tilde{\mathcal{E}}^{(n+m)} = \tilde{\mathcal{E}}^{(n)}$.

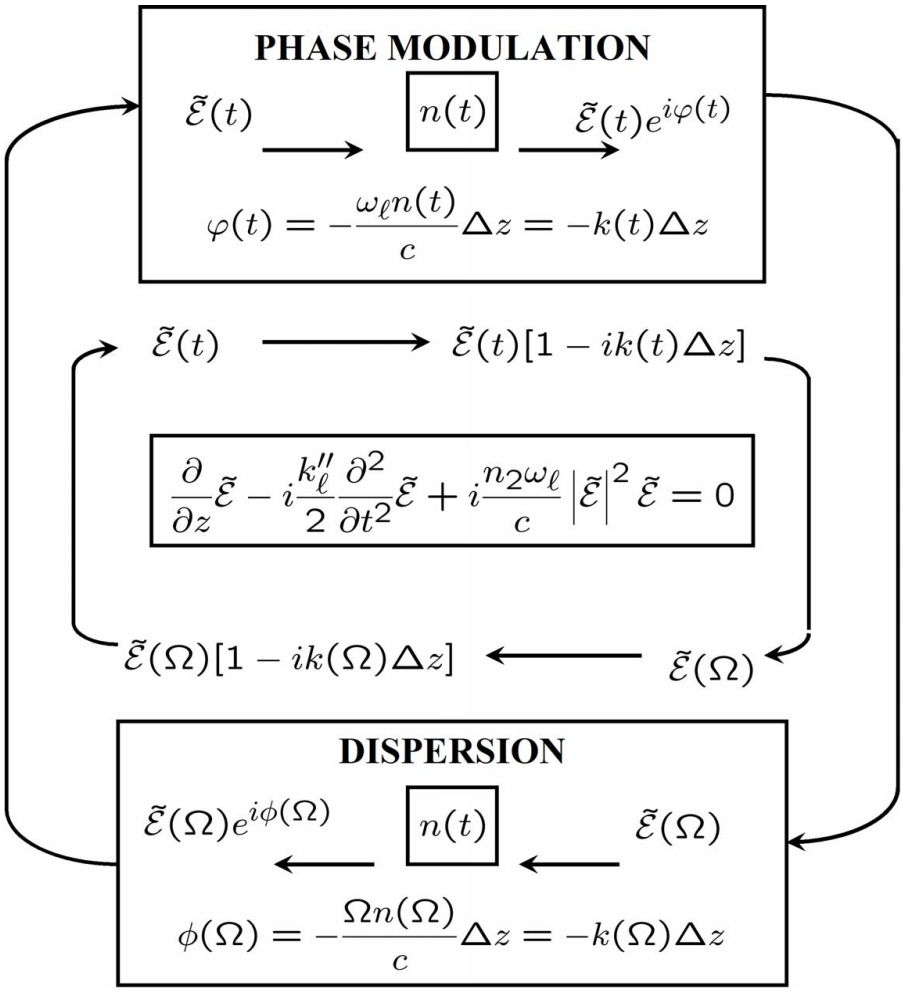

Figure 6.9: Model used to describe a "soliton" laser. Only infinitesimal self-phase modulation (top part) and dispersion (bottom part of the figure) are applied on the pulse circulating in the cavity. Phase modulation leads to a time-dependent wave vector $k(t) = \omega_\ell n(t)/c = \omega_\ell n_2|\tilde{\mathcal{E}}|^2/c$. The combined operation of phase modulation and dispersion results in the equation written in the center of the picture for which soliton solutions are known (nonlinear Schrödinger equation [7]). A steady state in which gain and loss compensate is assumed.

several subsystems have been found to lead to soliton solutions. For instance, considering *only* the amplifier and an absorber as cavity elements, soliton solutions can be found [8] which are related to the π and 2π pulse propagation, as detailed in Chapter 4. Another subsystem that has been used considers the laser to consist

only of a GVD and Kerr medium. It is this latter model, where absorption and gain are assumed to balance each other exactly, that will be discussed here in more detail.

The elegance of the theory is at the expense of simplifying assumptions that are not quite compatible with a pulse *formation* mechanism. Since the only compression mechanism assumed in the model presented below is purely dispersive, there is no intensity dependent mechanism that could preferably amplify the noise fluctuations of the laser in order to start the pulse operation. Even though the Kerr effect is taken into account, one assumes that the self-focusing associated with it has no influence.

The ring laser model reduces to a product of two operations, as sketched in Fig. 6.9: phase modulation in the time domain (upper part of the figure) and dispersion in the frequency domain. Both operations are combined into a single equation (see problem at the end of this chapter) shown in a square box in the middle of Fig. 6.9.

This resulting expression is the nonlinear Schrödinger equation, which has been analyzed in detail by Zakharov and Shabat [7], using the inverse scattering method [9]. The problem is reduced to a search for eigenvalues of coupled differential equations. The soliton is the eigenfunction associated with that eigenvalue. The order of the soliton is the number of poles associated with that solution. A soliton of order 1 is a sech-shaped pulse. It exhibits a stable pulse shape, propagating without distortion. Solitons of order n are periodic solutions with n characteristic frequencies. Periodic evolution of the pulse train has been observed in some dye lasers [10, 11]. Salin *et al.* [12] interpreted the periodicity in pulse evolution of a fs laser as a manifestation of a soliton of order larger than 1. In the case of a dye laser, however, the nonlinear Schrödinger equation is only a crude approximation of the complex pulse evolution. For lasers with large gain, such that the continuity approximation is no longer valid, periodic oscillation of the pulse energy can also be observed [13, 14]. Despite the oversimplifications of this soliton model, it appears to describe certain features of the stationary operation of a fs Ti:sapphire laser [15, 16]. For instance, the unchirped pulse that returns identical to itself after each round-trip is associated with the soliton of order 1. With some minor changes in alignment, a periodicity is observed in the pulse train. If this periodicity contains m frequencies, it is often possible to represent the pulse by a soliton of order $n = m - 1$.

Before we give a detailed description of the evolution of various pulse parameters and the role of the most common cavity elements, in the next two sections, the basic features of a numerical model and an analytical approach will be explained.

6.2.3 Elements of a numerical treatment

Because of its central importance in the description of the pulse evolution let us first elaborate on the successive treatment of processes in the time and frequency domain. If a single cavity element represents several processes it is often convenient to divide it into thin slices. The term "thin" means that the change in the complex pulse envelope caused by one slice is small. In this case the order of processes considered in one slice is unimportant. The choice about which processes are treated in which domain (time, frequency, spatial frequency) is made based on numerical or analytical convenience and feasibility. Gain and the Kerr effect are typically dealt with in the time domain ((x,y,z,t) space) while free-space propagation and dispersion are usually treated in the frequency domain ((k_x,k_y,z,t) or (x,y,z,Ω) space). For example, if gain and dispersion occur in one element, for each slice one has to solve a differential equation in the time domain to deal with the gain and subsequently treats the effect of the dispersion and diffraction in the frequency domain.

Figure 6.10 illustrates the procedure for the sequence of an element (or slice) with gain, free space propagation, phase modulation and dispersion. The illustration starts with an electric field $\tilde{E}_1(x,y,z,t) = \tilde{\mathcal{E}}_1(x,y,z,t)e^{i\omega_\ell t}$ entering the gain medium. This could be noise if we want to simulate the pulse evolution. This first step where all processes but the gain are neglected can formally be written using a transfer operator T_g.

$$\tilde{\mathcal{E}}_2(x,y,t) = T_g(t)\tilde{\mathcal{E}}_1(x,y,t). \tag{6.24}$$

In practice one solves the differential equations derived in Chapter 3 and Chap-

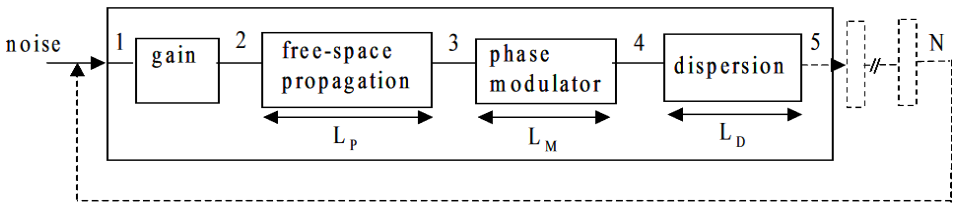

Figure 6.10: Illustration of some of the main elements and processes in a circulation model that describes pulse evolution in a laser. The numbers refer to the subscript of the electric field before and after a certain element or process.

ter **??** for a medium with population inversion. The next step involves propagation over a distance L_P. This diffraction problem is best described in the frequency domain. Fast Fourier-transform (FFT) algorithms are applied to obtain $\tilde{E}_2(\Omega,x,y)$. In Fresnel approximation the propagation step through free-space is described by

Eq. (1.245):

$$\tilde{E}_3(x,y,\Omega) = \frac{i\Omega}{2\pi c L_P} e^{i\Omega L_P/c} \int\int dx'dy' \tilde{E}_2(x',y',\Omega) \times \exp\left\{-\frac{i\Omega}{2L_P c}\left[(x'-x)^2+(y'-y)^2\right]^{1/2}\right\}. \quad (6.25)$$

Inverse FFT then produces the output in the time domain $\tilde{E}_3(x,y,t)$. Except for pulses of a few optical cycles or shorter the approximation $\Omega \approx \omega_\ell$ can be made in the terms preceding the integral and in the exponent in the integral. As explained in Chapter 1 this is equivalent to separating the space and time effects upon propagation.

The next element introduces a phase modulation. Let us assume that through some effect the (nondispersive) refractive index of the material is modulated in time and/or space, $n = n(x,y,t)$. Its effect on the pulse is advantageously described in the time picture

$$\tilde{\mathcal{E}}_4(x,y,t) = \tilde{\mathcal{E}}_3(x,y,t)\exp\left[-i\frac{\omega_\ell}{c}n(x,y,t)L_M\right]. \quad (6.26)$$

Note that the pulse envelope $|\mathcal{E}(t)|$ does not change while the pulse spectrum and spatial frequency spectrum are modified due to the action of such a phase modulator.

As detailed in Chapter 1, cf. Eq. (1.178), a dispersive element is characterized by its (linear) transfer function, which for a dispersive path of length L_D is simply the propagator $\exp[-ik(\Omega)L_D]$ with $k = \Omega n(\Omega)/c$. Thus

$$\tilde{E}_5(x,y,\Omega) = \tilde{E}_4(x,y,\Omega)\exp\left[-i\frac{\Omega}{c}n(\Omega)L_D\right]. \quad (6.27)$$

The necessary input field is obtained after FFT of the output of the phase modulator.

This procedure is continued until all resonator elements are taken into account. The final output pulse $\tilde{\mathcal{E}}_N(x,y,,t)$ is then coupled back into the first element (gain in our case) to start the next round-trip.

As pointed out earlier, the treatment of a single cavity element may require a procedure as just described. This, for example, is true for the gain crystal in a Kerr-lens mode-locked laser. This element is responsible for gain, dispersion, self-lensing and diffraction (beam propagation). The procedure is exemplified in Fig. 6.11. The crystal is divided into slices of thickness Δz and the various effects are dealt with one at a time in each slice. At the beginning of each slice the pulse properties are defined by the complex amplitude $\tilde{\mathcal{E}}(z,r,t) = \mathcal{E}(z,r,t)\exp(\varphi(z,r,t))$. At the end of each slice we obtain $\tilde{\mathcal{E}}(z+\Delta z,r,t)$ which acts as the input for the next slice, $z+\Delta z \to z$.

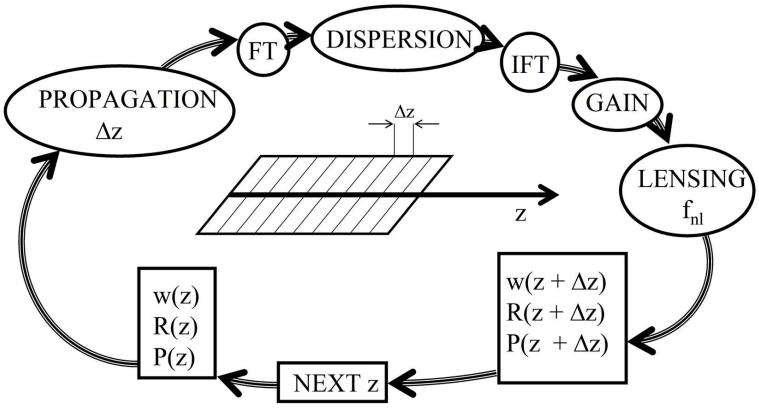

Figure 6.11: Successive calculations to be made to propagate a pulse through each slice Δz of a gain crystal. FT and IFT stand for Fourier transform and inverse Fourier transform and indicate that the treatment of dispersion can conveniently be done in the frequency domain.

In order to study the switch-on dynamics of a fs laser one starts from noise. The noise bandwidth is roughly given by the width of the fluorescence curve of the amplifier while its magnitude corresponds to the light emitted spontaneously into the solid angle defined by the cavity modes. In most cases the particular noise features vanish after few round trips and the final results are independent of the field originally injected. Figure 6.12 shows as an example the development of the pulse envelope, instantaneous frequency, and energy as a function of round trips completed after the switch-on of the laser mode-locked with a slow saturable absorber. Obviously the pulse parameters become stationary after several hundred round trips, which amounts to several microseconds.

6.2.4 Elements of an analytical treatment

A number of approximate analytical procedures has been developed by New [18, 19] and Haus [20] to describe the steady state regime. The problem often reduces to finding a complex pulse envelope $\tilde{\mathcal{E}}(t)$ that satisfies the steady state condition [20]:

$$\tilde{\mathcal{E}}(t+h) = \prod_{i=1}^{N} T_i \tilde{\mathcal{E}}(t). \tag{6.28}$$

Equation (6.28) states that the pulse envelope reproduces itself after each round trip, except for a temporal translation h including a constant pase shift. The main challenge is to find appropriate operator functions for the different resonator ele-

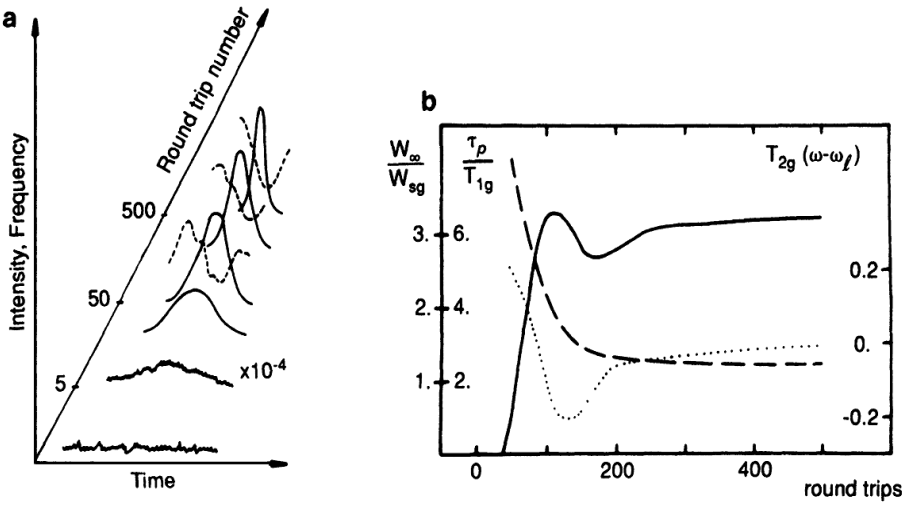

Figure 6.12: (a) Evolution of pulse envelope (solid line) and instantaneous frequency (dashed line) after switch on of the laser, and (b) corresponding steady-state pulse energy (solid line), pulse duration (dashed line), and frequency (dotted line). The active media were described by the density matrix equations introduced in Chapter 3. All pulse parameters including the average frequency develop as a result of the interplay of resonator elements. No extra frequency selective element was necessary to limit the pulse duration (normalized to the spectral width of the gain transition $2/T_{2g}$). (From [17].)

ments that are amenable to an analytical evaluation of Eq. (6.28). A convenient approximation is to assume that the modification introduced by each resonator element is small, which allows one to terminate the expansion of the corresponding operator functions after a few orders. Another consequence of that approximation is that the order of the resonator elements is no longer relevant. We will briefly describe this approach here with a small number of possible resonator elements and processes.

Some of the most frequently used operators representative of resonator elements are derived below. The transformation of the pulse envelope by a saturable loss/gain can be expressed as

$$\boxed{\tilde{\mathcal{E}}_{out}(t) = \left\{1 + \frac{1}{2}a_a^{(0)}\tilde{L}\left[1 - \frac{W(t)}{W_{sa}} + \frac{1}{2}\left(\frac{W(t)}{W_{sa}}\right)^2\right]\right\}\tilde{\mathcal{E}}_{in}(t).} \tag{6.29}$$

Equation (6.29) is the rate equation approximation ($T_2 \to 0$) of Eq. (**??**). The expansion parameters are the small signal absorption coefficient ($a_a < 0$) and the

ratio of pulse energy density to the saturation density of the transition. Equation (6.29) applies to a gain medium with the substitutions $a_a \rightarrow a_g$ and $W_{sa} \rightarrow W_{sg}$.

The transfer function of a group velocity dispersion (GVD) element can be derived from Eq. (1.184) and reads

$$\boxed{\tilde{\mathcal{E}}_{out}(t) = \left\{1 + ib_2 \frac{d^2}{dt^2}\right\} \tilde{\mathcal{E}}_{in}(t).} \tag{6.30}$$

For this expansion to be valid, the dispersion parameter b_2 has to be much smaller than τ_p^2. In the case of a transparent medium of thickness d, $b_2 = k"d/2$.

A corresponding expression for the action of a Kerr medium of length d is

$$\boxed{\tilde{\mathcal{E}}_{out}(t) = \left\{1 - i\frac{k_\ell n_2 d}{n_0} |\tilde{\mathcal{E}}_{in}(t)|^2\right\} \tilde{\mathcal{E}}_{in}(t)} \tag{6.31}$$

which can easily be derived from Eq. (4.67).

A linear loss element, which for example represents the out-coupling mirror, can be modelled according to

$$\boxed{\tilde{\mathcal{E}}_{out}(t) = \left\{1 - \frac{1}{2}\,\gamma\right\} \tilde{\mathcal{E}}_{in}(t)} \tag{6.32}$$

where γ is the intensity loss coefficient (transmission coefficient).

Each resonator contains frequency selective elements which can be used to tune the frequency. Such elements are for example prisms, Lyot-filters, and mirrors with a certain spectral response. Together with the finite gain profile, they ultimately restrict the bandwidth of the pulse in the laser. Let us assume a Lorentzian shape for the filter response in the frequency domain $\tilde{H} = [1 + i(\Omega - \omega_\ell)/\Delta\omega_F]^{-1}$ where the FWHM $\Delta\omega_F$ is much broader than the pulse spectrum. After expansion up to second order and re-transformation to the time domain:

$$\boxed{\tilde{\mathcal{E}}_{out}(t) = \left\{1 - \frac{2}{\Delta\omega_F}\frac{d}{dt} + \frac{4}{\Delta\omega_F^2}\frac{d^2}{dt^2}\right\} \tilde{\mathcal{E}}_{in}(t).} \tag{6.33}$$

If all passive elements are chosen to have an extremely broad frequency response, the finite transition profiles of the active media act as effective filters. This can be taken into account by using the operator defined in Eq. (**??**) for the media instead of Eq. (6.29) derived from the rate equations.

The operator describing the pulse change at each round-trip is obtained by multiplying the transfer functions of all elements of the cavity, neglecting products of

small quantities. To evaluate the steady state (6.28), $\tilde{\mathcal{E}}(t+h)$ can be conveniently written as $(1+h\frac{d}{dt}+\ldots)\tilde{\mathcal{E}}(t)$, leading to an integro-differential steady-state equation for the complex pulse envelope. The type of laser to be modelled determines the actual elements (operators) that need to be included. A parametric approach is generally taken to solve the steady state equation. An analytical expression is chosen for the pulse amplitude and phase, depending on a number of parameters. This ansatz is substituted in the steady state equation, leading to a set of algebraic equations for the unknown pulse parameters. Several types of mode-locked fs lasers have been modelled by this approach [21–24]. Changes in the beam profile due to the self lensing effect have been incorporated [25, 26]. The transverse dimension is included through a modification of the pulse matrices introduced in Chapter 2 to include the action of the various active resonator elements [26].

6.3 Evolution of the pulse energy

Before proceeding with a discussion of the various processes of pulse formation and compression, we will consider only the evolution of pulse energy in the presence of saturable gain and nonlinear losses. Based on the continuous model we will derive rate equations that describe the evolution of the pulse energy on time scales of the cavity round-trip time and longer. The rate equations will be written in terms of derivatives with respect to time. To relate this to the spatial derivatives used in the continuous model we apply

$$\frac{d}{dz} \approx \frac{1}{v_g}\frac{d}{dt} = \frac{\tau_{RT}}{2L}\frac{d}{dt}, \tag{6.34}$$

where L is the cavity length. Through most of this section we will neglect the transverse variation of the beam intensity (flat top beam) and diffraction effects. If we assume a beam cross section area A we may refer either to the total pulse energy $\mathcal{W}$ or the energy density $W = \mathcal{W}/A$.

We will concentrate first on parameters that may lead to a *continuous* mode-locked pulse train, as opposed to *Q-switched mode-locking*. Most broadband solid–state laser media being used for short pulse operation have a very long gain lifetime. As a result, there is a tendency for the intracavity pulse to grow until the gain has been depleted. The laser operation thereafter ceases until the gain is recovered, which takes a time of the order of the gain material lifetime (typically microseconds). The output of such a laser consists in bursts of "Q-switched-mode-locked" pulse trains.

This first subsection is dedicated to straightforward linear cavities. The case of ring cavities, and some linear cavities with two pulses per cavity round-trip, is

more complex because it involves mutual coupling between counterpropagating pulses in an absorber or nonlinear loss element.

6.3.1 Rate equations for the evolution of the pulse energy

Nonlinear element

The hypothetical laser to be considered here consists of a gain and a loss medium whose parameters vary with the intensity and the energy of the evolving pulse, depending on the time constant of the nonlinearity. Examples are saturable gain and loss as described in detail in Chapter 3. A nonlinear element will be said to provide *negative feedback* if it enhances the net cavity losses with increasing energy or intensity. The reverse (cavity losses decreasing with intensity or energy) occurs for a nonlinear element that provides *positive feedback*. "Saturable absorption" is an example of positive feedback: the loss decreases with increasing intensity. Positive feedback is needed for the establishment of a pulse train. It is generally desirable to have a positive feedback dominating the nonlinearities of the cavity at higher intensities. Examples of negative feedback are two-photon absorption and intracavity second harmonic generation. It will be shown in Section 6.4 that Kerr lensing contains both types of feedback. Another important example of positive and negative feedback is found with semiconductor absorbers, as discussed in Section 7.5.

We will consider in this section a combination of positive and negative passive feedback nonlinearities. The nonlinear losses can be expressed through their dependence on the pulse energy density W. We assume that at a certain energy, a negative feedback takes over, i.e. the loss start increasing with energy. The simplest form of nonlinear loss that will show a transition from positive to negative feedback is:

$$L(\mathcal{W}) = L_L + a(\mathcal{W} - \mathcal{W}_0)^2, \tag{6.35}$$

where $\mathcal{W}_0$ defines the energy at which the nonlinear losses switch over from saturable losses (positive feedback) to induced losses (negative feedback). As we will see when discussing specific examples of cavities, Eq. (6.35) is a second-order fit for the actual energy dependence of the losses, hence L_L is not simply a sum of the linear losses, but may also contain a contribution from the nonlinear elements.

The saturable gain is another factor that determines the dynamics of the pulse evolution in the cavity. We will show in an example of saturable absorption and intracavity two-photon absorption (cf. Section 6.3.2) how the parameters L_L, a and $\mathcal{W}_0$ are related to those material parameters. In the case of mode-locking dominated by self-lensing, we will show in Section 6.4.3 the connection between the phenomenological parameters L_L, a and $\mathcal{W}_0$ and properties such as the magnitude

of the nonlinearity, the transverse dimension of the beam, the length and position of the nonlinear element.

Rate equations

In the present derivation of the evolution of the pulse energy we will use a rate equation approximation for the gain medium. Referring for instance to Eq. (3.80) for a two level system, we can write for the population difference ΔN:

$$\frac{d\Delta N}{dt} = -\frac{I(t)\Delta N}{I_s T_1} - \frac{\Delta N - \Delta N_0}{T_1} - \frac{\Delta N + \Delta N_0}{2} R \tag{6.36}$$

where $I(t)$ is the laser intensity, R is a constant pumping rate[6], and $W_s = I_s T_1$ is the saturation energy density. ΔN_0 is the equilibrium population difference in the absence of the pump and laser field. For most gain media, the energy relaxation time T_1 is longer than the pulse duration. The above equation is equivalent to the rate equation often used to model a gain medium:

$$\frac{d\Delta N}{dt} = -\frac{I\Delta N}{I'_s T_p} - \frac{\Delta N - \Delta N_0}{T_p} + R' \tag{6.37}$$

which has a constant pump rate $R' = -R\Delta N_0$, and where the energy relaxation time T_1 has been replaced by a shorter characteristic constant T_p given by:

$$\frac{1}{T_p} = \frac{1}{T_1} + \frac{R}{2}. \tag{6.38}$$

The saturation density $I'_s = (T_1/T_p)I_s$. Without laser field ($I = 0$) the population difference, according to Eq. (6.37, approaches an equilibrium value

$$\Delta N_e = T_p R' + \Delta N_0, \tag{6.39}$$

which can be positive for a sufficiently large pumping $R' > -\Delta N_0/T_p$, or $R > 2/T_1$.[7] In terms of ΔN_e Eq. (6.37) can be written as

$$\frac{d\Delta N}{dt} = -\frac{I\Delta N}{W_s} - \frac{\Delta N - \Delta N_e}{T_p}. \tag{6.40}$$

[6]The pumping term is proportional to the population of the ground state which is $N_1 = (\Delta N + \Delta N_0)/2$. R is an effective (assumed to be constant) pump rate that also contains the properties of a third energy level involved in the pumping process.

[7]In the condition leading to population inversion, the recovery rate $1/T_p$ as defined by Eq. (6.38) is dominated by the pumping rate R.

Because we are neglecting effects of pulse shape, and will be considering gain media with relaxation times much longer than the cavity round-trip time, the effect of a short pulse on depleting the gain is equivalent to that of a constant intensity filling the cavity for a round-trip time $\tau_{\rm RT}$. Defining a gain factor $G = \sigma \Delta N \ell$, where σ is the cross section for stimulated emission, and ℓ is the length of the gain medium traversed per round-trip, an equivalent form for Eq. (6.40) is:

$$\frac{dG}{dt} = -\frac{G - G_e}{T_p} - \frac{G\mathcal{W}}{\mathcal{W}_{es} T_p}. \tag{6.41}$$

In Eq. (6.41), $\mathcal{W}_{es} = W_s \times A_g \times \tau_p / T_p$ is an effective saturation energy in the gain medium, where A_g is the cross section of the beam at that location. The physical meaning of the energy $\mathcal{W}_{es}$ is obvious from the steady state ($dG/dt = 0$) solution of Eq. (6.41):

$$G(\mathcal{W}) = \frac{G_e}{1 + \frac{\mathcal{W}}{\mathcal{W}_{es}}}. \tag{6.42}$$

Next we need a rate equation for the pulse energy. We assume that the laser consists only of the gain medium and the nonlinear loss element that was introduced in Eq. (6.35). The combined effect of gain and loss for the pulse energy per round trip is $d\mathcal{W}/(dt/\tau_{\rm rt}) = G - L$ or:

$$\frac{d\mathcal{W}}{dt} = \frac{G - L_L - a(\mathcal{W} - \mathcal{W}_0)^2}{\tau_{\rm RT}} \mathcal{W}. \tag{6.43}$$

The system of Eqs. (6.41) and (6.43) describes the evolution of the energy of a single pulse.

$$\boxed{\begin{aligned} \frac{d\mathcal{W}}{dt} &= \frac{G - L_L - a(\mathcal{W} - \mathcal{W}_0)^2}{\tau_{\rm RT}} \mathcal{W} && (6.44) \\ \frac{dG}{dt} &= -\frac{G - G_e}{T_p} - \frac{G\mathcal{W}}{\mathcal{W}_{es} T_p}. && (6.45) \end{aligned}}$$

It is useful to investigate first under which condition there is a steady-state solution for the evolution equations. Steady state, $d\mathcal{W}/dt = 0$, is reached when $G(\mathcal{W}) = L_L + a(\mathcal{W} - \mathcal{W}_0)^2$, cf. Eq. (6.44). With Eq. (6.42) for the gain coefficient, this condition becomes:

$$\frac{G_e}{1 + \frac{\mathcal{W}}{\mathcal{W}_{es}}} = L_L + a(\mathcal{W} - \mathcal{W}_0)^2 \tag{6.46}$$

The existence of a real solution for the pulse energy $\mathcal{W}$ indicates that a steady-state regime of the laser is possible.[8] This is exemplified in the two examples discussed below for a short and a long lifetime gain medium.

[8] Note that Eqs. (6.44) and (6.45) do not distinguish between mode-locked and cw laser. As such they can only be used to discuss the evolution of the pulse energy or cw power ($\mathcal{W}/\tau_{RT}$).

Immediately after the gain is turned on, the energy is given by the spontaneous emission into the lasing mode, $\mathcal{W}_{sp} \ll \mathcal{W}_0$. At this early time the evolution of energy and gain can be calculated using $\mathcal{W} = 0$ and $G = G_e$ in the right hand side of Eq. (6.44), and $\mathcal{W} = \mathcal{W}_{sp}$ and $G = G_e$ in Eq. (6.45):

$$\mathcal{W}(t) = \mathcal{W}_{sp} \exp\left(\frac{G_e - L_L - a\mathcal{W}_0^2}{\tau_{RT}}\, t \right) \tag{6.47}$$

$$G(t) = G_e \exp\left(-\frac{\mathcal{W}_{sp}}{\mathcal{W}_{es} T_p}\, t \right). \tag{6.48}$$

The laser is self starting (the energy increases) if the gain exceeds the loss ($G_e > L_L + a\mathcal{W}_0^2$). The gain decreases from its initial value G_e due to saturation.

Case of a laser with a short lifetime gain medium

The gain medium of a dye or a semiconductor laser is characterized by an energy relaxation time in the nanosecond range (typically a few nanoseconds), and a large gain cross section leading to a saturation energy density of the order of a few mJ/cm^2. Therefore, all the time constants in the system of Eqs. (6.44) and (6.45) are of the same order of magnitude. The saturable absorber saturates at an energy smaller than the gain medium. The case of a strong positive-negative feedback with $a = 0.008$ nJ^{-2}, with a turn-over energy $\mathcal{W}_0 = 5$ nJ and a larger gain saturation energy of $\mathcal{W}_{es} = 10$ nJ (this proportion would be typical in a dye laser) is illustrated in Fig. 6.13. The heavier solid line represents the losses $L(\mathcal{W})$ (linear loss $L_L = 0.1$) of Eq. (6.35). The other succession of curves represents the saturated gain $G(\mathcal{W})$, cf. Eq. (6.42), for various levels of pumping, i.e. the unsaturated gain G_e varies from 0.15 to 0.4, with increments of 0.5. Steady-state solutions $\mathcal{W}$ exist where the loss and the gain curves intersect, which represents a solution of Eq. (6.46). Obviously, the laser is self-starting for values of unsaturated gain larger than 0.3. Steady-state solutions can be expected only for $G_e > 0.15$.

The steady state pulse energy should correspond to the highest energy intersection of the saturated gain curves with the loss curve. The low-energy intersection is an unstable equilibrium; a small positive excursion of the pulse energy from this value will drive the system towards the high-energy intersection point. For values of initial gain less than 0.3, an initial energy larger than the first intersection of the saturated curve with the loss curve is required. For instance, if the unsaturated gain is 0.25, an initial pulse energy larger than 1 nJ is required to have evolution towards the steady state energy of 7.35 nJ.

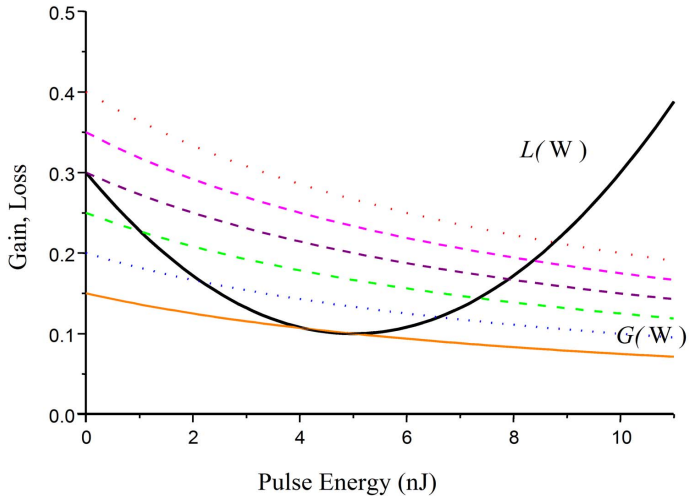

Figure 6.13: Saturated gain and loss of a laser with a short gain life time. The solid line describes the loss $L(\mathcal{W})$. The other lines represent the gain $G(\mathcal{W})$ for different small signal gain values $G_e = G(\mathcal{W} = 0)$. The laser parameters are defined in the text.

Case of a laser with a long lifetime gain medium

In most solid-state crystalline lasers, such as Ti:sapphire, Li:CAF, Nd:YAG, or Nd:vanadate, the energy relaxation time of the upper lasing level is orders of magnitude larger than the cavity round-trip time. The loss modulation is small $[a(\mathcal{W}_0 - \mathcal{W})^2 \ll 1]$, with a turn-over point for the nonlinear loss curve much higher than the gain saturation $\mathcal{W}_0 \gg \mathcal{W}_{es}$. In most solid state laser crystals used for fs pulse generation, the gain lifetime being in the microsecond range, the two Eqs. (6.41) and (6.43) operate on totally different time constants. Once the gain G_e has been switched on, the pulse energy reaches a value that corresponds to the steady state of Eq. (6.44). Because of the long lifetime T_p of the upper state, the gain [Eq. (6.45)] evolves on a much longer time scale of thousands of round-trips. Thus one can assume that the pulse energy derived from the steady-state solution of Eq. (6.44) follows the slowly evolving gain adiabatically. Substituting the steady state solution $\mathcal{W}$ of Eq. (6.44) into Eq. (6.45) yields:

$$\frac{dG}{dt} = -\frac{G - G_e}{T_p} - \frac{G\mathcal{W}_0}{T_p \mathcal{W}_{es}} \mp \sqrt{\frac{G - L_L}{a}} \frac{G}{T_p \mathcal{W}_{es}}. \tag{6.49}$$

A plot of the function dG/dt versus gain G is shown in Fig. 6.14. The steady-state condition corresponds to the intersection of these curves with the abscissa, $dG/dt = 0$. As initial condition, the pulse energy $\mathcal{W}$ is small, and the gain has its maximum value equal to the linear gain G_e, cf. Eqs. (6.48) and (6.49). The laser starts necessarily on the lower branch of any of these curves, where dG/dt is negative since the gain decreases as the laser power builds up. Referring to the solid line, the gain is expected to decrease until $dG/dt = 0$, which happens at the lower branch of this curve. The point $dG/dt = 0$ describes a stable steady-state, since an increase in pulse energy leading to a further decrease in gain leads to a positive dG/dt, hence an increase in gain and return towards the $dG/dt = 0$ point. This indicates the possibility of the existence of a stable pulse train.

The situation is different with the parameter set leading to the dotted curve. Here, dG/dt is still negative at the minimum gain value $G = L_L = 0.3$. At this point there are no real solutions to Eq. (6.49). Reducing the gain below L_L as required by the negative dG/dt drives the laser below threshold. Hence the laser will turn itself off, until the gain can recover to its small signal value, and the laser can start again. This describes the scenario of Q-switching.

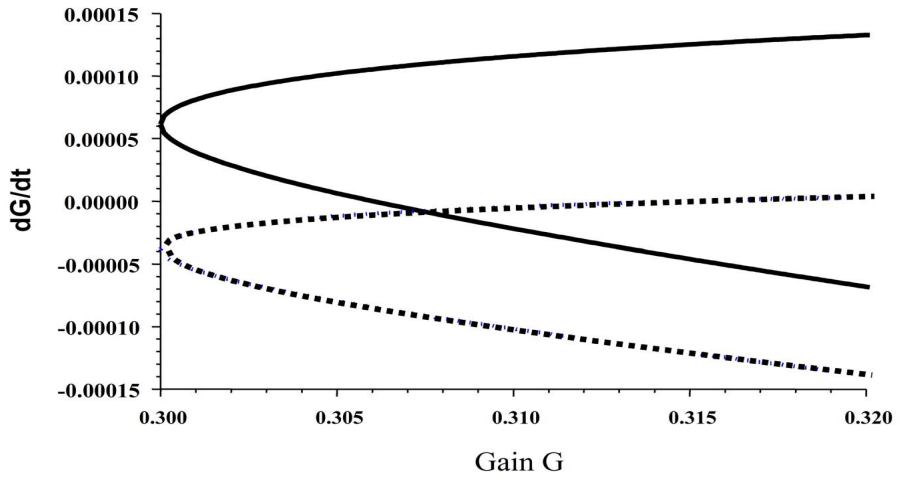

Figure 6.14: Plot of the function dG/dt from Eq. (6.49), taken for two sets of parameters leading either to cw mode-locking (solid line) or to Q-switched mode-locking (dotted line). The parameters are $\mathcal{W}_0 = 25$ nJ, $\mathcal{W}_s = 13$ nJ, Ge = 1 (solid line); and $L_L = 0.3$, $T_p = 2000$ ns and $G_e = 0.8$ (dotted line).

CW-mode-locking versus Q-switching

The condition for a cw regime (or a stable pulse train) is thus that at the minimum value $G = L_L$, the gain derivative as shown in Eq. (6.49) be positive, $\frac{dG}{dt}\big|_{G=L_L} > 0$. This can be expressed as:

$$\boxed{\epsilon_g = G_e - L_L\left(1 + \frac{\mathcal{W}_0}{\mathcal{W}_{es}}\right) > 0.} \tag{6.50}$$

The condition (6.50) was derived under the approximation that the gain lifetime is infinite. It remains a good approximation for the typical solid state laser cavities with a round-trip time of 10 ns, and a gain lifetime of 2 μs.

To illustrate this point Eqs. (6.44) and (6.45) were solved numerically and the results are plotted in Fig. 6.15. Figure (a) corresponds to a set of parameters leading to $\epsilon_g \approx 0$ [Eq. (6.50)], and shows that steady-state continuous mode-locking is reached after a few transients. The pulse energy initially rises quickly as Eq. (6.44) reaches equilibrium at the initial gain value. After a few transient oscillations the pulse energy settles to a value nearly equal to $\mathcal{W}_0$. At this point and for this choice of parameters, the gain is just balancing the linear losses. Figure 6.15 (b) corresponds to a slightly smaller gain (gain reduced from $G_e = 0.87$ to $G_e = 0.8$). Substituting the values in Eq. (6.50), we find a negative value for $\epsilon = -0.07$, which indicates Q-switching. Indeed, a periodic burst of mode-locked pulse trains is seen.

6.3.2 Connection of the model to microscopic parameters

In the previous sections we found a condition for continuous mode-locked operation, as opposed to Q-switched operation. The model was based on a simple model for the nonlinear intracavity losses of a hypothetical element [cf. Eq. (6.35)]. Although the exact functional behavior of the losses at the transition from positive to negative feedback depends on the actual cavity elements and processes involved, the general trend described by Eq. (6.35) is quite general. To illustrate this point we identify the terms of that expression with physical quantities for a specific example.

We consider here the case where the nonlinear losses are caused by a saturable absorber of thickness d_1 and a two photon absorber of thickness d_2. Each element is traversed once per roundtrip and we assume that the change in energy per roundtrip is small ($\Delta\mathcal{W}/\mathcal{W} << 1$). For a saturable absorber whose relaxation time is much longer than the pulse duration we derived a relation between the input and output pulse energy in Chapter 3, cf. Eq. (3.84):

$$\mathcal{W}_{out} = \mathcal{W}_{sa} \ln\left[1 - e^{-\alpha_0 d_1}\left(1 - e^{\mathcal{W}_{in}/\mathcal{W}_{sa}}\right)\right], \tag{6.51}$$

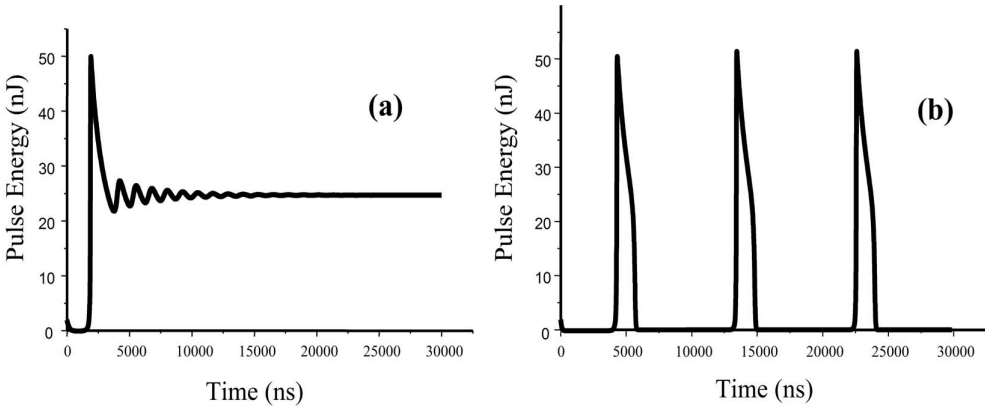

Figure 6.15: Pulse energy versus round-trip index. The lifetime of the upper laser level is 2000 ns. The round-trip time is 10 ns. The linear loss parameter is $L_L = 0.3$. The turnover energy is $\mathcal{W}_0 = 25$ nJ. The saturation energy is $\mathcal{W}_s = 13$ nJ. The amplitude coefficient for the nonlinear interaction is $a = 0.0006$ nJ^{-2}. The figure on the left (a) is for a linear gain of $G_e = 0.87$. The figure on the right (b) is for a linear gain of $G_e = 0.8$.

where $\mathcal{W}_{sa}$ is the saturation energy for the absorber. After expanding this expression into a Taylor series up to first order in the small signal absorption coefficient, $\alpha_0 d_1$, and up to third order in $(\mathcal{W}_{in}/\mathcal{W}_{sa})$ we obtain

$$\mathcal{W}_{out} = \mathcal{W}_{in} - \mathcal{W}_{sa}\alpha_0 d_1 \left[\frac{\mathcal{W}_{in}}{\mathcal{W}_{sa}} - \frac{1}{2}\left(\frac{\mathcal{W}_{in}}{\mathcal{W}_{sa}}\right)^2 + \frac{1}{6}\left(\frac{\mathcal{W}_{in}}{\mathcal{W}_{sa}}\right)^3 \right]. \tag{6.52}$$

The energy attenuation per round trip for the saturable absorber becomes:

$$\frac{d\mathcal{W}}{d(t/\tau_{RT})} = -\mathcal{W}_{sa}\alpha_0 d_1 \left[\frac{\mathcal{W}}{\mathcal{W}_{sa}} - \frac{1}{2}\left(\frac{\mathcal{W}}{\mathcal{W}_{sa}}\right)^2 + \frac{1}{6}\left(\frac{\mathcal{W}}{\mathcal{W}_{sa}}\right)^3 \right], \tag{6.53}$$

where we have replaced $\mathcal{W}_{in}$ by $\mathcal{W}$. Clearly, the transmission increases with increasing pulse energy (saturation). The opposite can be expected from a two-photon absorber. Here, a beam of intensity I is attenuated according to

$$\frac{dI}{dz} = -\beta_2 I^2, \tag{6.54}$$

where β_2 is the two-photon absorption cross section. Spatial integration relates the input to the output intensity

$$\frac{1}{I_{in}} - \frac{1}{I_{out}} = -\beta_2 d_2. \tag{6.55}$$

Assuming small changes per pass ($\Delta I = |I_{out} - I_{in}| \ll I_{in}, I_{out} \approx I$) we can approximate

$$\frac{dI}{d(t/\tau_{RT})} = -\beta_2 d_2 I^2. \tag{6.56}$$

Within our approximation of a fixed pulse shape (duration τ_p) and flat-top beam of area A we can obtain from Eq. (6.56) the rate of change for the pulse energy $\mathcal{W} = I\tau_p A$

$$\frac{d\mathcal{W}}{d(t/\tau_{RT})} = -\beta_w d_2 \mathcal{W}^2, \tag{6.57}$$

where $\beta_w = \beta_2/(A\tau_p)$ is the effective two-photon absorption cross section for the pulse energy[9].

If we add linear losses L_0 to the effect of the one-photon absorber [Eq. (6.53)] and the two-photon absorber [Eq. (6.57)], we find for the total beam attenuation/round trip:

$$\frac{d\mathcal{W}}{d(t/\tau_{RT})} = -\left\{L_0 + \alpha_0 d_1 - \frac{\alpha_0 d_1 \mathcal{W}}{2\mathcal{W}_{sa}} + \frac{\alpha_0 d_1 \mathcal{W}^2}{6\mathcal{W}_{sa}^2} + \beta_w d_2 \mathcal{W}\right\}\mathcal{W}. \tag{6.58}$$

This equation can be compared to the formal expression for the nonlinear loss introduced in Eq. (6.35):

$$L(\mathcal{W}) = L_L + a(\mathcal{W} - \mathcal{W}_0)^2. \tag{6.59}$$

We find the correspondences

$$L_L = L_0 + \alpha_0 d_1 - a\mathcal{W}_0^2, \tag{6.60}$$

where the turn-over energy is given by:

$$\mathcal{W}_0 = \frac{3\mathcal{W}_{sa}}{2}\left(1 - \frac{2\beta_w d_2 \mathcal{W}_{sa}}{\alpha_0 d_1}\right). \tag{6.61}$$

The "amplitude" of the nonlinear losses is characterized by the parameter a:

$$a = \frac{\alpha_0 d_1}{6\mathcal{W}_{sa}^2}. \tag{6.62}$$

[9]We have made the approximation in this section that reshaping and focusing effects are negligible.

Colliding pulses in the loss element

In some cases several pulses can circulate in the cavity. This is the case for a bidirectional ring laser and a linear laser where several pulses exist during one round-trip. If the cavity consists of a saturable gain and a saturable loss medium the pulses of a ring laser will collide in the loss medium if the attenuation decreases with energy. This favors optimum pulse overlap in the absorber because each pulse feels an absorption that is saturated by twice the energy. The same situation can occur in linear resonators where two (or more) pulses oscillate. If the absorber is in the cavity center equal pulse spacing results. Asymmetric pulse spacings have been observed that result in colliding pulses in nonlinear elements placed off center in linear cavities (see for example [27]). The evolution of such regimes is complex; at this point we want to sketch the modifications necessary for the nonlinear loss element only.

For a thin saturable absorber the transmitted pulse energy, according to Eq. (6.52), is:

$$\mathcal{W}_{out} = \mathcal{W}_{in}\left\{1 - \alpha_0 d_1\left[1 - \frac{\beta}{2}\frac{\mathcal{W}_{in}}{\mathcal{W}_{sa}} + \frac{\theta}{6}\left(\frac{\mathcal{W}_{in}}{\mathcal{W}_{sa}}\right)^2\right]\right\}. \tag{6.63}$$

We have introduced the coefficients β and θ to describe the colliding pulse effect on the saturation. If the absorber is geometrically thin compared to the pulse length and the pulses interact incoherently, for example due to crossed polarizations, $\mathcal{W}_{in}$ should be replaced by $2\mathcal{W}_{in}$ and $\theta = \beta^2 = 4$.

In the case of coherent overlap the two counterpropagating pulses produce an intensity grating in the absorber.

$$I(z) = I_0\,[1 + \cos(2kz)] \tag{6.64}$$

While at the nodes of the intensity modulation there is no saturation, the saturation at the maxima corresponds to an energy density of $4\mathcal{W}_{in}$. An analysis of the grating and its effect on the propagating field gives $\beta = 3$ and $\theta = 5$ [28] in Eq (6.63).

6.4 Pulse shaping in intracavity elements

In any description of a laser that follows the round-trip model, either numeric or analytical, each element is taken in sequence, represented either by a matrix or a scalar function. Essential intracavity elements are analyzed in this section. In the sections that follow and in Appendix **??**, we will derive expressions for the most essential combinations of intracavity elements. The term "element" refers here more to a function than a physical element, because each component of a laser

will have generally a plurality of properties which are most easily treated separately. For instance, the Ti:sapphire crystal in a laser may serve simultaneously as a gain medium, dispersive element, nonlinear-nonresonant element, astigmatism compensator. In each subsection characterizing an element, we will give expressions for its function at various levels of approximation, either in the time domain or in the frequency domain, as appropriate.

The various elements are organized in resonant, non-resonant passive elements and active elements. Under "resonant" elements we include saturable absorbers and gain, since they are generally associated with a near-resonant transition.

The organization of this section is as follows:

1. Saturable absorbers and gain
2. Nonlinear—non-resonant elements
   (a) Self-phase modulation and cross phase modulation
   (b) Polarization coupling and rotation
   (c) Two-photon absorption
3. Self Lensing
4. Summary of compression mechanisms
5. Dispersion

6.4.1 Saturation

Most fs mode-locked lasers involve some intensity dependent loss mechanism. Saturation of an absorber is the first one that comes to mind, and has been used for mode-locking. The typical passive mode-locking element favors pulsed over cw operation by reducing the cavity losses for high intensities. Through the sheer mechanism of saturation, an absorber/gain element can also produce phase modulation, and coupling between counter-propagating beams.

Since there should be at least one pulse per cavity round-trip time τ_{RT}, the recovery time τ_r of the device should not exceed that time: $\tau_r \leq \tau_{RT}$. Within that constraint, there is still room for a distinction between "slow" and "fast" intensity dependent elements. A "slow" element — such as the saturable absorber of a fs laser — will recover in a time long compared with the pulse duration. A "fast" element — such as a Kerr lens — will have its time constant(s) even shorter than the fs pulse.

The most commonly used saturable absorbers are dyes and semiconductors — specifically Multiple Quantum Wells (MQW's). When used in a free flowing dye

jet, the saturable absorber dye has the advantage of a continuously adjustable optical density (through its concentration) and a very high damage threshold. The latter is due to the fact that the tiny interaction volume (a tight focal spot) is replenished in microseconds. To ensure a good stability and optical quality of the jet, a viscous solvent — typically ethylene glycol — is used. Saturable absorber dyes have a saturation energy density of the order of 1 mJ/cm^2, and an energy relaxation time ranging from 1 ps to several ns. The obvious disadvantage of a dye is the inconvenience of having to deal with carcinogenic solutions and noisy, bulky circulation systems. There is a widespread effort to replace dyes by MQW saturable absorbers.

Multiple quantum wells (MQW's) provide the substitute saturable absorber with the smaller saturation energy required to mode-lock semiconductor lasers [29]. Measurements performed at room temperature with cw radiation, and a 5 μm spot size [30] indicate a saturation intensity of less than 1 kW/cm^2 for MQW, against 10 MW/cm^2 for pure GaAs. It has been possible to achieve even more control upon the parameters of the saturable absorber (in particular its saturation intensity) by inserting a MQW in a Fabry–Perot used in antiresonance [31, 32]. Such a device can be added to an end mirror of a mode-locked laser. Because of the antiresonance condition, the material inside the Fabry–Perot is subjected to a smaller field than the one present in the laser cavity, hence a better damage threshold and higher saturation intensity for the device than for the MQW used directly. Such a device has therefore been successfully applied to most cw mode-locked solid state lasers.

The general case of saturable gain and absorption was treated in Chapters 3 and 4. Here we want to summarize the main results for a fast and a slow element in the rate-equation approximation.

Fast absorber or amplifier

The propagation equation for the intensity through a fast saturable material

$$\frac{d}{dz}I = \frac{\alpha I}{1 + I/I_s}, \tag{6.65}$$

cf. Eq. (**??**), can be integrated and one obtains after a distance Δz an implicit solution for the output intensity

$$\ln \frac{I(\Delta z, t)}{I_0(t)} + \frac{I(\Delta z, t) - I_0(t)}{I_s} = \alpha \Delta z = a \tag{6.66}$$

Here $a = \alpha \Delta z$ is the small signal absorption ($a < 0$) or gain ($a > 0$) coefficient. For optically thin elements or a slice Δz of an arbitrary element, $|a| \ll 1$, the change in

intensity becomes

$$\Delta I(t) \simeq \frac{aI_0(t)}{1+I_0(t)/I_s}. \tag{6.67}$$

The phase modulation associated with saturation and interaction away from the line center, according to Eq. (**??**), is

$$\varphi(\Delta z,t) \simeq -\frac{1}{2}(\omega_\ell-\omega_{10})T_2 a \ln\frac{I(\Delta z,t)}{I_0(t)}. \tag{6.68}$$

These fast elements can follow the pulse instantaneously. The saturation and consequently the pulse shaping is therefore controlled by the intensity. As explained in detail in Chapter 3 this leads to pulse shortening in an absorber and broadening in an amplifier.

Slow absorber or amplifier

In slow elements the saturation is controlled by the pulse energy. The medium at a given time t accumulates the changes in the occupation numbers induced by all parts of the pulse arriving prior to t. From Eq. (3.82) we obtain for the intensity after such an element

$$I(z,t) = I_0(t)\frac{e^{W_0(t)/W_s}}{e^{-a}-1+e^{W_0(t)/W_s}}. \tag{6.69}$$

For weak absorption or gain ($|a| \ll 1$) this expression can be simplified, and the change of pulse intensity

$$\Delta I(t) \simeq aI_0(t)e^{-W(t)/W_s}. \tag{6.70}$$

In this limit the phase modulation is given by Eq. (**??**) and reads:

$$\varphi(t) \simeq -\frac{1}{2}(\omega_\ell-\omega_{10})T_2 a e^{-W_0(t)/W_s}. \tag{6.71}$$

The pulse shaping in these elements is a result of (unsaturated) attenuation or gain in the leading part of the pulse while the trailing part is less affected (saturated transition).

6.4.2 Nonlinear non-resonant elements

(a) Self-phase modulation

Some elements impress a nonlinear phase upon the propagating pulse. As detailed in Chapter 3, this phase is the result of a nonlinear process of third-order and

characterized by a nonlinear polarizability $\chi^{(3)}$. In the limit of a fast nonlinearity the response is instantaneous and is usually described by an intensity dependent refractive index. Acting only on the phase, such an element leaves the pulse envelope, $\mathcal{E}_0(t)$, unchanged. From Eq. (4.70)

$$\varphi(t,z) = \varphi_0(t) - \frac{k_\ell n_2}{n_0} z\mathcal{E}_0^2(t) = \varphi_0(t) - \frac{k_\ell \bar{n}_2}{n_0} z I_0^2(t). \tag{6.72}$$

If the actual profile of the incident beam is taken into account the index change becomes a function of the transverse coordinate, which leads to self-lensing effects. The general mechanism is described in Chapter 3; the effect of such an element in a fs laser is discussed in the next section.

(b) Polarization coupling and rotation

Nonlinear effects can also act on the polarization state of the laser pulse. This effect is used in some lasers (for instance in fiber lasers [33]) to produce mode-locking. Let us consider a pulse with arbitrary polarization, with complex amplitudes $\tilde{\mathcal{E}}_x(t)$ and $\tilde{\mathcal{E}}_y(t)$ along the principal axis characterized by the unit vectors $\hat{x}$ and $\hat{y}$:

$$\mathbf{E} = \frac{1}{2}\left(\hat{x}\tilde{\mathcal{E}}_{0x}(t) + \hat{y}\tilde{\mathcal{E}}_{0y}(t)\right) e^{i(\omega_\ell t - k_\ell z)} + c.c.. \tag{6.73}$$

The propagation of such a field through the nonlinear material leads to a coupling of the two polarization components. One can calculate, see [33], the nonlinear index change probed by polarizations along $\hat{x}$ and $\hat{y}$:

$$\begin{aligned} \Delta n_{\mathrm{nl},x} &= n_2\left[|\tilde{\mathcal{E}}_{0x}|^2 + \frac{2}{3}|\tilde{\mathcal{E}}_{0y}|^2\right] \\ \Delta n_{\mathrm{nl},y} &= n_2\left[|\tilde{\mathcal{E}}_{0y}|^2 + \frac{2}{3}|\tilde{\mathcal{E}}_{0x}|^2\right]. \end{aligned} \tag{6.74}$$

In an element of thickness d_m, this induced birefringence leads to a phase change between the x and y components of the field vector

$$\Delta\Phi(t) = \frac{2\pi}{\lambda_\ell}\left(\Delta n_{\mathrm{nl},x} - \Delta n_{\mathrm{nl},y}\right) = \frac{2\pi n_2 d_m}{3\lambda_\ell}\left[|\tilde{\mathcal{E}}_{0x}(t)|^2 - |\tilde{\mathcal{E}}_{0y}(t)|^2.\right] \tag{6.75}$$

The phase shift is time dependent, and, in combination with another element, can represent an intensity-dependent loss element.

To illustrate this further let us consider a sequence of such a birefringent element and a linear polarizer. We assume that the incident pulse, $\mathcal{E}_0\cos(\omega t)$, is linearly polarized with components

$$\begin{aligned} \mathcal{E}_{0x}(t) &= \mathcal{E}_0(t)\cos\alpha \\ \mathcal{E}_{0y}(t) &= \mathcal{E}_0(t)\sin\alpha. \end{aligned} \tag{6.76}$$

The pass direction of the polarizer is at $\alpha + 90^o$ resulting in zero transmission through the sequence for low-intensity light ($\Delta\Phi \approx 0$). Neglecting a common phase the field components at the output of the nonlinear element are

$$\begin{aligned} \mathcal{E}'_x(t) &= [\mathcal{E}_0(t)\cos\alpha]\cos(\omega_\ell t) \\ \mathcal{E}'_y(t) &= [\mathcal{E}_0(t)\sin\alpha]\cos[\omega_\ell t + \Delta\Phi(t)]\,. \end{aligned} \tag{6.77}$$

Next the pulse passes through the linear polarizer. The total transmitted field is the sum of the components from $\mathcal{E}'_x(t)$ and $\mathcal{E}'_y(t)$ along the polarizer's path direction

$$\mathcal{E}_{out}(t) = \mathcal{E}_0(t)\cos\alpha\sin\alpha\{\cos(\omega_\ell t) + \cos[\omega_\ell t + \Delta\Phi(t)]\} \tag{6.78}$$

The total output intensity $I_{out}(t) = \langle\mathcal{E}^2(t)\rangle$ is

$$I_{out}(t) = I_{in}(t)\frac{1}{2}[1 - \cos\Delta\Phi(t)]\sin^2(2\alpha). \tag{6.79}$$

Let us now assume a Gaussian input pulse $I_{in} = I_0\exp\left[-2(t/\tau_G)^2\right]$ and parameters of the nonlinear element so that for the pulse center the phase difference

$$\Delta\Phi(t=0) = \frac{2\pi n_2 d_m}{3\lambda_\ell}\mathcal{E}_0^2(t=0)\left(\sin^2\alpha - \cos^2\alpha\right) = \pi. \tag{6.80}$$

For this situation we obtain a transmitted pulse

$$I_{out}(t) = \frac{1}{2}I_{in}(t)\left\{1 - \cos\left[\pi e^{-2(t/\tau_G)^2}\right]\right\}. \tag{6.81}$$

The transmission is maximum (= 1) where the nonlinear element acts like a half-wave plate that rotates the polarization by 90^o, lining it up with the pass direction of the polarizer. For the parameters chosen here this happens at the pulse center (t = 0). The phase shift $\Delta\Phi$ is smaller away from the pulse center producing elliptically polarized output and an overall transmission that approaches zero in the pulse wings. Thus this sequence of elements can give rise to an intensity dependent transmission similar to a fast absorber.

(c) Two-photon absorption

In the case of an imaginary susceptibility of third-order [$\chi^{(3)}$] there is a resonant transition at twice the photon energy of the incident wave. As explained in Chapter 3 this may lead to two-photon absorption, which is governed by the propagation equation for the pulse intensity

$$\frac{d}{dz}I(t,z) = -\beta_2 I^2(t,z). \tag{6.82}$$

Integrating this equation over a propagation distance d yields for the output pulse $I_{out}(t)$ in terms of the input $I_{in}(t)$

$$I_{out}(t) - I_{in}(t) = -\beta_2 d I_{in}(t) I_{out}(t). \tag{6.83}$$

If the pulse modification introduced by this element is small the change in pulse intensity can be approximated:

$$\Delta I(t) = -\beta_2 d I^2(t) \tag{6.84}$$

For counter-propagating pulses of intensities I_1 and I_2 in an optically and geometrically thin ($d \ll \tau_p c$) absorber the induced change is

$$\Delta I_1(t,d) = -\beta_2 d \Big[I_1^2(t,0) + 2 I_2^2(t,0) \Big]. \tag{6.85}$$

This follows directly from integrating Eq. (4.87) using the approximations for thin absorbers.

6.4.3 Self-lensing

An intensity dependent index of refraction results in spatial phase modulation, because of the transverse variation of the intensity, as well as in temporal phase modulation through the time dependent intensity of the pulses. We will consider here laser beams with an intensity profile that peaks on axis. The radial intensity distribution causes a variation in index resulting in a wavefront curvature. Therefore, the nonlinear element can be adequately represented by a lens with an intensity dependent focal distance. Self lensing can be caused either by the Kerr effect (nonresonant nonlinearity), or by an off-resonance saturation (resonant nonlinearity). The calculations presented in this section will take as an example the Kerr nonlinearity. In Chapter 3, Eq. (4.89), we derived an expression for the radial dependence of the phase in the vicinity of the beam center, assuming a Gaussian beam profile

$$\varphi(r,t) = \frac{2\pi d}{\lambda_\ell} \Delta n_{\rm nl}(r,t) = -\bar{n}_2 \frac{2\pi}{\lambda_\ell} d I_0(t) e^{-(2r^2/w_0^2)} \approx -\bar{n}_2 \frac{2\pi}{\lambda_\ell} d I_0 \left(1 - 2\frac{r^2}{w_0^2} \right). \tag{6.86}$$

Here $I_0(t)$ is the intensity on axis ($r = 0$) and w_0 is the beam waist located at the input of a thin sample of thickness d. This expression should be compared to the phase factor that is introduced by a thin lens of focal length f, for example [34],

$$T(r) = \exp\left(i k_\ell \frac{r^2}{2f} \right). \tag{6.87}$$

Obviously the nonlinear element acts like a lens of focal length

$$f = \frac{w_0^2}{4\bar{n}_2 d I_0}. \tag{6.88}$$

Note that $f = f(t)$ is controlled by the time dependence of the pulse envelope $I_0(t)$. A similar expression applies to any nonlinear change in index that results in a parabolic radial phase dependence $\varphi(r) = Br^2$. The generalized expression for the focal length is

$$f = \frac{k_\ell}{2B}. \tag{6.89}$$

Another example is off-resonance interaction with a saturable absorber or amplifier.

Let us now consider the transmission of a pulse with a Gaussian beam and temporal profile,

$$I(r,t) = \hat{I} \exp\left[-4\ln 2(t/\tau_p)^2\right] \exp\left[-2r^2/w_0^2\right],$$

through a sequence of a nonlinear-lens element and an aperture of radius R a distance z away. To explain the time-dependence of the transmission analytically we will make certain restrictive assumptions. One of these assumptions is that the beam remains Gaussian after the nonlinear element. This requires to consider the element as a thin lens of certain focal length f. Strictly speaking, the latter is only true in the vicinity of the beam center. It will be obvious that similar effects occur in the general case; its treatment, however requires a numerical approach. The waist of the incident Gaussian beam with Rayleigh range $\rho_0 = \pi w_0^2/\lambda$ is placed at the nonlinear element (z = 0). After a lens of focal length f the waist of the Gaussian beam develops as, see for example [34],

$$w^2(z) = w_0'^2 \left[1 + \frac{(z_m - z)^2}{\rho_0'^2}\right] \tag{6.90}$$

where

$$w_0'^2 = w_0^2 \frac{f^2}{f^2 + \rho_0^2} \tag{6.91}$$

is the beam waist after the lens, which occurs at a distance

$$z = z_m(f) = f \frac{\rho_0^2}{f^2 + \rho_0^2}. \tag{6.92}$$

$\rho_0' = \pi w_0'^2/\lambda$ is the Rayleigh range of the beam after the nonlinear element. By way of Eq. (6.88) we can write the focal length of the nonlinear element

$$f(t) = f_0 \exp\left[4\ln 2\left(\frac{t}{\tau_p}\right)^2\right], \tag{6.93}$$

where $f_0 = w_0^2/(4d\bar{n}_2\hat{I})$. We will consider the behavior of the lens-aperture sequence in the vicinity of the pulse center, for which we can approximate

$$f(t) \approx f_0\left[1 + 4\ln 2(t/\tau_p)^2\right]. \tag{6.94}$$

The aperture is placed in the plane of the beam waist produced by the pulse center, that is, at $z = z_{m0} = z_m(f_0)$. The power transmitted through the aperture is then

$$\begin{aligned} P_{\text{out}} &= \int_0^R rdr \int_0^{2\pi} d\phi \; \frac{w_0^2}{w^2(z_{m0})}\hat{I}\exp\left[-2\left(\frac{r}{w(z_{m0})}\right)^2\right] \\ &= \left[1 - e^{-2R^2/w^2(z_{m0})}\right]P_{\text{in}} \approx \frac{2R^2}{w_0'^2(z_{m0})}P_{\text{in}}, \end{aligned} \tag{6.95}$$

where the input power $P_{in} = \hat{I}\pi w_0^2/2$, and $R \ll w(z_{m0})$ was assumed to derive the last equation. Inserting Eqs. (6.90) through (6.92) with $f(t)$ from Eq. (6.94) into Eq. (6.95) yields for the time dependent transmission through the lens - aperture sequence

$$\frac{P_{\text{out}}}{P_{\text{in}}} \approx \frac{2R^2\left(f_0^2 + \rho_0^2\right)}{w_0^2 f_0^2}\left(1 - \frac{2\rho_0^2}{f_0^2 + \rho_0^2}at^2\right), \tag{6.96}$$

where, consistent with Eq. (6.94), we have kept expansion terms up to t^2 only. The transmission is time dependent with the maximum at the pulse center. This reflects the fact that the shortest focal length is produced at the intensity maximum leading to the smallest beam size at the position of the aperture. Obviously, such a lens - aperture sequence is just another example of a fast element whose overall transmission is controlled by the pulse intensity.

Laser pulse induced lensing does take place in nearly all ultrashort pulse mode-locked lasers. In femtosecond pulse lasers, there is always a pulse shaping mechanism in the cavity, involving a balance of dispersion and temporal self-phase modulation. The latter effect implies necessarily a spatial modulation of the wavefront, hence self-lensing. As a result of self-lensing, the size of the cavity modes is modified, leading to an increase or reduction of losses because - (i) there is a change in transmission through an aperture (hard aperture), or (ii) there is a change in spatial overlap between the cavity mode and the pump beam in the gain medium (soft aperture).

6.4.4 Summary of compression mechanisms

Figure 6.16 summarizes the compression mechanisms and the associated pulse shaping that were discussed in the previous sections.

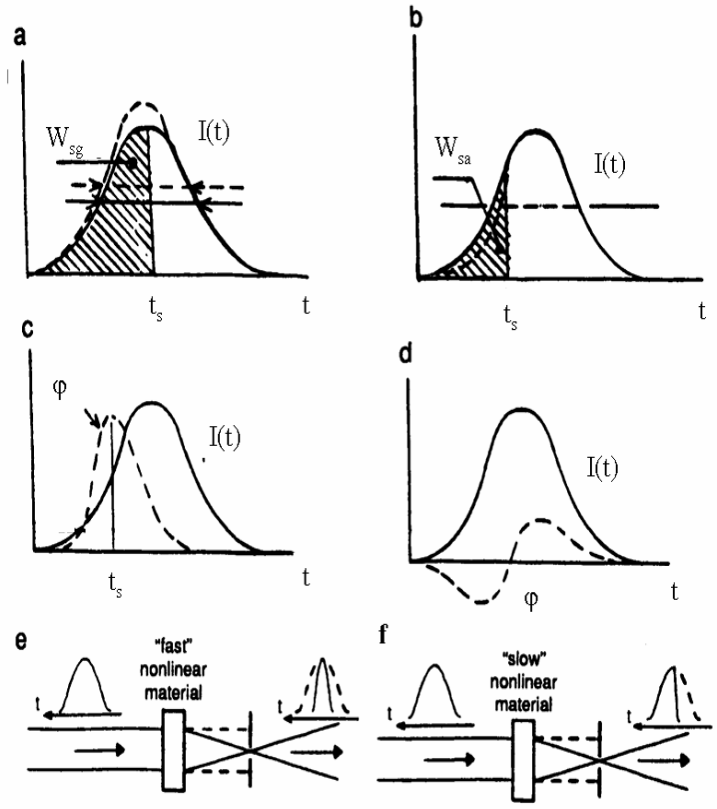

Figure 6.16: Various compression mechanisms. (a) Gain saturation: The original pulse and its pulse width are indicated by the solid line. The leading edge of the pulse is amplified, until the accumulated energy equals the saturation energy density W_{sg} at time t_s, as indicated by the dashed area. In the case of the figure, the pulse tail is not amplified, resulting in a shorter amplified pulse (dashed line). (b) Saturable absorption: The leading edge of the pulse is attenuated, until the saturation energy density W_{sa} is reached at t_s. (c) Frequency modulation (dotted line) due to saturation peaks at the time t_s when the saturation energy density W_{sa} is reached. For $t > t_s$, the pulse experiences a downchirp, if the carrier frequency of the pulse is smaller than the resonance frequency of the absorber. (d) Frequency modulation (dotted line) produced by the Kerr effect. The central part of the pulse (intensity profile indicated by the solid line) experiences an upchirp. (e) Self-focusing by a fast nonlinearity combined with an aperture, leads to a compression by attenuating both leading and trailing edges. (f) In the case of self-focusing by a slow nonlinearity combined with an aperture, only the trailing edge is trimmed.

6.4.5 Dispersion

The effect of dispersion is most simply treated in the frequency domain. Using the notations of Chapter 2, a dispersive element is characterized by a frequency

dependent phase factor $\psi(\Omega)$. In the particular case where the dispersion is due to propagation through a thickness d of an homogeneous medium of index $n(\Omega)$, the dispersive phase factor is simply $\psi(\Omega) = k(\Omega)d$. The most rigorous procedure to model dispersion is to take the temporal Fourier transform of the pulse, $\tilde{\mathcal{E}}_{in}(\Omega)$, and multiply by the dispersion factor, to find the field $\tilde{\mathcal{E}}_{out}(\Omega)$ after the dispersive element:

$$\tilde{\mathcal{E}}_{out}(\Omega) = \tilde{\mathcal{E}}_{in}(\Omega)e^{-i\psi(\Omega)}. \tag{6.97}$$

An inverse Fourier transform will lead to the field $\tilde{\mathcal{E}}_{out}(t)$ in the time domain.

When analytical expressions are sought to model the evolution of a pulse in a cavity and the dispersion per round-trip is small, one can use an approximate analytical solution in the time domain. We approximate $\psi(\Omega) \approx \psi''|_{\omega_\ell}(\Omega-\omega_\ell)^2/2$. This is the lowest order of a Taylor expansion that produces a change in pulse shape. Expanding the exponential function $\exp\left[-i\,\psi''|_{\omega_\ell}(\Omega-\omega_\ell)^2/2\right]$ up to first-order and Fourier transform to the time domain yields

$$\tilde{\mathcal{E}}_{out}(t) = \tilde{\mathcal{E}}_{in}(t) - \frac{i}{2}\,\psi''\Big|_{\omega_\ell}\frac{\partial^2}{\partial t^2}\tilde{\mathcal{E}}_{in}(t), \tag{6.98}$$

which is a special case of Eq. (6.30). Note that this treatment of dispersion is equivalent to solving the differential equation (1.104) for an incremental step Δz. There the dispersion was that of an optical material, $\psi(\Omega) = k''_\ell(\Omega)\Delta z$.

6.5 Cavities

Resonators are an essential part of any laser. We will review first the mode spectrum of a laser cavity and the standard ABCD-matrix cavity analysis. Since mirrors are used as focusing elements, astigmatism complicates significantly the calculation and design (optical positioning of the elements) of the resonator. Finally, we will analyze the effect of a Kerr-lens in a laser cavity.

6.5.1 Cavity modes and ABCD-matrix analysis

"Mode-locked" operation requires a well defined mode structure. It is generally understood that the longitudinal modes are locked in phase. A transverse mode structure will generally contribute to amplitude noise (at frequencies corresponding to the differences between mode frequencies). Most fs lasers operate in a single TEM_{00} transverse mode. We will see however that some multiple transverse mode lasers have the same longitudinal mode structure as the fundamental TEM_{00}.

This subsection reviews standard ABCD matrix calculations of the stability of laser resonators. Most fs laser cavities have at least one beam waist (for instance, one for the gain medium, and possibly one for a passive mode-locking element).

A beam with an electric field amplitude having a Gaussian radial dependence is uniquely defined by its complex $\tilde{q}$ parameter defined by Eq. (**??**). The phase variation on axis ($r = 0$) of the beam is determined by the phase angle $\Theta(z) = \arctan z/\rho_0$ according to Eq. (**??**).

The parameter of the fundamental Gaussian beam that can reproduce itself in a cavity can be determined by the standard technique using ABCD matrices [35]. Let A, B, C, and D be the elements of the 2×2 system matrix obtained by calculating the product of the matrices of all cavity components, defining a complete round-trip from a point P. The complex $\tilde{q}$ parameter of the Gaussian beam at the point P is given by:

$$\boxed{\frac{1}{\tilde{q}} = -\frac{A-D}{2B} - i\frac{\sqrt{1-(A+D)^2/4}}{|B|}.} \tag{6.99}$$

Identifying with the definition of the $\tilde{q}$ parameter, Eq. (**??**), leads to the beam characteristics at point P:

$$R = -\frac{2B}{A-D} \tag{6.100}$$

$$\frac{\pi w^2}{\lambda_\ell} = \frac{|B|}{\sqrt{1-(A+D)^2/4}}. \tag{6.101}$$

The "modes" of a cavity are determined by the condition that, after one round-trip from point P to point P, the total phase variation is a multiple of 2π. For the fundamental TEM_{00} mode, and a simple cavity consisting of two concave mirrors at distance d_1 and d_2 from the beam waist (which we will assume here to be inside the resonator), the phase variation for the half round-trip should be a multiple of π:

$$\begin{aligned} l\pi &= k(d_1+d_2) + \Theta(d_1) + \Theta(d_2) \\ &= k(d_1+d_2) + \Delta\Theta \\ &= k(d_1+d_2) + \arctan\left(\frac{d_1}{\rho_0}\right) + \arctan\left(\frac{d_2}{\rho_0}\right), \end{aligned} \tag{6.102}$$

where $k = 2\pi\nu/c$. If $d_{1,2} \ll \rho_0$, the mode-spacing frequency $\Delta\nu = \nu_{l+1} - \nu_l = c/[2(d_1 + d_2)]$.

The Fourier transform of the output of a continuously mode-locked laser is a "comb" of frequency spikes having a maximum overlap with the longitudinal mode structure represented by Eq. (6.102). Apertures are often inserted in the cavity of mode-locked lasers to avoid the complication introduced by a transverse mode-structure. In some lasers, a saturable absorber acts as an aperture. The small cross-section of the inverted region in the gain medium can also act as a mode-limiting aperture.

The fundamental TEM_{00} Gaussian beam is not necessarily the only existing mode in a fs laser. Let us consider the influence that the transverse mode structure can have on the operation of a mode-locked laser. If the laser is multimode, the electric field can be expressed as an expansion of Hermite–Gaussian modes (see, for instance, [35]):

$$E(x,y,z,t) = \sum_n \sum_m c_{nm} u_n(x) u_m(y) e^{i(\omega t - kz)} + c.c., \tag{6.103}$$

where

$$\begin{aligned} u_s(x) &= \left(\frac{2}{\pi}\right)^{\frac{1}{4}} \sqrt{\frac{\exp[i(2s+1)\Theta(z)]}{2^s s! w(z)}} \\ &\times H_s\left(\frac{\sqrt{2}x}{w(z)}\right) \exp\left\{-\left[i\frac{kx^2}{2R(z)} + \frac{x^2}{w^2(z)}\right]\right\}. \end{aligned} \tag{6.104}$$

Here H_s are Hermite–Gaussian polynomials of order s. The subscripts m and n are the transverse mode indices.

For the simple cavity consisting of the two curved mirrors introduced above, the spacing between transverse modes is:

$$\Delta\nu = \frac{c}{2(d_1+d_2)}(\Delta n + \Delta m)\left[\arctan\left(\frac{d_1}{\rho_0}\right) + \arctan\left(\frac{d_2}{\rho_0}\right)\right] \tag{6.105}$$

where Δn and Δm are the difference in transverse mode numbers [35]. If the various transverse modes oscillate independently with random phase, the output of the laser will have a noise component corresponding to the beating of the various transverse modes. This noise component will be periodic if the mode spacing is equal in the two transverse directions. In some cases [36], the transverse modes can be locked in phase, resulting in a periodic spatial scanning of the beam. The noise contribution corresponding to the transverse mode beating will be low frequency if $d_{1,2} < \rho_0$.

Calculation of the exact stability diagram, position and size of the beam waists, is a tedious but essential task in the design of fs lasers. Since it is not essentially different from the design of any laser, we will refer to the appropriate literature for details, for example [35]. A few general criteria to consider in the design of the laser cavity are:

- minimal losses
- a flexibility of varying the ratio of beam waists in various resonator elements in large proportions. The saturation level in the gain medium will be a factor

in determining the intracavity power. In the case of Kerr lensing, it is important to identify the location where the beam size variation due to self-lensing will be maximum (positioning of an aperture). In the case of passive mode-locking, the ratio of beam waists in the absorber/amplifier is important, since this is the parameter that determines the relative saturation of the gain and absorber.

- a small spot size in the amplifier may be desirable for efficient pumping and heat removal.

- a round spot is desirable in the passive mode-locking element (for instance, the amplifier rod in the case of a Ti:sapphire laser, or the saturable absorber jet in a dye laser) in order to have the most uniform possible wavefront across the beam, since it is a region of the cavity which contributes to the phase modulation

Mirrors or lenses can be used to create beam waists in a laser cavity. Because of the requirement of minimum losses and dispersion, one will generally choose reflective optics over lenses.

6.5.2 Astigmatism and its compensation

It is not always an easy task to create a waist of minimal size with off-axis reflective optics. Indeed, let us consider the typical focusing geometry sketched in Fig. 6.17. The smaller the focal spot in A, the larger the diameter w of the incident beam on the mirrors, hence the larger the clearance angle θ required to have the focal point fall outside of the incident beam cross section. However, the astigmatism caused by a large angle of incidence θ will make it impossible to obtain the desired small focal spot with a cylindrically symmetric Gaussian beam incident from the left.

Since a tight focusing is required in the nonlinear elements of a mode-locked laser, there is clearly a need for minimizing or reducing the astigmatism. There are some exceptions. A large astigmatism may sometimes be desirable in the gain medium. This is the case when it is desirable to take maximum advantage of a self-lensing effect. Another example of such a need is to match the elongated shape of the gain region of semiconductor lasers.

Let us choose as transverse coordinate y for the plane of incidence (the plane of the figure in Fig. 6.17), and x for the orthogonal direction. The locations of the two focal lines corresponding respectively to the plane of the figure and to the

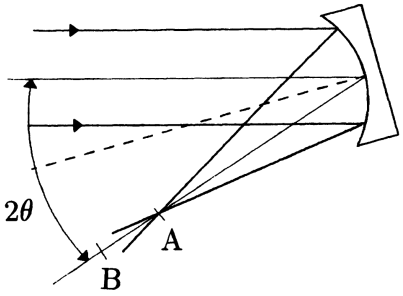

Figure 6.17: Off-axis focusing of a Gaussian beam leading to astigmatism. In the plane of the figure the focal distance of the mirror is $(R/2)\cos\theta$, where R is the radius of curvature of the mirror. The first focalization is therefore a line perpendicular to the plane of the figure originating from A. In the orthogonal plane the focal distance of the mirror is $(R/2)/\cos\theta$. There will therefore be a focal line in the plane of the figure at B.

orthogonal plane are:

$$\begin{aligned} f_y &= f\cos\theta \\ f_x &= \frac{f}{\cos\theta}, \end{aligned} \tag{6.106}$$

where θ is the angle of incidence and $f = R/2$ is the focal length of the mirror (see for example ref. [37]).

Other elements in a cavity, such as Brewster plates, also have astigmatic properties that can limit the performance of the system. The gain medium of a Ti:sapphire laser or of a dye laser is generally a plane-parallel element put at Brewster's angle. Kogelnik *et al.* [37] have shown under which condition the astigmatism can be compensated by such elements.

To analyze the astigmatism of such elements let us consider the propagation of a Gaussian beam through a plate of thickness d and refractive index n put at the Brewster angle directly next to the beam waist (size w_0) at $z = 0$, as sketched in Fig. 6.18.

Upon entering the medium, the beam waist takes the values:

$$\begin{aligned} w_{0x} &= w_0 \\ w_{0y} &= w_0\frac{\cos\theta_r}{\cos\theta_B} = w_0\frac{\sin\theta_B}{\cos\theta_B} = nw_0, \end{aligned} \tag{6.107}$$

where $\theta_B = \arctan n$ is the Brewster angle, and $\theta_r = 90^o - \theta_B$ is the angle of refraction. To a thickness d, there corresponds a propagation distance

$$\chi = \frac{d}{\cos\theta_r} = d\frac{\sqrt{1+n^2}}{n}. \tag{6.108}$$

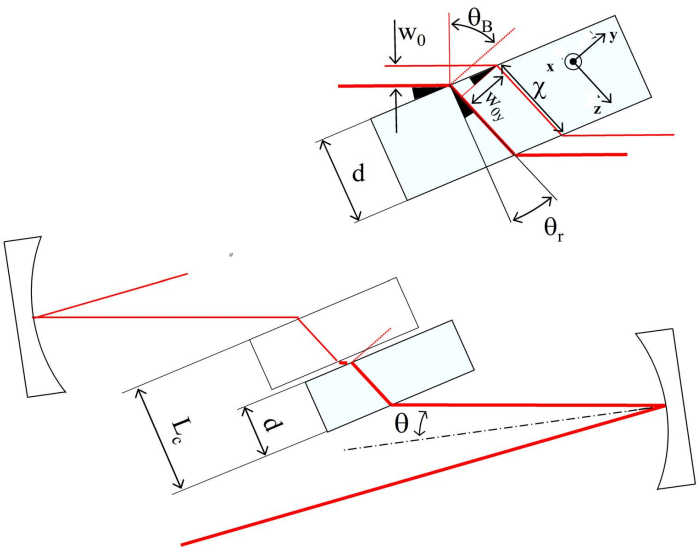

Figure 6.18: Brewster plate geometry for the calculation of astigmatism compensation. On the top right: a Brewster plate of thickness d is placed close to a beam waist (w_0). The propagation through the plate is calculated along z, for the plane of the figure (coordinate y) and orthogonal to the plane of the figure. Bottom part of the figure: a Brewster cut laser crystal of length L_c inserted in an X or Z configuration (the Z configuration is shown) between two curved mirrors can be considered to be made of two halves of thickness $d = L_c/2$.

Applying the propagation law (1.219) for the beam waist across the thickness d yields:

$$w_x = w_0\sqrt{1+\left(\frac{\lambda_\ell \chi}{n\pi w_0^2}\right)^2} = w_0\sqrt{1+\left(\frac{\lambda_\ell}{\pi w_0^2}\frac{d\sqrt{1+n^2}}{n^2}\right)^2} \tag{6.109}$$

$$w_y = nw_0\sqrt{1+\left(\frac{\lambda_\ell \chi}{n^3\pi w_0^2}\right)^2} = nw_0\sqrt{1+\left(\frac{\lambda_\ell}{\pi w_0^2}\frac{d\sqrt{1+n^2}}{n^4}\right)^2}. \tag{6.110}$$

Upon exiting the crystal, the beam waists take the values w_x and w_y/n, along x and y, respectively. Therefore, the Brewster plate can be seen from Eqs (6.109)

and (6.110) to be equivalent to propagation in free space of distances equal to

$$d_x = d\frac{\sqrt{1+n^2}}{n^2} \tag{6.111}$$

$$d_y = d\frac{\sqrt{1+n^2}}{n^4} \tag{6.112}$$

in the planes xz and yz, respectively. The beam issued from the waist w_0 after passing through the Brewster plate will be again collimated by a mirror of radius R at an angle θ if the difference between the two distances d_x and d_y compensates the difference in focal distances f_x and f_y. Using Eqs. (6.106),(6.111), and (6.112), this condition is equivalent to:

$$\frac{2d}{R}\frac{\sqrt{n^4-1}}{n^4} = \frac{\sin^2\theta}{\cos\theta}. \tag{6.113}$$

In the case of a typical Ti:sapphire laser, the crystal of length $L_c = 2d$ is inserted near the focal point between two curved mirrors. Each half crystal of thickness $d = L_c/2$ can compensate the astigmatism of each of the mirrors, provided the angle of incidence is chosen to be a solution of:

$$\frac{L_c}{R}\frac{\sqrt{n^4-1}}{n^4} = \frac{\sin^2\theta}{\cos\theta}. \tag{6.114}$$

For a 9 mm long Ti:sapphire crystal inserted between two mirrors of 10 cm curvature, Eq. (6.114) indicates that astigmatism compensation occurs at an angle of $\theta = 9.5^{\circ}$.

In the case of dye lasers, we find that for a typical jet thickness of 200 μm and a mirror curvature of 5 cm, the compensated angle is less than 2.5°. Compensation is impossible for tight focusing in a saturable absorber jet of typical thickness of 50 μm. Two options are available in such a situation:

- insert a glass window at Brewster angle between the two curved mirrors, of a thickness sufficient to compensate the astigmatism caused by the mirrors, or
- use the astigmatism of another part of the cavity, to obtain a minimum astigmatism-free spot between the two mirrors.

The latter approach is only possible in situations where there are two or more waists in the cavity. Calculations show that large angles can actually result in astigmatism compensation, and, even with angles of incidence on the focusing mirrors exceeding 10° , large stability ranges have been found [38]. Resonators for dye lasers

have been designed to provide a round and minimum size spot in the absorber jet, using the cavity geometry (relative location of the components) to compensate the astigmatism, without a need for inserting additional "compensating elements." The price to pay for an optimal focusing at one waist of the cavity, is a large astigmatism at another part of the cavity. Returning to Fig. 6.17, the beam incident from the left will focus first on a line originating from A, perpendicular to the plane of the figure, next in a line at B in the plane of the figure. However, if the beam incident from the left is collimated in the plane of the figure, but convergent in the orthogonal direction, the focal line B will recede towards the focus A. The incident beam parameters can be adjusted such as to create a tight round focal spot.

In order to assess the importance of astigmatism, let us consider a simple ring cavity with two beam waists. We assume that one beam waist is formed by two lenses of 15 mm focal distance, spaced by 30 mm. The other waist is formed by two mirrors of focal distance $f = 25$ mm separated by a distance d. The distances between the two waists are 1 m and 3 m in a 4 m perimeter ring cavity. From the expression for the ABCD matrix for this cavity one finds that the stability range is $f < d < 1.01f$. If astigmatism due to an angle of incidence θ on the two mirrors of $f = 25$ mm is taken into account, there will be a different stability condition corresponding to each of the two focal distances $f_x = f/\cos\theta$ and $f_y = f\cos\theta$. The cavity is stable if the two stability ranges overlap. For an angle $\theta \geq 5.7^{\circ}$, this cavity is no longer stable. In this situation other degrees of freedom, such as beam propagation out of plane and/or the insertion of additional elements are options.

6.5.3 Cavity with a Kerr-lens

In this section we will treat the effect of a Kerr-lens on the beam parameters in a laser cavity perturbatively based on Gaussian beam analysis. A simple, geometrical optics description of a nonlinear-lens - aperture sequence is presented in Appendix **??**.

General approach

It is convenient to use the ABCD matrix approach [39] to evaluate the intensity dependent losses introduced by Kerr lensing in a laser cavity [40]. The ABCD matrix of the resonator is calculated starting from a reference plane at the position of the Kerr medium. Let $\mathcal{M}_1 = \begin{pmatrix} A_1 & B_1 \\ C_1 & D_1 \end{pmatrix}$ be the ABCD matrix for low intensity (negligible Kerr effect). At high intensity, the nonlinear lensing effect modifies this

matrix as follows:

$$\begin{aligned}\mathcal{M} &= \begin{pmatrix} 1 & 0 \\ -\frac{1}{f_{\rm nl}} & 1 \end{pmatrix}\begin{pmatrix} A_1 & B_1 \\ C_1 & D_1 \end{pmatrix} = \begin{pmatrix} A_1 & B_1 \\ C_1+\delta C & D_1+\delta D \end{pmatrix} \\ &= \begin{pmatrix} A & B \\ C & D \end{pmatrix}, \end{aligned} \tag{6.115}$$

where $\delta C = -A_1/f_{nl}$; $\delta D = -B_1/f_{nl}$, and $f_{\rm nl}$ is the time dependent focal length of the Kerr medium, cf. Eq.(6.88). A Gaussian beam is uniquely characterized by its complex beam parameter $\tilde{q}$ (cf. Chapter 1 and Ref. [39]). In the absence of Kerr lensing, the eigenmode of the empty cavity is characterized by a complex beam parameter $\tilde{q}_1$, at the location the system matrix calculation was started. The inverse of this beam parameter is:

$$\begin{aligned}\tilde{s}_1 &= \frac{1}{\tilde{q}_1} = \frac{1}{R_1} - i\frac{\lambda_\ell}{\pi w_1^2} \\ &= \frac{C_1 + D_1\tilde{s}_1}{A_1 + B_1\tilde{s}_1} \end{aligned} \tag{6.116}$$

Solving the eigenvalue equation (6.116) yields the complex beam parameter at the location of the nonlinear crystal (Kerr medium):

$$w_1^2 = \frac{|B_1|\lambda}{\pi} \times \sqrt{\frac{1}{1-[(A_1+D_1)/2]^2}} \tag{6.117}$$

$$R_1 = \frac{2B_1}{D_1 - A_1}. \tag{6.118}$$

In the presence of the Kerr lensing, the eigenvalue $\tilde{s}$ is the solution of the eigenmode equation for the complete round-trip ABCD matrix:

$$\tilde{s} = \frac{C + D\tilde{s}}{A + B\tilde{s}}. \tag{6.119}$$

For $\tilde{s}$ we can make the ansatz:

$$\tilde{s} = \tilde{s}_1 + \delta\tilde{s} \tag{6.120}$$

where $\delta\tilde{s}$ is the small change in $\tilde{s}$ produced by the Kerr lens that we will determine next. For this we multiply both sides of Eq. (6.119) by $A + B\tilde{s}$, substitute Eq. (6.120) for $\tilde{s}$, and replace all four matrix elements X by $X_1 + \delta X$. Keeping only terms up to first order we obtain:

$$A_1\tilde{s}_1 + B_1\tilde{s}_1^2 + (2D_1\tilde{s}_1 + A_1)\delta\tilde{s} = C_1 + D_1\tilde{s}_1 + \delta C + \tilde{s}_1\delta D + D_1\delta\tilde{s}, \tag{6.121}$$

where we have made use of the fact that $\delta A = \delta B = 0$, cf. Eq. (6.115). Solving for $\delta\tilde{s}$ and using δC and δD from Eq. (6.115), and using Eq. (6.116) yields:

$$\delta\tilde{s} = \frac{1}{f_{\mathrm{nl}}}\left[\frac{-(A_1 + B_1\tilde{s}_1)}{A_1 + 2B_1\tilde{s}_1 - D_1}\right]. \tag{6.122}$$

The change in $\delta\tilde{s}$ implies that the lensing effect results in a change in beam size at any location in the cavity. Typically, an aperture is used at a particular location of the cavity, where, ideally, the self lensing results in the largest reduction in beam size. Let $\mathcal{M}_m = \begin{pmatrix} A_m & B_m \\ C_m & D_m \end{pmatrix}$ be the ABCD matrix that connects the reference point of the cavity (location of the Kerr lens) to the position of the aperture. The complex parameter $\tilde{s}_m$ at the aperture is:

$$\tilde{s}_m = \frac{C_m + D_m\tilde{s}}{A_m + B_m\tilde{s}}. \tag{6.123}$$

The relative change in beam size at the aperture $\delta w_m/w_m$ due to the Kerr lens is related to the change in $\tilde{s}_m$:

$$\frac{\delta w_m}{w_m} = -\frac{1}{2}\frac{\mathrm{Im}(\delta\tilde{s}_m)}{\mathrm{Im}(\tilde{s}_m)}. \tag{6.124}$$

The change in beam parameter at the aperture $\delta\tilde{s}_m$ can be inferred from the change in beam parameter $\delta\tilde{s}$ at the point of reference. Let us make the ansatz that $\tilde{s}_m = \tilde{s}_{m0} + \delta\tilde{s}_m$, where $\tilde{s}_{m0}$ is the complex s parameter without the Kerr lens [$\tilde{s}_{m0}$ is given by Eq. (6.123) for $\tilde{s}_1 = \tilde{s}$]. Inserting these expressions for $\tilde{s}_m$ and $\tilde{s} = \tilde{s}_1 + \delta\tilde{s}$ into Eq. (6.123) and keeping only terms up to first order, we find:

$$\delta\tilde{s}_m = \frac{D_m - B_m\delta\tilde{s}_{m0}}{A_m + B_m\tilde{s}_1}\delta\tilde{s}. \tag{6.125}$$

In this equation, $\tilde{s}_{m0}$ can be substituted from Eq. (6.123) where $\tilde{s}$ has been replaced by $\tilde{s}_1$, yielding:

$$\delta\tilde{s}_m = \frac{\delta\tilde{s}}{(A_m + B_m\tilde{s}_1)^2}. \tag{6.126}$$

Finally we substitute $\delta\tilde{s}$ with Eq. (6.122) to obtain:

$$\delta\tilde{s}_m = \frac{1}{f_{\mathrm{nl}}}\left[\frac{-(A_1 + B_1\tilde{s}_1)}{(A_1 + 2B_1 s_1 - D_1)(A_m + B_m\tilde{s}_1)^2}\right]. \tag{6.127}$$

The last equation (6.127) contains all the information necessary to estimate the effect of Kerr–induced lensing on a cavity. Let us consider an aperture of radius

w_a. Using Eq. (6.95), we can estimate the ratio of the energy loss through the aperture with Kerr effect ($\Delta\mathcal{W}$) to the loss without Kerr effect ($\Delta\mathcal{W}_0$):

$$\frac{\Delta\mathcal{W}}{\Delta\mathcal{W}_0} = \exp\left\{-2\left(\frac{w_a}{w_m+\delta w_m}\right)^2 + 2\left(\frac{w_a}{w_m}\right)^2\right\} = \exp\left\{4\left(\frac{w_a}{w_m}\right)^2 \frac{\delta w_m}{w_m}\right\} \tag{6.128}$$

where δw_m is determined by Eqs. (6.124) and (6.127).

6.6 Problems

1. By simple energy conservation arguments, find (in the approximation $T_1 \to \infty$) an expression for the energy gained (lost) per unit distance for an amplifier (absorber) $\frac{dW}{dz}$ as function of the change in population difference, and of the photon energy. Introduce into that expression the linear gain (absorption) coefficient, and combine with the rate equation to derive the evolution equation for the pulse energy density:

$$\frac{dW}{dz} = -\alpha_0 W_s\left[1 - e^{-W/W_s}\right], \tag{6.129}$$

where α_0 is the linear gain (absorption) coefficient, and W_s is the saturation energy density.

2. Derive an evolution equation for the pulse energy in a mode-locked laser ring cavity consisting of (a) the sequence output mirror (reflectivity r — gain — saturable absorber; (b) the sequence gain — mirror — absorber; and (c) the sequence absorber — gain — mirror. Neglect reshaping of the pulse, and integrate Eq. (6.129) to yield the energy $\mathcal{W}_{out} = W_{out}A_a$ at the end of a loss element of thickness d_a, as a function of the input energy $\mathcal{W}_{in} = W_{in}A_a$. A_a is the cross section of the beam in this particular element. Show that the output pulse of energy $\mathcal{W}_{out}$, after transmission of a pulse of input energy $\mathcal{W}_{in}$ through a saturable absorber is:

$$\mathcal{W}_{out} = A_a W_{sa} \ln\left[1 - e^{\alpha_a d_a}\left(1 - e^{\mathcal{W}_{in}/A_a W_{sa}}\right)\right]. \tag{6.130}$$

3. Consider the elementary round-trip model of Fig. 6.19. Choose a reference point just after the saturable loss, where the beam cross section is A_a. Show that the energy density W_4 at the end of series loss–gain–nonlinear-loss is related to the energy density W_1 entering this sequence by:

$$1 + e^{-a_a}\left[e^{W_4/W_{sa}} - 1\right] = \left\{1 + e^{a_g}\left[e^{RW_1A_a/(W_{sg}A_g)} - 1\right]\right\}^{\frac{W_{sg}A_g}{W_{sa}A_a}}, \tag{6.131}$$

where R is the output coupler (intensity) reflectivity, A_a and A_g are the beam cross sections in the absorber and gain elements, respectively; W_{sa} and W_{sg} the saturation energy densities in the absorber and gain media. Note that in a steady state, $\mathcal{W}_1 = \mathcal{W}_4$, and Eq. (6.131 can be used to calculate the pulse energy.

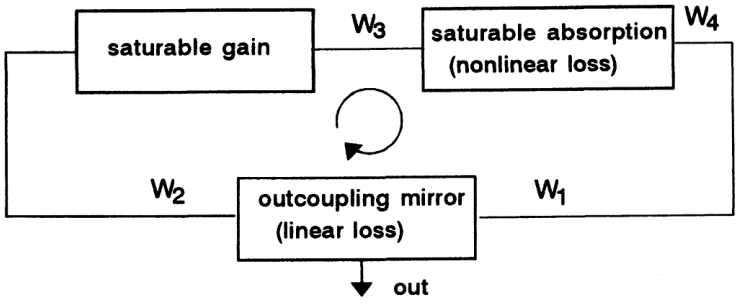

Figure 6.19: Simplified round-trip model for a passively mode-locked laser, showing the evolution of the pulse energy density, W.

Solve Eq. (6.131) in the approximation $W_4/W_{sa} \ll 1$ and $W_1/W_{sg} \ll 1$. Show that, even for a laser below threshold for cw operation ($R = r^2 < \exp\left[-(a_a + a_g)\right]$, two solutions can be found for W_1. The first solution is the minimum intracavity energy required to start mode-locked oscillation. The second solution is the steady state intracavity energy. Discuss the stability of both solutions. Under which condition can the first solution be small compared to the steady state intracavity energy?

4. Derive the equation for the soliton laser, following the procedure sketched in Fig. 6.9.

5. Calculate the spectrum of a continuously mode-locked Ti:sapphire laser emitting a continuous train of identical Gaussian pulses, 40 fs FWHM each, at a repetition rate of 80 MHz. The laser cavity is linear, with two prisms separated by 60 cm [$(dn/d\lambda)^2 = 10^{-9}$ nm^{-2}]. Neglecting all other contributions to the dispersion, calculate the longitudinal mode spectrum of the cavity. Is the latter spectrum identical to the Fourier amplitude (squared) of the train of pulses? If not, explain the difference(s).

6. Three mode-locked lasers generate pulses of 40 fs duration at the wavelengths of 620, 700 and 780 nm, respectively. Find under which condition the output of these lasers could be combined to provide a train of much shor-

ter pulses. What are the practical problems to be solved? Assuming perfect technology, how short would these pulses be?

7. Consider a passively mode-locked dye laser consisting of a saturable absorber, a depletable amplifier, an output-coupler and a bandwidth limiting element. Following the approach described in Section 6.2.4, write down the equation for the steady state pulse envelope assuming both absorber and amplifier are traversed at resonance. The result should be an integro-differential equation with differentials up to second-order (d^2/dt^2) and containing integrals of the type $W(t)$ and $[W(t)]^2$ where $W(t) = \int_{-\infty}^{t} F(t')dt'$.

8. In short cavity and distributed feedback lasers short pulse generation is possible in the single (longitudinal) mode regime. At first sight this seems to be in contradiction to the necessity of a broad laser spectrum. Make a quantitative estimate of the essential laser parameters required for the generation of a 500 fs pulse (Hint: consult the paragraph on miniature dye lasers in Section 7.8.1).

9. A Gaussian beam passes through a sequence of a Kerr medium of thickness d and an aperture of diameter D. The beam waist $w_0 = 25\ \mu$m is at the position of the Kerr medium ($d = 1$ mm, $\bar{n}_2 = 3 \cdot 10^{-16}$ cm^2/W). Find the distance from the Kerr medium to the aperture L, and the diameter of the aperture D, such that the overall transmission changes by 1% if the input illumination is switched from cw (no Kerr lens) to a 25 fs, 10 nJ pulse.

10. Recall Eq. (6.28) that determines the field envelope, $\mathcal{E}(t)$ at the output of a saturable absorber or amplifier, valid for small induced changes. Use this equation to derive an equation for the output pulse energy in terms of the input energy, cf. Eq. (6.51).

Bibliography

[1] W. H. Knox. *In situ* measurement of complete intracavity dispersion in an operating Ti:sapphire femtosecond laser. *Opt. Lett.*, 17:514–516, 1992.

[2] W. H. Knox and J. P. Gordon. Frequency-domain dispersion measurements in tunable mode-locked lasers. *J. Opt. Soc. Am. B*, 10:2071–2079, 1993.

[3] R. J. Jones, J. C. Diels, J. Jasapara, and W. Rudolph. Stabilization of the frequency, phase, and repetition rate of an ultra-short pulse train to a Fabry-Perot reference cavity. *Optics Comm.*, 175:409–418, 2000.

[4] Th. Udem, J. Reichert, R. Holzwarth, and T.W. Hänsch. Accurate measurement of large optical frequency differences with a mode-locked laser. *Opt. Lett.*, 24:881–883, 1999.

[5] J. Ye. Absolute measurement of a long, arbitrary distance to less than an optical fringe. *Opt. Lett.*, 29:1153–1155, 2004.

[6] S. V. Chekalin, P. G. Kryukov, Yu. A. Matveetz, and O. B. Shatherashvili. The processes of formation of ultrashort laser pulses. *Opto-Electronics*, 6:249–261, 1974.

[7] V. E. Zakharov and A. B. Shabat. Exact theory of two-dimensional self-focusing and one-dimensional self-modulation of waves in nonlinear media. *Sov. Phys. JETP*, 34:62–69, 1972.

[8] V. Petrov, W. Rudolph, and B. Wilhelmi. Evolution of chirped light pulses and the steady-state regime in passively mode-locked femtosecond dye lasers. *Rev. Phys. Appl.*, 22:1639–1650, 1987.

[9] C. S. Gardner, G. Green, M. Druskal, and R. Miura. Method for solving the Korteweg-deVries equation. *Phys. Rev. Lett.*, 19:1095, 1967.

[10] J.-C. Diels and H. Sallaba. Black magic with red dyes. *J. Opt. Soc. Am.*, 70:629, 1980.

[11] J.-C. Diels, J. Menders, and H. Sallaba. Generation of coherent pulses of 60 optical cycles through synchronization of the relaxation oscillations of a mode-locked dye laser. In R. M. Hochstrasser, W. Kaiser, and C. V. Shank, editors, *Picosecond Phenomena II*, page 41, Berlin, 1980. Springer-Verlag.

[12] F. Salin, P. Grangier, G. Roger, and A. Brun. Observation of high-order solitons directly produced by a femtosecond ring laser. *Phys. Rev. Lett.*, 56:11321135, 1986.

[13] T. Tsang. Observation of higher order solitons from a mode-locked Ti:sapphire laser. *Optics Lett.*, 18:293–295, 1993.

[14] J.-C. Diels. Femtosecond dye lasers. In F. Duarte and L. Hillman, editors, *Dye Laser Principles: With Applications*, volume ISBN 0-12-215492-4, chapter 3, pages 41–132. Academic Press, Boston, 1990.

[15] Y. Ishida, N. Sarukura, and H. Nakano. Soliton like pulse shaping in a passively mode locked Ti:sapphire laser. In C. B. Harris, E. P. Ippen, G. A. Mourou, and A. H. Zewail, editors, *Ultrafast Phenomena VII*, pages 75–77. Springer-Verlag, 1990.

[16] P. F. Curley, Ch. Spielmann, T. Brabec, F. Krausz, E. Wintner, and A. J. Schmidt. Operation of a fs Ti:sapphire solitary laser in the vicinity of zero group-delay dispersion. *Opt. Lett.*, 18:54–57, 1993.

[17] V. Petrov, W. Rudolph, and B. Wilhelmi. Computer simulation of passive mode locking of dye lasers with consideration of coherent light-matter interaction. *Optical and Quantum Electron.*, 19:377–384, 1987.

[18] G. H. C. New. Mode-locking of quasi-continuous lasers. *Optics Comm.*, 6:188–193, 1972.

[19] G. H. C. New. Pulse evolution in mode-locked quasi-continuous lasers. *IEEE J. of Quantum Electron.*, QE-10:115–124, 1974.

[20] H. A. Haus. Theory of mode-locking with a fast saturable absorber. *J. Appl. Phys.*, 46:3049, 1975.

[21] J.-C. Diels, J. J. Fontaine, I. C. McMichael, W. Rudolph, and B. Wilhelmi. Experimental and theoretical study of a femtosecond laser. *Sov. J. Quantum electron.*, 13:1562–1569, 1983.

[22] W. Rudolph and B. Wilhelmi. Calculation of light pulses with chirp in passively mode-locked lasers taking into account the phase memory of absorber and amplifier. *Appl. Phys.*, B-35:37–44, 1984.

[23] J.-C. Diels, W. Dietel, J. J. Fontaine, W. Rudolph, and B. Wilhelmi. Analysis of a mode-locked ring laser: chirped-solitary-pulse solutions. *J. Opt. Soc. Am. B*, 2:680–686, 1985.

[24] H. A. Haus and Y. Silberberg. Laser mode-locking with addition of nonlinear index. *IEEE J. of Quantum Electron.*, QE-22:325–331, 1986.

[25] Xin Miao Zhao and J.-C. Diels. Stability study of fs dye laser with self-lensing effects. *J. Optical Society America B*, 10(7):1159–1165, 1993.

[26] J. L. A. Chilla and O. E. Martinez. Spatial-temporal analysis of the self-mode-locked Ti:sapphire laser. *Journal of the Optical Society B*, 10:638–643, 1993.

[27] M. Lai, J. Nicholson, and W. Rudolph. Multiple pulse operation of a femtosecond Ti:sapphire laser. *Optics Communications*, 142:45–49, October 1997.

[28] D. Kuehlke, W. Rudolph, and B. Wilhelmi. Calculation of the colliding pulse mode locking in cw dye ring lasers. *IEEE J. Quant. Electr.*, QE-19:526–533, 1983.

[29] U. Keller, G. W. 'tHooft, W. H. Knox, and J. E. Cuninham. Femtosecond pulses from a continously self-starting passively mode-locked Ti:sapphire laser. *Opt. Lett.*, 16:1022–1024, 1991.

[30] P. W. Smith, Y. Silberberg, and D. Q. B. Miller. Mode-locking of semiconductor diode lasers using saturable excitonic nonlinearities. *J. Opt. Soc. Am.*, B-2:1228–1235, 1985.

[31] U. Keller. Ultrafast all-solid-state technology. *Appl. Phys. B*, 58:347–363, 1994.

[32] L. R. Brovelli, U. Keller, and T. H. Chiu. Design and operation of antiresonant Fabry–Perot saturable semiconductor absorbers for mode-locked solid-state lasers. *J. Opt. Soc. Am. B*, 12:311–322, 1995.

[33] G. P. Agrawal. *Nonlinear Fiber Optics*. Academic Press, ISBN 0-12-045142-5, Boston, 1995.

[34] Miles V. Klein and Thomas E. Furtak. *Optics*. John Wiley and Sons, ISBN 0-471-87297-0, New York, 1986.

[35] Anthony E. Siegman. *Lasers*. University Science Books, Mill Valley, CA, 1986.

[36] S. L. Shapiro, editor. *Ultrashort Light Pulses*. Springer Verlag, Berlin, Heidelberg, New York, 1977.

[37] H. W. Kogelnik, E. P. Ippen, A. Dienes, and C. V. Shank. Astigmatically compensated cavities for cw dye lasers. *IEEE Journal of Quantum Electron.*, QE-8:373–379, 1972.

[38] N. Jamasbi, J.-C. Diels, and L. Sarger. Study of a linear femtosecond laser in passive and hybrid operation. *J. of Modern Optics*, 35:1891–1906, 1988.

[39] H. W. Kogelnik and T. Li. Laser beams and resonators. *Appl. Opt.*, 5:1550–1567, 1966.

[40] A. Agnesi and G. C. Reali. Analysis of unidirectional operation of Kerr lens mode-locked ring oscillators. *Optics Comm.*, 110:109–114, 1994.

Chapter 7

Ultrashort Sources II - Examples

In the previous chapter the elements of passive mode-locking and their function for pulse shaping were described in detail. Analytical and numerical methods of characterizing mode-locked lasers were presented. Passive mode-locking is indeed the most widely applied and successful technique to produce pulses whose bandwidth approaches the limits imposed by the gain medium of dye and solid state lasers including fiber lasers. Passive mode-locking was the technique of choice to produce sub 50 fs pulses in dye lasers and, today, is routinely applied in solid-state and fiber lasers. Sub 5-fs pulses have been obtained from Ti:sapphire lasers without external pulse compression [1] using this method.

In this chapter we will review additional techniques of mode-locking and discuss examples of mode-locked lasers. The purely active or synchronous mode-locking will be covered first, followed by the hybrid passive-active technique. Other techniques not discussed in the previous chapter are additive mode-locking, methods based on second order nonlinearities, and passive negative feedback. For their important role as saturable absorbers we will review the relevant properties of semiconductor materials. The later part of this chapter is devoted to specific examples of popular lasers.

7.1 Synchronous mode-locking

A simple method to generate short pulses is to excite the gain medium at a repetition rate synchronized with the cavity mode spacing. This can be done by using a pump that emits pulses at the round-trip rate of the cavity to be pumped. One of the main advantages of synchronous mode-locking is that a much broader range of gain media can be used than in the case of passive mode-locking. This includes semiconductor lasers and, for instance, laser dyes such as styryl 8, 9, and 14, which

have too short a lifetime to be practical in cw operation, but are quite efficient when pumped with short pulses.

Ideally, the gain medium in a synchronously pumped laser should have a short lifetime, so that the duration of the inversion is not larger than that of the pump pulse. An extreme example is the case of optical parametric oscillators (OPO) where the gain lives only for the time of the pump pulse.

Synchronous pumping is sometimes used in situations that do not meet this criterion, just as starting mechanism. This is the case in some Ti:sapphire lasers, where the gain medium has a longer lifetime than the cavity round-trip time, and therefore synchronous pumping results in only a very small modulation of the gain. The small modulation of the gain coefficient $\alpha_g(t)$ is sufficient to start the pulse formation and compression mechanism by dispersion and self-phase-modulation [2]. The initial small gain modulation grows because of gain saturation by the modulated intracavity radiation, resulting in a shortening of the function $\alpha_g(t)$, and ultimately ultrashort pulses.

The simple considerations that follow, neglecting the influence of saturation, show the importance of cavity synchronism. If the laser cavity is slightly longer than required for exact synchronism with the pump radiation (train of pulses), stimulated emission and amplified spontaneous emission will constantly accumulate at the leading edge of the pulse, resulting in pulse durations that could be even longer than the pump pulse. Therefore, to avoid this situation, the cavity length should be slightly shorter than that required for exact synchronism with the pump radiation. Let us assume first perfect synchronism. The net gain factor per round-trip is

$$G(t) = e^{[\alpha_g(t)d_g - L]}, \tag{7.1}$$

where L is the natural logarithm of the loss per cavity round-trip. After n round-trips, the initial spontaneous emission of intensity I_{sp} has been amplified sufficiently to saturate the gain α_g, and thus the pulse intensity is approximately $I(t) \approx I_{sp} \times \left\{e^{[\alpha_{g0}(t)d_g - L]}\right\}^n = I_{sp} \times [G_0(t)]^n$. The pulse is thus $\sqrt{n}$ times narrower than the unsaturated gain function $G_0(t)$.

For a cavity shorter than required for exact synchronism, in a frame of reference synchronous with the pulsed gain $\alpha_g(t)$, the intracavity intensity of the j^{th} round-trip is related to the previous one by:

$$I_j(t) = I_{j-1}(t+\delta)e^{[\alpha_g(t)d_g - L]}, \tag{7.2}$$

where δ is the mismatch between cavity round-trip time and the pump pulse spacing. The net gain for the circulating pulse $e^{[\alpha_g(t)d_g - L]}$ exists in the cavity for a time $n\delta$ only, as can be seen from Fig. 7.1. The laser oscillation will start from a small

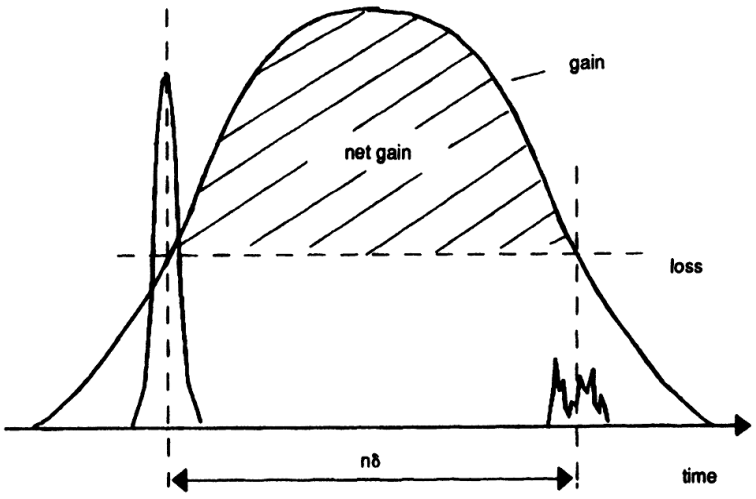

Figure 7.1: Net gain (gain minus loss) temporal profile as it appears at each periodicity of the pump pulse. If the round-trip time of the laser cavity is slightly shorter (by δ) than the pump period, radiation emitted at the right edge of the gain profile will reappear shifted to the left by that amount δ at each successive round-trip. A pulse will experience gain for a maximum of n passages, given by the ratio of the duration of the net gain to the mismatch δ.

noise burst $I_{sp}(t)$. The intracavity pulse after n round trips can be approximated by:

$$I(t) = I_{sp}(t + n\delta)\left[e^{(\alpha_{av} d_g - L)}\right]^n, \tag{7.3}$$

where $I_{sp}(t+n\delta)$ is the spontaneous emission noise present in the cavity in the time interval $(n-1)\delta \rightarrow n\delta$, and $\alpha_{av} = \frac{1}{n\delta}\int \alpha_g(t)dt$ is a gain coefficient averaged over the n round-trips.

These simple considerations indicate that in the absence of any spectral filtering mechanism and neglecting the distortion of the gain curve $\alpha_g(t)$ by saturation, the pulse should be roughly $\sqrt{n}$ times shorter than the duration of the gain window. The timing mismatch δ is an essential parameter of the operation of a synchronously mode-locked laser. The shape of the autocorrelation (see Chapter 10) is typically a double sided exponential, which — as pointed out by Van Stryland [3] — is a signature for a possible random distribution of pulse duration in the train. The interferometric autocorrelation also indicates a random (Gaussian) distribution of pulse frequencies [4]. These fluctuations in pulse duration and frequency

have also been observed in theoretical simulations by New and Catherall [5] and Stamm [6].

Gain saturation — neglected in the elementary model above — does play an essential role in pulse shaping and compression for synchronously pumped lasers. We refer to a paper by Nekhaenko *et al.* [7] for a detailed review of the various theories of synchronous pumping. In a typical synchronously pumped laser, the net gain (at each round-trip) is "terminated" by gain depletion at each passage of the circulating pulse. The shortening of the gain period results in a laser pulse much shorter than the pump pulse. This mechanism was analyzed in detail by Frigo *et al.* [8]. It has been verified experimentally [9] that the shortest pulse duration is approximately $\tau_p \approx \sqrt{\tau_{pump} T_{2g}}$. This result illustrates the fact that the finite spectral width of the gain profile, $\delta\nu_g \approx T_{2g}^{-1}$, ultimately limits the shortest obtained pulse duration. Numerical simulations have been made to relate the number of round-trips required to reach steady state to the single-pass gain [10].

Regenerative feedback As we have seen at the beginning of the previous section, the laser cavity should never be longer than the length corresponding to exact synchronism with the pump radiation in order to generate pulses shorter than the pump pulse. This implies strict stability criteria for the pump laser cavity, its mode-locking electronics, and the laser cavity (invar or quartz rods were generally used for synchronously pumped dye laser cavities). Considerations of thermal expansion of the support material and typical cavity lengths clearly shows the need for thermal stability. Indeed, the thermal expansion coefficient of most rigid materials for the laser support exceeds $10^{-5}/^{o}C$. Since the cavity length approaches typically 2 m, even a temperature drift of 0.5 ^{o}C would bring the laser out of its stability range. However, since it is the *relative* synchronism of the laser cavity with its pump source that is to be maintained, a simpler and efficient technique is to use the noise (longitudinal mode beating) of the laser itself, to drive the modulator of the pump laser [11]. This technique, sometimes called "regenerative feedback," has been applied to some commercial synchronously pumped mode-locked lasers, and even to a Ti:sapphire laser [2].

Seeding Even if somewhat oversimplified, the representation of Fig. 7.1 gives a clue to an important source of noise in the synchronously pumped dye laser. The seed $I_{sp}(t)$ has a complex electric field amplitude $\tilde{\epsilon}(t)$ with random phase. As pointed out in [12] and in [6] it is this spontaneous emission source that is at the origin of the noise of the laser. Could the noise be reduced by adding to $\tilde{\epsilon}$ a minimum fraction $\eta E(t)$ of the laser output, just large enough so that the phase of $\eta E(t) + \tilde{\epsilon}(t)$ is equal to the phase of the output fields $E(t)$ (which essentially

implies $\eta E(t) \gg \tilde{\epsilon}$). Both calculation and experiment have demonstrated a dramatic noise reduction by seeding the cavity with a small fraction of the pulse *in advance* of the main pulse [13]. The emphasis here is on small: only a fraction of the order of 10^{-7} (not exceeding 10^{-5}) of the output power should be re-injected. A possible implementation would consist of reflecting back a fraction of the output pulse delayed by slightly less than a cavity round-trip. This amounts to a weakly coupled external cavity. A much simpler implementation demonstrated by Peter *et al.* [13] consists in inserting a thin glass plate (microscope cover glass for instance) in front of the output mirror (Fig. 7.2). The amount of light re-injected is adjusted by translating the glass plate in front of the beam. The timing of the re-injected signal is determined by the thickness of the plate.

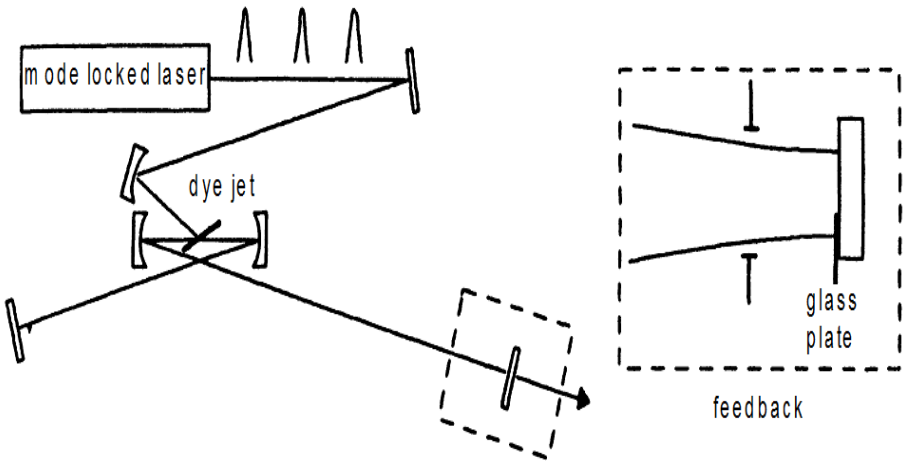

Figure 7.2: Typical synchronously pumped dye laser. The length of the dye laser cavity has to be matched to the repetition rate of the pump pulses. The noise in a synchronously pumped laser can be reduced by re-injection of a portion of the output *ahead* of the main intracavity pulse. A thin glass plate on the output mirror intercepts and reflects part of the beam into the cavity, with the desired advance. The fraction of energy reflected (of the order of 10^{-6}) is determined by the overlap of the aperture and the glass plate (adapted from [13]).

7.2 Hybrid mode-locking

Synchronous pumping alone can be considered as a good source of ps rather than fs pulses. The disadvantages of this technique, as compared to passive mode-locking, are:

- a longer pulse duration
- larger amplitude and phase noise,
- the duration of the pulses of the train are often randomly distributed [3],
- when attempting to achieve the shortest pulse durations, the pulse frequencies are randomly distributed [4].

One solution to these problems is to combine the techniques of passive and active mode-locking in a hybrid system [14,15]. Depending on the optical thickness of the absorber, the hybrid mode-locked laser is either a synchronously mode-locked laser perturbed by the addition of saturable absorption or a passively mode-locked laser pumped synchronously. The distinction is obvious to the user. The laser with little saturable absorption modulation will have the noise characteristics and cavity length sensitivity typical of synchronously pumped lasers, but a shorter pulse duration. The laser with a deep passive modulation (concentrated saturable absorber for a dye, or a large number of MQW for a semiconductor saturable absorber) shows intensity autocorrelation traces identical to those of the passively mode-locked laser [16]. The sensitivity of the laser to cavity detuning decreases. The reduction in noise can be explained as being related to the additional timing mismatch introduced by the absorber, which partially compensates the pulse advancing influence of the gain and spontaneous emission [17].

7.3 Additive pulse mode-locking

7.3.1 Generalities

There has been in the late 1980s a resurrection of interest in developing additive pulse mode-locking (APML), a technique involving coupled cavities. One of the basic ideas — to establish the mode coupling outside the main laser resonator — has been suggested in 1965 by Foster *et al.* [18] and applied to mode-locking a He-Ne laser [19]. In that earlier implementation, an acousto-optic modulator is used to modulate the laser output at half the inter-mode spacing of the laser. The frequency shifted beam is reflected back through the modulator, resulting in a first-order diffracted beam which is shifted in frequency by the total mode spacing, and re-injected into the laser cavity through the output mirror. The output mirror of the laser forms, with the mirror used to re-inject the modulated radiation, a cavity with the same mode spacing as the main laser cavity. If the laser is close to threshold, a small extracavity modulation fed back into the main cavity can be sufficient to lock the longitudinal modes.

Unlike this technique more recent APML implementations are based on passive methods. In the purely dispersive version, pulses from the coupled cavity are given some phase modulation, such that the first half of the pulse fed back into the laser adds in phase with the intracavity pulse, while the second half has opposite phase [20]. At each round-trip, the externally injected pulse thus contributes to compress the intracavity pulse, by adding a contribution to the leading edge and subtracting a certain amount from the trailing edge, as sketched in Fig. 7.3. This technique has first been applied to shortening pulses generated through other mode-locking mechanisms. A reduction in pulse duration by as much as two orders of magnitudes was demonstrated with color-center lasers [21–24] and with Ti:sapphire lasers [25].

It was subsequently realized that the mechanism of pulse addition through a nonlinear coupled cavity is sufficient to passively mode-lock a laser. This technique has been successfully demonstrated in a Ti:sapphire laser [26], Nd:YAG [27, 28], Nd:YLF [29, 30], Nd:glass [31], and KCl color-center lasers [32]. A detailed description of the coherent addition of pulses from the main laser and the extended cavity which takes place in the additive-pulse mode locking has been summarized by Ippen *et al.* [33].

Coherent field addition is only one aspect of the coupled cavity mode-locked laser. The nonlinearity from the coupled cavity can be for example an amplitude modulation, as in the "soliton" laser [34], or a resonant nonlinear reflectivity via a quantum well material [35].

7.3.2 Analysis of APML

Analysis of APML [23, 33] has shown that the coupling between a laser and an external nonlinear cavity can be modelled as an intensity-dependent reflectivity of the laser end mirror. Let r be the real (field amplitude) reflection coefficient of the output mirror. The radiation transmitted through that mirror into the auxiliary (external) cavity returns to the main cavity having experienced a field amplitude loss γ ($\gamma < 1$) and a total phase shift $-[\phi + \Phi(t)]$. The nonlinear phase shift $\Phi(t)$ induced by the nonlinearity is conventionally chosen to be zero at the pulse peak [33], so that the linear phase shift ϕ includes a bias due to the peak nonlinear phase shift. Therefore, if $r\tilde{\mathcal{E}}(t)$ is the field reflected at the mirror, the field transmitted through the output mirror, the auxiliary cavity (loss γ) and transmitted a second time through the output mirror is $(1-r^2)\gamma e^{-i\phi}\tilde{\mathcal{E}}(t)e^{-i\Phi(t)}$. If d is the length of the nonlinear medium, and assuming a $\bar{n}_2$ nonlinearity, according to Eq. (4.70):

$$\Phi(t) = \frac{2\pi\bar{n}_2}{\lambda_\ell}\left[I_{ax}(t) - I_{ax}(0)\right]d \tag{7.4}$$

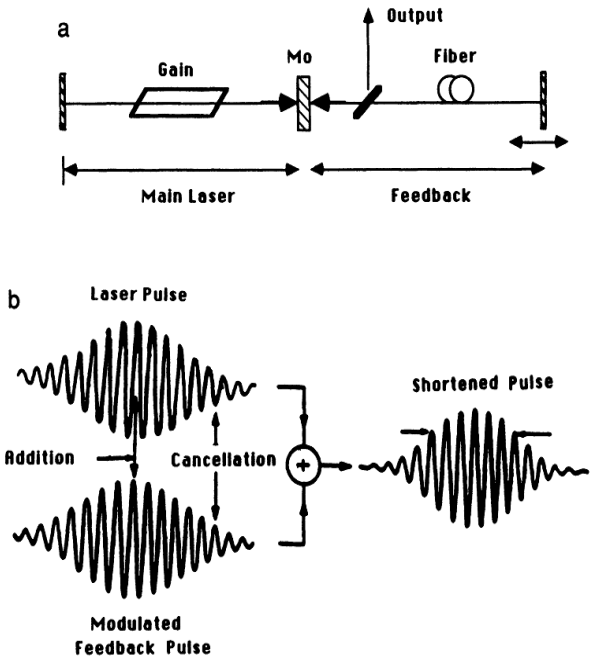

Figure 7.3: A typical additive-pulse mode locked laser (a). At the output mirror M_0, the pulse of the main cavity [(b), top left] adds coherently to the pulse of the auxiliary cavity [(b), bottom left], to result in a shortened pulse [(b), right] (courtesy E. Wintner).

where $I_{ax}(t)$ is the intensity of the field in the auxiliary cavity. For a qualitative discussion we determine the total reflection by adding the contribution of the re-injected field from the auxiliary cavity to the field reflection r of the output mirror, which leads to a time dependent complex "reflection coefficient" $\tilde{\Gamma}$:

$$\tilde{\Gamma}(t) = r + \gamma(1-r^2)e^{-i\phi}[1 - i\Phi(t)]. \tag{7.5}$$

In Eq. (7.5), it has been assumed that Φ is small, allowing us to substitute for the phase factor $e^{-i\Phi}$ its first order expansion. There is a differential reflectivity for different parts of the pulses. If one sets $\phi = -\pi/2$, then $|\tilde{\Gamma}|$ has a maximum value at the pulse center where $\Phi = 0$, and smaller values at the wings:

$$\tilde{\Gamma}(t) = r + \gamma(1-r^2)\Phi(t) + i[\gamma(1-r^2)]. \tag{7.6}$$

The reflection is thus decreasing when Φ becomes negative in the wings of the pulse, which is the "coherent field subtraction" sketched in Fig. 7.3. The compression factor is determined by the ratio of $\gamma(1-r^2)$ to r, which can be related to the

ratio of energy in the auxiliary cavity to that in the main cavity [Note that $\gamma(1-r^2)$ is the maximum amount of energy that can be subtracted from the pulse in the main cavity at each round-trip].

This dynamic reflectivity can be adjusted for pulse shortening at each reflection, until a steady-state balance is achieved between the pulse shortening and pulse spreading due to bandwidth limitation and dispersion.

7.4 Mode-locking based on non-resonant nonlinearity

Various techniques of mode locking using second order nonlinearities have been developed. A first method is a direct extension of Kerr-lens mode-locking, which has been analyzed in the previous chapter. A giant third order susceptibility can be found near phase matching conditions in second harmonic generation, not unlike the situation encountered with a third order susceptibility, which is seen to be enhanced near a two-photon resonance [36, 37]. In this method, called cascaded second-order nonlinearity mode-locking, the nonlinear crystal is used in mismatched conditions with a mirror that reflects totally both the fundamental and second-harmonic waves. The cascade of sum and difference frequency generation induces a transverse focusing of the fundamental beam in a way similar to Kerr self-focusing. This method has been applied to solid state lasers by Cerullo [38] and Danailov [39]. The resonance condition (the phase matching bandwidth) implied in this method does not make it applicable to the fs range.

Another technique was introduced by Stankov [40,41], who demonstrated passive mode-locking in a Q-switched laser by means of a nonlinear mirror consisting of a second harmonic generating crystal and a dichroic mirror. Dispersion between the crystal and the dichroic mirror is adjusted so that the reflected second harmonic is converted back to the fundamental.

A third method, based on polarization rotation occurring with type-II second harmonic generation, is the equivalent of Kerr-lens mode locking in fiber lasers. It has also been applied to some solid state lasers. The last two methods will be discussed in more details in the following subsections.

7.4.1 Nonlinear mirror

The principle of operation of the nonlinear mirror can be understood with the sketch of Fig. 7.4, showing the end cavity elements that provide the function of nonlinear reflection. A frequency-doubling crystal in phase-matched orientation is combined with a dichroic mirror output coupler that totally reflects the second-harmonic beam and only partially reflects the fundamental. These two elements

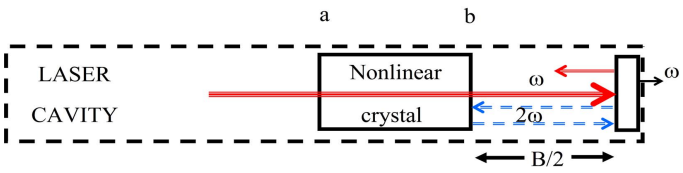

Figure 7.4: End cavity assembly constituting a nonlinear mirror. The end mirror is a total reflector for the second harmonic, and a partial reflector for the fundamental.

form a reflector, whose reflectivity at the fundamental wavelength can either increase or decrease, depending on the phases of the fundamental and second harmonic radiation. These phase relations between the first and second harmonics can be adjusted inserting a dispersive element between the nonlinear crystal and the dichroic mirror. The dispersive element can be either air (the phase adjustable parameter is the distance between the end mirror and the crystal) or a phase plate (of which the angle can be adjusted.

At low intensity, the cavity loss is roughly equal to the transmission coefficient of the output coupler at the fundamental wavelength. At high intensities, more second harmonic is generated, reflected back and reconverted to the intracavity fundamental, resulting in an increase in the effective reflection coefficient of the crystal– output coupler combination. The losses are thus decreasing with intensity, just as is the case with a saturable absorber. Figure 7.5 shows the variation of intensities of the fundamental and second harmonic in the first (left) and second (right) passage through the second harmonic generating crystal. Depletion of the fundamental through SHG reduced the intensity to 30% of its initial value. Only 10% of that fundamental is reflected back through the SHG crystal. However, since the full SH signal that was generated in the first passage is reflected back, and since it has reversed phase with respect to the fundamental, 30% of the initial fundamental is recovered. At the first passage, the conversion to second harmonic should be sufficient to have a sizeable depletion of the fundamental. Therefore, this method works best for high power lasers. The theoretical framework for the second harmonic generation has been set in Chapter 3 (Section 4.3.1) and can be applied for a theoretical analysis of this type of modelocking. A frequency domain analysis of the mode-locking process using a nonlinear mirror can be found in ref. [42]. Available software packages, such as — for example — *SNLO* software [43] can be used to compute the transmission of fundamental and second harmonic at each passage.

The electronic nonlinearity for harmonic generation responds in less than a few femtoseconds. However, because of the need to use long crystals to obtain suffi-

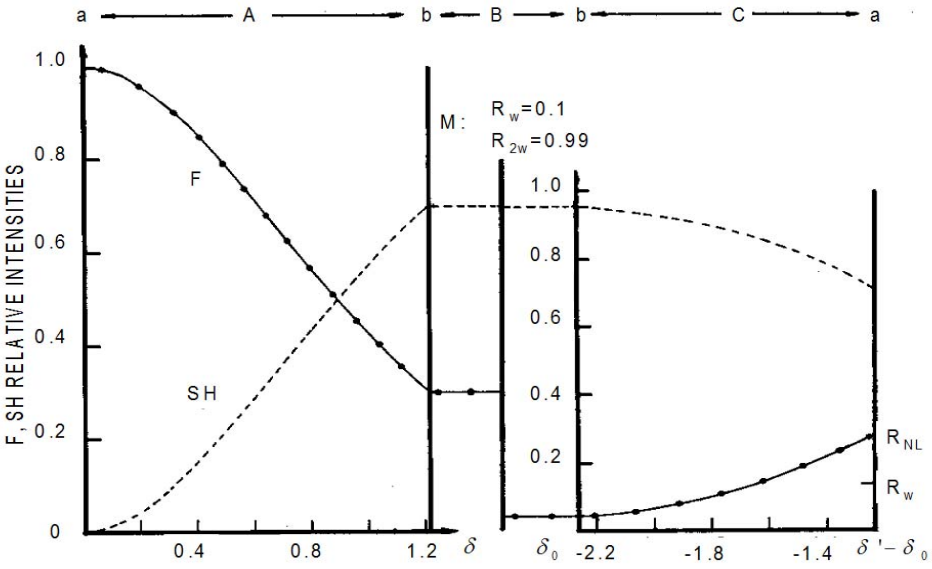

Figure 7.5: Variation of intensity of the fundamental (F, solid line) and the second harmonic (SH, dashed line) for two successive passages, A and B, through the nonlinear crystal. The entrance and exit surfaces a and b are labelled in Fig. 7.4. A fraction $R = 10\%$ of the fundamental intensity is reflected back into the crystal, together with the entire second harmonic. After propagation for a distance B in air, the phase of the second harmonic with respect to the fundamental has undergone a shift of π, resulting in a re-conversion of second harmonic into fundamental at the second passage.

cient conversion, the shortest pulse durations that can be obtained by this method are limited to the picosecond range by the phase matching bandwidth. The method has been applied successfully to flashlamp pumped lasers [44] and diode pumped lasers [45–48]. A review can be found in ref. [49].

The same principle has also been applied in a technique of parametric mode-locking [50], which can be viewed as a laser hybridly mode-locked by a nonlinear process. The third-order nonlinearity of a crystal applied to sum and difference frequency generation is used in the mode-locking process. The nonlinear mirror can also be used to provide negative feedback instead of positive feedback [51] by adjusting the phase shift between fundamental and second harmonic by the dispersive element.

7.4.2 Polarization Rotation

Nonlinear polarization rotation due to the nonlinear index associated with elliptical polarization has been described in Section 6.4.2 as an example of a third-order nonlinear process. Again, a second order nonlinearity can also be used for polarization rotation. As is the case when a phase-matched second harmonic generation is used, the minimum pulse duration is determined by the inverse of the phase matching bandwidth.

Under type-II phase-matching, the orientation of the fundamental field polarization (assumed to be linear) at the output of the nonlinear crystal is directly dependent on the relative intensity of the two orthogonal polarization components. The crystal cut and orientation is assumed to perfectly fulfill the phase-matching conditions for second harmonic generation. If the linearly polarized incoming field is split into two orthogonal components with strongly unbalanced intensity, then the wave of smallest initial amplitude may be completely depleted since the second harmonic generation process diminishes each component by the same amount. If the nonlinear propagation continues beyond that point the second harmonic generation is replaced by difference frequency generation between the generated harmonic and the remaining fundamental component. The new fundamental field appears on the polarization axis where the fundamental had disappeared but the phase of the created field is now shifted by π with respect to the initial field. Difference frequency generation then goes on with propagation distance until the power of the second harmonic goes to zero. If we assume that the crystal behaves in the linear regime like a full-wave or half-wave plate then the output polarization state remains linear in the nonlinear regime but the orientation of the output is intensity dependent. Two properly oriented polarizers placed on either side of the nonlinear crystal permit us to build a device with an intensity dependent transmission.

Details on the use of nonlinear polarization in a type-II SHG for mode-locking of a cw lamp-pumped Nd:YAG laser are given in ref [52].

7.5 Negative feedback

In this section we will describe a technique that limits the peak power of pulses circulating in the cavity. This can be accomplished by a combination of an element producing nonlinear defocusing and an aperture. Negative feedback has gained importance in Q-switched and modelocked solid-state lasers because it tends to lengthen the pulse train by limiting the peak power and thereby reducing the gain depletion. Moreover, a longer time for pulse formation usually leads to shorter

output pulses and more stable operation.[1]

We have seen that the pulse formation — in passively mode-locked lasers — is associated with a positive feedback element (Kerr lensing, saturable absorber) which enhances positive intensity fluctuations (generally through a decrease of losses with increasing intensity). While a positive feedback leads to pulse formation, it is inherently an unstable process, since intensity fluctuations are amplified. Therefore, it is desirable, in particular in high-power lasers, to have a *negative* feedback element that sets in at higher intensities than the positive feedback element.

Pulses of 10, 5, and less than 1 ps have been generated with this technique with Nd:YAG, Nd:YAP and Nd:glass lasers, respectively. More importantly for the fs field, the pulse-to-pulse reproducibility (better than 0.2% [53]) makes these lasers ideal pump sources for synchronous or hybrid mode-locking. The flashlamp pumped solid state laser with negative feedback provides a much higher energy per pulse, at shorter pulse duration, than the cw mode-locked laser used conventionally as pump for fs systems. The use of negative feedback to effectively pump a fs dye laser was demonstrated by Angel *et al.* [10].

In semiconductor laser pumped solid state lasers, negative feedback can be used to suppress Q-switched-mode-locked operation, in favor of cw mode-locked operation [54]. The mechanism is the same as for the flashlamp pumped laser: the energy limiting prevents the total gain depletion that ultimately interrupts the pulse train.

Electronic feedback

A typical flashlamp pumped, mode-locked Nd laser generates a train of only five to ten pulses of all different intensities. In the first implementation of "negative feedback," an electronic feedback loop *increases* the cavity losses if the pulse energy exceeds a well defined value. Martinez and Spinelli [55] proposed to use an electro-optic modulator to actively limit the intracavity energy in a passively mode locked glass laser. They demonstrated that the pulse train could be extended. A fast high voltage electronics led to the generation of μs pulse trains in a passively mode locked glass lasers [56] and in hybrid Nd:glass lasers [57].

Electronic Q-switching and negative feedback has the advantage that the timing of the pulses is electronically controlled. This is important in applications where several laser systems have to be synchronized. However, there is a minimum response time of one cavity roundtrip before the feedback can react [57].

[1] Note that in high-power solid-state lasers the typical Q-switched pulse is not much longer than a few cavity round trips.

Passive negative feedback

A passive feedback system can provide immediate response — i.e., on the time scale of the pulse rather than on the time scale of the cavity round-trip. We will here restrict our description to the Nd laser using a semiconductor (GaAs) for passive negative feedback. The semiconductor used in a passive feedback system produces nonlinear lensing. The analysis of the beam focusing is identical to that of the Kerr lensing, except that the sign of the lensing is opposite. The nonlinear index change is initiated by electrons generated by two-photon absorption into the conduction band. Various processes then contribute to the index change. The index change by free electrons, for example, can be estimated with the Drude model and is negative:

$$\Delta n_d(x,y,t) = -\frac{n_0 e^2}{2m^* \epsilon_0 \omega_\ell^2} N(x,y,t), \tag{7.7}$$

where N is the electron density, m^* is the electron's effective mass and n_0 is the linear index. We refer to the literature for additional contributions to Δn such as the interband contribution [58], and an additional electronic contribution [36, 59].

Other implementation of passive negative feedback [60] have used a second harmonic crystal near phase matching ("cascaded nonlineary") to produce a large nonlinear index required for the energy limiter.

A typical laser using passive negative feedback generally includes a saturable absorber for Q-switching and mode-locking, and an energy limiter. An energy limiter that can be used for passive negative feedback is illustrated in Fig. 7.6. A two-photon absorber (typically GaAs) is located near a cavity end mirror. After double passage through this sample, the beam is defocused by a self-induced lens originating mainly from the free carriers generated through two-photon absorption. The defocused portion of the beam is truncated by an aperture. Self-defocusing in the semiconducting two-photon absorber sets in at a power level that should be close to the saturation intensity of the saturable absorber used for Q-switching and mode-locking. Because the pulse intensity is close to the pulse saturation intensity, there is optimal pulse compression at the pulse leading edge by saturable absorption. Because of self defocusing in GaAs, the pulse trailing edge is clipped off, resulting in further pulse compression and energy loss.

The stabilization and compression of the individual pulses result from a delicate balance of numerous physical mechanisms. Details of the experimental implementation and theoretical analysis can be found in the literature [61–63].

At the end of this section we will discuss an experiment that illustrates the saturation and focusing properties of a particular nonlinear element. Often the nonlinear element [64] is just the substrate of a multiple quantum well. In that case, one has combined in one element the function of saturable absorber (the

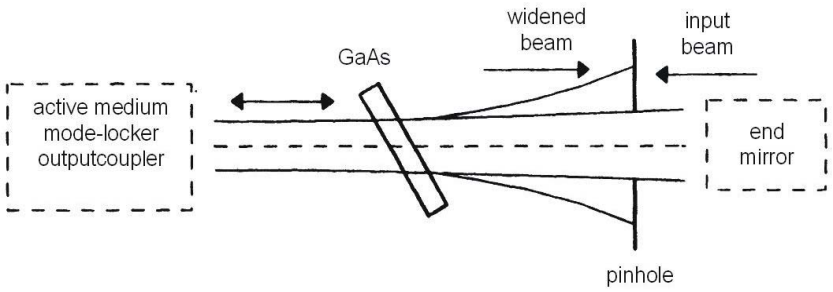

Figure 7.6: Passive negative feedback is typically achieved by inserting in the cavity an energy limiter, which can consist of a GaAs plate (acting as two-photon absorber and subsequent defocusing element) and an aperture (pinhole).

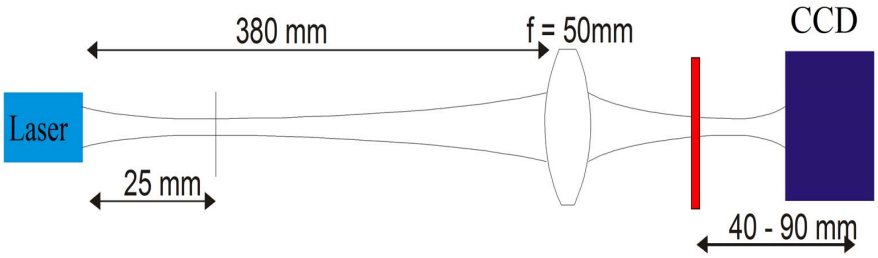

Figure 7.7: Experimental set-up to observe the saturable absorption, two-photon absorption and self lensing in a sample of 100 quantum wells on a GaAs substrate located in front of a CCD camera (from ref. [64]).

MQW, excited by one-photon absorption) and energy limiter (the substrate, excited by two-photon absorption). The properties of the MQW on its substrate are well demonstrated by the measurement illustrated in Fig. 7.7 and 7.8. A diode pumped microchip YAG laser is used to focus pulses of 3 μJ energy and 1 ns duration at a repetition rate of 15.26 kHz into a sample consisting of 100 quantum wells on a GaAs substrate. The lens has a focal distance of 50 mm. The output power from the laser was attenuated in order not to damage the MQW. The maximum power density in the focal point was 10 MW/cm^2. The spatial profile of the radiation transmitted through the sample was analyzed, using a CCD camera, as a function of the position of the sample. The various profiles are shown in Fig. 7.8. From this picture we can see that the initial low power transmission of 23% far from the focal point increases to 45% close to the focal point. The transmission of the

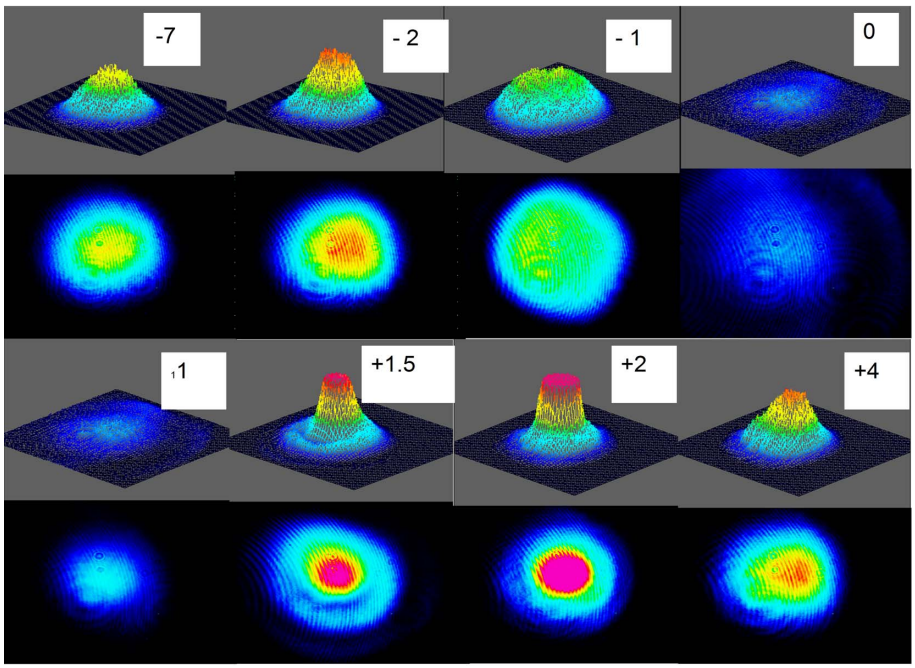

Figure 7.8: Spatial beam structure versus longitudinal position of the sample along the axis of the beam, after the lens. The distances from focus are indicated (in mm). The upper part of the figure corresponds to the positions left of the focus; the lower part right of the focus (from ref. [64]).

GaAs plate alone is 52%, indicating that the nonsaturable losses in the MQW are about 10%. The increase in transmission reflects the saturation of the quantum wells. Close to the focal point, the transmission drops and significant de-focusing is observed. This is a region of large two-photon absorption, creating an electron plasma sufficiently dense to scatter the beam. Self defocusing is observed with the sample positioned to the left of the focus, self-focusing to the right of the focus.

7.6 Semiconductor-based saturable absorbers

Progress in the fabrication of semiconductors and semiconductor based structures, such as multiple-quantum wells (MQWs), has led to the development of compact and efficient saturable absorbers whose linear and nonlinear optical properties can be custom tailored. These devices are particularly suited for mode-locking solid-state lasers, fiber lasers and semiconductor lasers. They can conveniently be de-

signed as laser mirrors, which makes them attractive for initiating and sustaining mode-locking in a variety of solid-state lasers and cavity configurations, for a review see [65].

In semiconductors a transition from the valence to the conduction band is mostly used. In MQWs an excitonic resonance near the band edge can be utilized [66], which leads to a lower saturation energy density [67].

As discussed in the previous chapter an important parameter is the relaxation time of the absorber. The recovery rate is the sum of the carrier relaxation rate $1/T_1$ and the rate of diffusion out of the excited volume $1/\tau_d$:

$$\frac{1}{\tau_A} = \frac{1}{T_1} + \frac{1}{\tau_d}. \tag{7.8}$$

For a beam waist w_0 at the absorber the characteristic diffusion time can be estimated by

$$\tau_d = \frac{w_0^2}{8D},$$

where D is the diffusion constant, which is related to the carrier mobility μ through the Einstein relation $D = k_B T\mu/e$. For a beam waist of 2 μm and $D = 10$ cm^2/s for example, the diffusion time $\tau_d \approx 500$ ps.

Typical carrier lifetimes in pure semiconductors are ns and thus too long for most mode-locking applications, where the cavity roundtrip time is of the order of a few ns. Several methods are available to reduce the effective absorption recovery rate of bulk semiconductors and MQWs:

1. tight focusing,
2. insertion of defects.

A commonly used technique to insert defects is proton bombardment with subsequent gentle annealing. For example, the bombardment of a MQW sample consisting of 80 periods of 102 Å GaAs and 101 Å $Ga_{0.71}Al_{0.29}As$, with 200-keV protons resulted in recovery times of 560 ps and 150 ps, respectively [67]. Structures with shorter wells (70 to 80 Å) separated by 100 Å barriers yield broader absorption bands [68], with the same recovery time of 150 ps after a 10^{13}/cm^2 proton bombardment and annealing.

Another technique to introduce defects is to grow the semiconductor at relatively low temperature. This can lead to a relatively large density of deep-level defects that can quickly trap excited carriers. As an example, Fig. 7.9 shows a plot of the carrier lifetime versus MBE growth temperature. The measurement is performed by focusing a 100 fs pump pulse onto a 20–30 μm spot on the semiconductor. A 10 times attenuated (as compared to the pump) probe pulse is focused

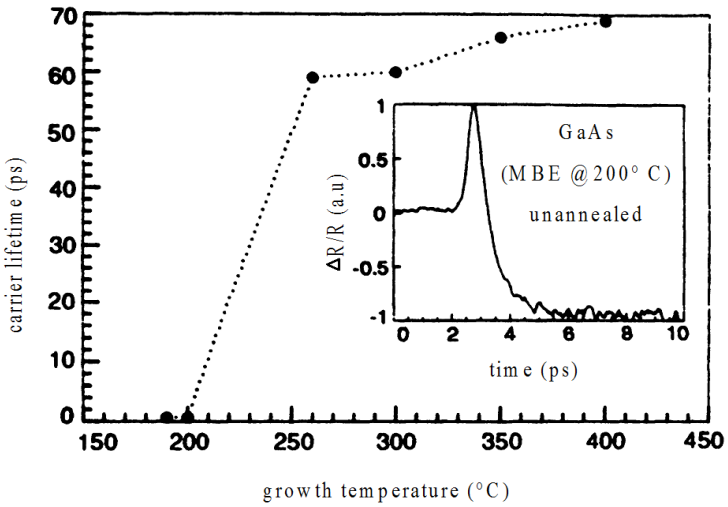

Figure 7.9: Carrier lifetime of GaAs versus MBE growth temperature. The inset shows the transient reflection measured in a pump-probe experiment, for a 200°C grown unannealed sample (from [69]).

into a 10 μm island within the pumped region. Both pump and probe are at 620 nm. The reflectance of the probe is measured as a function of probe delay (inset in Fig. 7.9). The carrier lifetime is defined as the initial decay ($1/e$) of the reflectance versus delay curve.

Table 7.1 lists carrier lifetimes and mobilities of some representative semiconductor materials.

7.7 Solid State Lasers

7.7.1 Generalities

Most common solid state lasers used for ultrashort pulse generation are media with a long lifetime (compared to typical cavity round-trip times). The laser efficiency can be very high if pumped by other lasers, for example semiconductor lasers, tuned to the pump transition. This is especially the case for lasers such as Ytterbium YAG that have a very small quantum defect[2].

Since these solid state lasers have small gain cross sections as compared to dye lasers and semiconductor lasers, gain modulation is ineffective for mode-locking.

[2]The quantum defect is the difference in energy of the pump photon and the laser emitting photon.

Material	Carrier lifetime T_1 (ps)	Mobility μ (cm^2/Vs)
Cr-doped GaAs	50-100	1000
Ion implanted InP	2-4	200
Ion-damaged Si-on-sapphire	0.6	30
Amorphous silicon	0.8-20	1
MOCVD CdTe	0.45	180
GaAs (MBE, 200^{o}C)	0.3	150
$In_{0.42}Al_{0.48}As$ (MBE, 150^{o}C)	0.4	5

Table 7.1: Semiconducting materials with carrier lifetimes and mobilities (from [69]).

With an upper state lifetime many orders of magnitude longer than the round-trip time, synchronous pumping is very seldom used [3].

The relatively low gain calls for longer lasing media, of the order of several mm, as opposed to the typical 100 μm used with dye and semiconductor lasers. The long gain crystal in turn favors large self-phase modulation. Therefore, mode-locking will most often occur through Kerr lensing and chirping in the gain medium. Some exception where saturable absorbers are used are

- Long pulse generation, tunable in wavelength.
- Mode-locking of LiCAF lasers, where the Kerr effect is very small.
- Bidirectional mode-locking of ring lasers (Kerr-lensing in the gain medium favors unidirectionality).

Also because of the longer gain medium, (as compared to dye and semiconductor lasers), the laser will be very sensitive to any parameter that influences the index of refraction. These are:

- Laser pulse intensity – an effect generally used for passive mode-locking (Kerr lensing).
- Temperature dependence of the index of refraction, which leads to thermal lensing and birefringence.
- Change in index of refraction associated with the change in polarizability of optically pumped active ions.

[3] Synchronous pumping has been used with some Ti:sapphire lasers to provide the modulation necessary to start the Kerr-lensing mode-locking, but not as a primary mode-locking mechanism.

The latter effect was investigated by Powell *et al.* [70] in Nd doped lasers, and found to be of the order of 50% of the thermal change in index.

Pumping of solid state lasers is done either by another laser (for instance argon ion laser, or frequency doubled vanadate (YVO4) laser, for Ti:sapphire) or by a semiconductor laser (Cr:LiSAF, Nd:vanadate) or by flashlamps (Nd:YAG). Diode laser pumping is the most advantageous from the point of view of wall-plug efficiency.

Mode-locked solid state lasers tend to specialize according to the property that is desired. So far Ti:sapphire lasers have been the choice for shortest pulse generation and stabilized frequency combs. Diode pumped Cr:LiSAF lasers can reach pulse durations in the tens of fs, and are the preferred laser when extremely low power consumption is desired. Nd:YAG lasers are most convenient for generating high power Q-switched mode-locked ps pulse trains, and are generally flashlamp pumped. Nd:vanadate is generally used as diode pumped Q-switched mode-locked source, although it is possible to achieve cw mode locked operation too. Both Nd:YAG and vanadate have a bandwidth that restricts their operation to a shortest pulse of approximately 10 ps. The laser with the lowest quantum defect is sought for high power application where efficiency is an issue. Yb:YAG can be pumped with 940 nm diode lasers, to emit at 1.05 micron. An optical to optical conversion efficiency of 35% has been obtained [71].

7.7.2 Ti:sapphire laser

The Ti:sapphire laser is the most popular source of fs pulses. The properties that make it one of the most attractive source of ultrashort pulses are listed in Table 7.2. Ti:sapphire is one of the materials with the largest gain bandwidth, excellent thermal and optical properties, and a reasonably large nonlinear index.

A typical configuration is sketched in Fig. 7.10. The pump laser is typically either a cw Ar ion laser or a frequency doubled Nd:vanadate laser. The operation of this laser is referred to as "self-mode-locked" [75]. The cavity configuration is usually linear, containing only the active element (the Ti:sapphire rod), mirrors and dispersive elements. The latter can be a pair of prisms (cf. Section 2.5.5), or negative dispersion mirrors (cf. Section 2.3.3), or other interferometric structures. Dispersion control by prisms [76] and by mirrors [77] led to the generation of pulses shorter than 12 fs in the early 90's. The output power typically can reach hundreds of mW at pump powers of less than 5 W. Sometimes, to start the pulse evolution and maintain a stable pulse regime, a saturable absorber, an acousto-optic modulator, a wobbling end mirror, or synchronous pumping is used.

The mode-locking mechanism most often used in the cavity of Fig. 7.10 is Kerr lens mode-locking. The cavity mode is adjusted in such a way that the lensing

Property	Value	Units	Reference
Index of refraction at 800 nm	1.76		[72]
Nonlinear index (electronic)	$10.5 \cdot 10^{-16}$	cm^2/W	[73]
Raman shift	419	cm^{-1}	[73]
Damping time T_R	6	ps	[73]
Raman contribution to $\tilde{n}_2$	$1.7 \cdot 10^{-17}$	cm^2/W	[73]
Raman shift	647	cm^{-1}	[73]
Damping time T_R	6	ps	[73]
Raman contribution to $\tilde{n}_2$	$0.8 \cdot 10^{-17}$	cm^2/W	[73]
Dispersion (k") at 800 nm	612	fs^2/cm	
Peak absorption at	500	nm	
σ_π	$6.5 \cdot 10^{-20}$	cm^2	[74]
σ_σ	$2.5 \cdot 10^{-20}$	cm^2	[74]
Number density of Ti^{3+}	$3.3 \cdot 10^{19}$	cm^{-3}	
at a concentration of	0.1	wt.% Ti_2O_3	
Peak gain at	795	nm	
σ_π	$5 \cdot 10^{-20}$	cm^2	[74]
σ_σ	$1.7 \cdot 10^{-20}$	cm^2	[74]
Fluorescence			
lifetime τ_F	3.15	μs	[74]
$d\tau_F/dT$	- 0.0265	$\mu s/^oK$	[74]

Table 7.2: Room temperature physical properties of Ti:sapphire. The gain cross-section increases with decreasing temperature, making it desirable to operate the laser rod at low temperatures. The values for the nonlinear index from ref. [73] take into account the conversion factor 4.61. Some data are given for σ (perpendicular to the optical axis) and π (parallel to the optical axis) polarization.

effect in the Ti:sapphire rod results in a better overlap with the pump beam, hence an increased gain for high peak power pulses (soft aperture). Another approach discussed in Section 6.4.3 and Appendix **??** is to insert an aperture in the cavity, at a location such that self-lensing results in reduced losses [increased transmission through the aperture (hard aperture)].

While Kerr-lensing in conjunction with a soft or a hard aperture initiates the amplitude modulation essential to start the mode-locking, the succession of self-phase modulation and quadratic dispersion is responsible for pulse compression. The prism pair provides a convenient means to tune the dispersion to an optimal value that will compensate the self-phase modulation, by translating the prism into the path of the beam, as shown in Fig. 7.10.

The shortest pulse duration that can be achieved is ultimately determined by

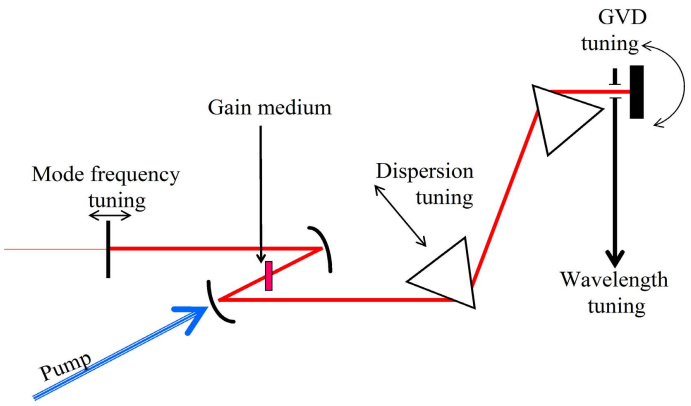

Figure 7.10: Typical Ti:sapphire laser cavity consisting (from the right) of an end mirror, an aperture, a prism pair, folding mirrors at both sides of the laser crystal, and an output coupler. The various controls that are possible on this laser are indicated.

higher order dispersion, which includes a contribution from the prism material, from the Ti:sapphire crystal, and the mirror coatings. To minimize the third order dispersion from the gain medium, short crystal lengths (2 to 4 mm) with the maximum doping compatible with an acceptable optical quality of the Ti:sapphire crystal are generally used. If the shortest pulses are desired, quartz prisms are generally preferred because of their low third order dispersion. However, since the second order dispersion of quartz is also small, the shortest pulse is compromised against a long round-trip time, since the intra-prism distance has to be large (> 1 m) to achieve negative dispersion. Another choice of prism material is LaK16, which has a sufficient second order dispersion to provide negative dispersion for distances of the order of 40 cm to 60 cm. Highly dispersive prisms such as SF10 or SF14 are used when a large number of dispersive intracavity elements has to be compensated with a large negative dispersion.

Several "control knobs" are indicated on the Ti:sapphire laser sketched in Fig. 7.10. After traversing the two prism sequence from left to right, the various wavelengths that constitute the pulse are displaced transversally before hitting the end mirror. An adjustable aperture located between the last prism and the end mirror can therefore be used either to narrow the pulse spectrum (hence elongate the pulse) or tune the central pulse wavelength. A small tilt of the end mirror — which can be performed with piezoelectric elements) — can by used to tune the group velocity (hence

the cavity round-trip time, or the "mode" spacing) without affecting the optical cavity length at the average pulse frequency (no translation of the "modes"). The position of the modes — in particular the mode at the average pulse frequency — can be controlled by translation of the of the end mirror with piezoelectric transducers. Such a motion also affects the repetition rate of the cavity. Ideally, orthogonal control of the repetition rate and mode position requires two linear combinations of the piezo controls just mentioned.

Cavities with chirped mirrors

Instead of intracavity prisms, negative dispersion mirrors are the preferred solution for the shortest pulses, provided a short Ti:sapphire rod is available, and there is no other dispersive intracavity element. Continuous tuning of the dispersion is not possible as was the case with the intracavity prism pair. Discrete tuning however is possible, through the number of multiple reflection at the dispersive mirrors. The minimum increment of dispersion is the dispersion upon single reflection of a coating.

As we have seen in Chapter 6, one of the applications of mode-locked lasers is to generate frequency combs for metrology. We will discuss such examples and the lasers applied in more detail in Chapter 14. For these applications it is desirable to have an octave spanning pulse spectrum, which implies pulses as short as 5 fs, or about 2 optical cycles [1]. This allows one to mix the second harmonic of the IR part of the mode comb with a mode from the short wavelength part of the spectrum - a technique to determine the carrier to envelope offset [78–81]. An example of such a 5-fs laser is sketched in Fig. 7.11. Mirrors with a smooth negative dispersion over the whole spectrum have been developed (see Section 2.3.3) and "double chirped mirrors" have been used for this laser [82]. Both the low and high index layers of these coatings are chirped. The spectral analysis of the reflectivity of these coatings still shows "phase ripples". To eliminate these ripples, the mirrors are used in pairs, manufactured in such a way that the ripples are 180 degrees out of phase.

Continuous dispersion tuning is achieved by the use of thin BaF_2 wedges. BaF_2 is the material with a low ratio of third- to second-order dispersion in the wavelength range from 600 to 1200 nm, and the slope of its dispersion is nearly identical to that of air. It is therefore possible to scale the cavity to, for instance, shorter dimensions, and maintain the same dispersion characteristics by adding the appropriate amount of BaF_2.

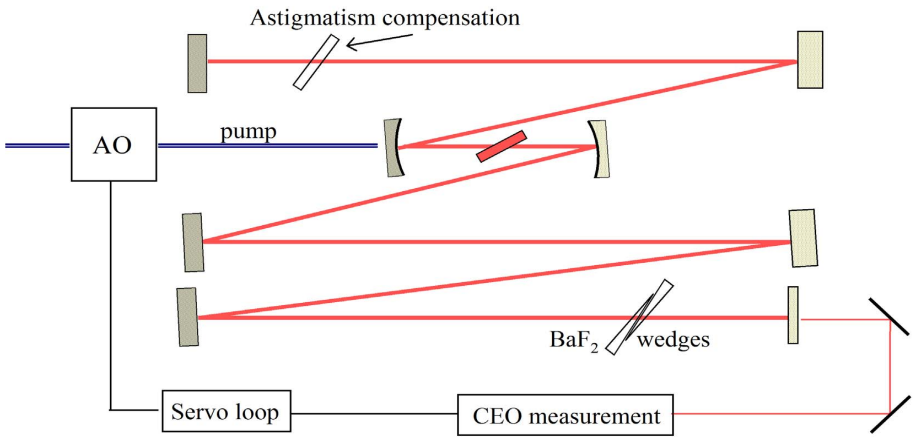

Figure 7.11: Ti:sapphire laser cavity with chirped mirrors for 5-fs pulse generation. Two wedges of BaF_2 are used for continuous dispersion control. The intracavity group velocity is tuned through the pump intensity. The servo loop takes the signal from the measurement of the CEO, and feeds it back to an acousto-optic modulator. Adapted from [1].

High power from oscillators

For some applications, for example laser micromachining, it is desirable to increase the pulse energy of the output of fs oscillators without amplification. Since the pump power is limited an increase in pulse energy can only be at the expense of repetition rate. Several different techniques have been developed.

A cavity dumper can be inserted in the Kerr-lens mode-locked Ti:sapphire laser resonator [83, 84]. This allows the fs pulse to build up in a high-Q cavity with essentially no outcoupling losses. When a certain energy is reached the outcoupler (typically based on an acousto-optic modulator) is turned on and the pulse is coupled out of the cavity. Repetition rates typically range from a few 100 kHz to a few MHz. Pulse energies of up to the 100-nJ level are possible.

Another method tries to capitalize on the inherent trend in solid-state lasers to show relaxation oscillations and self-Q switching. In such regimes the envelope of the modelocked pulse train is modulated. The Q-switched and modelocked output can be stabilized by (weakly) amplitude modulating the pump at a frequency of several hundred kHz that is derived from the Q-switched envelope in a feedback loop [85].

A third technique is based on long laser cavities (up to tens of meters) resulting in low repetition rates of a few MHz. Careful cavity and dispersion design are necessary to avoid the multiple pulse lasing and the instabilities that are usually associated with long cavities [86]. For example, 200-nJ, 30-fs pulses at a repetition

rate of 11 MHz were obtained with a chirped mirror cavity and external pulse compression with prisms [87].

7.7.3 Cr:LiSAF, Cr:LiGAF, Cr:LiSGAF and Alexandrite

The chromium ion has maintained its historical importance as a lasing medium. Ruby is produced by doping a sapphire host with Cr_2O_3. The ruby laser being a three level system, requires high pump intensities to reach population inversion. It is a high gain, narrow bandwidth, laser, hence not suited for ultrashort pulse applications.

A broadband lasing medium is alexandrite, consisting of chromium doped chrysoberyl ($BeAl_2O_4$:Cr^{3+}). The alexandrite laser is generally flashlamp pumped (absorption bands from 380 to 630 nm), with a gain bandwidth ranging from 700 to 820 nm, and is therefore sometimes used as an amplifier (mostly regenerative amplifier) for pulses from Ti:sapphire lasers. It is one of rare laser media in which the gain cross section increases with temperature, from $7 \cdot 10^{-21}$ cm^2 at 300°K to $2 \cdot 10^{-20}$ cm^2 at 475°K [72].

Of importance for femtosecond pulse generation are the Cr^{3+}:$LiSrAlF_6$ or Cr:LiSAF, Cr^{3+}:$LiSrGaF_6$ or Cr:LiSGAF and Cr^{3+}:$LiCaAlF_6$ or Cr:LiCAF lasers. These crystals have very similar properties as shown in Table 7.3. The gain cross section is relatively low compared with other diode pumped laser crystals (30× less than that of Nd:YAG for example). The thermal conductivity is 10× smaller than for Ti:sapphire. Therefore, very thin crystals are generally used for better cooling, which makes the mounting particularly delicate. The gain drops rapidly with temperature, because of increasing non-radiative decay. Stalder *et al.* [88] define a temperature $T_{1/2}$ at which the lifetime drops to half of the radiative decay time measured at low temperature. As shown in Table 7.3, this critical temperature is particularly low for Cr:LiSAF and Cr:LiSCAF (70°C) which, combined with their poor thermal conductivity, makes these crystals unsuitable for high power applications. Cr:LiCAF is preferred to the other two in applications such as regenerative amplifiers, because of its slightly larger saturation energy and better tolerance to a temperature increase.

The Cr^{3+}:$LiSrAlF_6$ is the most popular laser medium for low power, high efficiency operation. It is generally pumped by high brightness AlGaInP laser diodes. The emitting cross-section of a typical laser diode is rectangular, with a thickness of only a few micron, and a width equal to that of the diode. A "high brightness" diode is one for which the width does not exceed 200 μm. The shorter the diode stripe, the higher the brightness, and the lower the threshold for laser operation. Pump threshold powers as low as 2 mW [89] have been observed in diode pumped Cr^{3+}:$LiSrAlF_6$ lasers. Mode-locked operation with 75 fs pulses was achieved with

only 36 mW of pump power [90].

As can be seem from a comparison of Tables 7.2 and 7.3, the nonlinear index in LiSAF is significantly smaller than in Ti:sapphire. A very careful design of the cavity including astigmatism compensation is required in order to have tighter focusing in the LiSAF crystal, leading to the same Kerr lensing than in a typical Ti:sapphire laser [90]. A pair of BK7 prisms (prism separation 360 mm) was found to be optimal for second and third order dispersion compensation, leading to pulses as short as 12 fs (200 MHz repetition rate) for a Cr:LiSAF laser, pumped by two diode lasers of 500 mW and 350 mW output power [95]. The average output power of the fs laser was 6 mW. Diode laser technology is the limiting factor in reaching high output powers. Indeed, 70 mW and 100 mW powers (14 fs pulse duration) are easily obtained by Kr-ion laser pumping of LiSAF and LiGAF, respectively [96]. One solution to alleviate the drawback of a reduced brightness for higher power pump diodes, is to pump with a diode laser master oscillator power-amplifier system [97]. An output power of 50 mW was obtained with an absorbed pump power of 370 mW.

With chirped mirrors for dispersion compensation, the Cr:LiSAF laser should lend itself to very compact structures at high repetition rate, although most lasers were operated at less than 100 MHz [90–92, 96, 97]. The 12 fs Cr:LiSAF laser operating with a BK7 prism pair however had the shortest cavity, with a repetition rate of 200 MHz [95].

Because of the small nonlinear index $\bar{n}_2$, it is often more convenient to use a single quantum well to initiate and maintain the mode-locking. Mode-locking with saturable absorber quantum wells was discussed in Section 7.6.

7.7.4 Cr:Forsterite and Cr:Cunyite lasers

These two lasers use tetravalent chromium Cr^{4+} as a substitute for Si^{4+} in the host Mg_2SiO_4 (forsterite) [99, 100] and as a substitute for Ge in the host Ca_2GeO_4 (cunyite) [101, 102]. The properties of these two lasers are compared in Table 7.4. Forsterite based lasers have become important because they operate in the 1.3 μm range (1167 to 1345 nm), and can be pumped with Nd:YAG lasers. Attempts have also been made at diode pumping [103]. By careful intracavity dispersion compensation with a pair of SF58 prisms complemented by double chirped mirrors, a pulse duration of 14 fs was obtained [104]. This laser, pumped by a Nd:YAG laser, had a threshold of 800 mW for cw operation and 4 W for mode-locked operation. 100 mW output power could be achieved with a pump power of 6 W.

Property	Cr:LiSAF	Cr:LiSGAF	Cr:LiCAF	Units	Ref.
Sellmeir coeff.					
A_o	1.95823	1.95733	1.91850		
A_e	1.95784	1.95503	1.91408		
B_o	0.00253	0.00205	0.00113	μm^2	
B_e	0.00378	0.00252	0.00155	μm^2	
C_o	0.02671	0.03836	0.04553	μm^2	
C_e	0.01825	0.03413	0.04132	μm^2	
D_o	0.05155	0.04765	0.02525	μm^{-2}	
D_e	0.02768	0.03822	0.01566	μm^{-2}	
n_o (850 nm)	1.38730	1.38776	1.37910		
Nonlinear index	3.3 10^{-16}	3.3 10^{-16}	3.7 10^{-16}	cm^2/W	[73]
Dispersion k'' (850 nm, 0.8%)	210	280		fs^2/cm	[91,92]
Dispersion k'' (850 nm, 2%)	250			fs^2/cm	[91]
3^{rd} order dispersion k'''	1850	1540		fs^3/cm	[91,92]
Peak absorption	670	630		nm	
Peak gain at	850	835	763	nm	
cross section σ_π	4.8 10^{-20}	3.3 10^{-20}	1.3 10^{-20}	cm^2	[93]
Fluorescence τ_F (300^{o}K	67	88	170	μs	[93]
$T_{1/2}$	69	75	255	^{o}C	[88]
Expansion coeff. along c-axis	-10	0	3.6	10^{-6}/K	[93]
along a-axis	25	12	22	10^{-6}/K	[93]
c-axis thermal conductivity	3.3	3.6	5.14	W/mK	[94]
Thermal index dependence dn/dT	-4.0		-4.6	10^{-6}/K	[94]

Table 7.3: Room temperature physical properties of Cr:LiSAF, Cr:LiSGAF, and Cr:LiGAF. The second order dispersion of LiSAF is indicated for two different Cr doping concentrations. A, B, C and D are the parameters of the Sellmeir formula $n_i^2 = A_i + B_i/(\lambda_\ell^2 - C_i) - D_i\lambda_\ell^2$. with $i = o$ (ordinary) or e (extraordinary), and λ_ℓ expressed in μm.

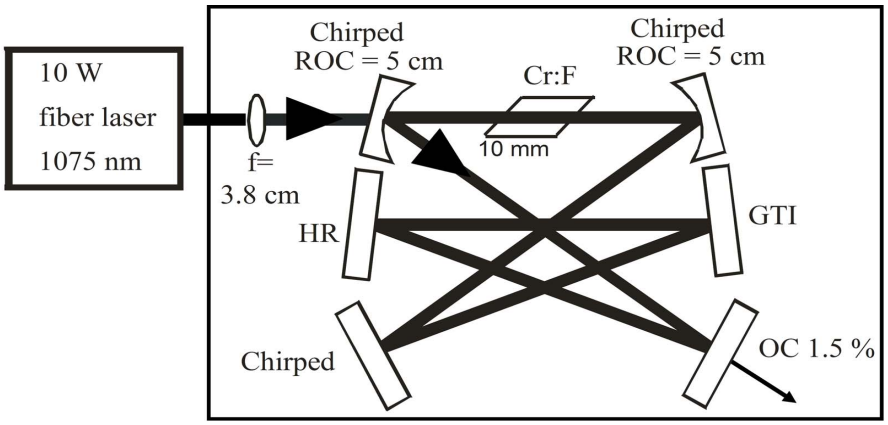

Figure 7.12: Compact ring cavity of a Cr:forsterite laser used in conjunction with HNLF fibers to generate an octave spanning continuum in the near IR (from ref. [98]. The curved mirrors of 5 cm radius of curvature as well as the first folding mirror (HR) have chirped multilayer coatings. The second folding mirror is a Gires-Tournois Interferometer (GTI), the third one a standard high reflector, and the output coupler has a transmission of 1.5%.

Property	$Cr:Mg_2SiO_4$	$Cr:Ca_2GeO_4$	Units	Ref.
Nonlinear index	$2\ 10^{-16}$	$1.5\ 10^{-16}$	cm^2/W	[72, 105]
Dispersion k" at (1280 nm)	185		fs^2/cm	[106]
Peak absorption at	670		nm	
Peak gain (1240 nm)	14.4	80	$10^{-20}cm^2$	[72]
Fluorescence lifetime				[101]
τ_F	2.7	15	μs	[102, 107]
Tuning range from	1167	1350	nm	[72]
to	1345	1500	nm	
Thermal conductivity		0.03	W/cm/K	

Table 7.4: Room temperature physical properties of Cr:Forsterite and Cr:Cunyite lasers.

The forsterite laser produces pulses short enough to create an octave spanning spectral broadening in fibers as discussed in Section 14.4.1[4].. A prismless compact ring cavity was designed with combination of chirped mirrors (GDD of -55 fs^2 from 1200 to 1415 nm) and Gires-Tournois interferometer mirrors (GDD of - 280 fs^2 from 1200 to 1325 nm) as sketched in Fig. 7.12. This laser, pumped by a 10 W fiber laser, combined short pulse output (28 fs) with a high repetition rate of 420 MHz [98].

[4]Germanium-doped silica fiber with a small effective area of 14 μm^2, nonlinear coefficient of 8.5 $W^{-1}km^{-1}$, zero dispersion near 1550 nm.

7.7.5 YAG lasers

The crystal $Y_3Al_5O_{12}$ or YAG is transparent from 300 nm to beyond 4 μm, optically isotropic, with a cubic lattice structure characteristic of garnets. It is one of the preferred laser hosts because of its good optical quality and high thermal conductivity. Some of the physical/optical properties are listed in Table 7.5. The two most important lasers using YAG as a host are Nd:YAG and Yb:YAG.

Property	YAG	Units
Index of refraction 1.064 μm	1.8169	
Index of refraction 1.030 μm	1.8173	
Dispersion (k'') at 1.064 μm	733	fs^2/cm
Dispersion (k'') at 1.030 μm	760	fs^2/cm
Nonlinear index	12.4	10^{-16} cm^2/W
Thermal expansion		
[100]	8.2	10^{-6} K^{-1}
[110]	7.7	10^{-6} K^{-1}
[111]	7.8	10^{-6} K^{-1}
Thermal Conductivity	0.129	W cm^{-1} K^{-1}
dn/dT	8.9	10^{-6} K^{-1}

Table 7.5: Room temperature physical properties of YAG. The second order dispersion is calculated from the derivative of the Sellmeier equation:
$n^2 = 1 + 2.2779\lambda_\ell^2/(\lambda_\ell^2 - 0.01142)$ with λ_ℓ in μm. The data are compiled from [70, 72, 106, 108–110].

Nd:YAG

Typical doping concentrations of the Nd^{3+} ion (substitution of Y^{3+}) range from 0.2 to 1.4% (atomic). Larger doping degrades the optical quality of the crystal. Nd:YAG has been the workhorse industrial laser for several decades, because of its relatively high gain and broad absorption bands that makes it suitable for flashlamp pumping. It has a UV absorption band from 300 to 400 nm and absorption lines between 500 and 600 nm. It has also an absorption band at 808.6 nm which coincides with the emission of GaAlAs diode lasers. Being a four level laser, Nd:YAG does not require as high a pump power to create an inversion as, for instance, the 3 level ruby laser or the Yb:YAG laser. The high gain is partly due to the narrow bandwidth of the fluorescence spectrum, limiting pulse durations to > 10 ps. Despite this limitation, Nd:YAG has still a place as a source of intense femtosecond pulses. Intracavity pulse compression by passive negative feedback (Section 7.5) yields mJ pulses as short as 8 ps directly from the oscillator [63, 64]. Efficient conversion

to the femtosecond range has been achieved either by harmonic generation [111] or parametric oscillation [112, 113]. The fundamentals of pulse compression associated with harmonic and parametric processes can be found in Section 4.3.2 and 4.4.

Yb:YAG

Yb:YAG is a popular crystal for high average power, subpicosecond pulse generation. Up to ten atomic percent of doping of the YAG crystal by Yb have been used. Table 7.6 compares some essential parameters of Nd:YAG and Yb:YAG. The main difference between the two crystals is that Yb:YAG is a quasi three level system, requiring large pump powers to reach an inversion. It does not have the broad absorption bands of Nd:YAG that would make it suitable for flashlamp pumping. The main advantage of Yb:YAG however is the very small quantum defect, when pumped with InGaAs diode lasers at 942 nm. A small quantum defect implies that a minimum amount of energy is dissipated in the crystal in the form of heat.

The combination of diode pumping (high wall-plug efficiency), broad bandwidth and small quantum defect has spurred the development of short pulse, high average power Yb:YAG sources. The main problem to be overcome in developing high average output power sources is the removal of the heat produced by pump intensities of the order of tens of kW/cm^2. Two solutions have been implemented, which led to pulse sources at 1.03 μm, subpicosecond pulse duration, and several tens of watts of average power:

1. A thin disk Yb:YAG laser [114]

2. Laser rods with undoped endcaps

The undoped endcaps allow for symmetrical heat extraction on either side of the beam waist. Typical average powers are between 20 and 30 W [71, 115]. Quantum wells are generally used for mode-locking, with the exception of a 21 W, 124 MHz repetition laser using a variation of additive pulse mode-locking [71] (cf. Section 7.3).

In a thin-disk laser, the laser material has a thickness much smaller than the diameter of the pump and laser mode. One end face of the disk is coated for high reflectivity, and put in direct contact with a heat sink. The resulting heat flow is longitudinal and nearly one-dimensional. Typical disks are 100 μm thick, for 10% doping with Yb. An average power of 60 W, for 810 fs pulses at a repetition rate of 34 MHz has been obtained [116].

Property	Nd:YAG	Yb:YAG	Units
Lasing wavelength	1064.1	1030	nm
Doping density (1% at.)	1.38	1.38	10^{20} atoms/cm^3
Diode pump band	808.6	942	nm
Absorption bandwidth	2.5	18	nm
Emission cross section	28	2.1	10^{-20}cm^2
Emission bandwidth	0.45	≈ 8	nm
Fluoresc. lifetime τ_F	230	951	μs

Table 7.6: Comparison of Nd:YAG and Yb:YAG (data from [72, 117]).

7.7.6 Nd:YVO_4 and Nd:YLF

Both neodymium doped lithium yttrium fluoride (YLF) and vanadate (YVO_4) have gained importance as diode pumped lasers. The emission bandwidth is only slightly larger than that of Nd:YAG, hence the shortest pulse durations that are possible with these lasers are in the range of a few picoseconds (3 ps [118] to 5 ps [119] have been reported). The absorption bandwidth of Nd:vanadate is roughly 18 nm, as opposed to 2.5 nm for Nd:YAG, making it a preferred crystal for diode pumping.

Nd:YLF, like Alexandrite, is a long lifetime medium (twice as long as Nd:YAG), hence an ideal storage medium for regenerative amplifiers. Its natural birefringence overwhelms the thermal induced birefringence, eliminating the depolarization problems of optically isotropic hosts like YAG. For example, a 15 W cw diode array was used to pump a Nd:YLF regenerative amplifier, amplifying at 1 kHz 15 ps, 20 pJ pulses to 0.5 mJ [120].

The main parameters of Nd:YLF and Nd:YVO_4 are summarized in Table 7.7.

7.8 Semiconductor and dye lasers

One of the main advantages of semiconductor and dye lasers, is that they can be engineered to cover various regions of the spectrum. As opposed to the solid state lasers of the previous sections, the semiconductor and dye lasers are characterized by a very high gain cross section, which implies also a short upper state lifetime, typically shorter than the cavity round-trip time. Consequently, mode-locking through gain modulation can be effective.

Property	$Nd:YVO_4$	Nd:YLF	Units
Lasing wavelength	1064.3	1053 (σ)	nm
		1047 (π)	nm
Index of refraction		1.4481 (n_o)	
		1.4704 (n_e)	
Absorption (1% doping)			
σ	9		cm^{-1}
at	809	806	nm
π	31	4.5	cm^{-1}
at	809	797	nm
Absorption bandwidth	15.7		nm
Emission cross section	15		
σ	21	12	$10^{-20}cm^2$
π	76	18	$10^{-20}cm^2$
Gain Bandwidth	0.96	1.3	nm
Fluorescence lifetime τ_F	90	480	μs
Thermal conductivity	0.05	0.06	W cm^{-1} K^{-1}
thermal expansion in σ	8.5	-2	10^{-6} K^{-1}
thermal expansion in π	3	-4.3	10^{-6} K^{-1}

Table 7.7: Properties of $Nd:YVO_4$ and Nd:YLF (data from [72, 117]). Parameters are listed for the radiation polarized parallel (π) or orthogonal (σ) to the optical axis of the crystal.

7.8.1 Dye lasers

Over the past fifteen years fs dye lasers have been replaced by solid-state and fiber lasers. It was, however, the dye laser that started the revolution of sub 100 fs laser science and technology. In 1981 Fork et al. [121] introduced the colliding pulse modelocked (CPM) dye laser that produced sub 100-fs pulses.

In this dye laser, the ring configuration allows two counterpropagating trains of pulses to evolve in the cavity [121] [5]. The gain medium is an organic dye in solution (for instance, Rh 6G in ethylene glycol), which, pumped through a nozzle, forms a thin ($\approx$100 μm) jet stream. Another flowing dye (for instance, diethyloxadicarbocyanine iodide, or DODCI, in ethylene glycol) acts as saturable absorber. The two counter-propagating pulses meet in the saturable absorber (this is the configuration of minimum losses).

[5] The same ring configuration is sometimes used with a Ti:sapphire gain medium, when a bidirectional mode of operation is sought.

A prism sequence (one, two, or four prisms) allows for the tuning of the resonator group velocity dispersion. The pulse wavelength is determined by the spectral profiles of the gain and absorber dyes. Limited tuning is achieved by changing the dye concentration. Pulses shorter than 25 fs have been observed at output powers generally not exceeding 10 mW with continuous (cw) pumping [122], and up to 60 mW with a pulsed (mode-locked argon laser) pump [123].

The palette of available organic dyes made it possible to cover practically all the visible to infrared with tunable and mode-locked sources. A table of gain-absorber dye combinations used for passively mode-locked lasers can be found in ref. [124]. Hybrid mode-locking of dye lasers has extended the palette of wavelength hitherto available through passive mode-locking, making it possible to cover a broad spectral range spanning from covering the visible from the UV to the near infrared. A list of dye combinations for hybrid-mode-locking is given in Table 7.8. Except when noted, the laser cavity is linear, with the absorber and the gain media at opposite ends. Another frequently used configuration is noted "anti-resonant ring". The saturable absorber jet is located near the pulse crossing point of a small auxiliary cavity, in which the main pulse is split into two halves, which are recombined in a standing wave configuration in the absorber [16,125]. The ring laser appears only once in Table 7.8 [126], because of the difficulty of adjusting the cavity length independently of all other parameters.

Dye lasers have been particularly successful in the visible part of the spectrum, where virtually all wavelengths have been covered. The advantage of using an organic dye in a viscous solvent is that the flowing dye jet allows for extremely high pump power densities — in excess of 10 MW/cm^2 — to be concentrated on the gain spot. The disadvantage of the dye laser lies also in the inconvenience associated with a circulating liquid system. One alternative for the liquid dye laser that conserves most of its characteristics is the dye-doped, polymer-nanoparticle gain medium. Significant progress has been made in developing a material with excellent optical quality [127, 128]. These laser media have yet to be applied as a femtosecond source.

Miniature dye lasers

The long (compared to the geometrical length of a fs pulse) cavity of most modelocked lasers serves an essential purpose when a sequence of pulses — rather than a single pulse — is needed. Emission of a short pulse by the long resonator laser requires — as we have seen at the beginning of the previous chapter — a coherent superposition of the oscillating cavity modes with fixed phase relation. If, however, only a single pulse is needed, there is no need for more than one longitudinal mode within the gain profile. Ultrashort pulses are generated in small cavity

Gain dye	Absorber[a]	λ_ℓ nm	range	τ_{pmin} fs	at λ_ℓ nm	Remarks
Disodium fluorescein	RhB	535	575	450	545	
Rh 110	RhB	545	585	250	560	
Rh6G	DODCI	574	611	300	603	
Rh6G	DODCI			110	620	Ring laser
Rh6G	DODCI			60	620	ANR ring
Kiton red S	DQOCI			29	615	
Rh B	Oxazine 720	616	658	190	650	
SRh101	DQTCI	652	682	55	675	Doubled
	DCCI	652	694	240	650	Nd:YAG p
Pyridine 1 [b]	DDI			103	695	
Rhodamine 700	DOTCI	710	718	470	713	
Pyridine 2	DDI,DOTCI			263	733	
Rhodamine 700	HITCI	770	781	550	776	
LDS-751	HITCI	790	810	100		
Styryl 8	HITCI		70	800		
Styryl 9 [b]	IR 140 [c]	840	880	65	865	Ring laser
Styryl 14	DaQTeC			228	974	

Table 7.8: Femtosecond pulse generation by hybrid mode-locking of dye lasers pumped by an argon ion laser, except as indicated (from [124]). (ANR - antiresonant, p - pump laser)
[a] See Appendix D for abbreviations.
[b] Solvent: propylene carbonate and ethylene glycol.
[c] in benzylalcohol.

lasers through resonator Q-switching and/or gain switching. Aside from gain bandwidth limitations, the pulse duration is set by the spectral width of the longitudinal mode, and hence the resonator lifetime. The latter in turn is limited by the resonator round trip time $2L/c$. Ideally, the laser cavity should have a free spectral range $c/2L$ exceeding the gain bandwidth.

Two methods of short pulse generation that use either ultrashort cavities (Fabry–Perot dye cells of thickness in the micron range) or no traditional cavity at all (distributed feedback lasers) have successfully been developed for (but are not limited to) dye lasers.

In distributed feedback lasers two pump beams create a spatially modulated excitation that acts as a Bragg grating. This grating serves as the feedback (resonator) of the laser and is destroyed during the pulse evolution. This short cavity lifetime

together with the small spatial extend of the gain volume can produce subps pulses whose frequency can be tuned by varying the grating period [129, 130]. The latter is determined by the overlap angle of the two pump beams.

In a typical "short cavity" laser [131], the wavelength is tuned by adjusting the thickness of the dye cell in a 3 to 5 μm range with a transducer bending slightly the back mirror of the cavity. With a round-trip time of the order of only 10 fs, it is obvious that the pulse duration will not be longer than that of a ps pump pulse. As with the distributed feedback laser, the dynamics of pump depletion can result in pulses considerably shorter than the pump pulses. The basic operational principles of this laser can be found in [132]. Technical details are given in [131]. For example, using an excimer laser, Szatmari and Schäfer [130] produced 500 fs pulses, tunable from 400 to 760 nm, in a cascade of distributed feedback and short cavity dye lasers. After self-phase modulation and recompression, pulses as short as 30 fs in a spectral range from 425 to 650 nm were obtained [133].

Another type of miniature laser is the integrated circuit semiconductor laser, which will be described in the next section.

7.8.2 Semiconductor lasers

Generalities

Semiconductor lasers are obvious candidates for fs pulse generation, because of their large bandwidth. A lower limit estimate for the bandwidth of a diode laser is $k_B T$ (where k_B is the Boltzmann constant and T the temperature), which at room temperature is (1/40) eV, corresponding to a 15 nm bandwidth at 850 nm, or a minimum pulse duration of 50 fs. The main advantage of semiconductor lasers is that they can be directly electrically pumped. In the conventional diode laser, the gain medium is a narrow inverted region of a p–n junction. We refer to a publication of Vasil'ev [134] for a detailed tutorial review on short pulse generation with diode lasers. We will mainly concentrate here on problems associated with fs pulse generation in external and internal cavity (integrated) semiconductor lasers. The main technical challenges associated with laser diodes result from the small cross-section of the active region (typically 1 μm by tens of μm), the large index of refraction of the material ($2.5 < n < 3.5$, typically) and the large nonlinearities of semiconductors.

The cleaved facets of a laser diode form a Fabry–Perot resonator with a mode spacing of the order of 1.5 THz. Two options are thus conceivable for the development of fs lasers: integrate the diode with a waveguide in the semiconductor, to construct fs lasers of THz repetition rates, or attempt to "neutralize" the Fabry–Perot effect of the chip, and couple the gain medium to an external cavity. We will

consider first the latter approach.

External cavity

Because of the high refractive index of the semiconductor, it is difficult to eliminate the Fabry–Perot resonances of the short resonator made by the cleaved facets of the crystal. Antireflection coatings have to be of exceptionally high quality. Even though reflectivities as low as 10^{-4} can be achieved, a good quality antireflection coating with a high optical damage threshold remains a technical challenge. A solution to this problem is the angled-stripe semiconductor laser [135], which has the gain channel making an angle of typically 5^{o} with the normal to the facets (Fig. 7.13). Because of that angle, the Fabry–Perot resonance of the crystal can easily be decoupled from that of the external cavity. A standard antireflection coating applied to the semiconductor chip is sufficient to operate the laser with an external cavity.

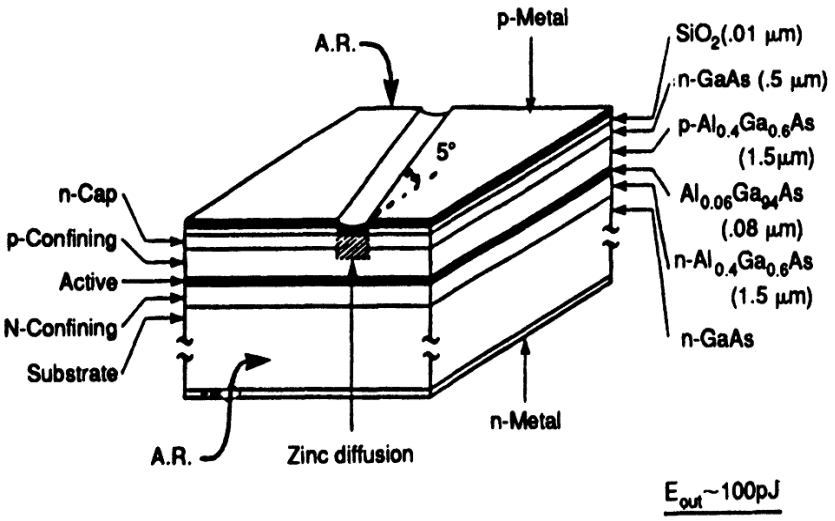

Figure 7.13: Structure of an angled stripe semiconductor laser (from [135]).

Femtosecond pulse operation in a semiconductor laser with an external cavity is similar to that of a dye laser. The laser can be cw pumped, as in ref. [136]. Best results so far were obtained in hybrid operation, using radio-frequency current modulation for gain modulation (synchronous pumping), and a saturable absorber. The low intracavity power of the external cavity semiconductor laser — as compared to the dye laser — makes the use of conventional saturable absorbers (i.e.,

dyes, bulk semiconductors) impractical. It has been necessary to develop absorbing structures with a very low saturation energy density. These are the multiple quantum well (MQW) absorbers, which were analyzed in Section 7.6. The laser diode is modulated at the cavity round-trip frequency (0.5 W RF power applied via a bias tee [68]). Modulation of the index of refraction is associated with the gain depletion and the saturation of the MQW. Since the gain depletion results in an increase of the index, a negative dispersion line appears appropriate. Bandwidth limited operation is difficult to achieve directly from a mode-locked semiconductor laser. An external dispersion line with gratings resulted in pulse durations of 200 fs [137].

The exact phase modulation mechanism of this laser is complex. The index of refraction of the diode is a function of temperature and free carrier density, which itself is a function of current, bias, light intensity, etc.. As with other high-gain solid state lasers, changes in the pulse parameters can be as large as 50% from one element to the next [68].

Current modulation To take full advantage of the fast lifetime of the gain in a semiconductor laser, one should have a circuit that drives ultrashort current pulses into the diode. As mentioned above, a feedback technique — generally referred to as "regenerative feedback" — can be used to produce a sine wave driving current exactly at the cavity repetition rate. The circuit consists essentially in a phase locked loop, synchronized by the signal of a photodiode monitoring the mode beat note of the laser, and a passive filter at the cavity round-trip frequency. A comb generator can be used to transform the sine wave in a train of short electrical pulses. A comb generator is a passive device which produces, in the frequency domain, a "comb" of higher harmonics which are integral multiples of the input frequency. As we had seen in the introduction of Chapter 6, to a regular frequency comb corresponds a periodic signal in the time domain. This periodic signal can correspond to ultrashort pulses, if — and only if — the teeth of the comb are in phase. Commercial comb generators are generally constructed to create higher harmonics, without being optimized for creating a phased comb. Therefore a selection should be made among these devices to find a generator with good temporal properties (shortest pulse generation).

To allow for the injection of a short current pulse into the laser diode, the latter should be designed with minimal capacitance. To this effect, the p and n contacts of the angle striped diode of Fig. 7.13 should not cover the whole area of the strip, but be limited to a narrow stripe which follows the gain line.

Integrated devices

Instead of trying to couple the semiconductor chip to a standard laser cavity, one can integrate the semiconductor into a waveguide cavity. Such devices ranging in length from 0.25 mm to 2 mm have been constructed and demonstrated for example by Chen et al. [138]. The end mirrors of the cavity are — as in a conventional diode laser — the cleaved faces of the crystal (InP) used as substrate. Waveguiding is provided by graded index confining InGaAsP layers. Gain and saturable absorber media consist of multiple quantum wells of InGaAs. The amount of gain and saturable absorption is controlled by the current flowing through these parts of the device (reverse bias for the absorber). As shown in the sketch of Fig. 7.14, the saturable absorber is located at the center of symmetry of the device, sandwiched between two gain regions. This configuration is analogous to that of the ring dye laser, in which the two counterpropagating pulses meet coherently in the absorber jet. In the case of this symmetric linear cavity, the laser operation of minimum losses will correspond to two circulating pulses overlapping as standing waves in the saturable absorber.

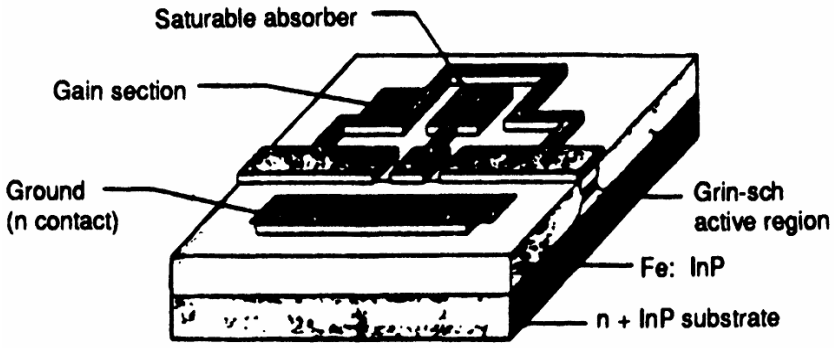

Figure 7.14: Layout of an integrated semiconductor fs laser (from [138]).

These devices are pumped continuously and are thus the solid-state equivalent of the passively mode-locked dye lasers. The laser parameters can, however, be significantly different. While the average output power is only slightly inferior to that of a dye laser (1 mW), at the much higher repetition rate (up to 350 GHz), the pulse energy is only in the fW range! For these ultrashort cavity lengths, there are only a handful of modes sustained by the gain bandwidth.

Semi-integrated circuit fs lasers

Total integration as shown above results in a very high duty cycle, at the expense of a lower energy per pulse. On can seek a compromise between the discrete elements semiconductor laser and the total integrated laser. For instance, the integration of the gain and saturable absorber of the integrated laser of Chen et al. [138] can be maintained in a single element coupled to an external cavity. Such a design has been successfully tested by Lin and Tang [139]. The absorber consists of a 10 μm island in middle of the gain region, with an electrical contact, isolated from the gain structure by two 10 μm shallow etched regions (without any electrical contact). The absorption — as in the case of the totally integrated laser — can be controlled through the bias potential of the central contact. To prevent lasing action of the 330 μm long gain module, the end facets — after cleavage — are etched (chemically assisted ion beam etching) at 10^{o} from the cleaved plane. The autocorrelation of the laser pulses from such a structure had a width of approximately 700 fs [139].

7.9 Fiber lasers

7.9.1 Introduction

In most lasers discussed so far, the radiation is a free propagating wave in the gain or other elements of the cavity. The gain length is limited by the volume that can be pumped. The length of a nonlinear interaction is also limited by the Rayleigh range (ρ_0). By confining the wave in a waveguide, it is possible to have arbitrarily long gain media, and nonlinear effects over arbitrarily long distances. A fiber is an ideal waveguide for this purpose. Its losses can be as small as a few dB/km. Yet the pulse confinement is such that substantial phase modulation can be achieved over distances ranging from cm to m. The fiber is particularly attractive in the wavelength range of negative dispersion (beyond 1.3 μm), since the combination of phase modulation and dispersion can lead to pulse (soliton) compression (see Chapter 9). The gain can be provided by Stimulated Raman Scattering (SRS) in the fiber material, Such "Raman soliton lasers" are reviewed in the next subsection. In the following subsection, we will consider the case of doped fibers, where the gain medium is of the same type as in conventional glass lasers.

Over the past twenty years ultrafast fiber lasers have matured dramatically. Compact, turn key systems are available commercially today and can deliver tens of mW of average power at pulse durations of the order of 100 fs. With amplification the micro Joule level is accessible. These lasers have applications as self-standing units or as compact seed sources for high-power fs amplifier systems.

7.9.2 Raman soliton fiber lasers

Stimulated Raman scattering (SRS) is associated with intense pulse propagation in optical fibers. A review of this topic can be found in [140] for example. The broad Raman gain profile for the Stokes pulse extends up to the frequency of the pump pulse. An overlap region exists because of the broad pump pulse spectrum. The lower frequency components of the pulse can experience gain at the expense of attenuation of the higher frequency components. In addition, the amplification of spontaneously scattered light is possible. Either process leads to the formation of a Stokes pulse which separates from the pump pulse after the walk-off distance due to GVD. These processes can be utilized for femtosecond Raman soliton generation in fibers, and fiber lasers [141–143]. An implementation of this idea is shown in Fig. 7.15. The pulses from a cw modelocked Nd:YAG laser (100 MHz, 100 ps, 1.32 μm) are coupled through a beam splitter BS into a ring laser containing an optical fiber. The fiber was tailored to have a negative dispersion for $\lambda_\ell > 1.46\,\mu$m. While travelling through the fiber the pump pulses at 1.319 μm produce Stokes pulses at $\lambda_1 = 1.41\,\mu$m. This first Stokes pulse in turn can act as pump source for the generation of a second Stokes pulse ($\lambda_2 = 1.495\,\mu$m), which is in the dispersion region that enables soliton formation. Of course, for efficient synchronous pumping, the length of the ring laser had to be matched to the repetition rate of the pump. Second Stokes pulses as short as 200 fs were obtained.

7.9.3 Doped fiber lasers

Fibers can be doped with any of the rare earth ions used for glass lasers. Whether pumped through the fiber end, or transversely, these amplifying media can have an exceptionally large optical thickness ($a_g = \alpha_g d_g \gg 1$). An initial demonstration of this device was made by Duling [144,145]. Passively mode locked rare earth doped fiber lasers have since evolved into compact, convenient, and reliable sources of pulses shorter than 100 fs. The gain media generally used are Nd^{3+} operating at 1050 nm and Er^{3+} at 1550 nm. The erbium doped fiber is sometimes co-doped with ytterbium, because of the broad absorption band of the latter centered at $\approx$ 980 nm and extending well beyond 1000 nm. Pump light at 1.06 μm can be absorbed by ytterbium, which then transfers the absorbed energy to the Er ions. Very high gain and signal powers can thus be obtained by using, for example, diode laser pumped miniature Nd:YAG lasers.

Because of the high gain in a typical fiber laser, it may include bulk optic components, e.g., mirror cavities, dispersion compensating prisms, or saturable absorbers. Obviously, the preferred configuration is that of an all-fiber laser, using a variety of pigtailed optical components and fused tapered couplers for output and

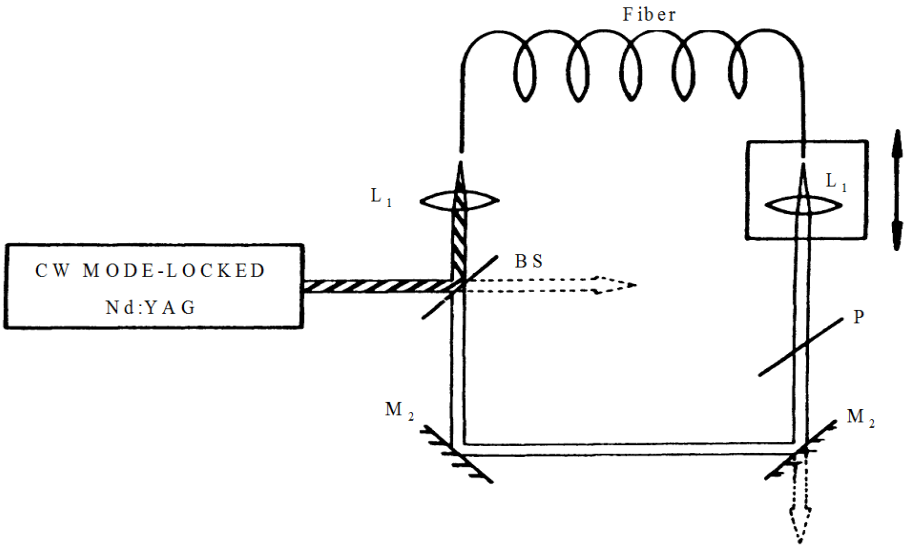

Figure 7.15: Experimental configuration of a synchronously pumped fiber ring Raman laser (from [143]).

pumping.

As compared to conventional solid state lasers, fibers have the advantage of a very large surface to volume ratio (hence efficient cooling is possible). The specific advantages of the single mode fiber geometry over bulk solid state (rare earth) media for mode locking are:

- Efficient conversion of the pump to the signal wavelength. Erbium, for example, is a three-level system and the tight mode confinement of the pump in a fiber allows for efficient depopulation of the ground state and thus high efficiency.

- Nonradiative ion–ion transitions which deplete the upper laser level are minimized. Such interactions are especially egregious in silica because of its high phonon energy and because the trivalent dopants do not mix well into the tetravalent silica matrix, tending instead to form strongly interacting clusters at the high concentrations necessary for practical bulk glass lasers [146]. The confinement of both the laser and pump modes allows the gain dopant to be distributed along greater lengths of fiber at lower concentration, obviating the need for high concentrations and so eliminating the interactions cited above.

- Diode laser pumping is practicable (due in large part to the previous two points). Single-mode laser diodes have been developed at 980 nm and 1480 nm for erbium fiber amplifiers in telecommunications applications. The four-level structure of neodymium allows for pumping even by multimode lasers, such as high-power laser diode arrays, by using fibers designed to guide the pump light in the cladding [147].

- Tight mode confinement and long propagation lengths maximize the self-phase modulation by the weak nonlinear index of silica ($\bar{n}_2 = 3\ 10^{-16}$ cm^2/W).

- The dispersion k" of fibers (including the sign) can be tailored to the application.

One drawback of the fiber laser is that the confinement limits the pulse energies that can be produced. In bulk solid state lasers, the problem of material damage can be overcome by beam expansion.

A number of techniques have been developed to mode-lock fiber lasers. The most successful methods are:

1. nonlinear polarization rotation [148].

2. nonlinear loop mirrors [149];

3. mode-locking with semiconductor saturable absorbers [150].

Femtosecond pulse output with durations of 100 fs and below has been observed with a variety of gain media – Nd, Yb, Er, Er/Yb, Pr, and Tm. For a detailed overview on such lasers we refer the reader to a review paper by Fermann *et al.* [151].

7.9.4 Mode-locking through polarization rotation

Because of its central importance in today's fs fiber lasers we will describe one of the mode-locking techniques - nonlinear polarization rotation - in more detail. As explained in Section 6.4.2 nonlinear polarization rotation in combination with polarizers can act as a fast saturable absorber, cf. Eq. (6.81). In a fiber laser using nonlinear polarization rotation, the differential accumulated phase yields an intensity dependent state of polarization across the pulse. This polarization state is then converted into an intensity dependent transmission by inserting a polarizer at the output of the birefringent element, oriented, for example, to transmit the high intensity central portion of the pulse and reject the wings. This approach is the fiber equivalent of the Kerr-lens mode-locked Ti:sapphire laser. Pulses as short as 36 fs have been obtained from an Yb fiber laser that used nonlinear polarization rotation [152], to name just one example.

A standard single mode fiber serves as nonlinear element. Such a fiber has generally a weak birefringence. The degree of birefringence is defined by the parameter:

$$B = \frac{|k_x - k_y|}{2\pi/\lambda_\ell} = |n_x - n_y|, \tag{7.9}$$

where n_x and n_y are the effective refractive indices in the two orthogonal polarization states. For a given value of B, the power between the two modes (field components along $\hat{x}$ and $\hat{y}$) is exchanged periodically, with a period L_B called the "beat length" given by [153]:

$$L_B = \frac{\lambda_\ell}{B}. \tag{7.10}$$

The axis with the larger mode index is called the slow axis. In a typical single mode fiber, the beat length is around 2 to 10 m at 1.55 μm [154]. As shown by Winful [155], nonlinear polarization effects can be observed at reasonably low power in weakly birefringent fibers (as opposed to polarization preserving fibers).

In a typical fiber ring cavity a first polarization controller produces an elliptical polarization whose major axis makes a small angle θ with the slow axis of the portion of fiber that follows. As shown in Section 6.4.2 the induced phase difference between two orthogonal polarization components depends on the propagation distance d and the pulse intensity. It can be adjusted such that after a distance d_m the polarization becomes linear. A polarizer can be used to maximize the loss for the lower intensities as compared to the higher intensities, as sketched in Fig. 7.16.

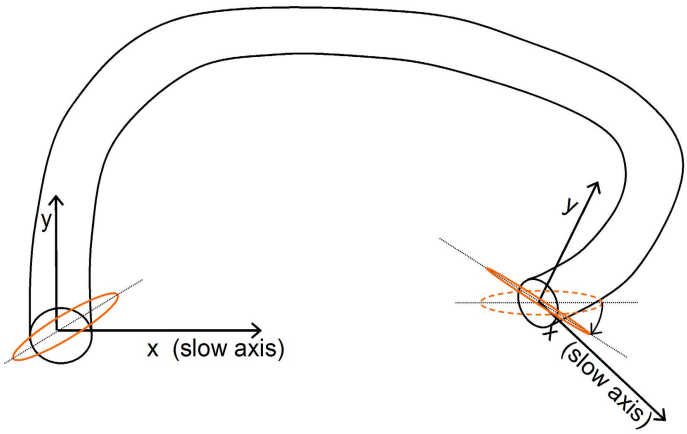

Figure 7.16: Sketch of the nonlinear polarization rotation in a fiber. The elliptically polarized input can be converted into linearly polarized light at the peak of the pulse for example.

We have derived in Section 6.4.2 the essential equations relating to nonlinear

polarization rotation. To describe a fiber laser we need to track the evolution of two polarization components. This can conveniently be done using a column vector for the electric field at a certain point in the cavity

$$\begin{pmatrix} \tilde{\mathcal{E}}_x \\ \tilde{\mathcal{E}}_y \end{pmatrix}, \tag{7.11}$$

and 2×2 matrices $(\mathcal{M})$ for the resonator elements [156, 157]. The effect of the nonlinear birefringent fiber of length L is the combination of a linear propagation problem and nonlinear phase modulation. The resulting matrix is thus a product of two matrices, and the field vector is given by:

$$\begin{aligned} \begin{pmatrix} \tilde{\mathcal{E}}_x(L) \\ \tilde{\mathcal{E}}_y(L) \end{pmatrix} &= \begin{pmatrix} e^{-i\Phi_{NL,x}} & 0 \\ 0 & e^{-i\Phi_{NL,y}} \end{pmatrix} \cdot \begin{pmatrix} e^{-ik_xL} & 0 \\ 0 & e^{-ik_yL} \end{pmatrix} \cdot \begin{pmatrix} \tilde{\mathcal{E}}_x(0) \\ \tilde{\mathcal{E}}_y(0) \end{pmatrix} \\ &= \begin{pmatrix} e^{-i\Phi_x} & 0 \\ 0 & e^{-i\Phi_y} \end{pmatrix} \cdot \begin{pmatrix} \tilde{\mathcal{E}}_x(0) \\ \tilde{\mathcal{E}}_y(0) \end{pmatrix}, \end{aligned} \tag{7.12}$$

where

$$\Phi_{x,y} = \frac{2\pi n_2 L}{\lambda_\ell}\left[|\tilde{\mathcal{E}}_{x,y}|^2 + \frac{2}{3}|\tilde{\mathcal{E}}_{y,x}|^2\right] - \frac{2\pi n_{x,y}L}{\lambda_\ell}.$$

We have used here the same approximations for the nonlinear phase as in Section 6.4.2. The linear propagation constants $k_{x,y} = \omega_\ell n_{x,y}/c$. Matrices of common polarizing elements like wave-plates and polarizers known from Jones calculus can easily be incorporated into this analysis.

Other components of the round-trip model like gain, saturable absorption, mirrors etc, usually do not distinguish between the two polarization components. The transfer functions $\mathcal{T}$ are those introduced in Chapter 6. For implementing these elements in a way consistent with the matrix approach we define a transfer matrix

$$(\mathcal{M}) = \mathcal{T}\begin{pmatrix} 1 & 0 \\ 0 & 1 \end{pmatrix}. \tag{7.13}$$

Fiber lasers have typically high gain and losses. The laser operates in a regime of strong saturation, with pulses much shorter than the energy relaxation time of the lasing transition. The gain transition is generally sufficiently broad for phase modulation due to saturation to be negligible. Therefore the $\mathcal{T}$ factor in the transfer matrix describing gain is real and can be obtained from Eq. (3.82):

$$\mathcal{T}_g = \left[\frac{e^{W_0(t)/W_s}}{e^{-a} - 1 + e^{W_0(t)/W_s}}\right]^{1/2}. \tag{7.14}$$

An alternative approach is to consider the fiber laser as a continuous medium, which leads to a coupled system of differential equations for the components $\tilde{\mathcal{E}}_x$

and $\tilde{\mathcal{E}}_y$. This is essentially a two-field component extension of Eq. (4.111) without the transverse differential operators. We refer to the literature [158, 159] for a derivation of this system of equations, and refs. [157, 160] for their application to the modelling of a mode-locked fiber ring laser using nonlinear polarization rotation.

7.9.5 Figure-eight laser

A widely studied fiber laser implementation of the nonlinear mirror is the figure-eight laser [144], so named for the schematic layout of its component fibers (see Fig. 7.17), with a nonlinear amplifying loop mirror [161]. In the example shown in Fig. 7.17, the laser consists of a nonlinear amplifying mirror (left lop) and an optical isolator with outcoupler (right loop). The two loops of the "figure eight" are connected by a 50% beam splitter.

Let us follow a pulse that propagates counter-clockwise in the right loop through the isolator (optical diode), through a polarization controller (to compensate for the natural birefringence of the fiber) and a 20% output-coupler. The remaining part of the circulating pulse is equally split into the two directions of the left loop (nonlinear mirror). The counter-propagating pulses experience the same gain in the Er-doped fiber section of about 2 to 3 dB. The switching fiber introduces a phase shift through self-phase modulation. Being amplified before entering this fiber section, the counter-clockwise circulating pulse experiences a larger phase shift than its replica propagating in the opposite direction. The two pulses arrive simultaneously at the beam splitter and recombine. The variation of the accumulated differential phase across the combined pulse will cause different parts of the pulse injected clockwise and counter-clockwise into the left loop. From the point of view of the counter-clockwise circulating pulse in the right loop, the left loop acts as a nonlinear mirror whose reflection varies sinusoidally as a function of intensity. Thus, the loop mirror behaves as a fast saturable absorber from low intensity to intensities corresponding to the first transmission maximum.

Fiber lasers operating on the 1050 nm transition of Nd^{3+} in silica require bulk optic elements (prism sequences) for compensating the substantial normal dispersion (30 ps/nm· km) of the gain fiber at the operating wavelength, and so are generally constructed as a bulk optic external cavity around the gain fiber. Passive mode locking is obtained via nonlinear polarization rotation in the gain fiber, and the Brewster angled prisms serve as the polarizer. Pulses as short as 100 fs have been demonstrated [162].

Femtosecond fiber lasers operating in the 1530–1570 nm gain band of erbium are of obvious interest for their potential application in telecommunications. This wavelength range is in the low loss window of silica fibers, and such a source is

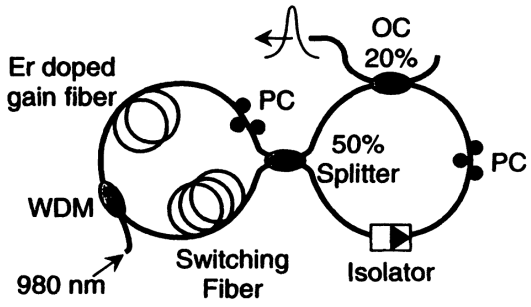

Figure 7.17: Schematic representation of the figure eight laser. The pump radiation at 980 nm is injected via the directional coupler WDM in the gain fiber (erbium doped). (Adapted from [144]).

obviously compatible with erbium fiber amplifiers. Of particular interest also is the anomalous dispersion exhibited by silica at this wavelength. The precise value of the dispersion may be tailored through the exact fiber design. This implies that a mode-locked laser with Er gain may be constructed entirely from fibers, with no need for dispersion compensating prisms as in the Nd fiber lasers or most other ultrafast sources. Indeed, subpicosecond erbium lasers have been demonstrated with all-fiber figure-eight, linear, and ring cavities, using both nonlinear mirrors and nonlinear polarization rotation. In addition, systems using semiconductor saturable absorbers have been demonstrated.

While soliton-like models have been used to describe a number of ultrafast laser systems as discussed in Chapter 6, the nonlinear dynamics of soliton propagation plays a more direct role in the erbium fiber laser than is seen in any other. The generated pulses are typically transform limited with a sech^2 intensity profile – the shape expected from the soliton solution of the nonlinear Schrödinger equation. The average intracavity energy per pulse corresponds reasonably well to the energy of a soliton of the same length propagating in fiber with dispersion equal to the average cavity dispersion.

It has been demonstrated that the minimum pulse length obtainable in erbium fiber lasers is approximately proportional to the total dispersion inside the cavity [163]. This is to some degree surprising: As the pulse propagation is soliton-like, the fiber dispersion is continuously balanced by the self-phase modulation of the fiber. In principle, solitons of any length will form as long as the amplitude of the input pulse exceeds the threshold value of Eq. (9.35) (cf. soliton description in Chapter 9). However, the coupling of energy into the dispersive wave increases

exponentially as the pulse shortens, thus limiting the minimum obtainable pulse width [164]. This loss becomes important only when the cavity length is of the order of the characteristic soliton length defined in Eq. (9.37). This is also why dispersive wave dynamics do not play an important role in other mode-locked lasers, which can be described by a soliton model: In such systems the soliton length corresponds to many cavity round trips, much longer than the cavity lifetime of the dispersive wave. To obtain very short pulses, then, it is necessary to minimize the total cavity dispersion, either by using dispersion shifted fiber components, or very short cavities, or by including lengths of dispersion compensating fiber specially designed to have normal dispersion at 1550 nm. Pulse widths of less than 100 fs [165] have been achieved. With such short pulses, third order dispersion plays an important role in limiting the pulse width and may impose a nonlinear chirp on the pulse [166].

Bibliography

[1] R. Ell, U. Morgner, F. X. Kärtner, J. G. Fujimoto, E. P. Ippen, V. Scheuer, G. Angelow, T. Tschudi, M. J. Lederer, A. Boiko, and B. Luther-Davis. Generation of 5-fs pulses and octave-spanning spectra directly from a Ti:sapphire laser. *Optics Lett.*, 26:373–375, 2001.

[2] D. E. Spence, J. M. Evans, W. E. Sleat, and W. Sibbett. Regeneratively initiated self-mode-locked ti:sapphire laser. *Optics Lett.*, 16:1762–1764, 1991.

[3] E. W. Van Stryland. The effect of pulse to pulse variation on ultrashort pulsewidth measurements. *Opt. Comm.*, 31:93–94, 1979.

[4] J.-C. Diels, J. J. Fontaine, I. C. McMichael, and F. Simoni. Control and measurement of ultrashort pulse shapes (in amplitude and phase) with femtosecond accuracy. *Applied Optics*, 24:1270–1282, 1985.

[5] G. H. C. New and J. M. Catherall. Advances in the theory of mode-locking by synchronous pumping. In G. Fleming and A. E. Siegman, editors, *Ultrafast Phenomena V*, pages 24–26, Berlin, 1986. Springer Verlag.

[6] U. Stamm. Numerical analysis of pulse generation in synchronously mode locked cw dye lasers. *Appl. Phys. B*, B45:101–108, 1988.

[7] V. A. Nekhaenko, S. M. Pershin, and A. A. Podshivalov. Synchronously pumped tunable picosecond lasers (review). *Sov. J. Quantum Electron.*, 16:299–315, 1986.

[8] N. J. Frigo, H. Mahr, and T. Daly. A study of forced mode locked cw dye lasers. *IEEE J. of Quantum Electron.*, QE-17:1134, 1977.

[9] A. M. Johnson and W. M. Simpson. Tunable femtosecond dye laser synchronously pumped by the compressed second harmonic of Nd:YAG. *J. Opt. Soc. Am. B*, B4:619–625, 1985.

[10] G. Angel, R. Gagel, and A. Laubereau. Generation of femtosecond pulses by a pulsed laser system. *Optics Comm.*, 63:259–263, 1987.

[11] L. Turi and F. Krausz. Amplitude modulation mode locking of lasers with regenerative feedback. *Appl. Phys. Lett.*, 58:810, 1991.

[12] J. M. Catherall and G. H. C. New. Role of spontaneous emission in the dynamics of mode-locking by synchronous pumping. *IEEE Journal of Quantum Electronics*, QE-22:1593, 1986.

[13] D. S. Peter, P. Beaud, W. Hodel, and H. P. Weber. Passive stabilazation of a synchronously pumped mode locked dye laser with the use of a modified outcoupling mirror. *Optics Lett.*, 16:405, 1991.

[14] J. P. Ryan, L. S. Goldberg, and D. J. Bradley. Comparison of synchronous pumping and passive mode-locking cw dye lasers for the generation of picosecond and subpicosecond light pulses. *Opt. Commun.*, 27:127–132, 1978.

[15] B. Couillaud, V. Fossati-Bellani, and G. Mitchel. Ultrashort pulse spectroscopy and applications. In *SPIE Proceedings*, volume 533, page 46. Springer-Verlag, 1985.

[16] N. Jamasbi, J.-C. Diels, and L. Sarger. Study of a linear femtosecond laser in passive and hybrid operation. *J. of Modern Optics*, 35:1891–1906, 1988.

[17] V. Petrov, W. Rudolph, U. Stamm, and B. Wilhelmi. Limits of ultrashort pulse generation in cw mode-locked dye lasers. *Physical Review A*, 40:1474–1483, 1989.

[18] L. C. Foster, M. D. Ewy, and C. B. Crumly. Laser mode locking by an external Doppler cell. *Appl. Phys. Lett.*, 6:6–8, 1965.

[19] R. W. Dunn, A. T. Hendow, J. G. Small, and E. Stijns. Gas laser mode-locking using an external acoustooptic modulator with a potential application to passive ring gyroscopes. *Applied Optics*, 21:3984–3986, 1982.

[20] K. J. Blow and D. Wood. Mode-locked lasers with nonlinear external cavities. *J. Opt. Soc. Am. B*, 5:629–632, 1988.

[21] K. J. Blow and B. P. Nelson. Improved mode locking of an f-center laser with a nonlinear nonsoliton external cavity. *Opt. Lett.*, 13:1026–1028, 1988.

[22] P. N. Kean, X. Zhu, D. W. Crust, R. S. Grant, N. Langford, and W. Sibbett. Enhanced mode locking of color-center lasers by coupled-cavity feedback control. *Opt. Lett.*, 14:39, 1989.

[23] J. Mark, L. Y.Liu, K. L. Hall, H. A. Haus, and E. P. Ippen. Femtosecond laser pumped by a frequency-doubled diode-pumped Nd:YLF laser. *Opt. Lett.*, 14:48–50, 1989.

[24] C. P. Yakymyshyn, J. F. Pinto, and C. R. Pollock. Additive-pulse mode-locked NaCl:OH^- laser. *Opt. Lett.*, 14:621–623, 1989.

[25] P. M. French, J. A. R. Williams, and R. Taylor. Femtosecond pulse generation from a titanium-doped sapphire laser using nonlinear external cavity feedback. *Opt. Lett.*, 14:686, 1989.

[26] J. Goodberlet, J. Wang, J. G. Fujimoto, and P. A. Shulz. Femtosecond passively mode-locked Ti:sapphire laser with a nonlinear external cavity. *Optics Lett.*, 14:1125–1127, 1989.

[27] J. Goodberlet, J. Jacobson, J. G. Fujimoto, P. A. Schulz, and T. Y. Fan. Self-starting additive-pulse mode-locked diode-pumped Nd:YAG laser. *Opt. Lett.*, 15:504–507, 1990.

[28] L. Y. Liu, J. M. Huxley, E. P. Ippen, and H. A. Haus. Self-starting additive-pulse mode-locking of a Nd:YAG laser. *Optics Lett.*, 15:553–555, 1990.

[29] J. M. Liu and J. K. Chee. Passive mode locking of a cw Nd:YLF laser with a nonlinear external coupled cavity. *Opt. Lett.*, 15:685, 1990.

[30] J. Goodberlet, J. Jackson, J. G. Fujimoto, and P. A. Schultz. Ultrashort pulse generation with additive pulse modelocking in solid state lasers: $Ti:Al_2O_3$, diode pumped Nd:YAG and Nd:YLF. In C. B. Harris, E. P. Ippen, G. A. Mourou, and A. H. Zewail, editors, *Ultrafast Phenomena VII*, page 11, Berlin, 1990. Springer-Verlag.

[31] F. Krausz, Ch. Spielmann, T. Brabec, E. Wintner, and A. J. Schmidt. Subpicosecond pulse generation from a Nd:glass laser using a nonlinear external cavity. *Opt. Lett.*, 15:737–739, 1990.

[32] W. Sibbett. Hybrid and passive mode-locking in coupled-cavity lasers. In C. B. Harris, E. P. Ippen, G. A. Mourou, and A. H. Zewail, editors, *Ultrafast Phenomena VII*, pages 2–7, Berlin, 1990. Springer-Verlag.

[33] E. P. Ippen, H. A. Haus, and L. Y. Liu. Additive pulse mode locking. *J. Opt. Soc. Am. B*, 6:1736, 1989.

[34] L. F. Mollenauer and R. H. Stolen. The soliton laser. *Opt. Lett.*, 9:13, 1984.

[35] U. Keller, G. W. 'tHooft, W. H. Knox, and J. E. Cuninham. Femtosecond pulses from a continously self-starting passively mode-locked Ti:sapphire laser. *Opt. Lett.*, 16:1022–1024, 1991.

[36] M. Sheik-Bahae, D. J. Hagan, and E. W. Van Stryland. Dispersion and band-gap scaling of the electronic kerr effect in solids associated with two-photon absorption. *Phys. Rev. Lett*, 65:96–99, 1990.

[37] M. Sheik-Bahae, D. C. Hutchings, D. J. Hagan, and E. W. Van Stryland. Dispersion of bound electronic nonlinear refraction in solids. *IEEE J. of Quan. Elec.*, QE-27:1296–1309, 1990.

[38] G. Cerullo, M.B. Danailov, S. De Silvestri, P. Laporta, V. Magni, D. Segala, and S. Taccheo. Nonlinear mirror mode-locking of a cw nd:yag laser. *Appl. Phys. Lett.*, 65:2392–2394, 1994.

[39] M.B. Danailov, G. Cerullo, V. Magni, D. Segala, and S. De Silvestri. Nonlinear mirror mode-locking of a CW Nd:YLF laser. *Opt. Lett.*, 19:792–794, 1994.

[40] K. A. Stankov. A new mode-locking technique using a nonlinear mirror. *Opt. Commun.*, 66:41, 1988.

[41] K. A. Stankov. Pulse shortening by a nonlinear mirror mode locker. *Appl. Opt.*, 28:942–945, 1989.

[42] K. A. Stankov. Frequency domain analysis of the mode-locking process in a laser with second-harmonic nonlinear mirror. *Opt. Lett.*, 16:639–641, 1991.

[43] Arlee Smith. URL http://www.sandia.gov/imrl/X1118/xxtal.htm, 2003.

[44] K.A. Stankov. 25 ps pulses from a pulsed Nd:YAG laser mode locked by a frequency doubling bbo crystal. *Appl.Phys. Lett.*, 58:2203–2204, 1991.

[45] V. Couderc, O. Guy, A. Barthelemy, V. Kubecek, and H. Jelinkova. Self-mode locked operation of a cw nd:yag laser using second-harmonic nonlinear mirror. In *International symposium on Advanced Materials for Optics and Optoelectronics*, volume 2777, pages 216–218, Prague, 1995. SPIE.

[46] A. Agnesi, C. Pennacchio, G. C. Reali, and V. Kubecek. High-power diode-pumped picosecond Nd^{3+}:YVO_4 laser. *Optics Lett.*, 22:1645–1647, 1997.

[47] A. Agnesi, G. C. Reali, and V. Kubecek. Nonlinear mirror operation of a diode-pumped quasi-cw picosecond Nd:YAG laser. *Appl. Phys. B.*, 66:283–285, 1998.

[48] A. Agnesi, G. C. Reali, and V. Kubecek. Nonlinear mirror operation of a diode-pumped quasi-cw picosecond nd:yag laser. *J. Opt. Soc. Am. B 16*, 66:1236–1239, 1999.

[49] V. Kubecek. Nonlinear mirror mode-locking of solid state lasers. volume 5259, pages 403–410, Bellingham, WA, 2003. SPIE.

[50] Xin Miao Zhao and Daniel McGraw. Parametric mode locking. *IEEE J. of Quantum Electronics*, QE-28:930, 1992.

[51] K.A. Stankov. Negative feedback by using a nonlinear mirror for generation of long train of short pulses. *Appl.Phys. B*, 52:158–162, 1991.

[52] V. Kubecek, V. Coudercand B. Bourliaguetand F. Loradour, and A. Barthelemy. 4-W and 23-ps pulses from a lamp-pumped Nd:YAG laser passively mode-locked by polarization switching in a KTP crystal. *Appl. Phys. B*, 69:99–101, 1999.

[53] A. V. Babushkin, N. S. Vorob'ev, A. M. Prokhorov, and M. Ya. Shchelev. Stable picosecond Y AlO_3:Nd crystal laser with hybrid mode-locking and passive intracavity feedback utilizing a GaAs crystal. *Sov. J. Quantum Electron.*, 19:1310–1311, 1989.

[54] Thien Trang Dang, Andreas Stintz, Jean-Claude Diels, and Yanshen Zhang. Active solid state short pulse laser gyroscope. In www.ion.org The Institute of Navigation, editor, *ION 57th Annual Meeting - Session D4*, Albuquerque, New Mexico, 2001.

[55] O. E. Martinez and L. A. Spinelli. Deterministic passive mode locking of solid-state lasers. *Appl. Phys. Lett.*, 39:875–877, 1981.

[56] K. Burneika, R. Grigonis, A. Piskarskas, G. Sinkyavichyus, and V. Sirutkaĭtis. Highly stable subpicosecond neodymium (Nd^{3+}) glass laser with passive mode-locking and negative feedback. *Kvantovaya Elektron.*, 15:1658–1659, 1988.

[57] P. Heinz, W. Kriegleder, and A. Laubereau. Feedback control of an actively-passively mode-locked Nd:glass laser. *Applied Physics A*, 43:209–212, 1987.

[58] D. H. Auston, S. McAfee, C. V. Shank, E. P. Ippen, and O. Teschke. Picosecond spectroscopy of semiconductors. *Solid State Electronics*, 21:147, 1978.

[59] W. A. Schroeder, T. S. Stark, M. D. Dawson, T. F. Boggess, A. L. Smirl, and G. C. Valley. Picosecond separation and measurement of coexisting photo-refractive, bound-electronic, and free-carrier grating dynamics in GaAs. *Optics Lett.*, 16:159–161, 1991.

[60] A. Agnesi, Annalisa Guandalini, and Giancarlo Reali. Continuous passive mode-locked and passive stabilized low pump power Yb:YAG laser. In *Europhysics Conference Abstracts*, volume 28C, Lausanne, Switzerland, 2004.

[61] J. Schwartz, W. Weiler, and R. K. Chang. Laser-pulse shaping using inducible absorption with controlled q-switch time behavior. *IEEE J. of Quantum Electronics*, QE-6:442–450, 1970.

[62] A. Hordvik. Pulse stretching utilizing two-photon-induced light absorption. *IEEE J. of Quantum Electronics*, QE-6:199–203, 1970.

[63] A. Agnesi, A. Del Corno, J.-C. Diels, P. Di Trapani, M. Fogliani, V. Kubecek, G. C. Reali, C.-Y. Yeh, and Xin Miao Zhao. Generation of extended pulse trains of minimum duration by passive negative feedback applied to solid state Q-switched lasers. *IEEE J. of Quantum Electron.*, 28:710–719, 1992.

[64] V. Kubecek, A. Dombrovsky, J.-C. Diels, and A. Stintz. Mode-locked Nd:YAG laser with passive negative feedback using multiple quantum well saturable absorber. In *Proceedings of SPIE; GC:/HPL 2004*, pages Paper 81–5, Prague, Czech Republic, 2004.

[65] U. Keller, K. J. Weingarten, F. X. Kartner, D. Kopf, B.Braun, I. D. Jung, R. Fluck, C. Honninger, N. Matuschek, and J. Aus der Au. Semiconductor saturable absorber mirrors (sesams) for femtosecond to nanosecond pulse generationin solid-state lasers. *" IEEE J. Sel. Topics Quantum Electron.*, 2:435–453, 1996.

[66] S. L. Chuang. *Physics of Optoelectronic Devices*. Wiley, New York, 1995.

[67] P. W. Smith, Y. Silberberg, and D. Q. B. Miller. Mode-locking of semiconductor diode lasers using saturable excitonic nonlinearities. *J. Opt. Soc. Am.*, B-2:1228–1235, 1985.

[68] P. J. Delfyett, L. Flores, N. Stoffel, T. Gmitter, N. Andreadakis, G. Alphonse, and W. Ceislik. 200 femtosecond optical pulse generation and intracavity pulse evolution in a hybrid modelocked semiconductor diode laser- amplifier system. *Optics Lett.*, 17:670–672, 1992.

[69] S. Gupta, J. F. Whitaker, and G. A. Mourou. Ultrafast carrier dynamics in III-V semiconductors grown by molecular-beam epitaxy at very low substrate temperatures. *IEEE J. of Quantum Electron.*, 28:2464–2472, 1992.

[70] R. C. Powell, S. A. Payne, L. L. Chase, and G. D. Wilke. Index-of-refraction change in optically pumped solid-state laser materials. *Optics LETT.*, 14:1204, 1989.

[71] M. Weitz, S. Reuter, R. Knappe, R. Wallenstein, and B. Henrich. In *CLEO, CTuCC1*, San Francisco, 2004. Optical Society of America.

[72] W. Koechner and M. Bass. *Solid-State Lasers*. Springer, ISBN 3-387-95590-9, Berlin, Heidelberg, New York, 2002.

[73] S. Smolorz and F. Wise. Time-resolved nonlinear refraction in femtosecond laser gain media. *Optics Lett.*, 23:1381–1383, 1998.

[74] P. F. Moulton. Spectroscopic and laser characteristics of Ti:Al_2O_3. *J. Opt. Soc. Am.B*, 3:125–133, 1986.

[75] D. E. Spence, P. N. Kean, and W. Sibbett. 60-fs pulse generation from a self-mode-locked Ti:sapphire laser. *Optics Lett.*, 16:42–44, 1991.

[76] M. T. Asaki, C. P. Huang, D. Garvey, J. Zhou, H. Kapteyn, and M. M. Murnane. Generation of 11 fs pulses from a self-mode-locked Ti:sapphire laser. *Opt. Lett.*, 18:977–979, 1993.

[77] A. Stingl, Ch. Spielmann, F. Krausz, and R. Szipöcs. Generation of 11 fs pulses from a Ti:sapphire laser without the use of prisms. *Optics Lett.*, 19:204–406, 1994.

[78] J. Reichert, R. Holzwarth, Th. Udem, and T. W. Hänsch. Measuring the frequency of light with mode-locked lasers. *Optics Comm.*, 172:59–68, 1999.

[79] H. R. Telle, G. Steinmeyer, A. E. Dunlop, S. Stenger, D. A. Sutter, and U. Keller. Carrier-envelope offset phase control: A novel concept for absolute optical frequency measurement and ultrashort pulse generation. *Appl. Phys. B*, 69:327, 1999.

[80] Scott A. Diddams, David J. Jones, Jun Ye, Steven T. Cundif, John L. Hall, Jinendra K. Ranka, Robert S. Windeler, Ronald Holzwarth, Thomas Udem, and T.W. H*ä*nsch. A direct link between microwave and optical frequencies with a 300 thz femtosecond laser comb. *Phys. Rev. Lett.*, 84:5102–5105, 2000.

[81] U. Morgner, R. Ell, G. Metzler, T. R. Schibli, F. X. Kärtner J. C. Fujimoto, H. A. Hauss, and E. P. Ippen. Nonlinear optics with phase-controlled pulses in the sub-two-cycle regime. *Phys. Rev. Lett.*, 86:5462–5465, 2001.

[82] F. X. Kärtner, N. Matuschek, T. Schibli, U. Keller, H. A. Haus, C. Heine, R. Morf, V. Scheuer, M. Tilsch, and T. Tschudi. Design and fabrication of double chirped mirrors. *Opt. Lett.*, 22:831–833, 1997.

[83] M. Ramaswamy, M. Ulman, J. Paye, and J. G. Fujimoto. Cavity dumped femtosecond kerr-lens modelocked ti:sapphire laser. *Opt. Lett.*, 18:1822–18824, 1993.

[84] M. S. Pshenichnikov, W. P. De Boeij, and D. A. Wiersma. Generation of 13 fs, 5-mw pulses from a cavity dumped ti:sapphire laser. *Opt. Lett.*, 19:572–574, 1994.

[85] J. Jasapara, V. L. Kalashnikov, D. O. Krimer, G. Poloyko, and and W. Rudolph M. Lenzner. Automodulations in kerr-lens modelocked solid-state lasers. *J. Opt. Soc. Am. B*, 17:319–326, 2000.

[86] S. H. Cho, F. X. Kärtner, U. Morgner, E. P. Ippen, J. G. Fujimoto, J. E. Cunningham, and W. H. Knox. Generation of 90-nj pulses with a 4-mhz repetition rate kerr-lens modelocked ti:sapphire oscillator. *Opt. Lett.*, 26:560–562, 2001.

[87] A. Apolonski, A. Fernandez, T. Fuji, K. Krausz, A. Fürbach, and A. Stingl. Scaleable high-energy femtosecond Ti:sapphire oscillator. In *CLEO, CThA2*, San Francisco, 2004. Optical Society of America.

[88] M. Stalder, M. Bass, and B. H. T. Chai. Thermal quenching of fluorescence in chromium-doped fluoride laser crystals. *J. Opt. Soc. Am. B*, 9:2271–2273, 1992.

[89] V. Kubecek, R. Quintero-Torres, and J.-C. Diels. Ultralow-pump-threshold laser diode pumped Cr:LiSAF laser. In Vladislav Ya. Panchenko Guenter Huber, Ivan A. Scherbakov, editor, *Advanced Lasers and Systems*, volume 5137, pages 43–47, Bellingham, WA, 2003. SPIE.

[90] G. J. Valentine, J. M. Hopkins, P. Loza-Alvarez, G. T. Kennedy, W. Sibbett, D. Burns, and A. Valster. Ultralow-pump-threshold, femtosecond Cr^{3+}:$LiSrAlF_6$. *Optics Lett.*, 22:1639–1641, 1997.

[91] R. Szip ocs and A. Köházi-Kis. Theory and design of chirped dielectric laser mirrors. *Appl. Phys. B*, 65:115–135, 1997.

[92] I. T. Sorokina, E. Sorokin, E. Wintner, A. Cassanho, H. P. Jenssen, and R. Szip ocs. Sub-20 fs pulse generation from the mirror dispersion controlled LiSGAF and LiSAF lasers. *Appl. Phys. B*, 65:245–253, 1997.

[93] L. K. Smith, S. A. Payne, W. L. Kway, L. L. Chase, and B. H. T. Chai. Investigation of the laser properties of Cr^{3+}:$LiSrGaF_6$. *IEEE Journal of Quantum Electronics*, 28:2612–2618, 1992.

[94] D. Kopf, K. J. Weingarten, G. Zhang, M. Moser, M. A. Emanuel, R. J. Beach, J. A. Skidmore, and U. Keller. High average power diode pumped femtosecond Cr:LiSAF lasers. *Applied Phys. B*, 65:235–243, 1997.

[95] S. Uemura and K. Torizuka. Generation of 12-fs pulses from a diode-pumped Kerr-lens mode-locked CrLiSAF laser. *Opt. Lett.*, 24:780–782, 1999.

[96] I. T. Sorokina, E. Sorokin, E. Wintner, A. Cassanho, and H. P. Jenssen. 14 fs pulse generation in Kerr-lens mode-locked prismless LiSGAF and LiSAF lasers: observation of pulse self-frequency shift. *Optics Lett.*, 22:1716–1718, 1997.

[97] R. Robertson, R. Knappe, and R. Wallenstein. Kerr-lens mode-locked Cr:LiSAF laser pumped by the diffraction limited output of a 672 nm diode laser master-oscillator power-amplifier system. *J. Opt Soc. Am. B*, 14:672–675, 1997.

[98] I. Thomann, A. Bartels, K. L. Corwin, N. R. Newbury, L. Hollberg, S. A. Diddams, J. W. Nicholson, and M. F. Yan. 420 MHz Cr: forsterite femtosecond ring laser and continuum generation in the 1—2 μm range. *Optics Lett.*, 28:1368–1370, 2003.

[99] V. Petricevic, S. K. Gayen, and R. Alfano. Laser action in chromium activated fosterite for near IR excitation, is Cr^{4+} the lasing ion? *Appl. Phys. Lett.*, 53:2590, 1988.

[100] A. Seas, V. Petricevic, and R. R. Alfano. Self-mode-locked chromium doped forsterite laser generates 50 fs pulses. *Optics Lett.*, 18:891–893, 1993.

[101] V. Petricevic, A. B. Bykov, J. M. Evans, and R. Alfano. Room temperature near IR tunable lasing operation of $Cr^{4+}Ca_2GeO_4$. *Optics Lett.*, 21:1750–1752, 1996.

[102] B. Xu, J. M. Evans, V. Petricevic, S. P. Guo, O. Maksimov, M. C. Tamargo, and R. R. Alfano. Continuous wave and passively mode-locked operation of a cunyite laser. *Applied Optics*, 39(27):4975, 2000.

[103] L. Qian, X. Liu, and F. Wise. Cr:forsterite laser pumped by broad area laser diodes. *Opt. Lett.*, 22:1707–1709, 1997.

[104] Chudoba, J. G. Fujimoto, E. Ippen, H. A. Haus, U. morgnere, F. .X. Kärtner, V. Scheuer, G. Angelow, and T. Tschudi. All-solid-state Cr:forsterite laser generating 14 fs pulses at 1.3μm. *Optics Lett.*, 26:292–294, 2001.

[105] V. Yanovsky, Y. Pang, F. Wise, and B. I. Minkov. Generation of 25-fs pulses from a self-mode-locked Cr:forsterite laser with optimized group-delay dispersion. *Optics Lett.*, 18:1541–1543, 1993.

[106] I. Thomann, L. Hollberg, S. A. Diddams, and R. Equal. Chromium-doped forsterite: Dispersion measurement with white-light interferometry. *Appl. Opt.*, 42:1661, 2003.

[107] J. M. Evans, V. Petricevic, A. B. Bykov, and R. R. Alfano. Direct diode-umped continuous wave near infrared tunable laser operation of Cr^{4+} forsterite and $Cr^{4+}Ca_2GeO_4$. *Opt. Lett.*, 22:1171–1173, 1997.

[108] R. Adair, L. L. Chase, and S. A. Payne. Nonlinear refractive index of optical materials. *Phys. Rev. B*, 39:3337–3345, 1989.

[109] W. F. Krupke, M. D. Shinn, J. E.Marion, J. A. Caird, and S. E. Stokowski. Spectroscopic, optical, and thermomechanical properties of neodymium- and chromium-doped gadolinium scandium gallium garnets. *J. Opt. Soc. Am. B*, 3:102, 1986.

[110] T. Kushida, H. M. Marcos, and G. E. Geusic. Laser transition cross section and fluorescence branching ratio for nd3+ in yttrium aluminum garnet. *Phys. Rev.*, 167:289, 1968.

[111] A. Umbrasas, J. C. Diels, G. Valiulis, J. Jacob, and A. Piskarskas. Generation of femtosecond pulses through second harmonic compression of the output of a Nd:YAG laser. *Opt. Lett.*, 20:2228–2230, 1995.

[112] A. Umbrasas, J. C. Diels, J. Jacob, and A. Piskarskas. Parametric oscillation and compression in KTP crystals. *Opt. Lett.*, 19:1753–1755, 1994.

[113] J. Biegert, V. Kubecek, and J. C. Diels. A new femtosecond uv source based on Nd:YAG. In *CLEO, 1999*, page 479, Baltimore, Maryland, 1999. Optical Society of America.

[114] A. Giesen, H. Hügel, A. Voss, K. Wittig, U. Brauch, and H. Opower. Scalable concept for diode-pumped high-power solid-state-lasers. *Appl. Phys. B*, 58:365, 1994.

[115] G. J. Spühler, T. Südmeyer, R. Paschotta, M. Moser, K. J. Weingarten, and U. Keller. Passively modelocked high-power Nd:YAG lasers with multiple laser heads. *Appl. Phys. B*, 71:19–25, 2000.

[116] E. Innerhofer, T. Südmeyer, F. Grunner, R. Häring, A. Aschwanden, and R. Paschotta. 60w average power in 810 fs pulses from a thin disk Yb:YAG laser. *Optics Lett.*, 28:367–369, 2003.

[117] A. Agnesi and G. C. Reali. Development of medium power, compact all-solid-state lasers. *La Rivista del Nuovo Cimento*, 21(4):1–31, 1998.

[118] J. R. Lincoln and A. I. Ferguson. All-solid-state self-mode locking of a nd:ylf laser. *Optics Lett.*, 19:2119–2121, 1994.

[119] R. Fluck, G. Zhang, U. Keller, K. J.Weingarten, and M. Moser. Diode-pumped passively mode-locked 1.3 μm Nd:YVO_4 and Nd:YLF lasers by use of semiconductor saturable absorbers. *Optics Lett.*, 21:1378–1380, 1996.

[120] L. Turi and J. Juhasz. High-power longitudinally end-diode-pumped Nd:YLF regenerative amplifier. *Optics Lett.*, 20:154–156, 1995.

[121] R. L. Fork and C. V. Shank. Generation of optical pulses shorter than 0.1 ps by colliding pulse mode-locking. *Appl. Phys. Lett.*, 38:671, 1981.

[122] A. Finch, G. Chen, W. Steat, and W. Sibbett. Pulse asymetry in the colliding-pulse mode-locked dye laser. *J. Mod. Opt.*, 35:345–349, 1988.

[123] H. Kubota, K. Kurokawa, and M. Nakazawa. 29 fs pulse generation from a linear cavity synchronously pumped dye laser. *Opt. Lett.*, 13:749–751, 1988.

[124] J.-C. Diels. Femtosecond dye lasers. In F. Duarte and L. Hillman, editors, *Dye Laser Principles: With Applications*, volume ISBN 0-12-215492-4, chapter 3, pages 41–132. Academic Press, Boston, 1990.

[125] A. E. Siegman. An antiresonant ring interferometer for coupled laser cavities, laser output coupling, mode-locking, and cavity dumping. *IEEE J. Quantum Electron.*, QE-9:247–250, 1973.

[126] M. C. Nuss, R. Leonhart, and W. Zinth. Stable operation of a synchronously pumped colliding-pulse mode-locked ring dye laser. *Opt. Lett.*, 10:16–18, 1985.

[127] F. J. Duarte and R. O. James. Tunable solid-state lasers incorporating dye-doped, polymer-nanoparticle gain media. *Optics Lett.*, 21:2088–2090, 2003.

[128] F. J. Duarte and R. O. James. Spatial structure of dye-doped polymer nanoparticle laser media. *Applied Optics*, 43:4088–4090, 2004.

[129] Zs. Bor and A. Muller. Picosecond distributed feedback dye lasers. *IEEE Journal of Quantum Electronics*, QE-22:1524–1533, 1986.

[130] S. Szatmari and F. P. Schaefer. Generation of high power UV femtosecond pulses. In T. Yajima, K. Yoshihara, C. B. Harris, and S. Shionoya, editors, *Ultrafast Phenomena VI*, pages 82–86, Berlin, 1988. Springer.

[131] P. H. Chin, P. Pex, L. Marshall, F. Wilson, and R. Aubert. A high energy, electromagnetically tuned single mode, short cavity picosecond dye laser system: design and performances. *Optics and Lasers in Engineering*, 10:55–68, 1989.

[132] H. P. Kurz, A. J. Cox, G. W. Scott, D. M. Guthals, H. Nathel, S. W. Yeh, S. P. Webb, and J. H. Clark. Amplification of tunable, picosecond pulses from a single mode, short cavity dye laser. *IEEE J. of Quantum Electron.*, QE-21:1795–1798, 1985.

[133] P. Simon, S. Szatmari, and F. P. Schafer. Generation of 30 fs pulses tunable over the visible spectrum. *Opt. Lett.*, 16:1569–1571, 1991.

[134] P. P. Vasil'ev. Ultrashort pulse generation in diode lasers. *Optical and Quantum ELectron.*, 24:801–824, 1992.

[135] G. A. Alphonse, D. B. Gilbert, M. G. Harvey, and M. Ettenberg. High power superluminescent diodes. *IEEE J. of Quantum Electron.*, 24:2454–2458, 1988.

[136] P. J. Delfyett, Y. Slberberg, G. A. Alphonse, and W. Ceislik. Hot-carrier thermalization induced self-phase modulation in semiconductor traveling wave amplifiers. *Appl. Phys. Lett.*, 59:10, 1991.

[137] P. J. Delfyett, C. H. Lee, L. Flores, N. Stoffel, T. Gmitter, N. Andreadakis, G. Alphonse, and J. C. Connolly. Generation of subpicosecond high-power optical pulses from a hybrid mode-locked semiconductor laser. *Optics Lett.*, 15:1371–1373, 1990.

[138] S. Chen and J. Wang. Self-starting issues of passive self-focusing mode-locking. *Opt. Lett.*, 16:1689–1691, 1991.

[139] C. F. Lin and C. L. Tang. Colliding pulse mode-locking of a semiconductor laser in an external ring cavity. *Appl. Phys. Lett.*, 62:1053–1055, 1993.

[140] W. Rudolph and B. Wilhelmi. *Light Pulse Compression*. Harwood Academic, Chur, London, Paris, New York, 1989.

[141] B. Zysset, P. Beaud, and W. Hodel. Generation of optical solitons in the wavelength region 1.37—1.43 μm. *Appl. Phys. Lett.*, 50:1027–1029, 1987.

[142] J. D. Kafka and T. Baer. Fiber raman soliton laser pumped by a Nd:YAG laser. *Optics Lett.*, 12:181–183, 1987.

[143] A. S. Gouveia-Neto, A. S. L. Gomes, and J. B. Taylor. Generation of 33 fs pulses at 1.32 μm through a high order soliton effect in a single mode optical fiber. *Opt. Lett.*, 12:395–397, 1987.

[144] I. N. Duling III. Subpicosecond all-fiber erbium laser. *Electron. Lett.*, 27:544–545, 1991.

[145] I. N. Duling. All fiber ring soliton laser mode locked with a nonlinear mirror. *Optics Lett.*, 16:539–541, 1991.

[146] S. P. Craig-Ryan and B. J. Ainslie. Glass structure and fabrication techniques. In P. W. France, editor, *Optical Fiber Lasers and Amplifiers*, pages 50–78. Blackies & Son, Ltd., Glasgow, 1991.

[147] I. N. Duling, R. P. Moeller, W. K. Burns, C. A. Villaruel, L. Goldberg, E. Snitzer, and H. Po. Output characteristics of diode pumped fiber ase sources. *IEEE J. Quantum Electron.*, 27:995–1003, 1991.

[148] M. Hofer, M. E. Fermann, F. Haberl, M. H. Ober, and A. J. Schmidt. Mode locking with cross-phase and self-phase modulation. *Opt. Lett.*, 16:502–504, 1991.

[149] N. J. Doran and D. Wood. Nonlinear-optical loop mirror. *Opt. Lett.*, 13:56–58, 1988.

[150] M. Zirngibl, L.W. Stulz, J. Stone, D. DiGiovanni, and P. B. Hansen. 1.2 ps pulses from passively modelocked laser diode pumped er-doped fiber ring laser. *Electron. Lett.*, 27:1734–5, 1991.

[151] M. E. Fermann, A. Galvanauskas, G. Sucha, and D. Harter. Fiber lasers for ultrafast optics. *Appl. Phys. B*, 65:259–275, 1997.

[152] F. Ö. Ilday, J. Buckley, L. Kuznetsova, and F. W. Wise. Generation of 36-fs pulses from an ytterbium fiber laser. *Optics Express*, 11:3550–54, 2003.

[153] I. Kaminow. Polarization in optical fibers. *IEEE J. of Quantum Electron.*, QE-17:15, 1981.

[154] K. Tamura, H. A. Haus, and E. P. Ippen. Self-starting additive pulse mode-locked erbium fiber ring laser. *Electron. Lett*, 28:2226–2228, 1992.

[155] H. G. Winful. Self-induced polarization changes in birefringent optical fibers. *Appl. Phys. Lett.*, 47:213, 1985.

[156] C. W. Chang and S. Chi. Mode-locked erbium-doper fibre ring laser using nonlinear polarization rotation. *Journal of Modern Optics*, 45:355–362, 1998.

[157] C. W. Chang and S. Chi. Ultrashort pulse generation from mode-locked erbium-doper fibre ring lasers. *Journal of Modern Optics*, 46:1431–1442, 1999.

[158] S. Chi, C. W. Chang, and S. Wen. Ultrashort soliton pulse train propagation in erbium-doped fiber amplifiers. *Optics Comm.*, 111:132, 1994.

[159] G. P. Agrawal. *Nonlinear Fiber Optics*. Academic Press, ISBN 0-12-045142-5, Boston, 1995.

[160] L. M. Spaulding, D. H. Yong, and A. D. Kimand J. N. Kutz. Nonlinear dynamics of mode-locking optical fiber ring lasers. *J. Opt. Soc. Am.*, B-19:1045–1054, 2002.

[161] M. E. Fermann, F. Haberl, M. Hofer, and H. Hochreiter. Nonlinear amplifying loop mirror. *Opt. Lett.*, 15:752–754, 1990.

[162] M. H. Ober, F. Haberl, and M. E. Fermann. 100 fs pulse generation from an all-solid-state Nd:glass fiber laser oscillator. *Appl. Phys. Lett.*, 60:2177–2179, 1992.

[163] M. L. Dennis and I. N. Duling. Role of dispersion in limiting pulse width in fiber lasers. *Appl. Phys. Lett.*, 62:2911–2913, 1993.

[164] M. L. Dennis and I. N. Duling. Experimental study of sideband generation in femtosecond fiber lasers. *IEEE J. Quantum Electron.*, 30:1469–1477, 1993.

[165] M. Nakazawa, E. Yoshida, and Y. Kimura. Generation of 98 fs optical pulses directly from an erbium-doped fibre ring laser at 1.57 μm. *Electron. Lett.*, 29:63–65, 1993.

[166] M. L. Dennis and I. N. Duling. Third order dispersion effects in femtosecond fiber lasers. *Opt. Lett.*, 19:1750–1752, 1993.

Chapter 10

Diagnostic Techniques

The femtosecond time scale is beyond the reach of standard electronic display instruments. New methods have to be designed to freeze and time resolve events as short as a few optical cycles. Any measurement technique introduces some perturbation on the parameter to be measured. This problem is particularly acute in attempting to time resolve fs signals. As we have seen in the chapter on fs optics, reflection and transmission through most optical element will modify the signal to be measured. In addition, most diagnostic schemes involve nonlinear elements which may also have an influence on the amplitude and phase of the pulse to be measured. A careful analysis of the diagnostic instrument is required to find its exact transfer function. The inverse of this instrument transfer function should be applied to the result of the measurement, to obtain the parameters of the signal *prior* to entering the measuring device.

We will start this chapter with the description of simple, coarse methods that provide some estimate of the pulse duration and a description of some measurement techniques commonly used for recording pulse correlations (Sections 10.1-10.3). Many of these techniques were developed with the emergence of ns and ps laser technology, for a review see [1]. In the second part of this chapter, Section 10.4, we will describe techniques that lead to a complete characterization of the pulse amplitude and phase.

10.1 Intensity correlations

10.1.1 General properties

The temporal profile $I_s(t)$ of an optical signal can be easily determined, if a shorter (reference) pulse of known shape $I_r(t)$ is available. The method is to measure the

intensity cross-correlation:

$$A_c(\tau) = \int_{-\infty}^{\infty} I_s(t) I_r(t-\tau) dt. \tag{10.1}$$

Let us define the Fourier transforms of the intensity profiles as:

$$\mathcal{I}_j(\Omega) = \int_{-\infty}^{\infty} I_j(t) e^{-i\Omega t} dt, \tag{10.2}$$

where the subscript j indicates either the reference (r) or signal (s) pulse. The Fourier transform of Eq. (10.2) should not be confused with the spectral intensity (proportional to $|\tilde{\mathcal{E}}(\Omega)|^2$). The Fourier transform of the correlation (10.1) is $A_c(\Omega)$, related to the Fourier transforms of the intensities by:

$$A_c(\Omega) = \mathcal{I}_r(\Omega) \mathcal{I}_s^*(\Omega). \tag{10.3}$$

The shape of the signal $I_s(t)$ can be determined by first taking the Fourier transform $A_c(\Omega)$ of the measured cross-correlation, and dividing by the Fourier transform $\mathcal{I}_r(\Omega)$ of the known reference pulse $I_r(t)$. The inverse Fourier transform of the complex conjugate of the ratio $A_c(\Omega)/\mathcal{I}_r(\Omega)$ is the temporal profile $I_s(t)$. In presence of noise, this operation leads to large errors unless the reference function is the (temporally) shorter of the two pulses being correlated (or the function with the broadest spectrum). The ideal limit is of course that of the reference being a delta-function. In the frequency domain, we are dividing by a constant. In the time domain, the shape of the correlation $A_c(\tau)$ is identical to that of the signal $I_s(t)$. Even in that ideal case, the intensity cross-correlation has an important limitation: it does not provide any information on the phase content (frequency or phase modulation) of the pulse being analyzed.

10.1.2 The intensity autocorrelation

In most practical situations, a reference pulse much shorter than the signal cannot be generated. In the ideal cases where such a pulse is available, there is still a need for a technique to determine the shape of the reference signal. It is therefore important to consider the limit where the signal itself has to be used as reference. The expression (10.1) with $I_s(t) = I_r(t) = I(t)$ is called an intensity autocorrelation. An autocorrelation is always a symmetric function – this property can be understood from a comparison of the overlap integral for positive and negative arguments τ. According to Eq. (10.3), the Fourier transform of the autocorrelation is a real function, consistent with a symmetric function in the time domain. As a result, the autocorrelation provides only very little information on the pulse shape,

since an infinity of symmetric and asymmetric pulse shapes can have very similar autocorrelations. Nevertheless, the intensity autocorrelation is a widely used diagnostic technique, because it can be easily implemented, and is the first tool used to determine whether a laser is producing short pulses rather than intensity fluctuations of a continuous background. Typical examples are given in Section 10.3. The intensity autocorrelation is also used to quote a "pulse duration". The most widely used procedure is to *assume* a pulse shape (generally a sech^2 or a Gaussian shape), and to "determine" the pulse duration from the known ratio between the FWHM of the autocorrelation and that of the pulse. The parameters pertaining to the various shapes are listed in Table 10.1 in Section 10.4.

10.1.3 Intensity correlations of higher order

Let us look at an intensity correlation of higher order defined as:

$$A_n(\tau) = \int_{-\infty}^{\infty} I(t) I^n(t-\tau) dt. \tag{10.4}$$

For $n > 1$, the function defined by Eq. (10.4) has the same symmetry as the pulse. In fact, for a reasonably peaked function $I(t)$, $\lim_{n\to\infty} I^n(t) \propto \delta(t)$, and the shape of the correlation $A_n(\tau)$ approaches the pulse shape $I(t)$. Such higher order correlations are convenient and powerful tools to determine intensity profiles.

10.2 Interferometric correlations

10.2.1 General expression

We have analyzed in Chapter 2 the Michelson interferometer, and defined the field[1] correlation measured by that instrument as:

$$G_1(\tau) = \tilde{A}_{12}^{+}(\tau) + c.c = \frac{1}{4}\int_{-\infty}^{\infty} \tilde{\mathcal{E}}_1(t)\tilde{\mathcal{E}}_2^{*}(t-\tau)e^{i\omega_\ell \tau} dt + c.c. \tag{10.5}$$

We have seen also [Eq. (2.6)] that the Fourier transform of $A_{12}^{+}(\tau)$ is equal to $\tilde{E}_1^{*}(\Omega)\tilde{E}_2(\Omega)$. Hence, the Fourier transform of the autocorrelation (identical fields) is proportional to the spectral intensity of the pulse. Therefore, a first order field autocorrelation does not carry any other information than that provided by a spectrometer.

In a Michelson interferometer, let us add to the detector a second harmonic generating crystal (type I) and a filter to eliminate the fundamental. Instead of the

[1] The field correlation is often referred to as a first order correlation.

expression (10.5), the detected signal is a second order interferometric correlation, proportional to the function:

$$G_2(\tau) = \int_{-\infty}^{\infty} \left\langle \left| [E_1(t-\tau) + E_2(t)]^2 \right|^2 \right\rangle dt \tag{10.6}$$

Here $\langle\rangle$ denotes averaging over the fast oscillations of the electric field and the integral stands for integration over the pulse envelope. A Mach-Zehnder interferometer can also be substituted for a Michelson interferometer for such a measurement [2]. Replacing the fields by the usual envelope and phase functions, $E_{1,2} = (\mathcal{E}_{1,2} e^{i\omega_\ell t} e^{i\varphi_{1,2}} + c.c.)/2$ and performing the $\langle\rangle$ average yields for the correlation apart from a constant factor:

$$G_2(\tau) = A(\tau) = A_0(\tau) + \mathrm{Re}\left[A_1(\tau) e^{-i\omega_\ell \tau}\right] + \mathrm{Re}\left[A_2(\tau) e^{-2i\omega_\ell \tau}\right], \tag{10.7}$$

where

$$A_0(\tau) = \int_{-\infty}^{\infty} \left[\mathcal{E}_1^4(t-\tau) + \mathcal{E}_2^4(t) + 4\mathcal{E}_1^2(t-\tau)\mathcal{E}_2^2(t)\right] dt \tag{10.8}$$

$$A_1(\tau) = 4 \int_{-\infty}^{\infty} \mathcal{E}_1(t-\tau)\mathcal{E}_2(t)\left[\mathcal{E}_1^2(t-\tau) + \mathcal{E}_2^2(t)\right] e^{i[\varphi_1(t-\tau) - \varphi_2(t)]} dt \tag{10.9}$$

$$A_2(\tau) = 2 \int_{-\infty}^{\infty} \mathcal{E}_1^2(t-\tau)\mathcal{E}_2^2(t)\, e^{2i[\varphi_1(t-\tau) - \varphi_2(t)]} dt. \tag{10.10}$$

The purpose of the decomposition (10.7) is to show that the correlation has three frequency components[2] centered respectively around zero frequency, around ω_ℓ and $2\omega_\ell$. Most often, the detection system of the correlator will act as a low pass filter, eliminating all but the first term of the expansion. The interferometric correlation reduces then to $A_0(\tau)$ – the sum of a background term and the (background-free) intensity correlation [labelled $A_c(\tau)$ in Eq. (10.1)]. The terms A_0, A_1 and A_2 of the expansion (10.7) can be extracted from a measurement by taking the Fourier transform of the data, identifying the cluster of data near the three characteristic frequencies, and recovering them by successive inverse Fourier transforms. Fast data acquisition and processing can also perform this task in real-time when working with fs oscillators [3]. The components A_1 and A_2 contain phase terms $[\varphi_1(t-\tau) - \varphi_2(t)]$, and thus carry information about pulse chirp.

Similarly the third-order interferometric correlation

$$G_3(\tau) = B(\tau) = \int \left\langle \left| [E_1(t-\tau) + E_2(t)]^3 \right|^2 \right\rangle dt \tag{10.11}$$

[2]Here "frequency" refers to the variation of the function $G_2(\tau)$ as a function of its argument τ. The latter argument τ is the delay parameter which is continuously tuned in the correlation measurement.

has four frequency components. In terms of pulse envelopes and phases it can be written as

$$B(\tau) = B_0(\tau) + \mathrm{Re}\left[B_1(\tau)e^{-i\omega_\ell\tau}\right] + \mathrm{Re}\left[B_2(\tau)e^{-2i\omega_\ell\tau}\right] + \mathrm{Re}\left[B_3(\tau)e^{-3i\omega_\ell\tau}\right], \quad (10.12)$$

where

$$B_0(\tau) = \int\left\{\mathcal{E}_1^6(t-\tau) + \mathcal{E}_2^6(t) + 9\mathcal{E}_1^2(t-\tau)\mathcal{E}_2^2(t)\left[\mathcal{E}_1^2(t-\tau) + \mathcal{E}_2^2(t)\right]\right\}dt \quad (10.13)$$

$$B_1(\tau) = 6\int\left[\mathcal{E}_1^4(t-\tau) + \mathcal{E}_2^4(t) + 3\mathcal{E}_1^2(t-\tau)\mathcal{E}_2^2(t)\right]\times \times\mathcal{E}_1(t-\tau)\mathcal{E}_2(t)\, e^{i\left[\varphi_1(t-\tau)-\varphi_2(t)\right]}\,dt \quad (10.14)$$

$$B_2(\tau) = 6\int\left[\mathcal{E}_1^2(t-\tau) + \mathcal{E}_2^2(t)\right]\mathcal{E}_1^2(t-\tau)\mathcal{E}_2^2(t)\, e^{2i\left[\varphi_1(t-\tau)-\varphi_2(t)\right]}\,dt \quad (10.15)$$

$$B_3(\tau) = 2\int\mathcal{E}_1^3(t-\tau)\mathcal{E}_2^3(t)\, e^{3i\left[\varphi_1(t-\tau)-\varphi_2(t)\right]}\,dt. \quad (10.16)$$

Again we have omitted a constant factor. The zero frequency component of this interferometric correlation, $B_0(\tau)$, corresponds to the third-order intensity correlation with background.

10.2.2 Interferometric autocorrelation

General properties

Let us consider in more detail the particular case of the expressions for the cross-correlation (10.6) through (10.10) where the two fields $E_1 = E_2 = E$. At $\tau = 0$, the peak value of the function $A(\tau = 0) = 16\int\mathcal{E}^4(t)dt$. For large delays compared to the pulse duration, cross products containing terms with $\mathcal{E}(t-\tau)\mathcal{E}(t)$ vanish, leaving a background of $A(\tau = \infty) = 2\int\mathcal{E}^4(t)dt$. The peak to background ratio for the interferometric autocorrelation is thus 8 to 1. The "d.c." term of the interferometric autocorrelation, $A_0(\tau)$, — which is in fact an intensity autocorrelation — has a peak to background of 3 to 1. The measurement leading to $A_0(\tau)$ is generally referred to as the *intensity autocorrelation with background*, as opposed to the *background free autocorrelation* leading to the expression $A_c(\tau)$ (10.1).

The fourth term of the expansion of Eq. (10.7) can be regarded as a correlation of the second harmonic fields. In the absence of phase modulation — i.e., for bandwidth limited pulses — this function is identical to the intensity autocorrelation. This property has been exploited to determine if a pulse is phase modulated or not [4].

As any autocorrelation, the interferometric autocorrelation is a symmetric function. However, as opposed to the intensity autocorrelation, it contains phase information. The shape and phase sensitivity of the interferometric autocorrelation can be exploited to:

1. *qualitatively* test the absence or presence of phase modulation, and eventually determine the type of modulation,

2. quantitatively measure a *linear* chirp,

3. determine, in combination with the pulse spectrum and linear filtering, the pulse shape and phase by fitting procedures (see Section 10.4).

Linearly chirped pulses

The sensitivity of the interferometric autocorrelation to chirp is well illustrated by the experimental recordings made with the beam from a Ti:sapphire laser in Ref. [5]. The lower and upper envelopes of the interference pattern split evenly from the background level in Fig. 10.1 pertaining to an unchirped 45 fs pulse. In the case of a phase modulated pulse as in Fig. 10.2, the interference pattern is much narrower than the pulse intensity autocorrelation. The wings of the interferometric autocorrelation are identical to those of the intensity autocorrelation. The level at which the interference pattern starts relative to the peak (2.8/8 in the case of Fig. 10.2) is a measure of the chirp, as explained below.

A simple tabulation of the chirp can be made by considering a linearly chirped Gaussian pulse ($\mathcal{E}(t) = \exp\left[-(1+ia)(t/\tau_G)^2\right]$), for which the interferometric autocorrelation can be determined analytically:

$$\begin{aligned} G_2(\tau) &= \left\{1+2\exp\left[-\left(\frac{\tau}{\tau_G}\right)^2\right]+4\exp\left[-\frac{a^2+3}{4}\left(\frac{\tau}{\tau_G}\right)^2\right]\cos\left[\frac{a}{2}\left(\frac{\tau}{\tau_G}\right)^2\right]\right. \\ &\quad \left.\times\cos(\omega_\ell\tau)+\exp\left[-(1+a^2)\left(\frac{\tau}{\tau_G}\right)^2\right]\cos 2\omega_\ell\tau\right\} \end{aligned} \tag{10.17}$$

A graphical representation of the upper and lower envelopes as a function of the chirp parameter a is shown in Fig. 10.3. Comparison of Figs. 10.2 and 10.3 indicate a chirp parameter of roughly $a = 20$ for the experimental pulse. This is of course only an approximation, but it gives a good estimate of the magnitude of the frequency modulation near the pulse center.

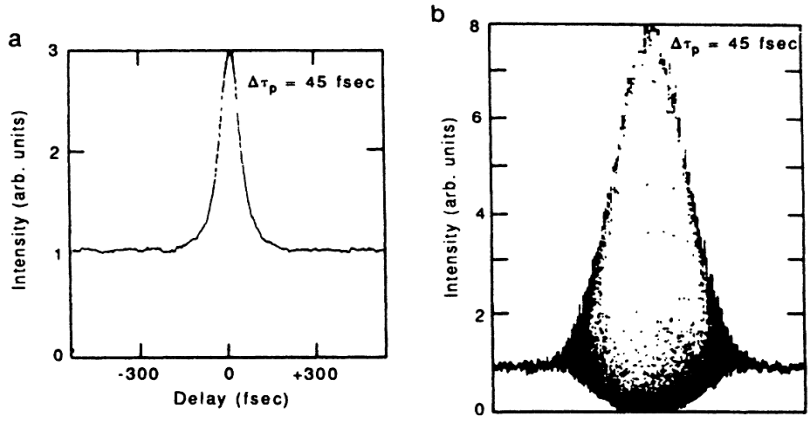

Figure 10.1: Intensity (with background) (a) and interferometric (b) autocorrelation traces of a mode-locked Ti:sapphire laser pulse after extracavity pulse compression. Note the peak to background ratios of 3/1 and 8/1 for the intensity and interferometric autocorrelations, respectively (from [5]).

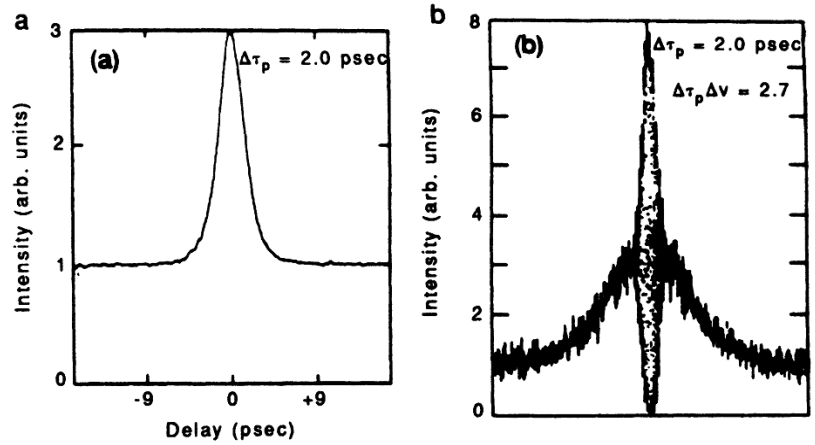

Figure 10.2: Intensity (a) and interferometric (b) autocorrelation traces of a mode-locked phase modulated Ti:sapphire laser pulse (from [5]).

Averaging over the pulse train

Most often, measurements are an average over a pulse train. It has been demonstrated by Van Stryland [6] that the intensity autocorrelation of pulses with a statistical distribution of pulse durations is shaped like a double sided exponential. This is

precisely the shape of the autocorrelation of a single sided exponential pulse. The autocorrelation of the output of synchronously pumped lasers have typically such a double sided exponential shape. It would be incorrect to conclude that the pulses generated by these lasers have a single sided exponential shape. Theoretical simulations [7, 8] have indeed confirmed that fluctuations of the pulse duration along the train are at the origin of the observed autocorrelation.

A similar ambiguity exists in the case of the interferometric autocorrelation of a train of pulses. The measurement can be either interpreted as the interferometric autocorrelation of identical chirped pulses, or as the average of interferometric autocorrelations of bandwidth limited pulses of different frequencies. To illustrate this point, let us consider unchirped Gaussian pulses with a Gaussian distribution of frequencies $F(\Delta\Omega)$ centered at ω_ℓ ($\Omega = \omega_\ell + \Delta\Omega$):

$$F(\Delta\Omega) = \frac{\tau_G}{b\sqrt{\pi}} e^{-(\Delta\Omega\ \tau_G/b)^2}. \tag{10.18}$$

The total autocorrelation (averaged over many pulses at each delay) is the statistical

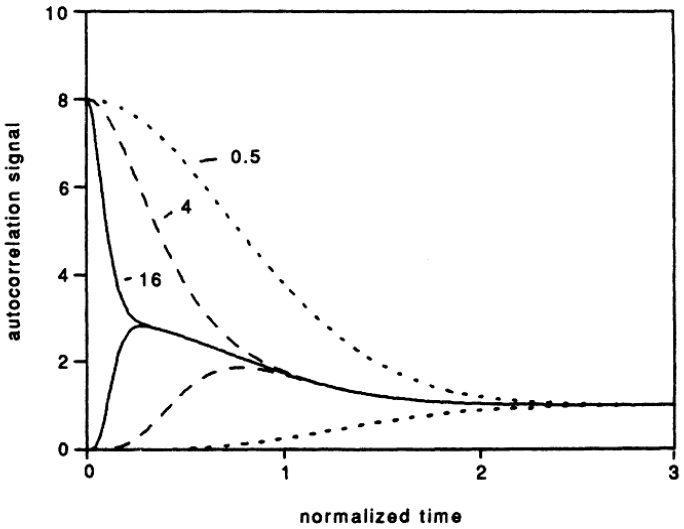

Chirp	Delay	Max. (l.e.)
2	1.30	1.161
4	0.78	1.866
6	0.59	2.278
8	0.48	2.505
10	0.41	2.639
12	0.36	2.725
14	0.32	2.783
16	0.29	2.824
18	0.26	2.855
20	0.24	2.878

Figure 10.3: Interferometric autocorrelations of Gaussian pulses $\tilde{\mathcal{E}}(t) = \exp\{-(1 + ia)(t/\tau_G)^2\}$ for various values of the linear chirp parameter a. The upper and lower envelopes of the autocorrelations are plotted for 3 values of the chirp parameter a. The upper and lower envelopes merge with the intensity autocorrelation. The table on the right shows the position (delay and value) of the maxima of the lower envelope (l.e.) of the interferometric autocorrelation as a function of chirp parameter a.

average of the autocorrelations at each frequency Ω:

$$G_2(\tau) = \int_{-\infty}^{\infty} \left\{ 1 + 2\exp\left[-\left(\frac{\tau}{\tau_G}\right)^2\right] + 4\exp\left[-\frac{3}{4}\left(\frac{\tau}{\tau_G}\right)^2\right]\cos\Omega\tau + \exp\left[-\left(\frac{\tau}{\tau_G}\right)^2\right]\cos 2\Omega\tau \right\} F(\Delta\Omega)d\Omega. \quad (10.19)$$

The integration over frequency can easily be performed. For small chirps, we can make the approximation in Eq. (10.17) that $\cos[\frac{a}{2}(\frac{\tau}{\tau_G})^2] \approx 1$. The equation obtained after substitution of (10.18) into Eq. (10.19) and subsequent integration is undistinguishable from Eq. (10.17) for $b = a$. Therefore, it is important to verify that the pulse train is constituted of *identical* pulses, in amplitude (energy), duration and frequency. It is relatively easy to check whether the pulses have constant energy and duration by displaying simultaneously the fundamental and the second harmonic of the pulse train. If both show no fluctuation, it can be said with reasonable certainty that the intensity autocorrelation represents pulses having the same energy and duration. It can be verified that there are no pulse to pulse variation in frequency by displaying the pulse train on an oscilloscope, after transmission through a spectrometer or reflection off a thin ($\ll 100\,\mu$m) etalon.

10.3 Measurement techniques

10.3.1 Nonlinear optical processes for measuring fs pulse correlations

In ultrafast optics, second harmonic generation is the most widely used technique for recording second order correlations. Because it is a nonresonant process of electronic origin, the nonlinearity is fast enough to measure pulses down to $10^{-14}s$ duration. While applicable through the IR and visible spectrum, the method is limited at short wavelength ($\lambda < 380$ nm) by the UV absorption edge of optical crystals. Techniques that have been used successfully for shorter wavelengths include multi-photon ionization [9] surface second harmonic generation [10], and two-photon luminescence [11]. Third order processes such as the optical Kerr effect have also been applied to the diagnostic of fs UV pulses [12–14]. These third-order correlations, as discussed in Section 10.1.3, have the additional advantage of being sensitive to pulse asymmetry. Photodetectors excited by a multi-photon absorption [15–18] are also convenient tools for correlation measurements as they produce a signal (current) that can be processed directly unlike most other nonlinear optical techniques.

10.3.2 Recurrent signals

It is assumed here that we have an ensemble of identical fs pulses, so that the correlations can be constructed from a large number of measurements taken for different delay parameters τ.

An example of a simple second order correlator is sketched in Fig. 10.4(a). The beams to be correlated are cross-polarized, and combined with a polarizing beam splitter. An optical delay is used to adjust the delay of the reference signal $I_r(t-\tau)$. The cross-polarized beams are sent orthogonally polarized into a nonlinear crystal phase matched for type II second harmonic generation. If the conditions outlined below are satisfied, the second harmonic signal is proportional to the function $A_c(\tau)$ defined in Eq. (10.1). This measurement — or function — is generally referred to as the "background-free" correlation, as opposed to the correlation with background. The latter is obtained by frequency-doubling the output of a Michelson interferometer (parallel polarization) in a crystal phase matched for type I second harmonic generation. An alternate technique to generate $A_c(\tau)$ is to use beams with parallel polarization intersecting in a nonlinear crystal. The "background free" signal is the second harmonic generated with wave vector $\mathbf{k_2}$ along the bisector of the two wave vectors $\mathbf{k}_s$ and $\mathbf{k}_r$. The crystal orientation has to satisfy the phase matching condition $\mathbf{k_2} = \mathbf{k}_s + \mathbf{k}_r$.

With either background-free techniques, the second harmonic field is proportional to the product of the fundamental fields:

$$\mathcal{E}_{SHG}(\Omega) = \eta(\Omega)\mathcal{E}_s(\Omega)\mathcal{E}_r(\Omega), \tag{10.20}$$

or, for the spectral intensities:

$$I_{SHG}(\Omega) = \frac{2\mu_0 c}{n}|\eta(\Omega)|^2 I_s(\Omega)I_r(\Omega). \tag{10.21}$$

In order for the instrument sketched in Fig. 10.4 to measure the true cross or autocorrelation, it is essential that the second harmonic conversion efficiency $\eta(\Omega)$ be a constant over the frequency range of the combined pulses. Another way to express the same condition is to state that the effective crystal length should be shorter than the coherence length of harmonic generation over the pulse bandwidth (cf. Chapter 3). The "effective length" can be either the physical crystal thickness, the Rayleigh range ρ_0 of the focused fundamental beams, or the overlapping region of the fundamental pulses in a noncolinear geometry. The shorter the crystal, the broader the bandwidth over which phase matched harmonic conversion is obtained, but the lower the conversion efficiency. There is clearly a compromise to be reached between bandwidth and sensitivity. In Eq. (10.21), the bandwidth efficiency factor $\eta(\Omega)$ includes only the frequency dependence of the phase matching condition, and

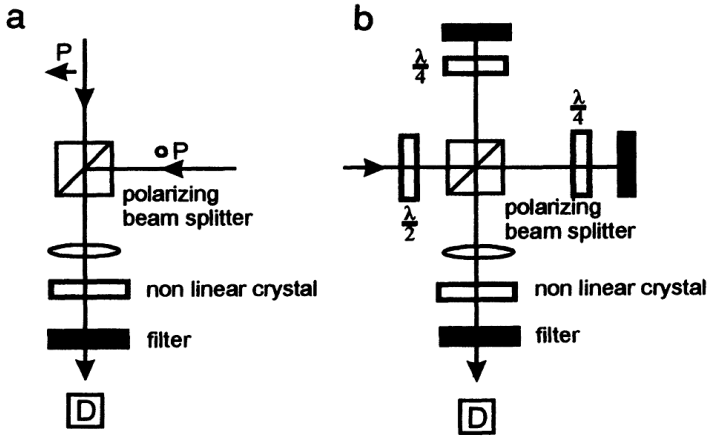

Figure 10.4: (a) Basic intensity cross-correlator, using second harmonic type II detection. A polarizing beam-splitter cube combines the beams to be correlated. The second harmonic signal generated by the crystal is proportional to the product of the fundamental intensities along the two orthogonal directions of polarization. The sketch on the right side, (b), shows a simple autocorrelator using the same type of detection. The same "recombining" polarizing beamsplitter cube can be used to split the beams into the two arms of the interferometer. Two quarter wave plates are used to rotate the polarization of the beam reflected by the mirrors of the two delay arms by 90^o.

not a finite response time for the harmonic generation process. It is assumed here that the response time of the second harmonic process is much shorter than the pulses to be measured, which is a reasonable assumption since the second order nonlinearity of wide bandgap crystals is a nonresonant electronic process.

Provided the pulses can be approximated by a Gaussian, a simple test can be performed to determine whether the proper focusing and crystal thickness has been chosen. In the case of the autocorrelation [Fig. 10.4(b)], a standard spectrometer (a 25 cm spectrometer is generally sufficient) is used to record the spectral intensities of the fundamental and second harmonic [2]. In case of perfect phase matchingg and zero dispersion, and for a conversion efficiency independent of frequency, the ratio of second harmonic to the *square* of the fundamental spectral intensity will be a constant in the case of Gaussian pulses, according to Eq. (4.27). The spectrum of the second harmonic will be narrower than the squared fundamental spectrum if the effective crystal length is too long. As a consequence of the second harmonic conversion efficiency being frequency dependent, the measured correlation width will be longer than the exact correlation length.

The background-free autocorrelation function A_c [Eq. (10.1)] for a fluctuating cw signal consists of a symmetric "bump" riding on an infinite background (Fig 10.5). The width of the bump is a measure of the temporal width of the fluctuations, and the contrast ratio (peak-to-background ratio of A_c) is a measure of the modulation depth. A 100% modulation depth results in a peak-to-background ratio of 2 to 1 [19]. Any "background free" signal of finite duration results in a function A_c of finite width [Fig 10.5(c)]. If that signal has some fine structure (amplitude modulation), a narrow spike will appear in the middle of the correlation function [Fig 10.5(d)]. This is the coherence spike, typical of a signal consisting of a burst of *amplitude* noise [20]. These considerations do not apply to the phase content or phase coherence of the pulse: the intensity correlations are the same whether the pulse is at a fixed carrier frequency, or has a random or deterministic frequency modulation.

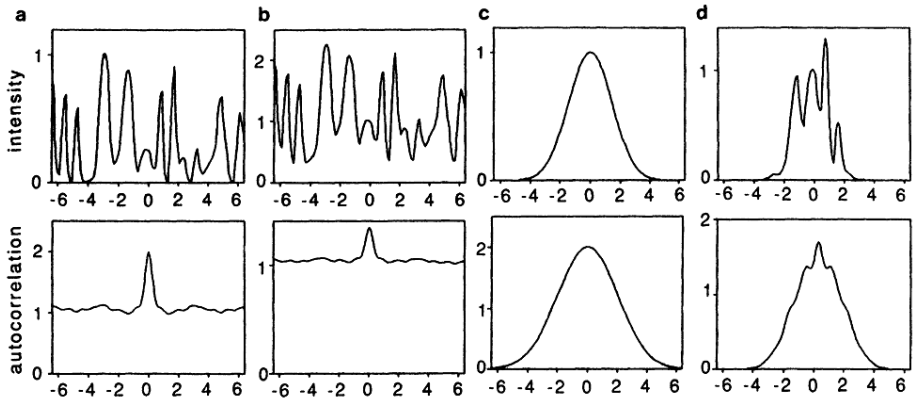

Figure 10.5: Some typical waveforms (intensity versus time) (top) and corresponding intensity autocorrelation $A_c(\tau)$ (bottom). From left to right: (a) continuous signal with 100 % amplitude modulation; (b) noisy cw signal; (c) pulse; and (d) noisy pulse.

10.3.3 Single shot measurements

Not all lasers provide a train of identical pulses and/or work at high repetition rate. Pulse to pulse fluctuation can be particularly severe in oscillator-amplifier systems. Single shot autocorrelators are therefore highly desirable. We will discuss in this section the simplest single shot autocorrelators. More sophisticated instruments for single shot amplitude and phase retrieval will be described in Section 10.4.

Intensity autocorrelators

One of the first intensity autocorrelators for mode-locked lasers was a single shot instrument [21]. The beam to be measured is split in two beams, which are thereafter sent with opposite propagation vector into a nonlinear medium. The first autocorrelator was based on two photon excitation rather than second harmonic generation: the medium (for instance a dye solution) was selected for its large two photon absorption and subsequent fluorescence. Because of the larger optical field in the region where the two counterpropagating pulses collide, the observed pattern of two-photon fluorescence essentially displays the intensity autocorrelation (with background). Because of the higher conversion efficiency of SHG, two-photon fluorescence is not widely used in the fs time scale, except in the UV, where no transparent nonlinear crystals can be found. To circumvent the difficulty of spatially resolving the μm size of the two-photon fluorescence trace, the beams are made to intersect at a small angle, thereby magnifying the fluorescence trace [11, 22].

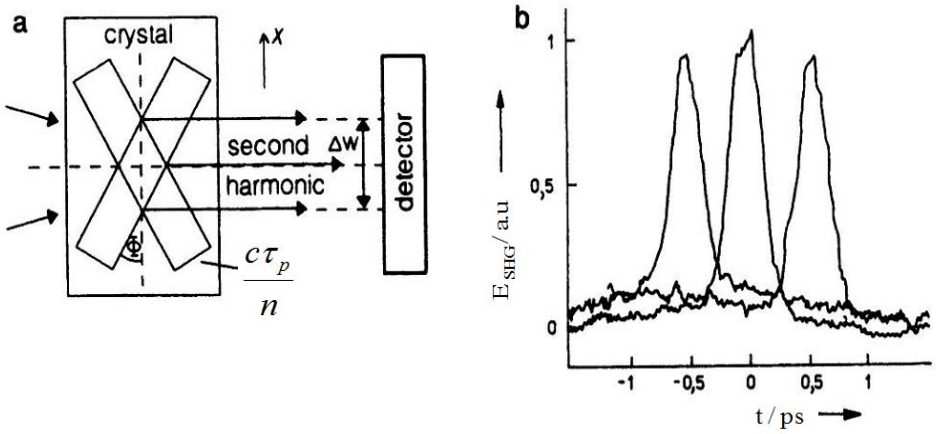

Figure 10.6: (a) Basic principle of the single shot autocorrelator of Jansky *et al* [23]. The nonlinear crystal is oriented for phase matched type I SHG for two beams intersecting at an angle 2Φ. Arrows indicate the propagation direction of the fundamental and the second harmonic (z direction). (b) Typical recording for a 250 fs pulse. Temporal calibration is made by recording the shift of the trace resulting from insertion of a 0.36 mm glass plate in either arm of the autocorrelator (from [24]).

Single shot autocorrelators using SHG have also been designed. In an arrangement developed for ps pulses by Jansky *et al.* [23] and Gyuzalian *et al.* [25], the autocorrelation in time is transformed into a spatial intensity distribution. This method has been applied by numerous investigators to the fs scale [24, 26, 27]. The

instrument is a typical non-colinear second harmonic autocorrelator. The nonlinear crystal is oriented for phase matched type I SHG for two beams intersecting at an angle 2Φ [Fig. 10.6(a)]. Provided the beam waist in the overlap region w_0 is much larger than the pulse length $v_g\tau_p$, the intensity distribution across the second harmonic beam corresponds to the intensity autocorrelation function. Cylindrical focusing, and a linear array detector can be used to capture the intensity profile of the autocorrelation. A typical measurement is shown in Fig. 10.6(b). The width of the autocorrelation function $\Delta\tau_a$ is proportional to the diameter Δw of the second harmonic beam:

$$\Delta w = \frac{\Delta\tau_a v_g}{\sin\Phi}. \tag{10.22}$$

Let us consider the projection of the two intersecting beams on axis z (along the direction of propagation) and x (the orthogonal direction). The components of the pulse envelope are co-propagating along the z direction, counterpropagating along the x axis. For a pulse with a temporal profile $\tilde{\mathcal{E}}(t)$, the component of the two envelopes propagating along the x direction are $\tilde{\mathcal{E}}_x = \tilde{\mathcal{E}}(t - x/L_x)$ and $\tilde{\mathcal{E}}_{-x} = \tilde{\mathcal{E}}(t + x/L_x)$ with $L_x = v_g/\sin\Phi$. The second harmonic intensity along the x direction is proportional to the product $\tilde{\mathcal{E}}_x\tilde{\mathcal{E}}_{-x}$ [23]. If we consider for instance a linearly chirped Gaussian pulse, the second harmonic just behind the crystal is also a Gaussian:

$$\tilde{\mathcal{E}}_{SHG}(t) \propto \exp\left[-2\left(\frac{t^2}{\tau_G^2} + \frac{x^2\sin^2\Phi}{v_g^2\tau_G^2}\right)\left(1 + i\frac{a}{2}\right)\right]. \tag{10.23}$$

The spatial dependence of the SH intensity is indeed an intensity autocorrelation, expanded transversely by the factor $1/\sin\Phi$. As noted by Jansky *et al.* [23] and further investigated by Danielius *et al.* [28], the spatial phase dependence of the second harmonic field indicates that the wavefront is no longer a plane wave, but has a (cylindrical) curvature proportional to the chirp parameter a. Referring to Gaussian beam propagation Eq. (**??**), the curvature is approximately $R = k_\ell v_G^2\tau_G^2/(2a\sin^2\Phi)$.

An analysis of the beam propagation after the crystal can be made by spatial Fourier transforms, starting with the wave equation in the retarded frame Eq. (1.189):

$$\frac{\partial}{\partial z}\tilde{\mathcal{E}}_{SHG} = -\frac{i}{2k_\ell}\frac{\partial^2}{\partial x^2}\tilde{\mathcal{E}}_{SHG}. \tag{10.24}$$

Taking the Fourier transform along the transverse spatial coordinate x and integrating along the propagation direction z:

$$\tilde{\mathcal{E}}_{SHG}(k_x, z, t) = \tilde{\mathcal{E}}_{SHG}(k_x, z = 0, t)e^{\frac{i}{2k_\ell}k_x^2 z}. \tag{10.25}$$

Taking the inverse Fourier transform leads to the field distribution after a propagation distance z:

$$\tilde{\mathcal{E}}_{SHG}(x, z, t) = \int_{-\infty}^{\infty}\tilde{\mathcal{E}}_{SHG}(k_x, z = 0, t)e^{-ik_x x}e^{\frac{i}{2k_\ell}k_x^2 z}dk_x. \tag{10.26}$$

Assuming that the overlapping region is short enough to produce an undistorted second harmonic, as discussed in Chapter3, the second harmonic field at the end of the crystal is:

$$\tilde{\mathcal{E}}_{SHG}(x, z = 0, t) = \eta \tilde{\mathcal{E}}\left(t - \frac{x}{L_x}\right)\tilde{\mathcal{E}}\left(t + \frac{x}{L_x}\right), \tag{10.27}$$

where η is the proportionality factor of Eq. (10.20) assumed to be constant over the frequency range of interest. Taking the Fourier transform gives us the function $\tilde{\mathcal{E}}_{SHG}(k_x, z = 0, t)$ to be inserted in Eq. (10.26):

$$\tilde{\mathcal{E}}_{SHG}(k_x, z = 0, t) = \int \eta e^{ik_x x} \tilde{\mathcal{E}}\left(t - \frac{x}{L_x}\right)\tilde{\mathcal{E}}\left(t + \frac{x}{L_x}\right) dx. \tag{10.28}$$

The spatial distribution given by Eq. (10.26) focuses after a distance z_F for which the phase factor $(i/2k_\ell)k_x^2 z_F$ compensates the phase factor due to chirp in Eq. (10.23). It is possible to reconstruct the chirp by matching the intensity distributions measured at $z = 0$ and $z = z_F$ to the distributions calculated with help of Eqs. (10.24) through (10.28).

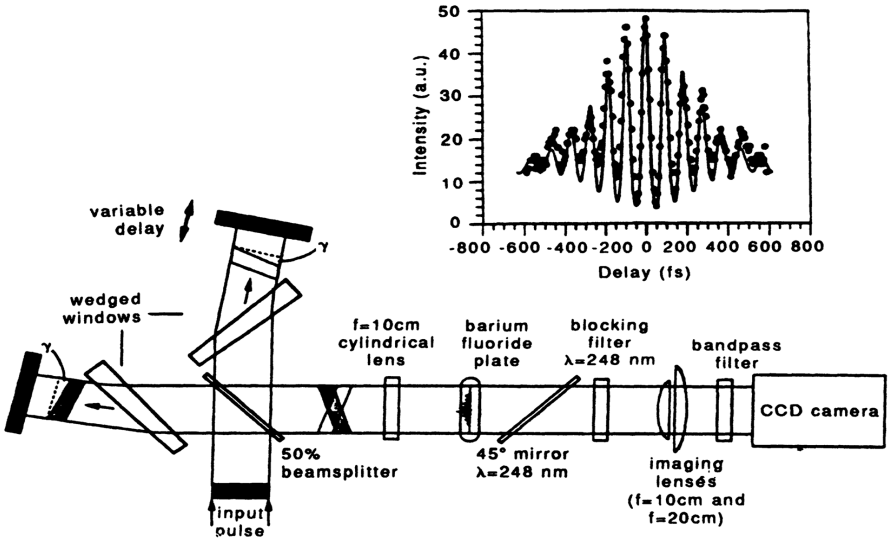

Figure 10.7: Sketch of the single shot interferometric autocorrelator using prisms (or wedged windows) to transfer the delay to the transverse coordinate of the beam, and typical recording of a 250 fs UV pulse. To record fs pulses, the angle of the prisms should not exceed a few degrees. The fringe spacing is adjusted by the tilt of a mirror in one arm of the autocorrelator (from [22]).

Interferometric autocorrelator

By recording the spatial profile of the second harmonic with interferometric accuracy, Salin *et al.* [29] showed that it was actually possible to record an interferometric autocorrelation. Because of diffraction effects, as explained earlier, the method is difficult to implement, and usually does not provide a recording with an 8 to 1 peak to background contrast. Simpler methods are available, making use of the tilt in energy front introduced by a dispersive element. We have seen in Chapter 2 that the energy front is tilted with respect to the wavefront by a prism (or any other element introducing angular dispersion). As shown by Szabo *et al* [30], this property can be exploited to provide a variable delay along a transverse coordinate of the beam. A glass wedge is inserted in one or both arm(s) of a Michelson type autocorrelator (Fig. 10.7). As in the previous method, the spatial (transverse) distribution of second harmonic is proportional to the pulse intensity autocorrelation. Obtaining such an intensity autocorrelation, however, assumes that the beams coming from both arms of the correlator add constructively towards the detector, destructively towards the source. Such a condition is difficult to implement, because it requires sub-wavelength stability and accuracy in controlling either arm. For this particular correlator, it is more convenient to introduce a small tilt of either end mirror of the Michelson interferometer. Such a tilt produces a pattern of parallel fringes at the output. Before the frequency doubling crystal, we have thus generated a first order correlation. The second harmonic of such a first order correlation is an interferometric correlation [22]. This arrangement has the advantage that one has complete control over the spacing of the fringes, which can be adjusted to accommodate the spatial resolution of the array detector used in this measurement. An example of an interferometric autocorrelation obtained with a fs UV pulse is shown in Fig. 10.7. For this particular case, the nonlinearity is two-photon fluorescence in BaF_2.

10.4 Pulse amplitude and phase reconstruction

10.4.1 Introduction

Since the second order autocorrelations are symmetric, and do not provide any information about the pulse asymmetry, either an additional measurement or a new technique is required to determine the signal shape. We will start with simple methods that complement the information of the autocorrelations, and proceed with an overview of various methods that have been introduced to provide amplitude and phase information on fs signals. The ideal diagnostic instrument is obviously one that would give a real time display of all pulse parameters. Because of the

ambiguity associated with an average over a large number of pulses, a single shot method is also desirable. The challenge in fs pulse characterization is that a tempo-

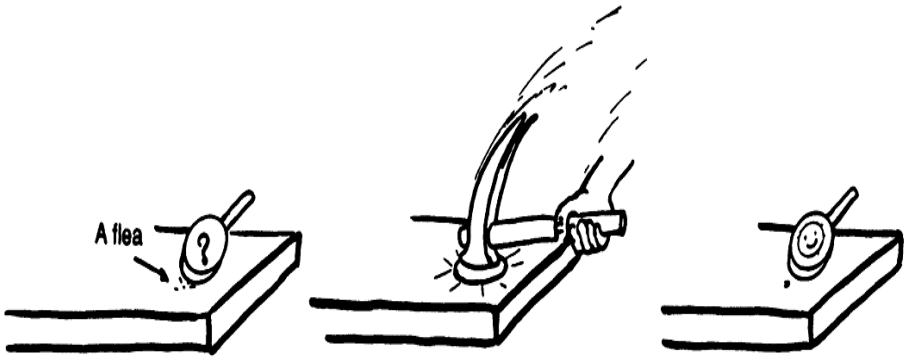

Figure 10.8: Applying a transfer function (b) to magnify the object (a) to be observed. The original object can be reconstructed by applying the inverse transfer function to the observed figure (c).

ral resolution is needed that is faster than the pulse itself. The solution, as sketched in Fig. 10.8, is to apply a transfer function to "expand" the signal. From the knowledge of the transfer function and the "expanded" signal the shape of the original object is recovered.

As introduced in Chapter 1 a light pulse in the time domain is characterized by its electric field

$$E(t) = \frac{1}{2}\mathcal{E}(t)e^{i\varphi_0}e^{i\varphi(t)}e^{i\omega_\ell t} + c.c. \tag{10.29}$$

In this section we are concerned with the retrieval of the pulse envelope $\mathcal{E}(t)$ and the time-dependent phase $\varphi(t)$ only. The measurement and control of the absolute phase φ_0 are described in Chapter 14.

More than 30 years ago Treacy measured a "sonogram" of ps pulses [31]. It took more than a decade before its importance for the full-field characterization of fs pulses was recognized [32]. Phase and amplitude of a pulse stretched in an optical fiber was measured using a cross correlation with a short sample pulse (compressed output pulse) [33] using an interferometric technique.

Early on methods based on interferometric autocorrelations and the pulse spectrum were developed to retrieve the complex field [2, 4, 34]. Efforts to use the pulse spectrum in conjunction with some kind of (nonlinear) correlation have been pursued [35–37].

With the development of more reliable and powerful fs lasers in the 90's a variety of other pulse characterization schemes have been discussed and demonstra-

ted [38–46]. While some rely on matching the measurements with a complex pulse amplitude iteratively, others permit a direct reconstruction. In the past decade, two techniques have emerged as most successful and versatile for a variety of different application scenarios - frequency-resolved optical gating (FROG) [14] and spectral phase interferometry for direct electric field reconstruction (SPIDER) [47].

In the next section we will discuss the general requirements on an experimental apparatus to retrieve amplitude and phase of ultrashort light pulses. In Section 10.4.3 we will review techniques based on the measurement of pulse correlations and spectrum with subsequent fitting. FROG and SPIDER will be introduced in Sections 10.4.4 and 10.4.5, respectively.

10.4.2 Methods for full-field characterization of ultrashort light pulses

Walmsley et al. [48, 49] used an elegant approach to discuss the general requirements on measurement techniques that permit the retrieval of both amplitude and phase of short light pulses. A necessary and sufficient condition is that the instrument contains at least one time-nonstationary and one time-stationary element. Four interferometric and four non-interferometric [49] schemes that consist of a minimal number of filters exist that satisfy these requirements. The detector is assumed to be time-integrating, that is, it has "zero" bandwidth.

Time-stationary filters whose output do not depend on the arrival time of the pulse act on the pulse field according to

$$E_{out}(t) = \int S(t-t')E_{in}(t')dt'. \tag{10.30}$$

Examples are passive devices such as mirrors, gratings, spectrometers, and dispersive delay lines. Time-nonstationary (or frequency stationary) filters produce an output that does not change with arbitrary spectral shifts of the input

$$E_{out}(\Omega) = \int N(\Omega-\Omega')E_{in}(\Omega')d\Omega'. \tag{10.31}$$

Examples are shutters, which may be controlled externally or by the light pulse itself.

Each of the two filter classes can be further divided into phase-only (P) and amplitude-only (A) filters. Examples of corresponding filter functions are:

$$N_A(t,\tau) = e^{-\Gamma^2(t-\tau)^2} \tag{10.32}$$

$$N_P(t,a) = e^{iat^2} \tag{10.33}$$

$$S_A(\Omega,\omega_c) = e^{-(\Omega-\omega_c)^2/\gamma^2} \tag{10.34}$$

$$S_P(\Omega,b) = e^{-ib\Omega^2}, \tag{10.35}$$

which represent a time gate, a phase modulator, a spectral filter, and a dispersive delay line, respectively.

In Chapter 1 we have introduced the Wigner function $\mathcal{W}$ as a convenient tool to completely characterize the field of an ultrashort pulse. It is related to the non-stationary two-time correlation function

$$C(t,t') = \left\langle E_{in}(t) E_{in}^{*}(t') \right\rangle$$

by

$$\mathcal{W}(\Omega,t) = \int dt' C\,(t+s/2, t-s/2)\, e^{i\Omega s}. \tag{10.36}$$

Note, that the correlation function C is what one could theoretically measure with a quadratic detector after a suitable set of filters. Any apparatus for complete pulse characterization must produce a function of two independent variables to carry the information about the pulse contained in $C(t,t')$ or $W(\Omega,t)$. The required two independently adjustable parameters have to be provided by the set of filters used. The detector then produces an output signal

$$D(p_i) = \int d\Omega \int dt \mathcal{W}(\Omega,t) F(\Omega,t,p_i). \tag{10.37}$$

Here F is a window function determined by the filter parameters p_i (type and sequence) of the instrument. If the window function of the apparatus is known the Wigner function (and from that the pulse parameters) can be retrieved from the measurement D. If the apparatus consists of only time-stationary (frequency-stationary filters) the window function becomes independent of time (frequency). The measured signal in these cases is the overlap of one of the marginals of the Wigner function, cf. Eqs. (1.49) and (1.50), and therefore contains no phase information. A necessary requirement for full-field reconstruction is thus the presence of at least one of either filters.

The general layout of a non-interferometric and an interferometric system is sketched in Fig. 10.9 (a) and (b) consisting of a minimum set of filters. Because the detector responds only to intensities (square in the field) only amplitude filters are meaningful elements just preceding the detector. A non-interferometric system consists of filters in sequence. In an interferometric device the pulse is split, each replica filtered separately before the combined and filtered output is detected. While FROG belongs to the first group of techniques, SPIDER is an example of an interferometric technique.

10.4.3 Retrieval from correlation and spectrum

While being always symmetric, the shape of an intensity and interferometric autocorrelation is (somewhat) sensitive to the pulse shape. It is conceivable that the

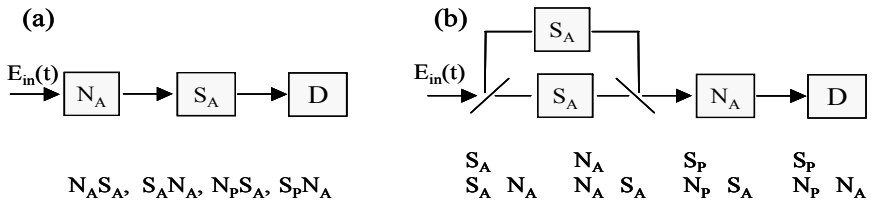

Figure 10.9: (a) Noninterferometric and (b) interferometric techniques for the measurement of amplitude and phase of short light pulses. Four possible combinations of filters (labelled by their transfer functions) are shown for each concept. Adapted from [47, 49].

pulse spectrum can complement the information provided by the symmetric second order autocorrelations, in order to determine the signal shape. As an illustration of

$\mathcal{E}^2(t)$	$\lvert\mathcal{E}(\Omega)\rvert^2$	$\tau_p\Delta\nu$	$A_c(\tau)$	τ_{ac}/τ_p	$G_2(\tau)-[1+3A_c(\tau)]$
e^{-t^2}	$e^{-\Omega^2}$	0.441	$e^{-\tau^2/2}$	1.414	$\pm e^{-(3/8)\tau^2}$
$\mathrm{sech}^2(t)$	$\mathrm{sech}^2(\frac{\pi\Omega}{2})$	0.315	$\frac{3\tau(\mathrm{ch}\tau-\mathrm{sh}\tau)}{\mathrm{sh}^3\tau}$	1.543	$\pm\frac{3(\mathrm{sh}2\tau-2\tau)}{\mathrm{sh}^3\tau}$
$[e^{t/(t-A)}+e^{-t/(t+A)}]^{-1}$					
$A=\frac{1}{4}$	$\frac{1+1/\sqrt{2}}{\mathrm{ch}\frac{15\pi}{16}\Omega+1/\sqrt{2}}$	0.306	$\frac{1}{\mathrm{ch}^3\frac{8}{15}\tau}$	1.544	$\pm4\left(\frac{\mathrm{ch}\frac{4}{15}\tau}{\mathrm{ch}\frac{8}{15}\tau}\right)^3$
$A=\frac{1}{2}$	$\mathrm{sech}\,\frac{2\pi}{4}\Omega$	0.278	$\frac{3\mathrm{sh}4x-8\tau}{4\,\mathrm{sh}^3\frac{4}{3}\tau}$	1.549	$\pm Q$
$A=\frac{3}{4}$	$\frac{1-1/\sqrt{2}}{\mathrm{ch}\frac{7\pi}{16}\Omega-1/\sqrt{2}}$	0.221	$\frac{2\mathrm{ch}4y+3}{5\mathrm{ch}^3 2y}$	1.570	$\pm4\frac{\mathrm{ch}^3 y(6\,\mathrm{ch}2y-1)}{5\,\mathrm{ch}^3 2y}$

Table 10.1: Typical pulse shapes, spectra, intensity and interferometric autocorrelations. To condense the notation, x has been substituted for $\frac{2}{3}\tau$, y for $\frac{4}{7}\tau$, ch for cosh, sh for sinh. τ_{ac} is the FWHM of the intensity autocorrelation. τ_p is the FWHM of the pulse intensity given in column 1. In the last column, $Q=\pm4[\tau\mathrm{ch}2\tau-\frac{3}{2}\mathrm{ch}^2x\mathrm{sh}x(2-\mathrm{ch}2x)]/[\mathrm{sh}^3 2x]$.

this, Table 10.1 shows analytical expressions [2] for the pulse spectrum, the intensity correlation, and the envelope of the interferometric correlation for various pulse shapes. For some typical shapes of the temporal intensity profile given in the first column, the spectral intensity (column 2) is used to compute the duration-bandwidth product $\tau_p\Delta\nu$ listed in column 3. The unit for the time t is such that the functional dependence takes the simplest form in column 1. The inverse of that time unit is used as unit of frequency Ω. The most often quoted parameter is

the ratio of the FWHM τ_{ac} of the intensity autocorrelation (column 4) to the pulse duration τ_p, and is given in column 5. Finally, the upper and lower envelopes of the interferometric autocorrelation $G_2(\tau)$ can be reconstructed from the expressions given in column 6.

As we have seen in the previous section, the interferometric autocorrelation also carries information about the pulse chirp. At the same time these correlation functions are one of the data sets that require relatively little experimental effort. It is therefore tempting to explore the feasibility of obtaining amplitude and phase of the optical pulse from such measurements. Indeed some of the earliest successful retrievals of the complex field of fs pulses were based on the simultaneous fitting of spectrum and interferometric autocorrelation [2, 4]. The reconstruction was facilitated after replacing the autocorrelation by a cross-correlation of pulses of different duration. The result of that cross-correlation approximated the longest of the two pulses. Figure 10.10 shows an example of a Michelson interferometer unbalanced with a phase-only filter (block of glass), and the recorded intensity and interferometric correlation functions.

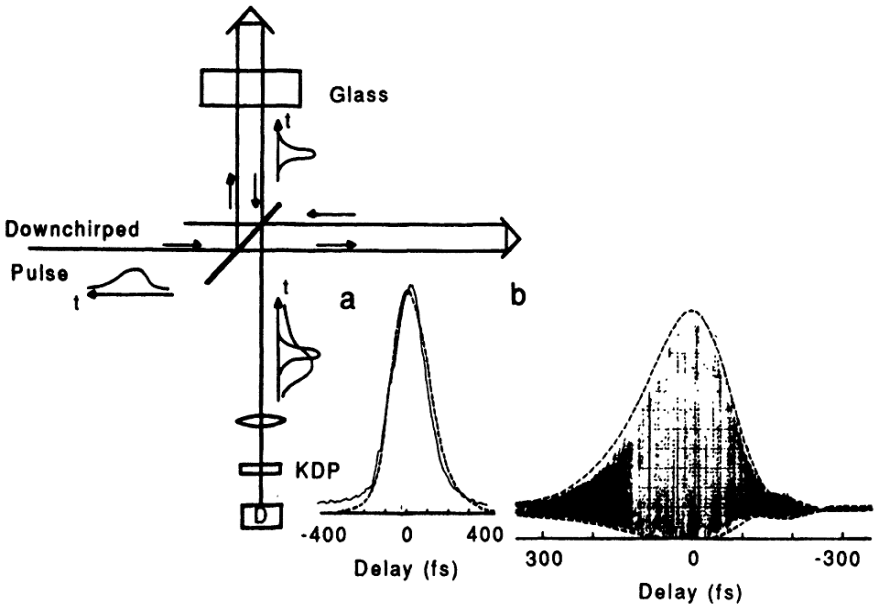

Figure 10.10: Sketch of an asymmetric correlator to record second-order correlation functions G_2 through SHG. An example of intensity (a) and interferometric (b) cross-correlation measured with this set-up is also shown. The input was an asymmetric downchirped pulse, which is compressed in the arm containing a 5-cm BK7 block. Adapted from [2].

In most cases the problem reduces to the task of measuring the pulse spectrum and suitable correlations and finding an amplitude and time-dependent phase that fits the data best. Care has to be taken to guarantee a unique retrieval, that is to avoid ambiguities hidden in the data sets (see, for example, Problem 3 at the end of this chapter). For this reason unbalanced correlators where a linear optical element of known transfer function is inserted into one arm of the correlator have been implemented [34, 36].

A possible retrieval algorithm is sketched in Fig 10.11. The pulse spectrum,

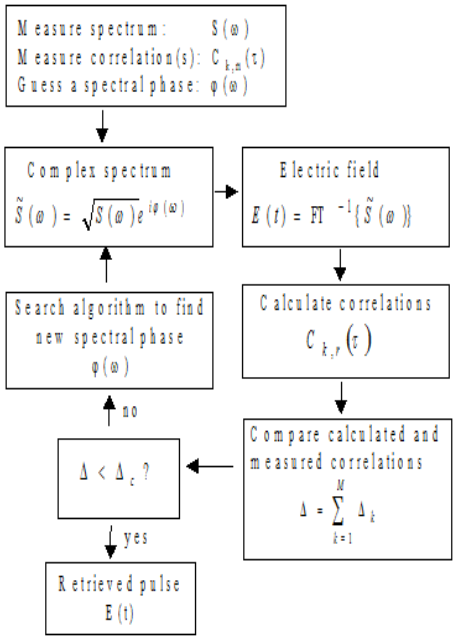

Figure 10.11: Schematic diagram of the retrieval of phase and intensity from correlation and spectrum only (PICASO) [36, 50].

$S(\Omega) = |\mathcal{E}(\Omega)|^2$, and a pulse correlation of type k or an ensemble of M correlations, $C_{k,m}$ are measured. The retrieval starts by guessing a spectral phase, $\varphi(\Omega)$, which combined with the measured spectrum results in an initial pulse $\sqrt{S(\Omega)}e^{i\varphi(\Omega)}$. This pulse is used to calculate the correlation(s) $C_{k,r}(\tau_i)$ that are recorded in the measurement. A root mean square deviation of measured and calculated correlation can be defined by

$$\Delta_k = \sum_{k=1}^{M} \sqrt{\frac{1}{N}\sum_{i=1}^{N}[C_{k,r}(\tau_i) - C_{k,m}(\tau_i)]^2}, \tag{10.38}$$

which serves as the figure of merit to be minimized during the search. The quality of the retrieval and its robustness against experimental noise depends on the data sets used for the correlation functions.

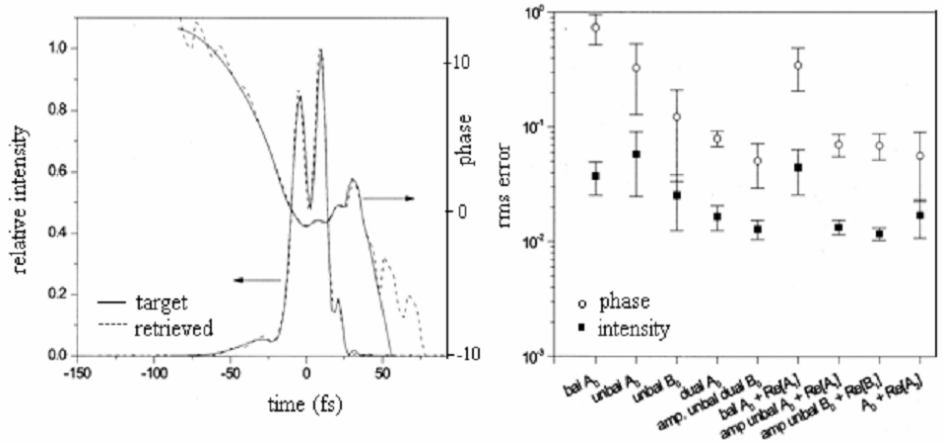

Figure 10.12: (a) - Target and retrieved pulse amplitude and phase using a third-order correlation, which was unbalanced with an amplitude-only filter. Field noise (3% additive and multiplicative) was considered. (b) - rms errors for different retrieval scenarios for the pulse shown in the left part of the figure. The labels refer to the components of the correlations used in the retrieval ("amp. unbal. dual B_0", for example, means that two intensity correlations of third order where used, measured with an amplitude-unbalanced Michelson interferometer. In one of the measurements an additional filter was placed in front of the detector.). The labels were defined in Eqs. (10.7) and (10.12). Adapted from [37]

.

If the correlation is chosen properly, the pulse can be retrieved reliably together with the spectrum. This is illustrated in Fig. 10.12. Part (a) shows a test pulse and its retrieved replica using a third-order correlation, which can be based on third-harmonic generation for example. Figure 10.12(b) depicts the rms error of the retrieval results for different measurement scenarios, that is, different types of correlation in addition to the spectrum.

10.4.4 Frequency-resolved optical gating (FROG)

Frequency-resolved optical gating (FROG) was introduced by Kane and Trebino in 1993 [13, 14] and since then has developed into a field of its own. Numerous versions of the original scheme have been introduced to increase accuracy, sensitivity, versatility, and practicality. Details of these developments can be found in a book devoted entirely to this subject [51].

A FROG measurement records a two-dimensional trace of the form

$$S_E(\Omega,\tau) = \left| \int_{-\infty}^{\infty} dt\, \tilde{\mathcal{E}}(t) g(t-\tau) e^{-i\Omega t} \right|^2, \tag{10.39}$$

where g is a gate function of variable delay τ and $\tilde{\mathcal{E}}(t)$ is the complex pulse amplitude to be determined. The gate function is usually provided by a nonlinear optical process. Assuming instantaneous response, $g(t-\tau) \approx |\tilde{\mathcal{E}}'(t-\tau)|^2$ for a Kerr nonlinearity and $g(t-\tau) \approx \tilde{\mathcal{E}}'^*(t-\tau)$ for sum-frequency generation. $\tilde{\mathcal{E}}'$ can be the original pulse in which case an autocorrelation is measured or a reference field for a cross-correlation (XFROG). The Fourier transform in Eq. (10.39) is realized using an optical spectrometer in front of the detector.

The original FROG apparatus involved a Kerr shutter and is sketched in Fig. 10.13. The signal transmitted by the Kerr gate, the sequence polarizer — Kerr medium

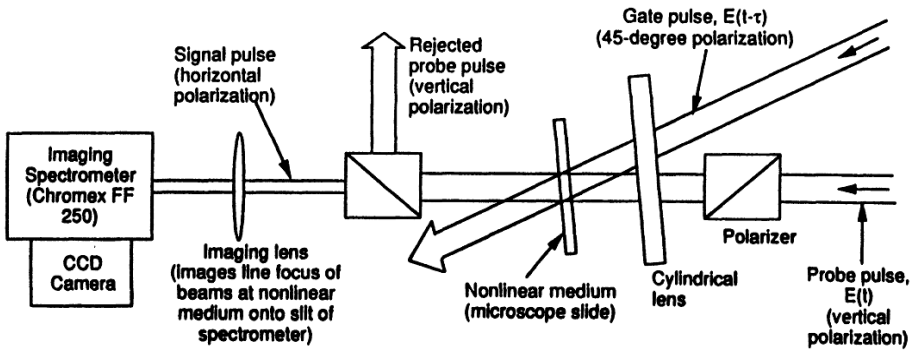

Figure 10.13: Experimental arrangement for frequency resolved optical gating. The pulse to be analyzed $\tilde{E}(t)$ is gated by its delayed replica $\tilde{E}(t-\tau)$ in a Kerr shutter assumed to respond instantaneously (from [13]).

— polarizer, is a pulse of electric field (complex) amplitude[3]:

$$\tilde{\mathcal{E}}_s(t,\tau) = \tilde{\mathcal{E}}(t)\; g(t-\tau), \tag{10.40}$$

A CCD camera at the output of the spectrometer records the spectrogram $S_E(\Omega,\tau)$ of $\tilde{\mathcal{E}}_s(t,\tau)$. The delay τ varies parallel to the entrance slit of the spectrometer since gate and signal pulse intersect at an angle in the Kerr medium.

The function represented by Eq. (10.39) is well known in acoustics [52] and used to display acoustic waves. The spectrogram of a strongly chirped pulse shown on the left side of Fig. 10.14 seems identical to the writing of many successive notes

[3] Apart from constants that do not affect the shape and that we will omit here.

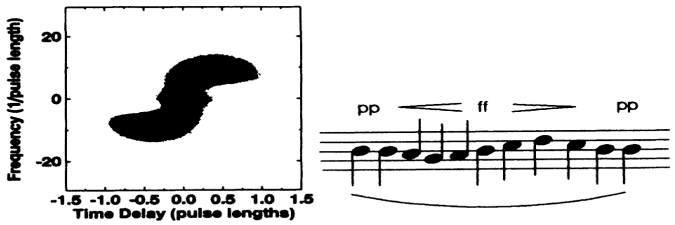

Figure 10.14: Spectrogram of a pulse with strong self phase modulation. The frequency sweeps from -12 to + 12 inverse pulse lengths during the pulse (from [13]). The acoustic analog (see also the reconstruction in Fig. 10.16).

(right side of Fig. 10.14), which can be considered a temporal sequence of spectral components. The difference is only that, in the case of music, the carrier frequency is in the kHz rather than PHz range, and the time delays are seconds rather than fs. The problem of reconstruction reduces essentially to extracting the function

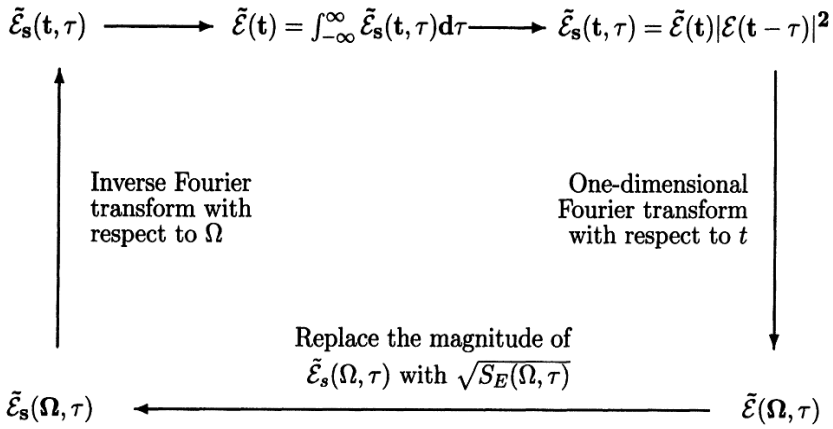

Figure 10.15: Flowchart of an iterative reconstruction algorithm. Adapted from [13].

$\tilde{\mathcal{E}}_s(t,\tau)$ from the spectrogram. Indeed, we note that the integral of Eq. (10.40) over

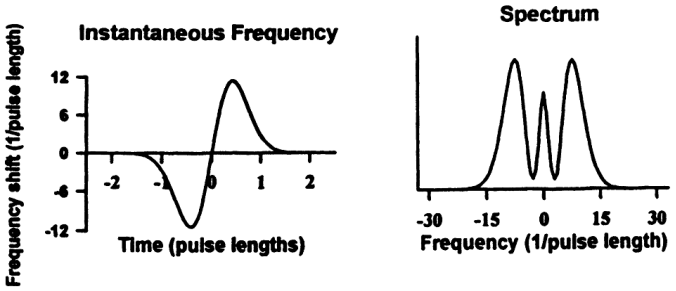

Figure 10.16: Instantaneous frequency versus time and spectrum reconstructed from the spectrogram on the left Fig. 10.14 (from [14]).

the delay τ is simply proportional to the pulse itself [4]

$$\tilde{\mathcal{E}}(t) \propto \int_{-\infty}^{\infty} \tilde{\mathcal{E}}_s(t,\tau)d\tau. \tag{10.41}$$

The FROG trace is related to the Fourier transform of $\tilde{\mathcal{E}}_s(t,\tau)$, $\tilde{\mathcal{E}}_s(t,\Omega_\tau)$, by

$$S_E(\Omega,\tau) = \left| \int_{-\infty}^{\infty} dt \int_{-\infty}^{\infty} d\Omega_\tau \tilde{\mathcal{E}}_s(t,\Omega_\tau) e^{-i\Omega t + i\Omega_\tau \tau} \right|^2. \tag{10.42}$$

Extraction of the unknown signal $\tilde{\mathcal{E}}_s(t,\Omega_\tau)$ from the spectrogram (10.42) is a two-dimensional (the two dimensions are t and τ) phase-retrieval problem. This (phase retrieval) problem is known to have a unique solution for two and higher dimensions [53,54]. The flowchart of the original FROG algorithm, which can be found in Refs. [13, 14], is shown in Fig. 10.15 for illustration.

Since we can write Eq. (10.39) as

$$S_E(\Omega,\tau) = |\tilde{\mathcal{E}}_s(\Omega,\tau)|^2,$$

by replacing the magnitude of $\tilde{\mathcal{E}}_s(\Omega,\tau)$ by $\sqrt{S_E(\Omega,\tau)}$ during each iteration cycle, Eq. (10.39) is always satisfied. Improved algorithms, based for example on generalized projections [55] known from phase retrieval of images, have been developed over the years [51]. Here the integration step to obtain $\tilde{\mathcal{E}}(t)$ is replaced by a search to minimize the figure of merit

$$Z = \sum_{i,j} \left| \tilde{\mathcal{E}}_s(t_i,\tau_j) - \tilde{\mathcal{E}}(t_i) |\tilde{\mathcal{E}}(t_i - \tau_j)|^2 \right|.$$

[4] The integration over the variable τ is equivalent to opening the gate function for all times in Eq. (10.40).

The reconstruction of the pulse defined by the spectrogram on the left side of Fig. 10.14 leads to the instantaneous frequency versus time and spectrum of Fig. 10.16.

10.4.5 Spectral phase interferometry for direct electric-field reconstruction (SPIDER)

Unlike the techniques discussed before SPIDER allows one to determine the pulse shape and phase non-iteratively by a set of linear transformations of the measured data. The technique developed by Iaconis and Walmsley [47] is an example of spectral shearing interferometry. Suppose we have two pulses that are identical except that they are shifted in frequency with respect to each other by an amount ω_s (spectral shear). These two pulses are delayed in time by τ and send into a spectrometer. At the output of the spectrometer, using a quadratic integrating detector, we measure a signal proportional to the square of the sum of the spectral fields $\tilde{E}(\Omega+\omega_s)$ and $\tilde{E}(\Omega)e^{-i\Omega\tau}$.

$$S(\Omega) = |\tilde{E}(\Omega+\omega_s)|^2 + |\tilde{E}(\Omega)|^2 + 2|\tilde{E}(\Omega+\omega_s)||\tilde{E}(\Omega)|\cos(\Delta\Phi) \tag{10.43}$$

where

$$\Delta\Phi = [\Phi(\Omega+\omega_s) - \Phi(\Omega) + \Omega\tau]\,. \tag{10.44}$$

Because of the cosine term the spectrogram is modulated with a period of about τ^{-1}. The data set $S(\Omega)$ can be processed noniteratively using a retrieval procedure known from spectral interferometry [56, 57] to obtain the spectral phase difference $\Phi(\Omega+\omega_s) - \Phi(\Omega)$ and from this the spectral phase $\Phi(\Omega)$. Note that the spectral phase $\Phi(\Omega)$ and amplitude $|E(\Omega)|$, which can be obtained from the square root of the spectral envelope, determine the pulse amplitude and phase unambiguously.

For example, the spectral interferogram is Fourier-transformed using a computer. The resulting spectrum (in time) has components centered at $t = 0$ (carrying information about the spectral envelope) and at $t = \pm\tau$. The $t = 0, -\tau$ components are removed by filtering and the result is inverse Fourier transformed. After removing the component $\Omega\tau$ the spectral phase difference is obtained, from which the spectral phase $\Phi(\Omega)$ can be calculated through concatenation.

The question is how to produce two pulse replicas that differ only in their center frequencies? A SPIDER apparatus is sketched in Fig. 10.17. The pulse to be characterized is split into two replicas. One replica is stretched and chirped in a dispersive device, for example a grating sequence. The second replica is split again into two time delayed pulses, for example in a Michelson interferometer. These two (identical) pulses are mixed (upconverted) with different parts of the stretched

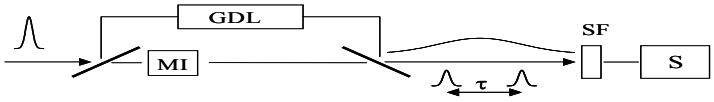

Figure 10.17: Schematic diagram of a SPIDER apparatus. One replica of the pulse to be characterized is stretched and chirped in an element with group delay dispersion (GDL), the other replica is split into identical time-delayed pulses in a Michelson interferometer (MI). The sum frequency is produced in a nonlinear crystal (SF) and recorded in a spectrometer (S). Adapted from [47].

pulse, each centered at a different frequency due to the chirp. The result is a pair of (up-converted) pulses that are identical except for a spectral shear.

The stretcher has to be designed so that the frequency of the stretched pulse does not change (much) during the time of the original pulse duration. Pulses consisting of few optical cycles have been successfully characterized using the SPIDER technique [58, 59]. By combining it with homodyne detection sensitivity and versatility are improved [60]. True single shot implementation of SPIDER has been demonstrated at a repetition rate of 1 kHz [61].

10.5 Problems

1. Show that the statistical average of the autocorrelation of Gaussian pulses distributed in frequency [distribution given by Eq. (10.18)] is approximately identical to the autocorrelation of a simple Gaussian pulse [perform the integration of Eq. (10.19), and compare to Eq. (10.17)].

2. Consider a Gaussian pulse, of 50 fs duration, at 800 nm, with an upchirp corresponding to $a = 1.5$. Determine analytically the result of a measurement using the cross-correlator in which a block of BK-7 glass has been inserted in one arm. Calculate the amount of glass required for pulse broadening by a factor 5, after double passage through the glass. Calculate the envelopes $A_1(\tau)$, $A_2(\tau)$, and $A_3(\tau)$ that will be obtained by measuring a second order cross-correlation, cf. Eq. (10.7). Write the expressions corresponding to the various steps of the procedure leading to the reconstruction of the original pulse following Section 10.2.

3. Derive Eq. (10.12), the expression for the third-order interferometric correlation. Determine the peak to background ratio of the fringe-resolved autocorrelation and of the intensity autocorrelation. Assume equal pulses, $E_1 = E_2$.

4. Let us assume that the spectral phase of a pulse is given by $\Phi(\Omega) = \phi_2(\Omega - \omega_\ell)^2 + \phi_3(\Omega - \omega_\ell)^3$ and the complex field is to be retrieved from the measurement of the pulse spectrum and (a) an amplitude unbalanced third-order correlation, and (b) an amplitude and phase unbalanced third-order correlation using the PICASO scheme, cf. Fig. 10.11. The search space $\Delta(\phi_2, \phi_3)$ is depicted in Fig. 10.18, with dark zones representing minima of the root-mean square deviation, cf. Eq. (10.38). Explain the reason for the ambiguity in case (a). How do the two possible pulses differ in the time domain? Why does adding a phase filter resolve the ambiguity?)

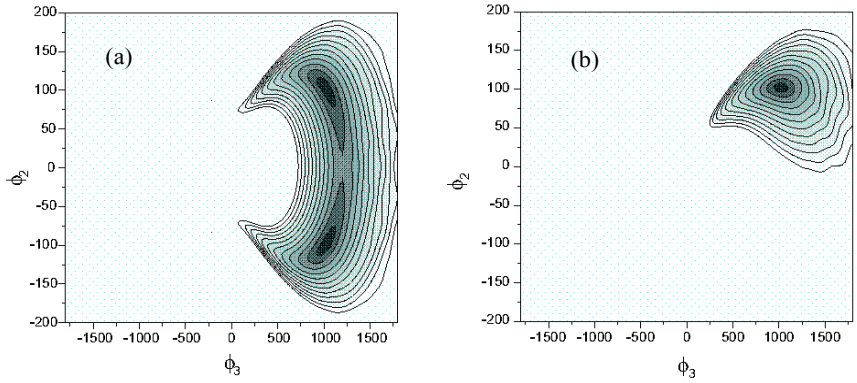

Figure 10.18: Figure of merit, cf. Eq. (10.38), of pulse retrieval based on a spectral measurement and (a) an amplitude unbalanced third-order correlation and (b) an amplitude and phase unbalanced third-order correlation.

Bibliography

[1] S. L. Shapiro, editor. *Ultrashort Light Pulses*. Springer Verlag, Berlin, Heidelberg, New York, 1977.

[2] J.-C. Diels, J. J. Fontaine, I. C. McMichael, and F. Simoni. Control and measurement of ultrashort pulse shapes (in amplitude and phase) with femtosecond accuracy. *Applied Optics*, 24:1270–1282, 1985.

[3] M. Sheik-Bahae T. Hirayama. Real-time chirp diagnostic for ultrashort laser pulses. *Opt. Lett.*, 27(10):860–862, 2002.

[4] K. Naganuma, K. Mogi, and H. Yamada. General method for ultrashort light pulse chirp measurement. *IEEE J. of Quantum Electronics*, QE-25:1225–1233, 1989.

[5] D. E. Spence, P. N. Kean, and W. Sibbett. 60-fs pulse generation from a self-mode-locked Ti:sapphire laser. *Optics Lett.*, 16:42–44, 1991.

[6] E. W. Van Stryland. The effect of pulse to pulse variation on ultrashort pulsewidth measurements. *Opt. Comm.*, 31:93–94, 1979.

[7] G. H. C. New and J. M. Catherall. Advances in the theory of mode-locking by synchronous pumping. In G. Fleming and A. E. Siegman, editors, *Ultrafast Phenomena V*, pages 24–26, Berlin, 1986. Springer Verlag.

[8] J. M. Catherall and G. H. C. New. Role of spontaneous emission in the dynamics of mode-locking by synchronous pumping. *IEEE Journal of Quantum Electronics*, QE-22:1593, 1986.

[9] S. Szatmari and F. P. Schaefer. Generation of high power UV femtosecond pulses. In T. Yajima, K. Yoshihara, C. B. Harris, and S. Shionoya, editors, *Ultrafast Phenomena VI*, pages 82–86, Berlin, Heidelberg, 1988. Springer Verlag.

[10] E. S. Kintzel and C. Rempel. Near surface second harmonic generation for autocorrelation measurements in the UV. *Appl. Phys.*, B28:Liu06 91–95, 1987.

[11] R. Deich, F. Noack, W. Rudolph, and V. Postovalos. Two-photon luminescence in CsI(Na) under UV femtosecond pulse excitation. *Solid state communications*, 74:269–273, 1990.

[12] H. S. Albrecht, P. Heist, J. Kleinschmidt, D. van Lap, and T. Schroeder. Single-shot measurement of femtosecond pulses using the optical kerr effect. *Meas. Sci. Technol.*, 4:1–7, 1993.

[13] R. Trebino and D. J. Kane. Using phase retrieval to measure the intensity and phase of ultrashort pulses: frequency-resolved optical gating. *Journal Opt. Soc. Am. A.*, 10:1101–1111, 1993.

[14] D. J. Kane and R. Trebino. Single-shot measurement of the intensity and phase of an arbitrary ultrashort pulse using frequency-resolved gating. *Optics Lett.*, 18:823–825, 1993.

[15] D. T. Reid, M. Padgett, C. McGowan, W. E. Sleat, and W. Sibbett. Light-emitting diodes as measurement devices for femtosecond laser pulses. *Optics Lett.*, 22:233–235, 1997.

[16] W. Rudolph, M. Sheik-Bahae, A. Bernstein, and L.F. Lester. Femtosecond autocorrelation measurements based on 2-photon photoconductivity in ZnSe. *Opt. Lett.*, 22:313–315, 1997.

[17] A.M. Streltsov, K.D. Moll, A.L. Gaeta, P. Kung, D. Walker, and M. Razeghi. Pulse autocorrelation measurements based on two- and three-photon conductivity in a GaN photodiode. *Appl. Phys. Lett.*, 75:3778–3780, 1999.

[18] P. Langlois and E. P. Ippen. Measurement of pulse asymmetry by three-photon-absorption autocorrelation in a GaAsP photodiode. *Opt. Lett.*, 24(24):1868–1870, 1999.

[19] H. P. Weber and H. G. Danielmeyer. Multimode effects in intensity correlations measurements. *Phys. Rev. A*, 2:2074–2078, 1970.

[20] G. H. C. New. Pulse evolution in mode-locked quasi-continuous lasers. *IEEE J. of Quantum Electron.*, QE-10:115–124, 1974.

[21] J. A. Giordmaine, P. M. Rentzepis, S. L. Shapiro, and K. W. Wecht. Two-photon excitation of fluorescence by picosecond light pulses. *Applied Physics Letters*, 11:216–218, 1967.

[22] S. P. LeBlanc, G. Szabo, and R. Sauerbrey. Femtosecond single-shot phase-sensitive autocorrelator for the ultraviolet. *Opt. Lett.*, 16:1508–1510, 1991.

[23] J. Jansky, G. Corradi, and R. N. Gyuzalian. On a possibility of analyzing the temporal characteristics of short light pulses. *Optics Comm.*, 23:293–298, 1977.

[24] C. Rempel and W. Rudolph. Single shot autocorrelator for femtosecond pulses. *Experimentell Technik der Physik*, 37:381–385, 1989.

[25] R. N. Gyuzalian, S. B. Sogomonian, and Z. G. Horvath. Background–free measurement of time behavior of an individual picosecond laser pulse. *Optics Comm.*, 29:239, 1979.

[26] F. Krausz, T. Juhasz, J. S. Bakos, and Cs. Kuti. Microprocessor based system for measurement of the characteristics of ultrashort laser pulses. *J. Phys. E: Sci. Instrum.*, 19:1027–1029, 1986.

[27] F. Salin, P. Georges, G. Roger, and A. Brun. Single-shot measurement of a 52-fs pulse. *Applied Optics*, 26:4528–4531, 1987.

[28] R. Danielius, V. Sirutkaitis, G. Valikulis, A. Stabinis, and A. Yankauskas. Characterization of phase modulated ultrashort pulses using single-shot autocorrelator. *Optics Comm.*, 105:67–71, 1994.

[29] F. Salin, P. Georges, G. Le Saux, G. Roger, and A. Brun. Autocorrelation interferometrique monocoup d'impulsions femtosecondes. *Revue de Physique Appliquée*, 22:1613–1618, 1987.

[30] G. Szabo, Z. Bor, and A. Mueller. Phase-sensitive single pulse autocorrelator for ultrashort laser pulses. *Opt. Lett.*, 13:746–748, 1988.

[31] E. B. Treacy. Measurement and interpretation of dynamic spectrograms of picosecond light pulses. *J. Appl. Phys.*, 42:3848–3858, 1971.

[32] J. L. A. Chilla and O. E. Martinez. Analysis of a methof of phase measurement of ultrashort pulses in the frequency domain. *IEEE Journal of Quantum Electr.*, 27:1228–1235, 1991.

[33] J. E. Rothenberg and D. Grischkowsky. Measurement of the optical phase with sub ps resolution. *Opt. Lett.*, 12:99–101, 1987.

[34] Chi Yan and J.-C. Diels. Amplitude and phase recording of ultrashort pulses. *J. of the Opt. Soc. Am. B*, 8:1259–1263, 1991.

[35] A. Baltuska, A. Pugzlys, M. Pshenichnikov, and D. A. Wiersma. Rapid amplitude-phase reconstruction of femtosecond pulses from intensity autocorrelation and spectrum. In *Conference on Lasers and Electro-Optics*, OSA Technical Digest, pages 264–265, Washington, DC, 1999. Optical Society of America.

[36] J. W. Nicholson, J. Jasapara, W. Rudolph, F. G. Omenetto, and A. J. Taylor. Full-field characterization of femtosecond pulses by spectrum and cross-correlation measurements. *Opt. Lett.*, 24(23):1774–1776, 1999.

[37] J. W. Nicholson and W. Rudolph. Noise sensitivity and accuracy of femtosecond pulse retrieval using PICASO. *J. Opt. Soc. of Am. B*, 19(2):330–339, 2002.

[38] J.-P. Foing, J.-P. Likforman, M. Joffe, and A. Migus. Femtoseond pulse phase measurement by spectrally resolved up-conversion. *IEEE J. Quant. Electron.*, 28:2285–2290, 1992.

[39] J. Paye, M. Ramaswamy, J. G. Fujimoto, and E. P. Ippen. Measurement of the amplitude and phase of ultrashort light pulses from spectrally resolved autocorrelation. *Opt. Lett.*, 18:1946–1048, 1993.

[40] M. Beck, M. G. Raymer, I. A. Walmsley, and V. Wong. Chronocyclic tomography for measuring the amplitude and phase structure of optical pulses. *Opt. Lett.*, 18(23):2041–2043, 1993.

[41] B. S. Prade, J. M. Schins, E. T. J. Nimbering, M. A. Franco, and A. Mysyrowicz. A simple method for the determination of the intensity and phase of ultrashort optical pulses. *Optics Comm.*, 113:79–84, 1994.

[42] S. P. LeBlanc and R. Sauerbrey. Ultrashort pulse characterization using plasma-induced cross-phase modulation. *Opt. Commun.*, 111:297–302, 1994.

[43] K. C. Chu, J. P. Heritage, R. S. Grand, K. X. Lie, A. Dienes, E. E. White, and A. Sullivan. Direct measurement of the spectral phase of femtosecond pulses. *Opt. Lett.*, 20:904–906, 1995.

[44] Steffen Prein, Scott Diddams, and Jean-Claude Diels. Complete characterization of femtosecond pulses using an all-electronic detector. *Optics Comm.*, 123:567–573, 1996.

[45] B. Haase. Determination of weak optical pulses in amplitude and phase by measurement of the transient polarization state. *Opt. Lett.*, 24(8):543–545, 1999.

[46] N. Nakajima and Y. Tomita. New approach to determine the intensity and phase of ultrashort pulses by use of time-to-space conversion and a noniterative phase-retrieval algorithm. *J. Opt. Soc. Am. A*, 16(6):1268–1276, 1999.

[47] C. Iaconis, V. Wong, and I. A. Walmsley. Direct interferometric techniques for characterizing ultrashort optical pulses. *IEEE Selected Topics in Quant. Electron.*, 4(2):285–294, 1998.

[48] V. Wong and I. A. Walmsley. Analysis of ultrashort pulse-shape measurement using linear interferometers. *Optics Lett.*, 19:287–289, 1994.

[49] I. A. Walmsley and V. Wong. Characterization of the electric field of ultrashort optical pulses. *J. Opt. Soc. B*, 13:2453–2463, 1996.

[50] J. W. Nicholson, M. Mero, J. Jasapara, and W. Rudolph. Unbalanced third order correlations for full characterization of femtosecond pulses. *Opt. Lett.*, 25(24):1801–1803, 2000.

[51] R. Trebino. *Frequency-Resolved Optical Gating, The Measurement of Ultrashort Laser Pulses*. Kluwer, 2002.

[52] W. Koenig, H. K. Dunn, and L. Y. Lacy. The sound spectrograph. *J. Acoust. Soc. Amer.*, 18:19–49, 1946.

[53] D. Israelevitz and J.S. Lim. A new direct algorithm for image reconstruction from fourier transform magnitude. *IEEE Trans. Acoust. Speech Signal Process.*, ASSP-35:511–519, 1987.

[54] J. R. Fienup. Reconstruction of a complex-valued object from the modulus of its fourier transform using a support constraint. *J. Opt. Soc. Amer. A.*, 4:118–123, 1987.

[55] Kennetch W. DeLong, David N. Fittinghoff, Rick Trebino, Bern Kohler, and Kent Wilson. Pulse retrieval in frequency-resolved optical gating based on the method of generalized projections. *Opt. Lett.*, 19(24):2152–2154, 1994.

[56] M. Takeda, H. Ina, and S. Kobayashi. Fourier-transform method of fringe-pattern analysis for computer-based topography and interferometry. *J. Opt. Soc. Am.*, 72:156, 1982.

[57] L. Lepetit, G. Cheriaux, and M. Joffre. Linear techninques of phase measurement by fs spectral interferometry for applications in spectroscopy. *J. Opt. Sco. Am. B*, 21:2467, 1995.

[58] L. Gallmann, D. H. Sutter, N. Matuschek, G. Steinmeyer, U. Keller, C. Iaconis, and I. A. Walmsley. Characterization of sub-6-fs optical pulses with spectral phase interferometry for direct electric-field reconstruction. *Opt. Lett.*, 24(18):1314–1316, 1999.

[59] B. Schenkeland J. Biegert, U. Keller, C. Vozzi, M. Nisoli, G. Sansone, S. Stagira, S. De Silvestri, and O. Svelto. Generation of 3.8-fs pulses from adaptive compression of a cascaded hollow fiber supercontinuum. *Optics Letters*, 28:1987–1989, 2003.

[60] C. Dorrer, P. Londero, and I. A. Walmsley. Homodyne detection in spectral phase interferometetry for direct electric-field reconstruction. *Opt. Lett.*, 26(19):1510–1512, 2001.

[61] W. Kornelis, J. Biegert, J. Tisch, M. Nisoli, G. Sansone, C. Vozzi, S. De Silvestri, and U. Keller. Single-shot kilohertz characterization of ultrashort pulses by spectral phase interferometry for direct electric-field reconstruction. *Optics Letters*, 28:281–283, 2003.

Chapter 11

Measurement Techniques of Femtosecond Spectroscopy

11.1 Introduction

Femtosecond pulses are an ideal tool to investigate ultrafast processes of various origins. There is usually more than one parameter that varies with time in any particular experiment. One of these parameters will often be the position. As an example of the types of time dependence that have to be distinguished, let us consider the example of an apple falling from a tree (Fig. 11.1). A photograph taken with a sufficiently short exposure time can "freeze" the motion of the falling apple as it reaches the position x. We can compare this picture with one of the apple still on the tree, which provides some information about the aging process. To establish either the law of motion $x(t)$ or the temporal behavior of aging, we need to know exactly the time elapsed from the moment the apple was shaken loose from the tree, until the photograph was taken. The standard experimental technique is to *trigger* the fall (for instance, ignite a small explosion) and simultaneously start a clock that synchronizes the shutter of the camera. By triggering the event, we do not have to wait days for the apple to fall down.

A pump-probe femtosecond experiment has analogies as well as fundamental differences with the falling apple measurement. The basic analogy is that a powerful light pulse — usually labeled the "pump pulse" or "excitation pulse" — interacts with the sample and excites it into a non-equilibrium state (Fig. 11.2). The sample thereafter relaxes towards a new equilibrium state. This process can be mapped by sending a second (much weaker) pulse, called a probe or test (pulse), onto the sample. The probe is the analogue of the snapshot photograph, aimed at detecting a change of optical properties without disturbing the object under inves-

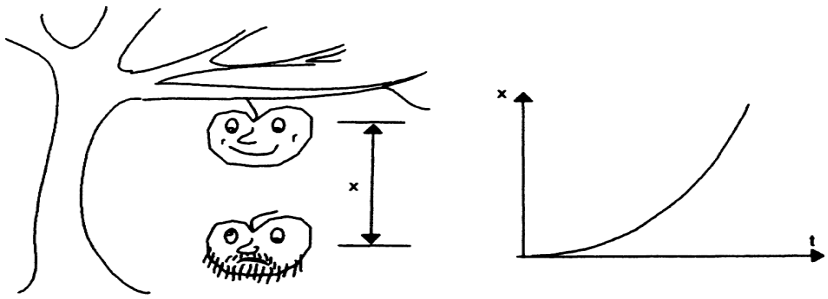

Figure 11.1: The falling apple and the aging apple.

tigation. The difference with the falling apple is that the speed of light is infinite compared to the velocity of the apple, whereas the propagation time of the probe radiation through the sample can be long compared with the event to be observed. Therefore, the geometry of interaction, the angle between probe and pump, the interaction length, and the group velocities in the sample are essential parameters in femtosecond pump-probe experiments.

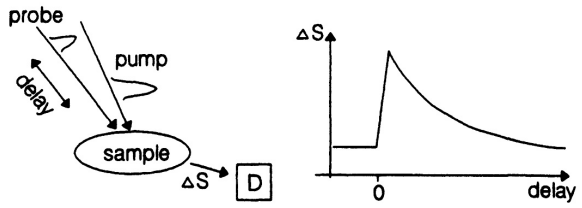

Figure 11.2: Schematic representation of a pump-probe experiment in ultrafast spectroscopy. The pump and probe pulses can be obtained from a single source and delayed with respect to each other in a Michelson or a Mach–Zehnder interferometer for example.

In a typical pump-probe experiment, the delayed weak pulse probes the change of an optical property ΔS, such as transmission or reflection, induced by the pump. Repeating the experiments for various delays τ_d provides the function $\Delta S(\tau_d)$. Depending on the actual light matter interaction, $\Delta S(\tau_d)$ is related to material parameters such as occupation numbers, carrier density, and molecular orientation. In

this chapter we discuss a selection of fs experimental techniques, many of them originally developed for ps and ns spectroscopy.

The obvious temporal limitation of the pump-probe technique is the duration of the pump and probe. The medium preparation should be completed before the material can be probed. If the physics of the interaction is well understood, a theoretical modeling (deconvolution) can provide some interpretation of data corresponding to partial temporal overlap of pump and probe.

A compromise often must be sought between spectral and temporal resolution. Either the probe or the pump pulse has to *select* a specific spectral feature. In order to excite the desired transition, rather than an adjacent one, the excitation spectrum (i.e., the pulse spectral width $\Delta\omega_p$, augmented by the Rabi frequency $\kappa\mathcal{E}$ or power broadening of the transition, if needed) should not exceed the separation between lines Δ. The spectral resolution imposes therefore a limit to the temporal resolution, since the pulse duration should not be less than $\tau_p \approx 1/(\Delta + \kappa\mathcal{E})$.

11.2 Data deconvolutions

In most fs time resolved experiments, a signal $S(\tau_d)$ is measured as a function of position or delay τ_d of a reference probe pulse of intensity $I_{\text{ref}}(t)$. We will consider the large class of measurements where the measured quantity is proportional to the product of a gating function I_g times the physical quantity $f(t)$ to be analyzed. The gate $I_g(t)$ is a direct function of the reference intensity $I_{\text{ref}}(t)$. Since — as pointed out in the previous chapter — the detection electronics has no fs resolution, the measured signal will be the time integral:

$$S(\tau_d) = \int_{-\infty}^{\infty} I_g(t-\tau_d) f(t) dt. \tag{11.1}$$

Deconvolution procedures should thus be applied to retrieve the physical quantity $f(t)$ from the measurement $S(\tau_d)$. A typical example is a measurement of time resolved fluorescence by upconversion. As detailed in Section 11.7, the detected upconversion radiation results from mixing the signal (fluorescence) and the reference pulse in a nonlinear crystal. Therefore, in that particular case, the gate function is the reference pulse itself $I_g(t) = I_{\text{ref}}(t)$. It is often assumed that the gating function in the correlation product [Eq. (11.1)] is much shorter than the fastest transient of the signal and thus can be approximated by a δ-function. With that simplifying assumption, the signal is directly proportional to the physical parameter to be measured: $S(\tau_d) \propto f(\tau_d)$. There are, however, very fast events — such as the rise of fluorescence — for which this simplifying assumption is not valid. The exact temporal dependence $f(\tau_d)$ can be extracted from the data if the gating function $I_g(t)$ is known. Indeed, if $\mathcal{I}(\Omega)$ is the Fourier transform of the gate

function $I_g(t)$, and $\mathcal{S}(\Omega)$ is the Fourier transform of the measured signal $S(\tau_d)$, the Fourier transform $f(\Omega)$ of the physical quantity $f(t)$ is just the ratio:

$$f(\Omega) = \frac{\mathcal{S}(\Omega)}{\mathcal{I}(\Omega)}. \tag{11.2}$$

The physical quantity $f(t)$ can be calculated by taking the inverse Fourier transform of Eq. (11.2). This deconvolution technique can be applied in numerous cases where the gate function $I_g(t)$ does not depend on the phase of the interaction[1].

11.3 Beam geometry and temporal resolution

To obtain a better quantitative understanding of the influence of the beam geometry on the temporal resolution, let us analyze a pump-probe experiment as sketched in Fig. 11.3. The pump pulse creates a small change of the transmission coefficient,

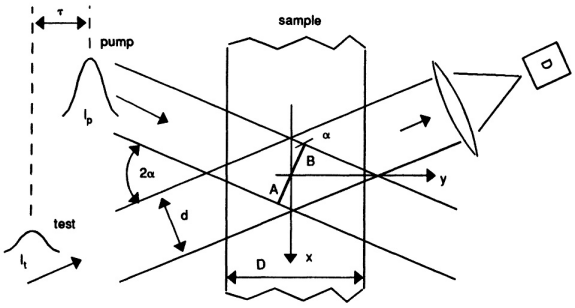

Figure 11.3: Schematic diagram of a pump-probe transmission experiment in non-collinear geometry. The line AB shows the position of the pump pulse maximum at $t = 0$. Refraction at the sample interfaces has been neglected.

$\Delta a(x, y, z, t)$, which is sampled by the time-delayed test pulse of intensity $I_t(t)$. The signal measured by the detector PD as function of the delay τ_d can be written as the sum of the transmitted test pulse energy $\mathcal{W}_{t0}$ in the absence of a pump, and a pump-induced change $\Delta\mathcal{W}_t(\tau_d)$:

$$\begin{aligned} \mathcal{W}_t(\tau_d) &= \mathcal{W}_{t0} + \Delta\mathcal{W}_t(\tau_d) \\ &\propto \int_{-\infty}^{\infty} dt \iiint dx\,dy\,dz\,[1 + a_o + \Delta a(x, y, z, t)]\, I_t(x, y, z, t - \tau_d) \end{aligned} \tag{11.3}$$

[1]The gate depends on the phase of the interaction in the case of coherent interaction. In that case the measured signal cannot be described by the simple expression (11.1).

where a_o is the transmission coefficient in the absence of the pump and $|a_0| \ll 1$ has been assumed: $e^a = 1 + a_0 + \Delta a$. In the overlapping volume of the two beams, a complex mixing of spatial and temporal effects occurs. We want to derive conditions under which the excitation geometry does not affect substantially the outcome of the experiment. For simplicity, the beam profiles of pump and test pulse are assumed to be uniform and of rectangular shape, the temporal profiles are Gaussian of equal FWHM τ_p, and the overlapping region is symmetric with respect to the sample center. The time axis is chosen so that the pump pulse maximum reaches the origin of the coordinate system at $t = 0$, and the test pulse reaches the origin at $t = \tau_d$. The sample response is assumed to follow the pump pulse instantaneously, $\Delta a \propto I_p(t)$, and we expect a signal $\Delta W_t(\tau_d)$ resembling the pulse autocorrelation in the absence of geometrical effects. An increase of the correlation FWHM is then a measure of the loss in temporal resolution of any pump-probe experiment due to geometrical effects.

In the following considerations we will omit constants for the sake of brevity. The delay-dependent part of the measured signal is

$$\Delta \mathcal{W}_t(\tau_d) \propto \int_{-\infty}^{\infty} dt \int dx \int dy I_t(x,y,t-\tau_d) I_p(x,y,t) \tag{11.4}$$

where we have already carried out the z-integration yielding a constant. The pulses propagate through the sample with the group velocity v_g. Lines of constant intensity (parallel to AB in Fig. 11.3) obey the equation

$$(x - v_g t \sin\alpha) = -(y - v_g t \cos\alpha)\frac{\cos\alpha}{\sin\alpha} \tag{11.5}$$

for the pump pulse and

$$\left[x + v_g(t-\tau_d)\sin\alpha\right] = \left[y - v_g(t-\tau_d)\cos\alpha\right]\frac{\cos\alpha}{\sin\alpha} \tag{11.6}$$

for the test pulse. Hence, the corresponding pulse intensities which are needed in the integral (11.4) can be written as

$$I_p = I_{p0}\exp\left\{-\frac{4\ln 2}{(v_g\tau_p)^2}[y\cos\alpha + x\sin\alpha - v_g t]^2\right\} \tag{11.7}$$

$$I_t = I_{t0}\exp\left\{-\frac{4\ln 2}{(v_g\tau_p)^2}\left[y\cos\alpha - x\sin\alpha - v_g(t-\tau_d)\right]^2\right\}. \tag{11.8}$$

Inserting these expressions into Eq. (11.4) and carrying out the time integration yields after some algebra

$$\Delta \mathcal{W}_t(\tau_d) \propto e^{-2\ln 2(\tau_d/\tau_p)^2} \int_{-y_m}^{y_m} dy \int_{l(y)}^{u(y)} dx \exp\left\{-\frac{8\ln 2}{(\tau_p v_g)^2}\left[x^2\sin^2\alpha - v_g x\tau_d\sin\alpha\right]\right\} \tag{11.9}$$

where

$$y_m = \min\left(\frac{d}{2\sin\alpha}, \frac{D}{2}\right) \tag{11.10}$$

$$l(y) = -\frac{d}{2\cos\alpha} + y\tan\alpha \tag{11.11}$$

$$u(y) = \frac{d}{2\cos\alpha} - y\tan\alpha. \tag{11.12}$$

The value of y_m depends on whether or not the overlapping area of the beams is completely inside the sample. The upper and lower limit of the x-integration form the diamond-shaped boundary of the overlapping region as sketched in Fig. 11.3.

The exponential function in front of the integrals is the autocorrelation function of a Gaussian pulse and represents the result of an ideal measurement where the geometrical effects do not play a part, i.e., the spatial integration yields a constant which does not depend on τ_d. This is obviously the case for a collinear beam geometry ($\alpha = 0°$). For all other cases one can evaluate Eq. (11.9) numerically. Figure 11.4 shows the FWHM of $\Delta\mathcal{W}_t(\tau_d)$ normalized to its value at $\alpha = 0°$ as a function of α and for different values of the parameter $K = v_g\tau_p/d$. The latter

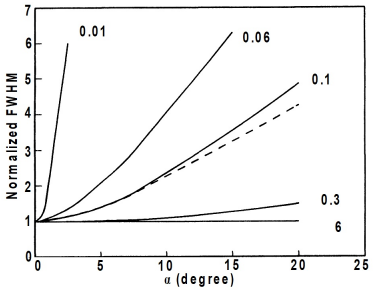

Figure 11.4: FWHM of $\Delta\mathcal{W}_t(\tau_d)$ according to Eq. (11.9), normalized to its value at $\alpha = 0°$ and shown as a function of the half-angle α between pump and probe pulse. The curves are depicted for different values of the ratio of the geometrical pulse length and beam width, $K = v_g\tau_p/d$. The sample thickness was chosen to be $D = 3v_g\tau_p$. For $K = 0.1$, a second curve for $D = 10v_g\tau_p$ is also shown for comparison (from [1]).

describes the ratio of the geometrical pulse length and the beam width. As can be seen, the shorter the pulses at a given beam width, the more critical becomes the beam geometry in a noncollinear experiment. The temporal broadening of $\Delta\mathcal{W}_t$ can be substantial, causing a loss in time resolution of a pump-probe experiment. The effect of the crystal thickness, on the other hand, is small at moderate values of the angle α. In the following sections we will always assume an experimental geometry which justifies neglecting these geometric effects.

11.4 Transient absorption spectroscopy

Transient absorption spectroscopy is a widely used form of a pump-probe technique. As a simple example to illustrate the method, we consider an ensemble of two-level systems at resonance with a fs pulse source. With all the particles in the ground state at thermal equilibrium, the sample acts as a saturable absorber. The physical quantity to be determined is the energy relaxation time T_1 of the excited state. This parameter is to be extracted from the measurement of attenuation of the probe versus delay.

A typical experimental arrangement is sketched in Fig. 11.5. In order for the probe to be much weaker than the pump, the reflectivity of the beam splitter (called BS in Fig. 11.5) should be larger than 0.5. Since only the transmission of the *probe* is measured, there is a need to devise a means to shield the pump pulse from the detector. Since pump and probe have the same wavelength, one is left with the following choices:

- separation by polarization
- separation by wave vector
- temporal separation in combination with a gated detector.

In the example sketched in Fig. 11.5, it is the wave vector separation that is used.

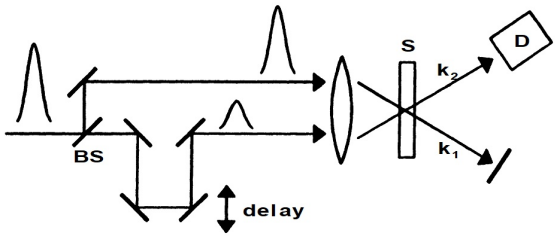

Figure 11.5: Typical geometry for measuring transient absorption. The two relatively delayed pulses are spatially separated before being sent onto the focusing optics, to provide for **k** vector separation in the sample S.

In a typical experiment, the first (pump) pulse will saturate the absorber, and the delayed probe pulse will sample the absorption coefficient. The interpretation of the data is straightforward if the transition can be considered as homogeneously broadened. For delays longer than the phase relaxation time T_2 of the transition, the probe pulse samples the absorption coefficient α:

$$\alpha = \sigma \Delta N \tag{11.13}$$

where σ is the absorption cross-section and ΔN is the population difference (density) between the upper and lower level of the transition. According to the rate equations, after excitation, the absorption coefficient relaxes exponentially with time:

$$\alpha(\tau_d) = \alpha_0 + \Delta\alpha\ e^{-\tau_d/T_1}, \tag{11.14}$$

where $\Delta\alpha$ is the change in absorption due to the pump pulse, τ_d the delay of the probe relative to the pump, and T_1 is the energy relaxation time of the absorbing transition.

Extraction of T_1 from the measurement can be made under a variety of experimental conditions. In the considerations that follow, we will not attempt to select the experimental conditions for best signal-to-noise ratio, but the ones that lead to the simplest analytical expression relating the measurement to T_1, without the need for numerical modeling. We assume a uniform beam profile. In addition to being "optically thin," the sample thickness d is assumed to be negligible compared with the overlap length of pump and probe beams. Finally, the pump and probe pulse duration is assumed to be much shorter than the relaxation time to be measured ($\tau_p \ll T_1$), to avoid the need of deconvolution procedures. The completion of the pumping process is taken as time origin. The measured signal $S(\tau_d)$ is the energy of the transmitted probe versus delay. For a probe signal of energy density $W = \int I dt$ sent through a sample of thickness d:

$$\begin{aligned} S(\tau_d) &= A\int_{-\infty}^{\infty} I(t-\tau_d)e^{\alpha(t)d}dt \\ &\approx AWe^{\alpha(\tau_d)d} \approx AW[1+\alpha(\tau_d)d], \end{aligned} \tag{11.15}$$

where A is the beam cross-section. Inserting Eq. (11.14) into Eq. (11.15) yields:

$$S(\tau_d) = AW\left[1+\alpha_0 d + \Delta\alpha\ d\ e^{-\tau_d/T_1}\right] \tag{11.16}$$

$$\approx S_{-\infty} + AW\Delta\alpha\ d\ e^{-\tau_d/T_1}, \tag{11.17}$$

where $S_{-\infty}$ is the probe transmission in the absence of the pump pulse. The energy relaxation time T_1 can be obtained directly from a logarithmic plot of $S(\tau_d) - S_{-\infty}$ versus τ_d. The key approximation in Eq. (11.15) is that the temporal variations of the absorption coefficient be slow compared to the duration of the probe pulse. A numerical deconvolution of the data can be made if this latter condition is not satisfied.

The expression (11.14) is only valid for delays sufficiently large such that the excitation of the pump has dephased before the arrival of the leading edge of the probe ($\tau_d \gg T_2 + \tau_p$). For short delays that do not satisfy the latter condition, the probe coherently interacts with the polarization created by the pump. For pump and

probe collinear and having the same polarization, the induced dipoles created by the pump will be in or out of phase with the probe field, depending on whether the delay is an even or odd number of half wavelengths. The transmitted energy versus delay will have an interference-like pattern similar to that observed in a "zero-area pulse" experiment (see the end of this chapter). This pattern is often referred to as the "coherent spike" of a pump-probe experiment. In the case of non-collinear pump-probe experiments, a "transient grating" is created by the spatial-temporal superposition of the probe and the polarization created by the pump. In the latter geometry, the coherent spike can be explained as a result of partial diffraction of the pump pulse into the direction of the probe.

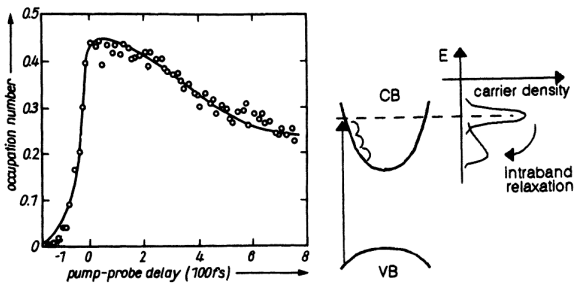

Figure 11.6: Transient transmission in CdS_xSe_{1-x}. The population numbers in the states excited by the pump can be determined from the measured changes in transmission of the 100 fs probe pulses at 618 nm. The change in occupation numbers is a measure of intraband relaxation (from [2]).

As a typical example of transient absorption, Fig. 11.6 shows the absorption recovery of a mixed crystal, CdS_xSe_{1-x}, after excitation with a 618 nm pulse. The pump pulse creates free carriers, i.e., electrons in the conduction band and holes in the valence band, which occupy states and subsequently increase the transmission of a test pulse at the corresponding wavelength. As the carriers relax towards the bottom of the band, the transmission decreases. The decay time is a measure of the intraband relaxation.

Much more information can be gained by using a fs white light continuum instead of a probe at the excitation frequency. In the previous example, the test pulse monitored the change in carrier density only for specific states above the band gap. A continuum fs pulse can probe simultaneously all states in a broad

energy range, providing detailed information on the time dependent carrier density distribution. An example of a pump-probe transmission experiment using a white light continuum is discussed in the next chapter.

11.5 Transient polarization rotation

A linearly polarized pump pulse can induce anisotropy in a sample, which can be probed subsequently with a delayed pulse. Anisotropy means here that the transmission depends on the polarization of the probing radiation. The decay in anisotropy can often be related to orientational relaxation of the dipoles excited by the pump. Such measurements have been applied successfully on a fs time scale to the determination of momentum (**k**-space) relaxation of photo-excited electrons in condensed matter (for instance, GaAs [3]).

A polarization rotation can also be induced in transparent media. The pump pulse acts through the optical Kerr effect causing birefringence. This polarization anisotropy can be seen as a polarization-direction dependence of the refractive index experienced by the probe.

A standard experimental arrangement to measure the temporal change in pump induced polarization anisotropy in shown in Fig. 11.7(a). Let us assume an absorbing sample. Subsequent to the excitation by the pump pulse, a probe pulse — of the same wavelength — is sent with its electric field vector oriented at an angle β with respect to that of the pump. The pump induces a polarization change (rotation) for the probe pulse, $\Delta\beta$.

We will first derive a relationship between the polarization rotation $\Delta\beta$ of the probe as a function of the anisotropy produced by the pump, and then relate $\Delta\beta$ to experimental parameters that are easily accessible. We make the assumptions of optically thin samples so that the absorption $e^a \approx 1 + a$ causing small rotations $\Delta\beta$ for which $\sin\Delta\beta = \tan\Delta\beta \approx \Delta\beta$ and $\cos\Delta\beta \approx 1$. Let us assume that the pump pulse causes the sample to have an absorption coefficient $a_\parallel$ and $a_\perp$ for the components of the probe field, $\mathcal{E}_\parallel$ and $\mathcal{E}_\perp$, that are polarized parallel and perpendicular to the pump, respectively. The two field components after the absorber are:

$$\mathcal{E}'_\parallel \approx \left(1+\frac{1}{2}a_\parallel\right)\mathcal{E}_\parallel = \left(1+\frac{1}{2}a_\parallel\right)\mathcal{E}\cos\beta = \mathcal{E}'\cos(\beta+\Delta\beta) \qquad (11.18)$$

$$\mathcal{E}'_\perp \approx \left(1+\frac{1}{2}a_\perp\right)\mathcal{E}_\perp = \left(1+\frac{1}{2}a_\parallel\right)\mathcal{E}\sin\beta = \mathcal{E}'\sin(\beta+\Delta\beta) \qquad (11.19)$$

where $\mathcal{E}$ and $\mathcal{E}'$ are the field amplitudes of the input and output probe fields, respectively. Dividing these two equations, $\mathcal{E}'_\perp/\mathcal{E}'_\parallel$, and using only the two last terms

yield:

$$\tan(\beta+\Delta\beta) = \frac{\left(1+\frac{1}{2}a_{\perp}\right)}{\left(1+\frac{1}{2}a_{\parallel}\right)}\tan\beta. \tag{11.20}$$

For $|a|, \Delta\beta << 1$ this can be approximated by

$$\Delta\beta \approx \frac{\sin(2\beta)}{4}(a_{\perp}-a_{\parallel}). \tag{11.21}$$

Clearly, the polarization rotation is caused by an induced anisotropy of the optical thickness of the sample by the pump, $(a_{\perp}-a_{\parallel})$.

To measure the small rotation angle it is advantageous to monitor the transmitted probe components at polarization angles of 45° and 135° with respect to the pump polarization [Fig. 11.7(a)]. The corresponding probe field components after the sample are:

$$\mathcal{E}'_{45} = \mathcal{E}'\cos\left(\frac{\pi}{4}-\beta-\Delta\beta\right) \approx \frac{1}{2}\sqrt{2}\mathcal{E}'\left[\cos\beta+\sin\beta+\Delta\beta(\cos\beta-\sin\beta)\right] \tag{11.22}$$

and

$$\mathcal{E}'_{135} = \mathcal{E}'\cos\left(\frac{\pi}{4}+\beta+\Delta\beta\right) \approx \frac{1}{2}\sqrt{2}\mathcal{E}'\left[\cos\beta-\sin\beta-\Delta\beta(\cos\beta+\sin\beta)\right]. \tag{11.23}$$

What is recorded in such a pump probe experiment is the ratio of the intensities (pule energies):

$$R' = \frac{(\mathcal{E}'_{45})^2}{(\mathcal{E}'_{135})^2}. \tag{11.24}$$

Eqs. (11.21) and (11.23) can be inserted into the equation for R'. After some basic algebra and making use of $\Delta\beta << 1$ again we find

$$R' \approx R\left(1+\frac{4\Delta\beta}{\cos(2\beta)}\right), \tag{11.25}$$

where $R = [1+\sin(2\beta)]/[1-\sin(2\beta)]$ is the ratio of the two probe components in the absence of the pump. From relation (11.25) the rotation angle $\Delta\beta$ can be determined from the measurement of R and R' and the known angle β.

The scattered pump intensity adds a noise component to the signals S_{135} and S_{45}. The angle β has to be sufficiently large, such that the scattered noise from the pump be negligible compared with the measured probe component $\mathcal{E}^2\sin^2\beta$. An angle of $\beta = 15^o$ is chosen in most applications [3, 4]. The measured anisotropy (rotation in probe beam polarization of the order of one degree) decays with probe delay and is a measure of relaxation processes following the excitation. An example of a polarization rotation measurement is shown in Fig. 11.8.

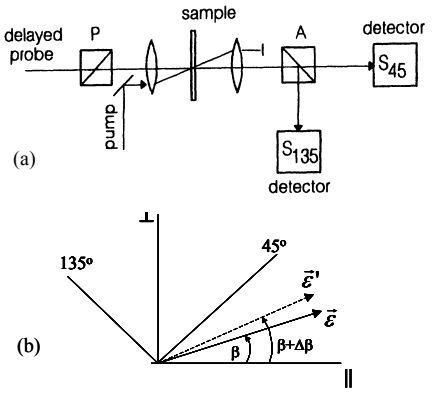

Figure 11.7: (a) Experimental setup to measure pump-induced birefringence. The Glan polarizer P sets the polarization of the probe at an angle β with respect to that of the pump. The analyzer A extracts the components of the transmitted probe at an angle of 45° and 135° with respect to the pump polarization. (b) Sketch showing the relation between the rotation angle $\Delta\beta$ of the probe $\mathcal{E}$ and the induced anisotropy in absorption. "in" and "out" denote the probe polarization before and after the sample.

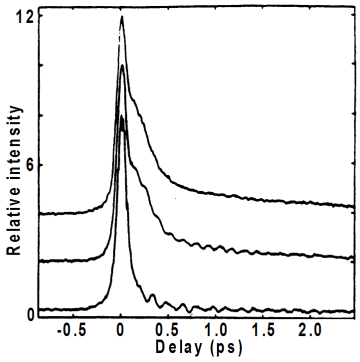

Figure 11.8: Optical Kerr signals for the liquids CH_2Cl_2, $CHCl_3$ and CCl_4 (top to bottom). Different time constants can be identified for each sample. They represent a complex interplay of intramolecular processes as well as interaction with the local environment (from [5]).

11.6 Transient grating techniques

11.6.1 General technique

There are numerous variations of transient grating techniques, providing a wide array of information on sample properties. A general review of these techniques

is given in a book by Eichler *et al.* [6]. The basic experimental setup is sketched in Fig. 11.9. Two pump pulses of different propagation direction overlap in the sample. If their relative delay (τ_1) is less than the phase relaxation time of the interaction, they produce an interference pattern of the sample excitation. The modulation of the sample excitation can manifest itself in a periodically changing transmission (amplitude grating) and/or a refractive index (phase grating). The grating vector is:

$$\mathbf{k}_G = \mathbf{k}_1 - \mathbf{k}_2, \tag{11.26}$$

where $\mathbf{k}_{1,2}$ are the propagation vectors of the pump pulses in the sample. The ex-

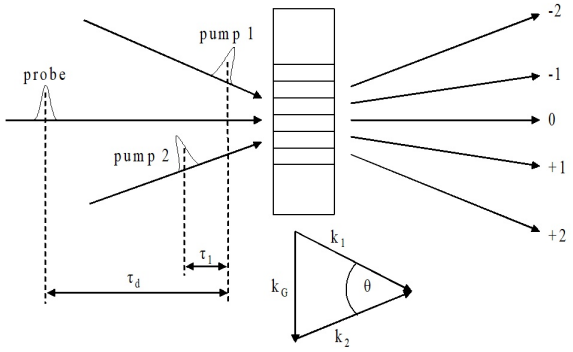

Figure 11.9: Schematic representation of a transient grating experiment.

istence and dynamics of the grating can be probed by the diffraction that a delayed (weak) probe pulse experiences. A series of detectors can probe simultaneously the behavior in several diffraction orders. If the excitation is weak, the absorption and refractive index modulation are small [$|\Delta\alpha/\alpha_0| \ll 1$, $(\Delta n/n) \ll 1$], and the relative diffracted probe intensity (first order) is given by [6]:

$$\frac{\Delta I_{\text{diff}}}{I_p} \propto (\Delta n)^2 + \left(\frac{\lambda_p}{2\pi}\right)^2 (\Delta\alpha)^2. \tag{11.27}$$

One has generally to distinguish between two mechanisms for the decay of diffraction efficiency with delay:

1. The pump-induced changes in the sample relax locally. For example, if $\Delta\alpha$ and Δn are the result of free carrier generation in a semiconductor, carrier relaxation towards the original equilibrium state will lower the modulation depth. The diffraction as a function of delay provides information on the carrier relaxation time.

2. The sample excitation diffuses spatially (non-local mechanism). In the example of free carrier generation in a semiconductor, the pump modulates the carrier density, and thus triggers diffusion of carriers into the low excitation regions (minima of the induced grating). The result is a gradual "wash-out" of the modulation, and decline of the diffraction signal. In many cases, the diffusion process can be described by a diffusion equation with a characteristic diffusion constant. From the characteristic decay time of the diffraction efficiency and the grating period one can determine the diffusion constant.

Both processes (1) and (2) have to be taken into account in the data evaluation. To distinguish between the local and non-local relaxation mechanisms (in particular when they occur on a comparable time scale), a series of measurements can be performed at various angles θ between the two pump beams producing the grating. Since the grating constant is modified by changing the angle θ [Eq. (11.26)], the decay component due to diffusion will also be modified. The local relaxation component to the decay should not depend on the angle θ. Another possibility to distinguish between local and non-local contributions to the decay is to compare transmitted (zero diffraction order) and diffracted signals.

Grating techniques also provide the possibility of measuring coherent effects by varying the delay τ_1 between the two pump pulses, at constant probe delay τ_d. The first arriving pump pulse generates a polarization oscillation in the sample which decays with the characteristic transverse relaxation time T_2. The second pump interferes with this polarization, which results in a modulation of the excitation (e.g., occupation numbers). The modulation depth and thus the diffraction efficiency experienced by the probe pulse and measured as function of τ_1 contain information on T_2.

The actual data evaluation in a transient grating experiment can be complex and requires a detailed model of the processes involved. An example of determination of phase relaxation times using collinear counter-propagating pump pulses is detailed in the next subsection.

11.6.2 Degenerate four-wave mixing (DFWM)

In this particular variation of transient grating experiment, the two pump pulses are two strong counter-propagating waves $\tilde{\mathcal{E}}_{p1}(t)\exp\Big[i(\omega_\ell t - k_p z)\Big]$ and $\tilde{\mathcal{E}}_{p2}(t)\exp\Big[i(\omega_\ell t + k_p z)\Big]$. The probe wave is sent along an intersecting direction x and has as electric field $\tilde{\mathcal{E}}_3(t-\tau_d)\exp[i(\omega_\ell t - k_x x)]$. The nonlinear interaction results in the generation of a signal $\tilde{\mathcal{E}}_4(t)\exp[i(\omega_\ell t + k_x x)]$, which, for momentum conservation, is counter-propagating to the probe direction (Fig. 11.10). In the case of continuous waves, and, for instance, a quadratic nonlinearity, it can be shown that the wavefront of the

generated signal wave $\tilde{\mathcal{E}}_4$ is the reverse of the wavefront of the probe $\tilde{\mathcal{E}}_3$ [7]. This property of spatial phase conjugation does not transpose directly in the time domain. Temporal phase conjugation is chirp reversal, which can be shown to occur only when the following conditions are met [8]:

- instantaneous nonlinearity,
- medium thickness $\ll$ than the pulse length,
- weak interaction ($|\tilde{\mathcal{E}}_4| \ll |\tilde{\mathcal{E}}_3|$).

It can easily be seen that if all but the second condition are met, each depth of the medium will generate a DFWM signal, resulting in a square pulse $\tilde{\mathcal{E}}_4$ with a length equal to twice the sample thickness [8].

We have so far assumed that all three waves meet simultaneously in the nonlinear medium. Interesting information on the dynamics of the interaction can be gathered from the study of the DFWM signal when all three waves are applied in a particular time sequence.

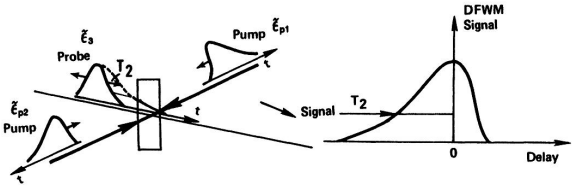

Figure 11.10: Coherent single-photon resonant DFWM. The probe pulse is trailed by a polarization wave, that forms a population grating with one of the pump pulses that follows. The other pump pulse scatters off that grating into the direction from which the probe originates. The *rise* of the signal energy versus delay is thus a measure of the phase relaxation time of the single-photon resonance.

We assume in the following discussion that the nonlinear medium is shorter than the optical pulses and is either at single- or at two-photon resonance with the radiation. Let us first consider the case of a single-photon resonant absorber being excited first by a weak probe, followed by two simultaneous strong counterpropagating pump pulses (Fig. 11.10). As we have seen in Chapter 3, the short pulse creates a pseudo-polarization $\tilde{Q}_3 = w_0 \sin\theta_0 \exp[-ik_x x]$ that decays with a characteristic time T_2. If a strong pump pulse enters the interaction region within that characteristic time, it will form a population grating [as seen from the Bloch equation (3.69)] corresponding to the interferences between waves of vector $\mathbf{k}_x$ and $\mathbf{k}_z$. If the second pump pulse impinges on this grating, it will be diffracted

along the opposite direction as the signal (wave vector $-\mathbf{k}_x$) according to the Bloch equation (3.68). The longer T_2 is, the more the probe can be launched in advance of the two pump pulses, and still produce a signal. As illustrated in Fig. 11.10, the rise-time of the signal versus delay is a measure of the phase relaxation time of a single photon transition.

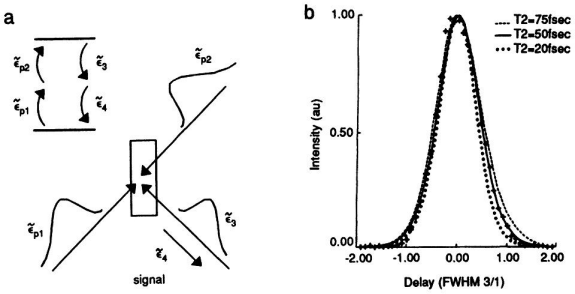

Figure 11.11: Coherent two-photon resonant DFWM. (a) The counter-propagating pump pulses create a two-photon excitation of frequency $2\omega_\ell$, which decays with the two-photon phase relaxation time $T_{2(2ph)}$. The signal is two-photon stimulated emission induced by subsequent passage of the probe pulse. It is thus the *fall* of the signal energy versus delay that is a measure of the phase relaxation time of the two-photon resonance. (b) Intensity of the DFWM signal versus probe delay. The sample is the saturable absorber jet of a mode-locked dye laser. The crosses indicate the experimental data points. Theoretical curves for the two-photon resonant interaction are plotted for three values of the phase relaxation time: 20 fs (dotted), 50 fs (solid), and 75 fs (dashed).

The same experiment performed on a two-photon resonant transition, as sketched in Fig. 11.11(a), leads to different results and interpretation. Since the interaction is a two-photon process, the weak probe alone cannot have any significant effect on the system, and there will be no signal if the probe is ahead of the pump pulses. We have seen in Chapter 3 that for a two-photon transition, Bloch's equations apply, except that the driving term is proportional to the square of the field. The two counter-propagating pump pulses can produce a two-photon excitation oscillating at $2\omega_\ell$, which will decay with the phase relaxation time $T_{2(2ph)}$ of the two-photon transition. One component of this two-photon excitation, ϱ_{12}, with no spatial modulation (zero spatial frequency), will interact with a probe to generate a counter-propagating signal by two-photon stimulated emission. A probe pulse sent through the interaction region with a subsequent delay τ_d will induce a signal by two-photon stimulated emission, $\tilde{\mathcal{E}}_4 \propto \varrho_{12}(\tau_d)\tilde{\mathcal{E}}_3^*$. Since the probe field corresponds to a phase factor $\omega_\ell + k_x x$ and the two-photon excitation to a phase factor $2\omega_\ell$, the signal E_4 has a phase factor $2\omega_\ell - \omega_\ell - k_x x = \omega_\ell - k_x x$, which describes a wave

propagating in the direction opposite to the probe. Since the two-photon excitation ϱ_{12} is the amplitude of an off-diagonal matrix element decaying with a two-photon phase relaxation time $T_{2(2ph)}$, the two photon stimulated emission being proportional to ϱ_{12} will only exist within $T_{2(2ph)}$ of the pump excitation. In the case of two-photon resonance, it is thus the trailing edge of the signal energy versus delay that is a measure of the phase relaxation time $T_{2(2ph)}$.

An example of determination of phase relaxation times through DFWM is given in Fig. 11.11(b). In this particular case, the sample is the saturable absorber jet (dye DODCI) of a mode-locked dye laser [9]. The two pump pulses are the counter-propagating pulses circulating inside the dye laser cavity. The probe is taken from one of the outputs of the dye laser, and focused with a 25 mm focal distance lens into the interaction region. Figure 11.11(b) shows the average intensity of the signal retro-reflected into the probe direction, as a function of the delay of the probe. The leading edge of the signal matches exactly the instantaneous response, given the pulse shape $\tilde{\mathcal{E}}(t) = \exp\left[-0.15ix^2\right]/\{\exp[-1.33x] + \exp[0.8x]\}$ (where $x = t/\tau_s$, and the pulse FWHM is $1.72\tau_s = 76$ fs). The instantaneous response, for the single-photon transition model, is calculated by taking the steady state solution of Bloch's equations (3.72) and (3.73) for the field consisting of the sum of the probe and pump fields. The trailing edge of the DFWM signal versus delay shows clearly the effect of a two-photon coherence. Following the procedure outlined above, the DFWM signal can be calculated as a function of delay for the two-photon excitation [9]. The result of the calculation (for the particular pulse shape mentioned above) is plotted in Fig. 11.11(b) for three values of the two-photon phase relaxation time $T_{2(2ph)} = 20$ fs (dotted line), $T_{2(2ph)} = 50$ fs (solid line), and $T_{2(2ph)} = 75$ fs (dashed line).

The experiment thus indicates a two-photon resonant DFWM and a phase relaxation time of 50 fs (decay of the DFWM signal versus delay) for the two-photon transition. There is no resolvable effect of a single-photon resonant DFWM (rise-time of DFWM signal versus delay). The dominance of the two-photon enhancement of DFWM in DODCI at 620 nm is confirmed by theory. Simple numerical estimates [9] indicate that indeed, the contribution of the two-photon resonance dominates the DFWM signal.

11.7 Femtosecond resolved fluorescence

If an excitation is followed by fluorescence (luminescence), the time resolved measurement of the transients of this radiation provides useful information on the evolution of occupation numbers and relaxation channels. Streak cameras are often used to measure fluorescence decay. The temporal resolution of this instrument

is limited to approximately one half of a picosecond. As noted earlier, all-optical techniques are needed to obtain even better time resolution. The general method of correlation introduced in Chapter 10 applies also to fluorescence measurements.

A pump pulse provides the time dependent excitation to be analyzed. The radiation to be measured as a function of time is correlated with a delayed replica of the pump (reference pulse). This cross-correlation is achieved by up-converting (sum frequency generation) the fluorescence with the fs reference pulse. This technique, pioneered by Mahr and Hirsch [10] with ps pulses, was first applied to the fs range to measure the risetime of fluorescence in organic dyes [11].

The basic experimental setup as sketched in Fig. 11.12 includes a polarizing beam splitter, two quarter wave plates, and a nonlinear crystal for type II sum frequency generation. Type II sum frequency generation is essential to provide an optimum signal-to-background ratio. In the first experiment, an unamplified dye laser at 620 nm was used. After the calcite polarizing beam splitter, one of the polarization components of the main pulse is focused into the sample, e.g., a concentrated solution of oxazine dye in ethylene glycol. The backscattered fluorescence radiation (at ω_f) is collected by the focusing lens and recollimated towards the calcite prism and the nonlinear detection. In this reflective geometry, the temporal resolution is limited by the optical depth of the sample or the confocal parameter of the focused beam, whichever is shorter. With the concentrated solution of oxazine dyes used, the optical depth of the sample was approximately 2 μm, limiting the temporal resolution to 6 fs. A half wave plate can be introduced before the calcite polarizer to control the fraction of radiation sent to the sample.

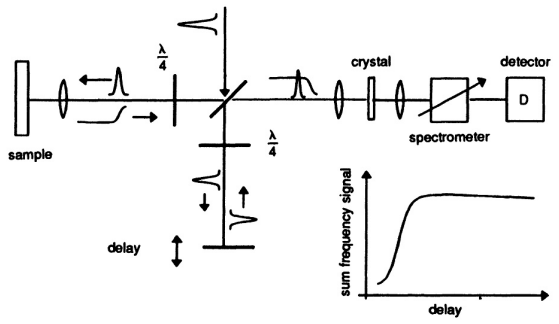

Figure 11.12: Setup for femtosecond resolved detection of fluorescence

The nonlinear crystal generates the sum frequency (of intensity I_{sum}) of the radiation components polarized along two orthogonal axes. If $I_{\text{ref}}(t-\tau_d)$ is the reference signal delayed by an amount τ_d and polarized along $\hat{x}$, and $I_s(t)$ is the

fluorescence signal polarized along the orthogonal direction $\hat{y}$:

$$I_{\rm sum}(\tau_d) \propto \int_{-\infty}^{\infty} I_{\rm ref}(t-\tau_d) I_s(t) dt. \tag{11.28}$$

To reach the ultimate resolution, the bandwidth of the conversion process should be larger than the bandwidth of the reference pulse. Both the imperfection of the crystal and the non-perfect rejection factor of the polarizing beam splitter contribute to a fraction ϵ_y of the reference beam polarized along the axis y, and hence a (τ_d independent) background signal:

$$I_b \propto \int_{-\infty}^{\infty} \epsilon_y I_{\rm ref}^2(t-\tau_d) dt. \tag{11.29}$$

The optical quality of the nonlinear crystal is essential in this experiment, since it helps discriminate between the signal and a background caused by second harmonic generation of the more intense reference beam. Additional background rejection can be obtained by spectrally separating the gated fluorescence (at $\omega_\ell + \omega_f$) from the second harmonic of the reference signal (at $2\omega_\ell$). The bandwidth of this filter should correspond to the pulse spectral bandwidth $\Delta\omega_p$ in order to ensure a temporal resolution given by the pulse duration. The focusing lens can be replaced by a parabolic mirror which collects fluorescence from a larger solid angle [12].

The number of upconverted photons per excitation pulse can formally be written as

$$N_{up} \approx V_1 V_2 Q \left(\frac{\nu_F \mathcal{W}_0}{\hbar \omega_F} \right) \frac{\Delta\omega_p}{\Delta\omega_F} \frac{\tau_p}{T_F}, \tag{11.30}$$

where V_1 is the linear loss of the experimental setup, V_2 is the fractional solid angle (i.e., solid angle divided by 4π) from which the focusing optics gathers the fluorescence, the term in parentheses describes the total number of fluorescence photons excited, $\Delta\omega_p/\Delta\omega_F$ is the fraction of the fluorescence spectrum which is upconverted and reaches the detector, τ_p/T_F with T_F as fluorescence lifetime is the fraction of fluorescence within the time window set by the pulse, and Q is the conversion efficiency of the sum frequency generation. For an upconversion experiment using a passively mode-locked dye laser to resolve the fluorescence dynamics of an organic dye and urea as nonlinear crystal, the following parameters are typical: $V_1 = 10^{-1}$, $V_2 = 2\ 10^{-3}$, $\mathcal{W}_0 = 150$ pJ, $\tau_p = 100$ fs, $T_F = 1$ ns, $Q = 5\ 10^{-4}$, $\nu_F = 1$. This yields $N_1 = 1.5\ 10^{-4}$ upconverted photons per pump pulse photon. This weak signal is detectable because the repetition rate of the source is $\approx 10^8$ Hz, resulting in a photon flux of $1.5\ 10^4$ s^{-1}. Figure 11.13 shows as an example the onset of fluorescence for the dye oxazine 720.

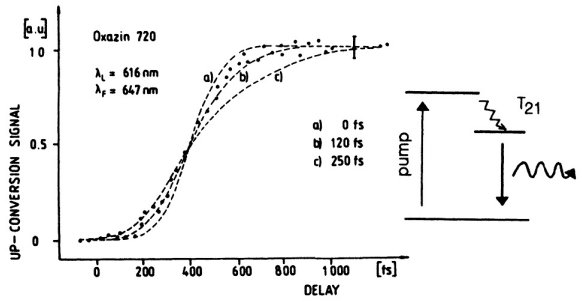

Figure 11.13: Onset of fluorescence of an organic dye (oxazin 720) measured by up-conversion. The number of photon counts is plotted versus delay. Theoretical curves corresponding to different relaxation times T_{21} of a simple three-level model system are shown.

11.8 Photon echoes

Photon echo is the standard method [13] — directly derived from spin echoes [14] — to determine the phase relaxation time T_2 of a transition. In the basic photon echo experiment, a sequence of two pulses is sent through the sample. Ideally, the first pulse will be a "$\pi/2$ pulse," and the second a "π pulse."

In an inhomogeneously broadened medium, the $\pi/2$ pulse excites the electric dipoles to oscillate with their characteristic frequency ω_0. Immediately after excitation all dipoles are in phase and the macroscopic polarization is maximum. As time progresses, because of their different eigenfrequencies, the dipoles dephase relative to each other. The macroscopic polarization is damped with a time constant given by the inverse of the width of the inhomogeneous line profile $g_{inh}(\omega_0 - \omega_{ih})$. The individual dipole groups still oscillate, with an amplitude damped with the phase relaxation time T_2 corresponding to the homogeneous line profile. The π pulse at delay τ_d adds a phase of π to each individual oscillator, which causes them to add again in phase after a time τ_d ($2\tau_d$ after the $\pi/2$ pulse). The associated macroscopic polarization results in a collective radiation effect called an "echo." The explanation of the echo in the Bloch vector model is as follows.

After the first pulse ($\pi/2$ pulse), the pseudo-polarization vector is aligned along the v axis, as shown in Fig. 11.14(a). Each component of the line $g_{inh}(\omega_0 - \omega_{ih})$ will precess around the "w axis" — thus in the u-v plane — at an angular velocity $(\omega_0 - \omega_\ell)$, for a time equal to the delay τ_d between the $\pi/2$ and π pulses. The effect of the π pulse, however, is to create the mirror image of the component of the pseudo-polarization vector, with respect to the u axis, as shown in Fig. 11.14(b). Each component of the line $g_{inh}(\omega_0 - \omega_{ih})$ is subsequently precessing at the velo-

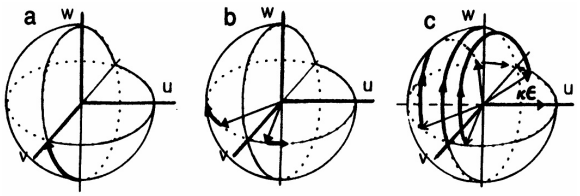

Figure 11.14: Photon echoes: A $\pi/2$ pulse (a) creates a macroscopic polarization (pseudo-polarization vector aligned along the v axis). Following the excitation, the components of the pseudo-polarization vector precess (b). After a π pulse is applied, the spreading process is reversed (c).

city ($\omega_\ell - \omega_0$), hence reversing the course of the previous "spreading." After a time τ_d following the π pulse, the components of the pseudo-polarization vector will be lined up again, resulting in a macroscopic echo signal [Fig. 11.14(c)]. The only decay mechanism for the echo is the nonreversible homogeneous decay. The pseudo-polarization vector of initial amplitude $\mathcal{P}_0$, after the delay $2\tau_d$, has been reduced exponentially to $\mathcal{P}_0 \exp(-2\tau_d/T_2)$; hence the echo intensity decays as $\exp(-4\tau_d/T_2)$. It should be noted that the $\pi/2$ and π pulse areas need not be reached in order to observe an echo. The amplitude however, is maximum for this particular choice.

The dephasing in condensed matter at room temperature is extremely fast. The challenge in photon echo measurement is to resolve the fast decaying echo from scattering from the tail of the preceding π pulse. The various possibilities to separate the signal are:

1. temporal gating of the echo
2. **k** vector separation
3. separation by polarization
4. separation by focalization

The time resolution necessary for the first technique could be achieved by upconverting the echo using type II second harmonic generation with a delayed excitation pulse (of polarization orthogonal to that of the echo). The other three techniques are commonly used. If $\mathbf{k_1}$ is the wave vector of the first ($\pi/2$) pulse, and $\mathbf{k_2}$ the wave vector of the second one, it can be shown that the angle of emission of the third pulse (the echo) is twice the angle between the direction of the two first pulses — hence $\mathbf{k_e} = 2\mathbf{k_2} - \mathbf{k_1}$ (cf. Fig. 11.15). This property can be easily

understood from momentum conservation considerations. Indeed, a photon echo is a particular case of degenerate four-wave mixing experiment, in which the first two waves form a grating. The latter waves do not need to be simultaneous; their interval only needs to be shorter than the phase relaxation time, to form a grating. The grating vector is $\mathbf{k}_2 - \mathbf{k}_1$. The second pulse with wave vector $\mathbf{k}_2$ scatters off that grating, to generate a first-order diffracted wave in the direction $\mathbf{k_e} = \mathbf{k}_2 - (\mathbf{k_1} - \mathbf{k_2})$. The latter property is directly related to the focusing properties of the echo. If the radius of curvature of the first $\pi/2$ pulse is R_1, and that of the π pulse R_2, the echo has the wavefront curvature given by [15]:

$$\frac{1}{R_e} = \frac{2}{R_2} - \frac{1}{R_1} \tag{11.31}$$

Polarization can also be used to distinguish the echo from the intense excitation pulses. The polarization dependence of the echo has been investigated by Alekseef and Evseev [16] and shown to depend on the total angular momentum number J of each of the two levels involved in the transition. For a J=1/2 $\rightarrow$ J=1/2 transition, the polarization of the echo makes an angle 2ψ with that of the first (linearly polarized) pulse (ψ being the angle between the polarization of the first and second pulse). In the latter case also, a linearly polarized pulse following a circularly pola-

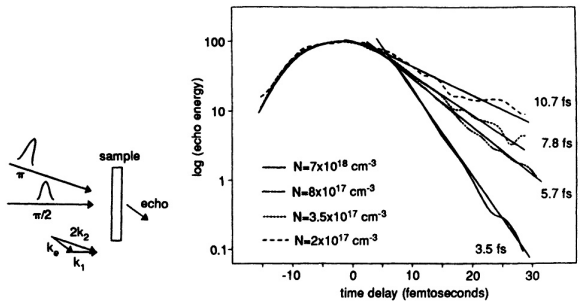

Figure 11.15: Photon echo applied to GaAs. Left: wave vector diagram. Right: echo amplitude versus delay for different carrier densities (adapted from [17]).

rized pulse, produces a photon echo with circular polarization. For transitions J=0 $\leftrightarrow$ J=1 and J=1 $\rightarrow$ J=1, the echo has the polarization of the second pulse, with an amplitude proportional to cosψ.

None of the echo separation techniques totally eliminates the background due to the first pulses. The duration of the exciting pulses should be shorter than the phase relaxation T_2 to be measured.

The fs photon echo technique has been applied to the study of dephasing of band-to-band transitions in the direct gap semiconductor GaAs [18]. Dephasing in

this system is due to momentum relaxation of the carriers, as verified by an independent method that specifically probes momentum relaxation (see previous sections). The data (Fig. 11.15) indicate a carrier concentration dependent phase relaxation time ranging from 14 to 44 fs [17,18], fitting the power law $T_2 = 6.2\ 10^6 \times N^{-0.3}$ (T_2 in fs, concentration of excited carriers N in cm^{-3}). This power law is characteristic of a three dimensional screening. A similar experiment performed on two-dimensional multiple quantum wells gave a density law $T_2 = 6.8\ 10^7 \times N^{-0.55}$, reflecting a two-dimensional screening of carriers [19]. Recent advances in fs photon echo spectroscopy of molecules and solids are summarized in papers by Fayer et al. [20] and Hannaford et al. [21].

In summary, the photon echo method is quite powerful and useful for the determination of relaxation times longer than the pulse duration. It has been one of the most commonly used.

11.9 Zero-area pulse propagation

The photon echo experiment is based on a sequence of two non-overlapping pulses whose relative phase is unimportant. An essential feature of coherent excitation is that the excitation depends on the phase of the applied signal. We have seen in Chapter 3 that a sequence of two pulses 180^o out of phase applied at resonance to a two-level system, will return that system to the ground state. There will be no energy loss for this particular pulse sequence, while there will be maximum absorption if the pulses are in phase. The contrast in absorption for the "in phase" pulse sequence — as opposed to the sequence of pulses out of phase — can be used as a measure of coherent interaction, and to determine T_2. The experimental setup consists essentially of a Michelson or a Mach–Zehnder interferometer (Fig. 11.16) to produce a zero-area pulse.

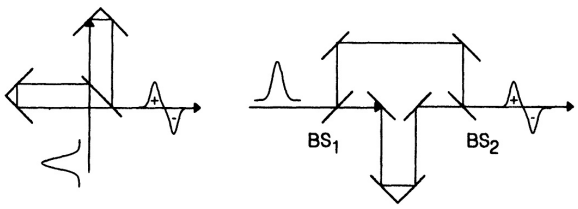

Figure 11.16: Michelson or Mach–Zehnder interferometers for the generation of zero-area pulses. The beam splitters BS_1 and BS_2 should be identical, in order to produce a zero-area pulse. The field envelopes of the pulses are shown.

The measurement is particularly simple and clear in the case of a single ho-

mogeneously broadened line. A linear (i.e., with a small area pulse) measurement provides all the information needed in that case. The zero-area pulse sequence has a zero spectral Fourier component at the average pulse frequency. The *linear* absorption for that pulse sequence — when applied at resonance with the line — is proportional to the spectral overlap of the line and the pulse spectrum. For $T_2 = \infty$, the infinitely narrow line coincides with the "node" of the spectrum of the zero-area pulse, and there is no absorption. The smaller T_2, the broader the line and its overlap with the pulse spectrum. With decreasing T_2, the ratio of absorption for an "out of phase" (zero-area) pulse sequence to the absorption for an "in phase" pulse sequence will also decrease. An illustration of such a measurement in Li-vapor is shown in Fig. 11.17. The energy of the second harmonic of the transmitted pulse sequence is plotted as function of the delay between the two components of the pulse.

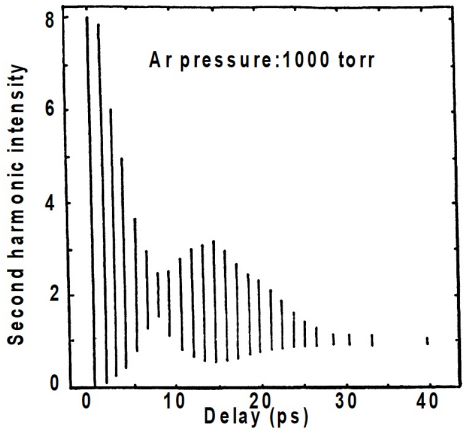

Figure 11.17: Second harmonic detection of the transmission of a zero-area pulse sequence consisting of two delayed pulses as a function of delay through lithium vapor in the presence of argon as buffer gas. The vertical lines indicate the contrast between in- and out-of-phase transmission. The second harmonic of the transmitted zero-area pulse sequence versus delay is recorded. The advantage of the second harmonic detection is that the first portion of the curve is approximately the interferometric autocorrelation of the pulse. The transmission corresponding to out-of-phase pulse sequence is the lower envelope near zero delay (weaker pulse because of destructive interference) and becomes the upper envelope for larger delays (larger transmission on resonance for out-of-phase pulse sequences).

In the time domain the experiment can be explained as follows. The first signal emerging out of the interferometer of Fig. 11.16 excites the resonant transition in lithium vapor. The induced dipoles reradiate a field which opposes the applied field and therefore cause absorption. The energy stored in the medium will be

restituted to the second signal emerging out of the interferometer if the latter is 180^o out of phase with the first pulse (the reradiated field adds in phase with the applied electromagnetic signal). Maximum absorption occurs for in-phase pulse sequences. The signal versus delay should therefore show an interference pattern with a periodicity in delay equal to the light period.

The constructive/destructive interferences that extend beyond the region of pulse overlap decay with the collision time of the resonant sodium atoms with a buffer gas (Ar, 1000 torr pressure). Second harmonic detection was used in that particular example [22]. By using second harmonic detection, the transition between the region corresponding to pulse interferences, and coherent interaction effects, can easily be identified. For delays smaller than the pulse duration, the pulse interference pattern is an interferometric autocorrelation (see Chapter 10).

In the case of an inhomogeneously broadened line, the phase dependence of the interaction disappears in the weak pulse limit. We have seen in Chapter 3 that the weak pulse absorption is proportional to the spectral overlap of the line and pulse. As shown by Eq. (3.95), in the case of purely inhomogeneous broadening and no saturation:

$$\frac{dW}{dz} \propto \int_{-\infty}^{\infty} g_{inh} |\mathcal{E}(\Omega)|^2 d\Omega = -\alpha_0 W, \tag{11.32}$$

and the absorbed energy is independent of the phase content of the pulse. There is, however, a difference in *nonlinear* transmission [for which the approximation of Eq. (11.32) does not apply] of "in-phase" and "out-of-phase" pulse sequences, even in the case of inhomogeneous broadening. Let us consider a sequence consisting of two pulses. If each half of the pulse sequence has an area between 0 and π, the zero-area pulse sequence will be absorbed more strongly than the "in-phase" pulse sequence. The physical reason can be explained simply by considering the originally uniform absorption spectrum [Fig. 11.18(a)] in which the first pulse burns a hole, which is seen by the second pulse as an inverted homogeneously broadened line [Fig. 11.18(b)]. For the "in phase" pulse sequence, there is less absorption because of the reduced absorption of spectral components at the pulse average frequency [Fig. 11.18(c)]. In contrast, the zero-area pulse sequence does not have spectral components overlapping with the center of the hole [Fig. 11.18(d)]. However, if each half of the pulse sequence is a π pulse, the system will be returned to ground state independently of the relative phase of the pulses.

The phase relaxation time T_2 can be extracted [23] by measuring the ratio of the energy transmission factor $\Delta\mathcal{W}/\mathcal{W}$ for a sequence of pulses 180^o out of phase to the same transmission factor for the "in phase" pulse sequence, as a function of total energy $\mathcal{W}$ in the pulse sequence. The corresponding values of α_π/α_0 are plotted in Fig. 11.19 for three values of the phase relaxation time T_2.

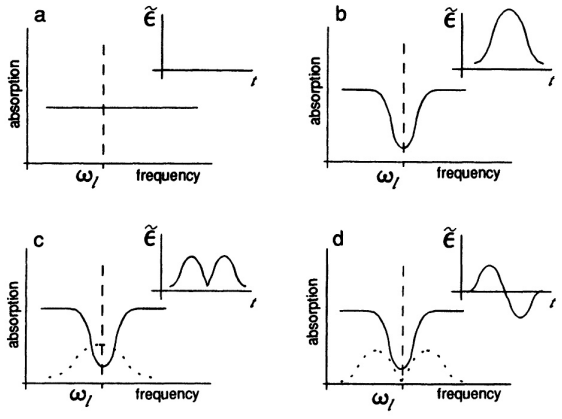

Figure 11.18: Interaction of an in-phase and out-of-phase two-pulse sequence with an homogeneously broadened absorbing transition. Initially (a), the line profile is uniform. At $t = t_1$, the first of a two-pulse sequence burns a hole in the uniformly inhomogeneously broadened absorption line (b). The second pulse no longer sees a uniform line, but an inverted homogeneously broadened line. The absorption will be smaller for the in-phase pulse sequence (c) which has more spectral components (dotted line) overlapping with the center of the hole, than with the out-of-phase pulse sequence (d).

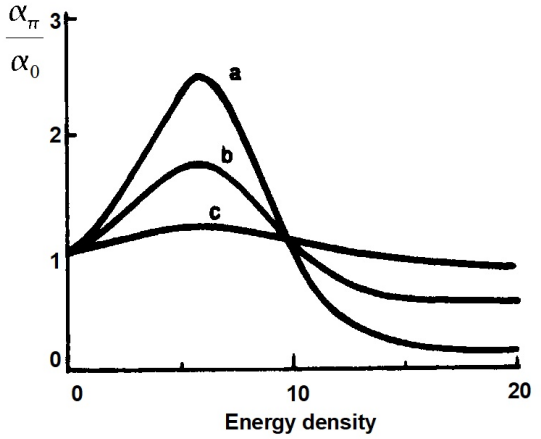

Figure 11.19: Ratio of the relative energy transmission for the 180^o out-of-phase α_π to the in-phase α_0 pulse sequence, as a function of pulse energy $\mathcal{W}$, for various values of the phase relaxation time T_2, for an absorption line with infinite inhomogeneous broadening. The pulses are Gaussian, with a temporal separation equal to twice their duration (FWHM). The phase relaxation times are 100× (a), 6× (b), and 1× (c) the pulse duration.

The main advantages of zero-area pulse excitation as applied to the determination of phase relaxation times are:

- the pulses of the sequence can overlap
- phase relaxation times shorter than the pulse duration can be measured
- the experimental technique is particularly simple
- a 180^o pulse sequence has zero area for transitions of different degeneracy and dipole moment

The last property results in an easier interpretation of the data when the measurement covers more than one type of transition. The extension of this method to molecular multiphoton transitions has been discussed in Refs. [24, 25]. In addition to the measurement of a dephasing time for a multiphoton transition, the pattern of absorption versus relative phase of the pulse sequence can be used to identify the type of resonance [25].

11.10 Impulsive stimulated Raman scattering

11.10.1 General description

Some molecular vibrations — for instance the stretching mode of a symmetric diatomic molecule such as N_2 — cannot be directly excited by a resonant electromagnetic field. However, such dipole forbidden transitions between states of equal parity and angular momentum can be accessed by a transition involving two photons. In resonant Raman scattering, the difference between the optical frequencies of the two photons involved in the transition is equal to the frequency of the mechanical vibration being excited. Let us consider, for instance, a molecular vibration of frequency ω_{21} between two states $|2\rangle$ and $|1\rangle$ of identical parity [Fig. 11.20(a)]. The molecule can be brought in the vibrationally excited state $|2\rangle$ by a succession of optical excitations via the dipole allowed transitions $|1\rangle \rightarrow \langle \ell|$ and $\langle \ell| \leftarrow |2\rangle$, involving photons of frequencies $\omega_{\ell 1}$ and $\omega_{\ell 2}$.

Because of the broad bandwidth of the fs pulse, stimulated Raman scattering can occur through the mixing of various spectral components of the ultrashort optical pulse [Fig. 11.20(b)]. For example, a molecular vibration is initiated by the sudden impulse exerted by the electric field of the pulse. The sample selects a pair of frequency components whose difference is in resonance with the eigenfrequencies of a Raman transition. This type of Raman scattering is called "impulsive stimulated Raman scattering" [26]. The fs excitation makes it possible to excite in

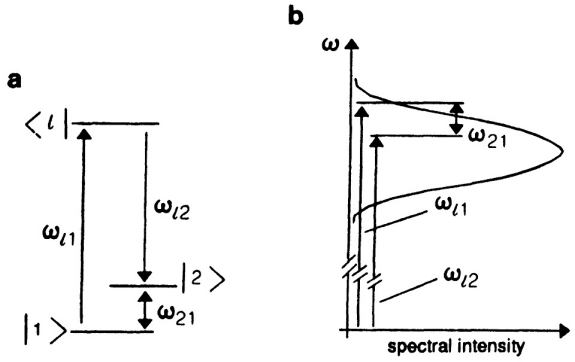

Figure 11.20: (a) Excitation of a Raman transition $|1\rangle \rightarrow |2\rangle$ via an electronically excited state $\langle \ell |$. (b) For a fs pulse of average carrier frequency ω_ℓ, the two frequency components of the Raman transition are contained within the pulse spectrum. The medium itself selects the frequency pairs suitable to drive the Raman transition.

phase a macroscopic ensemble of vibrating molecules. In solids, it is a coherent excitation of lattice vibrations that is achieved.

It is generally not possible to achieve a complete excitation of the Raman transition with a single fs pulse. Many Raman-active modes can sometimes be accessed by the same fs pulse. However, if the process of impulsive stimulated Raman scattering is repeated at each cycle $2\pi/\omega_v$ of a Raman transition, the excitation will be enhanced. The selectivity of the process is also increased by the periodic excitation [27].

Impulsive stimulated Raman scattering can be used to analyze vibrational motions — for instance to determine their decay through pump-probe techniques. Synchronous excitation by a train of pulses can lead to substantially larger amplitudes of motion. This excitation process can generate high-frequency vibration. A train of pulses spaced by a picosecond can generate THz LO phonons in semiconductors, which have a wavelength in the 100 Å range, and can therefore be used for high-resolution imaging in solids.

11.10.2 Detection

The change in matter properties associated with the Raman excitation can be probed in a variety of ways. One can, for instance, probe an induced birefringence, in which case the rotation of the probe polarization will be measured, as detailed in Section 11.5. In parallel polarization (probe polarization parallel to that of the

pump), the attenuation of the probe will be modulated with delay, because the probe pulse can also induce Raman transitions. The phase of the oscillations of attenuation versus delay of the probe depends on the particular spectral component that is being probed. In the example reproduced in Fig. 11.21, the pump and probe have the same polarization and are sent nearly collinearly through a sample of liquid CH_2Br_2 [26]. The transmitted probe is dispersed by a monochromator. Two frequency components (609 nm and 620 nm) are displayed as a function of delay in Fig. 11.21.

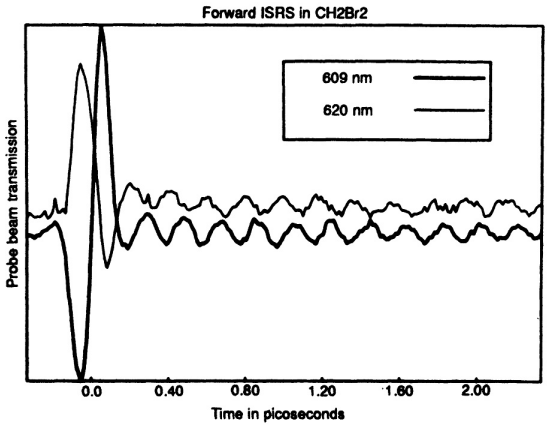

Figure 11.21: Transmission versus delay for two spectral components of the probe signal, for a sample of CH_2Br_2 pumped by a 65 fs pulse of a few μJ energy at 615 nm. The excitation and probe pulses are focused to a 200 μm spot size, at an angle of 5^o, into a 2 mm sample cuvette (from [26]).

Both spectral components are seen to oscillate with delay at the molecular vibration frequency, but with opposite phase. A simple explanation is that at a particular delay, the position of the vibrating coordinates is such that the 609 nm radiation is absorbed, and the 620 nm reinforced by the Raman transition. For a delay corresponding to half a vibration cycle later, the 609 nm transition will be reinforced, and the 620 nm attenuated.

So far we have assumed a single pump pulse to induce the Raman signal. A standing wave pattern can also be generated for the impulsive stimulated Raman signal, either through a periodic configuration of the sample, or through the use of two intersecting pump pulses.

An example of sample periodicity is a multiple quantum well structure, of which the spacing between wells is made to match the wavelength of the phonon to be generated. The phonon can be generated by a train of fs pulses spaced by the phonon period, tuned to the intraband absorption in the quantum wells. The

periodic spatial structure that is excited is responsible for the spatial coherence of the phonon [28]. The excitation by a periodic pulse sequence ensures temporal coherence of the created phonons.

It is also possible to create a standing wave Raman excitation with two intersecting pump pulses of the same frequency [26]. The temporal evolution of the vibration is easily analyzed through diffraction of a probe pulse by the standing wave pattern.

11.10.3 Theoretical framework

The same density matrix formalism as in Chapters 3 can be used to describe impulsive stimulated Raman scattering. As in Fig. 11.20, we will consider Raman transitions between a ground state $|1\rangle$ and a first excited state $|2\rangle$ of a vibrational mode with frequency ω_{21} . The states $|1\rangle$ and $|2\rangle$ are infrared inactive, i.e., there is no dipole allowed transition $|1\rangle \rightarrow |2\rangle$. Coupling between these two states can occur via any electronic state $\langle \ell|$. All states $|\ell\rangle$ connected to $|1\rangle$ and $|2\rangle$ via a dipole transition will contribute to the Raman transition. We assume the optical field E to be off-resonant with all single-photon transitions. For this assumption to hold, the detuning of the intermediate levels $\langle \ell|$ has to exceed several pulse bandwidths.

The evolution of the system is described by the density matrix equations (3.63). For the particular level system being considered:

$$\begin{aligned}
\frac{\partial \rho_{12}}{\partial t} &- i\omega_{21}\rho_{12} = -\frac{i\tilde{E}^+}{\hbar}\sum_{\ell}(\rho_{1\ell}p_{\ell 2} - p_{1\ell}\rho_{\ell 2}) \\
\frac{\partial \rho_{22}}{\partial t} &= -\frac{i\tilde{E}^+}{\hbar}\sum_{\ell}(\rho_{2\ell}p_{\ell 2} - p_{2\ell}\rho_{\ell 2}) \\
\frac{\partial \rho_{1\ell}}{\partial t} &- i\omega_{\ell 1}\rho_{1\ell} = -\frac{i\tilde{E}^+}{\hbar}\sum_{j}(\rho_{1j}p_{j\ell} - p_{1j}\rho_{j\ell}),
\end{aligned} \tag{11.33}$$

where the sum over j applies to any level connected to $\langle \ell|$ by a dipole transition, including levels 1 and 2. A similar equation applies for $\rho_{2\ell}$.

As we have seen in Chapter 1, it is more convenient to decompose the off-diagonal matrix elements $\rho_{1\ell}$ and $\rho_{2\ell}$ into an envelope and fast varying phase term. For instance:

$$\rho_{1\ell} = \varrho_{1\ell}\, e^{i\omega_\ell t} \tag{11.34}$$

and a similar equation for $\rho_{2\ell}$. Substituting Eq. (11.34) into the third equation (11.33), and keeping only the levels 1 and 2 as levels that are dipole connected to levels ℓ:

$$\frac{\partial \varrho_{1\ell}}{\partial t} + i(\omega_\ell - \omega_{\ell 1})\varrho_{1\ell} = -\frac{i\tilde{\mathcal{E}}}{2\hbar}(\rho_{11}p_{1\ell} + \rho_{12}p_{2\ell}). \tag{11.35}$$

The assumption of the intermediate levels $\langle \ell|$ being off-resonance enables us to use the adiabatic approximation. This is a standard approximation used routinely in the context of deriving interaction equations in condition of two (and more) photon resonance [29]. A detailed analysis of the use of the adiabatic approximation in the context of two-photon transitions can be found in [29]). Essentially, the second term in the left hand-side of Eq. (11.35) dominates, and we can approximate $\varrho_{1\ell}$ by its steady state value:

$$\varrho_{1\ell} = \frac{-\tilde{\mathcal{E}}(\rho_{11}p_{1\ell} + \rho_{12}p_{2\ell})}{2\hbar(\omega_\ell - \omega_{\ell 1})}, \tag{11.36}$$

and a similar equation for $\varrho_{2\ell}$. Substituting into the first equation (11.33), we find the evolution equation for the coherent Raman excitation:

$$\frac{\partial \rho_{12}}{\partial t} - i\omega_{21}\rho_{12} = -\frac{i}{4\hbar^2}\tilde{\mathcal{E}}\tilde{\mathcal{E}}^* \sum_\ell \left(\rho_{11}\frac{p_{1\ell}p_{\ell 2}}{\omega_\ell - \omega_{\ell 1}} - \frac{p_{1\ell}p_{\ell 2}}{\omega_\ell - \omega_{\ell 2}}\rho_{22} \right) \tag{11.37}$$

Of particular interest is the amplitude of the off-diagonal element ρ_{12}. Let us define a (complex) amplitude ϱ_{12} similarly as in Eq. (11.34): $\rho_{12} = \varrho_{12}\exp(i\omega_{12}t)$. In addition, to simplify the discussion, let us assume, that there is only one level $\langle \ell|$ that dominates the interaction. We note that $\omega_\ell - \omega_{\ell 2} = (\omega_\ell - \omega_{\ell 1})[1 + \omega_{21}/(\omega_\ell - \omega_{\ell 1})]$. Substituting in Eq. (11.37) yields:

$$\frac{\partial \varrho_{12}}{\partial t}e^{i\omega_{21}t} = \frac{ip_{1\ell}p_{\ell 2}}{4\hbar^2(\omega_\ell - \omega_{\ell 1})}\tilde{\mathcal{E}}\tilde{\mathcal{E}}^*(\varrho_{22} - \rho_{11}) \tag{11.38}$$

where $\varrho_{22} = \rho_{22}/[1 + \omega_{12}(\omega_\ell - \omega_{\ell 1})]$. We recognize in Eq. (11.38) a Rabi frequency similar to the two-photon Rabi frequency discussed in Chapter 3:

$$\frac{p_{1\ell}p_{\ell 2}}{4\hbar^2(\omega_\ell - \omega_{\ell 1})}\tilde{\mathcal{E}}(t)\tilde{\mathcal{E}}^*(t) = \frac{r_{12}}{\hbar^2}\tilde{\mathcal{E}}(t)\tilde{\mathcal{E}}^*(t). \tag{11.39}$$

The evolution equations for the density matrix components can be rewritten:

$$\begin{aligned} \frac{\partial \varrho_{12}}{\partial t} &= i\frac{r_{12}}{\hbar^2}\tilde{\mathcal{E}}\tilde{\mathcal{E}}^* e^{-i\omega_{21}t}[\varrho_{22} - \rho_{11}] \\ \frac{\partial \rho_{22}}{\partial t} &= -2\mathrm{Im}\left[\frac{r_{12}}{\hbar^2}\tilde{\mathcal{E}}\tilde{\mathcal{E}}^*\varrho_{12}e^{i\omega_{21}t}\right]. \end{aligned} \tag{11.40}$$

The form of the set of equations (11.40) is similar to Bloch's equations (3.68) and (3.69). In the weak pulse approximation ($\rho_{11} \approx 1$), after passage of the fs excitation, the off-diagonal matrix element oscillates at the Raman frequency:

$$\begin{aligned} \rho_{12} &\approx -ie^{i\omega_{21}t}\left[\int_{-\infty}^{\infty}\frac{r_{12}}{\hbar^2}\tilde{\mathcal{E}}(t')\tilde{\mathcal{E}}^*(t')e^{-i\omega_{21}t'}dt'\right] \\ &= -ie^{i\omega_{21}t}\left[\int_{-\infty}^{\infty}\frac{r_{12}}{\hbar^2}\tilde{\mathcal{E}}(\Omega)\tilde{\mathcal{E}}^*(\Omega - \omega_{21})d\Omega\right]. \end{aligned} \tag{11.41}$$

Equation (11.41) is obtained by integrating the first differential equation (11.40) with $\rho_{11} \approx 1$ and $\rho_{22} \approx 0$. It can be seen immediately from the convolution in Eq. (11.41) that, for efficient Raman excitation, the pulse spectrum should be broad compared with the Raman frequency ω_{21}. Indeed, for $\omega_{21} \gg \tau_p^{-1}$, there is no overlap between $\tilde{\mathcal{E}}(\Omega)$ and $\tilde{\mathcal{E}}(\Omega - \omega_{21})$. The dimensionless quantity

$$\theta_R = \int_{-\infty}^{\infty} \frac{r_{12}}{\hbar^2} \tilde{\mathcal{E}}(\Omega)\tilde{\mathcal{E}}^*(\Omega - \omega_{21}) d\Omega \tag{11.42}$$

is the analogue of the tipping angle of the polarization in the Bloch vector model. We recognize from the analogy between Eqs. (11.40) and Bloch's equations (3.68) and (3.69), and the description of the vector model in Chapter 3, that an angle θ_R on the order of unity will be required to bring the ground state population to a vibrational excited state of energy $\hbar\omega_{21}$. It is left as a problem at the end of this chapter to demonstrate that the convolution in θ_R can be maximized by using, instead of a single pulse, a train of pulses spaced in time by $\tau_d = 2n\pi/\omega_{21}$ (n integer). The increase in selectivity can be inferred from the form of θ_R in the frequency domain [Eq. (11.42)]: θ_R vanishes for a pulse spacing $\Delta t \neq 2\pi/\omega_{21}$, in the case of a large number of pulses and undamped oscillations. The technique of using a synchronized pulse train can also lead to much larger amplitudes of motion than a single pulse [27]. Methods of generating such pulse trains have been presented in Chapter 9.

11.10.4 Single pulse shaping versus mode-locked train

The expression (11.42) for θ_R can be maximized by a pulse train whose repetition rate is any submultiple of the frequency $\omega_{21}/2\pi$. With ω_{21} in the THz range, one technique is to "shape" a fs pulse into a sequence of pulses. Another possibility is to tune the mode-locked period of the laser to $T = 2n\pi/\omega_{21}$ (n integer). Such a technique is reminiscent of high-resolution coherence spectroscopy, where the repetition rate of mode-locked trains is tuned to a submultiple of an atomic resonance, leading, for instance, to enhanced quantum beats [30]. With advances in semiconductor lasers, repetition rates in the GHz to THz range are accessible with fs pulses. The repetition rate of passively mode-locked lasers can also be tuned continuously by adjusting the cavity length [31].

A question that arises is: what is the lowest repetition rate that can be used to excite a particular resonance ω_{21}? That question can be simply answered by modeling the resonant system by a classical oscillator, driven by an infinite series of δ function forces separated by a time T. Each successive pulse excites the particular oscillation corresponding to the resonance. This oscillation is represented in the classical model by the displacement x of an oscillator of mass m, restoring force

$-Kx$, and damping constant b. The oscillation is not completely damped before the time of arrival of the next pulse, which, if T is a multiple of $2\pi/\omega_{21}$, will reinforce the motion. After an infinite number of driving pulses, the damped oscillation between two successive driving pulses will be stationary (see Fig. 11.22). Assuming

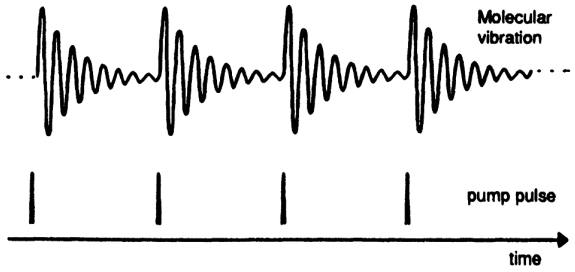

Figure 11.22: Damped molecular vibration, following impulsive stimulated Raman excitation by a train of ultrashort pulses. The amplitude of the oscillation will be maximum for a pulse separation equal to a multiple of the period of the molecular vibration.

$(2N+1)$ pulses in the train, the periodic driving force is represented by a series of δ functions: $F = F_0 \sum_{j=-N}^{N} \delta(t - jT)$. The equation of motion for the classical oscillator is:

$$m\ddot{x} + b\dot{x} + Kx = F_0 \sum_{j=-N}^{N} \delta(t - jT). \tag{11.43}$$

Simple Fourier transformation of this equation leads to a solution for the amplitude $x(\omega)$. Taking the inverse Fourier transform of that solution yields $x(t)$:

$$x(t) = \frac{F_0}{2\pi} \sum_j I_j \tag{11.44}$$

with

$$I_j = \int_{-\infty}^{\infty} \frac{e^{i\omega(t-jT)}}{(K - m\omega^2) + ib\omega} d\omega. \tag{11.45}$$

The integrand I_j in Eq. (11.45) has two poles at $\omega = i\Gamma \pm \omega_{21}$, and $\omega_{21}^2 = K/m - \Gamma^2$ and $\Gamma = b/2m$. The stationary solution for the oscillator is found by contour integration and summation (over j) of the geometric series:

$$x(t) = \frac{1}{2} A(T) e^{-\Gamma t + i\omega_{21} t} + c.c. \tag{11.46}$$

with

$$\begin{aligned} A(T) &= \frac{iF_0}{\omega_{21}} \frac{1}{1-e^{\Gamma T + i\omega_{21}T}} \\ &= \frac{iF_0}{\omega_{21}} \frac{1-e^{\Gamma T - i\omega_{21}T}}{1+e^{2\Gamma T}-2e^{\Gamma T}\cos\omega_{21}T}. \end{aligned} \tag{11.47}$$

$A(T)$ is essentially the amplitude of the first cycle of oscillation. Its value is maximum and equal to $iF_0/[\omega_{21}(1-e^{\Gamma T})]$ when $\omega_{21}T = 2n\pi$, and minimum, equal to $iF_0/[\omega_{21}(1+e^{\Gamma T})]$ for $\omega_{21}T = 2(n+1)\pi$. The modulation depth $(1-e^{\Gamma T})/(1+e^{\Gamma T})$ is thus determined solely by the damping rate and the period of the driving force T. When driving a system at a subharmonic of the resonant frequency, the term $\omega_{21}T$ in Eq. (11.47) can be very large ($\omega_{21}T = 2n\pi$, with n a large integer). The "resonances" (values of the periodicity T that satisfy the resonance condition) are closely spaced. The damping factor Γ determines which subharmonic N can still be used to drive effectively the resonance ω_{21}. Each δ-function force sets off an oscillation, which should not be completely damped before being reinforced by the next exciting pulse.

11.11 Self-action experiments

Pump-probe experiments are intended to provide information on linear and nonlinear properties of matter. As noted earlier, there is a fundamental temporal limitation. For the measurement interpretation, the pump or excitation process should be completed before the medium is probed. One could try to obtain information on the properties of matter by measuring the time resolved fields of a single pulse incident, reflected and/or transmitted by a thin sample (Fig. 11.23), using some of the techniques outlined in Chapter 10.

In the case of a linear interaction with the medium, the problem is analogous to the analysis of a linear circuit. For instance, referring to Chapter 1 [Eqs. (1.84) through (1.90)], the complex dielectric constant $\tilde{\epsilon}(\Omega) = \epsilon_0[1+\tilde{\chi}(\Omega)]$ can be extracted by taking the Fourier transform $\tilde{E}(\Omega)$ of the incident (i) and transmitted (t) fields:

$$1+\tilde{\chi}(\Omega) = -\frac{c^2}{z^2\Omega^2}\ln^2\left[\frac{\tilde{E}_t(\Omega)}{\tilde{E}_i(\Omega)}\right] \tag{11.48}$$

where z is the sample thickness.

There is no simple algorithm that can solve the general problem of retrieval of a nonlinear susceptibility $\chi^{(n)}(\Omega)$ from a series of measurements of incident, transmitted, and reflected fields. Some assumptions have to be made — for instance, that all nonlinear susceptibilities except the third order, $\chi^{(3)}$, can be neglected. Within

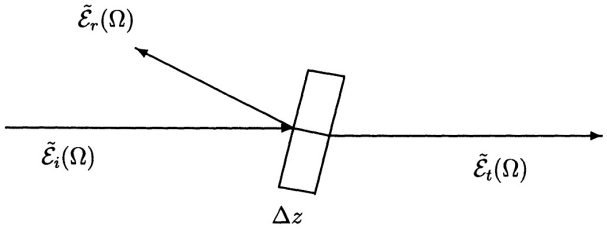

Figure 11.23: For linear systems, and some simple nonlinear systems, the complex susceptibility can be completely determined from single pulse transmission (reflection) measurements, provided the amplitude and phase of the incident, transmitted, and reflected signals can be completely determined.

this approximation, measurement of the third harmonic transmitted field $\tilde{\mathcal{E}}_{3\omega}$ leads to a determination of the third-order susceptibility:

$$\chi^{(3)}(\Omega) = \frac{2c\Delta z}{\omega_\ell} \frac{\tilde{\mathcal{E}}_{3\omega}(\Omega)}{\tilde{\mathcal{E}}^2(\Omega)}. \tag{11.49}$$

The transmission measurements provide information on the bulk properties of the sample. Properties at the surface can be analyzed by measuring the reflected field. For instance, at normal incidence, the reflection coefficient is approximately $\chi_s(\Omega)/[4+\chi_s(\Omega)]$, where $\chi_s(\Omega)$ is the complex susceptibility at the surface (assumed to be $\ll 1$). In the presence of resonances, these complex susceptibilities may have a complicated functional dependence on the optical field.

11.12 Problems

1. Referring to Section 11.3, derive in detail Eqs. (11.5) through (11.9). Find the effect of the beam geometry on the temporal resolution for a square temporal profile, and square spatial profile in x and y.

2. A transient grating experiment is performed with a semiconductor. Let us assume that we have an amplitude grating only and that the carrier density $n(x,t)$ obeys the equation for ambipolar diffusion (one-dimensional model):

$$\frac{\partial n}{\partial t} - D\frac{\partial^2 n}{\partial x^2} = 0. \tag{11.50}$$

Derive a formula that relates the diffraction signal versus τ_d to the diffusion parameter D to be determined. From the diffusion parameter one can then

obtain the carrier mobility $\mu = eD/(k_B T)$, where e is the electron charge, k_B Boltzmann's constant, and T the temperature.

3. Prove that in a transient grating experiment the diffraction of a probe pulse measured as function of the delay between the two pump pulses contains the information on the transverse relaxation time T_2. Assume an ensemble of homogeneously broadened two-level systems, weak excitation, thin samples.

4. The purpose of this problem is to compare impulsive stimulated Raman scattering excited by a single pulse and a train of identical pulses. The period of the Raman oscillation to be excited is 1 ps, and its damping time is 500 ps. The molecular system has a resonant absorption at 750 nm. The laser system delivers a Gaussian pulse of 50 fs duration, 1 nJ energy, at 770 nm, focused into the sample with a beam waist of $w_0 = 200$ μm. The dipole moment of the transitions $p_{1\ell} = p_{\ell 2} = 6\ 10^{-29}$ Cm. Calculate the off-diagonal matrix element ρ_{12} resulting from the excitation by the Gaussian pulses. Assume next each fs pulse is replaced by a train of 10 Gaussian pulses of 50 fs duration, but of 0.1 nJ energy each. Calculate the off-diagonal matrix element as a function of the period of this pulse train (in the range 1–10 ps).

Bibliography

[1] J. Krueger. Master thesis, Friedrich-Schiller-University Jena, 1988.

[2] W. Rudolph, J. Puls, F. Henneberger, and D. Lap. Femtosecond studies of transient nonlinearities in wide-gap II-VI semiconductor compounds. *Phys. Stat. sol. (b)*, 159:49–53, 1990.

[3] M. T. Portella, J.-Y. Rigot, R. W. Schoenlein, C. V. Shank, and J. E. Cunningham. k-space carrier dynamics in GaAs. In C. B. Harris, E. P. Ippen, G. A. Mourou, and A. H. Zewail, editors, *Ultrafast Phenomena VII*, pages 285–287, Berlin, 1990. Springer-Verlag.

[4] L. Oudar, A. Migus, D. Hulin, G. Grillon, J. Etchepare, and A. Antonetti. Femtosecond orientational relaxation of photoexcited carriers in GaAs. *Phys. Rev. Lett.*, 53:384–387, 1984.

[5] D. McMorrow, W. T. Lotshaw, and G. A. Kenney-Wallace. Femtosecond optical studies on the origin of the nonlinear responses in simple liquids. *IEEE J. of Quantum Electronics*, QE-24:443–454, 1988.

[6] H. J. Eichler, P. Guenther, and D. W. Pohl. *Laser-Induced Dynamic Gratings*. Springer, Berlin, Heidelberg, 1986.

[7] Y. R. Shen. *The Principles of Nonlinear Optics*. John Wiley & Sons, New York, 1984.

[8] J.-C. Diels, W.-C. Wang, and H. Winful. Dynamics of the nonlinear four-wave mixing interaction. *Applied Physics*, B26:105–110, 1981.

[9] J.-C. Diels and I. C. McMichael. Degenerate four-wave mixing of femtosecond pulses in an absorbing dye jet. *J. Opt. Soc. Am. B*, 3:535–543, 1986.

[10] H. Mahr and M. D. Hirsch. An optical upconversion light gate with picosecond resolution. *Optics Commun.*, 13:96–99, 1975.

[11] W. Rudolph and J.-C. Diels. Femtosecond time resolved fluorescence. In A. E. Siegman, editor, *Picosecond Phenomena V*, pages 71–74, Berlin, 1986. Springer-Verlag.

[12] J. Shah. Ultrafast luminescence spectroscopy using sum frequency generation. *IEEE J. of Quantum ELectron.*, QE-24:276–288, 1988.

[13] I. D. Abella, N. Q. Kurnit, and S. R. Hartmann. Photon echoes. *Phys. Rev.*, 141:391–406, 1966.

[14] E. L. Hahn. Spin echoes. *Phys. Rev.*, 80:580–594, 1950.

[15] C. V. Heer. Focusing of carr-purcell photon echoes, and collisional effects. *Phys. Rev. A*, 13:1908–1920, 1976.

[16] A. I. Alekseef and I. V. Evseev. Photon echo polarization in a gas medium. *Soviet Physics JETP*, 29:1139–1143, 1969.

[17] P .C. Becker, H. C. Fragnito, C. H. Brito-Cruz, R. L. Fork, J. E. Cunningham, J. E. Henry, and C. V. Shank. Femtosecond photon echoes from band-to-band transitions in GaAs. *Phys. Rev. Lett.*, 61:647–649, 1988.

[18] C. V. Shank, P. C. Becker, H. L. Fragnito, and R. L. Fork. Femtosecond photon echoes. In T. Yajima, K Yoshihara, C. B. Harris, and S. Shionoya, editors, *Ultrafast Phenomena VI*, pages 344–348, Berlin, 1988. Springer-Verlag.

[19] J.-Y. Rigot, M. T. Portella, R. W. Schoenlein, C. V. Shank, and J. E. Cunningham. Two-dimensional carrier-carrier screening studied with femtosecond photon echoes. In C. B. Harris, E. P. Ippen, G. A. Mourou, and A. H. Zewail, editors, *Ultrafast Phenomena VII*, pages 239–243, Berlin, 1990. Springer-Verlag.

[20] J. B. Ashbury, T. Steinel, and M. D. Fayer. In P. Hannaford, editor, *Femtosecond Laser Spectroscopy*, chapter Vibrational Echo Correlation Spectroscopy, pages 167–196. Springer, 2005.

[21] L. V. Dao, C. Lincoln, M. Lowe, and P. Hannaford. In P. Hannaford, editor, *Femtosecond Laser Spectroscopy*, chapter Spectrally resolved Two-Color Femtosecond Photon Echoes, pages 197–224. Springer, 2005.

[22] J.-C. Diels, W. C. Wang, and R. K. Jain. Experimental demonstration of a new technique to measure ultrashort dephasing times. In K. B. Eisenthal, R. M. Hochstrasser, W. Kaiser, and A. Laubereau, editors, *Ultrafast Phenomena III*, pages 120–122, Berlin, 1982. Springer-Verlag.

[23] J.-C. Diels. Feasibility of measuring phase relaxation time with subpicosecond pulses. *IEEE Journal of Quantum Electron.*, QE-16:1020–1021, 1980.

[24] J.-C. Diels, J. Stone, S. Besnainou, M. Goodman, and E. Thiele. Probing the phase coherence time of multiphoton excited molecules. *Optics Communications*, 37:11–14, 1981.

[25] V. I. Bespalov and V. I. Talanov. Molecular multiphoton excitation of phase coherent pulse pairs. *J. of Chem. and Phys.*, 81:143–149, 1984.

[26] S. Ruhman, A. Joly, and K. Nelson. Coherent molecular vibrational motion observed in the time domain through impulsive stimulated raman scattering. *IEEE Journal of Quantum Electron.*, 34:460–468, 1988.

[27] A. Weiner, D. Leaird, G. Wiederrecht, M. Banet, and K. Nelson. Spectroscopy with shaped femtosecond pulses:styles for the 1990s. In *SPIE Proceedings 1209*, pages 185–195, Los Angeles, CA, 1990.

[28] H. T. Grahn, H. J. Maris, and J. Tauc. Picosecond ultrasonics. *IEEE J. of Quantum Electron.*, 25:2562–2568, 1989.

[29] D. Grischkowsky, M. M. T. Loy, and P. F. Liao. Adiabatic following model for two-photon transitions: nonlinear mixing and pulse propagation. *Phys. Rev. A*, 12:2514–2533, 1975.

[30] J. Mlynek, W. Lange, H. Harde, and H. Burggraf. High-resolution coherence spectroscopy using pulse trains. *Phys. Rev. A*, 24:1099–1101, 1981.

[31] N. Jamasbi, J.-C. Diels, and L. Sarger. Study of a linear femtosecond laser in passive and hybrid operation. *J. of Modern Optics*, 35:1891–1906, 1988.

Chapter 12

Examples of Ultrafast Processes in Matter

12.1 Introduction

A microscopic analysis of many fundamental processes in matter starts at the ps or fs time scale. Primary events associated with macroscopic transformations that appear relatively slow, such as chemical reactions, photosynthesis, phase changes, and human vision, evolve on a fs time scale. A mere listing of all processes in biology, chemistry, and physics that are being actively investigated is already beyond the scope of this book. A detailed introduction of these topics can be found for example in the books by Kaiser et al. [1], De Schryver et al. [2], Shah [3] and Mukamel [4]. A periodic update of these topics is published in the proceedings of the bi-annual conferences on "Ultrafast Phenomena" [5].

Rather than to attempt an extensive review, this chapter will focus on a few examples of ultrafast events in matter, and their measurement. We shall proceed by order of material systems of increasing complexity. The simplest system is the single atom, in which wave packets representing the motion of the electron in a Rydberg orbit can be analyzed with ultrafast techniques. Next, we proceed from the single atom to simple molecules to dissociating molecules — a step towards chemical reactions. The next form of arrangement of atoms is condensed matter, in which fs techniques are particularly powerful in analyzing changes of phase. Finally, biological systems offer the ultimate in molecular complexity. Femtosecond techniques are an essential tool in unraveling, for example, the primary processes of vision and photosynthesis.

12.2 Ultrafast transients in atoms

12.2.1 The classical limit of the quantum mechanical atom

Bohr's model of the hydrogen atom was based on the concept of the electron describing a classical trajectory in the attractive potential of the nucleus. The quantization relation introduced empirically by Bohr (see, for instance Ref. [6]) states that the angular momentum of the orbits is quantized:

$$\frac{m_e m_p}{m_e + m_p} v r = p r = \hbar n \tag{12.1}$$

where v is the radial velocity of the electron (p its linear momentum) along the orbit of radius r, m_e and m_p are the masses of the electron and proton, and n is the quantum number. The classical picture of the orbiting electron violates the uncertainty principle for small quantum numbers n. In order to be able to describe the electron motion by a classical trajectory, the uncertainty in position (Δr) and momentum (Δp) should be smaller than r and p, respectively, or:

$$\frac{\Delta r}{r}\frac{\Delta p}{p} \ll 1 \tag{12.2}$$

$$\gg \frac{\hbar}{n\hbar}. \tag{12.3}$$

The last inequality (12.3) is simply obtained by substituting the uncertainty principle and the quantization condition (12.1) into the classical representation condition (12.2). The two conditions (12.2) and (12.3) are only compatible for large values of the quantum number n, or large orbits. States characterized by a high principal quantum number are called Rydberg states. The classical orbit becomes a reasonable approximation for these states with large quantum number n.

12.2.2 The radial wave packet

A fs pulse cannot be used to excite an atom from its ground state to a single Rydberg state, because Rydberg states are closely spaced as compared to the bandwidth of ultrashort pulses. Instead, a fs pulse will excite a superposition of many Rydberg states. This superposition is a wave packet localized in the *radial* coordinate. The period of oscillation corresponds to the period of the Kepler orbit of a classical particle with the energy corresponding to that of the average Rydberg state excited.

The experimental technique to observe the radial motion of the electrons along these Kepler orbits is a pump-probe experiment. The pump pulse excites the atoms to a superposition of Rydberg states. The number of ions (or free electrons) produced by a subsequent probe is recorded as a function of delay. As explained below,

the number of ions can be related to the position (velocity) of the electron along its Kepler orbit [7–9].

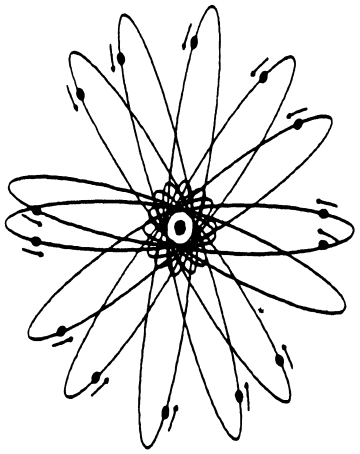

Figure 12.1: An ensemble of classical Kepler orbits make up the radially localized wave packet created by fs excitation of the ground state atom. The major axes of the ellipses are randomly distributed over all directions with a $\sin^2\theta$ distribution, but each electron has the same angular coordinate in various ellipses (from [7]).

There is no localization in the angular coordinates. If the ground state is an S state, the states forming the wave packet are P-states with various principal quantum numbers. Each of these states has as an angular dependence proportional to the square of a single spherical harmonic, a dependence in $\sin^2\theta$ in the case of the $l = m = 1$ state (where l and m are the usual eigenvalues of the orbital angular momentum and its projection along a z axis). The classical description of a Kepler orbit applies: Rather than a single orbiting electron, we should visualize an ensemble of non-interacting particles orbiting the nucleus, with their principal axes distributed according to the $\sin^2\theta$ distribution (Fig. 12.1). This "radial Rydberg wave packet" will move in the effective atomic potential between the two classical turning points. It is a radial wave packet, because only a few angular momentum eigenstates can be excited (selection rule $l \rightarrow l \pm 1$), and the angular coordinates of the Rydberg electron are delocalized in a quantum mechanical sense [10]. Each of these orbits correspond to approximately the same energy, hence the same classical period. Therefore, with all particles moving in phase along the various elliptical orbits, they arrive at the same time close to the nucleus, as illustrated in Fig. 12.1. To the motion of the charged particle is associated an electric current $\mathbf{J} = ev$ proportional to its velocity v. The Rydberg wave packet is excited by a pump pulse. The energy absorbed by a delayed probe pulse of electric field $\mathbf{E}_p$ is proportional

to $\mathbf{J}\cdot\mathbf{E}_p$. The absorbed energy is large if the delay is such that the pulse reaches the atoms with the electron near the nucleus (maximum velocity), and substantial ionization will result. At the other turning point far away from the core, the electron is nearly a free particle (which will not absorb radiation).

The photoionization versus probe delay is shown in Fig. 12.2. The signal oscillates at the classical orbital frequency. However, because the Rydberg states are not equally spaced in frequency, the states get out of phase, and the wavepacket decays. Owing to the finite number of states excited, the observed decay of the wave-packet shown in Fig. 12.2 is not an irreversible process: After a large number of cycles, the components of the wave packet come back in phase [11], a process called "revival" of the wave packet. One can also observe "fractional revivals" [9]. For instance, during the one-half fractional revival, every other state in the superposition comes into phase, leading to the formation of two wave packets. Experimental evidence of the formation of two wave packets is the change in oscillation frequency to twice the orbital frequency in Fig. 12.2.

12.2.3 The angularly localized wave packet

Radial localization was obtained by creating a superposition of states corresponding to a large radial quantum number n, spanning a group of values Δn. Similarly, angular localization will require the superposition of excitations to a large angular momentum l, spanning a group of values Δl. Since a single photon carries only one unit of angular momentum, many photons are required to reach the high angular momentum states from the ground state. The technique devised by Yeazell and Stroud [12] is to excite sodium atoms from the ground state to the $n \approx 50$ manifold of states via a two-photon transition, using circularly polarized light at 483.7 nm from an excimer pumped dye laser. A radio-frequency (rf) field is used to create the high angular momentum wave packet through 30-photon excitation from the $50d$ state to states grouped around $l = 32$ ($n = 50$, $29 < l < 37$, $m = l$). The orientation of the wave packet lies along the direction of the rf-field vector at the time of the optical excitation. Since the precession and rate of dispersion of the wave packet are very slow (order of ms), detection can be made through ionization with a pulsed electric field [12]. The wave packet is localized in the angular direction, but not in the radial direction. The classical description is that of an ensemble of elliptical orbits, all with their axes aligned along the direction of the rf field. However, the phases of the motion along the ellipses are not determined, resulting in an elliptical distribution in space that is approximately stationary in time.

Techniques involving ultrashort optical and electrical pulses have been proposed by Gaeta *et al.* [13] to localize wavepackets in the radial and angular coordinates. This would produce an atomic electron in a classical orbit.

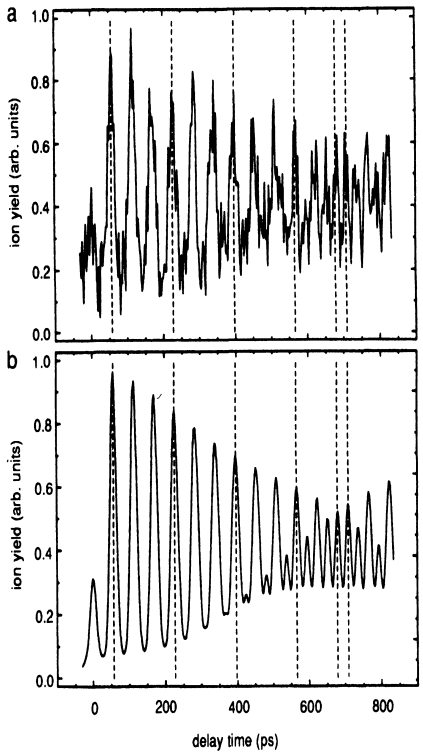

Figure 12.2: Photoionization signal as a function of probe delay. (a) Experimental recording. (b) Theoretical simulation. The Rydberg wave packet spans $\Delta n = 5$ and is centered around the Rydberg state $n = 72$ of atomic potassium (wavelength of pump pulse 285.6 nm). The probe is at 571.2 nm. (From Ref. [9].)

12.3 Ultrafast processes in molecules

12.3.1 Observation of molecular vibrations

Simple molecules

When single atoms combine to form molecules, additional internal degrees of freedom, such as rotations and vibrations, arise, with transients in the picosecond and femtosecond range.

Instead of an electron moving in the field of an atom, we shall now consider the case of an atom in a molecule. For the purpose of illustration let us consider as specific system the I_2 molecule for which the potential curves of the electronic states are reproduced in Figs. 12.3 and 12.4. A fs pulse is used to excite the $\mathbf{X}(v" = 0) \rightarrow \mathbf{B}(v' = n)$ transition in the 500–600 nm wavelength range (where v

characterizes the vibronic excitation). Owing to the broad excitation spectrum, the fs pulse creates a coherent superposition of vibronic states of mean quantum number n. Note that during the short fs interaction the nuclear motion can be neglected, which corresponds to a vertical transition in Figs. 12.4 or 12.3. The time evolution of this system can be viewed as the motion of this wave packet in the molecular potential. The classical limit is the mechanical (harmonic) oscillation with a characteristic vibration frequency ω_{vib}. As in the case of the electron in a Rydberg atom, the periodic motion of the wave packet can be observed with fs techniques.

There are several techniques available to monitor the quantum state of excited molecules. They are based on the fact that the interaction strength with a second light pulse depends on the instantaneous location and shape of the wave packet. If the experiment is carried out in a molecular beam, a delayed fs pulse can be used to excite the molecule from state **B** to a dissociative state. The fragments can be monitored with a mass spectrometer. If the measurement is carried out in a cell, the population of the **B** state can be observed simply through the fluorescence from the **B** state to the ground state. To probe the dynamics of the vibration, the molecule can be irradiated by probe pulses identical to those that created the excitation (except for the timing and phase). Since the excited state still represents a stable molecule, return to ground state stimulated by the second pulse will be possible at periodic intervals corresponding to the vibrational period of the electronically excited I_2 molecule (Fig. 12.3).

The experimental technique is essentially that of the zero-area pulse experiment described in the previous chapter. In the case of I_2, the excitation wavelength should be in the range of 608 to 613 nm. The zero-area pulses are generated in a Mach–Zehnder interferometer and sent through a 5 cm long room temperature I_2 cell at 0.25 torr [14]. The fluorescence is detected at a right angle. The return to ground state will occur if the delayed probe of the same wavelength as the pump is π out of phase with the exciting pulse. If instead the probe is in phase with the first pulse, the excitation will be reinforced. As in the case of the radial Rydberg wave packet, the classical picture for an oscillating particle fully applies. The envelope of the fluorescence pattern for in-phase and out-of-phase pulse sequences is shown in Fig. 12.3(b) (from [14]). The successive peaks are separated by 278 fs. This spacing corresponds to the superposition of the vibrational levels of the **B** state pumped by excitation at 611.2 nm from the thermally populated levels of the ground state. The classical picture is that we are seeing the period of the oscillation of the excited molecule, corresponding to a vibration frequency of 3.6 THz.

Another possibility to measure the dynamics of the wave packet is to probe the excitation of state **B** into a bound state $\mathbf{B}_1$ [Fig. 12.4(a)] with a time delayed pulse of different frequency (λ_2 = 310 nm) [15]. This was done by measuring the fluorescence from state $\mathbf{B}_1$ as a function of the delay between the excitation pulses, as

shown in Fig. 12.4(b). The short time oscillation has the period of vibration of the molecule, or period of wave packet motion in the **B** state. The periodical behavior of the oscillation period is due to a revival of the wave packet (see, for instance, Ref. [11]). The wave packet consists of a finite number of *nearly* equally spaced energy states (anharmonic potential). This causes the wave packet to spread as time progresses so that it is no longer localized. As a result, the periodic behavior of the fluorescence disappears. However, since only a finite number of states is excited by the fs pulse and forms the wave packet, a rephasing of the states occurs after a certain time period. As in the case of the Rydberg states, the wave packet again becomes localized, which manifests itself in an increased modulation amplitude of the fluorescence.

Complex molecules

Vibrations and other motions The interpretation of the vibrational studies is particularly simple for isolated diatomic molecules. Molecular vibration and vibrational relaxation, of course, occur in more complex systems, too. As an example, let us consider organic dye molecules in solution. As outlined in previous chapters these systems have gained importance as laser dyes and saturable absorbers, and have therefore been extensively studied. Because of the large number of internal degrees of freedom and the strong interaction with the solvent, the damping of coherently excited wave packets and the vibrational relaxation often proceed on a sub-picosecond time scale. Wise *et al.* [16] observed a damped sinusoidal decay in a pump-probe absorption experiment. For the dye Nile Blue, for example, they could identify eight different oscillation frequencies, documenting the large manifold of molecular eigenmodes of this complex system. Femtosecond techniques have also been successfully applied to the spectroscopic characterization of clusters, see, for example, [17].

An absorption spectrum of a dye solution taken with an ordinary spectrophotometer typically exhibits a resonance corresponding to the $S_0 \rightarrow S_1$ transition with a spectral width of several tens of nanometers. This broad absorption profile results from a very large number of rotational and vibrational states within one electronic state. An interesting question is whether the transition is homogeneously or inhomogeneously broadened. As explained in Chapter 3 (Fig. **??**), the answer depends on the time scale on which the experiment is performed. A convenient experimental technique is time resolved hole burning.

Hole burning Hole burning or saturation spectroscopy is the standard technique to determine the homogeneous linewidth (T_2^{-1}) in gases and vapors. In the case of condensed matter, a fs variation of that technique can be used. First, an intense fs

pump pulse is applied to saturate a particular transition. Let us consider as a specific example a hole burning experiment performed on cresyl violet [18]. The 60 fs wide pump pulse (centered at 618 nm) excites the $S_0(v = 0) \rightarrow S_1(v = 0)$ transition of the molecule (Fig. 12.5). Since the occupation numbers of the $v = 0$ transition in the S_0 and S_1 electronic state are modified, an absorption change in the $0 \rightarrow 1$ and $1 \rightarrow 0$ transition is also observed immediately after excitation. A fraction of the pump pulse is chirped and compressed — and hence spectrally broadened — to probe the modified absorption spectrum of the sample. Twelve millimeters of fiber and a pair of gratings compress that fraction of the pump down to 10 fs, using the technique outlined in Chapter 9. For every delay increment, the difference spectrum (with and without pump) is recorded. The resulting plot reproduced in Fig. 12.5 (b) shows clearly that three successive holes are burnt in the absorption profile. The inverse of the linewidth of the hole indicates a phase relaxation time of $T_2 = 75$ fs. A plot of the differential absorption versus time also shows a fast transient. The decay of the hole structure with time is a measure of the cross relaxation. The red shift of the peak in the differential absorption indicates vibrational relaxation. The spectral feature gives in this case a more positive identification of the homogeneous broadening than the more complex temporal transient.

12.3.2 Chemical reactions

One of the great frontiers in chemistry is detailed experimental investigations of chemical reactions in progress from reactants through a transition state to products. Until recently, understanding of the evolution of the transition state relied almost exclusively on theoretical treatments. For a three-atom system with a small number of electrons, calculations may provide potential energy surfaces on which to compute classical trajectories to simulate chemical reactivity. To adequately reflect observable chemical phenomena, the accuracy of these energy potential surfaces needs to be on the order of 1 kcal/mole, an appalling figure for spectroscopists, since it corresponds to a spectral uncertainty of 350 cm^{-1} (or 10^{13} s^{-1})! The uncertainty is even worse for more complex molecular systems with many more internal degrees of freedom, hence the need for an experimental technique that will directly measure the potential energy surfaces of the transition states.

Femtosecond pulses offer the possibility of separating the electronic and nuclear parts of the wave function, and therefore work directly within the framework of the Born–Oppenheimer approximation (see, for instance, [6]). One of the new methods discussed in the beginning of this section is to coherently excite or deexcite a transition from a ground to a higher energy potential surface. The advantage of the fs pulse excitation is that no substantial change in nuclear coordinates can take place during the interaction with light.

For the study of chemical reactions, the experimental difficulty is that measurements cannot be made on a single isolated molecule, and it seems difficult at best to synchronize (for instance) pairs of molecules involved in bimolecular reactions. In the case of unimolecular reactions, however, it is possible to use a femtosecond pulse to initiate synchronously the dissociation of a group of molecules (excitation to a repulsive potential surface V_1), and to monitor subsequently their evolution to products with delayed probe pulses [19] as sketched in Fig. 12.6.

Potential curves have been extracted from such measurements [21]. The probe pulse induces transitions from the repulsive potential surface V_1 (along which the dissociating molecule is moving, following excitation by the pump), to another potential surface V_2. For a given delay τ_d, the probe absorption versus probe wavelength approximates a step function, where the wavelength at the step is a measure of the energy difference between potential energy surfaces V_2 and V_1 at the particular delay τ_d. It is usually not practical to measure the absorption of the probe with low-density molecules. Instead, one can determine the number of molecules excited to the V_2 potential surface by laser induced fluorescence. Another possibility is to use a photoionizing probe (in which case the number of transitions is directly measured by an ion count). This technique has been applied to a detailed study of the unimolecular dissociation [19]:

$$\mathrm{ICN}^* \rightarrow \mathrm{I} + \mathrm{CN}. \tag{12.4}$$

The value of the resonance energy versus delay is a measure of the *difference* between the potential energy surfaces $V_2 - V_1$. In order to obtain an absolute measurement of an energy potential curve, it is necessary to know the shape of the upper curve V_2, or to make the assumption that this upper curve is flat. For the particular experiment reported in [19], the variation of the potential surface V_2 should not exceed 100 cm^{-1} [19]. Another approach is to use a theoretical model to calculate the upper potential surface. However, since the potential variation is on the order of 6000 cm^{-1} over the range of interest [19], the required accuracy is on the order of a few percent. Procedures to invert the data to obtain the energy surfaces for the ICN reaction have been developed by Bernstein and Zewail [21]. Because of the large energy changes along the potential energy surface in a short delay, the probe pulse duration has to be selected to obtain the optimal combination of temporal and spectral resolution. We refer the reader interested in a general overview of fs probing of dissociative reaction to [20, 22, 23].

The technique of probing chemical reactions has been successfully applied to unimolecular dissociations. The possibility of using a femtosecond technique to study bimolecular reactions at the individual collision level is complicated by the difficulties of spatial and temporal synchronization. One way to overcome this

problem is through the use of van der Waals complexes of weakly bound molecular clusters. In these complexes the moieties are held in a reasonably well-defined geometry, so that the prospective bimolecular reagents or their precursors may be frozen into a convenient geometry in preparation for reaction initiation. There are well established techniques to produce clusters of heterodimers [24, 25]. Once frozen collision complexes have been prepared by expansion of molecular beams after a supersonic nozzle, a bimolecular chemical reaction can be initiated by a fs photodissociation pulse producing a pair of reagents. Such a technique has been applied [26] to the reaction

$$\mathrm{H} + \mathrm{OCO} \rightarrow [\mathrm{HOCO}]^{\ddagger} \rightarrow \mathrm{OH} + \mathrm{CO}. \tag{12.5}$$

The van der Waals "precursor molecule" was [IH$\cdots$OCO] formed in a free-jet expansion of a mixture of HI and CO_2 in an excess of helium carrier gas. To clock the reaction, an ultrashort laser pulse photodissociates HI, ejecting an H atom towards the O atom of the CO_2. The delayed probe detects the formation of OH. Such an experiment establishes clearly that the reaction proceeds via an intermediate state, as shown in Eq. (12.5), and gives values for the lifetime of the intermediate complex $[\mathrm{HOCO}]^{\ddagger}$.

Femtosecond techniques are not limited to the *observation* of chemical reactions, but can even be exploited to influence the course of the reaction (see, for instance, Ref. [27]). This can open new relaxation channels or increase the yield of certain reaction products.

12.3.3 Molecules in solution

Considerable progress has been made towards the microscopic understanding of molecular vibration and chemical reactions in solution. For instance, we have shown at the beginning of this section techniques to study the wavepacket dynamics of the nuclear motions of iodine in the **B** state, in the collision-free limit. These techniques can be applied to solutions of different densities, and liquids. The primary effects of the solvent on the fs wave packet are dephasing, energy relaxation, caging and recombination [28]. Except for collision induced rapid nonradiative transitions in the liquid state, which cause the main fluorescence emission to originate from a lower transition, the experimental techniques are similar to the one used in the gaseous phase.

Femtosecond techniques have also been applied to more complex chemical problems, such as the study of photodissociation. The influence of the solvent on the dynamics of photodissociation of ICN can be dramatic [29]. The knowledge gained of how the solvent influences the decay of photofragment translation and rotation is useful in understanding the dynamics of thermally activated chemical

reactions [29]. Theoretical simulations have indeed shown that the fluctuations in reactant and product translational and rotational motions of thermally activated reactions proceed on the fs scale [30].

12.4 Ultrafast processes in solid state materials

12.4.1 Excitation across the band gap

Femtosecond techniques made it possible to resolve fundamental interaction mechanisms and times in solids at room temperature. These processes are of tremendous importance. For instance, they determine physical limits for speed and miniaturization in semiconductor devices. Figure 12.7 illustrates essential processes in semiconductors, following optical excitation above the band gap. For a comprehensive review of ultrafast processes semiconductors probed by laser pulses, see Shah [3].

An ultrashort light pulse of frequency ω_ℓ creates electron–hole pairs in states above the band gap. Their mean excess energy is $\Delta E = \hbar(\omega_\ell - \omega_{gap})$, and their initial energy distribution resembles the excitation spectrum. With large excited carrier densities, mainly carrier–carrier scattering leads to a thermalization within the Γ-valley without changing the mean carrier energy. This means that some carriers scatter out of their initial states, so that the distribution of occupied states becomes broader. Such processes are generally associated with momentum relaxation and are responsible for the dephasing of the polarization. Corresponding T_2 times can be measured by means of photon-echo experiments as described in the previous chapter. The temperature that can be attributed to the thermalized electronic system can exceed the lattice temperature by far. Depending on the band structure, and photon energy, inter-valley scattering can occur.

Energy is transferred to the lattice (heating) by inelastic electron–phonon collisions, and the carriers relax into states at the bottom of the band. The Fermi distribution which is finally reached can be characterized by a temperature which is equivalent to the lattice temperature. If the excitation density is sufficiently high, a local change in the lattice temperature can readily be observed. Extremely high excitation can even result in melting. While the initial carrier scattering proceeds on a time scale of tens of fs or less, the intraband energy relaxation times can amount to a few ps.

12.4.2 Excitons

Another interesting feature of the excitation spectrum of solids is the exciton resonance. Excitons can be viewed as an electron–hole pair bound together through

the Coulomb attraction, with properties similar to a hydrogen atom. Because of the positive Coulomb interaction, the corresponding energy levels are below the band gap (cf. Fig. 12.7). If the energy of the exciton is raised by an amount larger than the binding energy (E_b), the bound systems decays into a free electron and hole (exciton ionization). Such a process can be induced, for example, by longitudinal optical (LO) phonon scattering and typically proceeds on a time scale of about 100 fs in bulk materials at room temperature.

Owing to the strong excitonic oscillator strength and nonlinear susceptibilities, transient properties of excitons have attracted much attention. In particular in multiple quantum well (MQW) structures, the exciton resonances can be clearly distinguished from the bulk absorption at room temperature. Figure 12.8 displays the absorption spectrum of a CdZnTe–ZnTe MQW and the results of a pump-probe experiment [31]. The pump spectrum was chosen to excite predominantly excitons. The differential transmission at the exciton resonance shows a fast increase and a partial recovery. Its dynamics can be explained by exciton excitation, exciton ionization due to LO-phonon scattering, and the presence of a coherent artifact. The increase of the transmission at photon energies which probe the occupation of states at the bottom of the bands (λ = 610 nm) is a direct indication of the exciton ionization into free carriers. The characteristic ionization time was determined to be about 110 fs [31].

12.4.3 Intraband relaxation

Intraband relaxation processes can conveniently be observed using pump-probe absorption techniques. A pump pulse of certain energy creates carriers at corresponding states above the band gap. Temporally delayed probe pulses of various frequencies test the occupation of states at different energies above the gap. The results of such an experiment for $Al_{0.2}Ga_{0.3}As$ [32] are shown in Fig. 12.9. A quantitative evaluation of the data is rather complicated, in view of the complexity of the processes involved in highly excited semiconductors. The interested reader is referred to the book by Haug and Koch [33]. Qualitatively, however, the time resolved transmission data follow a pattern consistent with the basic properties of the band model.

A rapid transmission change occurs not only at the excitation energy, but over a broader spectral range, indicating a thermalization within a time range significantly shorter than 100 fs. At 1.88 eV and 1.94 eV, a reduced change in transmission can be attributed to the cooling of the electronic system through energy transfer to the phonon system (lattice). This cooling results in a relaxation of carriers towards the bottom of the band, thus emptying higher energy states. The increase of transmission at 1.78 eV accounts for the increase of occupied states at the band edge,

with a characteristic time constant of 1 to 2 ps. The transmission features observed at 2.07 eV are explained by intervalley scattering ($\Gamma \leftrightarrow L$) and confirmed by additional probing of the split-off transition [32].

12.4.4 Phonon dynamics

Phonons represent lattice vibrations. Just as in the case of molecular vibrations, they can be probed either by Raman techniques (frequency domain spectroscopy) or by ultrafast probing (time domain spectroscopy). The latter has the additional advantage of being able to retrieve not only the amplitude, but also the phase of the vibration. A simple model for coherent excitation of phonons was introduced in Section 11.10. The phonon vibration of frequency ω_{phonon} is excited by pairs of spectral components of the pulse spectrum ω_1 and ω_2 such that $\omega_{phonon} = \omega_2 - \omega_1$. The measurement of such collective atomic motion in crystals can be performed in reflection as well as in transmission (see, for example, Kütt *et al.* [34] and references therein). The vibrations are observable through optical probing because the atomic displacements directly affect the band structure, and consequently the dielectric function through the deformation potential and electro-optic coupling. In addition, in polar crystals, direct excitation of phonons is possible by an electric field containing suitable frequency components.

Transient reflectivity measurements performed on GaAs are presented in Fig. 12.10. A 50 fs pump pulse at 2 eV [34] is followed by an orthogonally polarized probe. The [010] crystal axis is oriented at an angle $\vartheta = 45^o$ and 135^o with respect to the probe polarization. After an initial peak, the reflectivity versus delay shows an oscillatory behavior, with a characteristic frequency of 8.8 THz that matches the frequency of the longitudinal (LO) phonons in GaAs. The dependence of the modulation amplitude on ϑ results from the electrooptic effect, which is here responsible for the phonon-induced reflectivity change.

12.4.5 Laser-induced surface disordering

In a strongly absorbing material, the energy deposited in a small surface layer by a short light pulse can locally raise the temperature beyond the melting point. What is the response of matter to a δ-function impulse of energy, sufficient to cause melting? "How fast does melting occur?" is a question of fundamental interest, which involves changes in order and structure. In addition to the possibility of observing melting through "femtosecond photography" [35], nonlinear techniques sensitive to the material symmetry can be applied [36]. Results of an experiment to monitor changes in symmetry in GaAs during melting are shown in Fig. 12.11. In GaAs, melting can be considered as a transition from a non-centrosymmetric material to

an isotropic liquid. The second-order nonlinear susceptibility $\chi^{(2)}$ is therefore expected to change from a relatively large value (for the crystal) to (almost) zero (for the liquid) during the phase transition. This second-order susceptibility can be monitored by measuring the second harmonic in reflection generated by a delayed probe [38–40]. The reflectivity for the fundamental increases from the solid reflectance value to that of liquid GaAs with a characteristic time of about 1 ps. On the other hand, the second harmonic signal drops substantially on a time scale of about 100 fs. These data suggest an intermediate state between the non-centrosymmetric crystal structure and the molten material. Note that a transition to a centrosymmetric crystal would only require a small displacement of the atoms and substantially less energy than required for the actual bond breaking that occurs with melting.

With the availability of ultrafast x-ray sources x-ray diffraction became a powerful new spectroscopic tool for time-resolved spectroscopy [41]. Since x-ray diffraction is sensitive to the crystal symmetry laser-induced phase changes can be probed directly by this technique [42].

12.5 Primary steps in photo-biological reactions

In the progression of increasingly complex systems, we have come to the role of fs tools in analyzing the most complex biological systems. Two important biological problems connected to fs spectroscopy are photosynthesis and vision. In both cases, light energy is converted to biochemical energy, either for the purpose of energy storage/transfer, or for the purpose of detection. The primary processes in the complex chain of reactions following light absorption, in vision or photosynthesis, takes place on a fs time scale. The quantum yield of these ultrafast transformations is remarkably high — typically between 50 and 100%.

12.5.1 Femtosecond isomerization of rhodopsin

The primary process of vision takes place in rhodopsin, a pigment embedded in the membranes of specialized photoreceptor cells, the rod and cone cells of the retina. The role of the pigment is light absorption followed by a molecular conformational change, which leads eventually to a change in membrane potential. This change in electrical potential across the photoreceptor cells is eventually transmitted to the nervous system [43]. We are interested here in the primary process of vision, which is the isomerization of the pigment following absorption of a photon.

The pigment is a complex molecule called rhodopsin consisting of an “opsin” protein bound to the 11-cis form of retinal chromophore. The absorption band of rhodopsin peaks at 500 nm which corresponds to the peak sensitivity of vision.

This main absorption corresponds to a transition from the S_0 ground state to a S_1 excited state in the potential energy surface representation of Fig. 12.12(a). The potential energy is plotted as a function of an angular torsional coordinate of the molecule. Absorption of a photon at 500 nm is followed by isomerization to the red-absorbing trans-isomer bathorhodopsin. The classical representation of the transformation is a "twist" of the chain [Fig. 12.12(b)]. The potential surfaces as a function of the corresponding coordinate angle have a minimum corresponding to the cis- and trans- configurations.

The quantum efficiency of this reaction is exceptionally high (0.67). The radiation lifetime of the excited state of rhodopsin is 10^{-8} s. The extinction coefficient is 6.4 10^4 $M^{-1}cm^{-1}$, a typical value for a strongly absorbing dye.

The reaction of photo-isomerization was studied through transient transmission spectroscopy through a jet of rhodopsin [45]. Adequate spectral selectivity was achieved with a pump pulse of 35 fs at 500 nm. A 10 fs probe pulse with a spectrum in the range of 450 nm to 570 nm was used. The differential transmission spectrum versus delay shown in Fig. 12.12 indicate disappearance of the 500 nm peak, and increased absorption at 530 nm, in the first 150 fs following excitation. The speed of that isomerization calls for a better classical representation of the cis versus trans configuration than Fig. 12.12(b). It is doubtful that the large motion of nuclei implied by the sketch could take place in a time as short as 100 fs.

12.5.2 Photosynthesis

Photosynthesis is the process by which plants convert solar energy into chemical energy. Its importance is obvious, since it is at the origin of life on our planet. This topic is too vast to be adequately covered in a section of this book. A general overview of the topic can be found in a review article by Fleming and Grondelle [46], and in topical books [1, 43].

There are pigment–protein complexes called reaction centers, where a directional electron transfer takes place across a biological membrane. Light harvesting molecules ("antenna" chlorophylls) transfer electronic excitation energy to a special pair (P in the sketch of Fig. 12.13) of chlorophyll molecules, which acts as the primary electron donor. The latter transfers an electron to a pheophytin (H_A) within 3 ps, and from it to a quinone (Q_A) in 200 ps, thence to the other quinone Q_B, hence establishing a potential difference across a biological membrane. Biochemical reactions that store the energy subsequently occur with these separated charges.

The energy dissipation in the first processes should be small (about 0.25 eV) as compared to the excitation energy (1.38 eV), in order to minimize the waste of excitation energy. The electron transfer should be fast in order to compete with

fluorescence and radiationless decay.

The complexity of the problem can be appreciated by looking at the representation of the molecular structure of a bacterium's photosynthetic reaction center, which was determined to atomic resolution by Deisenhover and Michel [46,48]. A block diagram of the electron carrying pigments in the reaction center is shown in Fig. 12.13.

Recent transient absorption experiments [49] have concentrated on the fast initial electron transfers. In a model proposed by Zinth *et al.* [47, 49], the bacteriochlorophyll anion B_A^- is created in the first 3 ps reaction. The subsequent electron transfer to the bacteriopheophytin H_A is faster, taking only 0.9 ps. In the experiment, after the main absorption band of the pigment is pumped, a probe is sent in the near IR, where the bacteriochlorophyll anions ($P^+B_A^-$) have a strong absorption. The transient absorption change at 1.02 μm is shown in Fig. 12.14. The 0.9 ps time constant would correspond to the electron transfer from the bacteriochlorophyll to the bacteriopheophytin ($P^+H_A^-$).

Bibliography

[1] W. Kaiser and D. H. Auston, editors. *Ultrashort laser pulses*, volume 60 of *Topics in Applied Phys.* Springer-Verlag, Berlin, 1988.

[2] F. C. De Schryver, S. De Feyter, and G. Schweitzer (Eds.). *Femtochemistry : With the Nobel Lecture of A. Zewail*. Wiley, 2001.

[3] J. Shah. *Ultrafast Spectroscopy of Semiconductors and Semiconductor Nanostructures*. Springer, 1999.

[4] S. Mukamel. *Principles of Nonlinear Optical Spectroscopy*. Oxford University Press, New York, 1995.

[5] *Ultrafast Phenomena*. Springer, Bi-annual conference Proceedings.

[6] C. Cohen-Tannoudji, B. Diu, and F. Laloe. *Quantum Mechanics*. John Wiley & Sons, New York, 1977.

[7] C. R. Stroud. The classical limit of an atom. In W. T. Grandy and P. W. Milonni, editors, *Physics and Probability: a symposium in honor of E. T. Jaynes*, pages 1–9. Cambridge University Press, 1993.

[8] A. ten Wolde, L. D. Noordam, H. G. Muller, A. Lagendijk, and H. B. van Linden van den Heuvell. Observation of radially localized atomic wave packets. *Phys. Rev. Lett.*, 61:2099–2102, 1988.

[9] J. A. Yeazell and Jr C. R. Stroud. Observation of fractional revivals in the evolution of a Rydberg atomic wave packet. *Phys. Rev. A*, 4:5153–5156, 1991.

[10] G. Alber and P. Zoller. Laser-induced excitation of electronic Rydberg wave packets. *Contemporary Physics*, 32:185–189, 1991.

[11] J. A. Yeazell, M. Mallalieu, J. Parker, and Jr C. R. Stroud. Observation of the collapse and revival of a Rydberg electronic wave packet. *Phys. Rev. Lett.*, 64:2007–2010, 1990.

[12] J. A. Yeazell and Jr C. R. Stroud. Observation of spatially localized atomic electron wave packets. *Phys. Rev. Lett.*, 60:1494–1497, 1988.

[13] Z. D. Gaeta, M. Noel, and C. R. Stroud. Excitation of the classical-limit state of an atom. *Phys. Rev. Lett.*, to be published, 1994.

[14] N. F. Scherer, R. J. Carlson, A. Matro, M. Du, A. J. Ruggiero, V. Romero-Rochin, J. A. Cina, G. F. Fleming, and S. A. Rice. Fluorescence-detected wave packet interferometry: time resolved molecular spectroscopy with sequences of femtosecond phase-locked pulses. *J. Chem. Phys.*, 95:1487–1511, 1991.

[15] R. M. Bowman, M. Dantus, and A. H. Zewail. Femtosecond transition state spectroscopy of iodine: from strongly bound to repulsive surface dynamics. *Chem. Phys. Lett.*, 161:297–302, 1989.

[16] F. W. Wise, M. J. Rosker, and C. L. Tang. Oscillatory femtosecond relaxation of photoexcited organic molecules. *J. Chem. Phys.*, 86:2827–2832, 1987.

[17] T. Baumert, R. Thalweiser, and G. Gerber. Femtosecond two-photon ionization spectroscopy of the B state of Na_3 clusters. *Chem. Phys. Lett.*, 209:29–32, 1993.

[18] C. H. Brito-Cruz, R. L. Fork, W. H. Knox, and C. V. Shank. Spectral hole burning in large molecules probed with 10 fs optical pulses. *Chem. Phys. Lett.*, 132:341–344, 1986.

[19] M. J. Rosker, M. Dantus, and A. H. Zewail. Femtosecond real-time probing of reactions, i. the technique. *J. Chem. Phys.*, 89:6113–6127, 1988.

[20] A. H. Zewail. Laser femtochemistry. *Science*, 242:1645–1653, 1988.

[21] R. B. Bernstein and A. H. Zewail. Femtosecond real-time probing of reactions, iii. inversion to the potential from femtosecond transition-state spectroscopy experiments. *J. Chem. Phys.*, 90:829–842, 1989.

[22] A. H. Zewail. The birth of molecules. *Scientific American*, 262:76–82, 1990.

[23] P.Cong, A. Mokhtari, and A. H. Zewail. Femtosecond probing of persistent wave wave packet motion in dissociativereactions: up to 40 ps. *Chemical Phys. Lett.*, 172:109–113, 1990.

[24] J. R. Grover and E. A. Walters. Optimization of weak neutral dimers in nozzle beams. *J. Phys. Chem.*, 90:6201–6206, 1986.

[25] J. R. Grover, E. A. Walters, D. L. Arneberg, and C. J. Santandrea. Competitive production of weakly bound heterodimers in free jet expansions. *Chem. Phys. Lett.*, 146:305–307, 1988.

[26] N. F. Scherer, L. R. Khundkar, R. B. Bernstein, and A. H. Zewail. Real-time picosecond clocking of the collision complex in a bimolecular reaction: The birth of OH from H + CO_2. *J. Chem. Phys.*, 87:1451–1453, 1987.

[27] E. D. Potter, J. L. Herek, S. Petersen, Q. Liu, and A. H. Zewail. Femtosecond laser control of a chemical reaction. *Nature*, 355:66–68, 1992.

[28] Y. Yan, R. M. Whitnell, K. R. Wilson, and A. H. Zewail. Femtosecond chemical dynamics in solution: wavepacket evolution and caging of i_2. *Chem. Phys. Lett.*, to be published, 1993.

[29] I. Benjamin and K. R. Wilson. Proposed experimental probes of chemical reaction molecular dynamics in solution:icn photodissociation. *J. Chem. Phys.*, 90:4176–4197, 1989.

[30] L. L. Lee, Y. S. Li, and K. R. Wilson. Reaction dynamics from liquid structure. *J. Chem. Phys.*, 95:2458–2464, 1991.

[31] P .C. Becker, D. Lee, M. R. Xavier de Barros, A. M. Johnson, A. G. Prosser, R. D. Feldman, R. F. Austin, and R. E. Behringer. Femtosecond dynamic exciton bleaching in room temperature II-VI quantum wells. *IEEE J. of Quantum Electron.*, 28:2535–2542, 1992.

[32] W. Z. Lin, R. W. Schoenlein, J. G. Fujimoto, and E. P. Ippen. Femtosecond absorption saturation studies of hot carriers in GaAs and AlGaAs. *IEEE J. of Quantum Electron.*, 24:267–275, 1988.

[33] H. Haug and S. W. Koch. *Quantum theory of the optical and electronic properties of semiconductors*. World Scientific, Singapore, 1990.

[34] W. Kuett, W. Albrecht, and H. Kurz. Generation of coherent phonons in condensed media. *IEEE J. 0f Quantum Electron.*, 42:2434–2444, 1992.

[35] M. C. Downer, R. L. Fork, and C. V. Shank. Femtosecond imaging of melting and evaporation of a photoexcited silicon surface. *J. of Optical Soc. Am. B*, 2:595–599, 1985.

[36] N. Bloembergen, A. M. Malvezzi, and J. M. Lin. Second harmonic generation in reflection from crystalline GaAs under intense picosecond laser irradiation. *Appl. Phys. Lett.*, 45:1019–1021, 1984.

[37] S. V. Govorkov, I. L. Shumay, W. Rudolph, and T. Schroeder. Time-resolved second-harmonic study of femtosecond laser-induced disordering of GaAs surfaces. *Optics Lett.*, 16:1013–1015, 1991.

[38] P. Saeta, J. K. Wang, Y. Siegal, and N. Bloembergen. Ultrafast electronic disordering during femtosecond laser melting of GaAs. *Phys. Rev. Lett.*, 67:1023–1025, 1991.

[39] K. Sokolowski-Tinten, H. Schultz, J. Bialkowski, and D. von der Linde. Two distinct transitions in ultrafast solid-liquid phase transformations of GaAs. *Appl. Phys.*, A53:227–234, 1991.

[40] T. Schroeder, W. Rudolph, S. V. Govorkov, and I. L. Shumay. Femtosecond laser induced melting of GaAs probed by optical second-harmonic generation. *Appl. Phys.*, A51:49–51, 1990.

[41] C. Rischel, C. Rischel, A. Rousse, I. Uschmann, P. A. Albouy, J. P. Geindre, P. Audebert, J. C. Gauthier, E. Forster, J. L. Martin, and A. Antonetti. Femtosecond time-resolved x-ray diffraction from laser-heated organic films. *Nature*, 390:490–492, 1997.

[42] S. H. Chin, R. W. Schoenlein, T. E. Glover, P. Balling, W. P. Leemans, and C. V. Shank. Ultrafast structural dynamics in insb probed by time- resolved x-ray diffraction. *Phys. Rev. Lett.*, 83:336–339, 1999.

[43] R. R. Alfano, editor. *Biological events probed by ultrafast laser spectroscopy*. Academic Press, New York, 1982.

[44] R. W. Schoenlein, L. A. Peteanu, R. A. Mathies, and C. V. Shank. The first step in vision: femtosecond isomerization of rhodopsin. *Science*, 254:412–415, 1991.

[45] R. W. Schoenlein, L.-A. Poteanis, R. A. Mathias, and C. V. Shank. Femtosecond isomerization of rhodopsin. Ultrafast Phenomena in Spectroscopy, UPS'91, October 1991. Bayreuth, Germany.

[46] G. R. Fleming and R. van Grondelle. The primary steps of photosynthesis. *Physics Today*, 47:48–55, 1994.

[47] W. Zinth, C. Lauterwasser, U. Finkele, P. Hamm, S. Schmidt, and W. Kaiser. Molecular processes in the primary reaction of photosynthetic reaction centers. In J.-L. Martin, A. Migus, G. A. Mourou, and A. H. Zewail, editors, *Ultrafast Phenomena VIII*, pages 535–538, Antibes, France, 1994. Springer Verlag, Berlin.

[48] J. Deisenhofer and H. Michel. The photosynthetic reaction center from the purple bakterium rhodopseudomonas viridis. *EMBO Journal*, 8:2419–2157, 1989.

[49] W. Zinth, S. Schmidt, T. Arlt, H. Huber, T. Naegele, M. Meyer, and H. Scheer. Direct observation of the accessory bacteriochlorophyll in the primary electron transfer in bacterial reaction centers. In G. A. Mourou and A. H. Zewail, editors, *Ultrafast Phenomena IX*, Dana Point, CA, 1994. Springer Verlag, Berlin.

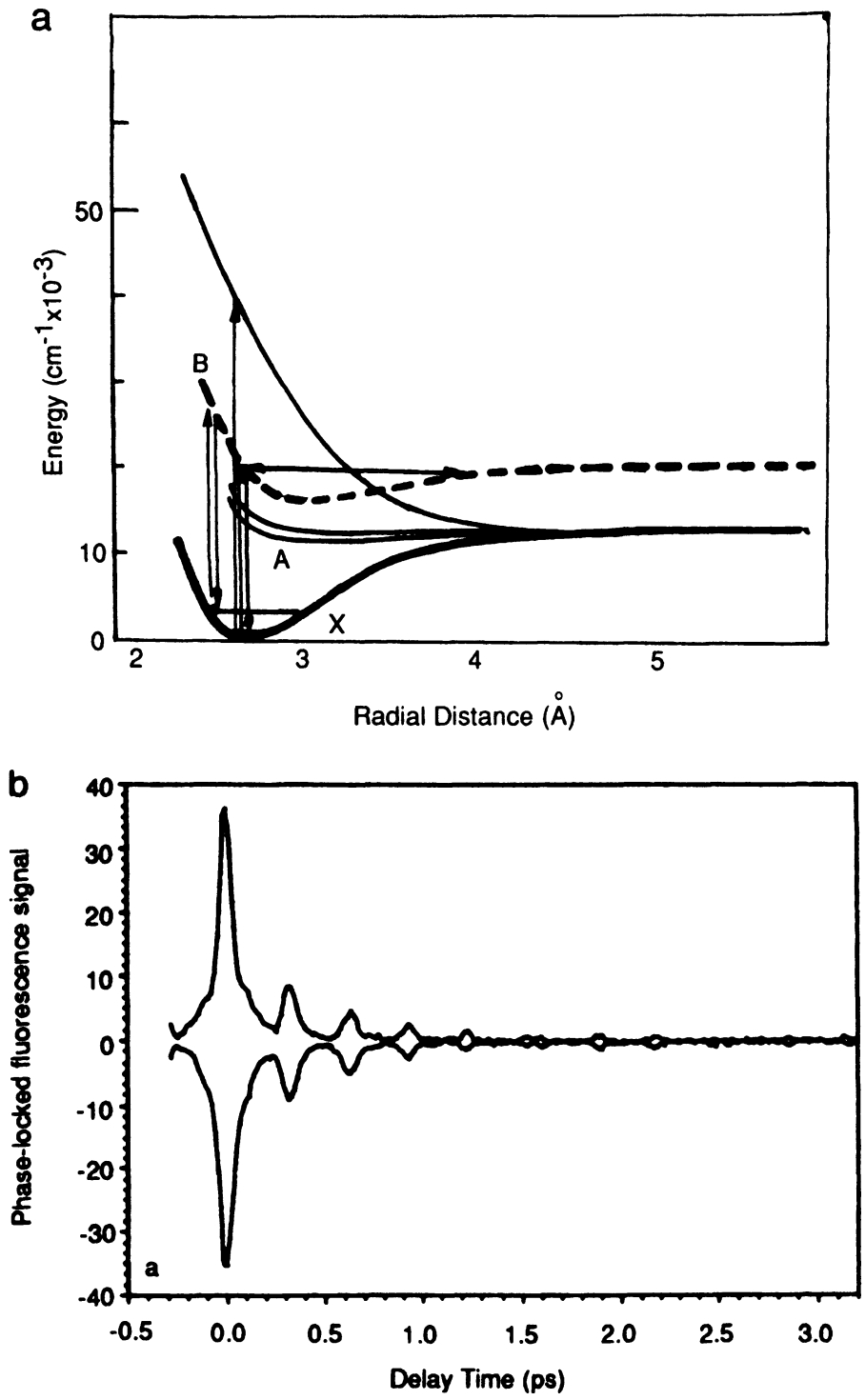

Figure 12.3: Study of the potential surface of I_2, using a pair of identical pulses with adjustable relative phase and delay. (a) Sketch of the potential surfaces. (b) Envelope of the fluorescence signal (only the contribution due to the two-pulse excitation) from the **B** state, corresponding to an in-phase sequence (upper envelope) and an out-of-phase sequence (lower envelope) (adapted from [14]).

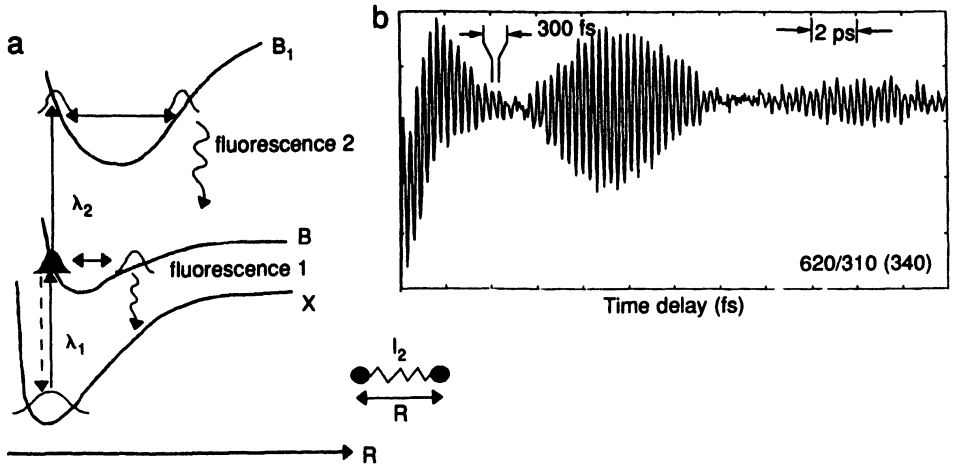

Figure 12.4: (a) Sketch of the bound potential energy surfaces relevant to the study of iodine through excited state fluorescence. (b) Fluorescence from the excited state $\mathbf{B}_1$ of I_2 as function of the delay between the two excitation pulses of wavelength λ_1 and λ_2 (adapted from [15]).

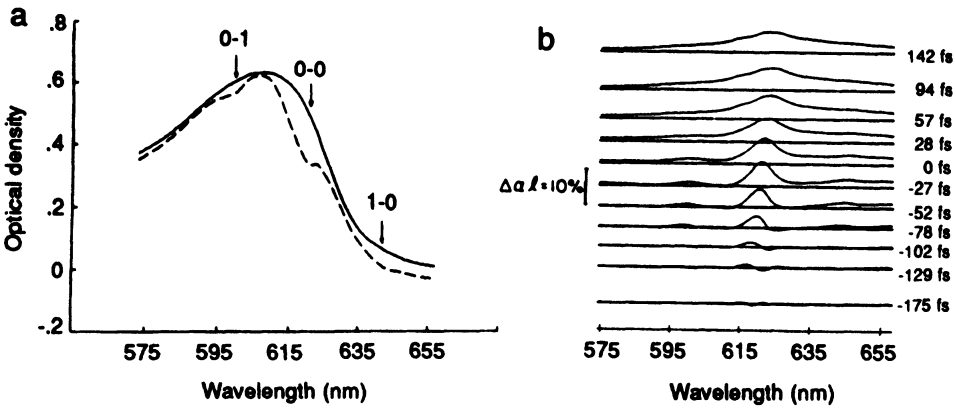

Figure 12.5: (a) Absorption spectrum of cresyl violet near the region of pumping. The dashed line illustrated qualitatively the spectral modification immediately after the 60 fs pump pulse. (b) Differential absorption spectra for successive delay increments after excitation of cresyl violet with a 60 fs pump pulse at 618 nm (from [18]).

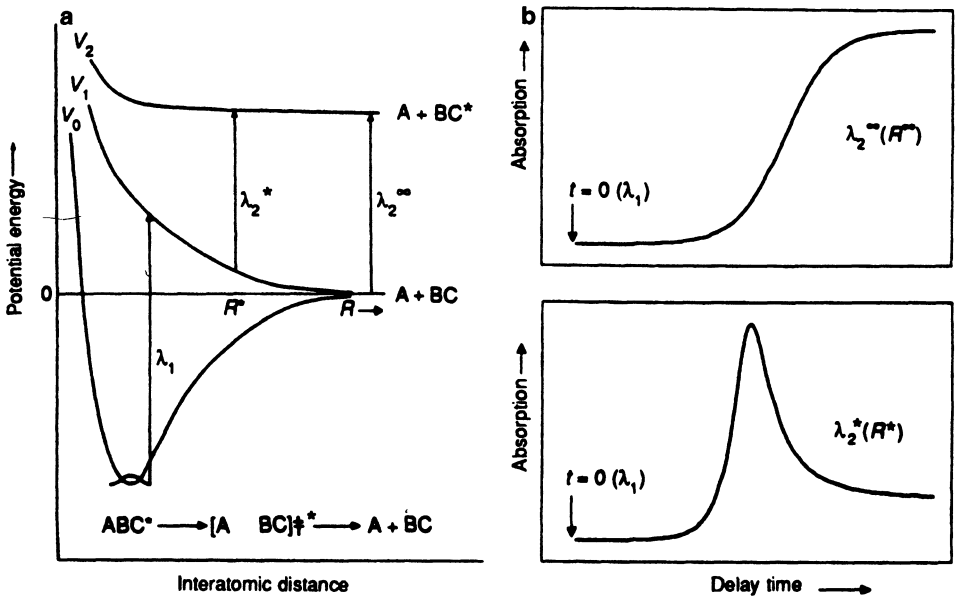

Figure 12.6: Pump-probe experiment to observe the transition region of a reaction. (a) The molecule is first excited by a pump pulse at λ_1 from the potential energy curves for the bound molecule V_0, to the dissociative state V_1. After a delay τ_d during which the fragment evolves along the repulsive potential V_1, a probe pulse at λ_2^* excites the complex to the dissociative (eventually ionizing) potential surface V_2. As the fragments recoil, the pulse at λ_2^* (or λ_2^∞) probes the transition region (or the free fragments). (b) The expected fs transients, signal versus delay τ_d at λ_2^* and λ_2^∞ (adapted from [20]).

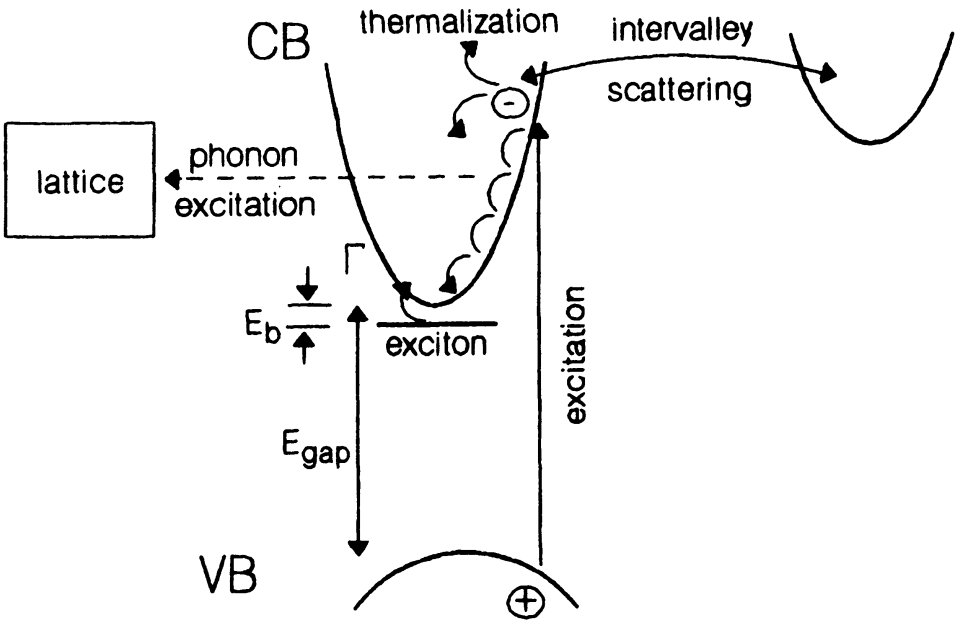

Figure 12.7: Simplified diagram of ultrafast processes occurring after above–band gap excitation in semiconductors.

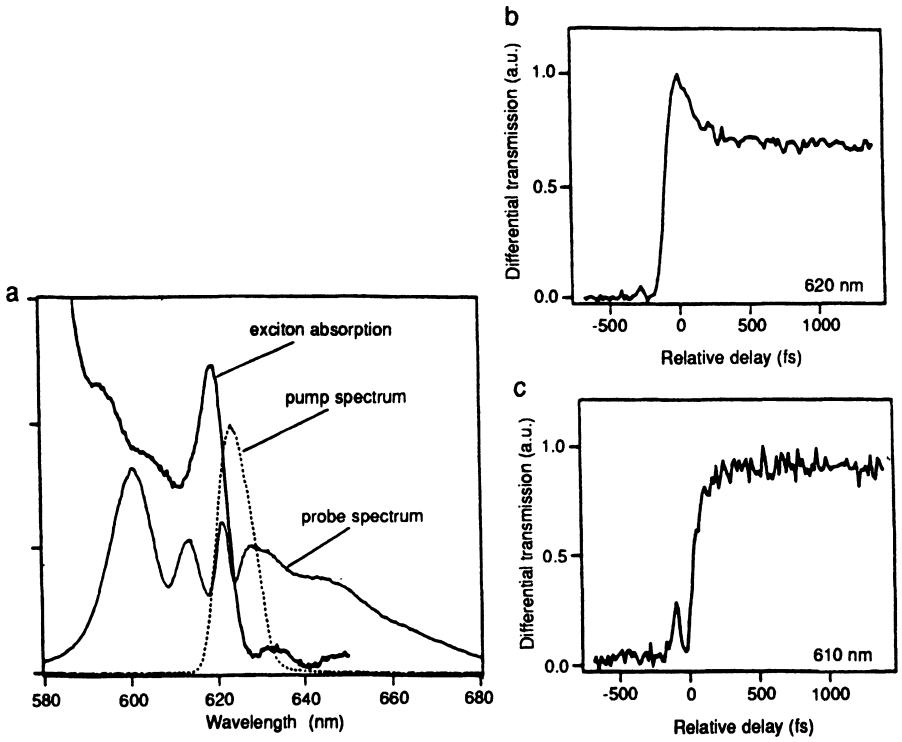

Figure 12.8: (a) Room temperature absorption spectrum of a CdZnTe–ZnTe MQW and the spectra of the 80 fs pump pulse and 14 fs probe pulse. The latter is a self-phase modulated and compressed part of the pump pulse. (b) Differential transmission at 620 nm and (c) 610 nm for a pump excitation level of 2×10^{11} carriers/cm^2. The wavelength filtering was done after the sample with a filter with a bandwidth of ≈8 nm. (From [31].)

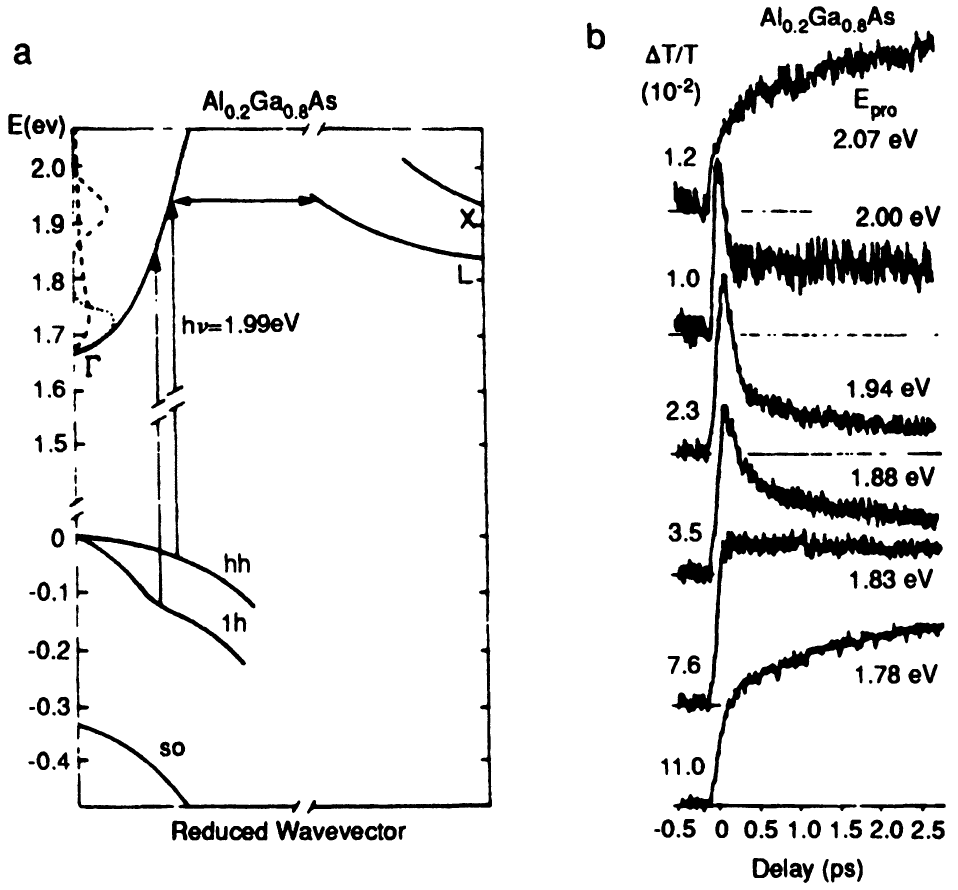

Figure 12.9: (a) Band structure for $Al_{0.2}Ga_{0.8}As$. The excitation photon energy being 1.99 eV, absorption from the light hole (ℓh) and heavy hole (hh) subbands into the Γ band are allowed. The carrier distribution is sketched for different instants (upper left corner). (b) Relative transmission change as seen by the test pulse for different photon energies and as function of the delay with respect to the pump pulse (adapted from [32]).

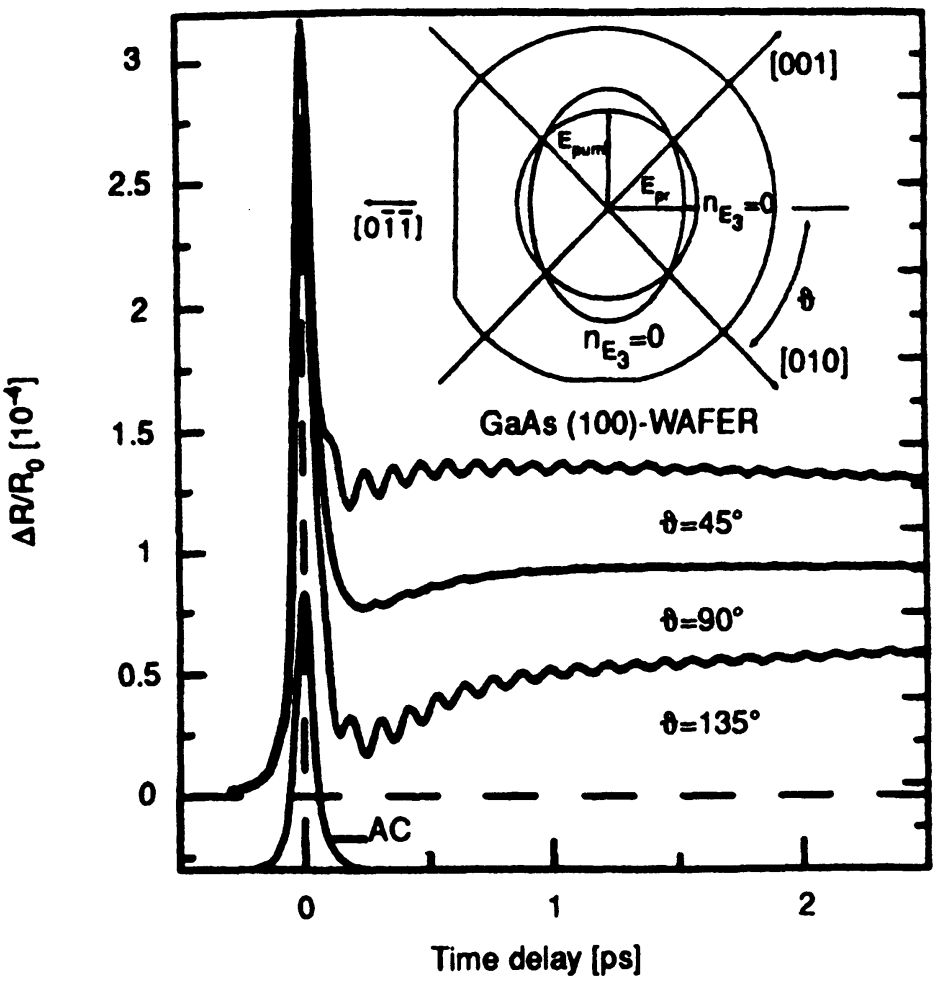

Figure 12.10: Relative reflection change of a [100] GaAs crystal excited by a 50 fs pulse at 2 eV. The generated carrier density is 10^{18} cm^{-3}. ϑ is the angle between the probe polarization and the [010] crystal axis. AC denotes the autocorrelation of the pump (probe) pulse (from [34]).

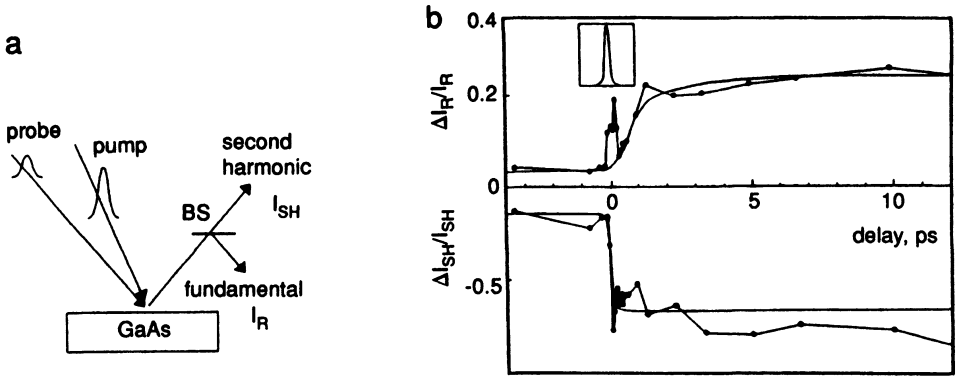

Figure 12.11: (a) Experimental setup to monitor ultrafast phase changes on a GaAs surface. A strong pump pulse induces the phase change. (b) The upper curve shows the reflectivity of a delayed probe. The lower curve is a plot of the second harmonic (in reflection) of the probe signal, which is a measure of the change in symmetry associated with the phase transition (adapted from [37]).

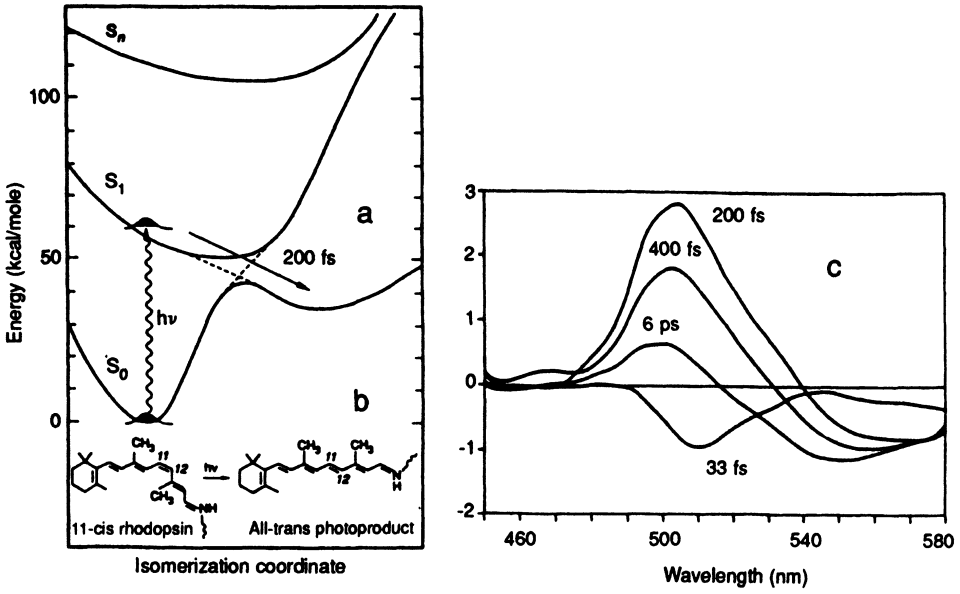

Figure 12.12: Schematic representation of the photo-isomerization reaction of rhodopsin. (a) Ground and excited state potential energy curves as a function of the torsional coordinate. The spectrum is red-shifted after absorption of a photon at 500 nm. The classical sketch of the cis-trans transformation is shown in (b). (c) Difference spectra measurements of 11–cis-rhodopsin at various delays following a 35 fs pump pulse at 500 nm ($\approx$10 fs probe). (From [44].)

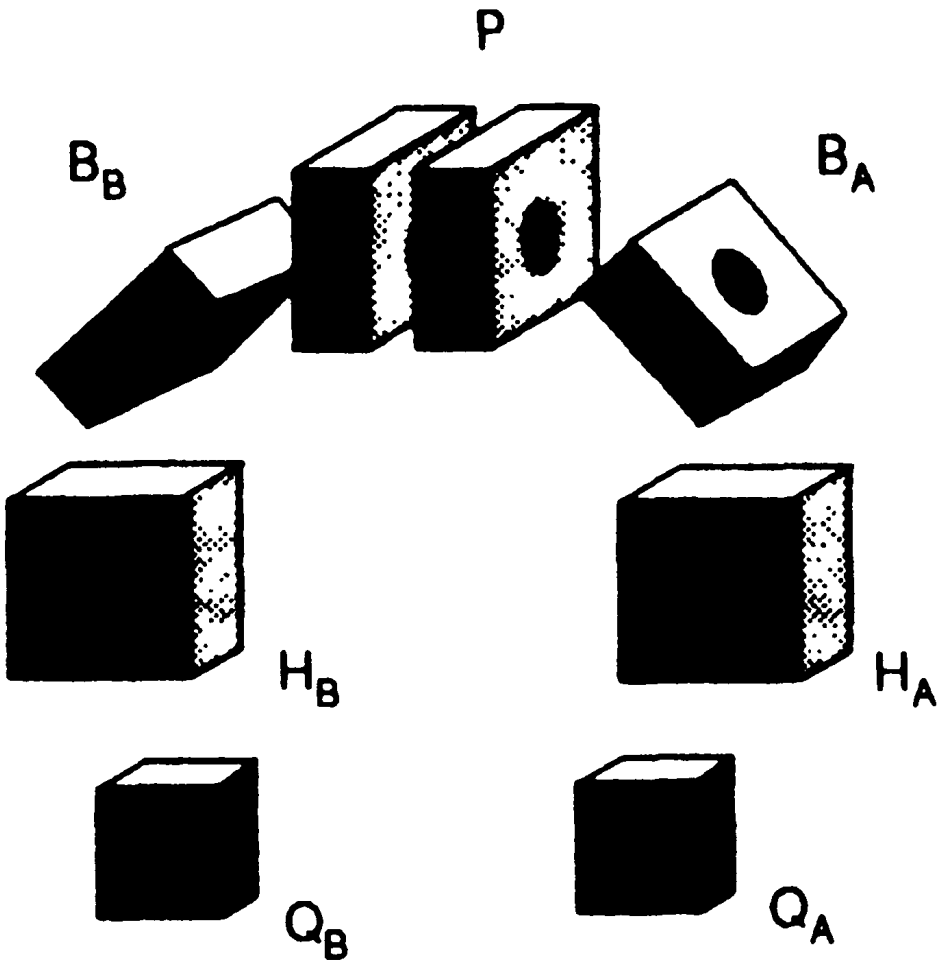

Figure 12.13: Sketch of the molecular arrangement of the four bacteriochlorophylls (P, B_A, B_B), the two bacteriopheophytins (H_A, H_B), and the two quinones (Q_A, Q_B) in reaction centers (from Ref. [47]).

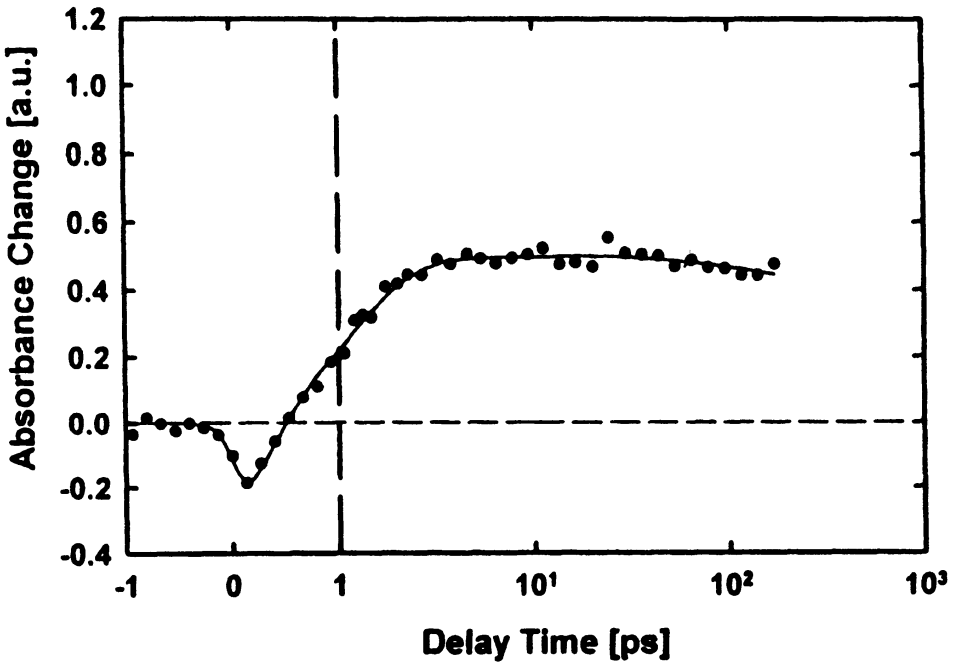

Figure 12.14: Transient absorption changes for native reaction centers at 1.02 μm associated with the photosynthesis. The large initial absorption increase has a time constant of 0.9 ps. It is related to the absorption change due to the formation of a bacteriochlorophyll anion (from Ref. [49]).

Chapter 13

Terahertz (THz) Radiation

Electromagnetic radiation in the far infrared (FIR) with frequencies from 0.1 to 10 THz (wavelengths from 3 mm to 30 μm) is usually referred to as Terahertz (THz) radiation. Situated between IR and millimeter waves that are relatively easily accessible by optical (laser) sources and electronic means, respectively, THz radiation did not gain a lot of interest for the lack of practical sources and attractive application fields. This changed in the 1980s when ultrashort laser pulses were successfully applied to generate wave packets with frequencies centered in the THz range [1, 2]. In the past decades this led to a surge in research efforts opening new application fields and triggering THz source developments also outside the realm of ultrafast photonics. Today THz waves are widely used for imaging, sensing, communication, and spectroscopy in research labs and are transcending into the commercial sector. Detailed summaries of THz science and technology can be found for example in references [3–9]. In this chapter we will discuss the basic principles of THz generation using short laser pulses and highlight example applications enabled by the availability of synchronized THz and optical pulses.

Resolving THz waveforms with fast detectors is still challenging and possible only if the features of interest are longer than a few ps. The method of choice to measure THz fields is through correlations with a synchronized, often shorter, optical pulse. In many cases the correlation utilizes a physical mechanism that is an inverse replica of the THz generating process, assuring adequate bandwidth. An additional benefit of such techniques is that the THz electric field $E_T(t)$ is often measured directly rather than the pulse (intensity) envelope.

In ultrafast optics one often distinguishes THz generation based on nonlinear optical mechanisms and transient currents although the boundaries are not clear-cut.

13.1 THz generation based on nonlinear optics

THz generation can be considered as a special case of frequency conversion, see Chapter 3. Spectral components of the participating fields couple so that the resulting photons have frequencies in the THz range. Since typically the nonlinear signals decrease with the order of the nonlinearity the lowest-order process, that is a process of second-order - difference frequency generation, is particularly interesting for efficient conversion.

The polarization of a second-order nonlinear optical process excited by a fundamental electric field E, according to Eq. (4.11), is

$$P^{NL}(\Omega) = P^{(2)}(\Omega) = \epsilon_0 \int \chi^{(2)}(\Omega, \Omega') d\Omega' E(\Omega - \Omega') E(\Omega'). \tag{13.1}$$

For a monochromatic incident field it can be shown, see problem at the end of this chapter, that this polarization has a component at twice the fundamental frequency and a dc component resulting in second-harmonic generation and optical rectification (OR), respectively. If the incident field is that of a short laser pulse the "dc" component varies with the pulse envelope and exhibits spectral components in the THz region if the pulse duration is shorter than a few ps. The frequency-domain picture is that two optical photons with frequencies from within the pulse spectrum produce a THz photon via difference frequency generation.

As with harmonic generation, for large conversion efficiencies large input fluences and a large product of sample length and nonlinear susceptibility are required. The wave vector mismatch of optical and THz wave, $\Delta\vec{k}$, limits the useful sample length to the coherence length $\pi/\Delta k$. In collinear geometry, zero wave vector mismatch means

$$\Delta k = k(\Omega + \omega_T) - k(\Omega) - k(\omega_T) = 0. \tag{13.2}$$

Here $\Omega + \omega_T$ and Ω are frequencies from within the optical pulse spectrum that couple to produce a THz photon of frequency ω_T. The dispersion of the nonlinear material controls to what extent the phase matching condition Eq. (13.2) can be satisfied for a given wavelength of the optical pulse.

Since $k(\Omega) = \Omega n(\omega)/c$ and $k(\Omega + \omega_T) \approx k(\Omega) + \frac{d}{d\Omega} n\omega_T$ the phase matching condition can also be written as

$$n(\Omega) + (\Omega - \omega_T)\frac{dn}{d\Omega} = n_T, \tag{13.3}$$

where n_T is the refractive index seen by the THz wave. Recall that the inverse of the optical group velocity $v_g^{-1} = n + \frac{dn}{d\Omega}\Omega$. After replacing the corresponding terms

in Eq. (13.3) by v_g and making use of $\omega_T << \Omega$, the phase matching condition becomes

$$v_g \approx \frac{c}{n_T} = v_{p,T}. \tag{13.4}$$

Thus, for efficient conversion, the phase velocity of the THz wave $v_{p,T}$, should match the group velocity of the generating optical pulse in the nonlinear material.

For a more quantitative understanding of OR we need to solve simultaneously the coupled wave equations for the fundamental pulse and the THz pulse. This is similar to what we discussed for second-harmonic generation in Chapter 3. There is however one important difference. The few-cycle THz waveform cannot be described in terms of a reduced wave equation for the envelope. Rather, the full wave equation with the nonlinear polarization term must be used [10, 11]. In the frequency domain, the generating equation for the THz field can be written as

$$\left(\frac{\partial^2}{\partial z^2} + \frac{\Omega^2}{c^2} n_T(\Omega)^2\right) \tilde{E}_T(\Omega, z) = \mu_0 \mathcal{F}\left\{\frac{\partial^2}{\partial t^2} P^{NL}(z,t)\right\}, \tag{13.5}$$

where $\mathcal{F}$ denotes Fourier transform. For simplification we restrict our discussion to plane waves propagating in $+z$ direction. Let us further assume that the optical pulse travels in the nonlinear medium with group velocity v_g and neglect its depletion and the group velocity dispersion. In this case its wave equation is decoupled from the THz field. The solution describes an optical pulse envelope propagating form-stable $\mathcal{E}(t,z) = \mathcal{E}(t - z/v_g, 0) = \mathcal{E}_0(\eta)$, where η is the local time in a reference frame moving with group velocity v_g.

For an instantaneous $\chi^{(2)}$ in the frequency range of interest the nonlinear polarization, according to Eq. (4.6), is $P^{(2)}(t) = \epsilon \chi_0^{(2)} E(t)^2$. In terms of the pulse envelope and local time the second derivative of the polarization needed in Eq. (13.5) can be expressed as

$$\frac{\partial^2}{\partial t^2} P^{(2)}(z,t) = \epsilon_0 \chi^{(2)} \frac{\partial^2}{\partial \eta^2} \mathcal{E}_0^2(\eta). \tag{13.6}$$

With this driving term the wave equation to be solved becomes

$$\left(\frac{\partial^2}{\partial z^2} + \frac{\Omega^2}{c^2} n_T(\Omega)^2\right) \tilde{E}_T(\Omega, z) = -\frac{\chi^{(2)}}{2c^2} \Omega^2 \tilde{I}_0(\Omega) e^{-i\frac{z}{v_g}\Omega}, \tag{13.7}$$

where $\tilde{I}_0(\Omega) = \mathcal{F}\{\mathcal{E}_0^2(\eta)\}$. Note, $\tilde{I}_0(\Omega)$ should not be confused with the spectral intensity of the laser pulse $\propto |\mathcal{F}\{\mathcal{E}_0(\eta)\}|^2$.

The forward-propagating wave solution with the boundary condition $\tilde{E}_T(\Omega, z = 0) = 0$ is

$$\tilde{E}_T(\Omega, z) = -i \frac{\chi^{(2)} \tilde{I}_0(\Omega)}{2c(n_T + n_g)} \Omega z e^{-i\frac{\Omega}{2c}(n_T + n_g)z} \mathrm{sinc}\left[\frac{(n_T - n_g)\Omega}{2c} z\right]. \tag{13.8}$$

Here n_T is the refractive index at the THz frequencies and $n_g = c/v_g$ is the group index at the carrier frequency of the optical pulse. This result illustrates a few important features of THz generation through optical rectification in collinear geometry.

1. As expected from a second-order nonlinear optical process the output (THz) field is proportional to $\chi^{(2)}$ and the square of the fundamental field amplitude $\mathcal{E}_0^2$.

2. The argument of the sinc function suggests that optimal phase matching leading to maximum conversion occurs when the refractive index n_T and the group index n_g are equal, in other words, when the *phase* velocity of the THz wave matches the *group* velocity of the optical pulse. In this ideal case, the THz field increases linearly with the length of the nonlinear material. Since $n_T = n_T(\Omega)$ the phase matching condition can only be satisfied approximately in real (dispersive) materials.

3. The THz field peaks at a certain nonzero frequency ν_p. For perfect phase matching and Gaussian optical pulses of duration (FWHM) τ_p, it can be shown that $\Omega_p = 2\pi\nu_p = \sqrt{8\ln 2}/\tau_p$.

4. The time dependent THz field can be obtained from Eq. (13.8) through an inverse Fourier transform. For perfect phase matching, $E_T(\eta) \propto \frac{\partial}{\partial\eta}\mathcal{E}_0^2(\eta)$.

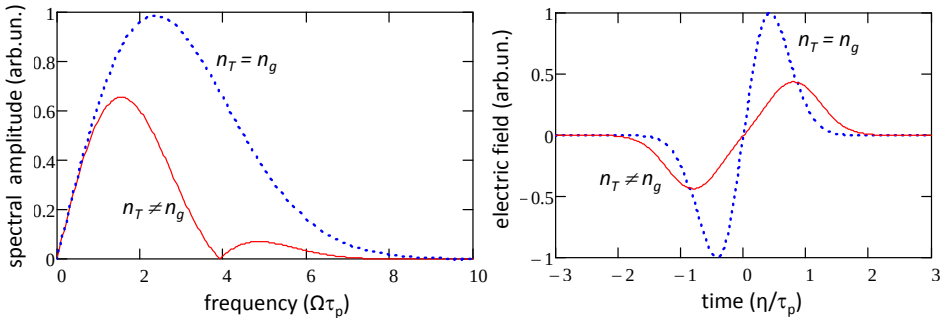

Figure 13.1: Field spectral amplitude and time-dependent electric field of a THz pulse according to Eq. (13.8) with $n_T(\Omega)$ = const. in the THz range of interest. The optical pulse is Gaussian with duration (FWHM) τ_p. Perfect phase matching is compared to $\Delta\Omega(n_T - n_g)z/2c = \pi$, where $\Delta\Omega$ is the FWHM of $\tilde{I}(\Omega)$.

Figure 13.1 depicts the spectrum and temporal shape of the THz field for perfect and non-perfect phase matching. For efficient, collinear THz generation via optical

rectification (OR) nonlinear materials are desired whose dispersion produces conditions $\langle n_T \rangle \approx n_g$. Imperfect phase matching reduces the THz bandwidth. Other limiting factors are absorption by phonons.

As an example Table 13.1 shows relevant parameters of two distinctly different materials for THz generation. ZnTe is widely used for collinear OR. The similar values of the indices indicate that the phase-matching condition can approximately be satisfied for pump pulses in the near IR at about 800 nm.

The second material listed, $LiTaO_3$, shows a considerably larger nonlinear coefficient but also a larger mismatch of the relevant refractive indices. This material was used in the original OR schema with near IR fs pulses by Auston *et al.* [1]. In this experiment, femtosecond pulses with an energy of about 100 pJ were focu-

material	d (pm/V)	n	n_T	α_T (cm^{-1})	band gap (eV)
ZnTe	4	2.85	3.17	1.3	2.4 [12]
$LiTaO_3$	31	2.18	6.5	46	4.5 - 4.6 [13]

Table 13.1: Order of magnitude values of material parameters important for THz generation for two selected crystals. n is the refractive index at the optical frequency and α is the absorption coefficient at the THz frequency. The electrooptic coefficient is related to the nonlinear susceptibility $d = |\chi^{(2)}|/2$. Data are from [8], Table 1, unless noted otherwise.

sed into a $LiTaO_3$ crystal, see Fig. 13.2. The optical pulse propagating through the crystal produces a polarization pulse via optical rectification as explained before. The optical rectification pulse is basically an electric dipole field that moves with the group velocity of the optical pulse. At a given position along its path in the crystal, this dipole emits a field that travels with the phase velocity $v_{p,T}$ associated with its low carrier frequency. The phase velocity in $LiTaO_3$, $v_{p,T} \approx 0.153c$, is considerably smaller than the group velocity of the optical pulse $v_g \approx 0.433c$ because (quasi-resonant) lattice vibrations contribute substantially to the dispersion behavior in the THz spectral range. The condition $v_g > (>) v_{p,T}$ leads to the formation of an electromagnetic shock wave, also called Cherenkov radiation, propagating on a conical surface in the crystal. The characteristic angle between the surface normal of the cone and its symmetry axis (propagation direction of the optical pulse) is

$$\cos\theta_c = \frac{v_{p,T}}{v_g}, \tag{13.9}$$

which is 69° for $LiTaO_3$ [1]. The emission of the conical wavefronts can be analyzed more rigorously by adding the transverse coordinate to the wave equation, Eq. (13.5) [10]. If the (external) angle of incidence of the optical pulse is chosen

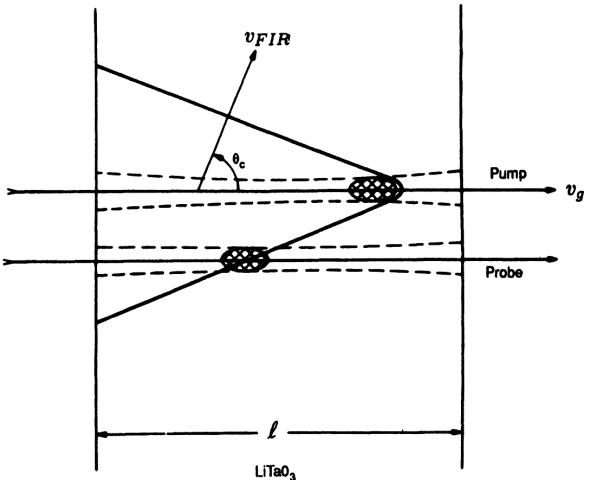

Figure 13.2: Schematic diagram for the generation of terahertz radiation through optical rectification (adapted from [1]). A time delayed optical pulse sampled the FIR field by probing the induced birefringence. (Note $v_{FIR} \equiv v_{p,T}$.)

to be $\alpha = 51°$, a portion of the Cherenkov cone propagates normally to the crystal surface [14] and thus can propagate into free space (air). In this manner the crystal acts like an emitter for THz radiation.

There are some practical drawbacks of high-power THz generation under conditions of Cerenkov radiation. It is the difficult to collect the THz radiation efficiently for applications downstream. The requirement that the lateral extension of the pump beam waist has to be smaller than λ_T (for efficient dipole emission) makes it difficult to increase the energy of the THz pulse at λ_T by increasing pump energy and spot size.

These problems can be mediated by using an optical pulse front that is tilted with respect to the propagation direction [15]. How to produce tilted pulse fronts, for example using optical elements with angular dispersion like prisms and gratings, was discussed in Chapter 2. The idea is illustrated schematically in Fig. 13.3(a). The pulse front is tilted at an angle γ that matches the angle between the propagation direction of the THz wave and the optical pulse, $\gamma = \theta_c$. A prismatic sample is used to couple out plane THz wave fronts.

It is interesting to note that the condition $v_g \cos\gamma = v_{p,T}$ can also be derived from the requirement of photon momentum conservation (zero wave vector mismatch) typically used to analyze difference frequency generation. The corresponding wave vectors add to form the THz wave vector, see Fig. 13.3(b). This is described mat-

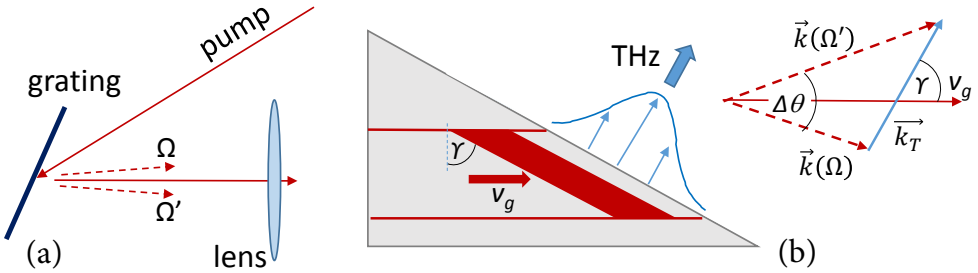

Figure 13.3: (a) THz generation via optical rectification using tilted pump pulse fronts produced by a reflection grating. The exit face of the nonlinear material is cut parallel to the pulse front and normal to the generated THz wave, respectively. (b) Wave vector diagram showing the THz wave vector $\vec{k}_T$ at frequency $\omega_T = \Omega' - \Omega$. Adapted from [16].

hematically by the phase matching condition Eq. (13.2) in vector format

$$\Delta\vec{k} = \vec{k}(\Omega + \omega_T) - \vec{k}(\Omega) - \vec{k}(\omega_T) = 0. \tag{13.10}$$

As discussed in Chapter 2 pulse front tilt from angular dispersion is associated with different spectral components propagating at different angles within the beam, cf. Eq. (2.72). It turns out that the angular spread of two plane wave components that couple to produce a THz wave at frequency $\omega_T = \Omega' - \Omega$ is just what is needed so that the THz wave vector includes an angle γ with respect to the direction of the average optical wave vector [15, 16], satisfying the phase-matching condition.

Conversion efficiencies of a few percent have been reported with tilted pump pulse fronts using $LiNbO_3$ crystals [17]. The nonlinear material was cooled to reduce phonon absorption.

13.2 THz generation from a current surge

The electric field of an electromagnetic wave emitted from a localized transient current $J(t)$ is proportional to

$$E_T(t) \propto \frac{d}{dt} J(t) \propto \frac{d}{dt}[N(t)v(t)], \tag{13.11}$$

where N and v are local charge density and velocity, respectively. Let us assume that the current is produced by a focused laser pulse and its rise and/or fall time are controlled by the optical pulse envelope $\mathcal{E}(t)$. The power spectrum of the emitted radiation $|\tilde{E}_T(\Omega)|^2$ contains frequency components in the THz range if the optical pulse duration is shorter than a few ps.

13.2.1 Biased photoconductive switches

Emission of THz radiation from a transient current was first observed with biased photo-conductive switches [2], see Fig. 13.4.

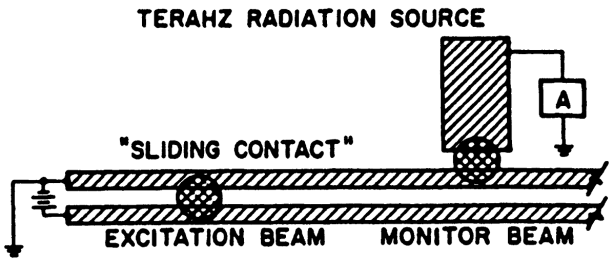

Figure 13.4: THz radiation through ultrafast switching of a charged coplanar transmission line. A fs pulse shortens the transmission line creating a subps electrical pulse. Its transients, after propagation over a certain length L, can be measured by a time delayed second pulse that excites a fast photoconductive switch (from [2]).

The transmission line consisted of two 5-μm wide, 5-μm thick aluminum lines separated by 10 μm. The substrate was heavily implanted silicon on sapphire to ensure a short carrier life time of about 600 fs [18]. The latter is crucial for generating the short electrical transients and for a short response time of the detection switch. The transient current emitted a THz pulse that propagated through free space. Conversion efficiencies on the order of a few tenths of a percent have been achieved [19] using photoconductive switches.

13.2.2 Two-color THz generation in plasmas

The electric field of a laser pulse can move charged carriers directly without the presence of an external bias field. However the symmetric nature of the field oscillations typically does not lead to a directional net current when averaged over the optical pulse envelope. This is a consequence of the fact that $\int E(t)dt = 0$. The symmetry can be broken by simultaneous irradiation with the fundamental pulse and its second-harmonic. THz emission from laser plasmas under such illumination conditions was observed [20] and gained interest because some of the bandwidth limiting effects in solids, such as absorption by phonons, can be avoided.

While the THz generation in plasmas involves a complex interplay of contributions from several processes in the neutral and ionized gas [21] we will focus here on the contribution from a net drift current in the plasma [22].

A fs pulse $E_1(t)$ and its second-harmonic $E_2(t,\theta)$ are focused into a gas. The

combined field

$$E(t) = \mathcal{E}_1(t)\cos(\omega_\ell t) + \mathcal{E}_2(t)\cos(2\omega_\ell t + \theta) \tag{13.12}$$

ionizes atoms and molecules if the intensity is sufficiently high. Let

$$\Delta N_e(t_e) = \left.\frac{dN}{dt}\right|_{t_e} \Delta t. \tag{13.13}$$

be the electron density created at time t_e during an interval Δt. The electrons are accelerated by the optical field, and at time t have acquired a velocity

$$v_e(t, t_e) = \frac{e}{m_e}\int_{t_e}^{t} E(t)dt, \tag{13.14}$$

where e, m_e are the electron charge and mass, respectively. This group of moving electrons represents a current, which at time t is

$$\Delta J(t, t_e) = e\Delta N_e(t_e) v_e(t, t_e). \tag{13.15}$$

The total current responsible for field emission, cf. Eq. (13.11), is obtained after adding the contributions from electrons liberated at different times t_e. It turns out that efficient THz generation occurs for a relative phase $\theta = \pi/2$ while for $\theta = 0$ no THz emission is observed [22].

For a qualitative understanding of this surprising fact let us first analyze the trajectory of an electron in a monochromatic, linearly polarized field $\mathcal{E}_1\cos(\omega_\ell t)$. We assume that the electron, by a process yet to be defined, is injected into the field at time t_e and position $x = 0$ with zero initial velocity. The equation of motion

$$\frac{d^2}{dt^2}x = \frac{e\mathcal{E}_1}{m_e}\cos(\omega t) \tag{13.16}$$

can be integrated to obtain the velocity

$$v_e(t, t_e) = \frac{e\mathcal{E}_1}{m_e}\int_{t_e}^{t}\cos(\omega_\ell t')dt' = \frac{e\mathcal{E}_1}{m_e\omega_\ell}\left[\sin(\omega_\ell t) - \sin(\omega_\ell t_e)\right] \tag{13.17}$$

and the electron displacement

$$x(t, t_e) = \int_{t_e}^{t} v_e(t')dt' = \frac{e\mathcal{E}_1}{m_e\omega_\ell}\left\{\frac{1}{\omega_\ell}\left[\cos(\omega_\ell t_e) - \cos(\omega_\ell t)\right] - (t - t_e)\sin(\omega_\ell t_e)\right\}. \tag{13.18}$$

The electron velocity has two components - a term that oscillates with time and a constant term. The latter is called drift velocity v_d and, in general, is obtained by averaging $v_e(t)$:

$$v_d(t_e) = \langle v_e(t, t_e)\rangle_t = -\frac{e\mathcal{E}_1}{m_e\omega_\ell}\sin(\omega_\ell t_e). \tag{13.19}$$

For $t_e = n\pi/\omega_\ell$ with n being an integer the drift velocity is zero and the electron wiggles about $x = e\mathcal{E}_1/(m_e\omega_\ell^2)$. For all other t_e there is a net drift of electrons either in positive or negative direction depending on when during the optical cycle the electron injection occurs. Example electron trajectories are depicted in Fig. 13.5.

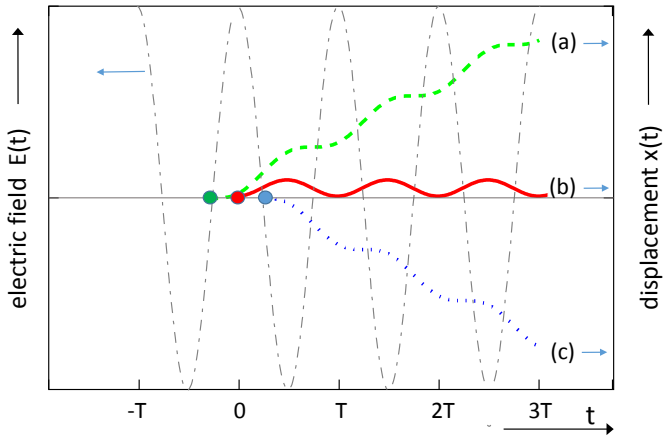

Figure 13.5: Electron displacements due to the action of an electric field according to Eq. (13.18). The electrons are born at different times during the optical cycle – (a) $-T/4$, (b) 0, (c) $T/4$. Adapted from [22].

For an ensemble of electrons "created" symmetrically around the peak field amplitude[1], the net drift current is zero. For each electron with a positive drift velocity of certain magnitude there is an electron with the same v_d but of opposite sign. Mathematically we can express this using an ensemble average of the current with respect to the phase angle $\epsilon = \omega t_e$

$$\left\langle \int_{-\epsilon_m}^{\epsilon_m} N(t_e) v_d(t_e) d(\omega t_e) \right\rangle_\epsilon = 0 \tag{13.20}$$

Thus, (efficient) generation of THz radiation from a laser induced current surge is not expected.

As mentioned before, the symmetry of the problem can be broken if fundamental and second harmonic waves are incident simultaneously and have certain relative phase θ, cf. Eq. (13.12). To illustrate that this leads to a nonzero total drift current we can follow the same approach as above. We find for the velocity of an

[1] This assumption makes sense since the ionization is controlled by multi-photon absorption and tunneling, cf. section **??**.

electron injected into the two-component field Eq. (13.12) at time t_e

$$v_e(t,t_e) = \frac{e\mathcal{E}_1}{m_e\omega_\ell}\left[\sin(\omega_\ell t) - \sin(\omega_\ell t_e)\right] + \frac{e\mathcal{E}_2}{2m_e\omega_\ell}\left[\sin(2\omega_\ell t + \theta) - \sin(2\omega_\ell t_e + \theta)\right]. \tag{13.21}$$

The oscillatory parts again average to zero and the drift velocity becomes

$$v_d(t_e) = -\frac{e\mathcal{E}_1}{m_e\omega_\ell}\sin(\omega_\ell t_e) - \frac{e\mathcal{E}_2}{2m_e\omega_\ell}\sin(2\omega_\ell t_e + \theta). \tag{13.22}$$

For $\theta = 0$ we have essentially the same situation as for the case of a single field, cf. Eq. (13.20). Each wave produces a zero net drift current if the electrons are born symmetric with respect to the maxima of the total field.

For a relative phase $\theta = \pi/2$, the maxima of the total field are shifted relative to the maxima of the constituting waves. It is left to a problem at the end of the chapter to show that the extrema of the sum of two monochromatic waves with frequencies ω_ℓ and $2\omega_\ell$

$$E(t, \theta = \pi/2) = \mathcal{E}_1\cos(\omega_\ell t) - \mathcal{E}_2\sin(2\omega_\ell t) \tag{13.23}$$

occur at phase angles $\Phi_m = \omega_\ell t \approx m\pi - (-1)^m 2\beta$, where m is an integer and $\beta = \mathcal{E}_2/\mathcal{E}_1$ was assumed to be $<< 1$. The result is an asymmetry in the electron drift current if the electrons are born at equal density symmetric, now with respect to $\omega_\ell t_e = \Phi_m$.

The drift velocity of electrons created near the maximum of the total field, at time $t = (\Phi_m + \epsilon)/\omega_\ell$, can now be estimated. Near the "central" maximum at phase angle $\Phi_0 = -2\beta$ we obtain for example

$$v_d(-2\beta + \epsilon) = -\frac{e\mathcal{E}_1}{m_e\omega}\left[\sin(-2\beta + \epsilon) + \frac{1}{2}\beta\cos(-4\beta + 2\epsilon)\right]. \tag{13.24}$$

The ensemble average of the drift velocities over a symmetric interval $[-2\beta - \epsilon, -2\beta + \epsilon]$

$$\langle v_d\rangle_\epsilon \approx -\frac{e\mathcal{E}_1}{m_e\omega}\frac{1}{2\epsilon}\left[-2\sin(2\beta)\sin(\epsilon) + \frac{1}{2}\beta\cos(4\beta)\sin(2\epsilon)\right], \tag{13.25}$$

which for small β and ϵ simplifies to

$$\langle v_d\rangle_\epsilon \approx -3\mathcal{E}_2/(2m_e\omega_\ell).$$

For $\beta = 0$ we recover the result $\langle v_d\rangle_\epsilon = 0$ for a single field. For nonzero values of β we obtain a net drift velocity resulting in a transient current. Not surprisingly, its magnitude is controlled by the amplitude $\mathcal{E}_2$ of the second-harmonic field, which

caused the field asymmetry. What was left out in our simple discussion is the ionization of the gas, which requires the strong fundamental field. It is important to note that a drift current of the same sign is produced during each (half-) cycle, independent of m, resulting in efficient THz generation. This is not the case if the frequencies of the two incident laser fields are not integer multiples of each other.

Figure 13.6 shows the results of detailed numerical calculations of plasma generation and emission of THz radiation in molecular nitrogen gas when excited by 50-fs pulses at ω_ℓ and $2\omega_\ell$ [22]. Multiphoton ionization as described by the Keldysh formalism , cf. section **??**, controls the creation of free electrons during the pulse envelope. For a relative phase $\theta = \pi/2$ the spectrum of the emitted wave

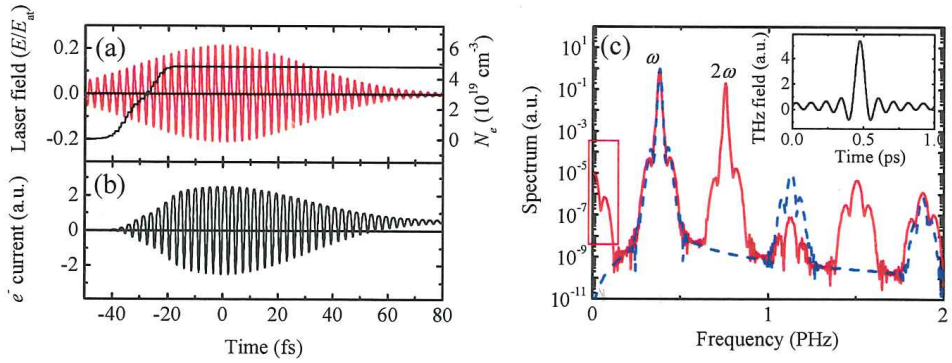

Figure 13.6: Generation of THz radiation in N_2 gas by simultaneous excitation with a fs laser pulse and its second-harmonic replica.(a) Total incident laser field for $\mathcal{E}_2/\mathcal{E}_1 = 0.2$ and $\theta = \pi/2$ and created electron density. The pulses have a duration of 50 fs and the peak intensity of the fundamental $I = 10^{15}$ W/cm^2. (b) Resulting electron current. (c) Spectrum of the emitted electromagnetic radiation for $\theta = \pi/2$ (solid line) and $\theta = 0$ (dashed line) for comparison. The inset shows the emitted field in the time domain after a 10-THz low-pass filter. From [22].

contains distributions in the THz region. In addition emission (scattering) of the fundamental and higher harmonics are also obvious. In contrast, for $\theta = 0$, THz contributions and even harmonics in the spectrum are missing.

In solids, the achievable THz bandwidth is often limited by absorption by phonon bands even if the phase matching condition is satisfied. Because of the lack of strong low-frequency absorption in plasmas the achievable bandwidths are larger and bandwidths of tens of THz have been demonstrated [20, 23].

13.3 Measurement of THz field transients

Direct all-electronic techniques are still too slow to resolve transients of a few ps and less. We discussed in Chapter **??** how amplitude and phase of an optical pulse can be retrieved from nonlinear (auto-) correlation measurements. Fortunately, by virtue of their generation, the THz pulses of interest in this chapter are accompanied by a synchronous optical pulse of comparable or often shorter duration. This allows for cross-correlation measurements avoiding complex retrieval procedures. In addition the electric field can be sampled yielding amplitude and phase of the THz waveform directly. Often the physical process applied for the cross-correlation is a replica of the THz generation mechanism.

In one of the first THz experiments, the THz pulse emitted from a transient electric current was recorded using a fast photo-conductive switch [24]. A schematic diagram is shown in Fig. 13.7. The THz wave to be resolved illuminates a

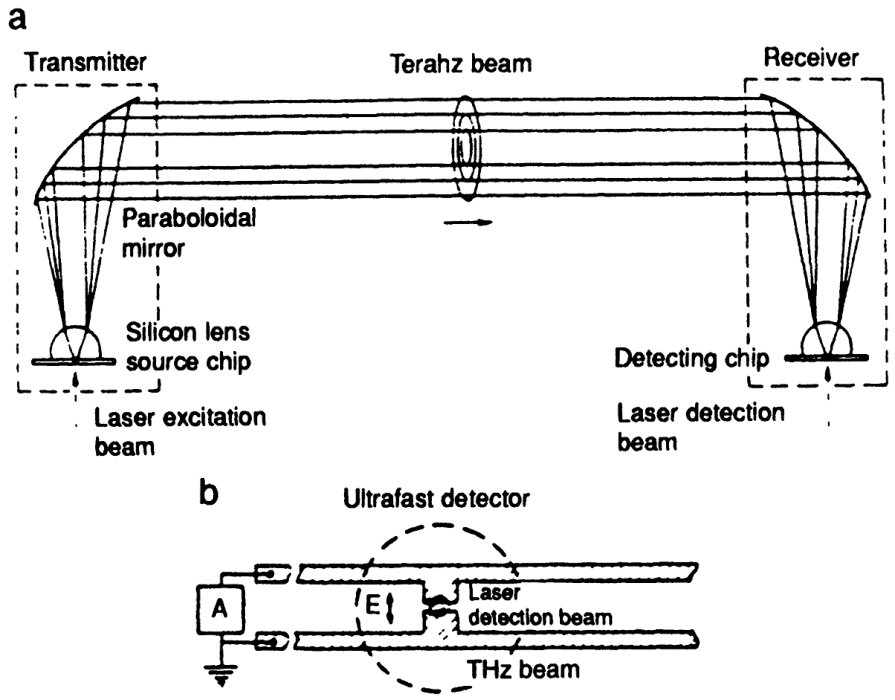

Figure 13.7: (a) Setup for generating and transmitting ultrashort THz radiation. (b) Detector for the time resolved measurement of the THz field. (From [24].)

photoconductive switch and acts as "bias voltage". The conductivity is switched by an optical pulse focused onto the gap between the two electrodes. For maxi-

mum time resolution the switch should only be conductive during the optical pulse. This requires that the excited carrier lifetime is short, $T_c \leq \tau_p$, which is difficult to achieve for short fs pulses.

A widely used THz measurement technique relies on the linear electro-optic effect (Pockels effect). An applied electric field changes the refractive index of an electro-optic (eo) material proportionally to the field strength. Originally applied to measure ps and subps electric transients using shorter optical pulses [25], electro-optic sampling was introduced for resolving free-space THz wave forms [26]. Figure 13.8 shows a schematic diagram of such a measurement. A THz and an optical

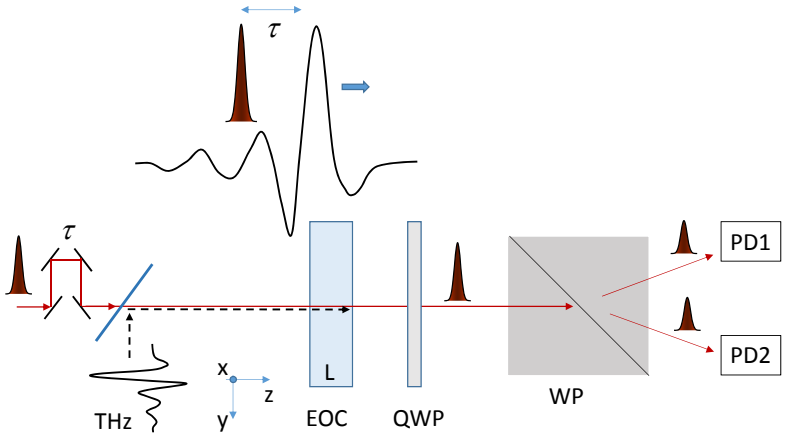

Figure 13.8: Electro-optic sampling of a THz field by a time-delayed optical pulse in an electro-optic crystal (EOC) in collinear geometry. The laser pulse is split from the pump pulse generating the THz wave. QWP - quarter-wave plate, WP - Wollaston prism, PD1, PD2 - photodetectors.

pulse propagate collinearly in an electro-optic crystal. The THz-field induces birefringence, which is probed by a shorter optical pulse as a function of the delay τ. After a quarter-wave plate (QWP) two perpendicular polarization components of the optical pulse are separated by a Wollaston prism (WP) and measured simultaneously with detectors PD1 and PD2.

While details depend on the actual properties of the crystal, the THz wave and the optical pulse, a simple picture suffices to explain the basic principle of operation of electro-optic sampling. Let us assume that the THz field only affects the refractive index seen by the optical field polarized along x

$$\begin{aligned} n_x &= n_0 + \frac{n_0^3}{2} r E_T \\ n_y &= n_0, \end{aligned} \tag{13.26}$$

where r is the electro-optic coefficient. The additional phase shift experienced by the field component polarized along x is $\phi_x = (\omega_\ell n_0^3/2c)LrE_T$ after a crystal of length L. The QWP and WP translate this phase shift into an imbalance in the two detection channels. The normalized difference signal for small induced phase shifts ($|\phi_x| << 1$)

$$\begin{aligned} S(\tau) &= \frac{S_1 - S_2}{S_1 + S_2} \\ &= \frac{\omega_\ell n_0^3 L}{2c} r E_T(\tau) \end{aligned} \tag{13.27}$$

is directly proportional to the THz field strength, see also a problem at the end of the chapter. The crystal length L should be short compared to the coherence length since THz field and optical pulse propagate collinearly. As usual, additional deconvolution steps need to be applied if the optical pulse is not sufficiently short to resolve the THz transients of interest. In reality, the crystal properties (susceptibility tensor) will determine which input polarizations of THz and optical field are convenient, and the prefactor of E_T in Eq. (13.27) will need to be modified accordingly [27].

13.4 Examples of THz spectroscopy

THz pulses alone or in combination with synchronized optical pulses have been extensively applied to study properties of matter [3–9]. The THz spectral range overlaps with inter and intraband transitions in solids, rotational and vibrational spectra in gases and liquids, and with phonon energies to name a few examples of elementary excitations that become accessible. THz and optical pulses can serve as pump as well as probe depending on the task in question and allow for simultaneous time and frequency resolved studies.

Figure 13.9 shows an example of an experimental setup for time-resolved THz pump-probe measurements. The setup contains many components typical for experiments that involve optical and THz pulses. The fs laser pulse is split fourfold to generate a (i) THz pump and (ii) THz probe pulse via optical rectification and to (iii,iv) record both fields E_T after the sample using eo sampling. Parabolic mirrors image the THz sources onto the sample and the sample output to the electro-optic crystals. A pair of grid polarizers serve as variable attenuators. The delays between the THz pump and probe pulse and for the eo sampling are adjusted by delay lines in the optical beam paths. Various other configurations are possible and have been applied. For example, optical pulse(s) can be used for excitation (pump) and THz pulse as probe.

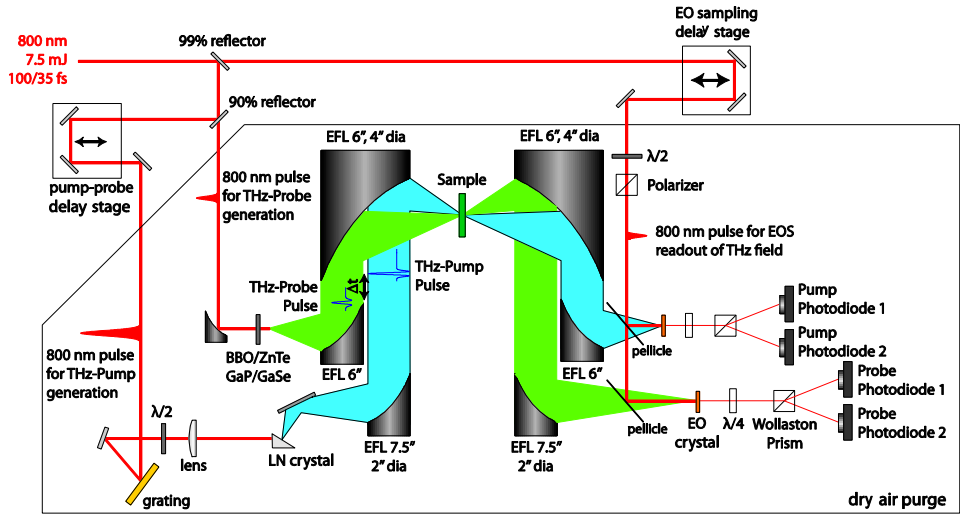

Figure 13.9: Example of an experimental setup of THz pump-probe spectroscopy. The optical pulse is used to produce the THz pulses and resolve the THz fields after the sample by electro-optic sampling. The THz probe is generated by OR in collinear geometry. The higher power THz pump is produced by OR with tilted pulse fronts. From Ref. [6] with permission.

Without the THz pump pulse the (linear) transmission of the sample is probed. If the interaction is completely incoherent, that is relevant dephasing times are much shorter than the THz waveform, the ratio of the Fourier transforms of the THz field with and without sample yield the ordinary transmission spectrum over the frequency range covered by the FIR field. Peak THz fields > 1 MV/cm are possible, which also allows to study nonlinear sample responses and to perform THz pump-probe experiments.

In the following sections we will briefly describe two THz application examples - rotational spectroscopy in gases and time-resolved charge carrier dynamics in graphite.

13.4.1 Rotational Spectroscopy

In one of the earliest THz applications the molecular response of N_2O to THz excitation was studied in the coherent regime [28]. Figure 13.10 shows measurements on N_2O as an example. The rotational spectrum of N_2O between 0 and 1 THz consists essentially of regularly spaced narrow lines [28]. The rotational frequencies

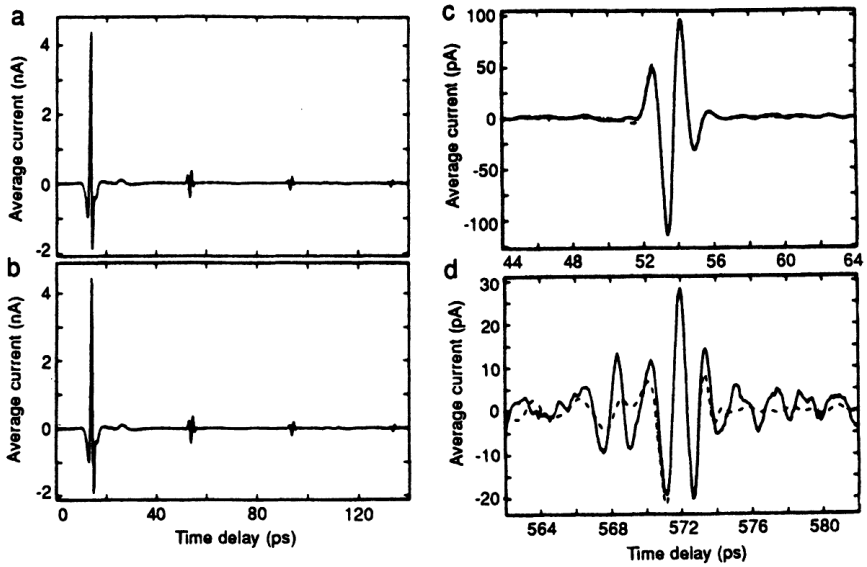

Figure 13.10: Coherent THz rotational spectroscopy of N_2O. THz radiation transmitted (a) and calculated (b) through N_2O. Measurement (solid line) and calculation (dashed lines) of (c) the first, and (d) the 14th radiated coherent pulse (from [28]).

are given by:

$$\nu_R = 2B(J+1) - 4D(J+1)^2 \tag{13.28}$$

where J is the rotational quantum number, B the rotational constant and D the centrifugal stretching constant. As many as 70 transitions can be excited simultaneously by the THz pulse. Bloch's equations (cf. Chapter **??**) apply to this system. They can be simplified assuming small pulse area and a long T_2 time. Indeed, at a pressure of 600 torr (which corresponds to an optical thickness of the sample $\alpha d = 1.2$), the dephasing time due to collisions is 65 ps, thus much longer than the exciting pulse. Each of the excited molecules, for a particular J value, acts as a vibrating dipole. These dipoles — nearly equally spaced in frequency — radiate in phase following the pulsed excitation (free induction decay), resulting in a train of ultrashort pulses (Fig. 13.10). The directly transmitted pulse is followed by a series of THz pulses at a repetition rate of 25.1 GHz, equal to the frequency separation between adjacent lines [$2B$ in Eq. (13.28) if the anharmonicity is negligibly small], as shown in Fig. 13.10(a). Since the incident and transmitted fields are measured with high precision in amplitude and phase (the signal-to-noise ratio in this experiment was better than 20,000), a detailed comparison of theory and experiment is possible [Fig. 13.10(b) and Fig. 13.10(a)].

13.4.2 Time-resolved charge carrier dynamics

Optical pulses from a fs oscillator (10 fs, 780 nm) were split to (i) generate THz probe pulses (100 fs, 8 - 30 THz), (ii) excite hot electrons in graphite films, and (iii) sample the THz waveforms passing through excited and nascent sample volumes [29]. Figure 13.11 shows results of the time-resolved pump-probe measurements and data analysis.

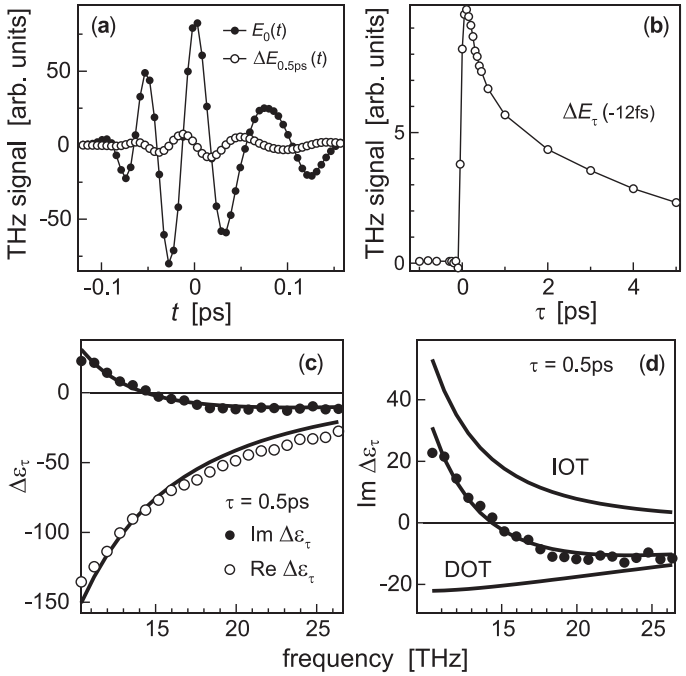

Figure 13.11: Time-resolved optical pump - THz-probe transmission experiment on graphite film. (a) - $E_0(t)$ is the THz waveform transmitted through the graphite measured with eo sampling. $\Delta E_\tau(t)$ is the pump-induced change of the THz field at a delay $\tau = 0.5$ ps. (b) - Transmitted THz signal at time -12 fs as a function of delay after excitation. (c) and (d) - Retrieved changes of real and imaginary part of the dielectric function versus frequency. The solid lines are modeling results taking into account direct optical transitions (DOT) and indirect optical electron transitions (IOT) excited by the THz wave. The latter require participation of a third (collision) partner such as phonons, defects or electrons. From Ref. [29].

The THz waveform transmitted through the unexcited sample and the changes when an excited sample volume is probed 500 fs after the pump are depicted in Figure 13.11(a). The hot (excited) electrons relax primarily through electron-phonon

energy transfer on a time scale of a few ps. The initial decay within the first 500 fs is attributed to the thermalization of hot electrons towards a Fermi-Dirac distribution that can be characterized by an electron temperature T_e. Initially, T_e is larger than the sample (lattice) temperature. The two different decay constants can be seen in the transient THz transmission shown in panel (b) for a certain time slice (-12 fs) within the THz pulse. The excitation of the electronic system and subsequent relaxation leads to a change of the dielectric function, $\Delta\epsilon$, of the graphite film. The THz pulse samples this change as a function of time. Panel (c) and (d) depict the real and the imaginary of $\Delta\epsilon$ for fixed delay (0.5 ps) as a function of frequency over the range covered by the THz probe.

13.5 Problems

1. Show that the nonlinear optical polarization of second-order driven by a monochromatic incident field $E(t) = \mathcal{E}_0 e^{i\omega_\ell t} + c.c.$ has frequency components at $\Omega = 2\omega_\ell$ and $\Omega = 0$. Are these two signals controlled by the same nonlinear optical susceptibility? Explain.

2. Derive Eq. (13.8). Apply it to find the frequency dependent THz field produced by a Gaussian laser pulse of duration (FWHM) τ_p. Show that the maximum of the spectral amplitude occurs at a frequency $\nu_p = \sqrt{2\ln 2}/\pi/\tau_p$.

3. Explain why a freely propagating (THz) pulse cannot possess an electric field according to $E(t) = e^{-at^2}\cos(bt)$? Find possible fields with the same "envelope".

4. Derive equations (13.24) and (13.25) and verify that there is a nonzero drift current if the fundamental and second harmonic field are phase shifted with respect to each other by $\pi/2$. Verify that the sign of the expected drift current is the same in each half cycle of the pulse if the two-color excitation uses frequencies that are integer multiples of each other.

5. Consider electro-optic sampling to measure a THz wave packet using a much shorter optical pulse, cf. Fig. 13.8. Assume that one of the axes (fast or slow) of the QWP is aligned with the input polarization of the optical wave and that the two output waves after the WP have polarizations along this axis and perpendicular to it, respectively. Prove the relationship between measured signals S_1, S_2 and the THz field strength given by Eq. (13.27) for small phase shifts. Which features of the setup can be changed to ensure the correct sign? (Hint: Use Jones matrices and vectors.)

Bibliography

[1] D. H. Auston, K. P. Cheung, J. A. Valdmanis, and D. A. Kleinman. Cherenkov radiation from femtosecond optical pulses in electrooptic media. *Phys. Rev. Lett.*, 35:1555–1558, 1984.

[2] Ch. Fattinger and D. Grischkowsky. Point source terahertz optics. *Appl. Phys. Lett.*, 53:1480–1482, 1988.

[3] Susan L. Dexheimer. *Terahertz spectroscopy: principles and applications*. CRC Press, Boca Raton, 2008.

[4] Erik Bründermann, Heinz-Wilhelm Hübers, and Maurice FitzGerald Kimmitt. *Terahertz Techniques*. Springer, 2012.

[5] Ho-Jin Song and Tadao Nagatsuma. *Handbook of Terahertz Technologies: Devices and Applications*. Springer, 2015.

[6] Harold Y. Hwang, Sharly Fleischer, Nathaniel C. Brandt, Bradford G. Perkins Jr., Mengkun Liu, Kebin Fan, Aaron Sternbach, Xin Zhang, and Richard D. Averitt and Keith A. Nelson. A review of non-linear terahertz spectroscopy with ultrashort tabletop-laser pulses. *J. Mod. Optics*, 62:1447–1479, 2015.

[7] Thomas Elsaesser, Klaus Reimann, and Michael Woerner. *Concepts and Applications of Nonlinear Terahertz Spectroscopy*. Morgan & Claypool Publ., San Rafael, CA, 2019.

[8] H. A. Hafez, X. Chai, A. Ibrahim, S. Mondal, X. Ropagnol D. Frachou, and T. Ozaki. Intense terahertz radiation and their applications. *J. Opt.*, 18:039004, 2016.

[9] Daniel M. Mittleman. Perspective: Terahertz science and technology. *J. of Appl. Phys.*, 122:230901, 2017.

[10] S. A. Akhmanov, V. A. Vysloukh, and A. S. Chirkin. *Optics of Femtosecond Laser Pulses*. American Institute of Physics, New York, 1992.

[11] Yujie J. Ding. Efficient generation of high-power quasi-single-cycle terahertz pulses from a single infrared beam in a second-order nonlinear medium. *Opt. Lett.*, 29(22):2650–2652, 2014.

[12] D. J. Chadi. Doping in ZnSe, ZnTe, MgSe and MgTe wide-band-gap semiconductors. *Phys. Rev. Lett.*, 72(4):534–538, 1994.

[13] C. Baumer, C. David, A. Tunyagi, K. Betzler, H. Hesse, E. Kratzig, and M. Wohlecke. Composition dependence of the ultraviolet absorption edge in lithium tantalate. *J. Appl. Phys.*, 93:3102–3104, 2003.

[14] B. B. Hu, X. C. Zhang, D. H. Auston, and R. R. Smith. Free-space radiation from electrooptic crystals. *Appl. Phys. Lett.*, 56:506–508, 1990.

[15] J. Hebling, G. Almasi, I. Z. Kozma, and J. Kuhl. Velocity matching by pulse front tilting for large area THz-pulse generation. *Opt. Express*, 10:1161–1166, 2002.

[16] Janos Hebling, Ka-Lo Yeh, Matthias C. Hoffmann and Balzs Bartal, and A. Nelson. Generation of high-power terahertz pulses by tilted-pulse-front excitation and their application possibilities. *Opt. Soc. Am. B*, 25:B6–B19, 2008.

[17] Shu-Wei Huang, Eduardo Granados, Wenqian Ronny Huang, Kyung-Han Hong, Luis E. Zapata, and Franz X. Kärtner. High conversion efficiency, high energy terahertz pulses by optical rectification in cryogenically cooled lithium niobate. *Opt. Lett.*, 38:796–798, 2013.

[18] F. E. Doany, D. Grischkowsky, and C. C. Chi. Carrier life time versus ion-implantation dose in silicon on sapphire. *Appl. Phys. Lett.*, 50:460–462, 1987.

[19] Z. D. Talor, E. R. Brown, J. E. Bjarnason, M. E. Hanson, and A. C. Gossard. Resonant-optical-cavity photoconductive switch with 0.5% conversion efficiency and 1.0w peak power. *Opt. Lett.*, 31:1729–1731, 2006.

[20] Jianming Dai, Jingle Liu, and Xi-Cheng Zhang. Terahertz wave air photonics: Terahertz wave generation and detection with laser-induced gas plasma. *IEEE J. of Selected Topics in Quant. Electron.*, 17:183–190, 2010.

[21] V. A. Andreeva, O. G. Kosareva, N. A. Panovand D. E. Shipilo, P. M. Solyankin and M. N. Esaulkov, P. Gonzlez de Alaiza Martnez, A. P. Shkurinov, V. A. Makarov, L. Berg, and S. L. Chin. Ultrabroad terahertz spectrum generation from an air-based filament plasma. *Phys. Rev. Lett.*, 116:063902, 2016.

[22] K. Y. Kim, J. H. Glownia, A. J. Taylor, and G. Rodriguez. Terahertz emission from ultrafast ionization in air in symmetry broken laser fields. *Optics Express*, 15(8):4577–4584, 2007.

[23] K. Y. Kim, A. J. Taylor, J. H. Glownia, and G. Rodriguez. Coherent control of terahertz supercontinuum generation in ultrafast lasergas interactions. *Nature Photonics*, 2:605–609, 2008.

[24] M. van Exter and D. Grischkowsky. Characterization of an optoelectronic terahertz beam system. *IEEE J. of Quantum Electron.*, QE-28:1684–1691, 1990.

[25] J. A. Valdmanis and G. Mourou. Subpicosecond electrooptic sampling: Principles and applications. *IEEE J. Quantum Electron.*, 22:69–78, 1986.

[26] Q.Wu and X. C. Zhang. Free-space electro-optics sampling of thz beams. *Appl. Phys. Lett.*, 67:3523–3525, 1999.

[27] Paul C. M. Planken, Han-Kwang Nienhuys, Huib J. Bakker, and Tom Wenckebach. Measurement and calculation of theorientation dependenceof terahertz pulse detection in znte. *J. Opt. Soc. Am. B*, 18:313–317, 2001.

[28] H. Harde and D. Grischkowski. Coherent transients excited by subpicosecond pulses of teraherz radiation. *J. Opt. Soc. Am. B*, 8:1642–1651, 1991.

[29] Tobias Kampfrath, Luca Perfetti, Florian Schapper, Christian Frischkorn, and Martin Wolf. Strongly coupled optical phonons in the ultrafast dynamics of the electronic energyand current relaxation in graphite. *Phys. Rev. Lett.*, 95:187403, 2005.

Chapter 14

Selected Applications

In previous chapters we have emphasized the role of femtosecond pulses in basic research. Ultrashort pulses are not limited to esoteric research on ultrafast events. We want to emphasize here more down-to-the-earth applications, for which the femtosecond source can have practical advantages. The topics covered are short pulse imaging, solitons, fs lasers as sensors, and stabilized fs lasers for applications in metrology.

14.1 Imaging

14.1.1 Introduction

It does not come as a surprise that ultrashort pulses contribute to the most fundamental function of light: imaging. The intensity information of light is sufficient to record two-dimensional images. Additional information provided by the phase of the optical field makes it possible to record an image along all three space coordinates. This technique, combining phase and amplitude retrieval of the light scattered by objects, is called holography, and is the most accurate of all macroscopic imaging methods. It can easily measure deformations much smaller than one wavelength. The price to pay for the high accuracy of holography is that an excessive amount of data has to be recorded. Since all the three-dimensional information of the object has to be stored in a single recording, high optical energy densities are used, with the possibility of laser damage if the material absorbs light.

"Range gating" is another method to obtain depth information, by measuring the transit time of the radiation from the source to the object and thereafter to the detector. If — as is often the case — the source and detector are co-located, the distance z from source to object is simply $c\times$ (round trip time)/2. This technique

has been used since World War II for localizing and tracking moving objects. The resolution has shifted from meter (radar) to centimeter (lidar). Femtosecond pulses offer the possibility of a depth resolution of a few microns. Another function of ultrashort range gating is to discriminate against scattering, as will be shown later in this chapter.

14.1.2 Range gating with ultrashort pulses

A basic sketch of principle for range gating 3D images with fs pulses is shown in Fig. 14.1. The source fs beam is split into a reference and an object beam. The reference beam, after an appropriate delay line, triggers the optical gate at a delay time τ. The light backscattered from various depths z of the object reaches the optical gate at time intervals spaced out by $2z/c$. A particular depth is selected by

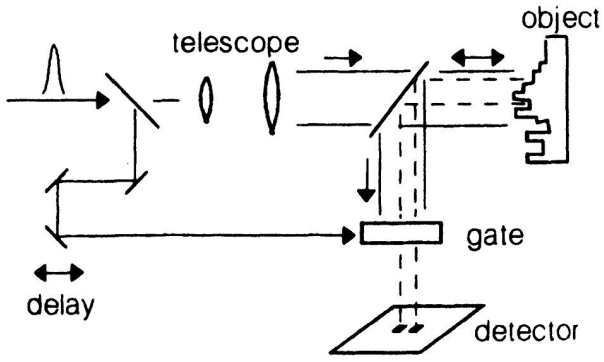

Figure 14.1: Recording of a three-dimensional object through range gating with ultrashort pulses. The gate is "opened" by a fs reference pulse derived from the illuminating source and appropriately delayed. An ultrafast gating function can be achieved, for example, with a Kerr gate or a nonlinear crystal for sum frequency generation. In the latter case, transverse resolution is generally obtained by scanning a narrow beam across the object.

the delay time at which the shutter is opened. The signal S received by the detector, as a function of delay τ, for a particular position (x,y) in the transverse plane of the beam, is the correlation of the gating function $g(t)$ and the intensity from the object $I_s(t)$:

$$S(\tau) = \int_{-\infty}^{\infty} I_s(t) g(t-\tau) dt. \tag{14.1}$$

If the gating function can be assimilated to a δ-function with respect to the variations of the signal $I_s(t)$, the measured transmitted signal is simply $S(\tau) \approx I_s(\tau) =$

$I_s(2z/c)$, where the depth of observation z is determined by the position of the reference mirror (delay). In general, the higher the order of the gating process is, the better is the depth resolution. For instance, if three-photon interaction ($\omega_d = 2\omega_r + \omega_s$, where ω_d, ω_r and ω_s are respectively the frequencies of the detected, reference, and signal photons) is used to gate the signal light, since $g(t) \propto I_r(t)^2$, the gating signal is approximately $\sqrt{2}\times$ shorter than the signal pulse. A compromise has to be reached: The higher the order of the gating process, the greater the required reference intensity. Given the power limitation of the source, the intensity requirement for the reference pulse limits the beam cross-section that can be utilized. Lateral scanning is therefore often used to obtain the transverse information on the object.

Bruckner [1] proposed using a fast Kerr shutter to gate the radiation reflected by index discontinuities in eyes. A Kerr shutter consists of a Kerr liquid between crossed polarizers. The shutter is "opened" by an intense ultrashort pulse inducing birefringence in the liquid. The gating time is either the pulse duration or the response time of the liquid, whichever is longer. Kerr gates have been applied to picosecond gating [2, 3]. Femtosecond temporal resolution can be achieved, for example, by gating through second harmonic or sum frequency generation [4, 5]. The technique consists of generating a second harmonic signal $I_2(t)$ proportional to the product of a reference pulse $I_r(t)$, derived directly from the source, and the signal $I_s(t)$. The second harmonic energy $S_{2\omega}(\tau)$ recorded as a function of reference delay τ is simply the correlation function defined in Chapter 10. This technique has been applied in one dimension to fibers, to locate defects in fibers and connectors with a resolution of the order of a few microns [6]. The method has been extended to three dimensions (three-dimensional imaging of the eyes) by scanning the beam transversely [7]. The transverse resolution, limited by the size of the beam, can be improved by illuminating each point of the 3D object and using tomographic reconstruction algorithms [4].

Linear correlation techniques, such as heterodyning, can also be applied. Here the reference pulse is frequency-shifted. Gating is achieved by interfering reference and object pulse and detection at the heterodyne frequency. Because no nonlinear optical processes are involved, these linear techniques are very sensitive even at low illumination power. A particular example is Doppler interferometry. The backscattered signal is mixed with the reference signal, which is continuously scanned. Because of the scanning, the reference is Doppler-shifted, and the mixing produces a beat note observable only in the regions where the reference and signal are coherent with each other. In this particular application, either ultrashort pulses, or light with a short coherence length are used. The technique was initially applied to fibers and integrated optics structures [8].

Fujimoto and co-workers [9] introduced a greatly improved method as optical

coherence tomography (OCT) in the early 90's. Since then OCT has developed into a field of its own with impressive applications initially in the imaging of eyes [10], and later in biomedical non-invasive imaging in general. We refer the reader to several books devoted to OCT [11, 12].

Speed is an essential element in 3D imaging of in vivo biological objects. There is a compromise between speed and sensitivity: Very sensitive detectors require a longer integration time. One possibility to reduce the time needed for data acquisition is to reduce the multidimensional scanning to only one dimension (the depth). It is possible in the case of nonlinear gating (second harmonic or parametric generation) to record a single-shot transverse picture for each depth increment. Direct recording of 2D images in "depth slices" has been demonstrated with high-contrast objects [5, 13]. The optical arrangement is sketched in Fig. 14.2. The laser beam is expanded to the size of the object after being split by a calcite prism (polarizing beam-splitter) between a reference and probing beam. The amount of beam splitting is controlled by a half-wave plate, in order to have the maximum probing intensity that the sample can accommodate. A quarter-wave plate in both the reference and object arms ensures that the returning beams are re-directed toward the detector. The backscattered signal beam and the orthogonally polarized retroreflected reference are sent into a nonlinear crystal cut for type-II phase matched second harmonic generation. Assuming the reference has a uniform transverse intensity profile, the second harmonic contains the image information contained in the fundamental beam. The time of arrival of the reference ultrashort pulse determines the depth d at which a cross-section through the object is imaged into the CCD, as illustrated in Fig. 14.2.

The ultrashort pulse source used for the preliminary tests was a fs dye laser operating at 620 nm [5]. Urea crystals were chosen for these tests as being the only phase-matchable type II crystals at that wavelength. Unfortunately, good-quality urea crystals are not readily available. Despite these limitations, a spatial transverse resolution of the order of 100 μm has been achieved in experiments with a configuration in which the reference and object beams have the same size [5, 13]. The titanium sapphire femtosecond lasers appear promising for this particular application, because of the better transmission of biological tissues in its wavelength range of 750 nm to 850 nm, and the possibility of using KDP crystals (type II) for the gating.

There is a subtle interplay among sensitivity, depth, and transverse resolution in the setup shown in Fig. 14.2. One cannot have the three parameters simultaneously optimized. For instance, an optimum conversion efficiency of one single second-harmonic photon for one signal photon can be achieved, provided the crystal length and the reference power density are sufficient. A simple estimate given as a problem at the end of this chapter illustrates this problem. A minimum crystal

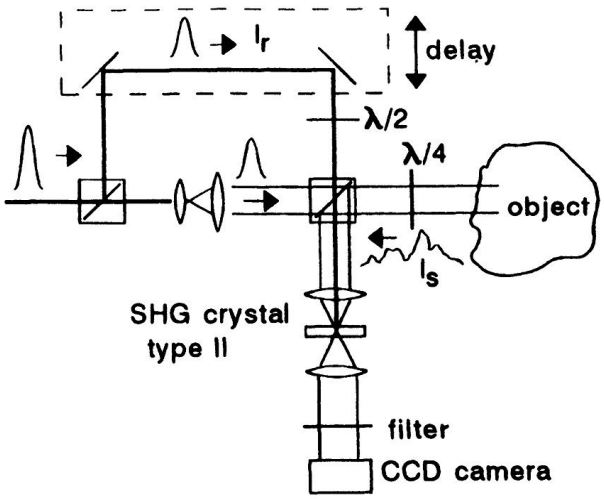

Figure 14.2: Setup for recording successive two-dimensional "slices" of a transparent 3D object based on SHG. The backscattered radiation I_s from the object is stretched out in time, corresponding to the time of arrival from various depths. In the nonlinear crystal, the second harmonic, being proportional to the product of the reference I_r and signal I_s, selects a portion of the signal corresponding to a certain depth (set by the reference delay).

length is required to achieve single photon upconversion (i.e., one second harmonic photon for each signal photon). But to this minimum crystal length corresponds a phase matching bandwidth, hence a limitation to the temporal resolution of the up-conversion. In addition, the waist of the reference beam acts as a spatial filter, limiting the transverse resolution of the imaging system.

14.1.3 Imaging through scatterers

One of the main medical motivations for this type of research is early detection of tumors. The photon energy of visible and infrared light is too small for direct ionization of most tissues. Hence, an optical method seems to be an attractive and safe alternative to x-rays. Large differences in absorption have been reported between in vivo normal tissue and some types of tumor [14].

In medical and biological imaging, the biggest challenge is generally posed by scattering. To illustrate the effect of scattering on short light pulses, let us consider a femtosecond pulse being incident on a slab of thickness L made of isotropic scatterers as shown in Fig. 14.3. If we time resolve the transmission, we observe a peak on the leading edge of the transmitted pulse, which corresponds to the unscattered light ("ballistic" component) followed by a broad distribution

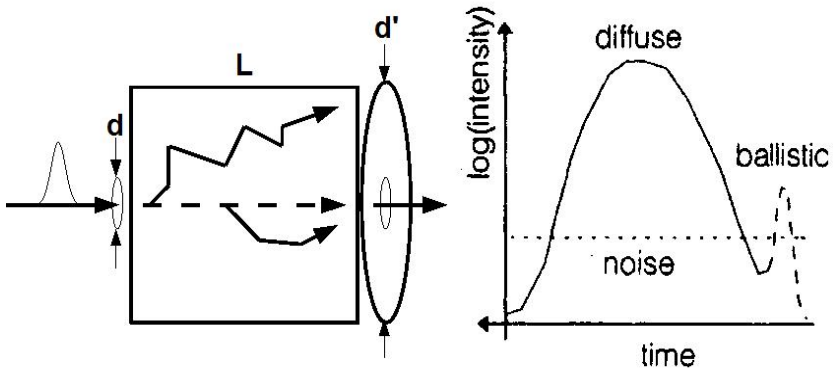

Figure 14.3: Sketch of pulse propagation through a scattering medium.

of scattered light. Diffraction-limited resolution in an imaging process can only be obtained with the ballistic light. The latter can be separated from the diffuse light by appropriate time gating. The ballistic component of the transmitted light is attenuated exponentially:

$$I_{\text{ball}} = I_0 e^{-\mu_s L}, \tag{14.2}$$

where $\mu_s = l_t^{-1}$ is the scattering coefficient, and l_t is the scattering mean free pathlength. There have been numerous attempts to visualize objects embedded in dense scatterers by range gating the backscattered or transmitted ballistic radiation [3, 13, 15]. Very high sensitivity is required in order to compensate for the large attenuation of the return signal. In the case of nonlinear detection, the second harmonic that is recorded is proportional to the product of a reference intensity by the weak backscattered radiation. Therefore, high peak powers (of the reference signal) are required to obtain a good conversion efficiency at the detection.

Problems arise if the scatterer is dense and I_{ball} approaches the noise level of the detection system. Here techniques are needed which provide not only the time gating but also an optical amplification. Nonlinear techniques, such as Raman amplification, and linear methods, such as heterodyning, have been applied successfully [16–19] leading to micrometer resolution through dense scatterers. The ultimate limit to the resolution is the quantum noise (photon shot noise) which essentially implies that at least one photon should be detected per element or pixel of the image. In the case of biological and medical samples that can only withstand average powers of irradiation of a few mW, these noise considerations limit the applicability of diffraction limited imaging to scattering densities $\mu_s L \leq 35$.

The multiply scattered photon path can be described by a diffusion model [20]. For $L \gg l_t$, it can be shown that a collimated input beam of diameter $d < l_t$ at the sample input broadens to a diameter d', which is approximately given by [21]:

$$d' = 0.2L \tag{14.3}$$

if we refer to the early-arriving scattered light that exceeds the detection noise and to illumination intensities below the critical values for biomedical samples. The quantity d' gives a reasonable measure of the resolution which can be achieved in imaging an object buried in a dense scatterer. With a sample thickness of several mm to several cm, the achievable resolution cannot be better than a few mm.

Several approaches are being attempted to utilize the large diffuse light component for imaging through very dense scatterers, such as several cm of tissue. One direction that promises to improve the resolution is to use the earlier portion of the scattered light, which may or may not follow a diffusion-like path [17, 22] for imaging.

An overview of activities in the field of imaging with short light pulses can be found for example in refs. [23, 24].

14.1.4 Prospects for four-dimensional imaging

Ultrashort pulses can be used as a substitute for holographic techniques to record three-dimensional images, provided the object does not move on the time scale of the ultrashort pulses. Holography with ultrashort pulses should be used to record the temporal evolution of ultrafast 3D events. A method called "light-in-flight holography" (LIFH) has been proposed by N. Abramson [25, 26] to convert the rapid time information obtained with ultrashort illumination holography into space information that is stored. The basic principle is that the holographic fringes can only be recorded if the object and reference beams arrive simultaneously at the recording medium. An ultrashort reference beam sent at oblique incidence to the recording medium sets a time axis (Fig. 14.4). Point A is illuminated first and point B last after a time interval $\Delta t_{AB} = D\tan\theta/c$. At any point on the line AB, a hologram of the object beam corresponding to a particular instant within the time interval Δt_{AB} is recorded.

This technique has been used to detect the first arriving light through scattering media [27, 28] — the "ballistic" component cited earlier. The holographic data can be recorded on a CCD camera (provided the reference and object beam make a sufficiently small angle for the fringes to be resolved by the camera), and reconstructed through numerical fast Fourier transform [28, 29]. The advantage of the electronic recording and numerical processing is the possibility to integrate a large number of successive (reconstructed) images. The speckle pattern is averaged out

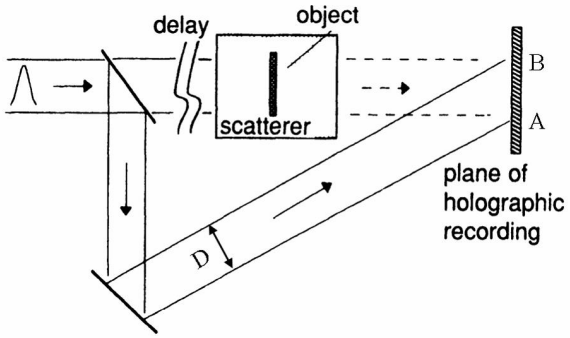

Figure 14.4: Light-in-flight holography illustrated for a simple one-dimensional transparent object (uniform in the transverse dimension of the object).

if the time interval between exposures is greater than the correlation time of the speckle.

14.1.5 Microscopy

Laser-scanning microscopy (see, for example, [30]) is ideally suited to combine microscopic imaging with fs pulse illumination. There are several attractive application fields of femtosecond microscopy — (i) nonlinear microscopy, (ii) microscopy with simultaneous space and time resolution, and (iii) microscopy of structures immersed in a scattering environment —. An early review can be found in [19]. In nonlinear microscopy the image signal is generated by a nonlinear optical process, such as surface second-harmonic generation and two-photon excited fluorescence. An image is a map of the distribution of the corresponding nonlinear susceptibility. Multi-photon fluorescence is particularly attractive for microscopy of biological cells because of the depth selectivity of the excitation process. Since its invention in 1990 by Denk, Strickler and Webb [31], the two-photon fluorescence microscope has greatly improved the microscopic imaging capabilities, in particular in the life sciences. Femtosecond pulses are needed because of their great peak power at comparatively small pulse energy (i.e., small heat consumption in the specimen). A recent overview of ultrafast optics for biological imaging can be found in a review by Squier [32].

Simultaneous μm spatial and temporal resolution is of great desire for the inspection of ultrafast opto-electronic circuits. Another direction is to combine techniques of ultrafast spectroscopy with spatial resolution — to monitor, for example, diffusion and relaxation of excited carriers in semiconductors. In fluorescence microscopy additional information can be gained by measuring the lifetime

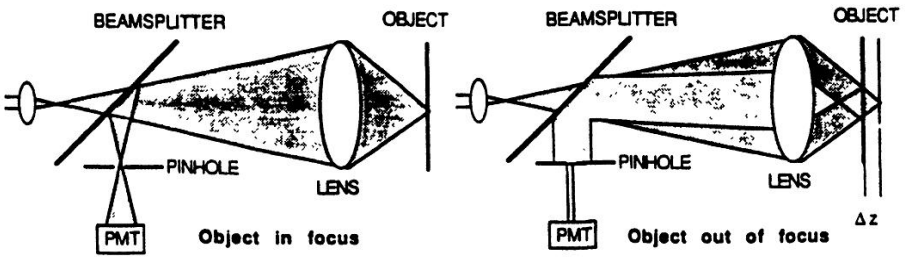

Figure 14.5: Schematic diagram of (reflection) confocal microscopy. Only light from layers that are in-focus can pass through the pinhole and reach the detector. The beam (or object) is scanned in transverse direction to obtain a two-dimensional image of the layer that can be displayed by a computer.

of the fluorescence. Since this relaxation depends sensitively on the interaction of the fluorescing dye with the environment, the "lifetime" image can describe local field and ion concentrations in cells [33].

Another example where scanning can be complemented by temporal correlation with a reference pulse is confocal imaging of objects buried under scattering layers. Confocal microscopy distinguishes itself by its depth selectivity [see Fig. 14.5]. Enhanced depth selectivity and optical amplification of the image signal are desirable for imaging through scattering layers that strongly attenuate the ballistic light. Both aspects can be addressed with scanning microscopy based on a sensitive correlation technique, such as heterodyning [34]. A realization of such a microscope is shown in Fig. 14.6. It consists of a Michelson interferometer which contains a scanning microscope in one arm and a piezoelectric transducer for Doppler-shifting the reference pulse in the other arm. The role of the pinhole is played by the coherent overlap of the plane reference wave and the image light. A maximum heterodyne signal is obtained if the wave front from the object is plane (parallel to the reference wave front), that is, if the object is in focus.

Assuming a layer of thickness L with scattering coefficient μ_s on top of an object with reflectivity R, the image signal of the correlation microscope can be written as:

$$S_d \propto \left(\mathcal{E}_{r0}\mathcal{E}_{s0}e^{-2\mu_s L}\right)\left(R \otimes \tilde{h}^2\right)\left[\frac{\langle \mathcal{E}(t)\mathcal{E}(t-\tau)\rangle}{\mathcal{E}_{r0}\mathcal{E}_{s0}}\right]. \tag{14.4}$$

$\mathcal{E}_{r0}$, $\mathcal{E}_{s0}$ are the amplitudes of the reference and the object pulse, respectively, $\tilde{h}$ is the amplitude point spread function (APF) of the objective, $\otimes$ describes convolu-

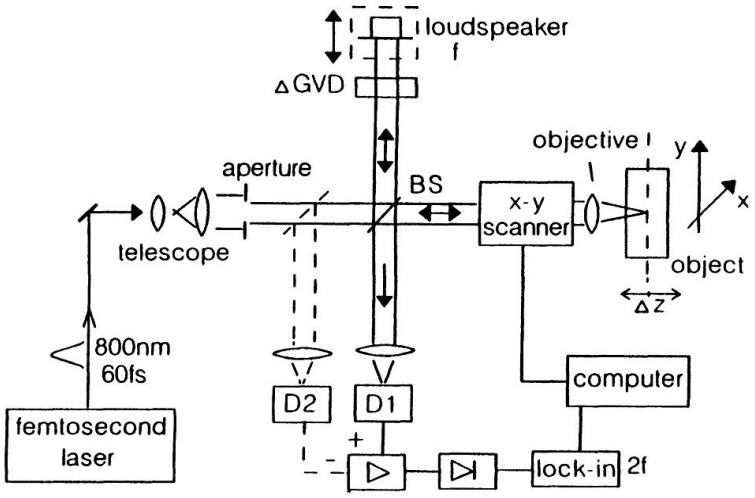

Figure 14.6: Schematic diagram of a correlation microscope based on heterodyne detection (from [35]).

tion and $\langle\rangle$ denotes correlation. As can be seen from the first term in Eq. (14.4), the attenuation of the ballistic light can be compensated by a large enough amplitude of the reference wave (optical amplification). The second term is the convolution of the object response with the APF. This term is essentially the square root of the response of a confocal microscope and describes the transverse and depth resolution. Additional depth selectivity and discrimination of scattered light from layers close to the object is possible due to the correlation (third) term in Eq.(14.4). It is nonzero only if the length mismatch of reference and image arm is smaller than the pulse duration (coherence length). Monte-Carlo simulations of photon paths showed that time gating in addition to the confocal (spatial) gate substantially increases the maximum scattering density $\mu_s L$ through which nearly diffraction limited imaging is possible, see for example ref. [36].

The depth resolution of a microscope is usually measured by scanning a reflecting object through the focus. The improved depth resolution of the correlation as compared to the confocal microscope is shown in Fig. 14.7(a). Figure 14.7(b) illustrates the transverse resolution as measured by scanning the beam focus over a straight edge buried under 5 mm of scattering material (96 nm latex spheres dissolved in water).

If the system is able to detect ballistic light, there is no loss in resolution. Microscopic techniques through scatterers have great potentials for noninvasive ima-

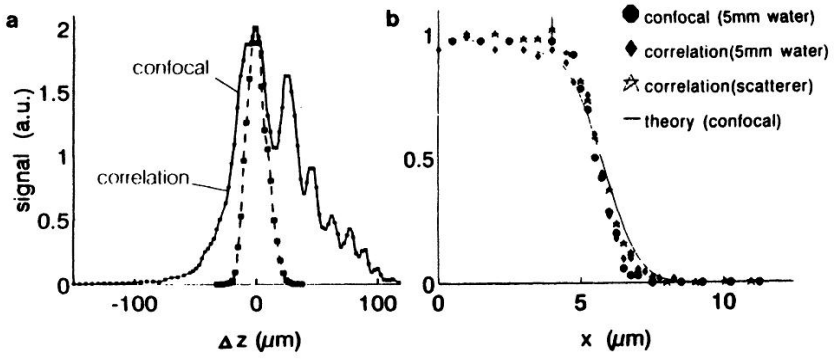

Figure 14.7: (a) Depth scan through a 10 mm glass layer that introduces spherical aberration and decreases the depth resolution of the confocal microscope (from [35]). (b) Scan over a straight edge. The scatter density was $2\mu_s L \approx 20$.

ging of biological and medical samples, see, for example, [37]. Figure 14.8 shows the images from a confocal and a correlation microscope of a cell layer of a leaf. The depth position of the layer was 80 μm from the lower epidermis.

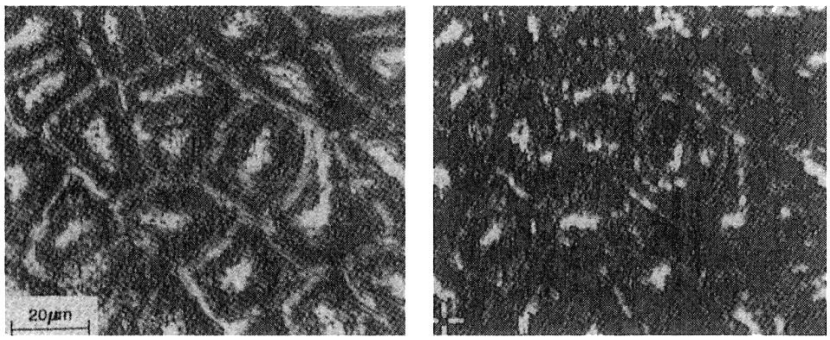

Figure 14.8: Correlation (left) and confocal (right) image of a cell layer 80 μm buried under the lower epidermis (from [38]).

14.2 Solitons

The concept of solitons has already appeared in various chapters of this book. For instance, we have seen in Chapter 6 how an elementary model for a laser cavity, including only self-phase modulation and dispersion, leads to the nonlinear Schrödinger equation, which has steady-state "soliton" solutions. The same model applied to fibers finds stable pulse shapes propagating without distortion over long distances. We have seen in Chapter 9 how solitons could be used for the shaping of fs pulses. This application transcends the fs time domain: In communication, pulse durations in the range of 20 to 80 ps are propagated without distortion through tens of km of fibers, or over 10^6 pulse lengths. The solitons used for pulse-coded communication which are *solitons in the time domain* will be briefly reviewed later. The nonlinear Schrödinger equation was first derived and solved by Zacharov and Shabat [39] in the context of self-focusing and self-filamentation. The solutions of this equation describing stable filaments are *solitons in the space domain*. The high intensities of fs pulses can also lead to spatial solitons, such as the observed filamentation in air of fs pulses [40–42]. A more complex problem is that of solitons both in the temporal and spatial domain, which we will discuss at the end of this section.

14.2.1 Temporal solitons

We have seen in Chapter 9 that ultrashort pulses of sufficient intensity launched in a single-mode glass fiber above the zero-dispersion wavelength evolve into a soliton. As mentioned earlier, since the soliton maintains its characteristics over long distances, it is an ideal signal for pulse-coded long-distance communication. Since any wavelength above the zero-dispersion point can be used, wavelength multiplexing is possible. The following problems must be overcome for-long distance propagation:

1. Decrease of the soliton pulse energy over long distances due to linear fiber losses.

2. Variations of the soliton propagation velocity resulting in timing jitter, hence loss of information.

3. Sliding of the soliton frequency, resulting in a mixture of adjacent frequency channels.

The first problem is solved with erbium-doped fibers (cf. Chapter 7) used as optical amplifiers. For example, in a test of a trans-Pacific soliton link [43], an Er-doped

amplifier was located every 26 km to restore the original soliton pulse energy, as sketched in Fig. 14.9.

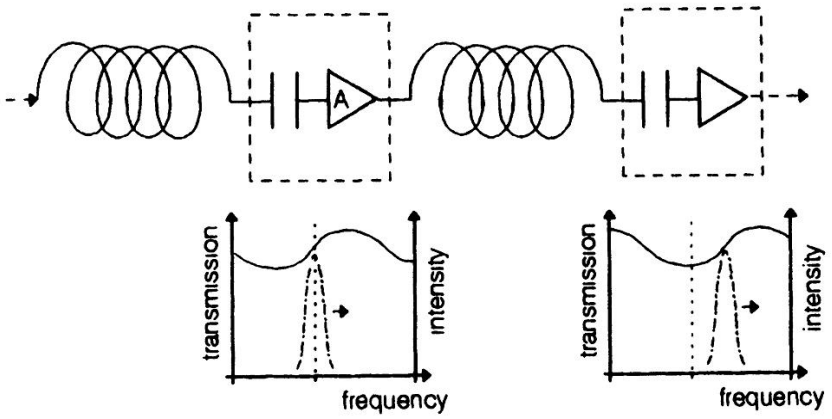

Figure 14.9: Optical soliton transmission line, showing schematically two units of fiber-repeater. Each unit consists of a single-mode, low-loss communication fiber, a Fabry–Perot filter, and an erbium-doped amplifier. The soliton spectrum makes its way through the successive filters with sliding transmission peaks, while the noise sees the overall attenuation of the overlapping filters.

Gordon and Haus [44] showed that the timing jitter is related to a jitter in the pulses' central frequency. They found that a certain component of noise added to the soliton will instantly shift its optical frequency, and consequently its velocity, hence its time of arrival. A consequence of the Gordon–Haus theory is that a soliton has the property to shift its average frequency toward the frequency of maximum transmission of a filter. Let us consider, for instance, a soliton whose frequency is slightly shifted from the filter peak transmission. The differential loss across the soliton spectrum, *in conjunction* with the ability of the nonlinear effect to generate new frequency components, provides a force to push the soliton back towards the filter peak. A frequency filter can therefore solve the time jitter problem by preventing the soliton frequency from drifting around.

In an actual system, to accommodate frequency multiplexing, a Fabry–Perot filter is used at the same location as the amplifier. Each transmission peak of the Fabry–Perot interferometer defines a particular communication channel. One disadvantage of the optical amplifiers is that the noise is also amplified. Because of the property of the soliton to shift its frequency in the presence of differential noise, filters of slightly different frequency can be put at the successive amplifier location, cf. Fig. 14.9. The soliton makes its way through the different filters located at each

successive amplifier, while the noise, being linear, sees the attenuation provided by the overlapping filters centered at different frequencies. Typical etalons [43] used as filters are Fabry–Perot interferometers of 1.5 mm length and 9% reflectivity. The fiber can support communication channels at frequency intervals of 100 GHz, which is the free spectral range of such an etalon.

In the example of trans-Pacific communication, the frequency of the etalons at successive amplifiers was shifted by 0.18 GHz at each successive amplifier spaced 26 km apart. The total shift over the 9,000 km trans-Pacific distance is still smaller than the 100 GHz frequency spacing between channels [43]. The soliton pulse duration was 16 ps at 1557 nm. The fiber had an average dispersion $D = 0.5$ ps/(nm km). We recall (cf. Fig. 9.4) that the parameter $D = dk'_\ell/d\lambda = -(2\pi c_0/\lambda^2)k''_\ell$ is generally used to characterize fibers, because it relates directly to the group delay (in ps) per nm of bandwidth, and per km propagation length.

While this particular example is not specifically in the femtosecond time scale, the concept and implementation originate directly from the properties of fs pulse propagation discussed in Chapters 1 and 2, and the pulse compression techniques explained in Chapter 9. Stable soliton propagation requires a balance of positive (negative) self-phase modulation and negative (positive) group velocity dispersion, and negligible losses. The diffraction losses are eliminated in fibers by confining the high-intensity pulse in a waveguide. In a bulk material, a mechanism for transverse confinement of the beam is required to compensate for diffraction losses. Such a mechanism is provided by self-focusing and self-filamentation, a problem addressed in the next subsection.

14.2.2 Spatial solitons and filaments

In this section, spatial solitons relate to the confinement of pulses in a self-guided waveguide. Because of their high peak power, femtosecond pulses are a primary source to observe this phenomenon.

Chiao, Garmire, and Townes [45] showed that the propagation equations for a time-independent field, in the presence of a self-focusing nonlinearity, reduce to the nonlinear Schrödinger equation. As we have seen in Chapters 6 and 9, the nonlinear Schrödinger equation has stationary solutions. These solutions were precisely investigated in the context of self-focusing [39]. Steady-state solutions, however, are not a proof of the existence of stable filaments, in particular for pulsed radiation.

As detailed in Chapter 3, Akhmanov *et al.* [46] showed that a nonlinearity of order larger than n_2 and of opposite sign can result in the formation of stable filaments. As the beam collapses because of self-focusing, the intensity on axis increases until the self-defocusing (for instance, from a negative term in $\bar{n}_4 I^2$) balances

the self-focusing due to the positive $\bar{n}_2 I$ term. The filament stabilizes at a diameter w such that the defocusing and focusing are in equilibrium. Such filaments have been observed with continuous radiation in materials of large, slow nonlinearities, such as suspensions of latex spheres, aerosols, and microemulsions [47,48]. In the case of pulsed radiation, the existence of filaments has been questioned. Instead, it has been postulated that a "moving focus," which in solids leaves a filament-like trace, can be generated with pulses [49,50].

Figure 14.10 illustrates the mechanism by which a self-focused pulse is expected to create a moving focus. On the left of the figure the initial pulse is shown at the beam waist characterized by w_0. The pulse is divided in successive slices of equal energy approximating the pulse profile. In the sketch of Fig. 14.10 the first and last slice start at the pulse FWHM. This first slice is assumed to be sufficiently above the critical power to focus at point A at a distance z_{SF} given by Eq. (4.94); the central slice focuses at point B. The length $AB = L$ is equal to $z_F(P_{max/2}) - z_F(P_{max})$. It is interesting to note that the pulse intensity of the input pulse is actually higher than the intensity in any plane within the focal region L for fs pulses. For ns pulses, the opposite is true. While this can be shown numerically, a simple model shall suffice here to bring this point home.

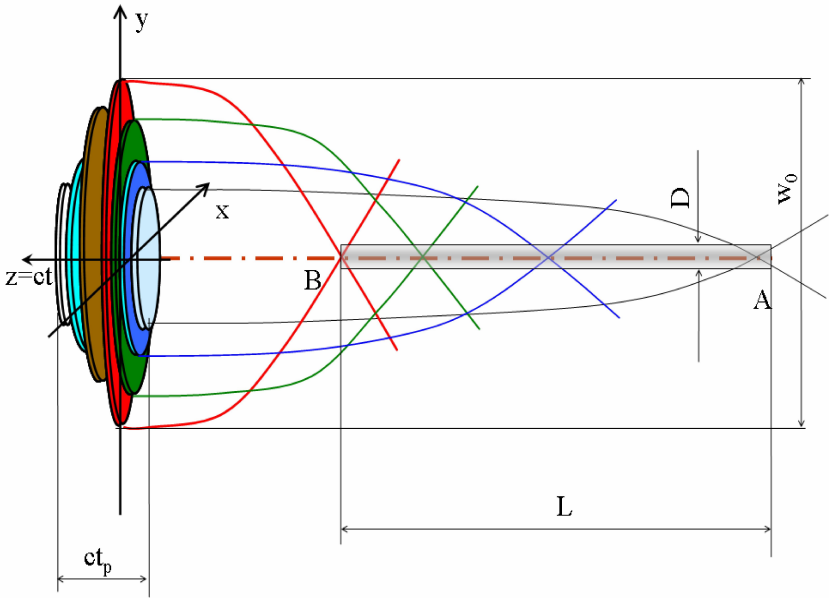

Figure 14.10: Illustration of the moving focus phenomena, for a pulse of duration t_p. Each disk represents a slice of the input pulse of certain power. Self-focusing leads to focusing at different locations depending on the power of a particular slice.

Each slice of the original pulse gets focused at various (cylindrical) focal volumes distributed along the line AB. The diameter of the cylinders (focus spot) D is finite for the reasons discussed in Section 4.8.1; from experiments $D \approx 100$ μm [42, 51]. Since each of the focal volumes contains the same number of photons as the original slice, the total energy in the cylindrical volume made up of all the focused slices is equal to the energy of the pancake shaped original pulse. We neglect here the contribution from the out-of-focus light in a particular slice since the intensity is mainly determined by the in-focus components. The total energy of the pulse is initially distributed in a volume of approximately $V_i = c\tau_p \times \pi w_0^2/2$. This energy is thereafter distributed along the "focal volume" of approximately $V_f = \pi D^2 L/4$, which controls the pulse intensity. For the comparison of fs and ns pulse focusing let us assume that in both cases $L = 1$ m. In the case of a 10 ns pulses of $w_0 = 1$ cm, V_i is of the order of $0.5 \cdot 10^5$ mm^3, while V_f is of the order of 10^{-3} mm^3. A considerable increase in energy density is thus taking place in the "filament" region, hence the filament like damage tracks observed after high power nanosecond irradiation of solids.

In the case of fs pulses as sketched in Fig. 14.10, the pancake shaped initial pulse volume is only $V_i \leq 0.5$ mm^3, while the intense pulse sweeps a focal volume of $V_f \geq 15$ mm^3. In the case of a fs pulse, there is thus *less energy density* in the focal region than in the original pulse. Therefore, in the case of self-trapping of fs pulses in air, the strong nonlinear phenomena such as conical emission [41, 42] and multiphoton ionization [40] can only be explained if a significant portion of the original pulse is trapped as a "light bullet" within the filament as opposed to a moving focus.

We discussed in Section 4.8 possible mechanisms of beam trapping. In the simple theory of steady state self-focusing, the filament remains confined through a balance of the self-focusing (term $n_2\mathcal{E}^2$) and a self-defocusing [term $n_3\mathcal{E}^3$ in Eq. (4.100)] of opposite sign. The simple interpretation most commonly cited is that the stabilizing higher order index due to an electron plasma leads to defocusing. In the case of air, the electron plasma is created by (multiphoton) ionization. A second contribution to the negative index change stems from the shift of the absorption edge towards shorter wavelengths (because of the replacement of neutral molecules by ions).

The physical reality is more complex, since numerous effects other than the negative lensing of an electron plasma contribute to compensate self-focusing. Some of these effects are illustrated in a model of filamentation without ionization [52]. Any nonlinear phenomenon (of order higher than 3) that limits the pulse intensity will have a stabilizing influence on the filament. One example is third harmonic generation, that has been shown to be quasi phase-matched and to play a role in sustaining the propagation of filaments produced by IR pulses [53–55]. At the op-

posite end of the spectrum, optical rectification has been observed and — because of the short duration of the propagating optical pulse — has resulted in the generation of THz radiation. The experimental observation of a THz pulse emitted by a filament [56] was explained as being the result of a longitudinal plasma oscillation created by the Lorenz force [57]. Both of these nonlinear effects reduce the $n_2\mathcal{E}^2$ term by drawing power from the beam, hence acting similarly as a saturation of the focusing term.

A similar saturation effect can occur as a result of pulse splitting [58]. Multiple pulse splitting results from self-phase modulation and dispersion only, far below the power required for plasma formation, as demonstrated by Bernstein *et al* [59, 60], in a measurements where the pulse temporal and spatial profiles for a self-focusing beam. Because the beam, with an initially Gaussian profile (4 mm diameter FWHM), was focused down to not less than 1 mm over 23 m, the intensity never reached a level at which conical emission, harmonic generation or ionization become significant. Therefore, the multiple pulse splitting that was observed resulted purely from phase modulation and dispersion. The phase modulation leads to a lower frequency of the pulse leading edge, and to a higher frequency at the pulse trailing edge. Because of the normal dispersion of air, the leading edge travels faster than the trailing edge, resulting in pulse splitting. As the pulse splits, the peak intensity is reduced, resulting again in an apparent saturation of the self-focusing effect.

Application to remote sensing

Associated with the filaments is an intense white light or conical emission, which can be used to probe remotely the atmosphere [61, 62]. Two physical phenomena giving rise to that white light emission are illustrated in Fig. 14.11. Figure 14.11 (a) is the pulse intensity profile. SPM results in a similar phase modulation profile [Fig. 14.11 (b)], leading to a frequency sweep [Fig. 14.11 (c)]. The latter frequency excursion adds frequency components to the pulse, thereby broadening its spectrum. In combination with normal dispersion, the self-phase modulation results in pulse splitting. The low-frequency components generated in the leading edge of the pulse propagate faster than the high-frequency components generated in the tail of the pulse. This mechanism accounts for spectral broadening in the formation stage of filaments. As filamentation sets in, further spectral broadening is due mainly to amplitude modulation rather than phase modulation [63, 64]. This results from the self-steepening effect due to the first order correction to the SVEA ($\partial\mathcal{P}_{NL}/\partial t$), as detailed in Section 4.5.3 and illustrated in Figs. 14.11 (d) through (f). The responsible nonlinear polarization is sketched in Fig. 14.11 (d). Its impact on the propagating pulse can be illustrated by subtracting a field distribution of shape

similar to curve (e) from the original pulse, leading to Fig. 14.11 (f).

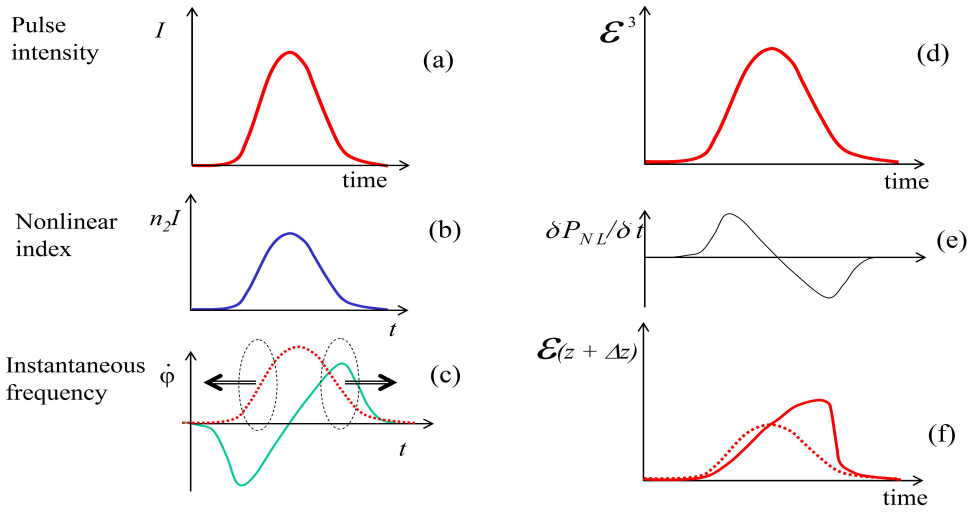

Figure 14.11: Left: illustration of the influence on pulse propagation of the Kerr effect nonlinearity. The pulse intensity represented in (a) gives rise to a nonlinear index (b), hence the frequency modulation shown in (c). Right: influence of the shock term, proportional to the derivative (e) of the nonlinear polarization (d), leading to the asymmetric shape (f) for the field.

The white light emission of filaments has been studied extensively both theoretically and experimentally (see for instance refs. [64, 65]). Launched vertically, the white light emission has been used to irradiate the atmosphere up to 13 km altitude [61, 62]. Spectral analysis of the time-gated return provides a means to study the composition of the atmosphere [66]. Measurements of the angular distribution of the supercontinuum emission show that it is peaked towards the backward direction [67], an effect that could be attributed to an inversion created in multiphoton excited nitrogen [68].

Application to laser induced discharges

The ionizing properties of a filament, combined with the relatively long spatial extension, should make it an ideal tool for laser induced discharges. The process by which seeding of a low density of charges in a uniform electric field results in a discharge has been investigated theoretically and experimentally [40]. High voltage electrical discharges were triggered and guided with UV pulses (248 nm) of only a few mJ energy over a gap of the order of 0.5 meter [69, 70]. The gap or reduction of breakdown voltage do not scale with the pulse energy. Even with 400

times higher pulse energies, the length over which a discharge could be guided reliably was only 2 or 3 times longer [71]. Plasma interferometry measurements [72] have shown that the ionization created in air by a filament exists for only 200 ps. A typical electron density of 10^{17} cm^{-3} in air causes a decrease in the index of refraction, which lasts for about 200 ps because of electron-ion recombination and the attachment of electrons to oxygen. There is a subsequent decrease in the index of refraction because of expansion of the air heated by the laser excitation. The rarefied air can provide a preferential path for the discharge, but does not efficiently reduce the minimum field required to produce a discharge over a given gap. This explains the difficulties in achieving breakdown reduction and discharge guiding over large gaps. A solution to the problem of triggering and guiding discharges over long distances is to maintain the ionized channel created by the UV or IR filament through inverse Bremstrahlung (plasma heating) and photodetachment of oxygen. Pulse intensities ranging from 1 to 10 MW/cm^2 have to be maintained in the channel, for the time duration required to trigger the discharge [70].

The ability to trigger a discharge depends also on the initial electron density deposited by the fs pulse in the filament path. Various evaluations of the electron density have been based on conductivity measurements. The values reported vary between 10^{12} cm^{-3} [73], 10^{14} cm^{-3} [51] and 10^{16} cm^{-3} [74]. Measurements performed with the same set-ups and 1-ps UV pulses (250 nm) and 100-fs IR pulses (800 nm) [51] indicate a 20 $\times$ larger conductivity induced by the UV filament than by an IR filament, the latter produced by a 10 $\times$ more energetic pulse. The larger conductivity in the UV filament is important for laser discharge applications and is attributed to the fact that the nonlinear ionization is only a three-photon process compared to a 9- to 10-photon process for the IR filaments. In both cases a diameter of the filaments of 100 μm was obtained, implying an intensity of 1 TW/cm^2 in the "UV" filament versus 100 TW/cm^2 in the "IR" filament. Using these intensities and typical cross sections for the multi-photon absorption one estimates electron densities that are consistent with the conductivity measurements [1].

14.2.3 Spatial and temporal solitons

The GVD parameter k''_ℓ of air is approximately 0.15 fs^2/cm at 800 nm [77,78]. For a 50 fs pulse that is often used to produce filaments, this dispersion corresponds to a characteristic distance [as defined by Eq. (1.139)] of $L_D \approx 160$ m. All dispersion effects of the atmosphere are thus negligible at that wavelength.

[1] Couairon and Bergé [75] however, using the Keldysh formula [76] for the evaluation of the three photon ionization of oxygen, infer from their calculations a beam diameter of 40 μm for the UV filament and 200 μm for the IR, leading to the same intensity in UV and IR filaments.

If we consider instead the dispersion of air at 248 nm, $k''_\ell \approx 1$ fs^2/cm and for a 50 fs pulse $L_D \approx 25$ m. Thus pulse broadening should occur over distances of the order of 10 m with UV fs pulses. Therefore, the existence of filaments over tens of meters requires that the pulse be trapped in space *and* in time.

A similar situation arises with filaments created at 800 nm with pulses of less than 10 fs duration: the dispersion length in air is now only $L_D \approx 6$ m. Using gases other than air (such as Ar) at higher pressure the characteristic length can be made of the order of tens of cm, and spatial-temporal soliton formation is possible. A recent application of filaments involves compressing intense fs pulses (i.e. < 20 fs, ≈ 1 mJ) down to a few fs (5.7 fs to 5.1 fs reported in Hauri *et al.* [79, 80]). This mechanism of (soliton) compression is based on phase modulation and dispersion, as was explained in Chapter 9. Numerical simulations relating to this compression mechanism have been published by Couairon *et al.* [81].

14.3 Sensors based on fs lasers

14.3.1 Description of the operation

This section is dedicated to some applications of femtosecond lasers as sensors. Rather than to use the beam radiated by the laser to perform measurements, this type of metrology uses the laser as a differential interferometer. Two or more pulses that are circulating in the laser resonator are made to interfere and a beat note is measured. A form of amplitude coupling is required to ensure that the pulses cross at the same two points during each round-trip, which also ensures that the two output pulse trains corresponding to each of these pulses have the same repetition rate. Any phase coupling (for instance backscattering from one pulse into the other) at a crossing point should be avoided, since it leads to frequency locking of the two pulses, which washes out the differential measurement. Two possible ways to achieve the desired two-pulse per cavity round-trip operation are:

1. Inserting of a saturable absorber *flowing dye jet* in the laser resonator
2. Use of an intracavity pumped OPO

The first method is relatively straightforward, but limited to laboratory applications [82, 83]. The pulses meet at the saturable absorber, because this is the configuration of minimum loss, since — as discussed in Section 6.3.2 — standing wave saturation is more effective than travelling wave saturation. In order to prevent locking of the two pulse frequencies to each other, liquid jet saturable absorbers are used, because the phase of the backscattered pulse is averaged out [82]. In the case of a ring laser (Fig. 14.12) the two pulses circulate in opposite directions

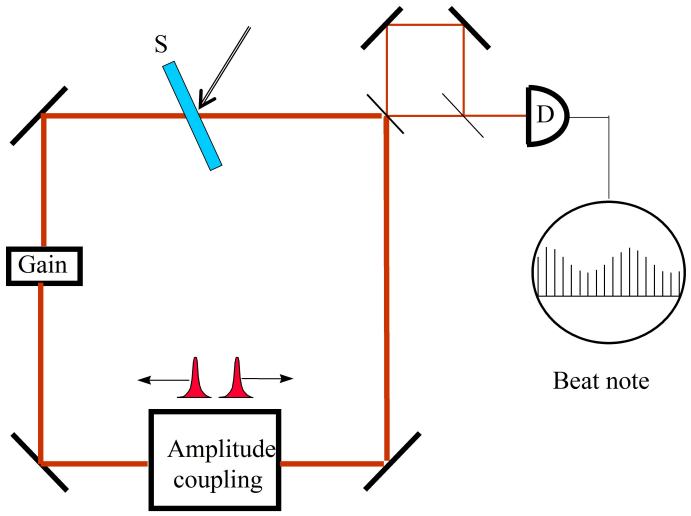

Figure 14.12: General configuration of sensors based on interfering the outputs of a laser with two intracavity pulses per round-trip, in a ring configuration. A saturable absorber dye jet sets the intracavity pulse crossing point. An extracavity detector is located at equal optical path from the pulse crossing point in the cavity. The gain medium is located at 1/4 cavity perimeter from the pulse crossing point to ensure equal gain recovery after each pulse passage. S is a possible sample of which certain properties are to be measured (sensed). For this an excitation can be applied synchronized to the pulse round trip if needed.

in the cavity. The pulse crossing point is "imaged" on a detector via a "detection interferometer" (the optical path for the two pulses from the crossing point to the detector is the same).

The second method consists essentially in having a fs "pump" laser, in the cavity of which an optical parametric oscillator (OPO) crystal is inserted (Fig. 14.13). That same crystal is also part of the "signal" cavity [84]. At each passage of the pump pulse through the OPO crystal, a signal pulse is generated. There are therefore two signal pulses per cavity round-trip time. The repetition rate is the same for both pulse trains, since it is uniquely determined by the length of the pump cavity ($\tau_{RT} = L_p/v_{gp}$ where L_p is the pump cavity length, and v_{gp} the group velocity averaged over one round-trip) in the pump cavity. In the case of the intracavity pumped OPO, it is the fixed repetition rate for the two pulses that results in a fixed crossing point.

Whether in a linear or a ring cavity, two circulating pulse trains (labelled by the index "1" and "2" below) of identical repetition frequency Δ are generated, which,

in the frequency domain, correspond to mode combs of frequency

$$\nu_{m,1} = f_{0,1} + m\Delta$$

and

$$\nu_{m,2} = f_{0,2} + m\Delta,$$

as discussed in detail in Chapter 6 [cf. Eq. (6.11)]. Mixing these frequencies in a quadratic detector (photodiode) produces a beatnote $\Delta\nu$ at the difference frequency of the two carrier to envelope offsets:

$$\Delta\nu = |f_{0,1} - f_{0,2}|. \tag{14.5}$$

Let us now assume that by some process (to be defined later) the dispersive properties of sample S (Fig. 14.12) are different for each circulating pulse, which changes the effective index of the cavity $n(\nu)$ defined in Eq. (6.1). As a result the mode combs become

$$\nu'_{m,j} = f'_{0,j} + m\Delta'$$

resulting in a new beat note of

$$\Delta\nu = |f'_{0,1} - f'_{0,2}|, \tag{14.6}$$

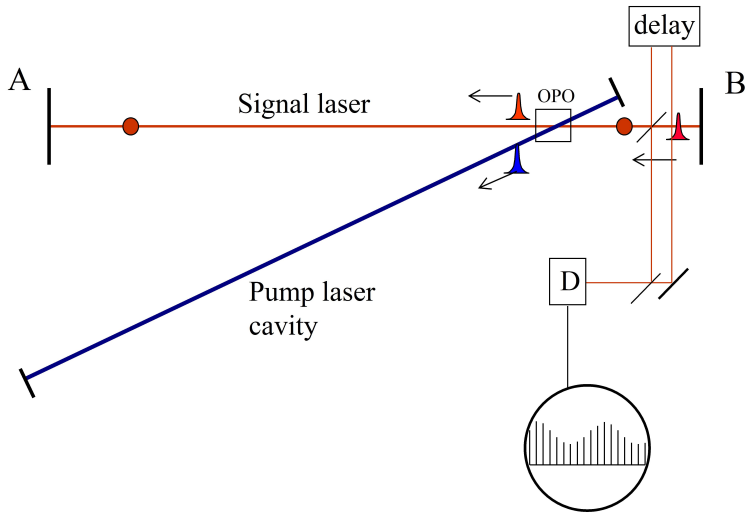

Figure 14.13: Linear cavity configuration of an intracavity pumped OPO. An OPO crystal is common to the pump and signal cavities. The two pulses generated in the signal cavity cross at the two points marked by a dot. As in Fig. 14.12, the two outputs are made to interfere after an appropriate delay line at the detector D.

because the repetition rate Δ' is locked to the same value for either train of pulses. Experiments have shown that the difference $|f'_{0,1} - f'_{0,2}|$ is proportional to the phase difference $\Delta\varphi$ between the two pulses experienced at each round-trip:

$$\Delta\nu \propto \frac{\Delta\varphi}{2\pi\tau_{RT}}. \tag{14.7}$$

In many cases the constant of proportionality is close to one, some examples will be discussed below. Thus, the sensor described in this section is basically a phase detector ($\Delta\varphi$). In contrast to standard techniques that convert a phase difference into an amplitude difference in an interferometer, this method converts the phase difference into a beat frequency. As we have seen in Fig. 6.6, even with an unstabilized laser it is possible to record a change in $\Delta\nu$ of 1 Hz, which, according to Eq. (14.7) corresponds to a phase sensitivity of 10^{-7} in a cavity of $\tau_{RT} = 16$ ns. If — as is often the case — the phase difference is due to a differential change in cavity length or perimeter ΔP: $\Delta\varphi = k_\ell \Delta P$, then Eq. (14.7) can be written:

$$\frac{\Delta\nu}{\nu} = \frac{\Delta P}{P}. \tag{14.8}$$

With $\nu \approx 3 \cdot 10^{14}$ Hz, $\Delta\nu \approx 1$ Hz and a cavity perimeter P (corresponding to 2 L for a linear cavity), of the order of 1 m, this sensor should be sensitive to changes of cavity length of the order of 10^{-15} m.

The different types of sensors distinguish themselves by the particular process of converting a physical quantity into a phase shift. Some examples will be given next, pertaining to two categories of detectors:

1. Detector of non-reciprocal effects. The "sample" can be the laser itself (rotation sensing), a flowing fluid (motion measurement by Fresnel drag), a material with a high Verdet constant (magnetic field measurement), or a resonant atomic vapor (intracavity phase spectroscopy). This type of response exists also with cw lasers, but, with mode-locked ring lasers, the sensitivity is not limited by a dead band.

2. Detector of changes of the optical cavity length externally synchronized by processes such as the electro-optic effect, or the displacement of reflecting surfaces by phonons, or the change of cavity length due to nonlinear indices.

The latter type of measurement is unique to mode-locked lasers, because it exploits the property that the two intracavity pulses occupy different positions in the cavity at different times, and can thus be distinguished. This is not the case if the cavity is filled uniformly by a cw beam, as is the case in a He-Ne ring laser for instance.

14.3.2 Inertial measurements (rotation and acceleration)

Rotation

The mechanical gyroscope (gyro) is an instrument based on the conservation of angular momentum of a spinning wheel. The fixed orientation of the angular momentum provides information on the motion of a moving frame of reference. An optical gyro based on a fs laser is essentially the instrument sketched in Fig. 14.12, without any intracavity addition.

There are three possible descriptions of the operational principle of this instrument. that were initially introduced for cw lasers. It turns out that, with some caution, one can also apply the same arguments to explain the behavior of modelocked laser gyros. The key is that an intracavity element always ensures that the pulse round trip time τ_{RT} remains the same for both pulse trains. Let us assume a ring laser of diameter R and rotating with angular velocity Ω. The first model is considers the interference pattern created by the two "counter-rotating" beams. The two beams having the same frequency, this standing wave pattern (of period $\lambda_\ell/2$) is fixed in an absolute (i.e. non accelerating) frame of reference. A detector in the rotating laboratory frame will produce a sinusoidal signal from these interference fringes passing by at a rate $2R\Omega/\lambda$.

A second approach to consider is that, for the observer in the laboratory frame rotating at the angular velocity Ω, the two circulating beams will be Doppler shifted up and down by $\nu_\ell R\Omega/c$, resulting in a total shift (or beat note) of $\Delta\nu = 4A\Omega/(P\lambda_\ell)$ (A and P being the area and perimeter of the ring, respectively). The factor $\mathcal{R} = 4A/(\lambda P)$ is called the "scale factor" of a ring laser, and is valid for cavities of arbitrary shape [85, 86].

A third point of view, now with the laboratory frame at rest and the laser rotating, is that the two counter-rotating beams are resonating in a cavity that is lengthened in the sense of rotation (cavity perimeter P_2), shortened in the other direction (cavity perimeter P_1). Hence, the corresponding mode combs (cf. Eq. (14.6) will be shifted in frequency by the amount $\Delta\nu = |f'_{0,1} - f_{0,2}| = \nu_\ell(P_2 - P_1)/c = 4A\Omega/(P\lambda_\ell)$.

Compact single-mode He–Ne ring lasers are extensively used as navigation gyroscopes in commercial aircrafts. Continuous-wave laser gyros are plagued by a phenomenon called lock-in: the response of continuous-wave laser gyros is zero for a range of small rotation rates. This dead band is due to the scattering of one circulating beam of the ring laser into the other direction. This weak coupling may "injection lock" the counterpropagating modes, i.e., force each of them to operate at the same frequency as radiation injected from the other mode.[2]

[2]Hence the label "mode-locking" which is sometimes given to this effect, since the scattering of

The "lock-in" problem can be avoided with ultrashort pulse lasers, where the two counterpropagating pulses meet in only two places. If the phase coupling at these meeting points is avoided, (as is the case in the examples presented so far), the dead band is eliminated. There is no phase coupling in the case of an intracavity pumped OPO such as sketched in Fig. 14.13. Such is also the case for a phase conjugated interaction through degenerate four-wave mixing, such as occurs in a saturable absorber dye jet [87] as in Fig. 14.12. This lock-in problem will be dealt with in more detail in Section 14.3.3 to follow.

Acceleration

We have seen in the previous section that the ring configuration of Fig. 14.12 leads naturally to a form of inertial sensing of rotation. Similarly, the linear configuration of Fig. 14.13 has an inertial response as accelerometer. Let us consider indeed that the whole laser is accelerating along the direction BA (the laser cavity is rigid and the distance from A to B is L). Let us consider a pair of pulses issued at the crossing point at a distance ℓ from mirror B. One of the two intracavity pulses travelling to the right hits mirror B, receives a Doppler shift $\nu_\ell v/c$, before proceeding to the left and sending an output to the delay line. Meanwhile, the other pulse travels to the right, receives a Doppler shift $\nu_\ell[v + a(L-2\ell)/c]/c$, before proceeding to the right and sending an output to the detector, to interfere with the other output. The measured beat note is thus $\Delta\nu = a(L-2\ell)\nu_\ell/c^2$. If the detection delay arm is increased by the amount $N\tau_{RT}$, where N is a large integer, the beat note is

$$\Delta\nu = a[N\tau_{RT} + (L-2\ell)/c]\nu_\ell/c. \tag{14.9}$$

14.3.3 Measurement of changes in index

In this subsection we will describe how a change in refractive index synchronized to the cavity repetition rate can be sensed. A straightforward measurement is that of the nonlinear index of a sample inserted in the cavity of Fig. 14.13. The sample can be the lithium niobate crystal of the OPO itself [88]. If the two pulses circulating in the OPO cavity have an intensity I_1 and I_2, a beat note appears because of the different phase shift introduced by the nonlinear index of $LiNbO_3$. The beat note frequency

$$\Delta\nu \propto \frac{2\pi}{\lambda_\ell}\bar{n}_2\langle I_2 - I_1\rangle \tag{14.10}$$

is proportional to the nonlinear index of the crystal. $\langle\rangle$ denotes averaging over the pulse and beam profile.

one circulating mode locks the frequency of the other. This is not to be confused with the mode-locking creating ultrashort pulse trains.

In Fig. 14.12, an arrow at the sample S indicates a possibility to change some property of a cavity element by an external signal that has the same periodicity as the pulse rate. An example is a voltage applied to a Pockels cell. The synchronization can be ensured by using the voltage from a photodetector monitoring the pulse train. To demonstrate the concept, a Pockels cell oriented as a phase

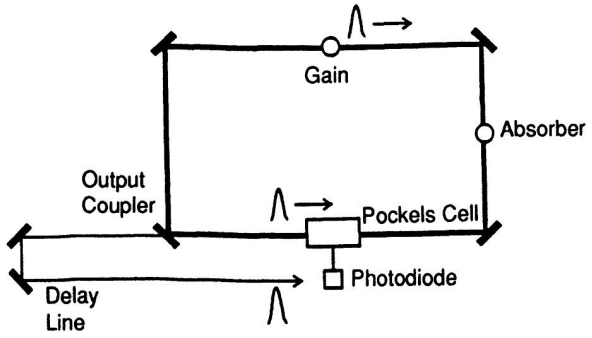

Figure 14.14: The output of the clockwise pulse of the ring cavity reaches the avalanche photodiode shortly before the time of arrival of the counterclockwise pulse in the Pockels cell. The electrical pulse from the photodiode is applied to the Pockels cell, resulting in a change in index, and therefore also in cavity length for the counterclockwise pulse.

modulator is inserted in the cavity as shown in Fig. 14.14. An avalanche photodiode detects the pulse train from the laser and applies an electrical pulse to the Pockels cell. Appropriate optical delay ensures temporal coincidence of the electrical pulses and *one* of the cavity pulses at the electro-optic crystal. Because the other cavity pulse always reaches the Pockel's cell between electrical pulses, the two counterpropagating pulses experience different indices in the cell. The optical length of the cavity is therefore different for the two senses of circulation of the intracavity pulses. Therefore, interfering the two outputs on a detector will result in a beat frequency between the two outputs that is equal to the difference in the CEO frequencies. The voltage $V_0 \cos(2\pi t/\tau_{rt})$ applied across the thickness e of the electro-optic crystal results in a change of index $\Delta n = (d_{\text{eff}} V_0/e)\cos 2\pi t/\tau_{rt}$ over a crystal length ℓ. The resulting beat note is:

$$\Delta\nu = K\frac{\Delta n\ell}{\lambda_\ell \tau_{RT}} = K\frac{V_0 d_{\text{eff}}\ell}{e\lambda_\ell \tau_{RT}}, \tag{14.11}$$

where K is a constant of proportionality shown to be close to one in this experiment, and d_{eff} is the electro-optic constant.

Figure 14.15(a) shows a plot of the beat frequency versus the amplitude of the electric pulse applied to the modulator. By varying the optical delay, one can

record the temporal response of the detector/electro-optic crystal combination as shown in Fig. 14.15(b). The temporal resolution is that of the detector-crystal combination. The particular measurement reproduced here [82] was performed with an avalanche photodiode, and 1 m cable delay to the crystal. Figure 14.15(b) shows a resolution of about 300 ps. The intrinsic resolution of the method, however, is in the fs regime, limited only by the pulse duration. This arrangement is a fast and sensitive tool for studying the intrinsic response of photodetectors (by measuring directly the change of index due to the generated carriers) or photodetector/modulator combinations. The best sensitivity in these measurements can be

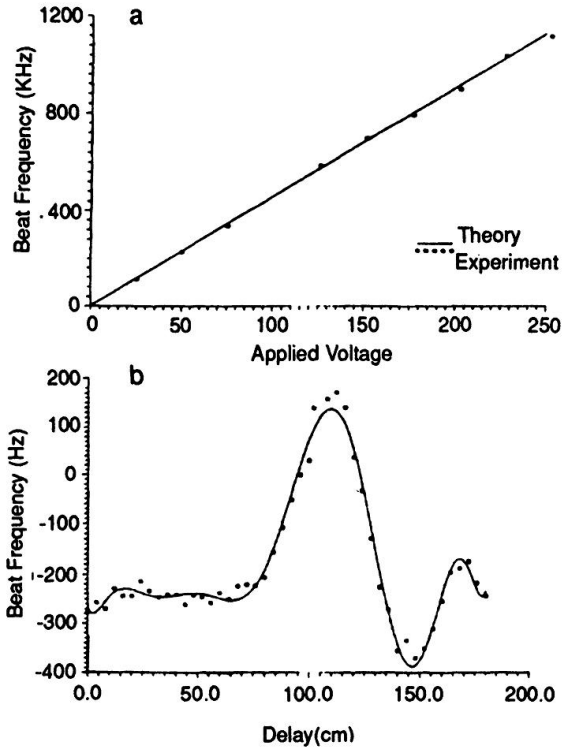

Figure 14.15: Beat note versus amplitude of the signal from the avalanche photodiode (a), all other parameters being kept constant. (b) Change in beat note versus the optical delay of the pulse impinging on the photodiode.

achieved when all other contributions to the beat note (such as rotation [89] or air currents [90]) can be eliminated. The linear laser is therefore to be preferred for this class of measurements. There is no "bias beat note" in the linear laser, because the intracavity circulating pulses travel through the same optical elements in the same order.

Dead band, and measurement of low level scattering

If there is an optical element at one of the crossing points of the two intracavity pulses, the fields may couple into each other. This "injection lock-in" modifies the otherwise linear relationship between beat note and mode spacing between the two pulse trains generated by the laser, leading to what is known as the "dead band" in cw laser gyros. This problem is similar to frequency pulling and locking though injection seeding. Theoretical treatments for the cw case can be found in ref. [91], for example. With small modifications they can also be applied to modelocked lasers as described below.

The phenomenon of coupling in the case of the mode-locked laser with two intracavity pulses can be modelled best by considering the time evolution of the spectral modes of the pulse trains. We note that this problem involves only one time scale t: the time scale of the evolution of the phase and amplitude of the pulses from the two trains over a large number of round-trips. Obviously this time scale is much larger than the pulse duration. It is because of this that the main characteristics of the cw models apply.

We consider each of the pulses of index $i = 1, 2$ to be represented by their spectral field envelope $\tilde{\mathcal{E}}_i(\Omega, t)\exp[i\phi_i(\Omega, t)]$. If $\tilde{r}$ is the complex scattering coefficient for one field into the counterpropagating field, at each round-trip, a fraction $\tilde{r}\tilde{\mathcal{E}}_1$ of the field $\tilde{\mathcal{E}}_1$ of pulse 1 is injected into the field $\tilde{\mathcal{E}}_2$, and vice versa. We make the approximation that the pulses are unchirped, and preserve their shape. The pulse belonging to train i can be written as:

$$\tilde{\mathcal{E}}_i(\Omega, t)e^{i[\phi_i(\Omega,t)]} \approx \tilde{\mathcal{E}}(\Omega)\left[\mathcal{E}_{0,i}(t)e^{[i\phi_i(t)]}\right]. \tag{14.12}$$

The equations of (slow) motion for each frequency mode of each pulse are:

$$\begin{aligned}
\frac{d\mathcal{E}_{0,1}(t)e^{i[\phi_1(t)]}}{dt/\tau_{RT}} &= \frac{\alpha_1}{2}\mathcal{E}_{0,1}(t)e^{i[\phi_1(t)-]} + re^{i\theta}\mathcal{E}_{0,2}(t)e^{i[\phi_2(t)]} \\
\frac{d\mathcal{E}_{0,2}(t)e^{i[\phi_2(t)]}}{dt/\tau_{RT}} &= \frac{\alpha_2}{2}\mathcal{E}_{0,2}(t)e^{i[\phi_2(t)2]} + re^{i\theta}\mathcal{E}_{0,1}(t)e^{i[\phi_1(t)]}
\end{aligned} \tag{14.13}$$

where $\tilde{r} = r\exp(i\theta)$ is the (complex) backscattering coefficient coupling the two pulses at their meeting point. The net gain coefficient α_i at each round-trip is defined as the difference of the saturated gain and the loss/round-trip. Separating

real and imaginary parts, leads to the system of equations:

$$\frac{d(\mathcal{E}_{0,1}/\mathcal{E}_{0,2})}{dt/\tau_{RT}} = r\cos(\theta-\psi) - r\frac{\mathcal{E}_{0,1}^2}{\mathcal{E}_{0,2}^2}\cos(\theta+\psi) \tag{14.14}$$

$$\frac{d\psi}{dt} = \Delta\omega + \frac{r}{\tau_{RT}}\left[\frac{\mathcal{E}_{0,2}}{\mathcal{E}_{0,1}}\sin(\theta-\psi) - \frac{\mathcal{E}_{0,1}}{\mathcal{E}_{0,2}}\sin(\theta+\psi)\right], \tag{14.15}$$

where $\psi = \phi_1 - \phi_2$, and we made the approximation that $\alpha_1 \approx \alpha_2$, consistent with a laser with a high Q cavity. The term $\Delta\omega$ on the right side of Eq. (14.15) is the externally imposed relative shift between the two mode combs. The instantaneous angular beat note frequency is thus $\dot{\psi} = 2\pi\Delta\nu_b$ as defined by Eq. (14.15). Instead of a linear relation between the differential CEO and the beat note of Eq (14.6), the coupling through the scattering results in a smaller beat note signal characteristic for frequency pulling:

$$\Delta\nu_b = \frac{\Delta\omega}{2\pi} + \frac{r}{2\pi\tau_{RT}}\left\{\sqrt{\frac{I_{0,2}}{I_{0,1}}}\sin(\theta-\psi) - \sqrt{\frac{I_{0,1}}{I_{0,2}}}\sin(\theta+\psi)\right\}, \tag{14.16}$$

where we have substituted the intensities for the fields. Note that these intensities have the meaning of average pulse intensities changing on a time scale of several round trips. If the scattering occurs through randomly moving scatterers (such as in a dye jet), expression (14.16) has to be averaged over r and θ. For a given r, the largest coupling occurs for $\theta = 0$. For this case and "steady-state" where the time derivatives in Eqs. (14.14) and (14.15) are zero, we find a particular solution:

$$\psi = 0 \quad \text{and} \quad \frac{I_{0,1}}{I_{0,2}} = 1 \quad \text{for} \quad \frac{|\Delta\omega|}{2\pi} \leq \frac{r}{\tau_{RT}}. \tag{14.17}$$

This steady-state with its zero beatnote frequency relates the width $\Delta\omega$ of the dead band to the magnitude of the backscattering coefficient.

Measurements such as those shown in Fig. 14.16 yield the largest value of $\Delta\omega = \Delta\omega_{max}$ for which the beat note response $\Delta\nu_b = 0$. This value corresponds to the equal sign in the last expression of Eq. (14.17), and thus leads directly to the measurement of the scattering coefficient r [92]. As shown in the example of Fig. 6.6 the beat note resolution corresponds to 1 Hz in a laser with a round-trip time of 10 ns. Therefore one can resolve an intensity backscattering coefficient of $r^2 \approx 10^{-16}$. Figure 14.16 shows the change in linear response of the beat note, when a dielectric mirror is inserted at a pulse crossing point. The observed dead band corresponds to an intensity backscattering coefficient of that mirror of about $2 \cdot 10^{-11}$, obtained when the mirror was used at an angle of incidence of 20°.

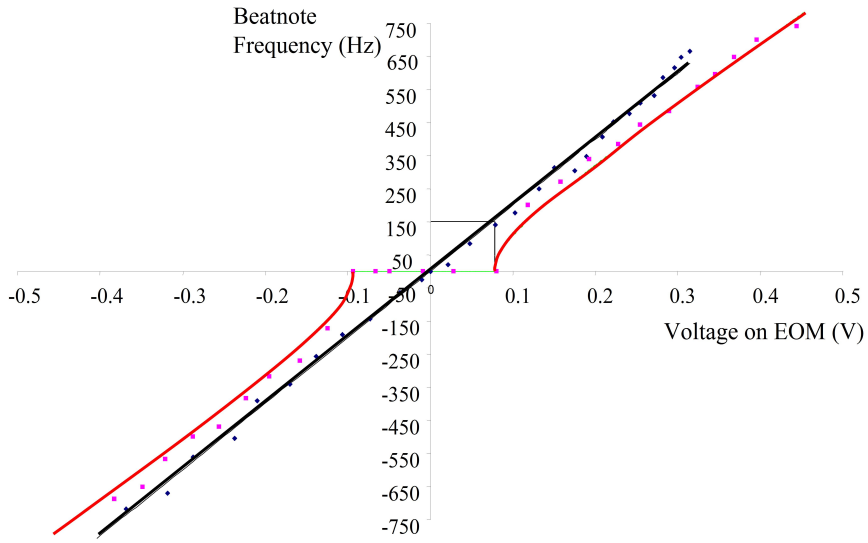

Figure 14.16: Beat note versus amplitude of the signal applied to the Pockel's cell (artificial rotation). The straight line is the empty cavity response. With a mirror inserted at 20° at the pulse crossing point, the beat note characteristics shows a dead band due to a small amount of backscattering from the mirror.

Reduction of the beat note bandwidth through stabilization

The 1-Hz linewidth of the beat note noticed in the previous example is due mainly to vibrations of the mirrors. Let us consider a particular mirror of the cavity, vibrating with an amplitude $a \approx 0.1$ μm, at a mechanical resonance frequency corresponding to a period $T_b \approx 10$ ms. The vibration of the mirrors contribute to the bandwidth $\Delta\nu_{\text{laser}}$ of the individual modes of the two frequency combs emitted by the laser. The maximum possible change in phase per round-trip due to vibration is $8\pi a/\lambda$; for a mean value averaged over many round trips and vibration periods let us use a/λ. The broadening of a laser mode can now be estimated:

$$\Delta\nu_{\text{laser}} = \frac{a}{\lambda\tau_{RT}} = \frac{\nu_\ell\, a}{P}. \tag{14.18}$$

Obviously, this bandwidth depends on the pulse repetition rate or the perimeter ($P = 2L$ for a linear cavity) of the cavity.

During the short time of a pulse roundtrip, the two pulses hit the vibrating mirror at a different location. Hence a slightly different cavity perimeter ΔP_b seen by the two pulses. If δt is the difference in time of arrival at the mirror, a maximum cavity length difference of $\Delta P_b \approx a \times 2\pi\delta t/T_b$ results. For instance, to $\delta t = 1$ ns

there corresponds a mirror displacement between the two pulses of $2\pi \cdot 10^{-14}$m. The cumulative effect of interfering the two pulse trains on the detector results in a beat note bandwidth $\Delta\nu_b$:

$$\Delta\nu_b \approx \frac{\Delta P_b \nu_\ell}{P} = \frac{a\tau_{RT}}{T_b}\frac{\nu_\ell}{P} = \left(\frac{\tau_{RT}}{T_b}\right)\Delta\nu_{\text{laser}} \tag{14.19}$$

where we have made use of Eq. (14.18). The beat note bandwidth is thus typically three orders of magnitude smaller than that of an isolated mode of the laser. Because the beat note is *proportional* to the laser bandwidth, a stabilization that reduces the laser mode bandwidth by three orders of magnitude will also reduce that of the beat note by the same amount, hence a sensitivity to rotation of the order of 10^{-4} degrees/hour can be expected. The stabilization should be applied to both pulses circulating in the cavity simultaneously. This requirement puts some constraints on the geometry of the cavity and the location of the control elements. For example, in the OPO configuration of Fig. 14.13, the beat note bandwidth of the signal can be reduced by mode stabilization, provided the correction to the cavity length is applied symmetrically with respect to the pulse crossing point (in such a configuration, both pulses travelling in opposite direction receive the same modification at various points of the cavity).

14.4 Stabilized mode-locked lasers for metrology

In Chapter 6 we explained the ability of a stabilized fs laser to act as an extremely sensitive frequency ruler and most accurate clock at the same time. Recall that the frequency comb describing the laser output in the spectral domain

$$\nu_m = f_0 + m\Delta \tag{14.20}$$

relates optical frequencies ν_m to radio frequencies $\Delta = 1/\tau_{RT}$. As is obvious from this relation, two parameters are required to define the femtosecond frequency comb corresponding to a mode-locked pulse train. Likewise, to stabilize the comb, two parameters must be controlled (and stabilized) independently. These two parameters can for instance be the pulse repetition rate, and the exact frequency of a particular optical mode. A second option is to make an exact measurement of the frequency of two modes, which requires two optical standards within the bandwidth of the pulse. A third option is to measure one optical mode, and the carrier to envelope offset (CEO). Only one calibrated measurement is required, if the carrier to envelope offset can be measured, controlled and set to a constant value. We will next present the technique to measure the CEO. As will be shown in the next two sections, this technique is limited to pulses shorter than 100 fs. For picosecond

pulses, the CEO can be extracted from a precise measurement of the repetition rate and one optical mode. At the end of this section we will then describe how a fs laser can be stabilized to external cavities.

14.4.1 Measurement of the carrier to envelope offset (CEO)

We will first describe the most commonly applied techniques to measure the CEO based on "f to 2f interferometry". We will then introduce a technique to produce the required octave-spanning spectrum using continuum generation in special fibers.

f to 2f interferometry

This is a "self-referencing" method, in which a mode from the high-frequency part of the spectrum (mode number m_h) is made to interfere with a frequency doubled mode from the low-frequency portion of the spectrum (mode number m_l) [93–95]. The lowest component of the beat note spectrum

$$\Delta\nu = |2(f_0 + m_l\Delta) - (f_0 + m_h\Delta)| = |f_0 + (2m_l - m_h)\Delta| \tag{14.21}$$

is the CEO f_0.

An experimental setup of this self-referencing technique is shown in Fig. 14.17. A two-prism spectrometer is used to separate the red and blue parts of the spectrum. An aperture A selects the desired blue portion of the spectrum, which is retro-reflected through the two prisms before being sent by a beam splitter to the f/2f interferometer. In one arm of the interferometer, a nonlinear crystal is inserted to frequency double the infrared pulse (shown as dotted line in Fig. 14.17). With a frequency doubling crystal type I, (BBO crystal phase matched for the infrared end of the pulse spectrum) the second harmonic is polarized orthogonally to the fundamental, and can thus be combined with a polarizing beam splitter with the blue portion of the fundamental pulse. A polarizer oriented to project equal components of the two orthogonally polarized signals along its axis, ensures maximum contrast of the beat signal on the photodetector APD.

There is no need for a wavelength selective aperture in the infrared portion of the spectrum, since the phase matching condition of the SHG crystal will provide the required spectral selection. Ideally, the two prisms should be configured for zero GVD, according to the calculations of Section 2.5.5, in order to prevent pulse broadening and phase modulation due to dispersion. The amount of intracavity glass and the prism separation can be selected for zero group velocity dispersion according to Eq. (C.18).

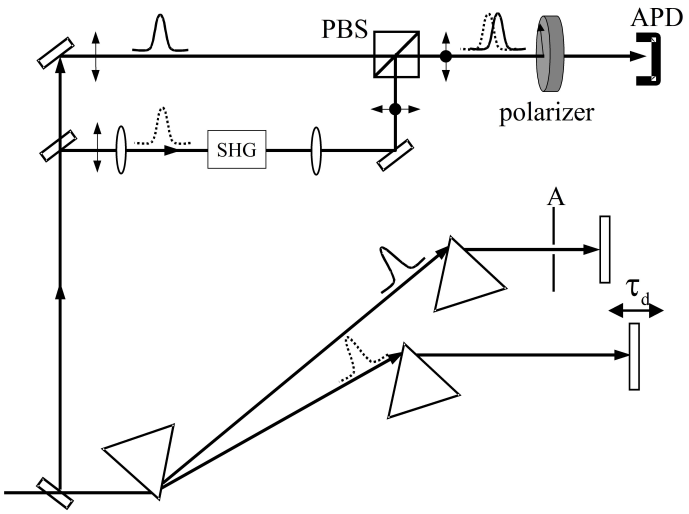

Figure 14.17: Measurement of the carrier to envelope offset (CEO) frequency of a fs comb by "f to $2f$" interferometry. The relevant high and low frequency parts of the spectrum are selected by a spectrometer with zero GVD. A high frequency part of the spectrum is selected by an aperture A. The pulses from the blue and IR part of the spectrum are sent to a Mach Zehnder interferometer. The beams are reflected after the prism pairs at a lower level, so that they can be picked up by a mirror diverting them towards the Mach Zehnder interferometer. A frequency doubling crystal (phase matched for SHG type I) is inserted in one arm of a Mach Zehnder interferometer. The orthogonally polarized blue part of the pulse spectrum and the second harmonic of the infrared are combined with a polarizing beam splitter (PBS). An adjustable delay τ_d ensures that these two orthogonally polarized pulses meet on the beam splitter. A polarizer selects an equal component of both pulses to record their beat note with an avalanche photodetector (APD).

Creating pulse spectra spanning an octave

There are two main approaches to produce pulses whose spectra span a full octave - (i) build lasers that emit extremely short (5 fs in the NIR) pulses, and (ii) broaden the spectrum of longer pulses outside the laser oscillator without destroying the mode structure and coherence. Since the first approach was described in Section 7.7.2 we will concentrate now on the spectral broadening.

Techniques based on optical fibers to generate a broad spectral continuum, while preserving the coherence of the comb, have been developed, cf. Section 4.6. Microstructured fibers [96], tapered fibers [97], and highly-nonlinear dispersion shifted (HNLF) fibers [98–100] have been used to demonstrate octave-spanning continua. Figure 14.18 compares the dispersion of microstructered fibers and HNLF's. In all these fibers the key issue is low dispersion at the wavelength of

the input pulse allowing for long interaction lengths. This together with the small confined beam diameter (guided mode) can produce large nonlinear effects, like continuum generation, with the relatively low pulse energies available from laser oscillators. Some characteristic parameters of fibers for continuum generation with

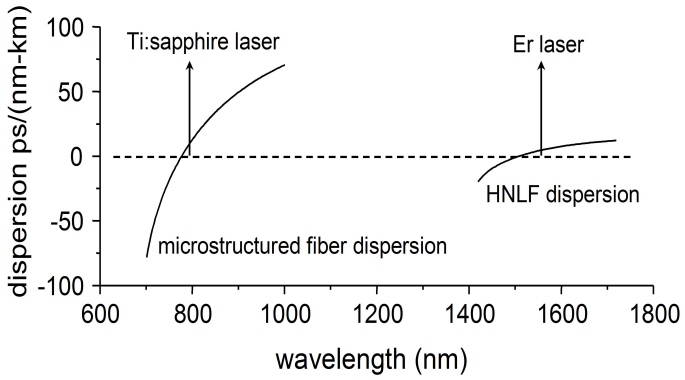

Figure 14.18: Dispersion of a typical small-core microstructured fiber in relation to the Ti:sapphire wavelength, compared to HNLF dispersion and an Er fiber laser (from ref. [100]).

low power lasers are listed in Table 14.1. The HNLF are ideally suited for the con-

Type	Wavelength nm	GVD ps/(nm km)	nonlinearity
Standard SMF	800	-110	$\bar{n}_2 = 310^{-16}$ cm^2/W
Microstructure	770	0	
	780	10	$\gamma = 0.07$ W^{-1}m^{-1}
	900	70	
Tapered	850	122	$L_{NL} = 0.6$ mm
HNLF	1550	2.2	$\gamma = 9$ W^{-1}m^{-1}

Table 14.1: Some characteristic parameters of fibers used for continuum generation compared to standard single-mode silica fibers (SMF's). The last column lists the Kerr nonlinearity in terms of parameters introduced in Chapter 3. The parameter γ is related to the nonlinear phase shift Φ_{NL} that is induced by a laser power P over a propagation distance L by $\gamma = \Phi_{NL}/(PL) = \omega\bar{n}_2/(cA_{\text{eff}})$, where A_{eff} is the effective fiber cross section, cf. Chapter 9.

tinuum generation with Er based fiber lasers operating at pulse durations in the range of 50 fs to 200 fs.

The nonlinear Schrödinger equation, Eq. (4.111), has been used successfully to simulate the pulse propagation and broadening in microstructure fibers [101, 102].

It is observed that the broadest continuum is generated when the laser pulse is in the anomalous-dispersion regime of the fiber, cf. Fig 14.18.

The method of f to $2f$ interferometry requires that some phase correlation between the pulse and the train is maintained in the continuum generation. One method to study the coherence properties of the continuum is to interfere independently generated continua. Two possible setups to perform such experiments are sketched in Fig. 14.19. A continuum is generated in each branch of a Michelson interferometer [Fig. 14.19 (a)]. The length of one arm can be varied to introduce a delay τ_d between the spectrally broadened pulses entering the spectrometer. This delay is observed as fringes across the combined spectrum of the pulses (spectral interferometry). The visibility of fringes recorded as the spectrum is being scanned is measured. The modulation depth of these fringes is a measure of the coherence. Bellini and Hänsch [103] performed a coherence experiment with continua generated in microstructure fibers by a Ti:sapphire laser using Young's double slit instead of the spectrometer. There, the visibility of the spatial fringe pattern was analyzed.

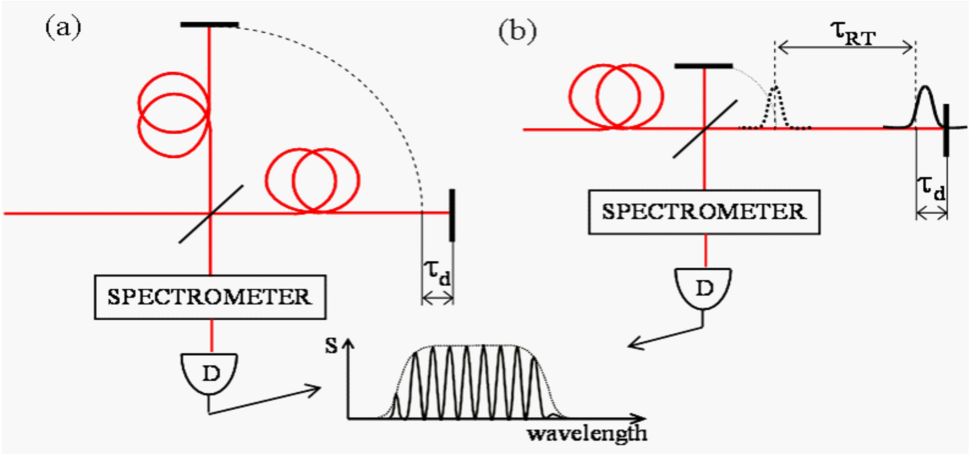

Figure 14.19: Spectral interferometry applied to the study of the coherence of the continuum. (a) The continuum is generated in each arm of the interferometer. (b) The continuum is generated outside the interferometer, but the relative delay of the two arms is close to the delay between successive pulses of the train. Therefore, it is the coherence between the continuum generated by two successive pulses that is being analyzed.

The configuration shown in Fig. 14.19(b) with an integrated fiber interferometer was used to study the coherence of continua produced by fiber lasers operating at 1550 nm [104]. The result of the measurements of refs. [103,104] is that the continuum can be highly coherent (fringe visibility ≈ 1) when generated by ultrashort

pulses (< 150 fs). The fringe structure disappeared in a broad continuum generated by 1 ps pulses.

Experimental investigation of pulses of 190 fs duration in microstructure fibers [105] shows that the pulse initially begins to self-Raman shift to longer wavelengths. The interplay of anomalous dispersion and Kerr nonlinearity enables the formation and propagation of solitons propagating at different velocities. As these higher-order solitons break up, parametric four-wave mixing generates frequencies at wavelengths shorter than the zero-dispersion wavelength, eventually leading to an intense blue radiation coexisting with a broad infrared supercontinuum [105]. One conclusion was that special fibers can only be used to extend the frequency comb of sub-150 fs pulse trains.

14.4.2 Locking of fs lasers to stable reference cavities

Earlier stabilization experiments with mode-locked lasers often used short Fabry-Perot etalons to stabilize the *average position* of the comb, directly employing the techniques developed for single mode lasers [106, 107]. More recent experiments have used external Fabry-Perot cavities as "mode filters", transmitting every 20^{th} comb component, such that any individual mode of the comb can be unambiguously identified with a wavemeter [93, 108]. Ultimate stability is reached by stabilizing one mode to an atomic resonance while at the same time keeping the CEO f_0 constant. The use of the frequency comb as a "ruler" has been introduced by the group of Hänsch as a powerful means to compare frequency standards [93, 109, 110]. It was first applied to a measurement of the cesium D_1 line using a mode-locked laser [108].

Another example of the application of a frequency ruler involves linking the ytterbium to the iodine standard. The beat frequency between one mode of the comb and a frequency standard such as an Yb^+ stabilized laser at 871 nm provides a calibration of the entire comb. Another mode of the same comb is made to beat with an I_2 stabilized laser at 1064 nm. This measurement thus provides the ratio of the two frequency standards [111]. The noise in this direct ratio measurement is the same as that of a direct comparison between two independent I_2 standards, indicating that this ratio measurement was limited only by the noise of the I_2 stabilized laser. It is estimated that the excess fractional frequency noise introduced by the comb can be as low as 10^{-19} [112].

A building block of this time and frequency standard is a fs laser stabilized to an external Fabry-Perot cavity. A close-up of such an experiment is shown in Fig. 14.20 [113]. The reference cavity is a long (62.5 cm) Fabry-Perot resonator made of a solid block of ultra-low expansion quartz, with high reflectivity mirrors of the same substrate material optically contacted on both ends. The cavity was

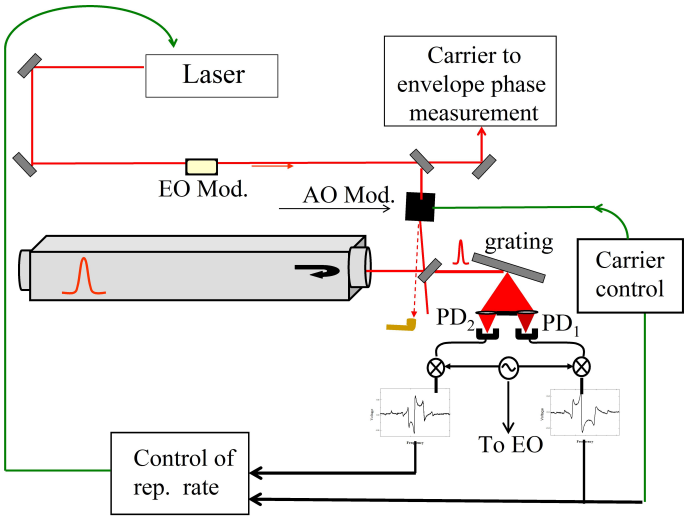

Figure 14.20: Stabilization of a mode-locked laser to a reference cavity. A phase modulator (EO) produces sidebands of opposite sign for each mode of the laser. The beam is mode-matched to the reference cavity. The beam reflected off the reference cavity is dispersed by a grating. The spectral component picked up by detector PD_1 is mixed with the modulation signal (which was applied to the phase modulator) to produce an error signal which is amplified and added as a correction frequency to the laser via an acousto-optic modulator. The difference between the signals from PD_2 and PD_1 provides an error signal for the repetition rate. The group velocity correction is either a tilt of an end mirror (following a prism sequence in the laser cavity) or an intensity adjustment of the pump laser of the fs laser.

placed in a vacuum chamber to isolate it from thermal and acoustic noise and, if needed, to control the ambient pressure. The vacuum chamber usually kept the pressure inside the reference cavity below 15 mTorr. The laser cavity length is twice the length of the reference cavity, so that every other fs laser mode can be transmitted[3]. The Kerr lens mode-locked laser produced pulses of ≈ 40 fs duration.

The standard technique to stabilize a single mode laser is the Pound-Drever-Hall method [114]. The basic principle is to create sidebands (of opposite phase) of the laser with a phase modulator (EO Mod. in Fig. 14.20). The phase modulated signal is detected after reflection by the reference cavity, and the detector output is mixed with the original modulation signal (not shown). At exact resonance (between laser and reference cavity mode), the reflected signal has still equal and op-

[3] A shorter cavity is not desirable: if N is the ratio of the laser to reference cavity lengths, the effective cavity finesse is reduced since the intensity of the pulse in the reference cavity is reduced by a factor $(1-R)^N$ between incident laser pulses due to reflections at the mirrors.

posite sidebands, and the result of the mixing is a null signal. The balance between the two sidebands is lost outside of resonance, resulting in a negative or positive mixing signal below or above resonance, which is the error signal to apply as correction to some controlling element within the laser. In the case of a single mode laser, this will generally be a piezo-element (PZT) controlling the cavity length.

As we have seen in Chapter 6, in the case of the mode-locked laser, both the repetition rate and the carrier frequency have to be stabilized. A single mode can be stabilized using the same Pound-Drever-Hall [114] technique as for the cw laser, by selecting a single mode with a grating [4]. The "single mode" error signal is obtained by mixing the signal from the detector PD_1 with the phase modulation (at f_{EO} = 10.7 MHz, for example). Ideally this error signal should be applied to an element that only corrects the mode frequency, without affecting the repetition rate. Such a correcting intracavity element does not exist. A PZT on an end-cavity mirror does offer good control of the mode position, but not without affecting the repetition rate somewhat. An acousto-optic modulator outside the laser cavity can be used as a fast frequency shifter, that does not affect the repetition rate.

Two techniques are commonly used to apply a correction to the laser repetition rate, with minimum perturbation on other parameters. The first one is to tilt (using PZT) the end mirror that follows the prism sequence [93]. This technique modifies the group velocity through the prism sequence, and affect the cavity length (mode-spacing) only to second order. A major disadvantage for some applications is that it also affects the overall spectrum of the pulse train. A second technique is to act on the pump beam intensity [115].

Once a mode of the laser comb has been "locked" to a mode of the reference cavity, the mode comb is still free to "breathe" about that central mode. Fluctuations in the laser repetition rate result in the largest mode frequency excursion between the extreme ends of the spectrum. A convenient error signal is provided by mixing the *difference* between the signals of PD_1 and PD_2 with the original modulation at frequency f_{EO}. The error signal obtained in this way is the composite signal from *all* longitudinal modes detected within the spectral region spanned by the detectors.

14.5 Problem

Consider a range gating setup like that in Fig. 14.1, with second-harmonic generation as gating mechanism. Both the reference pulse and the backscattered radiation are focused, with crossed polarization, into a second-harmonic crystal phase matched for second-harmonic generation type II at 620 nm. The crystal is urea, with

[4] In practice it will be a group of modes that will be selected by the grating.

a nonlinear coefficient of $d = 1.04\,10^{-23}$ C/V^2, and an index of refraction of 1.48. Given that both the reference beam and the signal beam are collimated with a diameter of 0.7 mm, and focused into the crystal with a 2.5 cm focal distance lens, find the peak power of the reference beam required to achieve single photon upconversion. What should the crystal length be? Given that crystal length, is there a limitation to the depth resolution of this 3D imaging system? Is there a limitation to the transverse resolution? Estimate these limits.

Bibliography

[1] A. P. Bruckner. Some applications of picosecond optical range gating. *SPIE*, 94, 1976.

[2] J. L. Martin, A. Antonetti, A. Astier, J. Etchepare, G. Grillon, and A. Migus. Subpicosecond spectroscopic techniques in biological materials. *SPIE*, 211:128–132, 1979.

[3] J. L. Martin, Y. Lecarpentier, A. Antonetti, and G. Grillon. Picosecond laser stereometry light scattering measurements on biological material. *Medical & Biological Engineering & Computing*, 18:250–252, 1980.

[4] J.-C. Diels and J. J. Fontaine. Imaging with short optical pulses. *Optics and Lasers in Engineering*, 4:145–162, 1983.

[5] J.-C. Diels, J. J. Fontaine, and W. Rudolph. Ultrafast diagnostics. *Revue Phys. Appl.*, 22:1605–1611, 1987.

[6] J. J. Fontaine, J.-C. Diels, Ching Yue Wang, and H. Sallaba. Subpicosecond time domain reflectometry. *Optics Lett.*, 6:495–498, 1981.

[7] J. G. Fujimoto, S. De Silvestri, E. P. Ippen, C. A. Puliafito, R. Margolis, and A. Oscroff. Femtosecond optical ranging in biological systems. *Opt. Lett.*, 11:150–152, 1986.

[8] R. C. Younquist, S. Carr, and D. E. Davies. Optical coherence-domain reflectometry: a new optical evaluation technique. *Optics Lett.*, 12:158–160, 1987.

[9] D. Huang, E. A. Swanson, C. P. Lin, J. S. Schuman, W. G. Stinson, W. Chang, H. R. Hee and T. Flotte, K. Gregory, C. A. Puliafito, and J. G. Fujimoto. Optical coherence tomography. *Science*, 254:1178–1181, 1991.

[10] E. A. Swanson, J. A. Izatt, M. R. Hee, D. Huang, C. P. Liu, J. S. Schuman, G. A. Puliafito, and J. G. Fujimoto. In vivo retinal imaging by optical coherence tomography. *Optics Lett.*, 18:1864–1866, 1993.

[11] B. E. Bouma and G. J. Tearney (Eds.). *Handbook of Optical Coherence Tomography*. Marcell Dekker, 2001.

[12] J. S. Schuman, C. Puliafito, and J. G. Fujimoto (Eds.). *Optical Coherence Tomography of Ocular Diseases*. Slack, 2004.

[13] Chi Yan and Jean-Claude. 3D imaging with ultrashort pulses. *Appl. Opt.*, 34:6869–6873, 1991.

[14] S. Ertefai and A. E. Profio. Spectral transmittance and contrast in breast diaphanography. *Med. Phys.*, 12:393–400, 1985.

[15] K. M. Yoo, Qirong Xing, and R. R. Alfano. Imaging objects hidden in highly scattering media using femtosecond second-harmonic-generation cross-correlation time gating. *Optics Letters*, 16:1019–1021, 1991.

[16] M. D. Duncan, R. Mahon, L. L. Tankersley, and J. Reintjes. Time-gated imaging through scattering media using stimulated Raman amplification. *Optics Lett.*, 16:1868–1870, 1991.

[17] M. Bashkansky, C. L. Adler, and J. Reintjes. Coherently amplified Raman polarization gate for imaging through scattering media. *Optics Lett.*, 19:350–352, 1994.

[18] J. Izatt, M. R. Hee, and G. M. Owen. Optical coherence microscopy in scattering media. *Optics Lett.*, 19:590–592, 1994.

[19] M. Kempe and W. Rudolph. Microscopy with ultrashort light pulses. *Nonlinear Optics*, 7:129–151, 1994.

[20] A. Ishimaru. *Wave propagation and scattering in Random media*. Academic Press, New York, 1978.

[21] J. A. Moon, R. Mahon, M. D. Duncan, and J. Reintjes. Resolution limits for imaging through turbid media with diffuse light. *Optics Lett.*, 18:1591–1593, 1993.

[22] J. C. Hebden and D. T. Delpy. Enhanced time resolved imaging with a diffusion model of photon transport. *Optics Lett.*, 19:311–313, 1994.

[23] *Proceedings of SPIE and OSA on optical biomedical imaging*, annual meetings.

[24] M. Kempe and W. Rudolph. Topical review: Trends in optical biomedical imaging. *J. Mod. Optics*, 44:1617–1642, 1997.

[25] N. Abramson. Light-in-flight recording: high speed holographic motion pictures of ultrafast phenomena. *Appl. Opt.*, 22:215–232, 1983.

[26] N. Abramson. Light-in-flight recording. 2: compensation for the limited speed of the light used for observation. *Appl. Opt.*, 23:1481–1492, 1984.

[27] H. J. Gerritsen. *Proc. Soc. Photo-Opt. Instrum. Eng.*, 519:250, 1984.

[28] H. Chen, Y. Chen, D. Dilworth, E. Leith, J. Lopez, and J. Valdmanis. Two-dimensional imaging through diffusing media using 150-fs gated electronic holography techniques. *Opt. Lett.*, 16:487–489, 1991.

[29] E. Leith, C. Chen, Y. Chen, D. Dilworth, J. Lopez, J. Rudd, P.C. Sun, J. Valdmanis, and G. Vossler. Imaging through scattering media with holography. *J. Opt. Soc. Am. A*, 9:1148–1153, 1992.

[30] T. Wilson and C. J. R. Sheppard. *Theory and practice of scanning optical microscopy*. Academic Press, London, 1984.

[31] W. Denk, J. M. Strickler, and W. W. Webb. Two-photon laser scanning fluorescence microscopy. *Science*, 248:73–76, 1990.

[32] J. Squier. Ultrafast optics: Opening new windows in biology. *Optics and Photonics News*, April:42–45, 2002.

[33] J. R. Lakowicz. Fluorescence lifetime sensing. *Laser Focus World*, 28-5:60–80, 1992.

[34] T. Sawatari. Optical heterodyne scanning microscope. *Applied Optics*, 12:2768–2772, 1973.

[35] M. Kempe and W. Rudolph. Scanning microscopy through thick layers based on linear correlation. *Optics Lett.*, 19:1919–1921, 1994.

[36] M. Magnor, P. Dorn, and W. Rudolph. Simulation of confocal microscopy though scattering media with and without time gating. *J. Opt. Soc. A*, 18:1695–1700, 2001.

[37] J. M. Schmitt, M. Yadloswky, and R. F. Bonner. Subsurface imaging of living skin with optical coherence microscopy. *Dermatology*, to be published, 1995.

[38] M. Kempe and W. Rudolph. Analysis of heterodyne and confocal microscopy for illumination with broad-bandwidth light. *J. Mod. Optics*, 43:2189–2204, 1997.

[39] V. E. Zakharov and A. B. Shabat. Exact theory of two-dimensional self-focusing and one-dimensional self-modulation of waves in nonlinear media. *Sov. Phys. JETP*, 34:62–69, 1972.

[40] Xin Miao Zhao, Jean-Claude Diels, A. Braun, X. Liu, D. Du, G. Korn, G. Mourou, and Juan Elizondo. Use of self-trapped filaments in air to trigger lightning. In P. F. Barbara, W. H. Knox, G. A. Mourou, and A. H. Zewail, editors, *Ultrafast Phenomena IX*, pages 233–235, Dana Point, CA, 1994. Springer Verlag, Berlin.

[41] A. Braun, C. Y. Chien, S. Coe, and G. Mourou. Long range, high resolution laser radar. *Opt. Comm.*, 105:63–66, 1993.

[42] A. Braun, G. Korn, X. Liu, D. Du, J. Squier, and G. Mourou. Self-channeling of high-peak-power femtosecond laser pulses in air. *Optics Lett.*, 20:73–75, 1995.

[43] L. F. Mollenauer. Soliton transmission speeds greatly multiplied by sliding-frequency guiding filters. *Optics and Photonics news*, pages 15–19, 1994.

[44] J. P. Gordon and H. A. Haus. Random walk of coherently amplified solitons in optical fiber. *Opt. Lett.*, 11:665–667, 1986.

[45] R. Y. Chiao, E. Garmire, and C. H. Townes. Self-trapping of optical beams. *Physics Review Letter*, 13:479–482, 1964.

[46] S. A. Akhmanov, A. P. Sukhorukov, and R. V. Khokhlov. Self focusing and self trapping of intense light beams in a nonlinear medium. *Sov. Phys JETP*, 23:1025–1033, 1966.

[47] M. Giglio and A. Vendramini. Soret-type motion of macromolecules in solution. *Phys. Rev. Lett.*, 38:26–29, 1977.

[48] E. Freysz, M. Afifi, A. Ducasse, B. Pouligny, and J. R. Lalanne. Critical microemulsions as optically nonlinear media. *Journal of the Optical Society of America B*, 1:433, 1984.

[49] Y. R. Shen and M. M. Loy. Theoretical interpretation of small-scale filaments of light originating from moving focal spots. *Physical Review A*, 3:2099–2105, 1971.

[50] G. K. L. Wong and R. Y. Shen. Transient self-focusing in a nematic liquid crystal in the isotropic phase. *Physical Review Letter*, 32:527–530, 1974.

[51] J. Schwarz, P. K. Rambo, J.-C. Diels, M. Kolesik, E. Wright, and J. V. Moloney. UV filamentation in air. *Optics Comm.*, 180:383–390, 2000.

[52] G. Mechain, A. Couairon, Y. B. Andre, C. D'Amico, M. Franco, B. Prade, S. Tzortzakis, A. Mysyrowicz, and R. Sauerbrey. Long-range self-channeling of infrared laser pulses in air: a new propagation regime without ionization. *Applied Physics B*, 79:379–382, 2004.

[53] L. Bergé, S. Skupin, C. Méjean, J. Kasparian, J. Yu, S. Frey, E. Salmon, and J. P. Wolf. Supercontinuum emission and enhanced self-guiding of infrared femtosecond filaments sustained by third harmonic generation in air. *Phys. Rev. E*, 71:016602–1–016602–13, 2005.

[54] N. Aközbek, M. Scalora, C.M. Bowden, and S.L. Chin. Third-harmonic generation and self-channeling in air using high-power femtosecond laser pulses. *Phys. Rev. Lett.*, 89:143901, 2002.

[55] H. Yang, J. Zhang, L. Z. Zhao, Y. J. Li, H. Teng, Y. T. Li, Z. Wang, Z. Chen, Z. Wei, J. Ma, W. Yu, and Z. M. Sheng. Third-order harmonic generation by self-guided femtosecond pulses in air. *Phys. Rev. E*, pages 015401 –1–015401–4(R), 2003.

[56] A. Proulx, A. Talebpour, S. Petit, and S. L. Chin. Fast pulsed electric field created from the self-generated filament of a femtosecond Ti:sapphire laser pulse in air. *Optics Comm.*, 174:305–309, 2000.

[57] C.-C. Cheng, E.M. Wright, and J.V. Moloney. Generation of electromagnetic pulses from plasma channels induced by femtosecond light strings. *Phys. Rev.Lett.*, 87:213001–1—213001–4, 2001.

[58] J. E. Rothenberg. Pulse splitting during self-focusing in normally dispersive media. *Optics Lett.*, 17:583–586, 1992.

[59] A.C. Bernstein, T.S. Luk, T.R. Nelson, A. McPherson, J.-C. Diels, and S.M. Cameron. Asymmetric ultra-short pulse splitting measured in air using frog. *Applied Physics B (Lasers and Optics)*, B75(1):119 – 122, July 2002.

[60] A.C. Bernstein, T.R. Nelson, T.S. Luk, A. McPherson, S.M. Cameron, and J.-C. Diels. Time-resolved measurements of self-focusing pulses in air. *Optics Lett.*, 28:2354–2355, 2003.

[61] P. Rairoux, H. Schillinger, S. Niedermeier, M. Rodriguez, F. Ronneberger, R. Sauerbrey, B. Stein, D. Waite, C. Wedeking, H. Wille, L. Woeste, and C. Ziener. Remote sensing of the atmosphere using ultrashort laser pulses. *Appl. Phys. B*, 71:573–580, 2000.

[62] L. Woeste, S. Wedeking, J. Wille, P. Rairouis, B. Stein, S. Nikolov, C. Werner, S. Niedermeier, F. Ronneberger, H. Schillinger, and R. Sauerbrey. Femtosecond atmospheric lamp. *Laser und Optoelektronik*, 29:51–53, 1997.

[63] A. L. Gaeta. Catastrophic collapse of ultrashort pulses. *Phys. Rev. Lett.*, 84:3582–3585, 2000.

[64] N. Aközbek, M. Scalora, C.M. Bowden, and S.L. Chin. White-light continuum generation and filamentation during the propagation of ultra-short laser pulses in air. *Optics Comm.*, 191:353–362, 2001.

[65] J. Kasparian, R. Sauerbrey, D.. Mndelain, S. niedermeier, J. Yu, J. P. Wolf, Y.-B.André, M. Franco, B. Prade, S. Tzortzakis, A. Mysyrowicz, M. Rodriguez, H. Wille, and L. Wöste. Infrared extension of the supercontinuum generated by femtosecond terawatt laser pulses propagating in the atmosphere. *Opt. Lett.*, 25:1397–1399, 2000.

[66] J. Kasparian, M. Rodriguez, J. Méjean, J. Yu, E. Salmon, H. Wille, R. Bourayou, S. Frey, Y.-B.André, A. Mysyrowicz, R. Sauerbrey, J. P. Wolf, and L. Wöste. White-light filaments for atmospheric analysis. *Science*, 301:61–64, 2003.

[67] J. Yu, D. Mondelain, G. Ange, R. Volk, S. Niedermeier, J. P. Wolf, J. Kasparian, and R. Sauerbrey. Backward supercontinuum emission from a filament generated by ultrashort laser pulses in air. *Optics Lett.*, 26:533–535, 2001.

[68] Q. Luo, W. Liu, and S. L. Chin. Lasing action in air induced by ultra-fast laser filamentation. *Appl. Phys. B*, 76:337–340, 2003.

[69] Jean-Claude Diels, Ralph Bernstein, Karl Stahlkopf, and Xin Miao Zhao. Lightning control with lasers. *Scientific American*, 277:50–55, 1997.

[70] P. K. Rambo, J. Schwarz, and J. C. Diels. High voltage electrical discharges induced by an ultrashort pulse UV laser system. *Journal of Optics A*, 3:146–158, 2001.

[71] M. Rodriguez, R. Sauerbrey, H. Wille, L. Woeste, T. Fujii, Y. B. Andre, A. Mysyrowicz, L. Klingbeil, K. Rethmeier, and W. Kalkner; et al. Triggering and guiding megavolt discharges by use of laser-induced ionized filaments. *Optics Lett.*, 27:772–774, 2002.

[72] P. K. Rambo, J. Schwarz, and J. C. Diels. Interferometry with 2-dimensional spatial and high temporal resolution. *Opt. Comm*, 197:145–159, 2001.

[73] H. Schillinger and R. Sauerbrey. Electrical conductivity of long plasma channels in air generated by self-guided femtosecond laser pulses. *Applied Physics B*, 68:753–756, 1999.

[74] S. Tzortzakis, M. A. Franco, Y. B. André, A. Chiron, B. Lamouroux, B. S. Prade, and A. Mysyrowicz. Formation of a conducting channel in air by self-guided femtosecond laser pulses. *Phys. Rev. E*, 60:R3505–R3507, 1999.

[75] A. Couairon and L. Bergé. Light filaments in air for ultraviolet and infrared wavelengths. *Phys. Rev. Lett*, 88:13503–1—13503–4, 2002.

[76] L. V. Keldysh. Ionization in the field of a strong electromagnetic wave. *Soviet Physics JET*, 20(5):1307–1314, 1965.

[77] Scott Diddams, A. Van Engen, and T. S. Clement. Measurement of air dispersion by white light interferometry. In *CLEO*, Baltimore, MD, 1999. Optical Society of America.

[78] J.-C. Diels, Jason Jones, and Ladan Arissian. Applications to sensors of extreme sensitivity. In Jun Ye and Stephen Cundiff, editors, *Femtosecond Optical Frequency Comb: Principle, Operation and Applications*, chapter 12, pages 333–354. Springer, New York, NY, 2005.

[79] C. P. Hauri, W. Kornelis, F. W. Helbing, A. Heinrich, A. Couairon, A. Mysyrowicz, J. Biegert, and U. Keller. Generation of intense, carrier-envelope phase-locked few-cycle laser pulses through filamentation. *Applied Physics B*, 79:673–677, 2004.

[80] C. P. Hauri, A. Guandalini, P. Eckle, W. Kornelis, J. Biegert, and U. Keller. Generation of intense few-cycle laser pulses through filamentation – parameter dependence. *Optics Express*, 13:7541, 2005.

[81] A. Couairon, J. Biegert, C. P. Hauri, U. Keller, and A. Mysyrowicz. Self-generation of near-single-cycle pulses through filamentation. *Journal of Modern Optics*, 53:75–85, 2005.

[82] Scott Diddams, Briggs Atherton, and Jean-Claude Diels. Frequency locking and unlocking in a femtosecond ring laser with the application to intracavity phase measurements. *Applied Physics B*, 63:473–480, 1996.

[83] Matthew J. Bohn, Jean-Claude Diels, and R. K. Jain. Measuring intracavity phase changes using double pulses in a linear cavity. *Optics Lett.*, 22:642–644, 1997.

[84] Xianmei Meng, Raphael Quintero, and Jean-Claude Diels. Intracavity pumped optical parametric bidirectional ring laser as a differential interferometer. *Opt. Comm*, 233:167–172, 2004.

[85] E. J. Post. Sagnac effect. *Rev. Mod. Phys.*, 39:475–493, 1967.

[86] E. O. Schulz-Dubois. Alternative interpretation of rotation rate sensing by ring laser. *IEEE J. Quant. Electr.*, QE-2:299–305, 1966.

[87] J.-C. Diels and I. C. McMichael. Degenerate four-wave mixing of femtosecond pulses in an absorbing dye jet. *J. Opt. Soc. Am. B*, 3:535–543, 1986.

[88] Xianmei Meng, Jean-Claude Diels, Dietrich Kuehlke, Robert Batchko, and Robert Byer. Bidirectional, synchronously pumped, ring optical parametric oscillator. *Opt. Letters*, 26:265–267, 2001.

[89] Ming Lai, Jean-Claude Diels, and Michael Dennis. Nonreciprocal measurements in fs ring lasers. *Optics Letters*, 17:1535–1537, 1992.

[90] M. L. Dennis, J.-C. Diels, and M. Lai. The femtosecond ring dye laser: a potential new laser gyro. *Optics Letters*, 16:529–531, 1991.

[91] A. E. Siegman. *Lasers*. University Science Books, Mill Valley, CA., 1986.

[92] Rafael Quintero-Torres, Mark Ackerman, Martha Navarro, and Jean-Claude Diels. Scatterometer using a bidirectional ring laser. *Opt. Comm.*, 241:179–183, 2004.

[93] J. Reichert, R. Holzwarth, Th. Udem, and T. W. Hänsch. Measuring the frequency of light with mode-locked lasers. *Optics Comm.*, 172:59–68, 1999.

[94] H. R. Telle, G. Steinmeyer, A. E. Dunlop, S. Stenger, D. A. Sutter, and U. Keller. Carrier-envelope offset phase control: A novel concept for absolute optical frequency measurement and ultrashort pulse generation. *Appl. Phys. B*, 69:327, 1999.

[95] D. J. Jones, S. A. Diddams, J. K. Ranka, A. Stentz, R. S. Windeler, J. L. Hall, and S. T. Cundiff. Carrier-envelope phase control of femtosecond mode-locked lasers and direct optical frequency synthesis. *Science*, 288:635–639, 2000.

[96] J. K. Ranka, R. .S. Windeler, and A. J. Stentz. Visible continuum generation in air-silica microstructure optical fibers with anomalous dispersion at 800 nm. *Optics Lett.*, 25:25–27, 2000.

[97] T. A. Birks, W. J. Wadsworth, and P. S. Russel. Supercontinuum generation in tapered fibers. *Optics Lett.*, 25:1415–1417, 2000.

[98] T. Okuno, M. Nishi, and M. Nishimura. Silica-based functional fibers with enhanced nonlinearity and their applications. *IEEE J. Sel. Top. Quantum Electron.*, 5:1385–1391, 1999.

[99] N. Nishizawa and T. Goto. Widely broadened super continuum generation using highly nonlinear dispersion shifted fibers and femtosecond fiber laser. *Jpn. J. Appl. Phys.*, 40:L365–L367, 2001.

[100] J. W. Nicholson, M. F. Yan, P. Wisk, J. Fleming, F. DiMarcello, E. Monberg, A. Yablon, C. Jorgensen, and T. Veng. All-fiber, octave-spanning supercontinuum. *Optics Lett.*, 28:643–645, 2003.

[101] S. Coen, A. H. L. Chau, R. Leonhardt, J. D. Harvey, J. C. Knight, W. J. Wadsworth, and P. St. J. Russell. Supercontinuum generation by stimulated Raman scattering and parametric four-wave mixing in photonic crystal fibers. *J. Opt.Soc. Am. B*, 19:753–764, 2002.

[102] B. R. Washburn, S. E. Ralph, and R. S. Windeler. Ultrashort pulse propagation in air-silica microstructure fiber. *Optics Express*, 10:575–580, 2002.

[103] M. Bellini and T. W. Hänsch. Phase-locked white-light continuum pulses: towards a universal optical frequency-comb synthesizer. *Optics Lett.*, 25:1049–1051, 2000.

[104] J. W. Nicholson and M. F. Yan. Cross-coherence measurements of supercontinua generated in highly-nonlinear, dispersion shifted fiber at 1550 nm. *Optics Express*, 12:679–688, 2004.

[105] L. Tartara, I. Cristiani, and V. Degiorgio. Blue light and infrared continuum generation by soliton fission in a microstructured fiber. *Applied Physics B: Lasers and Optics*, 77:307–311, 2003.

[106] A. I.Ferguson and R. A. Taylor. Active mode stabilization of a synchronously pumped mode-locked dye laser. *Optics Comm.*, 41:271–276, 1982.

[107] E. Krüger. Frequency stabilization and control of a mode-locked dye laser. *Rev. Sci. Instrum.*, 66:4806–4812, 1995.

[108] Th. Udem, J. Reichert, R. Holzwarth, and T.W. Hänsch. Absolute optical frequency measurement of the cesium D_1 line with a mode-locked laser. *Phys. Rev. Lett.*, 82:3568–3571, 1999.

[109] Th. Udem, J. Reichert, R. Holzwarth, and T.W. Hänsch. Accurate measurement of large optical frequency differences with a mode-locked laser. *Opt. Lett.*, 24:881–883, 1999.

[110] J. Reichert, M. Neiring, R. Holzwarth, M. Weitz, Th.Udem, and T. W. Hänsch. Phase coherent vacuum-ultraviolet to radio frequency comparison with a mode-locked laser. *Phys. Rev. Lett.*, 84:3232–3235, 2000.

[111] H. Schnatz, J. Stenger, B. Lipphardt, N. Haverkamp, and C.-O. Weiss. Optical frequency measurement using frequency multiplication and frequency combs. In Jun Ye and Stephen Cundiff, editors, *Femtosecond Optical Frequency Comb: Principle, Operation and Applications*, pages 198–224. Springer, New York, NY, 2005.

[112] S. Diddams, J. Ye, and L. Hollberg. Femtosecond lasers for optical clocks and low noise frequency synthesis. In Jun Ye and Stephen Cundiff, editors, *Femtosecond Optical Frequency Comb: Principle, Operation and Applications*, pages 225–262. Springer, New York, NY, 2005.

[113] R. J. Jones, J. C. Diels, J. Jasapara, and W. Rudolph. Stabilization of the frequency, phase, and repetition rate of an ultra-short pulse train to a Fabry-Perot reference cavity. *Optics Comm.*, 175:409–418, 2000.

[114] K. H. Drever, J. L. Hall, F. V. Kowalski, J. Hough, G. M. Ford, A. J. Munley, and H. W. Ward. Laser phase and frequency stabilization using an optical resonator. *Appl. Phys.B*, 31:97–105, 1983.

[115] J. Ye. Absolute measurement of a long, arbitrary distance to less than an optical fringe. *Opt. Lett.*, 29:1153–1155, 2004.

Appendix A

Phase Shifts upon Transmission and Reflection

Most often, phase shifts at interfaces are a simple consequence of energy conservation. Conversely, the phase shift properties in simple devices can be used to determine the direction of the flow of energy. A few simple examples are given here.

A.1 The symmetrical interface

Let us consider first the very simple situation sketched in Fig. A.1. The interface can be a mirror with a reflecting coating on the front face and an antireflection coating on the back face. We are only interested in fields propagating *outside* the mirror. The energy conservation relation between the reflected (field reflection coefficient $\tilde{r}$) and transmitted (field transmission coefficient $\tilde{t}$) waves implies:

$$|\tilde{r}|^2 + |\tilde{t}|^2 = 1, \tag{A.1}$$

where we assumed a unity field amplitude incident from the left.
Taking next a field incident from the right, we have:

$$|\tilde{r'}|^2 + |\tilde{t'}|^2 = 1, \tag{A.2}$$

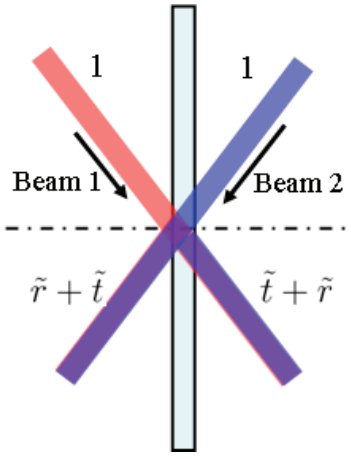

Figure A.1: Reflection and transmission by an interface between two identical media

Another relation can be found by summing the intensities on both sides of the symmetry line (dash-dotted line):

$$|\tilde{r}+\tilde{t}'|^2+|\tilde{r}'+\tilde{t}|^2=2. \tag{A.3}$$

Combination of Eqs. (A.1) and (A.3) leads to

$$2[\tilde{r}\tilde{t}'^*+\tilde{r}'^*\tilde{t}]=0, \tag{A.4}$$

which implies that the phase shifts upon transmission and reflection are complementary in the case of symmetric intefaces:

$$\varphi_r-\varphi_t=\frac{\pi}{2}. \tag{A.5}$$

It is because of the latter phase relation that the antiresonant ring reflects back all the incident radiation, and has zero losses if $|\tilde{r}|^2=|\tilde{t}|^2=0.5$. In the case of zero phase shift in transmission $\varphi_t=0$, Eq. (A.4) implies $r=-r'^*$, which corresponds to conservative coupling.

Note that Eq. (A.5) is not necessarily true if the structure is not symmetric, such as for a Fabry-Perot with different coatings on both sides. In the case, Eq. (A.4) has to be replaced by:

$$[\tilde{r}_1\tilde{t}_2^*+\tilde{r}_1^*\tilde{t}_2+\tilde{r}_2\tilde{t}_1^*+\tilde{r}_2^*\tilde{t}_1]=0, \tag{A.6}$$

where the indices 1 and 2 refer to the reflection/transmittion of beam 1 and 2, respectively. Equation (A.5) has then to be replaced by:

$$\cos(\varphi_{r1}-\varphi_{t2})+\cos(\varphi_{r2}-\varphi_{t1})=0. \tag{A.7}$$

A.2 Coated interface between two different dielectrics

Let us consider – as in Fig. A.2 – a partially reflecting coating at an interface between air (index 1) and a medium of index n. A light beam of amplitude $\mathcal{E}_1=1/\sqrt{\cos\theta_1}$ is incident from the air, at an angle of incidence θ_1. The transmitted beam is refracted at

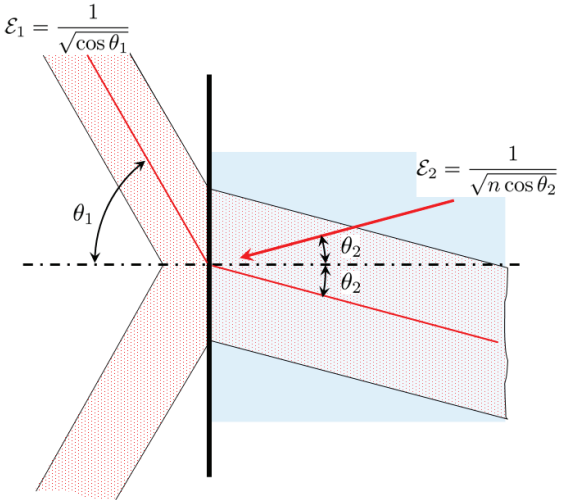

Figure A.2: Reflection and transmission by an interface between air and a dielectric.

the angle θ_2, and has an amplitude $\tilde{t}_1/\sqrt{cos\theta_1}$. The reflected beam has an amplitude $\tilde{r}_1/\sqrt{cos\theta_1}$. We take the vertical (orthogonal to the figure) dimension of the beam to be unity, as well as the distance covered by the beam on the interface in the plane of the figure. To calculate energy conservation, we compare the products $n_i|\tilde{\mathcal{E}}|^2A$ where $n_i = 1$ left of the interface, $n_i = n$ right of the interface, and $A = 1 \times \cos\theta$. As in the previous section, we will be considering a similar beam incident from the right, with an amplitude $\mathcal{E}_2 = 1/\sqrt{n\cos\theta_2}$ incident at an angle θ_2 on the dielectric/air interface. The choice of these incident electric field amplitudes is such that the same "energy" products $n_i|\tilde{\mathcal{E}}|^2A = A$ apply on both sides of the interface, above the dash-dotted line in Fig. A.2.

Energy conservation leads to the relation:

$$|\tilde{r}_1|^2 + |\tilde{t}_1|^2 \frac{n\cos\theta_2}{\cos\theta_1} = 1, \tag{A.8}$$

where we took into account the change in beam cross section upon refraction. We have a similar energy conservation equation for a beam of amplitude $\mathcal{E}_2 = 1/\sqrt{n\cos\theta_2}$ incident at an angle θ_2 on the dielectric/air interface:

$$|\tilde{r}_2|^2 + |\tilde{t}_2|^2 \frac{\cos\theta_1}{n\cos\theta_2} = 1. \tag{A.9}$$

From Eqs. (A.8) and (A.9) we get directly the relation:

$$|t_1|^2 \cdot |t_2|^2 = T_1T_2 = (1-|r_1|^2)(1-|r_2|^2) = (1-R_1)(1-R_2) \tag{A.10}$$

which is a trivial energy conservation equation. The amplitude of the reflection coefficient is equal on both sides of the interface. Since $|\tilde{r}_1|^2 = |\tilde{r}_2|^2$, Eqs (A.8) and (A.9) lead to:

$$\boxed{|t_1|\sqrt{\frac{n\cos\theta_2}{\cos\theta_1}} = |t_2|\sqrt{\frac{\cos\theta_1}{n\cos\theta_2}}.} \tag{A.11}$$

The amplitudes of the transmission coefficients are not equal, but in the ratio $|t_2|/|t_1| = n\cos\theta_2/\cos\theta_1$, a relation that satisfies Fresnel equations, and results simply from energy conservation.

In order to find a relation between the phase shift upon transmission and reflection, we consider the energy conservation for light incident from the upper half of the figure (the axis of symmetry being the dashed normal to the interface):

$$1+1=\cos\theta_1\left|\frac{\tilde{r}_1}{\sqrt{\cos\theta_1}}+\frac{\tilde{t}_2}{\sqrt{n\cos\theta_2}}\right|^2 + n\cos\theta_2\left|\frac{\tilde{r}_2}{\sqrt{n\cos\theta_2}}+\frac{\tilde{t}_1}{\sqrt{\cos\theta_1}}\right|^2. \tag{A.12}$$

Expanding:

$$2=|r_1|^2+|r_2|^2+|t_2|^2\frac{\cos\theta_1}{n\cos\theta_2}+|t_1|^2\frac{n\cos\theta_2}{\cos\theta_2} +(\tilde{r}_1\tilde{t}_2^*+\tilde{r}_1^*\tilde{t}_2)\sqrt{\frac{\cos\theta_1}{n\cos\theta_2}}+(\tilde{r}_2\tilde{t}_1^*+\tilde{r}_2^*\tilde{t}_1)\sqrt{\frac{n\cos\theta_2}{\cos\theta_1}} \tag{A.13}$$

Taking into account the energy conservation relations (A.8) and (A.9), leads to:

$$\boxed{(\tilde{r}_1\tilde{t}_2^*+\tilde{r}_1^*\tilde{t}_2)\cos\theta_1+(\tilde{r}_2\tilde{t}_1^*+\tilde{r}_2^*\tilde{t}_1)n\cos\theta_2=0.} \tag{A.14}$$

We can re-write Eq. (A.14)

$$2|r_1||t_2|\{\cos(\varphi_{r,1}-\varphi_{t,2})\}\cos\theta_1=-2|r_2||t_1|\{\cos(\varphi_{r,2}-\varphi_{t,1})\}n\cos\theta_2. \tag{A.15}$$

Equation A.14 leads also to the following trigonometric relations between phase shifts upon transmission and reflection:

$$\frac{\cos(\varphi_{r,1}-\varphi_{t,2})}{\cos(\varphi_{r,2}-\varphi_{t,1})}=-1, \tag{A.16}$$

which leads to the relation between phase angles:

$$\varphi_{t,2}-\varphi_{r,1}=\varphi_{r,2}-\varphi_{t,1}+(2n+1)\pi. \tag{A.17}$$

or

$$\varphi_{t,1}+\varphi_{t,2}=\varphi_{r,1}+\varphi_{r,2}+(2n+1)\pi. \tag{A.18}$$

The relations for normal incidence, where $|\tilde{r}_1|=|\tilde{r}_2|$ and $n_1|\tilde{t}_2|=n_2|\tilde{t}_1$, are:

$$n_1(\tilde{r}_1\tilde{t}_2^*+\tilde{r}_1^*\tilde{t}_2)+(\tilde{r}_2\tilde{t}_1^*+\tilde{r}_2^*\tilde{t}_1)n_2=0.$$
$$\varphi_{t,1}+\varphi_{t,2}=\varphi_{r,1}+\varphi_{r,2}+(2n+1)\pi.$$

A.3 Matrix method

A.3.1 The "S" matrix

Coatings play an important role in femtosecond optics, by shaping pulses through the amplitude and phase of their reflection coefficient. Matrix methods have been developed to predict all properties of a coating. A coated optical surface can be modeled as a stack of simple thin interfaces separated by propagation in a dielectric. The transmission and reflection of a right propagating field are the result from the interference from all of the layers. To calculate these resultant fields, the right moving and left moving waves must be recorded at each interface. At each simple thin layer interface, the incoming fields (from each direction) are split according to a scattering matrix S defined as:

$$\begin{bmatrix} E_2 \\ E_1' \end{bmatrix} = \begin{bmatrix} t_{12} & r_{21} \\ r_{12} & t_{21} \end{bmatrix} \begin{bmatrix} E_1 \\ E_2' \end{bmatrix}. \tag{A.19}$$

the electric field subscripts $(1,2)$ describe whether the field is on the left or right side of the interface, while the no prime and prime discern whether the field is right-propagating or left-propagating, respectively. The coefficients syntax is such that t_{12} and r_{12} describe the transmission and reflection coefficient of the wave starting on side 1 while t_{21} and r_{21} describe the coefficients of a field incoming from side 2.. The S matrix is a 2×2 matrix connecting an input column matrices (incident fields) to an output one (transmitted and reflected fields). The first line of each is a right moving field, and the second one a left moving field. The 2×2 S matrix connects the input fields to the "output" fields

A.3.2 The "M" matrix

The elements of the S matrix have real physical significance; they are the field reflection and transmission amplitudes of a layer. Unfortunately, the S matrix is not useful for building up multilayer surfaces as these matrices cannot be cascaded. What is needed is a matrix defining each layer that can be multiplied by the matrices corresponding to the other layers to create an effective total matrix for the whole structure. Instead of equations defining the relationship between incoming and outgoing fields at each layer, the equations need to define the relationship between the fields on the left and the right side of the layer (regardless of whether they are incoming or outgoing). In other words, in order to cascade the matrix layers, the matrix equation needs to move through the surface spatially (left to right) instead of causally (incoming to outgoing). Such a matrix is defined as the wave-transfer, M, matrix. The column matrices it connects are bound to a surface, with

as first line is a right moving field, and as second line a left moving field. The relationship between the M and S matrices is,

$$M = \begin{bmatrix} A & B \\ C & D \end{bmatrix} = \frac{1}{t_{21}} \begin{bmatrix} t_{12}t_{21} - r_{12}r_{21} & r_{21} \\ -r_{12} & 1 \end{bmatrix} \tag{A.20}$$

$$S = \begin{bmatrix} t_{12} & r_{21} \\ r_{12} & t_{21} \end{bmatrix} = \frac{1}{D} \begin{bmatrix} AD - BC & B \\ -C & 1 \end{bmatrix}. \tag{A.21}$$

A.3.3 Calculating the multilayer transmission and reflection

In order to use the cascaded matrix method, each layer is defined using its physical S matrix. Each S is converted into an M matrix, which are then multiplied together to give an effective total M_T matrix for the entire surface. This ultimate M_T matrix is converted back into a total S_T matrix to extract the effective physical parameters of the multilayer interface. Where the total effective scattering matrix, S_T, has elements that represent,

$$S_T = \begin{bmatrix} \mathcal{T} & \mathcal{R}' \\ \mathcal{R} & \mathcal{T}' \end{bmatrix}, \tag{A.22}$$

where $\mathcal{T}$ and $\mathcal{R}$ are the transmission and reflection coefficients for a beam incoming to the front surface, and $\mathcal{T}'$, $\mathcal{R}'$ are the similar coefficients for a beam incoming to the back surface.

The matrices involved in the calculations of a coating are given in Table A.1.

Type	Free Propagation	Interface
S	$\begin{pmatrix} e^{-inkd} & 0 \\ 0 & e^{-inkd} \end{pmatrix}$	$\frac{1}{n_1+n_2}\begin{pmatrix} 2n_1 & n_2-n_1 \\ n_1-n_2 & 2n_2 \end{pmatrix}$
M	$\begin{pmatrix} e^{-inkd} & 0 \\ 0 & e^{inkd} \end{pmatrix}$	$\frac{1}{2n_2}\begin{pmatrix} n_1+n_2 & n_2-n_1 \\ n_2-n_1 & n_1+n_2 \end{pmatrix}$

Table A.1: Multilayer matrices. The second column displays the propagation matrices through a niform dielectric of index n and thickness d. The third column show matrices for an interface between two media of index n_1 and n_2.

It can be verified that energy conservation and the phase relations derived in this appendix are automatically satisfied by applying the matrix procedure. The matrix calculation can also be applied to the Fabry-Perot to derive Eqs. (2.34) and (2.35).

.

.

Appendix B

The Uncertainty Principle

This demonstration of the uncertainty principle presented here is an example of application of various Fourier transform properties. We will give here a simple derivation of the uncertainty relation (1.65) that we wrote between the conjugated variables time t and frequency Ω. This uncertainty relation and its derivation also apply in all generality between any pair of conjugated variables, for instance between the transverse beam dimension x and the corresponding wave vector k. To derive the uncertainty relation (1.65), we will use a family of functions defined by the relation:

$$g(t) = tf(t) + \mu \frac{d}{dt} f(t) \tag{B.1}$$

where t and μ are real variables. The total "energy" associated with that distribution is proportional to:

$$\begin{aligned} \int_{-\infty}^{\infty} |g(t)|^2 \, dt &= \int t^2 |f|^2 \, dt + \mu \int \left[tf \frac{df^*}{dt} + tf^* \frac{df}{dt} \right] dt + \mu^2 \int \left| \frac{df}{dt} \right|^2 dt \\ &\geq 0. \end{aligned} \tag{B.2}$$

While the first term of the inequality defines the second order moment $\langle t^2 \rangle$:

$$\int t^2 |f(t)|^2 dt = \langle t^2 \rangle \int |f(t)|^2 dt. \tag{B.3}$$

we can apply Parseval's theorem to the last term to obtain:

$$\begin{aligned} \int_{-\infty}^{\infty} \left| \frac{df}{dt} \right|^2 dt &= \frac{1}{2\pi} \int \left| \mathcal{F}\left(\frac{df}{dt} \right) \right|^2 d\Omega \\ &= \frac{1}{2\pi} \int \Omega^2 |f(\Omega)|^2 d\Omega = \langle \Omega^2 \rangle \int |f(t)|^2 \, dt. \end{aligned} \tag{B.4}$$

If the function $|f|$ has finite boundaries so that $\lim_{t\to\pm\infty}\left(t|f|^2\right) = 0$, as is true for the modulus of the electric field of a laser pulse for example, one can write:

$$\int_{-\infty}^{\infty}\frac{d}{dt}\left[tf(t)f^*(t)\right]dt = \int_{-\infty}^{\infty}|f(t)|^2\,dt + \int_{-\infty}^{\infty}tf^*(t)\frac{df}{dt}dt + \int_{-\infty}^{\infty}tf(t)\frac{df^*}{dt}dt = 0. \tag{B.5}$$

Substituting the terms of Eqs. (B.4), (B.3) and (B.5) into the inequality (B.2) leads, after division by $\int_{-\infty}^{\infty}|f(t)|^2\,dt$, to:

$$\langle\Omega^2\rangle\mu^2 - \mu + \langle t^2\rangle \geq 0. \tag{B.6}$$

The left-hand side of the inequality is a quadratic polynomial in μ. Since $\langle\Omega^2\rangle > 0$, the polynomial is non-negative if the ordinate of the vertex of the parabola is ≥ 0. This is the case if

$$1 - 4\langle t^2\rangle\langle\Omega^2\rangle \leq 0, \tag{B.7}$$

which is equivalent to the uncertainty relation (1.65).

Appendix C

Prism pair dispersion

In order to compensate the angular dispersion, the two prisms are put in opposition, in such a way that, to any face of one prism corresponds a parallel face of the other prism (Fig. 2.25).

We consider in this section a prism sequence that controls GVD, but avoids the beam divergence and energy front tilt introduced by angular dispersion.

The optical path $\overline{ABB'A'D}$ at a frequency Ω is represented by the solid line in Fig. 2.25, while the path for a ray upshifted by $d\Omega$ is represented by the dashed line. The successive angles of incidence/refraction are θ_0 and θ_1 at point A), θ_2 and θ_3 at point B, θ_4 and θ_5 at point B', and finally θ_6 and θ_7 at point A'. The two prisms are identical, with equal apex angle α and with pairs of faces oriented parallel as shown in Fig. 2.25. At any wavelength or frequency Ω:

- $\theta_3 = \theta_4$
- $\theta_2 = \theta_5$
- $\theta_1 = \theta_6$
- $\theta_0 = \theta_7$
- $\theta_1 + \theta_2 = \alpha$
- $d\theta_1/d\Omega = -d\theta_2/d\Omega$.

If the prisms are used at minimum deviation at the central wavelength, $\theta_0 = \theta_3 = \theta_4 = \theta_7$. If, in addition to being used at minimum deviation, the prisms are cut for Brewster incidence, the apex angles of both prisms are $\alpha = \pi - 2\theta_0 = \pi - 2\arctan(n)$.

The challenge is to find the frequency dependence of the optical path $\overline{ABB'A'D}$. The initial (geometrical) conditions are defined by

- The distance $a = \overline{OA}$ from the point of impact of the beam to the apex O of the first prisms. For convenience, we will use in the calculations the distance $\overline{OH} = h = \overline{OA}\cos\alpha = a\cos\alpha$,
- the separation s between the parallel faces of the prisms,
- the distance t between the apex O and O', measured along the exit face of the first prism, cf. Fig. 2.25.

The changes in path length due to dispersion can be understood from a glance at the figure, comparing the optical paths at Ω (solid line) and $\Omega + d\Omega$ (dashed line). The contributions that increase the path length are:

1. positive dispersion because of propagation through the prism material of positive dispersion ($\overline{AB}$ and $\overline{B'A'}$)
2. positive dispersion because of the increased path length $\overline{BB'}$ in air (increment $\overline{SB'''}$ in Fig. C.2)
3. positive dispersion because of the increased path length $\overline{A'D}$ in air (projection of $\overline{A'A'''}$ along the beam propagation direction).

The contributions that decrease the path length (negative dispersion) of the frequency upshifted beam can best be understood with Fig. C.1 and Fig. C.2. Fig C.1 shows the configurations of the beams if the two prisms were brought together, i.e. $\overline{BB'} = 0$. Fig. C.2 shows an expanded view of the second prism. The negative dispersion contributions emanate from:

1. The shortened path length in glass because of the angular dispersion ($\overline{AA''}$ versus $\overline{AA'}$ in Fig. C.1),
2. the shorter path length in the second prism due to the deflection of the beam by the first one (path difference $\overline{B''T}$ in Fig. C.2).

Path through glass The total path in glass is $L_g = \overline{AB} + \overline{B'A'}$ where $\overline{AB} = a\sin\alpha/\cos\theta_2$ and $\overline{B'A'} = \overline{O'B'}\sin\alpha/\cos(\alpha-\theta_2) = \overline{O'B'}\sin\alpha/\cos\theta_1$, with:

$$\overline{O'B'} = t - s\tan\theta_3 - a(\cos\alpha + \sin\alpha\tan\theta_2). \tag{C.1}$$

We thus have for the total transmitted path in glass:

$$\begin{aligned} L_g = \overline{AB} + \overline{B'A'} &= \frac{a\sin\alpha}{\cos\theta_2} + [t - s\tan\theta_3 - a(\cos\alpha + \sin\alpha\tan\theta_2)]\,\frac{\sin\alpha}{\cos\theta_1} \\ &= (t - s\tan\theta_3)\,\frac{\sin\alpha}{\cos\theta_1}. \end{aligned} \tag{C.2}$$

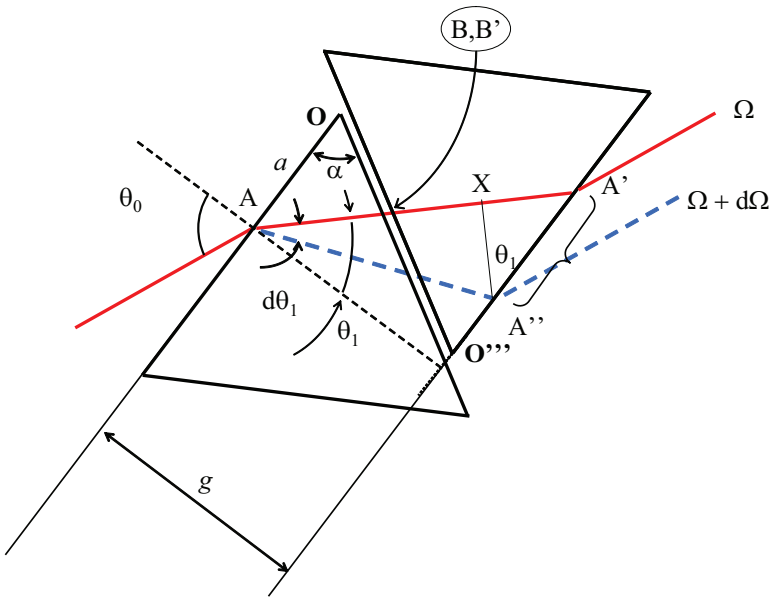

Figure C.1: Beam passage through the two prisms, when the distance $\overline{BB'}$ (in Fig. 2.25) has been reduced to zero. The distance between the apexes O and O' has been reduced to $\overline{OO'''} = t - \overline{BB'}\sin\theta_3$ (referring to Fig. 2.25). The distance between parallel faces is then $g = \overline{OO'''}\sin\alpha = (t - \overline{BB'}\sin\theta_3)\sin\alpha$.

As expected, the total path through glass is independent of the starting position defined by a. If the two prisms are brought together as in Fig. C.1, they act as a slab of glass with parallel faces, of thickness $g = L_g\cos\theta_1$. There are three contributions to the optical path change from Fig. C.1: one due to the change in index, a second due to the change in angle, and a third because the path length L_g is frequency dependent. Taking the derivative of $\Omega n L_g/c$ with L_g defined by Eq. (C.2):

$$\begin{aligned}\frac{d(kL_g)}{d\Omega} &= \frac{d}{d\Omega}\left(\frac{n\Omega L_g}{c}\right)\\ &= \frac{L_g}{c}\left(n+\Omega\frac{dn}{d\Omega}\right)+\left(\frac{n\Omega L_g}{c}\tan\theta_1\right)\frac{d\theta_1}{d\Omega}\\ &\quad -\left(\frac{n\Omega s}{c\cos^2\theta_3}\right)\frac{\sin\alpha}{\cos\theta_1}\frac{d\theta_3}{d\Omega}\end{aligned} \tag{C.3}$$

The first term can be attributed solely to material dispersion. The next term is the change in length in glass due to the angular dispersion $d\theta_1/d\Omega$, and the last expresses the reduction in path length in the second prism due to the propagation of the angularly dispersed beam in air. The expression above only partly accounts for

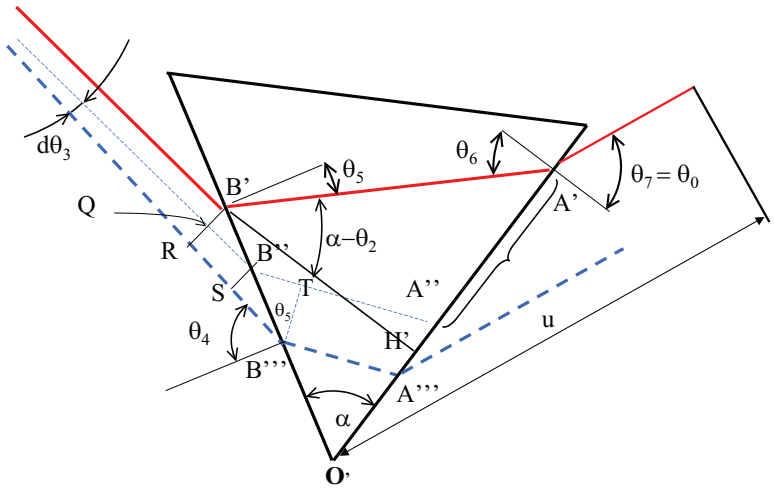

Figure C.2: Details of the beam passage through the second prism.

the energy tilt associated with the angular dispersion $d\theta_3/d\Omega$. Another contribution arises from the path through air to a reference plane.

Path through air between and after the prisms We have here to account for the contributions of the pathlengths $\overline{BB'}$ and $\overline{A'D}$ to the group delay:

$$\frac{d}{d\Omega}\left(\frac{\Omega}{c}\overline{BB'}\right) = \frac{\Omega}{c}\frac{d\overline{BB'}}{d\Omega} + \frac{\overline{BB'}}{c}. \tag{C.4}$$

For the path $\overline{BB'} = s/\cos\theta_3$, there is only a change in length equal to $\overline{S\,B'''}$, which can be obtained by either differentiating $s/\cos\theta_3$, or simply from geometrical considerations using Fig. 2.25 ($\overline{S\,B'''} = \overline{S\,B''}\tan\theta_3 = \overline{BB'}\tan\theta_3 d\theta_3$):

$$\frac{d\overline{BB'}}{d\Omega} = \frac{s}{\cos\theta_3}\tan\theta_3\frac{d\theta_3}{d\Omega}. \tag{C.5}$$

The path in air after the second prism can be expressed as:

$$\overline{A'D} = u - \overline{O'A'}\sin\theta_0. \tag{C.6}$$

Because u is not a function of Ω, the contribution to the group delay is:

$$\frac{1}{c}\frac{d\left(\Omega\overline{A'D}\right)}{d\Omega} = -\frac{\sin\theta_0}{c}\frac{d}{d\Omega}(\Omega\overline{O'A'}). \tag{C.7}$$

For $\overline{O'A'}$ we find:

$$\begin{aligned}\overline{O'A'} &= \overline{O'H'} + \overline{H'A'} = \overline{O'B'}\,[\cos\alpha + \sin\alpha\tan(\alpha-\theta_2)] \\ &= [t - s\tan\theta_3 - a(\cos\alpha + \sin\alpha\tan\theta_2)]\,[\cos\alpha + \sin\alpha\tan(\alpha-\theta_2)] \\ &= \left[t - s\tan\theta_3 - a\frac{\cos\theta_1}{\cos\theta_2}\right][\cos\alpha + \sin\alpha\tan(\alpha-\theta_2)] \\ &= [t - s\tan\theta_3]\,[\cos\alpha + \sin\alpha\tan\theta_1] - a, \end{aligned} \tag{C.8}$$

where we have used $\cos\alpha + \sin\alpha\tan\theta_2 = \cos(\alpha-\theta_2)\cos\theta_2$. The contribution of $\overline{A'D}$ to the group delay is:

$$\begin{aligned}-\frac{\sin\theta_0}{c}\frac{d(\Omega\overline{O'A'})}{d\Omega} &= \frac{\overline{O'A'}\sin\theta_0}{c} - \frac{\Omega s\sin\theta_0}{c\cos^2\theta_3}\,[\cos\alpha + \sin\alpha\tan\theta_1]\,\frac{d\theta_3}{d\Omega} \\ &\quad + \frac{\Omega\sin\theta_0}{c}\,[t - s\tan\theta_3]\,\frac{\sin\alpha}{\cos^2\theta_1}\,\frac{d\theta_1}{d\Omega} \\ &= -\frac{\overline{A'D}}{c} - \frac{n\Omega s}{c\cos^2\theta_3}\left[\cos\alpha\sin\theta_1 + \sin\alpha\frac{\sin^2\theta_1}{\cos\theta_1}\right]\frac{d\theta_3}{d\Omega} \\ &\quad + \frac{n\Omega}{c}\,[t - s\tan\theta_3]\,\frac{\sin\alpha\sin\theta_1}{\cos^2\theta_1}\,\frac{d\theta_1}{d\Omega}. \end{aligned} \tag{C.9}$$

In the last equation we used the fact that u is an arbitrary constant, for example zero, so that $\overline{A'D} = -\overline{O'A'}\sin\theta_0$.

Total path in glass and air After adding all contributions to the total phase

$$\Psi = \frac{\Omega}{c}\left(nL_g + \overline{BB'} + \overline{A'D}\right),$$

we obtain for the group delay using Eqs. (C.3),(C.4) and (C.5), and (C.7) and (C.9):

$$\begin{aligned}
\frac{d\Psi}{d\Omega} &= \frac{d}{d\Omega}\left(\frac{\Omega n L_g}{c}\right) + \frac{d}{d\Omega}\left(\frac{\Omega\overline{BB'}}{c}\right) + \frac{d}{d\Omega}\left(\frac{\Omega\overline{A'D}}{c}\right) \\
&= \frac{nL_g}{c} + \frac{(\overline{BB'}+\overline{A'D})}{c} + \frac{L_g\Omega}{c}\frac{dn}{d\Omega} + \frac{n\Omega L_g}{c}\tan\theta_1\frac{d\theta_1}{d\Omega} \\
&\quad + \left\{-\frac{n\Omega s}{c\cos^2\theta_3}\frac{\sin\alpha}{\cos\theta_1} + \frac{\Omega s}{c\cos\theta_3}\tan\theta_3 + \frac{n\Omega s}{c\cos^2\theta_3}\left[\cos\alpha\sin\theta_1\right.\right. \\
&\quad \left.\left. + \frac{\sin\alpha\sin^2\theta_1}{\cos\theta_1}\right]\right\}\frac{d\theta_3}{d\Omega} - \frac{n\Omega}{c}\left[t - s\tan\theta_3\right]\frac{\sin\alpha\sin\theta_1}{\cos^2\theta_1}\frac{d\theta_1}{d\Omega} \\
&= \frac{OPL(ABB'A'D)}{c} + \frac{L_g\Omega}{c}\frac{dn}{d\Omega} \\
&\quad + \left(\frac{\Omega s}{c\cos^2\theta_3}\right)\left(-n\sin\alpha\cos\theta_1 + \cos\theta_3\tan\theta_3 + n\cos\alpha\sin\theta_1\right)\frac{d\theta_3}{d\Omega},
\end{aligned} \tag{C.10}$$

where we have defined the optical path length $OPL(ABB'A'D) = nL_g + (\overline{BB'}+\overline{A'D})$. The factor preceding $d\theta_3/d\Omega$ cancels, since:

$$\begin{aligned}
\cos\alpha\sin\theta_1 - \sin\alpha\cos\theta_1 + \frac{\sin\theta_3}{n} & \\
&= \cos(\theta_1+\theta_2)\sin\theta_1 - \sin(\theta_1+\theta_2)\cos\theta_1 + \sin\theta_2 \\
&= 0.
\end{aligned}$$

The complete expression for the group delay through the pair of prism reduces to:

$$\boxed{\frac{d\Psi}{d\Omega} = \frac{OPL(ABB'A'D)}{c} + \frac{L_g\Omega}{c}\frac{dn}{d\Omega}} \tag{C.11}$$

The first terms in the last equation represents the travel delay at the phase velocity:

$$\frac{OPL(ABB'A'D)}{c} = \frac{L_g n}{c} + \frac{s}{c\cos\theta_3} + \frac{\overline{A'D}}{c} \tag{C.12}$$

The second part of Eq. (C.11) is the carrier to envelope delay caused by the pair of prisms[1]:

$$\tau_{CE}(\Omega) = \frac{\Omega}{c}\frac{d}{d\Omega}OPL(ABB'A'D) = \frac{L_g\Omega}{c}\frac{dn}{d\Omega}. \tag{C.13}$$

[1] We are assuming that the prisms are in vacuum, i.e. the contribution to the dispersion from air is neglected.

The second derivative of the phase, obtained by taking the derivative of Eq. (C.11), is:

$$\left.\frac{d^2\Psi}{d\Omega^2}\right|_{\omega_\ell} = L_g\left[2\left.\frac{dn}{d\Omega}\right|_{\omega_\ell} + \omega_\ell \left.\frac{d^2n}{d\Omega^2}\right|_{\omega_\ell}\right] - \frac{\omega_\ell}{c\cos\theta_1}\left.\frac{dn}{d\Omega}\right|_{\omega_\ell}\frac{s\sin\alpha}{\cos^2\theta_3}\left.\frac{d\theta_3}{d\Omega}\right|_{\omega_\ell} + \frac{\omega_\ell}{c}\left.\frac{dn}{d\Omega}\right|_{\omega_\ell}\left(L_g\tan\theta_1\left.\frac{d\theta_1}{d\Omega}\right|_{\omega_\ell}\right). \tag{C.14}$$

The derivatives with respect to Ω are related. By differentiating Snell's law for the first interface:

$$d\theta_1 = -\frac{\tan\theta_1}{n}dn = -d\theta_2. \tag{C.15}$$

For the second interface, taking the previous relation into account, we find:

$$\begin{aligned}\cos\theta_3 d\theta_3 &= n\cos\theta_2 d\theta_2 + \sin\theta_2 dn = n\cos\theta_2\left(\frac{\tan\theta_1}{n} + \sin\theta_2\right)dn \\ &= (\cos\theta_2\tan\theta_1 + \sin\theta_2)\,dn = \frac{\sin\alpha}{\cos\theta_1}dn,\end{aligned} \tag{C.16}$$

or:

$$d\theta_3 = \frac{\sin\alpha}{\cos\theta_1\cos\theta_3}dn. \tag{C.17}$$

Therefore, the second order dispersion Eq. (C.14) reduces to an easily interpretable form:

$$\boxed{\left.\frac{d^2\Psi}{d\Omega^2}\right|_{\omega_\ell} = \frac{L_g}{c}\left[2\left.\frac{dn}{d\Omega}\right|_{\omega_\ell} + \omega_\ell\left.\frac{d^2n}{d\Omega^2}\right|_{\omega_\ell}\right] - \frac{\omega_\ell}{c}\left(\frac{s}{\cos\theta_3}\right)\left(\left.\frac{d\theta_3}{d\Omega}\right|_{\omega_\ell}\right)^2 - \frac{n\omega_\ell}{c}L_g\left(\left.\frac{d\theta_1}{d\Omega}\right|_{\omega_\ell}\right)^2} \tag{C.18}$$

Appendix D

The role of space-time variables in the quantum nonlinear Schrödinger equation

D.1 The retarded frame of reference

As we have seen in Chapter 1, any phenomena that propagates with relatively little distortion around a fixed velocity v_g is most conveniently studied in a moving frame of reference. This is the case for a soliton, or more generally an envelope function $\tilde{\mathcal{E}}(z,t)$ that evolves in the laboratory frame according to an equation of the form:

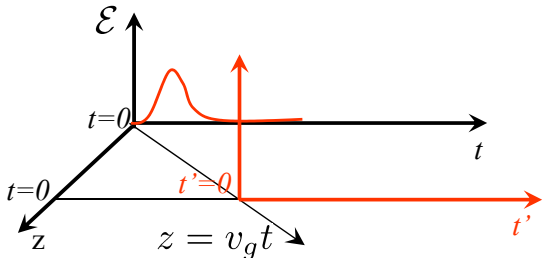

Figure D.1: Standard moving coordinates.

$$\frac{\partial\tilde{\mathcal{E}}}{\partial z} + \frac{1}{v_g}\frac{\partial\tilde{\mathcal{E}}}{\partial t} = f(t,z). \tag{D.1}$$

The traditional transformation to study the function $f(t,z)$ in the moving frame of reference is:

$$\begin{aligned} z' &= z \\ t' &= t - \frac{z}{v}, \end{aligned} \tag{D.2}$$

which transforms Eq (D.1) into:

$$\frac{\partial \tilde{\mathcal{E}}}{\partial z} = f(t,z). \tag{D.3}$$

In the case of the soliton, this means following its distortion in a frame moving at v_g as sketched in Fig. D.1.

D.2 The running space coordinate

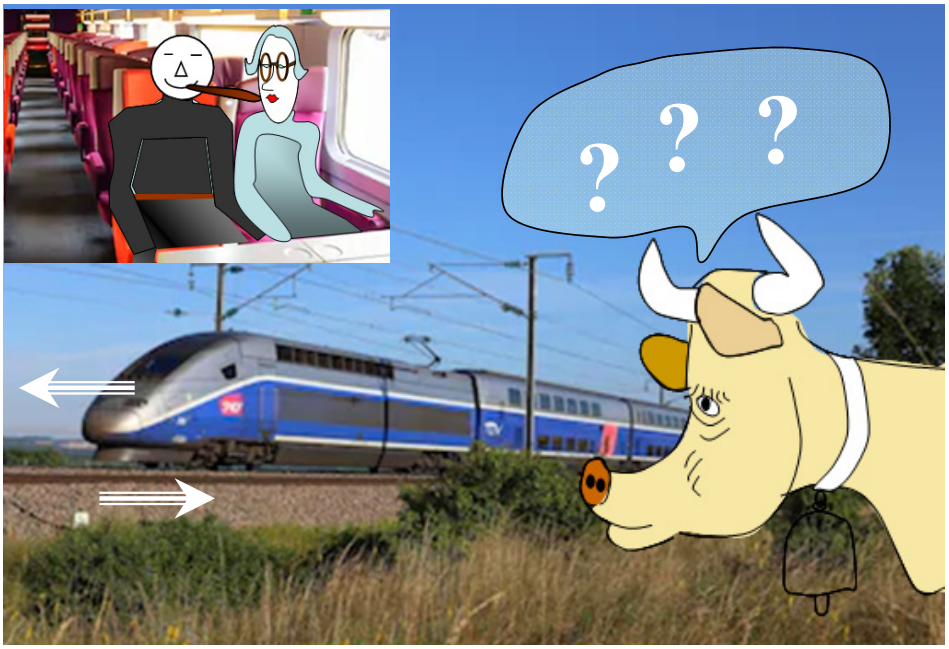

Figure D.2: CEO's in the moving TGV, cow in the laboratory frame pondering on the meaning of the running space coordinates.

The cow-watching-the-train is in the laboratory frame. In order to follow the moves of the CEO's in the TGV, she should hop in the TGV to be in the moving frame. Sadly, this moving frame is scorned by the quantum physicist, because if leads to Eq. (5.159) which does not look like the standard Schrödinger equation. Therefore, a "running space coordinate" transformation is generally:

$$\begin{aligned} z' &= z - v_g t \\ t' &= t \end{aligned} \tag{D.4}$$

which transforms Eq. (D.1) into:

$$\frac{1}{v}\frac{\partial\tilde{\mathcal{E}}}{\partial t'} = f(t', z'). \tag{D.5}$$

With this transformation, space and time have been flipped in Eq. (5.159), and the quantum physicist is happy since he basic Eq. (D.1) takes the form of a Schrödinger equation

$$i\hbar\frac{\partial\tilde{\mathcal{E}}}{\partial t} = iv_g\hbar f(t,z) = H\tilde{\mathcal{E}}$$

The cow-watching-the-TGV-is-not (Fig D.2). She must be ruminating on the physical meaning of the "running space coordinate". Does it mean that the rails are moving opposite to the train velocity so that the TGV is at standstill?

Appendix E

Complement to the chapter "semi-quantum"

E.1 Link between commutator and uncertainty relation

Let us consider two operators $\hat{Q}$ and $\hat{P}$ that do not commute, such that:

$$[\hat{Q}, \hat{P}] = i. \tag{E.1}$$

Consider the linear combination:

$$|\varphi\rangle = (\hat{Q} + i\lambda\hat{P})|\psi\rangle \tag{E.2}$$

where λ is a real number. For all value of λ, the square of the norm $\langle\varphi\rangle$ should be positive:

$$\begin{aligned}\langle\psi\rangle &= \langle\psi|(\hat{Q}^* - i\lambda\hat{P}^*)(\hat{Q} + i\lambda\hat{P})|\psi\rangle \\ &= \langle\psi|\hat{Q}^2|\rangle + \langle\psi|i\lambda\hat{Q}\hat{P} - i\lambda\hat{P}\hat{Q}|\psi\rangle + \langle\psi|\lambda^2\hat{P}^2|\rangle \\ &= \langle\psi|\hat{Q}^2|\rangle - i\lambda\langle[\hat{Q}, \hat{P}]\rangle + \lambda^2\langle\hat{P}^2\rangle \\ &= \langle\psi|\hat{Q}^2|\rangle - \lambda + \lambda^2\langle\hat{P}^2\rangle \geq 0.\end{aligned} \tag{E.3}$$

In order for this parabola (in λ) not to have intersection with the abscissa, we should have:

$$1 - 4\langle\hat{P}^2\rangle\langle\hat{Q}^2|\rangle \leq 0, \tag{E.4}$$

which implies the uncertainty relation:

$$\langle\hat{P}^2\rangle\langle\hat{Q}^2\rangle \geq \frac{1}{4}. \tag{E.5}$$

E.2 If $[\hat{X}_1, \hat{X}_2] = i$, Then $[\hat{N}, \hat{\varphi}] = i$

As shown in the previous section, the commutator $[\hat{X}_1, \hat{X}_2] = i$ between the quadrature components implies the uncertainty relation $\langle \Delta X_1^2 \rangle \langle \Delta X_2^2 \rangle \geq \frac{1}{4}$. It is shown here that this commutation relation implies the same commutation relation (hence the uncertainty relation) between amplitude (number N) and phase ($\varphi = \arctan(X_2/X_1)$. We have the two commutation relations:

$$\begin{aligned}
[\hat{X_1}^2, \arctan\left(\frac{\hat{X}_2}{\hat{X}_1}\right)] &= \hat{X_1}[\hat{X_1}, \arctan\left(\frac{\hat{X}_2}{\hat{X}_1}\right)] + [\hat{X_1}, \arctan\left(\frac{\hat{X}_2}{\hat{X}_1}\right)]\hat{X_1} \\
[\hat{X_2}^2, \arctan\left(\frac{\hat{X}_2}{\hat{X}_1}\right)] &= \hat{X_2}[\hat{X_2}, \arctan\left(\frac{\hat{X}_2}{\hat{X}_1}\right)] + [\hat{X_2}, \arctan\left(\frac{\hat{X}_2}{\hat{X}_1}\right)]\hat{X_2}
\end{aligned} \tag{E.6}$$

We use the property that, for any arbitrary function f:

$$\begin{aligned}
[\hat{X}_1, f(\hat{X}_2)] &= \sum_{n=0}^{\infty} \frac{f^{(n)} n!}{[} \hat{X}_1, \hat{X}_2^n] = i \sum_{n=0}^{\infty} \frac{f^{(n)} n!}{n} \hat{X}_2^{(n-1)} = i f'(\hat{X}_2) \\
&= \sum_{n=0}^{\infty} \frac{f^{(n)} n!}{[} \hat{X}_2, \hat{X}_1^n] = -i \sum_{n=0}^{\infty} \frac{f^{(n)} n!}{n} \hat{X}_1^{(n-1)} = i f'(\hat{X}_1)
\end{aligned} \tag{E.7}$$

Applying this property to Eqs. (E.6):

$$\begin{aligned}
[\hat{X_1}^2, \arctan\left(\frac{\hat{X}_2}{\hat{X}_1}\right)] &= \frac{2i{X_1}^2}{{X_1}^2 + {X_2}^2} \\
[\hat{X_2}^2, \arctan\left(\frac{\hat{X}_2}{\hat{X}_1}\right)] &= \frac{2i{X_2}^2}{{X_1}^2 + {X_2}^2}
\end{aligned} \tag{E.8}$$

Since the number operator $\hat{N} = \hat{X_1}^2 + \hat{X_2}^2$,

$$[\hat{N}, \varphi] = \frac{1}{2}[\hat{X_1}^2 + \hat{X_2}^2, \arctan\left(\frac{\hat{X}_2}{\hat{X}_1}\right)] = i, \tag{E.9}$$

which implies that $\langle \Delta N^2 \rangle \langle \Delta \varphi^2 \rangle \geq \frac{1}{4}$.

E.3 Link between commutator and uncertainty relation

We have seen that the main term in the number operator at the output of the Michelson in Eq. (5.88) is the interference term involving $(\hat{A}^\dagger \hat{B} - \hat{B}^\dagger \hat{A})$. The uncertainty is the expectation value of the square of the interference operator. We have assumed

in the derivation of Eq. (5.88) that $\hat{A}$ refers to a coherent field [$\hat{A}|\alpha\rangle = \alpha|\alpha\rangle$], with phase aligned with the X_1 axis.

$$\langle(\hat{A}^\dagger\hat{B} - \hat{B}^\dagger\hat{A})^2\rangle = \alpha^{*2}\langle\hat{B}^2\rangle + \alpha^2\langle\hat{B}^{\dagger 2}\rangle - \langle\hat{A}^\dagger\hat{A}\hat{B}\hat{B}^\dagger\rangle - \langle\hat{B}^\dagger\hat{B}\hat{A}\hat{A}^\dagger\rangle. \tag{E.10}$$

Because of the commutation relation $[\hat{A}\hat{A}^\dagger] = 1$, he last term can be replaced by $\langle(\hat{A}^\dagger\hat{A} + 1)\hat{B}\hat{B}^\dagger\rangle$. Substituting:

$$\begin{aligned}\langle(\hat{A}^\dagger\hat{B} - \hat{B}^\dagger\hat{A})^2\rangle &= \alpha^{*2}\langle\hat{B}^2\rangle + \alpha^2\langle\hat{B}^{\dagger 2}\rangle - \langle\hat{A}^\dagger\hat{A}\hat{B}\hat{B}^\dagger\rangle - \langle\hat{B}^\dagger\hat{B}\left(\langle\hat{A}^\dagger\hat{A}\rangle + 1\right)\\ &= \alpha^{*2}\langle\hat{B}^2\rangle + \alpha^2\langle\hat{B}^{\dagger 2}\rangle - \langle\hat{A}^\dagger\hat{A}\left(\hat{B}\hat{B}^\dagger + \hat{B}^\dagger\hat{B}\right)\rangle - \langle\hat{B}\hat{B}^\dagger\rangle.\end{aligned}$$

The following relations:

$$\begin{aligned}&\alpha^{*2}\langle\hat{B}^2\rangle \approx 0\\ &\alpha^2\langle\hat{B}^{\dagger 2}\rangle \approx 0\\ &\left(\hat{B} - \hat{B}^\dagger\right)^2 = \hat{B}^2 + \hat{B}^{\dagger 2} - \left(\hat{B}\hat{B}^\dagger + \hat{B}^\dagger\hat{B}\right) \approx -\left(\hat{B}\hat{B}^\dagger + \hat{B}^\dagger\hat{B}\right)\end{aligned}$$

lead to:

$$\begin{aligned}\langle(\hat{A}^\dagger\hat{B} - \hat{B}^\dagger\hat{A})^2\rangle &= \langle\hat{A}^\dagger\hat{A}\rangle\langle(\hat{B} - \hat{B}^\dagger)^2\rangle - \langle\hat{B}^\dagger\hat{B}\rangle\\ &= 4\langle\hat{N}\rangle\langle\Delta\hat{B}_2^2\rangle - \langle\hat{N}_b\rangle,\end{aligned} \tag{E.11}$$

where we introduced the number operators $\hat{N} = \hat{A}^\dagger\hat{A}$ and $\hat{N}_b = \hat{B}^\dagger\hat{B}$. the term $\langle\left(\hat{B} - \hat{B}^\dagger\right)^2\rangle$ represents the mean square deviation of the vacuum fluctuations

Appendix F

Slowly Evolving Wave Approximation

The derivation here essentially follows [1]. We start with the wave equation in the frequency domain for a scalar electric field propagating in the z direction, including a nonlinear polarization and the diffraction term

$$\left[\frac{\partial^2}{\partial z^2} + \nabla_\perp^2 + \tilde{k}^2(\Omega)\right] E(x,y,z,\Omega) = \mu_0 \mathcal{F}\left\{\frac{\partial^2}{\partial t^2} P^{NL}(t,x,y,z)\right\} \tag{F.1}$$

where $\nabla_\perp^2 = \frac{\partial^2}{\partial x^2} + \frac{\partial^2}{\partial x^2}$. Note that the effect of the linear polarization is included in $\tilde{k}^2(\Omega) = \Omega^2 \epsilon(\Omega)\mu_0 = \Omega^2 n^2/c^2$. We start with the following ansatz for the electric field and the nonlinear polarization:

$$E(\Omega) = \frac{1}{2}\tilde{\mathcal{E}}(\Omega - \omega_\ell, x, y, z) e^{-ik_\ell z} + c.c. \tag{F.2}$$

$$P(t) = \frac{1}{2}\tilde{\mathcal{P}}(t,x,y,z) e^{-i(\omega_\ell t - k_\ell z)} + c.c. \tag{F.3}$$

and neglect processes leading to backscattering, that is, coupling of opposite propagation directions. This ansatz inserted in Eq. (F.1) yields

$$\left[\left(\frac{\partial}{\partial z} - ik_\ell\right)^2 + \nabla_\perp^2 + \tilde{k}^2(\Omega)\right] \tilde{\mathcal{E}}(\Omega - \omega_\ell) = \mu_0 \mathcal{F}\left\{e^{i\omega_\ell t}\left(\frac{\partial}{\partial t} - i\omega_\ell\right)^2 \tilde{\mathcal{P}}(t)\right\}. \tag{F.4}$$

We now expand the complex $\tilde{k}(\Omega) = k + i\alpha/2$ into a Taylor series about ω_ℓ

$$\tilde{k}(\Omega) = k_\ell + i\frac{\alpha_0}{2} + k_1(\Omega - \omega_\ell) + \tilde{D}(\Omega), \tag{F.5}$$

where

$$\tilde{D}(\Omega) = i\frac{\alpha_1}{2}(\Omega-\omega_\ell) + \sum_{m=2}^{\infty}\frac{k_m + i\alpha_m/2}{m!}(\Omega-\omega_\ell)^m \tag{F.6}$$

with

$$k_m = \left.\frac{\partial^m}{\partial\Omega^m}\mathrm{Re}(\tilde{k})\right|_{\omega_\ell} \tag{F.7}$$

$$\alpha_m = \left.\frac{\partial^m}{\partial\Omega^m}\mathrm{Im}(\tilde{k})\right|_{\omega_\ell}. \tag{F.8}$$

The quantities α_m are related to linear loss coefficients for the field intensity. The next step is to insert Eq. (F.6) into Eq. (F.4) and inverse Fourier transform the resulting expression into the time domain. For this step we use the fact that an expression of the kind $(\Omega-\omega_\ell)^m A(\Omega-\omega_\ell)$ transforms into $\left(-i\frac{\partial}{\partial t}\right)^m A(t)$ where $A(t) = \mathcal{F}^{-1}\{A(\Omega-\omega_\ell)\}$. The resulting wave equation now reads

$$\left\{\left(\frac{\partial}{\partial z} - ik_\ell\right)^2 + \nabla_\perp^2 + \left[k_\ell - ik_1\frac{\partial}{\partial t} + i\frac{\alpha_0}{2} + \hat{D}(t)\right]^2\right\}\tilde{\mathcal{E}}(t) = \mu_0\left(\frac{\partial}{\partial t} - i\omega_\ell\right)^2\tilde{\mathcal{P}}(t), \tag{F.9}$$

where

$$\hat{D}(t) = \frac{\alpha_1}{2}\frac{\partial}{\partial t} + \sum_{m=2}^{\infty}\frac{k_m + i\alpha_m/2}{m!}\left(-i\frac{\partial}{\partial t}\right)^m. \tag{F.10}$$

The terms in Eq. (F.9) can be re-grouped, factoring out the operator $(1-\frac{i}{\omega_\ell}\frac{\partial}{\partial t})$. To this end, the third term in Eq. (F.9) can be written as:

$$\begin{aligned}
&\left[k_\ell - ik_1\frac{\partial}{\partial t} + i\frac{\alpha_0}{2} + \hat{D}(t)\right]^2 \\
&\quad= k_\ell^2 - 2ik_\ell k_1\frac{\partial}{\partial t} + 2ik_\ell\left(1 - i\frac{k_1}{k_\ell}\frac{\partial}{\partial t}\right)\left(\frac{\alpha_0}{2} - i\hat{D}\right) \\
&\qquad + i\alpha_0\hat{D} - k_1^2\frac{\partial}{\partial t} - \frac{\alpha_0^2}{4} + \hat{D}^2 \\
&\quad= k_\ell^2 - 2ik_\ell k_1\frac{\partial}{\partial t} + 2ik_\ell\left(1 - \frac{i}{\omega_\ell}\frac{\partial}{\partial t}\right)\left(\frac{\alpha_0}{2} - i\hat{D}\right) \\
&\qquad + 2ik_\ell\left(\frac{i}{\omega_\ell}\right)\left(1 - \frac{c}{nv_g}\right)\frac{\partial}{\partial t}\left(\frac{\alpha_0}{2} - i\hat{D}\right) + i\alpha_0\hat{D} - k_1^2\frac{\partial}{\partial t} - \frac{\alpha_0^2}{4} + \hat{D}^2.
\end{aligned} \tag{F.11}$$

We use a retarded frame of reference, i.e. the transformation $\xi = z$ and $\eta = t - z/v_g$. We note that the first squared expression in Eq. (F.9) is:

$$\begin{aligned}\left(\partial\xi - \frac{1}{v_g}\partial\eta - ik_\ell\right)^2 &= -2ik_\ell\left(1 - \frac{i}{k_\ell v_g}\partial_\eta\right)\partial_\xi - k_\ell^2 + 2ik_\ell\frac{1}{v_g}\partial_\eta \\ &= -2ik_\ell\left(1 - \frac{i}{\omega_\ell}\partial_\eta\right)\partial_\xi - k_\ell^2 + 2ik_\ell\frac{1}{v_g}\partial_\eta \\ &\quad + 2\left(\frac{n}{c} - \frac{1}{v_g}\right)\partial_\xi\partial_\eta. \end{aligned} \tag{F.12}$$

Substituting Eq. (F.11) and Eq. (F.12) into Eq. (F.10) yields:

$$\begin{aligned}&\left(1 - \frac{i}{\omega_\ell}\frac{\partial}{\partial\eta}\right)\left[\left(\frac{\partial}{\partial\xi} - \frac{\alpha_0}{2} + i\hat{D}\right)\tilde{\mathcal{E}} + i\frac{\omega_\ell c\mu_0}{2n_0}\left(1 - \frac{i}{\omega_\ell}\frac{\partial}{\partial\eta}\right)\tilde{\mathcal{P}}\right] - \frac{1}{2ik_\ell}\nabla_\perp^2\tilde{\mathcal{E}} \\ &= \left(1 - \frac{c}{nv_g}\right)\frac{i}{\omega_\ell}\frac{\partial}{\partial\eta}\left(\frac{\partial}{\partial\xi} - \frac{\alpha_0}{2} + i\hat{D}\right)\tilde{\mathcal{E}} - \frac{1}{2ik_\ell}\left(\frac{\partial^2}{\partial\xi^2} + \hat{D}^2 - \frac{\alpha_0^2}{4} + i\alpha_0\hat{D}\right)\tilde{\mathcal{E}}. \end{aligned} \tag{F.13}$$

So far the propagation equation is still exact and no approximations have been made. The terms on the right hand side are small compared to those on the left hand side and can be neglected if the conditions

$$|(\partial/\partial z)\tilde{\mathcal{E}}| << k_\ell|\tilde{\mathcal{E}}| \tag{F.14}$$

and

$$\left|1 - \frac{v_p}{v_g}\right| << 1 \tag{F.15}$$

are satisfied. Equation (F.13) reduces then to:

$$\left[\frac{\partial}{\partial z} + \frac{i}{2k_\ell}\left(1 - \frac{i}{\omega_\ell}\frac{\partial}{\partial t}\right)^{-1}\nabla_\perp^2 - \frac{\alpha_0}{2} + i\hat{D}\right]\tilde{\mathcal{E}} = -i\frac{\omega_\ell c\mu_0}{2n_0}\left(1 - \frac{i}{\omega_0}\frac{\partial}{\partial t}\right)\tilde{\mathcal{P}}^{(NL)}, \tag{F.16}$$

One should exercise caution in the application of Eq. (F.16) up to an arbitrary order in the expansion of $\hat{D}$. Depending on the particular pulse duration, the higher order terms in the expansion of $\hat{D}$ on the right hand side of Eq. (F.13) may not be negligible as compared to the highest order term of the left hand side of that expression.

In general, when a nonlinear polarization is involved, there will not be just one propagation equation, but as many as the number of waves that participate in the nonlinear optical process. For instance, a third order polarization excited by a field

at frequency ω_ℓ will create a polarization at $3\omega_\ell = \omega_\ell + \omega_\ell + \omega_\ell$, and a polarization at $\omega_\ell = \omega_\ell - \omega_\ell + \omega_\ell$. The first process is generation of a third harmonic field, and the second is either two-photon absorption or a nonlinear index of refraction, depending on the phase of the nonlinear susceptibility. The generated field at $3\omega_\ell$ will propagate, and interfere with the field at $3\omega_\ell$ produced at a different location by the fundamental. The third harmonic field may also lead to the generation of other frequencies, through the third order process. For instance, there will be regeneration of the fundamental frequency through the third order process $\omega_\ell = 3\omega_\ell - \omega_\ell - \omega_\ell$, and the latter field will also interfere with the propagated fundamental. The third harmonic may also create a 9^{th} harmonic through the nonlinear susceptibility. At a minimum, there will be at least two differential equations, with a third order susceptibility, corresponding to the fundamental and third harmonic fields. More equations have to be added if more frequencies are generated.

$$\left(\frac{\partial}{\partial z}\tilde{\mathcal{E}} - \frac{i}{2}k_\ell''\frac{\partial^2}{\partial t^2}\tilde{\mathcal{E}} + \mathcal{D}\right)e^{i(\omega_\ell t - k_\ell z)} + c.c. = i\frac{\mu_0}{k_\ell}\frac{\partial^2}{\partial t^2}P^{NL}. \tag{F.17}$$

The polarization appearing in the right hand side can be instantaneous, or be the solution of a differential equation as in the case of most interactions with resonant atomic or molecular systems. If we represent the polarization as a product of a slowly varying envelope $\tilde{\mathcal{P}}$ and a term oscillating with an optical frequency ω_p, $e^{i\omega_p t}$, the right-hand side of Eq. (F.17) can be written as

$$\frac{\partial^2}{\partial t^2}\left(\tilde{\mathcal{P}}e^{i\omega_p t} + c.c.\right) = \left(\frac{\partial^2}{\partial t^2}\tilde{\mathcal{P}} + 2i\omega_p\frac{\partial}{\partial t}\tilde{\mathcal{P}} - \omega_p^2\tilde{\mathcal{P}}\right)e^{i\omega_p t} + c.c.. \tag{F.18}$$

Bibliography

[1] T. Brabec and F. Krausz. Nonlinear optical pulse propagation in the single-cycle regime. *Phys. Rev. Lett.*, 78:3282–3284, 1997.

Index